SPACE SCIENCES SERIES OF ISSI

# Remote Sensing and Water Resources

A. Cazenave · N. Champollion · J. Benveniste
J. Chen *Editors*

Springer

INTERNATIONAL SPACE SCIENCE INSTITUTE

**Space Sciences Series of ISSI**

Volume 55

More information about this series at http://www.springer.com/series/6592

A. Cazenave · N. Champollion
J. Benveniste · J. Chen
Editors

# Remote Sensing and Water Resources

Previously published in *Surveys in Geophysics*, Volume 37, Issue 2, 2016

Springer

*Editors*
A. Cazenave
International Space Science Institute
Bern
Switzerland

and

LEGOS-CNES
Toulouse
France

N. Champollion
International Space Science Institute
Bern
Switzerland

J. Benveniste
European Space Agency
European Space Research Institute
Frascati
Italy

J. Chen
Center for Space Research
University of Texas at Austin
Austin, TX
USA

ISSN 1385-7525
Space Sciences Series of ISSI
ISBN 978-3-319-32448-7 ISBN 978-3-319-32449-4 (eBook)
DOI 10.1007/978-3-319-32449-4

Library of Congress Control Number: 2016935393



*Cover illustration*: Lake Balkhash, Kazakhstan. Image of the lake was taken by the NASA Space Shuttle Discovery on Mission STS039 in April 1991 (*Source* NASA). Image amended by A. Fisher, ISSI, Bern, Switzerland.

Printed on acid-free paper

This Springer imprint is published by Springer Nature
The registered company is Springer International Publishing AG Switzerland

# Contents

DOI 10.1007/978-3-319-32449-4_1
Reprinted from *Surveys in Geophysics* Journal, DOI 10.1007/s10712-016-9356-4

# Foreword: International Space Science Institute (ISSI) Workshop on Remote Sensing and Water Resources

**A. Cazenave[1,2] · N. Champollion[2] · J. Benveniste[3] · J. Chen[4]**

Received: 3 January 2016 / Accepted: 4 January 2016 / Published online: 22 January 2016


About 97 % of the total amount of water on Earth is found in the oceans and 2 % is stored in the Greenland and Antarctic ice sheets. It is only the remaining 1 % that is the amount of water available for the biospheric processes and for all human needs. This fresh water component is stored in both surface and subsurface reservoirs. On the surface, the storage volumes consist of rivers, lakes, man-made reservoirs, wetlands and inundated areas. Subsurface reservoirs include root zones (the uppermost few metres of the soil), as well as confined and unconfined aquifers and other geological formations. Except for the deep aquifers that evolve on thousand-year timescales, terrestrial waters are continuously exchanged with the atmosphere and oceans through vertical and horizontal mass fluxes (i.e. precipitation, evaporation, transpiration of the vegetation and surface and underground runoff). These exchanges as well as the associated storage of water in the different components of the climate system characterize the global water cycle.

On land, changes in the global water storage result from climate variations, from direct human interventions in the water cycle and from human modifications of the physical characteristics of the land surface. Climate variations (which are due to both natural and

✉ A. Cazenave
anny.cazenave@issibern.ch; anny.cazenave@legos.obs-mip.fr

N. Champollion
champollion@issibern.ch

J. Benveniste
Jerome.benveniste@esa.int

J. Chen
chen@csr.utexas.edu

[1] LEGOS, CNES, 18 Avenue Edouard Belin, 31401 Toulouse Cedex 9, France

[2] ISSI, Hallerstrasse 6, 3012 Bern, Switzerland

[3] ESA-ESRIN, Via Galileo Galilei, 0044 Frascati, Italy

[4] CSR, University of Texas at Austin, Austin, TX, USA

anthropogenic causes) produce changes in the land water balance, leading to either an increase or a decrease in water storage. For example, cold and wet climatic conditions have the tendency to increase water storage, while a warm and dry climate has the opposite effect. Many human activities directly affect land water storage; examples are groundwater pumping in aquifers, the construction of dams on rivers to form artificial man-made reservoirs and irrigation for improved agricultural production. Anthropogenic changes in land surfaces such as urbanization, agriculture and deforestation also lead to water storage changes.

Being an integral part of the climate system, terrestrial waters have important links to, and feedbacks with and from, the atmosphere and oceans via energy and moisture fluxes. Gaining a better understanding of the global hydrological cycle, in particular its terrestrial component, is thus a key issue in climate research today. It is also of significant importance for creating an inventory of water resources and for managing them.

In the last two to three decades, global estimates of the spatio-temporal changes in land water storage (surface, soil and underground waters, as well as snow packs) have relied on hydrological models, either coupled with atmosphere–ocean global circulation models or forced by meteorological observations. However, hydrological phenomena are so complex that it is very difficult to represent the hydrological system in such a simple way. What is needed is the acquisition of a huge amount of observations and their assimilation into complex models.

In situ gauging networks have been installed for several decades in many lakes and river basins. However, they are distributed non-uniformly throughout the world, and they often suffer from intermittent operation. In situ measurements provide time series of water levels and discharge rates, which are used for studies of regional climate variability, as well as for socio-economic applications (e.g., water resources inventory, navigation, land use, planning infrastructures, hydroelectric energy, flood hazards) and environmental studies (rivers, lakes, wetlands and floodplains hydroecology). However, for more than two decades, ground-based gauge networks have declined in many regions (Alsdorf and Lettenmaier 2003), because of economic pressures or for political reasons. For example, over 20 % of the freshwater discharge to the Arctic Ocean is ungauged; surface water across much of Africa and portions of the Arctic is either not measured at all or has experienced the loss of over two-thirds of the gauges (Shiklomanov et al. 2002). The physical removal of gauges from many lakes and river basins is, unfortunately, a common situation in many parts of the world. Besides, the distribution of collected data is often restricted, because water-related data are often considered to be sensitive national information. Therefore, to accurately measure, monitor and forecast global supplies of fresh water using in situ methods is almost impossible because of the lack of access to an adequate amount of in situ measurements worldwide.

For the past 10–15 years, remote sensing techniques have demonstrated their excellent capability to monitor several components of the water balance of large rivers, lakes and reservoirs, on timescales ranging from months to decades (e.g., Alsdorf and Lettenmaier 2003; Alsdorf et al. 2007; Famiglietti et al. 2015). For example, radar and laser satellite altimetry are routinely used for systematic monitoring of the water levels of large rivers, lakes, reservoirs and floodplains. If combined with satellite imagery, satellite altimeter observations also enable the variations of surface water volumes to be estimated. Passive and active microwave sensors offer important information on soil moisture (e.g., the SMOS mission) as well as on wetlands and snowpacks. Space gravity missions (in particular the GRACE mission) directly measure the spatio-temporal variations of vertically integrated terrestrial water storage. When combined with hydrological model estimates or

other observations of surface waters and soil moisture made from space (e.g., from satellite altimetry and SMOS), satellite gravity data can be used to study groundwater storage variations. Synthetic Aperture Radar Interferometry (InSAR) can be also used to estimate river flow.

In the very near future, the Surface Water Ocean Topography (SWOT) mission will provide frequently updated two-dimensional maps of surface water levels and river discharges, with global coverage and with unprecedented resolution ($\sim$100 m globally on land). All these observations, as well as those planned in the near future (e.g., the European Sentinel missions), will become increasingly important in improving our understanding of hydrological processes at work in large river basins and their links with climate variability and socio-economic activities. Significant new information can be expected by combining models and surface observations with space observations, which offer global geographical coverage, good spatio-temporal sampling, continuously repeated monitoring and the capability of measuring water mass changes occurring at or below the Earth's surface.

The scientific papers presented in this volume represent the outcome of a workshop on 'Remote Sensing and Water Resources' held in October 2014, in Bern, Switzerland, as part of the International Space Science Institute (ISSI) Earth Observation Programme. The objective of the workshop was to bring together leading scientists involved in the global water cycle, land hydrology and water resources research, either processing observations or running hydrological models or combining both. Two main issues were addressed during the workshop: (1) promoting the synergistic use of space observations for monitoring water storage changes in river basins worldwide, and (2) using the space data in hydrological models either by data assimilation or as external constraints. Participants in the workshop were experts in different disciplines, including remote sensing, hydrological modelling, meteorology, geophysics and climate science.

The first two articles address hydrological modelling, at the global scale ('Modelling fresh water resources at the global scale; challenges and prospects' by Döll et al.) and at the regional scale in a river basin that has been highly modified by human activities ('Hydrological modelling in highly anthropized river basins; example from the Garonne Basin' by Martin et al.). The paper by Zhang et al. 'On creating global gridded terrestrial water budget estimates from satellite remote sensing' investigates the reliability of global remote sensing products in closing estimates of the global water budget.

Three papers deal with the use of satellite altimetry and other remote sensing techniques to study surface waters. The paper by Crétaux et al. is an overview of lake monitoring from space. Biancamaria et al. demonstrate the high potential of the future SWOT mission to study surface waters with a precision, spatial resolution and temporal sampling that was previously unavailable. The issue of monitoring wetlands is addressed by Prigent et al. in an overview article entitled 'Towards high resolution monitoring of continental surface water extent and dynamics at global scale; from GIEMS (Global Inundation Extent from Multi-Satellites) to SWOT'.

The next three papers deal with the GRACE-based space gravimetry technique and its capability to measure total terrestrial water storage, accessing groundwater storage by removing model-predicted surface water storage change. The paper by Humphrey et al. 'Assessing global water storage variability from GRACE: trends, seasonal cycle, intra-annual anomalies and extremes' focuses on short-term water storage anomalies, as well as on extreme events such as droughts. The recovery of estimates of groundwater depletion in aquifers from GRACE measurements is discussed by Chen et al. in a paper entitled 'Groundwater storage changes: present status from GRACE observations'. The paper by Wada et al. 'Modelling global groundwater depletion: present state and future prospects'

evaluates the recent advances which modelling approaches bring to enable groundwater depletion to be estimated at a global scale.

The capability of future space gravity missions with new on-board interferometric laser systems to improve both the precision and resolution of water storage measurements is evaluated in Flechtner et al. 'What can we expect from the GRACE-FO Laser ranging interferometer for Earth sciences applications?'. The next paper by Lopez et al. 'Subsurface hydrology in the Lake Chad Basin from space-based and hydrogeological data' investigates how space radiometry combined with hydrogeological data and modelling can provide constraints on groundwater circulation in semi-arid regions. Finally, an overview of the significant issue of the provision for human beings of 'Water and Food in the 21st century' is given by de Marsily and Abarca Del Rio.

This Special Issue includes the majority of the lectures presented at the workshop, in some instances grouped into a single article in order to reflect a broader view of the subject. This volume focuses on terrestrial waters and, as such, complements the book published as the outcome of a previous ISSI workshop which was mostly devoted to the atmospheric water cycle (Bengtsson et al. 2014).

Clearly, studying the global water cycle is a very complex problem as many Earth processes are at play, and we recognize that several other volumes would be necessary to fully cover the ongoing research in this domain. However, we hope that the present issue will contribute to

1. fostering the interests of the science community around future spaceborne missions,
2. supporting the exploitation of past, present and future invaluable spaceborne measurements, and
3. gathering multidisciplinary teams working together on satellite observations, in situ data, modelling and data assimilation techniques.

We thank ISSI and the European Space Agency for providing an inspiring framework which made such a fruitful workshop possible.

## References

Alsdorf DE, Lettenmaier DP (2003) Tracking fresh water from space. Science 301:1492–1494

Alsdorf D, Fu LL, Mognard N, Cazenave A, Rodriguez E, Chelton D, Lettemaier D (2007) Measuring global oceans and terrestrial fresh water from space. EOS Trans AGU 88(24):253

Bengtsson L, Bonnet R-M, Calisto M, Destouni G, Gurney R, Johannessen J, Kerr Y, Lahoz WA, Rast M (eds) (2014) The Earth's hydrological cycle. Space sciences series of ISSI vol 46. ISBN 978-94-017-8788-8

Famiglietti J, Cazenave A, Eicker A, Reager JT, Rodell M, Velicogna I (2015) Satellites provide the 'big picture' for global hydrology. Science 349(6249):684–685

Shiklomanov AI et al (2002) Widespread decline in hydrological monitoring threatens Pan-Arctic research. EOS Trans AGU 83:13–16

DOI 10.1007/978-3-319-32449-4_2
Reprinted from *Surveys in Geophysics* Journal, DOI 10.1007/s10712-015-9343-1

# Modelling Freshwater Resources at the Global Scale: Challenges and Prospects

**Petra Döll[1] · Hervé Douville[2] · Andreas Güntner[3] · Hannes Müller Schmied[1] · Yoshihide Wada[4,5,6]**

Received: 12 March 2015 / Accepted: 26 September 2015 / Published online: 12 October 2015


**Abstract** Quantification of spatially and temporally resolved water flows and water storage variations for all land areas of the globe is required to assess water resources, water scarcity and flood hazards, and to understand the Earth system. This quantification is done with the help of global hydrological models (GHMs). What are the challenges and prospects in the development and application of GHMs? Seven important challenges are presented. (1) Data scarcity makes quantification of human water use difficult even though significant progress has been achieved in the last decade. (2) Uncertainty of meteorological input data strongly affects model outputs. (3) The reaction of vegetation to changing climate and $CO_2$ concentrations is uncertain and not taken into account in most GHMs that serve to estimate climate change impacts. (4) Reasons for discrepant responses of GHMs to changing climate have yet to be identified. (5) More accurate estimates of monthly time

✉ Petra Döll
p.doell@em.uni-frankfurt.de

Hervé Douville
herve.douville@meteo.fr

Andreas Güntner
guentner@gfz-potsdam.de

Yoshihide Wada
y.wada@uu.nl

[1] Institute of Physical Geography, Goethe University Frankfurt, 60629 Frankfurt, Germany

[2] Centre National de Recherches Météorologiques, Météo-France, 42 av. Coriolis, 31057 Toulouse, France

[3] Helmholtz Centre Potsdam, German Research Centre for Geosciences, Telegrafenberg, 14473 Potsdam, Germany

[4] Center for Climate Systems Research, Columbia University, 2880 Broadway, New York, NY 10025, USA

[5] NASA Goddard Institute for Space Studies, 2880 Broadway, New York, NY 10025, USA

[6] Department of Physical Geography, Faculty of Geosciences, Utrecht University, Heidelberglaan 2, 3584 CS Utrecht, The Netherlands

series of water availability and use are needed to provide good indicators of water scarcity. (6) Integration of gradient-based groundwater modelling into GHMs is necessary for a better simulation of groundwater–surface water interactions and capillary rise. (7) Detection and attribution of human interference with freshwater systems by using GHMs are constrained by data of insufficient quality but also GHM uncertainty itself. Regarding prospects for progress, we propose to decrease the uncertainty of GHM output by making better use of in situ and remotely sensed observations of output variables such as river discharge or total water storage variations by multi-criteria validation, calibration or data assimilation. Finally, we present an initiative that works towards the vision of hyperresolution global hydrological modelling where GHM outputs would be provided at a 1-km resolution with reasonable accuracy.

**Keywords** Global hydrological model · Climate data · Water abstraction · Model uncertainty · Calibration · Remote sensing data

## 1 Introduction

Water flows as well as water storage at and below the land surface of the Earth affect water availability for humans and ecosystems, result in hazards such as floods and affect atmospheric processes, sea level and global biogeochemical cycles. They have been increasingly altered by human actions including emissions of greenhouse gases, land use, water abstractions and the construction of dams and dykes (e.g., Vörösmarty and Sahagian 2000; Sterling et al. 2013). Ecosystems suffer from these alterations and, in many regions, human development is constrained by water scarcity. Freshwater systems including their natural and human components need to be characterized regarding both water quantity and quality to support a sustainable land and water management and a better understanding of the Earth system. Global-scale quantification of water flows and storage in freshwater systems under current and future conditions is of particular interest in a globalized world and can support the wise development of global-scale water management and governance (Vörösmarty et al. 2015).

Quantification is best achieved by combining in situ and remote sensing data with physical modelling. Global hydrological modelling serves to estimate water flows on the land areas of the globe such as evapotranspiration, river discharge or groundwater recharge as well as water storage (or only water storage variations) in different compartments, e.g., in soil or in groundwater and surface water bodies. It uses data on precipitation and other climate variables over land areas as input and computes water flows from the land areas to the oceans (or into internal sinks on the continents), thus covering the terrestrial part of the global water cycle. While global hydrological modelling has been refined and extended with respect to modelled processes (in particular regarding human impacts on natural water flows and storages) and computed indicators in the last decade, modelling uncertainties have not become less albeit better known. These uncertainties are generally categorized into uncertainties due to model inputs (e.g., climate variables or soil properties), parameter values and model structure, but uncertainty of observations used for model validation or calibration also has to be considered (Sood and Smakhtin 2015). Different models compute contradictory estimates of, for example, mean annual evapotranspiration and low, mean and high flows in river basins (Gudmundsson et al. 2012) or groundwater depletion (Döll

et al. 2014a). They result in strongly varying projected impacts of climate change on river discharge (Schewe et al. 2014) or irrigation water requirements (Wada et al. 2013). Even global mean annual evaporation estimates as derived from global hydrological modelling (or satellite observations) differ by almost a factor of 2 (Jiménez et al. 2011), which is an important obstacle for the detection and attribution of changes in evapotranspiration due to global warming (Douville et al. 2012). Reasons for the discrepant model output have not been sufficiently analysed.

With this paper, the authors wish to share their perspectives on important challenges of and prospects for modelling continental water flows and storages at the global scale. In the next section, we briefly present existing modelling approaches. In Sect. 3, we discuss seven challenges and illustrate them with results of two global hydrological models (GHMs), WaterGAP (Döll et al. 2003; Müller Schmied et al. 2014) and PCR-GLOBWB (Wada et al. 2014). In Sect. 4, we present three advancements that may help to better characterize freshwater flows and storages at the global scale in the future. Finally, we draw our conclusions.

## 2 Approaches for Modelling Global Hydrology

To understand and quantify natural and human-induced water flows and storage changes across large scales, a number of models that simulate the continental part of the hydrological cycle on a regional to global scale have been developed in recent decades. Models developed to simulate global hydrology can be roughly classified into GHMs, land surface models (LSMs) and dynamic global vegetation models (DGVMs). Most DGVMs, however, do not include lateral water flows or surface water bodies, and can therefore only be used to assess runoff but not discharge. GHMs focus on simulation of water resources; they have a comprehensive representation of continental hydrological processes and often take into account human water use as well as man-made reservoirs. LSMs serve as a module of global climate models (GCMs) and therefore model both water and energy balances at the land surface. Due to this, they often represent the soil with a higher vertical resolution than GHMs and represent evapotranspiration and snow melt in a less conceptual manner than GHMs. LSMs often lack a groundwater reservoir, lateral routing or consideration of surface water bodies, and in most cases, they do not model the impact of human water use or man-made reservoirs. Finally, some LSMs are able to also model vegetation dynamics, or DGVMs have been extended to simulate global hydrology including not only vertical but lateral water flows as well as human water use and man-made reservoirs. In addition, simulation of irrigation water use is not only done by some GHMs, LSMs and DGVMs but also by global crop models (e.g., Elliott et al. 2014).

In the following, we do not distinguish between GHMs, LSMs and DVGMs but summarily refer to all of them as GHMs (like Schewe et al. 2014 or Hagemann et al. 2013 did) because existing models cannot be strictly classified into the three categories and because we focus on their ability to simulate terrestrial water flows and storages. GHMs typically simulate the dynamics of soil moisture storage due to precipitation and evapotranspiration, the generation of runoff and the discharge through the river network. The majority of these models are based on the water balance concept and track the transfer of water through a number of storage compartments with time steps ranging from a month to less than 1 day. Conceptual models are chosen as they are deemed to be more robust than empirical models and more parsimonious in their data requirements than fully physically based models,

while they maintain the ability to translate the effects of global change on water flows and storages in a consistent manner. Over time process descriptions have become more physically based. Few models simulate human water use that is essential to quantify river discharge, water availability and water stress, and even fewer models represent groundwater including groundwater recharge and abstractions, which is crucial to assess groundwater resources. Sood and Smakhtin (2015) presented an overview over 12 GHMs, and Bierkens et al. (2015) provided a table that describes the main features of GHMs and regional-scale hydrological models.

## 3 Challenges

Aiming at an improved representation of freshwater systems at the global scale, global hydrological modelling faces diverse challenges. We select some of the most important challenges that have been identified by the scientific community, i.e. constraints that lead to uncertain model output and thus limit the usefulness of global hydrological modelling for understanding freshwater systems.

### 3.1 Modelling Human Water Use

Human water use leads to anthropogenic water flows in the form of water abstractions from and return flows to surface water or groundwater bodies (Döll et al. 2012; Wada et al. 2011). Quantification of these flows is important for two reasons. On the one hand, water abstractions, consumptive water use (the part of the withdrawn water that evapotranspires during use) or net water abstractions (water abstractions minus return flows) are used in combination with estimates of water availability to compute indicators of water stress (or water scarcity). On the other hand, these anthropogenic water flows alter natural groundwater and surface water flows and storages (Döll et al. 2014a, b; Wada et al. 2012). It was estimated that around the year 2000, mean annual river discharge had been decreased due to water abstractions and man-made reservoirs by more than 10 % on one-sixth of the global land area (excluding Greenland and Antarctica), as compared to natural discharge (Döll et al. 2009). The strongest alterations, with, e.g., both decreases and increases of mean annual water storage (Döll et al. 2012), are found in semi-arid and arid areas of the globe, where irrigation is the dominant water use and alterations of river flow regimes by water abstractions are more important than alterations due to man-made reservoirs (Döll et al. 2009).

In global hydrological modelling, water abstractions and return flows are mostly estimated at a spatial resolution of 0.5° by 0.5° (55 km by 55 km at the equator) or 5′ by 5′ (9 km by 9 km). While water use for domestic and industrial purposes is assumed to vary negligibly throughout the year, monthly estimates of irrigation water use are required due to the often high seasonal variation of irrigation requirements. Modelling of water use for households and manufacturing strongly relies on statistical water abstraction data provided by countries, but data generally exist for a few years only. To derive annual time series by country, abstractions are modelled taking into account structural and technological change (Flörke et al. 2013). In addition, downscaling to the grid cell level is required and is mainly done based on urban and rural population in grid cells (Flörke et al. 2013; Vassolo and Döll 2005). Cooling water requirements for thermoelectric power plants are computed for each

power plant as a function of power plant type and cooling system, as well as values of national thermal electricity production (Flörke et al. 2013).

Unlike domestic and industrial water abstractions, irrigation water abstractions are very rarely measured, and statistical data for countries are generally based on either modelling or rough assumptions on per hectare irrigation water use. Consumptive irrigation water use in a grid cell is modelled as a function of irrigated area, crops and climate (e.g., Döll and Siebert 2002; Rost et al. 2008). Estimation of areas equipped for irrigation and even more estimation of areas actually irrigated are prone to large uncertainties as quality of statistical information is very heterogeneous (comp. information of map quality of the Global Map of Irrigation Areas GMIA v5.0, http://www.fao.org/nr/water/aquastat/irrigationmap/index40.stm). Assumed cropping patterns describing crop-specific growing periods throughout the year strongly impact the seasonality of estimated irrigation water demands (Zhou et al. 2015) and to a lesser degree annual values. Global consumptive irrigation water use as computed by six state-of-the-art global water use models varies between 1000 and 1500 $km^3$/year (Zhou et al. 2015, Siebert and Döll 2010), but this range may underestimate total uncertainty as all models used the same map of irrigated areas (GMIA). Estimated consumptive use strongly depends on the algorithm to compute potential (or reference crop) evapotranspiration, with global values ranging from 1180 to 1450 $km^3$/year just due to using three different equally plausible algorithms (FAO Penman–Monteith and two versions of Priestley–Taylor; Siebert and Döll 2010). To estimate water abstractions for irrigation, irrigation water use efficiencies (water consumption-to-abstraction ratios) need to be defined, e.g., for individual world regions (Döll and Siebert 2002), or simulated depending on the crop (in particular paddy rice; Wisser et al. 2008) or type of irrigation system (surface, sprinkler and drip; Jägermeyr et al. 2015). By modelling water flows in the three irrigation systems in a processed-based manner for different crops, Jägermeyr et al. (2015) computed grid cell-specific irrigation water use efficiencies as well as beneficial consumptive use due to transpiration. They estimated that global abstractions for irrigation are twice as high as the global consumptive irrigation water use of 1260 $km^3$/year, while 52 % of consumptive use is beneficial.

Irrigation water use is normally computed under the assumption that the crops receive enough irrigation water to allow actual evapotranspiration to become equal to the potential evapotranspiration value. However, it is likely that farmers irrigate less in case of water scarcity. Backed by independent information on worldwide groundwater depletion, application of a GHM indicated that in areas with groundwater depletion, farmers irrigated with only 70 % of the optimal water volume (Döll et al. 2014a).

An important uncertainty in human water use modelling relates to the distinction between the groundwater and surface water abstractions, and also to which degree return flows caused by irrigation recharge groundwater. Currently, the distinction of the source of water abstraction appears to more uncertain in the domestic and manufacturing sector than in the irrigation sector (Döll et al. 2012). Table 1 summarizes major uncertainties in modelling sectoral human water use at the global scale.

### 3.2 Uncertain Climate Input

A number of studies have shown the very strong dependence of computed continental water flows on applied climate input (Biemans et al. 2009; Döll and Fiedler 2008; Guo et al. 2006; Müller Schmied et al. 2014; Nasonova et al. 2011). Not only precipitation, but also radiation data are strong drivers of water flows and storages around the globe, while temperature data have the strongest impact in case of snow and ice. However, both historic

**Table 1** Major challenges in modelling sectoral human water use at the global scale (livestock water use is neglected)

| Water use sector | Challenges |
|---|---|
| Irrigation | Areas equipped for irrigation and areas actually irrigated; irrigated crop calendars; degree of deficit irrigation; climate input; equation for computing potential evapotranspiration; fraction of return flows to groundwater and surface water |
| Domestic | Downscaling to grid cells |
| Manufacturing | For many countries, only data on sum of water use for manufacturing and thermal power plant cooling available; downscaling to grid cells |
| Thermal power plant cooling, TP | Temporal development of cooling systems |
| All sectors | Technological change rates leading to water saving; water consumption-to-abstraction ratio (except TP); differentiation between groundwater and surface water abstractions (except TP) |

and future climate information are prone to multiple types of uncertainty which represents a major challenge for providing reliable GHM output.

### 3.2.1 *Uncertainties in Historic Climate Information and Their Impact on Simulating Water Resources*

Historic climate information applicable for global-scale studies suffers mainly from insufficient density of high-quality observations but also from observation errors. The effect of incomplete knowledge about the spatio-temporal distribution of climate variables during historic periods on global sums of water flows and storage changes is illustrated in Table 2 where simulation results of the GHM WaterGAP 2.2 (Müller Schmied et al. 2014) are listed. The considered model output encompasses global mean annual river discharge into oceans and inlands sinks (equal to renewable water resources in the case of model runs

**Table 2** Mean annual (2000–2009) water flows (precipitation *P*, discharge into oceans and inland sinks/total water resources *Q*, actual evapotranspiration AET, consumptive water use WCa) and change in total water storage (dTWS) calculated for different WaterGAP 2.2 model variants, in $km^3$/year

| | 1 | 2 | 3 | 4 | 5 | 6 | 7 | 8 |
|---|---|---|---|---|---|---|---|---|
| *P* | 111,819 | 113,215 | 111,819 | 113,215 | 104,768 | 111,819 | 111,819 | 111,819 |
| *Q* | 39,799 | 42,470 | 45,743 | 49,998 | 41,405 | 46,908 | 51,567 | 44,031 |
| AET | 70,948 | 69,791 | 64,884 | 62,154 | 63,405 | 64,937 | 60,282 | 67,808 |
| WCa | 1326 | 1184 | 1368 | 1208 | 0 | 0 | 0 | 0 |
| dTWS | −246 | −220 | −167 | −135 | −34 | −18 | −22 | −12 |

1: STANDARD, 2: CLIMATE, 3: STANDARD NoCal, 4: CLIMATE NoCal, 5: PRINCETON NoCal NoUse, 6: STANDARD NoCal NoUse, 7: STANDARD NoCal NoUse −20 % net radiation, 8: STANDARD NoCal NoUse +20 % net radiation

NoCal: model version without calibration, NoUse: model version assuming no human water use (for details on model variants, refer to Müller Schmied et al. 2014)

that neglect human water abstractions), actual evapotranspiration, consumptive water use by humans and water storage changes for the time period 2000–2009. Three different climate data sets were used to generate the table, all of which are available at the spatial resolution of WaterGAP (0.5° grids). For the STANDARD model runs, the WFDEI data were used that combine observational data with ERA-Interim reanalysis data for the years 1979–2009, resulting in climate input with a daily resolution (Weedon et al. 2014). In variant CLIMATE, the monthly data set CRU TS 3.2 (Harris et al. 2014) was used, but monthly precipitation totals were replaced by the GPCC v6 precipitation monitoring product (Schneider et al. 2014) because it includes more observation stations. Downscaling to daily values was done within WaterGAP, in case of precipitation based on the number of wet days in each month. Precipitation input used to drive both STANDARD and CLIMATE variants is based on monthly precipitation data from GPCC, but correction of precipitation error and the GPCC product version differ, leading to small differences in global precipitation (Table 2). Further details on climate input for the two model variants can be found in Müller Schmied et al. (2014). The PRINCETON model variant is forced by the "Global Meteorological Forcing Dataset for land surface modelling v2" from Princeton University which is a combination of global observation-based datasets and the NCEP-NCAR reanalysis (Sheffield et al. 2006) and is available at http://hydrology.princeton.edu/data.pgf.php.

WaterGAP 2.2 is calibrated against observed mean annual river discharge at 1319 stations worldwide, by adjusting 1–3 parameters in the basin cells. Table 2 shows that this calibration reduces the impact of uncertain climate variables on global river discharge into oceans and inland sinks Q, actual evapotranspiration AET, actual consumptive water use WCa and change in total water storage dTWS (comp. differences between columns 1 and 2 to differences between columns 3 and 4 in Table 2). While the difference in global precipitation between CLIMATE and STANDARD of 1396 $km^3$/year is increased to a difference in Q of 4255 $km^3$/year without calibration, this difference, i.e. sensitivity to climate input, is reduced by calibration to 2671 $km^3$/year. The difference is still appreciable even in the calibrated model version due to areas without observed river discharge. Global AET reacts much less sensitive to the different climate inputs. This is also seen when comparing the results of two uncalibrated model runs (no human water abstractions assumed) that are driven by either the Princeton or WFDEI climate data (columns 5 and 6). The Princeton climate data, with global precipitation estimated to be 7051 $km^3$/year less than in case of the WFDEI data, result in global total water resources that are 5503 $km^3$/year less than with the WFDEI data.

To perform a first sensitivity analysis regarding uncertain radiation data, daily net radiation in the uncalibrated STANDARD variant of WaterGAP 2.2 (without human water abstractions, column 6 in Table 2) was decreased or increased by 20 % in each grid cell (columns 7 and 8 in Table 2). At least at the scale of 0.5° grid cells, an uncertainty of 20 % for net radiation is not exaggerated. In case of −20 % net radiation, global actual evapotranspiration decreases by 7.2 %, while with +20 % net radiation, it increases by only 4.4 %. The asymmetry is due to water availability limiting actual evapotranspiration; radiation-limited areas become water limited when net radiation is increased. With a 20 % lower global net radiation on the continents, renewable water resources (i.e. runoff) would increase by 9.9 %, while with a 20 % higher global net radiation, it would decrease by 6.1 %. Figure 1 shows the spatial distribution of the changes in renewable water resources that are computed by WaterGAP 2.2 to result from a 20 % decrease or increase in net radiation (average for 2000–2009), in addition to a global map of the baseline net radiation computed by WaterGAP 2.2. While renewable water resources decrease in most grid cells

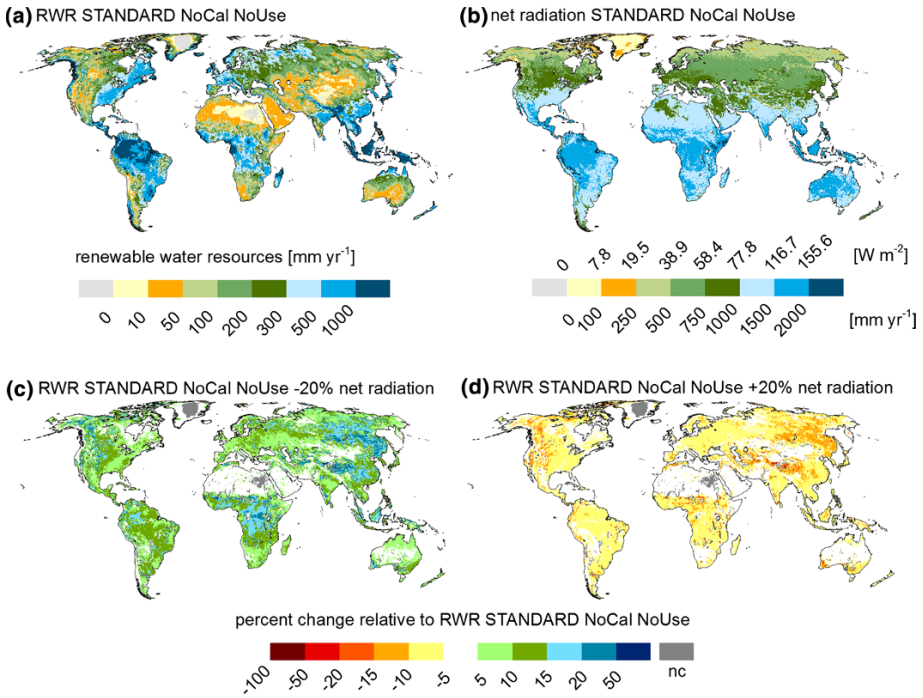


**Fig. 1** Sensitivity of renewable water resources RWR during 2000–2009 to a decrease or increase in daily net radiation by 20 % as simulated by WaterGAP 2.2 (Müller Schmied et al. 2014). RWR, i.e. net cell runoff, as computed with uncalibrated model variant STANDARD (**a**) and the related net radiation (**b**), and RWR changes relative to STANDARD in case of decreased (**c**) and increased (**d**) net radiation. nc: Per cent change cannot be meaningfully computed in case of zero or negative values of renewable water resources for STANDARD NoCal NoUse and where the value changes the sign. Negative RWR values occur in cells with lakes or wetlands if evapotranspiration of water flowing in from upstream cells exceeds precipitation

by less than 10 % in case of +20 % net radiation, they increase by more than 10 % in many regions of the globe in case of −20 % net radiation. Changes in per cent of water resources are highest in radiation-limited areas, i.e. in many grid cells with surface water bodies (e.g., in Tibet) but also in tropical and cold regions (even without surface water bodies). In water-limited areas, simulated water resources vary less (Fig. 1).

### *3.2.2 Uncertainties in Global and Regional Climate Projections and Their Impact on Simulating Future Water Resources*

Land and water management as well as assessment of climate change impacts in support of climate change mitigation require quantitative climate projections from seasonal to multi-decadal timescales that can be used as input to GHMs. These projections are subject to uncertainties that are different from the uncertainties of historic climate. The first uncertainty is related to future scenarios of anthropogenic perturbations including emissions of greenhouse gases and sulphate aerosols, land use change and water management itself all of which affect future climate at least on multi-decadal timescales. The second uncertainty, which is related to model deficiencies as illustrated by the different GCM responses to identical radiative forcings, is important at all timescales. Model uncertainty is generally

higher for precipitation than for temperature and arises partly from the limited spatial resolution of GCMs and the need to parameterize unresolved processes within atmosphere and ocean and at the land surface. Higher-resolution regional climate models still show significant biases when driven by atmospheric reanalyses and still require bias correction based on observations for use in impact studies. While there is hope to narrow model uncertainty by further increasing model resolution down to a few kilometres, at least for resolving explicitly atmospheric convective processes, the need of ensemble simulations at both seasonal and multi-decadal timescales will remain a major obstacle for at least a decade and raises the issue of both climate model formulation (structural model uncertainty) and model calibration (parameter uncertainty).

The need of large ensembles is related to the third source of uncertainty: the internal variability of the climate system, that is, the natural fluctuations that arise in the absence of any anthropogenic forcing (and any natural radiative forcing such as solar activity or volcanic eruptions). Appreciation of these fluctuations is an important matter for decision makers because they have the potential to reverse—for a decade or so—the longer-term trends that are associated with anthropogenic climate change (e.g., Douville et al. 2015). While they have been recognized as a fundamental limit to predictability from the early beginning of seasonal forecasting, their relevance in climate scenarios has been emphasized more recently and is probably still underestimated in most impact studies which often use a single realization of a given GCM for driving the impact model.

The relative importance of the three sources of uncertainty varies with prediction lead time and with spatial and temporal averaging scale, but is also variable dependent. Focusing on seasonal precipitation at the regional scale from the CMIP3 archive, Hawkins and Sutton (2011) showed that internal variability contributes 50–90 % of the total uncertainty for all regions for precipitation projections of the next decade and is the most important uncertainty for many regions for lead times up to 30 years. Model uncertainty is generally dominant thereafter. Scenario uncertainty was found to be small or over land areas. This is different for other climate inputs such as surface air temperature or surface radiation, and hydrological impacts of climate change differ appreciably between low and high emissions scenarios in the second half of the twenty-first century (Jiménez Cisneros et al. 2014).

The fourth source of uncertainty is related to the statistical bias correction of GCM outputs (e.g., Hagemann et al. 2011). Such techniques are sometimes included in statistical downscaling tools but, again, must be also implemented on top of dynamical downscaling tools. Statistical bias correction is commonly applied in climate impact modelling to correct GCM output for systematic deviations of the simulated historical data from observations. It has been found that evapotranspiration and river discharge as computed by GHMs that are driven by GCM output differ significantly for historic time periods if climate model output is not bias corrected; bias correction of precipitation and temperature is more important than bias correction of radiation, humidity and wind speed (Haddeland et al. 2012). Bias correction methods are generally based on transfer functions generated to map the distribution of the simulated historical GCM output to that of the observations. Those are subsequently applied to correct the future projections, thus making the assumption that GCM biases are constant over time. While such an assumption is not necessarily true, especially for precipitation biases (Chen et al. 2015), there are other challenging assumptions in most bias correction techniques.

### 3.3 Quantification of the Role of Active Vegetation Under Changing Climate and $CO_2$ Concentrations

When climate and atmospheric $CO_2$ concentrations change due to anthropogenic climate change, vegetation changes too. Therefore, evapotranspiration and runoff are not only affected directly by changes in climatic variables but in addition by the vegetation reaction to changes in climatic variables and $CO_2$ concentration. Rising $CO_2$ concentration causes two counteracting effects (Gerten et al. 2014). On the one hand, the physiological effect reduces opening of leaf stomata, as less water is required to assimilate carbon in case of higher $CO_2$ concentration; this decreases transpiration for the same climatic conditions. On the other hand, $CO_2$ fertilization may cause increased plant growth leading to increased transpiration per unit area (structural effect). Current quantification of these effects is highly uncertain, due to diverse observational evidence but also algorithms in DGVMs (Gerten et al. 2014). This is true not only for natural vegetation but also for crops (Elliott et al. 2014). In addition, the changing climate itself affects the vegetation, e.g., altering biomass production or vegetation cover or even leading of a biome shift.

It is uncertain how vegetation responses to increasing $CO_2$ and changing climate will affect water flows, which adds uncertainty to the response of water flows to climate change. Effects may be large, in particular where the type of vegetation changes. A modelling study with a DGVM indicated that until the end of the twenty-first century the active vegetation may cause a relative increase in runoff in response to increased atmospheric $CO_2$ concentration (physiological effect dominant), except in areas where grassland changes to deep-rooted vegetation in a warmer climate (Murray et al. 2012). In case of 4 °C global warming, the high temperatures lead to decreased vegetation cover, such that runoff as a ratio of precipitation is projected to increase worldwide (Murray et al. 2012). Large uncertainties also surround the response of vegetation to persistent droughts in both present-day and future climates, especially over the Amazon rainforest (Joetzjer et al. 2014).

Most GHMs, like most basin-scale hydrological models, do not model vegetation responses to changes in climate and atmospheric $CO_2$ concentrations. Thus, if, for example, the physiological effect were dominant, those GHM would underestimate future runoff and thus renewable water resources. Neglecting the reaction of crops to increased $CO_2$ may lead to an overestimation of future irrigation water demand (Wada et al. 2013; Elliott et al. 2014; Gerten et al. 2014). In the multi-model study of Wada et al. (2013), the only model that considered $CO_2$ effects on crop photosynthesis and transpiration shows a decreasing trend in future irrigation water demand (about 10 % by the end of this century) and increasing yields, while model runs without $CO_2$ effect indicated pronounced increases in future irrigation water demand (>20 % by the end of this century).

Unfortunately, models that simulate vegetation responses strongly disagree among each other on the effect of active vegetation on evapotranspiration and runoff. In a multi-model study on projected runoff changes between 1981–2010 and 2070–2099, two DGVMs computed higher runoff, and two computed lower runoff compared to GHMs with passive vegetation (Fig. 2; Davie et al. 2013). Comparing the runs of the four models with elevated $CO_2$ to runs with constant $CO_2$, they found that modelling the $CO_2$ effect on vegetation contributes to an increased spread in runoff projections. The challenge is to (1) improve modelling of climatic and $CO_2$ effects on vegetation with respect to evapotranspiration and runoff and (2) to include the effect of the active vegetation on evapotranspiration and runoff also in the majority of GHMs that do not model vegetation dynamics.

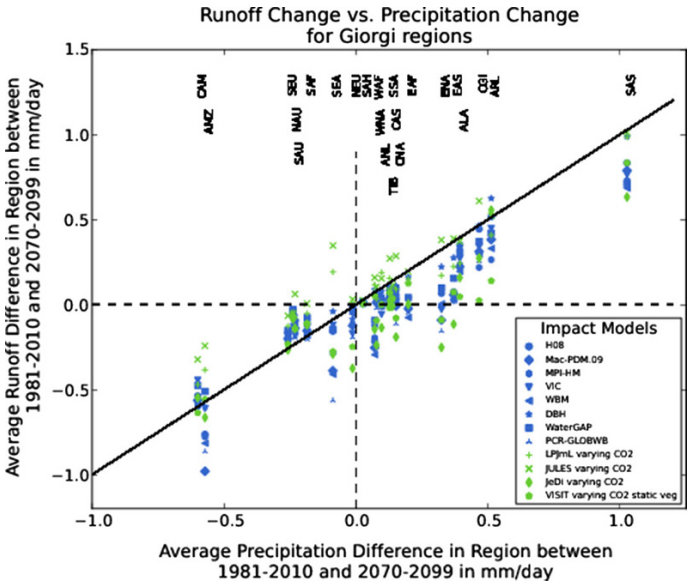


**Fig. 2** Uncertain impact of vegetation response on runoff changes under future anthropogenic climate change: scatterplot of runoff change against precipitation change between 1981–2010 and 2070–2099 in mm/day for world regions as computed by global hydrological models not taking into account active vegetation (*blue*) and global vegetation models that do (*green*). All models are forced with HadGEM2-ES RCP8.5 climate. Figure by Davie et al. (2013)

### 3.4 Understanding of Why GHMs (Including Global Irrigation Models) Respond Differently to Changed Climate Input

Traditionally, GCMs have been considered as a major source of the uncertainty in future hydrological assessments. Therefore, hydrological studies on the impact of climate change applied not only the output of one but multiple GCMs as input to the hydrological model (Jiménez Cisneros et al. 2014). However, recent model intercomparison projects (WaterMIP and ISI-MIP) where various GHMs were driven by either standard historic climate data or the bias-corrected output of multiple GCMs showed that differences among GHMs are also a major source of uncertainty regarding evapotranspiration, runoff and discharge (Dankers et al. 2014; Davie et al. 2013; Gosling et al. 2011; Haddeland et al. 2011, 2014; Hagemann et al. 2011, 2013; Schewe et al. 2014) and irrigation water demand (Wada et al. 2013; Elliott et al. 2014). The uncertainty can be larger than that arising from GCMs, depending on the region and the output variable. Considering eight GHMs but only three GCMs, Hagemann et al. (2013) found that the spread in projected changes of actual evapotranspiration dominantly caused by the different GHMs in most areas of the world, while the spread in projected runoff was dominantly caused either by the GCM or by the greenhouse gas emissions scenario (considering changes until the end of the twenty-first century). However, the small number of applied GCMs and bias correction of GCM output has limited the spread of GCM output. Applying eleven GHMs driven by five bias-corrected GCMs, Schewe et al. (2014) determined that GHMs were responsible for a larger spread in river discharge than the GCMs on most of the global land area. This can be explained by the fact that they compared model results not for a specific time period but for

a specific global warming for which the GCM outputs are more similar. Projections of the impact of climate change on optimal irrigation water abstractions as computed by seven GHMs driven the same GCMs were dominated by GHM uncertainty throughout the twenty-first century (Wada et al. 2014). With these studies, it has become state-of-the-art that an ensemble of model runs that has been generated by driving multiple GHMs with the output of multiple GCMs should be evaluated in water-related climate change impact studies. Analysis of such multi-model ensembles should not be restricted to the ensemble mean but also consider results of individual models that would imply a high risk, i.e. results that may have strong negative impacts due to high vulnerability (Döll et al. 2015).

Why do the responses of GHMs (and hydrological models in general) to climate change projections vary so widely? Possible reasons include (1) different model algorithms for the computation of potential and actual evapotranspiration as well as runoff generation, (2) modelling (or not) of energy balance in addition to water balance, (3) modelling irrigation water requirements based on soil water deficits as derived from soil water balances or as the difference between optimal evapotranspiration and available water, (4) different physiographic input parameters such as soil properties and land use and (5) different simulation of vegetation, including the $CO_2$ effect on crops and other vegetation. The latter aspect has already been discussed in the previous section.

None of the multi-model studies has been able to analyse in depth the reasons for the discrepant results of the individual GHMs. Hagemann et al. (2013) concluded that large differences in projected changes between the GHMs may be attributed to different model formulations of evapotranspiration but provide no further detail. Different methods for computing potential evapotranspiration (e.g., taking into account only temperature, or also radiation or humidity and wind speed) may explain the disagreement not only in energy-limited regions (Haddeland et al. 2012). Among eleven hydrological models applied for the ISI-MIP project, a few models used temperature-based methods for simulating potential evapotranspiration (Schewe et al. 2014), which has likely contributed to the spread. Haddeland et al. (2011) analysed differences among eleven GHMs driven by the same historic climate input, discussing the impact of energy balance-based snow algorithms as compared to degree day-based snow algorithms (affecting seasonal flows) and the impact of differing parameter values. They found that regarding "the interannual variation in runoff and evapotranspiration, no major differences have been found between the models run at daily or subdaily time steps or between models using different evapotranspiration or runoff schemes" (Haddeland et al. 2011, p. 882).

Model intercomparison studies should go beyond the identification of the spread of the model ensemble but also try to understand reasons for the spread and identify routes towards model improvement. However, the challenge of understanding why a large number of complex GHMs with a high spatial and temporal resolution react differently to a spatially and temporally heterogeneous change in input variables may appear overwhelming. A step towards progress could be to devise feasible intercomparison strategies that aim at understanding the major drivers of the spread. Another step would be to assess the capability of the GHMs to simulate hydrological effects of past climate variability, under the assumption that a model that does a good job in simulating hydrological responses to, e.g., inter-annual climate variability is also able to better simulate impacts of climate change. Hydrologists should study lessons learnt in model intercomparison of climate (e.g., Knutti and Sedlacek 2013) or dynamic vegetation models (Sitch et al. 2008; Warszawski et al. 2013). Regarding GCMs, Knutti and Sedlacek (2013) found that model spread regarding future temperature change has not decreased in the new CMIP5 model ensemble as compared to the CMIP3 ensemble, i.e. after about than 6 years of massive

efforts in model improvements. They argue that GCMs have improved and now represent more processes in greater detail, which implies greater confidence in projections even if model spread, which is often called model uncertainty, has not decreased. A decreased spread might even misleading if caused only by using more similar model input or more similar algorithms that become to be considered "state-of-the-art" within the scientific community even without firm scientific support. Regarding DGVMs, the study of Sitch et al. (2008. p. 2035) showed "the ability of models to satisfy contemporary global carbon cycle constraints, while future projections diverge markedly", as many different parameter combinations allow recreating the historical record but lead to divergent future projections.

### 3.5 Modelling of Monthly Time Series of River Discharge and Human Water Use to Support More Meaningful Indicators of Water Stress for Both Humans and Ecosystems

Currently, indicators of water stress are mostly defined based on mean annual values of water availability and use (e.g., Kiguchi et al. 2015, Arnell and Lloyd-Hughes 2014). Water stress for humans and freshwater ecosystems as well as environmental flow requirements could be defined more meaningfully at the monthly timescale (Hoekstra and Mekonnen 2011) as use of mean annual values masks differences in seasonality and interannual variability. Consideration of mean annual values only leads to an underestimation of water stress in highly seasonal flow regimes, e.g., in monsoon regions, as well as in regions with high interannual flow variability, e.g., in semi-arid and arid regions.

However, WaterGAP and most likely all other GHMs are not capable of satisfactorily simulating monthly time series or even mean monthly values of river discharge and human water use. Müller Schmied et al. (2014) found that even for most of the 1319 gauging stations used for model calibration (that considers only mean annual river discharge), monthly (their Figs. 6 and 7, and Table 4) or mean monthly river discharge (their Fig. 5) was not well simulated. In case of the best model version (STANDARD), only 28 % of the basins showed a modelling efficiency (Nash–Sutcliffe coefficient) of more than 0.7, while 46 % of the basins had a value of less than 0.5. Simulation of seasonality of irrigation water use is known to be highly uncertain as cropping patterns and calendars are not well known (Portmann et al. 2010). Besides, cropping patterns and calendars would ideally be simulated as a function of climate. Therefore, we believe that it is currently not reasonable to compute, in global-scale studies, water stress indicators based on monthly water availability and use. The challenge is to improve both GHMs and their input data such that reliable monthly time series of river discharge and human water use are computed.

An alternative to indicators based on monthly discharge values is to consider statistical monthly low and high flows, e.g., $Q_{90}$ and $Q_{10}$, the river discharge that is exceeded in 9 out of 10 months and 1 out of 10 months, respectively. These statistical low and high flows include seasonal and inter-annual variability of monthly river discharge, which is particularly high in the dry regions of the globe, and are ecologically relevant indicators of the flow regime. They can be computed reasonably well by the GHMs WaterGAP and PCR-GLOBWB, at least for the gauging stations whose mean annual discharge was used for calibrating WaterGAP (Fig. 3). Simulation of high flows is better than simulation of low flows. In case of observed $Q_{90}$ values of less than 1 km$^3$/month or 10 mm/month, $Q_{90}$ as simulated by WaterGAP simulations may differ very strongly from the observed value even though WaterGAP was calibrated against mean annual river discharge of these stations (Fig. 3 top). WaterGAP tends to overestimate $Q_{90}$ (with 592 of the simulated 821 values being larger than the observed ones) and to underestimate $Q_{10}$ (with 608 of the

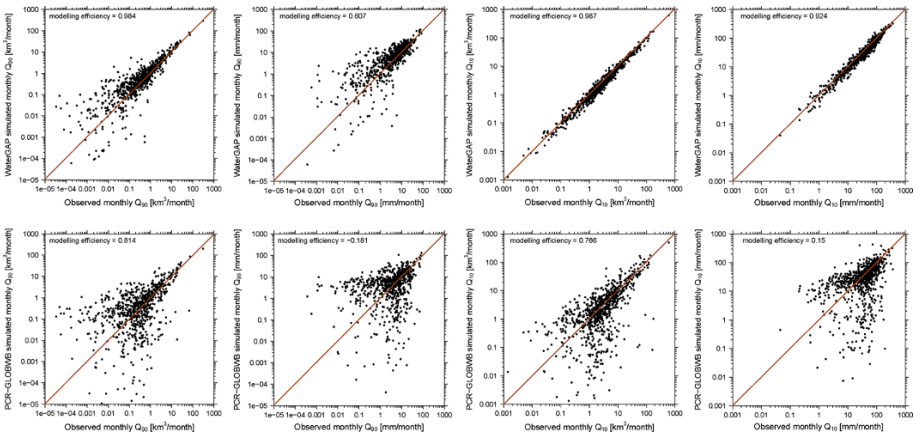


**Fig. 3** Validation of monthly low and high flows $Q_{90}$ (*left*) and $Q_{10}$ (*right*) as simulated by the global hydrological models WaterGAP 2.2 (Müller Schmied et al. 2014) (*top*) and PCR-GLOBWB (Wada et al. 2014) (*bottom*) against observations at 821 of the 1319 WaterGAP calibration stations with at least 15 years of data and basin area of at least 20,000 km$^2$. Note that different from WaterGAP, PCR-GLOBWB is not calibrated to mean annual observed discharge at the depicted gauging stations

simulated 821 values being smaller than the observed ones). PCR-GLOBWB shows the same behaviour but to a much lesser extent ($Q_{90}$: 497 of the simulated 821 values are larger than the observed ones; $Q_{10}$: 449 of the simulated 821 values are smaller than the observed ones). However, model results of PCR-GLOBWB show a lower fit to observed low and high flow values as the model is not calibrated against mean annual discharge at the depicted gauging stations. Water stress indicators based on monthly $Q_{90}$, where water use is often taken to be mean annual consumptive water use instead of mean annual water abstraction, were applied, e.g., by Alcamo et al. (2007) and Hanasaki et al. (2008).

### 3.6 Simulation of Groundwater–Surface Water Interaction and Capillary Rise by Gradient-Based Groundwater Modelling

Groundwater is the largest store of freshwater available for human use. It is replenished by precipitation in the form of diffuse groundwater recharge through the soil and sometimes by concentrated recharge from surface water bodies (Taylor et al. 2013). Groundwater flows along gradients of hydraulic head, but this is not represented yet in GHMs. In particular, groundwater flow between grid cells is not simulated. If at all, groundwater is represented in GHMs mainly as a linear storage compartments that discharge groundwater as baseflow into surface water bodies, baseflow being a function of groundwater storage. With a linear groundwater store, the relative temporal changes of groundwater storage can be computed, also as affected by groundwater abstractions (Döll et al. 2014a, b). Groundwater storage changes can be translated to variations of groundwater table elevations, but there is no information of the absolute elevation of the groundwater table or depth to groundwater table. An approach for taking into account groundwater in climate models by Niu et al. (2007) allows to compute depth to groundwater table and capillary rise but does not simulate lateral groundwater flow (nor groundwater recharge from surface water bodies).

Without dynamic modelling of the elevation of the groundwater table, groundwater recharge from surface water bodies, which is particularly important in dry regions, cannot be represented well. Döll et al. (2014a) used a very rough estimate of groundwater recharge from lakes and wetland in semi-arid and arid regions of the globe to avoid underestimation of groundwater recharge and thus overestimation of groundwater depletion. Equally, capillary rise from groundwater to the soil cannot be represented well if the distance of the groundwater table to the land surface is not simulated. Thus, for a simulation of groundwater–surface water interaction and capillary rise, it is necessary to estimate the temporally changing elevation of the groundwater table well; this can only be achieved if lateral groundwater flow driven by gradients of hydraulic head (or groundwater table) is computed (Fan et al. 2007; Jones et al. 2008; Kollet and Maxwell 2008; Krakauer et al. 2014; Maxwell et al. 2007; Maxwell et al. 2015). Lateral groundwater flow is described by a partial differential equation the solution of which is computationally more involved than solving the ordinary differential equation that is used to describe groundwater storage and outflow in typical hydrological models. However, the main reason for not including gradient-based groundwater flow modelling in GHMs may be the extreme lack of information on groundwater that is available for global-scale studies (Taylor et al. 2013; de Graaf et al. 2015).

For North America, Miguez-Macho et al. (2007) linked a land surface scheme with a two-dimensional gradient-based groundwater model and computed, with a daily time step, gradient-based groundwater flow, water table elevation, groundwater–surface water interaction and capillary rise, using a spatial resolution of 12.5 km. One challenge was the determination of the river conductance that affects the degree of groundwater–surface water interaction. Capillary rise was computed using the Richards' equation for a soil column reaching down to the groundwater table by soil layers of variable thickness; the model appears to overestimate capillary rise that is computed to dominate in all flat regions during May–October. Vergnes et al. (2012, 2014) established a gradient-based groundwater model applicable for global-scale modelling and applied it to France with spatial resolutions of 0.5° and 5 arc-min. The transient model simulates two-dimensional groundwater flow dynamics and also accounts for groundwater–river exchange and capillary rise. It is currently being implemented in the GHM of CNMR (Centre National de Recherches Météorologiques, France). Fan et al. (2013) developed a high-resolution (30 arc-s) steady-state global groundwater flow model driven by diffuse groundwater recharge, taking into account land surface elevation. The results indicated that patterns in water table depth explain patterns in wetlands at the global scale and vegetation gradients at regional and local scales. This study was an important step towards simulating groundwater dynamics globally. However, in the chosen approach, neither the important hydraulic connection between rivers, surface water bodies and groundwater nor spatially distributed hydrogeological information was taken into account. A subsequent study by de Graaf et al. (2015) presented an alternative global-scale steady-state groundwater flow model of a shallow aquifer (spatial resolution 6 arc-min), estimating aquifer depths and using a global lithological map (Hartmann and Moosdorf 2012) in combination with estimates of lithology-specific hydraulic conductivity (Gleeson et al. 2014). The results showed the importance of lateral groundwater flows over catchment boundaries as inter-basin flow paths. Both models are likely to overestimate the depth to groundwater. They are not dynamic and are not coupled to a model that dynamically models groundwater recharge and surface water levels. Therefore, the simulation of groundwater–surface water interactions is very limited, and neither capillary rise nor groundwater pumping or groundwater recharge by irrigation return flows is considered.

At a continental scale, Maxwell et al. (2015) showed the possibility of setting up an integrated hydrological model that simulates surface and subsurface flow at a high spatial resolution (1 km). The model solves surface and subsurface flow simultaneously and is constructed entirely of available datasets including topography, soil texture and hydrogeology. However, the steady-state simulation did not take into consideration runoff generation, transient dynamics or human activities such as groundwater pumping that affect the quantity of surface water fluxes and groundwater recharge (Döll et al. 2014a, b). Maxwell et al. (2015) concluded that these limitations can be addressed within the current modelling framework but require additional computational resources. Advanced soil–groundwater–surface water modelling systems such HydroGeoSphere (Brunner and Simmons 2012) that are widely applied at local scales would require not only faster computers and better calibration strategies but also good quality data to be applicable at the global scale.

Given the poor knowledge on the three-dimensional shape and distribution of aquifer bodies as well as restricted computational resources, gradient-based groundwater modelling cannot aim, in the near future, at modelling groundwater flows in three dimensions or at supporting the sustainable management of specific aquifers. The focus is on better representing groundwater–surface water interactions and capillary rise. Here, the major challenge is to achieve a reasonable representation even with relatively large grid sizes such that it is computationally feasible to perform transient groundwater flow simulations that are coupled to soil water and surface water dynamics.

### 3.7 Detection and Attribution of Observed Changes in Freshwater Systems

Detection is the process of demonstrating that an observed change cannot be explained by internal climate variability only. Attribution of a change to anthropogenic influence requires the additional demonstration that the detected change is consistent with the change simulated in response to a combination of external forcings. While detection is generally done using statistical methods, attribution almost always requires the use of models. Most often in hydrology, detected change, e.g., of river discharge, is attributed to observed changes in climate or $CO_2$ concentrations (Jiménez Cisneros et al. 2014). Attribution of hydrological changes to human climate-altering activities is seldom attempted because it requires the application of climate models. An exception is the study of Pall et al. (2011) where citizens allowed the researchers to perform a very large ensemble of climate model runs on their computers such that it could be shown that increased greenhouse gas concentrations increased the likelihood of a specific historic flood event in the UK by approximately a factor of 2–3.

Detection of changes of water flows and storages is limited by availability of, e.g., river discharge data or data on groundwater recharge. In the case of river discharge, available data are inhomogeneous as records of many stations end in the 1990s or even earlier, and there are a large number of ungauged basins around the world so that there is no good global coverage of river discharge by gauging stations. In case of the important variable groundwater recharge, there are no measured time series at all. In addition, the strong spatio-temporal variability of hydrological variables makes it hard to detect changes, e.g., changes in flood frequency. Attribution of detected changes of river discharge is challenging because river discharge is affected not only by climatic (and $CO_2$) changes but also by changes in land use and water abstractions (Jiménez Cisneros et al. 2014).

There are studies that tried to attribute changes in river discharge to changes in climate, $CO_2$ and land use (Gedney et al. 2006) and, more recently, to the radiative effect of

anthropogenic aerosols (Gedney et al. 2014). Such studies were based on the comparison between annual river discharge derived from offline land surface simulations on the one hand and from observed river discharges on the other hand. The river basins with significant irrigation were ignored so that the role of human water use was considered as negligible. Yet, the conclusions of Gedney et al. (2006) that $CO_2$ increase played a large role in causing increased global river discharge were challenged. They are highly uncertain not only due to the specific model assumptions on physiological versus structural effects on evapotranspiration but also because the applied precipitation data set is not suitable for evaluating trends as it is based on a temporally varying number of precipitation gauging stations, and because a more recent compilation of observed river discharge resulted in a decrease in global river discharge over time (Gerten et al. 2014). Alkama et al. (2011) were successful in simulating recent river discharge trends without accounting for physiological effects and emphasized the possible relevance of permafrost thawing for capturing the discharge trends of northern high-latitude rivers.

As far as evapotranspiration (ET) is concerned, changes at the continental to global scale are even more difficult to analyse due to lack of direct measurements. Only relatively few monitoring sites operate around the world and the period of record is quite short. Two studies (Jung et al. 2010, Wang et al. 2010) have used such in situ measurements for tuning global empirical ET schemes based on remote sensing and standard meteorological data. They agreed on a global increase in annual mean ET by about 7 mm per year per decade from 1982 to the late 1990s. These results were compared with ET outputs of process-oriented land surface models and were found to be relatively robust (Jung et al. 2010). The 1982–2008 period was, however, too short for a formal detection and attribution. More recently, Douville et al. (2012) used several global ET reconstructions based on two land surface models driven by two precipitation forcings and attributed the reconstructed multi-decadal variations of annual mean ET in three latitudinal belts to anthropogenic climate change. The ET reconstructions neither accounted for direct $CO_2$ effects on ET nor accounted for changes in land or water use, thereby allowing a fair comparison with GCM outputs and a more robust attribution of the effect of anthropogenic climate change. Yet, this strategy did not allow the authors to assess the possible impacts of other human activities on ET, such as water abstractions.

## 4 Prospects

The role of global hydrological modelling is to combine large amounts of diverse and mostly spatially and temporally resolved data in order to estimate continental water flows and storages and resulting policy-relevant indicators of the water situation worldwide. To decrease the uncertainty of the computed estimates, it will be fruitful to generate and utilize improved GHM input data such as climate data but also to make better use of observations of GHM output variables such as river discharge or total water storage variations. This can be done by multi-criteria validation, calibration or data assimilation. A higher spatial resolution of GHM models beyond the current 0.5° resolution (55 km × 55 km at the equator) will increase the policy relevance of GHM output, e.g., for supporting integrated water resources management at the scale of river basins.

### 4.1 Multi-criteria Validation Against River Discharge and Geodetic/Remote Sensing Observations

Observations of river discharge are ideally suited for validating macro-scale hydrological models because the point observation integrates over processes in the whole upstream basin of the gauging station. Besides, river discharge is a flow that can be related quite easily to water availability which is the focus of many assessments. Finally, long time series of observational data exist for many stations around the globe and some of them are compiled by the Global Runoff Data Centre (GRDC). When validating model output against observed river discharge, measurement errors should be taken into account, ideally in a station- and discharge-specific manner. None of the 500 UK gauging stations has a discharge observation uncertainty of less than 10 % (for individual measurements at mean flow conditions) due to uncertain stage–discharge relationships, while 83 % of the stations for which uncertainty could be determined has an uncertainty of less than 40 % (Coxon et al. 2015).

Observational data of other components of the water cycle in addition to river discharge are needed to validate hydrological models due to the well-known equifinality problem (Beven and Freer 2001); more than one parameter combination (or model) can lead to a good fit between discharge observations and simulations, while other water flows or storages would be projected very differently by model variants that result in equally good simulations of the river discharge. Therefore, a multi-criteria validation that considers other observed flows or water storage variations or any other observation that are related to flows and storages can be expected to be highly informative.

As an example, total water storage (TWS) variations as modelled by GHMs can be validated against satellite-based geodetic observations of monthly gravity variations of the GRACE satellites (Tapley et al. 2004), at least if all important storage compartments like the groundwater and large surface water bodies are taken into account in the GHM. Simulated TWS variations can also be validated by continuous GPS observations at more than 200 network stations worldwide because water storage variations cause crustal deformations which lead to displacements of the GPS reference point (Döll et al. 2014b). Comparing simulated TWS variations against both GRACE and GPS, Döll et al. (2014b) identified regions where the WaterGAP GHM underestimates seasonal variability of TWS and found that maximum TWS occurs 1 month too early in WaterGAP for most land areas (based on GRACE only). Validating groundwater depletion as computed by WaterGAP against both in situ well observations and GRACE TWS allowed the conclusion that farmers in groundwater depletion area irrigate with only 70 % of the optimal value (Döll et al. 2014a). In the future, combined validation of GHM model output against river discharge and TWS (e.g., Alkama et al. 2010) should be intensified, and time series of lake or river water tables as measured by radar altimetry should serve as additional observational data sets.

### 4.2 Multi-criteria Calibration and Data Assimilation

Multi-criteria calibration and data assimilation goes beyond multi-criteria model validation. In model calibration, model parameters are adjusted in a way that simulated water flux or storage (state) variables optimally match historic observations with respect to one or more performance criteria. A primary goal of calibration is to obtain a model (including parameter values) that allows simulations for periods without observation data, such as for

simulations of the global water resources for the time period 1971–2000 or of future climate change impacts. GHMs have rarely been calibrated, with few exceptions such as WaterGAP (Döll et al. 2003; Hunger and Döll 2008) and WASMOD-M (Widén-Nilsson et al. 2007) for which one or more parameters were adjusted by evaluating simulation results against observed river discharge. Without basin-specific calibration, even mean annual simulated river discharge may differ strongly from the observed value (Müller Schmied et al. 2014; Haddeland et al. 2011).

Model calibration is usually hampered by parameter equifinality (see Sect. 4.1), and calibration against more than one observable and performance criterion has long been recognized as an option to allow adjustment of a larger number of model parameters and to constrain the number of plausible model realizations (e.g., Gupta et al. 1999). For continental to global-scale modelling, however, there is not yet much experience with multi-criteria calibration, presumably because adequate satellite-based observation data with sufficient spatial and temporal extent and resolution have become available only recently. While considerable uncertainties of remote sensing data products may still limit their value in a multi-criteria calibration strategy (Livneh and Lettenmaier 2012), large-scale calibration examples demonstrated the benefit of using, in addition to river discharge, satellite-based monitoring data, such as near-surface soil moisture from Envisat (Milzow et al. 2011), MODIS-based evapotranspiration (Livneh and Lettenmaier 2012), altimetry-based water levels (Milzow et al. 2011), MODIS-based snow cover (Parajka and Blöschl 2008) or total water storage (TWS) variations from GRACE (Werth et al. 2009, Xie et al. 2012). GRACE TWS and river discharge were incorporated into a multi-criteria calibration scheme for WaterGAP by Werth and Güntner (2010) by adjusting the most sensitive 6–8 parameters in the 28 largest river basins worldwide. Improved simulations of TWS variations and river discharge were achieved for most basins after calibration, but calibrated mean annual discharge was still poor compared to the observed values in some basins, and a better fit to GRACE TWS did not necessarily lead to a better fit of simulated discharge to observed discharge. In the study of Xie et al. (2012), model parameters appear to be less sensitive to TWS than to river discharge. While large trade-offs in model performance for different objective functions leave the model with considerable uncertainties, they can help to unravel deficiencies of the model structure (e.g., Duethmann et al. 2014).

Direct multi-criteria calibration for the essential terms of the continental water balance (river discharge and TWS changes, and evapotranspiration if monitoring data were available) is particularly appealing if one strives for a closed water balance model of the continental areas. Nevertheless, the particular nature of GRACE TWS data based on the Earth's time-variable gravity field requires specific consideration of the storage compartments considered, data filtering and error terms to make the calibration scheme consistent between model and observations (Güntner 2008). Multi-criteria calibration should comprise more than two observables to further constrain the space of plausible model realizations. Besides the types of satellite-based data on states and fluxes mentioned above, information on water storage in surface water bodies has a high potential as a large-scale calibration constraint, based on currently available multi-sensor combination data (for example, Papa et al. 2013) and future satellite missions such as SWOT. With the development of multi-scale modelling and parameterization concepts (Samaniego et al. 2010), even observation data with a small spatial measurement support but a global coverage such as evapotranspiration from Fluxnet eddy-covariance sites (Jung et al. 2011) or near-surface soil moisture based on GNSS reflectometry (Larson et al. 2008), for instance, may inform parameter adjustment in global models within a multi-criteria calibration approach.

For observing systems that require complex operators to transform the sensor signal into a hydrological variable simulated by a GHM, an inverse strategy can be promising. In this case, the state or flux variable of the hydrological model is forward-transformed to a quantity at the sensor level and, thus, parameter adjustment is done by measuring the performance directly relative to the sensor signal. This avoids the need for using an operator which in turn often is a nonlinear model that is afflicted with uncertainty. An example is to convert simulated water storage variations of a hydrological model into K-Band range rate data which is the key observable of GRACE at the level of the twin satellites, i.e. the inter-satellite distance changes as determined by a K-Band Ranging (KBR) System between the two GRACE satellites (Krogh 2011). Parameters in the hydrological model are then adjusted by minimizing the difference between modelled and observed range rate data.

Data assimilation, i.e. an integration strategy of models and data that primarily adjust state variables of the model, and possibly also parameters, may allow for an optimal quantification of the system status for a period where observations are available, and if the respective errors can be adequately specified. With early developments of data assimilation for large-scale applications being tailored towards appropriate initial conditions in land surface schemes of weather forecasting systems, there are now numerous examples for continental to global-scale assimilation of a variety of data types into LSMs with the general aim of hydrological forecasting and provide land surface hydrological states that are superior to satellite observations or model estimates alone (see, e.g., overviews in Li et al. 2012; Reichle et al. 2014; Lahoz and de Lannoy 2014). However, there are only very few examples of data assimilation for large-scale water cycle modelling and operational water resources assessment so far (Renzullo et al. 2014), presumably because of limited availability of usable data at this scale, but also because of the complexity and computational costs of these techniques (van Dijk et al. 2014). The most widely adopted technique is the ensemble Kalman filter (EnKF) or Smoother, where the otherwise unknown error characteristics of the model are estimated by a Monte Carlo-based ensemble approach to determine the error covariance matrix of the model. First assimilation studies using GRACE TWS show its value for informing simulated subsurface water storage (Zaitchik et al. 2008; Li et al. 2012; Houborg et al. 2012). Eicker et al. (2014) presented an EnKF approach for assimilating GRACE TWS into WaterGAP with combined state and parameter updating and a full error propagation from the monthly GRACE spherical harmonic coefficients. They showed that GRACE data inform the model even at higher spatial resolution than resolved by the GRACE data themselves, with varying gains in time, space and among the different storage compartments. Some of the major challenges for the further development of data assimilation techniques include strategies for conserving mass during the assimilation process, error characterization of model and observation data, and adequate mapping functions between observed and simulated variables.

Data assimilation or fusion techniques can also be applied in an offline mode to provide consistent water balance estimates of continental hydrology. A global water cycle reanalysis product has recently been presented by van Dijk et al. (2014), merging prior estimates of monthly water storage changes based on an ensemble of several LSM outputs and complementary data with GRACE TWS data in a sequential data assimilation framework.

### 4.3 Hyperresolution Global Hydrological Modelling

There is the vision that one day it may be feasible to perform global-scale hydrological modelling with an acceptable accuracy at a much higher resolution than today, with grid cells of 100 m to 1 km instead of the current 50 km (Wood et al. 2011). Then, global-scale modelling would allow improved global assessment of, e.g., food security and could support river basin management everywhere. This has particular relevance in developing countries where basin models are not yet available or a poorly constrained because of lack of local data; in these cases, information about water resources derived from GHMs that can exploit non-local remote sensing data would be a great asset if it is locally relevant (Bierkens et al. 2015). In addition, highly resolved global-scale information on water flows and storages would be very beneficial for freshwater ecosystem management and for assessing global biogeochemical cycles.

The HyperHydro initiative (www.hyperhydro.org) aims at advancing hyperresolution global hydrological modelling. It is a network of scientists that is open to the broader scientific community and invites anyone who wishes to cooperate. Current efforts include the establishment of testbeds, overcoming of computational challenges and the compilation of input data sets. For further information on motivation, challenges and prospects of hyperresolution global hydrological modelling, please refer to Wood et al. (2011) (including a comment of Beven and Cloke 2012 and the reply of Wood et al. 2012) and Bierkens et al. (2015). Beven et al. (2015) provide valuable critical comments on hyperresolution modelling of water on the land areas of the globe, pointing out that unknown heterogeneities in the subsurface and ignorance about subsurface processes result in a lower gain of accuracy by increased resolution than is the case in atmosphere and ocean modelling. However, a prospect of hyperresolution modelling is that its output can be evaluated more meaningfully than current GHM output by local experts and stakeholders who can help identify model deficiencies.

## 5 Conclusions

The capabilities and the sheer number of GHMs have increased significantly over the last decade such that global-scale quantification of water resources has improved and uncertainties are better known. We conclude that major challenges remain until GHMs can serve as reliable tools for characterizing current and potential future water resources worldwide. We hope that our presentation of selected challenges informs not only on the state-of-the-art of global hydrological modelling but also indicates fruitful research directions. As outlined in the previous section, we believe that major advancements will be possible if in situ and remotely sensed observational data of model output variables are utilized more efficiently in global hydrological modelling and if spatially more resolved model output can be provided with reasonable accuracy.

**Acknowledgments** We acknowledge the International Space Science Institute in Bern, Switzerland, and specifically Anny Cazenave and Nicolas Champollion, for hosting the ISSI Workshop on Remote Sensing and Water Resources that motivated us to write this paper. In addition, we are thankful for the helpful comments of an anonymous reviewer.

## References

Alcamo J, Flörke M, Märker M (2007) Future long-term changes in global water resources driven by socio-economic and climatic changes. Hydrol Sci J 52(2):247–275. doi:10.1623/hysj.52.2.247

Alkama R, Decharme B, Douville H, Becker M, Cazenave A, Sheffield J, Voldoire V, Tyteca S, Le Moigne P (2010) Global evaluation of the ISBA-TRIP continental hydrologic system. Part 1: a twofold constraint using GRACE Terrestrial Water Storage estimates and in situ river discharges. J Hydrometeorol 11:583–600. doi:10.1175/2010JHM1211.1

Alkama R, Decharme B, Douville H, Ribes A (2011) Trends in global and basin-scale runoff over the late 20th century? Methodological issues and sources of uncertainty. J Climate 24:2983–2999. doi:10.1175/2010JCLI3921.1

Arnell NW, Lloyd-Hughes B (2014) The global-scale impacts of climate change on water resources and flooding under new climate and socio-economic scenarios. Clim Change 122(1–2):127–140. doi:10.1007/s10584-013-0948-4

Beven K, Cloke H (2012) Comment on "Hyperresolution global land surface modeling: meeting a grand challenge for monitoring Earth's terrestrial water" by Eric F. Wood et al. Water Resour Res 48:W01801. doi:10.1029/2011WR010982

Beven KJ, Freer J (2001) Equifinality, data assimilation, and uncertainty estimation in mechanistic modelling of complex environmental systems. J Hydrol 249:11–29. doi:10.1016/S0022-1694(01)00421-8

Beven K, Cloke H, Pappenberger F, Lamb R, Hunter N (2015) Hyperresolution information and hyperresolution ignorance in modelling the hydrology of the land surface. Sci China Earth Sci 58:25–35. doi:10.1007/s11430-014-5003-4

Biemans H, Hutjes RWA, Kabat P, Strengers BJ, Gerten D, Rost S (2009) Effects of precipitation uncertainty on discharge calculations for main river basins. J Hydrometeorol 10(4):1011–1025. doi:10.1175/2008JHM1067.1

Bierkens MFP, Bell VA, Burek P, Chaney N, Condon LE, David CH, de Roo A, Döll P, Drost N, Famiglietti JS, Flörke M, Gochis DJ, Houser P, Hut R, Keune J, Kollet S, Maxwell RM, Reager JT, Samaniego L, Sudicky E, Sutanudjaja EH, van de Giesen N, Winsemius H, Wood EF (2015) Hyper-resolution global hydrological modelling: what is next? Hydrol Process 29(2):310–320. doi:10.1002/hyp.10391

Brunner P, Simmons CT (2012) HydroGeoSphere: a fully integrated, physically based hydrological model. Groundwater 50:170–176. doi:10.1111/j.1745-6584.2011.00882.x

Chen J, Brissette FP, Lucas-Picher P (2015) Assessing the limits of bias-correcting climate model outputs for climate change impact studies. J Geophys Res Atmos 120:1123–1136. doi:10.1002/2014JD022635

Coxon G, Freer J, Westerberg IK, Wagener T, Woods R, Smith PJ (2015) A novel framework for discharge uncertainty quantification applied to 500 UK gauging stations. Water Resour Res 51:5531–5546. doi:10.1002/2014WR016532

Dankers R, Arnell NW, Clark DB, Falloon PD, Fekete BM, Gosling SN, Heinke J, Kim H, Masaki Y, Satoh Y, Stacke T, Wada Y, Wisser D (2014) First look at changes in flood hazard in the Inter-Sectoral Impact Model Intercomparison Project ensemble. Proc Natl Acad Sci USA 111(9):3257–3261. doi:10.1073/pnas.1302078110

Davie JCS, Falloon PD, Kahana R, Dankers R, Betts R, Portmann FT, Wisser D, Clark DB, Ito A, Masaki Y, Nishina K, Fekete B, Tessler Z, Wada Y, Liu X, Tang Q, Hagemann S, Stacke T, Pavlick R, Schaphoff S, Gosling SN, Franssen W, Arnell NW (2013) Comparing projections of future changes in runoff from hydrological and biome models. Earth Syst Dynam 4:359–374. doi:10.5194/esd-4-359-2013

de Graaf IEM, Sutanudjaja EH, van Beek LPH, Bierkens MFP (2015) A high-resolution global-scale groundwater model. Hydrol Earth Syst Sci 19:823–837. doi:10.5194/hess-19-823-2015

Döll P, Fiedler K (2008) Global-scale modeling of groundwater recharge. Hydrol Earth Syst Sci 12(3):863–885. doi:10.5194/hess-12-863-2008

Döll P, Siebert S (2002) Global modeling of irrigation water requirements. Water Resour Res 38(4):8-1–8-10. doi:10.1029/2001WR000355

Döll P, Kaspar F, Lehner B (2003) A global hydrological model for deriving water availability indicators: model tuning and validation. J Hydrol 270(1–2):105–134. doi:10.1016/S0022-1694(02)00283-4

Döll P, Fiedler K, Zhang J (2009) Global-scale analysis of river flow alterations due to water withdrawals and reservoirs. Hydrol Earth Syst Sci 13:2413–2432. doi:10.5194/hess-13-2413-2009

Döll P, Hoffmann-Dobrev H, Portmann FT, Siebert S, Eicker A, Rodell M, Strassberg G, Scanlon B (2012) Impact of water withdrawals from groundwater and surface water on continental water storage variations. J Geodyn 59–60:143–156. doi:10.1016/j.jog.2011.05.001

Döll P, Fritsche M, Eicker A, Müller Schmied H (2014a) Seasonal water storage variations as impacted by water abstractions: comparing the output of a global hydrological model with GRACE and GPS observations. Surv Geophys 35(6):1311–1331. doi:10.1007/s10712-014-9282-2

Döll P, Müller Schmied H, Schuh C, Portmann F, Eicker A (2014b) Global-scale assessment of groundwater depletion and related groundwater abstractions: combining hydrological modeling with information from well observations and GRACE satellites. Water Resour Res 50:5698–5720. doi:10.1002/2014WR015595

Döll P, Jiménez Cisneros B, Oki T, Arnell NW, Benito G, Cogley JG, Jiang T, Kundzewicz ZW, Mwakalila S, Nishijima A (2015) Integrating risks of climate change into water management. J Hydrol Sci 60(1):3–14. doi:10.1080/02626667.2014.967250

Douville H, Decharme B, Ribes A, Alkama R, Sheffield J (2012) Anthropogenic influence on multi-decadal changes in reconstructed global evapotranspiration. Nat Clim Change. doi:10.1038/NCLIMATE1632

Douville H, Voldoire A, Geoffroy O (2015) The recent global warming hiatus: What is the role of Pacific variability? Geophys Res Lett. doi:10.1002/2014GL062775

Duethmann D, Peters J, Blume T, Vorogushyn S, Güntner A (2014) The value of satellite-derived snow cover images for calibrating a hydrological model in snow-dominated catchments in Central Asia. Water Resour Res 50(3):2002–2021. doi:10.1002/2013WR014382

Eicker A, Schumacher M, Kusche J, Döll P, Müller Schmied H (2014) Calibration/data assimilation approach for integrating GRACE data into the WaterGAP Global Hydrology Model (WGHM) using an ensemble Kalman filter: first results. Surv Geophys 35(6):1285–1309. doi:10.1007/s10712-014-9309-8

Elliott J, Deryng D, Müller C, Frieler K, Konzmann M, Gerten D, Glotter M, Flörke M, Wada Y, Eisner S, Folberth C, Foster I, Gosling SN, Haddeland I, Khabarov N, Ludwig F, Masaki Y, Olin S, Rosenzweig C, Ruane AC, Satoh Y, Schmid E, Stacke T, Tang Q, Wisser D (2014) Constraints and potentials of future irrigation water availability on agricultural production under climate change. Proc Natl Acad Sci USA 111(9):3239–3244. doi:10.1073/pnas.1222474110

Fan Y, Miguez-Macho G, Weaver CP, Walko R, Robock A (2007) Incorporating water table dynamics in climate modeling: 1. Water table observations and equilibrium water table simulations. J Geophys Res Atmos 112:D10125. doi:10.1029/2006JD008111

Fan Y, Li H, Miguez-Macho G (2013) Global patterns of groundwater table depth. Science 339:940–943. doi:10.1126/science.1229881

Flörke M, Kynast E, Bärlund I, Eisner S, Wimmer F, Alcamo J (2013) Domestic and industrial water uses of the past 60 years as a mirror of socio-economic development: a global simulation study. Global Environ Change 23:144–156. doi:10.1016/j.gloenvcha.2012.10.018

Gedney N, Cox PM, Betts RA, Boucher O, Huntingford C, Stott PA (2006) Detection of a direct carbon dioxide effect in continental river runoff records. Nature 439:835–838. doi:10.1038/nature04504

Gedney N, Huntingford C, Weedon GP, Bellouin N, Boucher O, Cox PM (2014) Detection of solar dimming and brightening effects on Northern Hemisphere river flow. Nature Geosci 7:796–800. doi:10.1038/ngeo2263

Gerten D, Betts R, Döll P (2014) Cross-chapter box on the active role of vegetation in altering water flows under climate change. In: Field CB, Barros VR, Dokken DJ, Mach KJ, Mastrandrea MD, Bilir TE, Chatterjee M, Ebi KL, Estrada YO, Genova RC, Girma B, Kissel ES, Levy AN, MacCracken S, Mastrandrea PR, White LL (eds) Climate Change 2014: impacts, adaptation, and vulnerability. Part A: global and sectoral aspects. Contribution of working group II to the 5th assessment report of the intergovernmental panel on climate change. Cambridge University Press, Cambridge, pp 157–161

Gleeson T, Moosdorf N, Hartmann J, van Beek LPH (2014) A glimpse beneath earth's surface: gLobal HYdrogeological MaPS (GLHYMPS) of permeability and porosity. Geophys Res Lett 41:3891–3898. doi:10.1002/2014GL059856

Gosling SN, Taylor RG, Arnell NW, Todd MC (2011) A comparative analysis of projected impacts of climate change on river runoff from global and catchment-scale hydrological models. Hydrol Earth Syst Sci 15:279–294. doi:10.5194/hess-15-279-2011

Gudmundsson L, Tallaksen LM, Stahl K, Clark DB, Dumont E, Hagemann S, Bertrand N, Gerten D, Heinke J, Hanasaki N, Voss F, Koirala S (2012) Comparing large-scale hydrological model simulations to observed runoff percentiles in Europe. J Hydrometeorol 13(2):604–620. doi:10.1175/JHM-D-11-083.1

Güntner A (2008) Improvement of global hydrological models using GRACE data. Surv Geophys 29(4):375–397. doi:10.1007/s10712-008-9038-y

Guo Z, Dirmeyer PA, Hu Z-Z, Gao X, Zhao M (2006) Evaluation of the Second Global Soil Wetness Project soil moisture simulations: 2. Sensitivity to external meteorological forcing. J Geophys Res 111(D22):D22S03. doi:10.1029/2006JD007845

Gupta HV, Bastidas LA, Sorooshian S, Shuttleworth WJ, Yang ZL (1999) Parameter estimation of a land surface scheme using multicriteria methods. J Geophys Res 104(D16):491–503. doi:10.1029/1999JD900154

Haddeland I, Clark DB, Franssen W, Ludwig F, Voß F, Arnell NW, Bertrand N, Best M, Folwell S, Gerten D, Gomes S, Gosling SN, Hagemann S, Hanasaki N, Harding R, Heinke J, Kabat P, Koirala S, Oki T, Polcher J, Stacke T, Viterbo P, Weedon GP, Yeh P (2011) Multi-model estimate of the global terrestrial water balance: setup and first results. J Hydrometeorol 12:869–884. doi:10.1175/2011JHM1324.1

Haddeland I, Heinke J, Voß F, Eisner S, Chen C, Hagemann S, Ludwig F (2012) Effects of climate model radiation, humidity and wind estimates on hydrological simulations. Hydrol Earth Syst Sci 16:305–318. doi:10.5194/hess-16-305-2012

Haddeland I, Heinke J, Biemans H, Eisner S, Flörke M, Hanasaki N, Konzmann M, Ludwig F, Masaki Y, Schewe J, Stacke T, Tessler Z, Wada Y, Wisser D (2014) Global water resources affected by human interventions and climate change. Proc Natl Acad Sci USA 111(9):3251–3256. doi:10.1073/pnas.1302078110

Hagemann S, Chen C, Haerter JO, Heinke J, Gerten D, Piani C (2011) Impact of a statistical bias correction on the projected hydrological changes obtained from three GCMs and two hydrology models. J Hydrometeorol 12(4):556–578. doi:10.1175/2011JHM1336.1

Hagemann S, Chen C, Clark DB, Folwell S, Gosling SN, Haddeland I, Hanasaki N, Heinke J, Ludwig F, Voss F, Wiltshire AJ (2013) Climate change impact on available water resources obtained using multiple global climate and hydrology models. Earth Syst Dynam 4:129–144. doi:10.5194/esd-4-129-2013

Hanasaki N, Kanae S, Oki T, Masuda K, Motoya K, Shirakawa N, Shen Y, Tanaka K (2008) An integrated model for the assessment of global water resources—part 2: applications and assessments. Hydrol Earth Syst Sci 12(4):1027–1037. doi:10.5194/hess-12-1027-2008

Harris I, Jones PD, Osborn TJ, Lister DH (2014) Updated high-resolution grids of monthly climatic observations—the CRU TS3.10 dataset. Int J Climatol 34(3):623–642. doi:10.1002/joc.3711

Hartmann J, Moosdorf N (2012) The new global lithological map database GLiM: a representation of rock properties at the Earth surface. Geochem Geophys Geosyst 13:Q12004. doi:10.1029/2012GC004370

Hawkins E, Sutton R (2011) The potential to narrow uncertainty in projections of regional precipitation change. Clim Dyn 37:407–418. doi:10.1007/s00382-010-0810-6

Hoekstra AY, Mekonnen MM (2011) Global water scarcity: monthly blue water footprint compared to blue water availability for the world's major river basins. Value of Water Research Report Series No. 53. UNESCO-IHE Institute for Water Education. Delft, The Netherlands

Houborg R, Rodell M, Li BL, Reichle R, Zaitchik BF (2012) Drought indicators based on model-assimilated Gravity Recovery and Climate Experiment (GRACE) terrestrial water storage observations. Water Resour Res 48:W07525. doi:10.1029/2011WR011291

Hunger M, Döll P (2008) Value of river discharge data for global-scale hydrological modeling. Hydrol Earth Syst Sci 12(3):841–861. doi:10.5194/hess-12-841-2008

Jägermeyr J, Gerten D, Heinke J, Schaphoff S, Kummu M, Lucht W (2015) Water savings potentials of irrigation systems: global simulation of processes and linkages. Hydrol Earth Syst Sci 19:3073–3091. doi:10.5194/hess-19-3073-2015

Jiménez C, Prigent C, Mueller B, Seneviratne SI, McCabe MF, Wood EF, Rossow WB, Balsamo G, Betts AK, Dirmeyer PA, Fisher JB, Jung M, Kanamitsu M, Reichle RH, Reichstein M, Rodell M, Sheffield J, Tu K, Wang K (2011) Global intercomparison of 12 land surface heat flux estimates. J Geophys Res. doi:10.1029/2010JD014545

Jiménez Cisneros BE, Oki T, Arnell NW, Benito G, Cogley JG, Döll P, Jiang T, Mwakalila SS (2014) Freshwater resources. In: Field CB, Barros VR, Dokken DJ, Mach KJ, Mastrandrea MD, Bilir TE, Chatterjee M, Ebi KL, Estrada YO, Genova RC, Girma B, Kissel ES, Levy AN, MacCracken S, Mastrandrea PR, White LL (eds). Climate Change 2014: impacts, adaptation, and vulnerability. Part a: global and sectoral aspects. Contribution of working group II to the fifth assessment report of the intergovernmental panel on climate change. Cambridge University Press, Cambridge, pp 229–269

Joetzjer E, Delire C, Douville H, Ciais P, Decharme B, Fisher R, Christoffersen B, Calvet JC, da Costa ACL, Ferreira LV, Meir P (2014) Predicting the response of the Amazon rainforest to persistent drought conditions under current and future climates: a major challenge for global land surface models. Geosci Model Dev 7:2933–2950. doi:10.5194/gmd-7-2933-2014

Jones JP, Sudicky EA, McLaren RG (2008) Application of a fully-integrated surface-subsurface flow model at the watershed-scale: a case study. Water Resour Res 44:W03407. doi:10.1029/2006wr005603

Jung M, Reichstein M, Ciais P, Seneviratne SI, Sheffield J, Goulden ML, Bonan G, Cescatti A, Chen J, de Jeu R, Dolman AJ, Eugster W, Gerten D, Gianelle D, Gobron N, Heinke J, Kimball J, Law BE, Montagnani L, Mu Q, Mueller B, Oleson K, Papale D, Richardson AD, Roupsard O, Running S, Tomelleri E, Viovy N, Weber U, Williams C, Wood E, Zaehle S, Zhang K (2010) Recent decline in the global land evapotranspiration trend due to limited moisture supply. Nature 467:951–954. doi:10.1038/nature09396

Jung M, Reichstein M, Margolis HA, Cescatti A, Richardson AD, Arain MA, Arneth A, Bernhofer C, Bonal D, Chen J, Gianelle D, Gobron N, Kiely G, Kutsch W, Lasslop G, Law BE, Lindroth A, Merbold L, Montagnani L, Moors EJ, Papale D, Sottocornola M, Vaccari F, Williams C (2011) Global patterns of land-atmosphere fluxes of carbon dioxide, latent heat, and sensible heat derived from eddy covariance, satellite, and meteorological observations. J Geophys Res Biogeosci 116(G3):2156–2202. doi:10.1029/2010JG001566

Kiguchi M, Shen Y, Kanae S, Oki T (2015) Re-evaluation of future water stress due to socio-economic and climate factors under a warming climate. Hydrol Sci J 60(1–2):14–29. doi:10.1080/02626667.2014.888067

Knutti R, Sedlacek J (2013) Robustness and uncertainties in the new CMIP5 climate model projections. Nat Clim Change 3:369–373. doi:10.1038/nclimate1716

Kollet SJ, Maxwell RM (2008) Capturing the influence of groundwater dynamics on land surface processes using an integrated, distributed watershed model. Water Resour Res 44:W02402. doi:10.1029/2007WR006004

Krakauer NY, Li H, Fan Y (2014) Groundwater flow across spatial scales: importance for climate modeling. Environ Res Lett 9:034003. doi:10.1088/1748-9326/9/3/034003

Krogh PE (2011) Large scale hydrological model calibration with remote sensing data from GRACE. PhD thesis, DTU space, National Space Institute, Technical University of Denmark, Copenhagen

Lahoz WA, De Lannoy GJM (2014) Closing the gaps in our knowledge of the hydrological cycle over land: conceptual problems. Surv Geophys 35(3):623–660. doi:10.1007/s10712-013-9221-7

Larson KM, Small EE, Gutmann ED, Bilich AL, Braun JJ, Zavorotny VU (2008) Use of GPS receivers as a soil moisture network for water cycle studies. Geophys Res Lett 35(24):L24405. doi:10.1029/2008GL036013

Li BL, Rodell M, Zaitchik BF, Reichle RH, Koster RD, van Dam TM (2012) Assimilation of GRACE terrestrial water storage into a land surface model: evaluation and potential value for drought monitoring in western and central Europe. J Hydrol 446:103–115. doi:10.1175/2007JHM951.1

Livneh B, Lettenmaier DP (2012) Multi-criteria parameter estimation for the Unified Land Model. Hydrol Earth Syst Sci 16(8):3029–3048. doi:10.5194/hess-16-3029-2012

Maxwell RM, Chow FK, Kollet SJ (2007) The groundwater-land-surface-atmosphere connection: soil moisture effects on the atmospheric boundary layer in fully-coupled simulations. Adv Water Resour 30:2447–2466. doi:10.1016/j.advwatres.2007.05.018

Maxwell RM, Condon LE, Kollet SJ (2015) A high-resolution simulation of groundwater and surface water over most of the continental US with the integrated hydrologic model ParFlow v3. Geosci Model Dev 8:923–937. doi:10.5194/gmd-8-923-2015

Miguez-Macho G, Fan Y, Weaver CP, Walko R, Robock A (2007) Incorporating water table dynamics in climate modeling: 2. Formulation, validation, and soil moisture simulation. J Geophys Res Atmos 112:D13108. doi:10.1029/2006JD008112

Milzow C, Krogh PE, Bauer-Gottwein P (2011) Combining satellite radar altimetry, SAR surface soil moisture and GRACE total storage changes for hydrological model calibration in a large poorly gauged catchment. Hydrol Earth Syst Sci 15(6):1729–1743. doi:10.5194/hess-15-1729-2011

Müller Schmied H, Eisner S, Franz D, Wattenbach M, Portmann FT, Flörke M, Döll P (2014) Sensitivity of simulated global-scale freshwater fluxes and storages to input data, hydrological model structure, human water use and calibration. Hydrol Earth Syst Sci 18:3511–3538. doi:10.5194/hess-18-3511-2014

Murray SJ, Foster PN, Prentice IC (2012) Future global water resources with respect to climate change and water withdrawals as estimated by a dynamic global vegetation model. J Hydrol 448–449:14–29. doi:10.1016/j.jhydrol.2012.02.044

Nasonova ON, Gusev YM, Kovalev YE (2011) Impact of uncertainties in meteorological forcing data and land surface parameters on global estimates of terrestrial water balance components. Hydrol Process 25(7):1074–1090. doi:10.1002/hyp.7651

Niu GY, Yang ZL, Dickinson RE, Gulden LE (2007) Su H (2007) Development of a simple groundwater model for use in climate models and evaluation with Gravity Recovery and Climate Experiment data. J Geophys Res 112:D07103. doi:10.1029/2006JD007522

Pall P, Aina T, Stone DA, Stott PA, Nozawa T, Hilberts AGJ, Lohmann D, Allen MR (2011) Anthropogenic greenhouse gas contribution to flood risk in England and Wales in autumn 2000. Nature 470(7334):382–385. doi:10.1038/nature09762

Papa F, Frappart F, Güntner A, Prigent C, Aires F, Getirana ACV, Maurer R (2013) Surface freshwater storage and variability in the Amazon basin from multi-satellite observations, 1993–2007. J Geophys Res Atmos 118(21):11951–11965. doi:10.1002/2013JD020500

Parajka J, Blöschl G (2008) The value of MODIS snow cover data in validating and calibrating conceptual hydrologic models. J Hydrol 358(3–4):240–258. doi:10.1016/j.jhydrol.2008.06.006

Portmann F, Siebert S, Döll P (2010) MIRCA2000—global monthly irrigated and rainfed crop areas around the year 2000: a new high resolution data set for agricultural and hydrological modelling. Global Biogeochem Cy 24:GB1011. doi:10.1029/2008GB003435

Reichle RH, De Lannoy GJM, Forman BA, Draper CS, Liu Q (2014) Connecting satellite observations with water cycle variables through land data assimilation: examples using the NASA GEOS-5 LDAS. Surv Geophys 35(3):577–606. doi:10.1007/s10712-013-9220-8

Renzullo LJ, van Dijk AIJM, Perraud JM, Collins D, Henderson B, Jin H, Smith AB, McJannet DL (2014) Continental satellite soil moisture data assimilation improves root-zone moisture analysis for water resources assessment. J Hydrol 519:2747–2762. doi:10.1016/j.jhydrol.2014.08.008

Rost S, Gerten D, Bondeau A, Lucht W, Rohwer J, Schaphoff S (2008) Agricultural green and blue water consumption and its influence on the global water system. Water Resour Res 44:W09405. doi:10.1029/2007WR006331

Samaniego L, Kumar R, Attinger S (2010) Multiscale parameter regionalization of a grid-based hydrologic model at the mesoscale. Water Resour Res 46:W05523. doi:10.1029/2008WR007327

Schewe J, Heinke J, Gerten D, Haddeland I, Arnell NW, Clark DB, Dankers R, Eisner S, Fekete BM, Colon-Gonzalez FJ, Gosling SN, Kim H, Liu X, Masaki Y, Portmann FT, Satoh Y, Stacke T, Tang Q, Wada Y, Wisser D, Albrecht T, Frieler K, Piontek F, Warszawski L, Kabat P (2014) Multimodel assessment of water scarcity under climate change. Proc Natl Acad Sci USA 111(9):3245–3250. doi:10.1073/pnas.1222460110

Schneider U, Becker A, Finger P, Meyer-Christoffer A, Ziese M, Rudolf B (2014) GPCC's new land surface precipitation climatology based on quality-controlled in situ data and its role in quantifying the global water cycle. Theor Appl Climatol 115:15–40. doi:10.1007/s00704-013-0860-x

Sheffield J, Goteti G, Wood EF (2006) Development of a 50-year high-resolution global dataset of meteorological forcings for land surface modeling. J Clim 19:3088–3111. doi:10.1175/JCLI3790.1

Siebert S, Döll P (2010) Quantifying blue and green water uses and virtual water contents in global crop production as well as potential production losses without irrigation. J Hydrol 384:198–217. doi:10.1016/j.jhydrol.2009.07.031

Sitch S, Huntingford C, Gedney N, Levy PE, Lomas M, Piao SL, Betts R, Ciais P, Cox P, Friedlingstein P, Jones CD, Prentice IC, Woodward FI (2008) Evaluation of the terrestrial carbon cycle, future plant geography and climate-carbon cycle feedbacks using five dynamic global vegetation models (DGVMs). Global Change Biol 14:2015–2039. doi:10.1111/j.1365-2486.2008.01626.x

Sood A, Smakhtin V (2015) Global hydrological models: a review. Hydrol Sci J. doi:10.1080/02626667.2014.950580

Sterling SM, Ducharne A, Polcher J (2013) The impact of global land-cover change on the terrestrial water cycle. Nat Clim Change 3:385–390. doi:10.1038/nclimate1690

Tapley BD, Bettadpur S, Watkins M, Reigber C (2004) The gravity recovery and climate experiment: mission overview and early results. Geophys Res Lett 31:L09607. doi:10.1029/2004GL019920

Taylor RG, Scanlon B, Döll P, Rodell M, van Beek R, Wada Y, Longuevergne L, Leblanc M, Famiglietti JS, Edmunds M, Konikow L, Green TR, Chen J, Taniguchi M, Bierkens MFP, MacDonald A, Fan Y, Maxwell RM, Yechieli Y, Gurdak JJ, Allen DM, Shamsudduha M, Hiscock K, Yeh PJF, Holman I, Treidel H (2013) Ground water and climate change. Nat Clim Change 3:322–329. doi:10.1038/nclimate1744

van Dijk AIJM, Renzullo LJ, Wada Y, Tregoning P (2014) A global water cycle reanalysis (2003–2012) merging satellite gravimetry and altimetry observations with a hydrological multi-model ensemble. Hydrol Earth Syst Sci 18:2955–2973. doi:10.5194/hess-18-2955-2014

Vassolo S, Döll P (2005) Global-scale gridded estimates of thermoelectric power and manufacturing water use. Wat Resour Res 41:W04010. doi:10.1029/2004WR003360

Vergnes J-P, Decharme B, Alkama R, Martin E, Habets F, Douville H (2012) A simple groundwater scheme for hydrological and climate applications: description and off-line evaluation over France. J Hydrometeorol 13:1149–1171. doi:10.1175/JHM-D-11-0149

Vergnes J-P, Decharme B, Habets F (2014) Introduction of groundwater capillary rises using subgrid spatial variability of topography into the ISBA land surface model. J Geophys Res Atmos 119:11065–11086. doi:10.1002/2014JD021573

Vörösmarty CJ, Sahagian D (2000) Anthropogenic disturbance of the terrestrial water cycle. Bioscience 50(9):753–765. doi:10.1641/0006-3568(2000)050[0753:ADOTTW]2.0.CO;2

Vörösmarty CJ, Hoekstra AY, Bunn SE, Conway D, Gupta J (2015) Fresh water goes global. Science 349(6247):478–479. doi:10.1126/science.aac6009

Wada Y, van Beek LPH, Bierkens MFP (2011) Modelling global water stress of the recent past: on the relative importance of trends in water demand and climate variability. Hydrol Earth Syst Sci 15:3785–3808. doi:10.5194/hess-15-3785-2011

Wada Y, van Beek LPH, Bierkens MFP (2012) Nonsustainable groundwater sustaining irrigation: a global assessment. Water Resour Res 48:W00L06. doi:10.1029/2011WR010562

Wada Y, Wisser D, Eisner S, Flörke M, Gerten D, Haddeland I, Hanasaki N, Masaki Y, Portmann FT, Stacke T, Tessler Z, Schewe J (2013) Multi-model projections and uncertainties of irrigation water demand under climate change. Geophys Res Lett 40:4626–4632. doi:10.1002/grl.50686

Wada Y, Wisser D, Bierkens MFP (2014) Global modeling of withdrawal, allocation and consumptive use of surface water and groundwater resources. Earth Syst Dynam 5:15–40. doi:10.5194/esd-5-15-2014

Wang K, Dickinson ED, Wild M, Liang S (2010) Evidence for decadal variation in global terrestrial evapotranspiration between 1982 and 2002: 2. Results. J Geophys Res 115:D20113. doi:10.1029/2009JD013671

Warszawski L, Friend A, Ostberg S, Frieler K, Lucht W, Schaphoff S, Beerling D, Cadule P, Ciais P, Clark DB, Kahana R, Ito A, Keribin R, Kleidon A, Lomas M, Nishina K, Pavlick R, Rademacher TT, Buechner M, Piontek F, Schewe J, Serdeczny O, Schellnhuber HJ (2013) A multi-model analysis of risk of ecosystem shifts under climate change. Environ Res Lett 8:044018. doi:10.1088/1748-9326/8/4/044018

Weedon GP, Balsamo G, Bellouin N, Gomes S, Best M, Viterbo P (2014) The WFDEI meteorological forcing data set: WATCH forcing data methodology applied to ERA-interim reanalysis data. Water Resour Res 50(9):7505–7514. doi:10.1002/2014WR015638

Werth S, Güntner A (2010) Calibration analysis for water storage variability of the global hydrological model WGHM. Hydrol Earth Syst Sci 14(1):59–78. doi:10.5194/hess-14-59-2010

Werth S, Güntner A, Schmidt R, Petrovic S (2009) Integration of GRACE mass variations into a global hydrological model. Earth Planet Sci Lett 277:166–173. doi:10.1016/j.epsl.2008.10.021

Widén-Nilsson E, Halldin S, Xu C (2007) Global water-balance modelling with WASMOD-M: parameter estimation and regionalization. J Hydrol 340:105–118. doi:10.1016/j.jhydrol.2007.04.002

Wisser D, Frolking S, Douglas EM, Fekete BM, Vörösmarty CJ, Schumann AH (2008) Global irrigation water demand: variability and uncertainties arising from agricultural and climate data sets. Geophys Res Lett 35(24):L24408. doi:10.1029/2008GL035296

Wood E, Roundy JK, Troy TJ, van Beek R, Bierkens M, Blyth E, de Roo A, Döll P, Ek M, Famiglietti J, Gochis D, van de Giesen N, Houser P, Jaffe P, Kollet S, Lehner B, Lettenmaier DP, Peters-Lidard C, Sivapalan M, Sheffield J, Wade A, Whitehead P (2011) Hyper-resolution global land surface modeling: meeting a grand challenge for monitoring Earth's terrestrial water. Water Resour Res 47:W05301. doi:10.1029/2010WR010090

Wood E, Roundy JK, Troy TJ, van Beek R, Bierkens M, Blyth E, de Roo A, Döll P, Ek M, Famiglietti J, Gochis D, van de Giesen N, Houser P, Jaffe P, Kollet S, Lehner B, Lettenmaier DP, Peters-Lidard C., Sivapalan M, Sheffield J, Wade A, Whitehead P (2012) Reply to comment by Keith J. Beven and Hannah L. Cloke on "Hyperresolution global land surface modeling: meeting a grand challenge for monitoring Earth's terrestrial water". Water Resour Res 48:W01802. doi:10.1029/2011WR011202

Xie H, Longuevergne L, Ringler C, Scanlon BR (2012) Calibration and evaluation of a semi-distributed watershed model of Sub-Saharan Africa using GRACE data. Hydrol Earth Syst Sci 16(9):3083–3099. doi:10.5194/hess-16-3083-2012

Zaitchik BF, Rodell M, Reichle RH (2008) Assimilation of GRACE terrestrial water storage data into a land surface model: results for the Mississippi River basin. J Hydrometeorol 9(3):535–548. doi:10.1175/2007JHM951.1

Zhou T, Haddeland I, Nijssen B, Lettenmaier DP (2015) Human induced changes in the global water cycle. AGU Geophysical Monograph Series, Submitted

DOI 10.1007/978-3-319-32449-4_3
Reprinted from *Surveys in Geophysics* Journal, DOI 10.1007/s10712-016-9366-2

# On the Use of Hydrological Models and Satellite Data to Study the Water Budget of River Basins Affected by Human Activities: Examples from the Garonne Basin of France

**Eric Martin[1,2] · Simon Gascoin[3] · Youen Grusson[4,5] · Clément Murgue[6,7,8] · Mélanie Bardeau[10] · François Anctil[5] · Sylvain Ferrant[3] · Romain Lardy[6,7,9] · Patrick Le Moigne[1] · Delphine Leenhardt[6,7] · Vincent Rivalland[3] · José-Miguel Sánchez Pérez[4] · Sabine Sauvage[4] · Olivier Therond[6,7]**

Received: 29 April 2015 / Accepted: 28 January 2016 / Published online: 24 February 2016


**Abstract** Natural and anthropogenic forcing factors and their changes significantly impact water resources in many river basins around the world. Information on such changes can be derived from fine scale in situ and satellite observations, used in combination with hydrological models. The latter need to account for hydrological changes caused by human activities to correctly estimate the actual water resource. In this study, we consider the catchment area of the Garonne river (in France) to investigate the capabilities of space-based observations and up-to-date hydrological modeling in estimating water resources of a river basin modified by human activities and a changing climate. Using the

✉ Eric Martin
Eric.Martin@irstea.fr

✉ Olivier Therond
olivier.therond@toulouse.inra.fr

1 CNRM-GAME (Météo-France, CNRS), 42 avenue Coriolis, 31057 Toulouse, France

2 UR RECOVER, IRSTEA, 3275 route de Cézanne, 13182 Aix-en-Provence Cedex 5, France

3 UPS/CNRS/IRD/CNES, Centre d'Études Spatiales de la Biosphère (CESBIO), 18 avenue E. Belin bpi 2801, 31401 Toulouse, France

4 INPT, UPS, Laboratoire Ecologie Fonctionnelle et Environnement (EcoLab), University of Toulouse, Avenue de l'Agrobiopole, 31326 Castanet Tolosan Cedex, France

5 Chaire de recherche EDS en previsions et actions hydrologiques, Department of Civil and Water Engineering, Université Laval, Québec G1V 0A6, Canada

6 UMR AGIR, INRA, BP 52627, 31326 Castanet Tolosan, France

7 UMR AGIR, INP Toulouse, BP 52627, 31326 Castanet Tolosan, France

8 CACG, BP 449, 65004 Tarbes, France

9 ARVALIS - Institut du Végétal, 3 rue Joseph et Marie Hackin, 75016 Paris, France

10 BRGM, 3 Rue Marie Curie, 31520 Ramonville-Saint-Agne, France

ISBA–MODCOU and SWAT hydrological models, we find that the water resources of the Garonne basin display a negative climate trend since 1960. The snow component of the two models is validated using the moderate-resolution imaging spectroradiometer snow cover extent climatology. Crop sowing dates based on remote sensing studies are also considered in the validation procedure. Use of this dataset improves the simulated evapotranspiration and river discharge amounts when compared to conventional data. Finally, we investigate the benefit of using the MAELIA multi-agent model that accounts for a realistic agricultural and management scenario. Among other results, we find that changes in crop systems have significant impacts on water uptake for agriculture. This work constitutes a basis for the construction of a future modeling framework of the sociological and hydrological system of the Garonne river region.

**Keywords** Modeling · Hydrology · Agriculture · Anthropogenic changes · Sociological and hydrological system · Remote sensing

## 1 Introduction

Human-induced land use changes are now widespread over the planet. The primary objectives of land use are to satisfy immediate human needs (Foley et al. 2005). Agriculture and urbanization are important drivers of these changes. The hydrological cycle has been transformed in many places to provide freshwater for irrigation, domestic uses and industry (Vörösmarty et al. 2000). The number of dams along rivers and associated reservoirs has rapidly increased over recent decades (Lehner et al. 2011). Groundwater resources are being extensively used in regions with large aquifers and frequent water stresses (Wada et al. 2010). As a consequence, water fluxes, including evapotranspiration, are modified in many regions of the world (Asokan and Destouni 2014). Depending on the region and the hydrological variable considered, the signal can be dominated by climatic variability and trends or human activities (Vörösmarty et al. 2000; Moss et al. 2010). In south India, for instance, irrigation relies totally on groundwater extraction. The imbalance between recharge and extraction leads to local groundwater depletion and hence water scarcity episodes that depend on local settings, e.g., small surface reservoir capacity maintained by farmers to catch monsoon runoff, aquifer capacity to store this recharge, and irrigated area extent that conditions the water demand (Perrin et al. 2012).

These water scarcity episodes are expected to increase due to dry climatic extremes projected for the Garonne region in the future (Ferrant et al. 2014b). In the Upper Mississippi basin, climate change is the dominant driver of runoff changes over the twentieth century, while land use changes (e.g., in forested areas, grasslands and croplands) can influence the river runoff locally (Frans et al. 2013). The impact of irrigation on local climate varies according to climatic zones and the degree of anthropization (Lobell et al. 2009; Destouni et al. 2013). For example, Grouillet et al. (2015) found that, by 2050, in two Mediterranean catchments (Herault in France and Ebro in Spain) anthropogenic impacts on water demand will dominate the impacts due to climate change.

Explicitly taking into account direct human forcing in hydrological modeling is now a recognized need in order to correctly simulate hydrological evolution of highly anthropized basins. Some models already attempt to do this as is the case, for example, of the global-scale WaterGAP model (Alcamo et al. 2003). This consists of the WaterGAP Global

Hydrology Model (Döll et al. 2003) and five water use models for irrigation, livestock, household, manufacturing and cooling of thermal power plants. This type of model is highly relevant for simulating large scale hydrological patterns, e.g., groundwater depletion (Döll et al. 2014). This type of approach is also implemented at the scale of individual catchments smaller than the typical catchments simulated by WaterGAP (Grouillet et al. 2015). The main limitations for small scale applications are the level of details needed to reproduce human processes and the availability of databases.

Nowadays there is a growing interest to better account for the coevolutionary dynamics of coupled water–human systems. Sivapalan et al. (2012) introduced the concept of socio-hydrology, a new science coupling people and water resources, to highlight the need to study the coupled human–water system using an interdisciplinary approach. Preliminary attempts in this direction have been able to explain the multiples changes that occurred over the Murrumbidgee river basin in Australia during the twentieth century (Kandasamy et al. 2014). In this example, the underlying modeling framework (van Emmerik et al. 2014) is composed of five subsystems (hydrology, population, irrigation, ecology and environmental awareness) that non-linearly interact and have two external drivers—climate and socioeconomic. The model results highlight the competition between human productive and environmental restorative forces that lead to a so-called pendulum swing between agricultural development and environmental health. Due to oversimplifications, the model cannot describe the precise evolution of the system, but contains enough key elements to describe it. Another approach to describe a socio-hydrology system is to use agent-based models able to handle multiple interactions between numerous agents (Gaudou et al. 2014; Therond et al. 2014). The main advantage of this new approach is a greater flexibility in simulating individual processes and their interactions. However, it is quite complex and sensitive to small variations in the parameterization of the interaction rules between agents.

Accounting for both climatic and anthropogenic changes remains a challenge for hydrological models. While in situ and space-based hydrological measurements are able to provide information on human-induced changes, a large number of hydrological models do not simulate all the components of these changes and only account for the corresponding processes indirectly.

Satellite observations are able to document fine scale processes with a high spatiotemporal resolution. For example, Formosat-2, launched in 2004, is able to observe vegetation development at a high spatial resolution ($\sim$10 m) with a frequent revisit time (few days). This allows the detection of biophysical variables such as the leaf area index (LAI) for selected areas (Courault et al. 2010; Claverie 2012). The Sentinel-2 mission provides similar observations at the global scale. The Surface Water and Ocean Topography (SWOT) mission (whose launch is planned for 2020) is a swath-mapping radar interferometer designed to measure temporal changes in surface water elevation (lakes, reservoirs and river channels) with a quasi-global coverage between 78°S and 78°N (Durand et al. 2014; Biancamaria et al. 2015, see also https://swot.jpl.nasa.gov). Concerning rivers, the basic SWOT measurements will consist of river water surface elevation, slope and width at a very fine scale. It is anticipated that rivers wider than 100 m and lake or reservoir areas larger than 250 $\times$ 250 m will be observed with good accuracy. The SWOT revisit time depends on longitude: It is about 4 days at midlatitudes. In anthropized basins, river gauges' networks are usually relatively dense, but SWOT may be used to estimate flows between gauges or measure the water volumes of man-made reservoirs. Such data are usually not easily available, unless in situ networks depend on public bodies.

On the modeling side, several human processes need to be taken into account. Large alpine dams modify water regimes; other dams may be used to sustain low flows. In general, only a

small number of large reservoirs are involved and the associated processes may be taken into account relatively easily, if data are available. Irrigation is a critical process. Models should be able to account for the balance between crop water demand and resource availability (from groundwater, reservoirs and rivers, Döll et al. 2012; Perrin et al. 2012; Ferrant et al. 2014b). For instance, two major opposing effects of irrigation on aquifer dynamics may be identified: groundwater depletion in regions with primarily groundwater-fed irrigation and groundwater accumulation in regions dominated by return flows from irrigation fed by surface water (Goderniaux et al. 2009; Holman et al. 2009; Scibeck and Allen 2006; Jyrkama and Sykes 2007; Döll 2009; Gurdak and Roe 2010; Kovalevskii 2007; Green et al. 2007). The main difficulty is to account for water management practices that depend on the basin, as well as on local and national governance (Mazzega et al. 2014). The simulation of human processes requires integrated modeling tools, able to simulate spatiotemporal interactions (including feedbacks) within and between socio-ecological systems, at relevant scale, and accounting for water management and associated agricultural practices (Therond et al. 2014). Another important parameter is land use change that can lead to threshold effects (e.g., change from agriculture to forest, Donohue et al. 2007; Qiu et al. 2011; Murgue et al. 2015) or more diffuse variations (e.g., crop rotation, Parajuli et al. 2013).

The objective of this paper is to discuss some challenges in estimating the water budget of a highly anthropized basin subject to climate change. We take advantage of recent studies dedicated to the Garonne basin (a river basin that is highly modified by human activities, in France, with complex irrigation systems and frequent water management problems) to discuss how the combination of modeling, and space-based observations can be used to improve the water budget estimate. Section 2 describes the Garonne basin and its current hydrological behavior. Section 3 shows how fine scale satellite observations of snow cover and vegetation can be used to validate and calibrate the hydrological models. Section 4 presents an example of the use of a multi-agent platform developed for the Garonne basin to assess realistic crop rotation scenarios.

## 2 The Water Balance at the Scale of the Entire Garonne Basin

### 2.1 Climate and Physical Properties

The Garonne river basin (56,000 $km^2$ in total—50,000 $km^2$ at the Tonneins station—see Fig. 1) is located in southwestern France. It drains water from the northern slopes of the Pyrenees Mountains (along the French border with Spain) and the southern slopes of the Massif Central. The mean annual discharge based on 103 years of in situ data at the Tonneins gauging station is estimated to be 600 $m^3\ s^{-1}$. The main tributaries of the Garonne river are the Ariège (flowing from the Pyrénées), and the Tarn and Lot (flowing from the Massif Central). The broad range of altitudes and slopes within the Garonne watershed leads to a diversity of hydrological behaviors that can be associated with three geographic zones: the Pyrenees to the south, the Massif Central to the north east and the plain between them (Probst 1983). The Pyrenean portion of the watershed (i.e., elevated mountains—with some peaks exceeding 3000 m—above a large plain where the topography does not exceed a few hundred meters) largely influences the hydrological regime. The watershed altitudes range from 150 to 3145 m, with 44 % of the watershed below 500 m and 20 % above 1500 m.

The basin climate is influenced by oceanic conditions in its western part. It is characterized by heavy rainfall events during winter and relatively warm weather during summer.

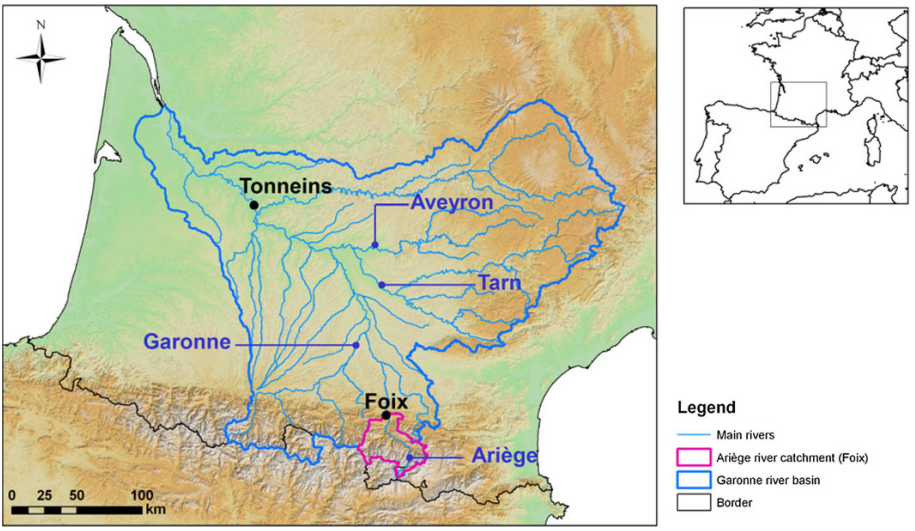


**Fig. 1** Map of the Garonne river basin, showing the main rivers and discharge stations mentioned in the paper

There is an important precipitation gradient from west to east, ranging from approximately 1200 mm year$^{-1}$ in the Atlantic coastal region to about 600 mm year$^{-1}$ 300 km to the east in the plain area. The upper Garonne and the Ariège river regimes are marked by spring snowmelt in the Pyrenees (Caballero et al. 2007), while summer flows are very low due to relatively dry conditions then.

From a geological point of view, the basin was marked by several marine invasions during the Jurassic and Cretaceous eras that led to the formation of limestone aquifers (some being heavily karstified) toward the north and the east. Some of these aquifers are exploited. More recently, the erosion of the Pyrenees, Massif Central and the Montagne Noire has led to the accumulation of a high amount of molasse substratum in the center of the basin. The hydrographic network, marked by the recent succession of glaciation and deglaciation, is composed of alluvial terraces. If the river is not deeply incised, the alluvial aquifer feeds the river during most of the time, while water is transferred to the aquifer during flooding periods. If the river is deeply incised, the aquifer only feeds the river; these aquifers are also exploited. According to the FAO soil classification on the European Soils Database map (ESDB 2006), the soil composition is dominated by different types of cambisols (65 % of the catchment).

The Garonne river flows into the Atlantic Ocean through the Gironde estuary, one of the most important estuaries in Western Europe. Due to this geographic arrangement, the hydrological influence of tides can be measured relatively far upstream. For this reason, the model domain is limited to the catchment area at the Tonneins gauge station, where there is no tidal effect.

## 2.2 Anthropization, Environmental Change due to Human Actions

Land use analyses from the Corine Land Cover (CLC2000) reveal that the plain is dominated by crops and pastures (Fig. 2). Agricultural activities cover 49 % of the watershed,

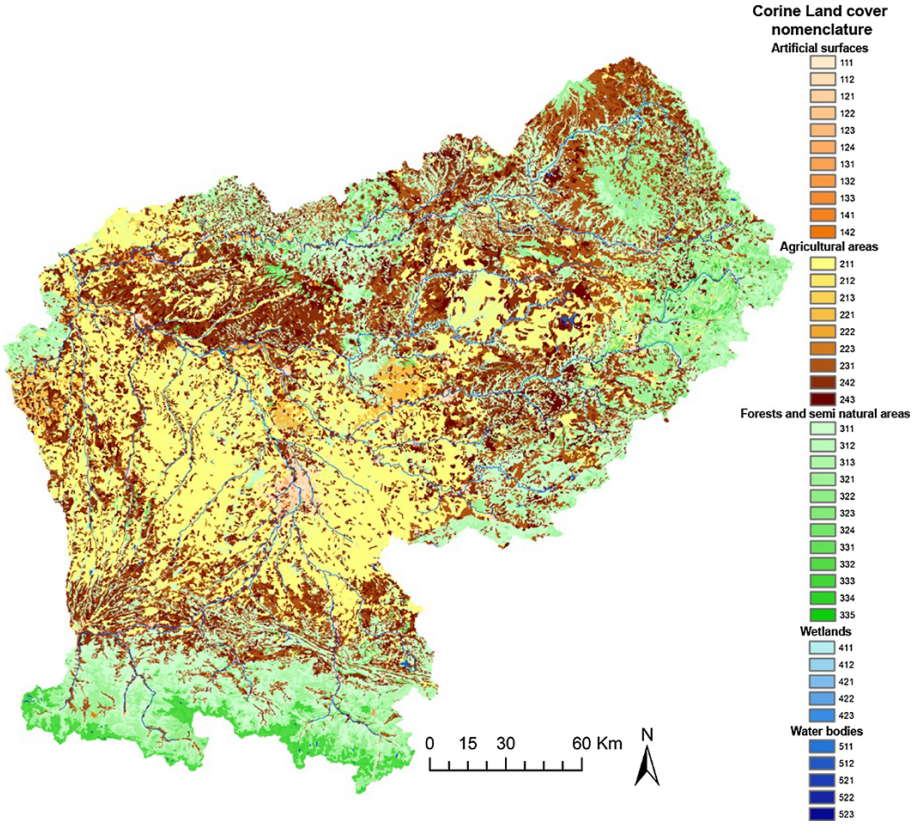


**Fig. 2** Map of the land use of the Garonne river basin. *Subclassification with numbers* corresponds to the Corine Land Cover classification http://www.eea.europa.eu/publications/COR0-landcover

while the hillsides of the Pyrenees (35 % of the watershed) are covered with forests. For altitudes above 2500 m, the vegetation is composed of alpine grassland and shrub covers. The influence of human activities is high in the basin (irrigated agriculture). The irrigated surface area became five times larger between the 1970s and the 1990s and has now stabilized at 160,000 ha (Sauquet et al. 2009). About 60 % of the irrigated surface is devoted to maize, the second main irrigated crops being sunflower and wheat. Water uptake for irrigation represents about 70 % of the total during low-flow period. Uptake comes primarily from surface waters (more that 80 %), reservoirs (8 %) and groundwater (9 %). In some areas, e.g., the plain near the confluence of the Tarn and the Garonne, groundwater uptake can reach 23 %.

At the basin scale, Sauquet et al. (2009) estimated that the total water uptake for agriculture, industry and drinking water amounted to 7 % of the discharge. Agricultural usage is dominant, especially during the summer months. Compared to other river basins in France, the Garonne basin has the largest deficit between supply and demand. Hence, regulation and management plans are implemented at the basin (or sub-basin) and departmental (administrative district) levels (Mazzega et al. 2014). At the basin level, the Master Scheme for Water Planning and Management (Mazzega et al. 2014) defines the general orientation for the management of water resources and water demands. It fixes (for

41 river gauges located in the Garonne catchment) two regulation rules: the "objective low-water flow" corresponding to the minimum flow that ensures a good functioning of the aquatic environment (and should be respected 8 years out of 10), and the "crisis flow," corresponding to the level under which the drinking water supply and the survival of aquatic species are in danger.

Low-water management plans define medium-term strategies and public policies to manage the imbalance between supply and demand. At the administrative level, departmental state services enforce water use restriction rules when they are required. Drought commissions are established when a crisis is foreseen in order to evaluate the most relevant strategy. The input data to the commission can be observations (flow, water level in reservoirs or in aquifers) or model results. In order to evaluate how much water can be withdrawn from the aquifers, hydrodynamic models of alluvial aquifers of the upper Garonne, Tarn and lower Aveyron were developed in 2009 by the French Geological Survey (BRGM) (Bardeau and Bouardaa 2010); these have been in continuous use since this date.

## 2.3 Hydrological Regime of the Garonne Basin: Trends and Variability

The mean annual air surface temperature over the basin increased by 1.1 °C from 1901 to 2000, while over this time span the precipitation decreased (with a negative trend that is barely significant, however) (Moisselin et al. 2002). Discharge trends are clearly negative, especially since the mid 1990s. Figure 3 shows the observed rainfall and snowfall based on meteorological data analyzed by the Safran system (Vidal et al. 2010), the observed discharge and the estimated pseudo-natural discharge. The pseudo-natural discharges

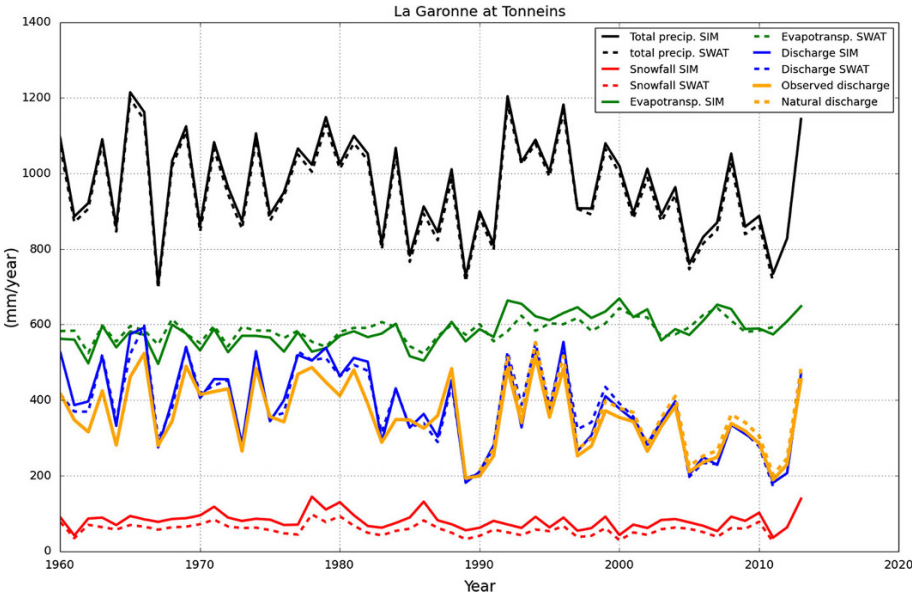


**Fig. 3** Variation in the main components of the water balance over the period 1960–2013 for the Garonne at Tonneins, as estimated by the Safran analysis system (precipitation) and the ISBA–MODCOU and SWAT models (evapotranspiration, discharge, snowfall)

estimated by Sauquet et al. (2009) over the period 1995–2005 have been extended back to 1990 (the epoch when the irrigated surface area stabilized).

Evaporation is evaluated using two hydrological models. The first model is the ISBA–MODCOU model developed at Meteo-France (SIM, Habets et al. 2008; Decharme et al. 2013). It has two components: the land surface model Interaction Soil–Biosphere–Atmosphere (ISBA) and the distributed hydrological model MODélisation COUplée (MODCOU). The mesh size is 8 km over the basin for the land surface model and varies between 0.25 and 2 km for the hydrological model. The land surface model transfers runoff from the surface and to the bottom of the hydrological model. Aquifers are only taken into account implicitly through conceptual transfer reservoirs (Artinyan et al. 2008).

The second model considered in this study is the SWAT model (Soil and Water Assessment Tool, Arnold et al. 1993), a comprehensive, physically based, semi-distributed and watershed-scale hydrological model that allows the simulation of a large number of hydrology-related physical processes (Douglas-Mankin et al. 2010; Gassman et al. 2007). In SWAT, the basin is discretized into sub-watersheds, which thereafter are divided into hydrological response units (HRUs), based on homogeneous soil, land use and slope. The HRUs are then used to compute a water balance, considering four reservoirs: snowpack, soil, shallow aquifer and deep aquifer. Hydrological processes connecting those reservoirs include infiltration, runoff, evapotranspiration, lateral flow and percolation. Computation is performed at the HRU level, aggregated at the sub-basin level and routed through reaches toward the catchment outlet. SWAT was applied to the upper part of the Garonne basin by Grusson et al. (2015). It must be noted that originally the two models had different objectives. SIM aims to simulate the coupled energy and mass balance of continental surfaces, while SWAT is a hydro-agro-environmental model, able to simulate the impact of climate, land use and agricultural practices on hydrology. We use both as they offer different kinds of information and thus are complementary.

The results for both models presented in this paper include the whole Garonne river watershed up to Tonneins. The SWAT model has been calibrated at monthly time steps over the 2000–2010 period using 21 stations spread over the watershed. SIM was not specifically calibrated for this study; the performance is the same as in Habets et al. (2008).

Figure 3 shows the main components of the water balance at the outlet (Tonneins) between 1960 and 2013, including analyses, observations and model outputs. The total precipitation and snowfall come from the Safran reanalysis (Vidal et al. 2010). The small differences between the two models are due to the spatial interpolation of the original 8 km Safran grid used by SIM that have been re-interpolated at the sub-watershed scale for SWAT (150 sub-watersheds and 3156 HRUs from the minimum surface of 0.0174 $km^2$ and maximum 316 $km^2$). The mean total precipitation over the period is 966 mm, but there is a marked negative trend since the middle of the 1990s. The linear trend over the common period of the two models (1960–2011) is small but significant ($-0.38$ mm $year^{-1}$ for SIM, $-0.36$ mm $year^{-1}$ for SWAT, 99 % confidence using a Monte Carlo nonparametric test). During the same period, the evapotranspiration calculated by the two models presents a significant positive trend of $+1.55$ mm $year^{-1}$ for SIM and $+0.76$ mm $year^{-1}$ for SWAT. Concerning the discharge, the linear trend is $-3.82$ mm $year^{-1}$ for SIM, $-3.25$ mm $year^{-1}$ for SWAT and only $-2.30$ mm $year^{-1}$ from the observations.

However, it must be noted that the largest differences appear during the first half of the period, which make an important impact on the computed trends. The reasons for these differences are many, but it is difficult to determine the main factor: uncertainties in meteorological forcing, changes in land use, anthropization or model calibration. It must be noted that anthropogenic forcing factors were not explicitly accounted for in the two

models but were only indirectly considered in the calibration procedure. Land use and vegetation characteristics are based on the ECOCLIMAP database (Faroux et al. 2013). SWAT is calibrated for the period 2000–2010 using the observed discharge, so that it indirectly accounts for anthropization. In addition to agricultural changes in the plain area, rapid land cover changes are occurring in the mountainous areas of the Garonne catchment due to the abandonment of agro-pastoral areas, i.e., due to reforestation. These human-induced land cover changes also impact some key hydrological processes such as storm runoff and snow melt in the Garonne river headwaters (Szczypta et al. 2015). Further work on observation and model errors is needed to explain the larger differences at the beginning of the period.

Figure 3 shows that the observed or modeled discharge trends at the annual discharge are mainly linked to climate variability and change, and not to anthropization. The trends are due to the natural variability [from annual to multi-decadal scales (Boé and Habets 2014)] and the human-induced climate change.

## 3 Interest of Fine Scale Data to Validate or Constrain Models

At the scale of the entire Garonne basin, uncertainties in the meteorological forcing and observation errors cause uncertainties in the discharge trend estimates which are larger than the averaged effects of anthropization. This is not the case for smaller sub-basins or at the seasonal scale, as irrigation is most prevalent during the summer months, and hydro-electric power production is dominant in winter, due to the high proportion of electrically heated houses in France. Discharge variability is also underestimated by the models because both land use and vegetation cycles are assumed to be constant over the whole period. In addition to discharge data, there is a need for additional data to either validate or constrain the models. Satellite data are especially adapted, provided that they have a high enough resolution. In the remaining part of this section, we provide two examples that demonstrate the added value of fine scale satellite data for hydrological modeling.

### 3.1 Snow Cover

The Ariège basin at Foix is one of the major mountainous sub-basins of the Garonne basin. Its area is 1340 $km^2$ and its mean annual discharge is around 40 $m^3\ s^{-1}$. As it contains a complex network of dams used for hydropower, the observed discharge is not representative of natural processes (in particular snow melt). Recently, Gascoin et al. (2015) built a snow cover dataset based on the space-based moderate-resolution imaging spectroradiometer (MODIS) products, MOD10A1 and MYD10A1 (Hall and Riggs 2007), for the Pyrenees. This dataset provides snow cover extent at a daily time step over the region since 2000, with 500 m resolution. The MODIS dataset was validated against in situ and Landsat data. This dataset complemented the in situ snow cover and discharge observations that are available for the basin. In addition, Hendrickx and Sauquet (2013) produced a series of pseudo-natural discharge values for the Ariège river at Foix, based on dam operations.

The snow cover dataset was used to validate the snow cover extent simulated by SIM. The snow model of SIM is the multilayer model ISBA–ES (Boone and Etchevers 2001). The snow cover fraction is a function of snow water equivalent. SIM is a distributed model using an 8 km grid; two versions of the model were considered. The first is the standard version (ISBA), whereas the second is a version taking into account up to four elevation bands in mountainous grid cells, characterized by a high sub-grid variability of orography

(ISBA-M). Figure 4 shows the comparison between snow observations and the two model versions for two contrasting winters (2008/2009 and 2009/2010). Over the whole period (from 2000 to 2013), the correlation for daily data is very high (0.96), but the model has a small negative bias (0.05), which is especially visible during, or immediately after, snowfalls (e.g., in November 2008). A possible explanation for these temporary biases may be the very simple relation between snow cover equivalent and the snow fraction implemented in the model. Indeed, in a study of an alpine catchment (the Durance), Magand et al. (2013) highlighted the fact that the snow cover extent varies faster during winter than during the ablation season because melting occurs at preferential locations. In our case, underestimation mainly occurs from December to March. The difference between the simulations with and without elevation bands is usually low, except at the end of the season, when the snow cover fractions simulated using elevation bands are higher.

The snow water equivalent produced by ISBA was also compared to the snow water equivalent simulated by the SWAT model applied to the Garonne basin (Grusson et al. 2015). In this version, the snow module of SWAT used 10 elevation bands over each snow dominated sub-watershed, where each band covers one-tenth of total sub-watershed elevation. The agreement between the two models is high (Fig. 5), even if the SWAT model tends to overestimate the snow cover in spring and summer (as also shown by Grusson et al. 2015, using in situ measurements), the mean bias being less than 13 mm snow water equivalent (SWE).

Grusson et al. (2015) highlighted the positive impact of elevation bands in SWAT on the river discharge simulation. Even if the snow cover extents simulated by ISBA and ISBA-M are very close, the impact on the river discharge is substantial: The monthly efficiency improved from 0.48 to 0.68 when compared to the operational measurements at Foix and from 0.63 to 0.85 when compared to the naturalized discharge proposed by Hendrickx and Sauquet (2013).

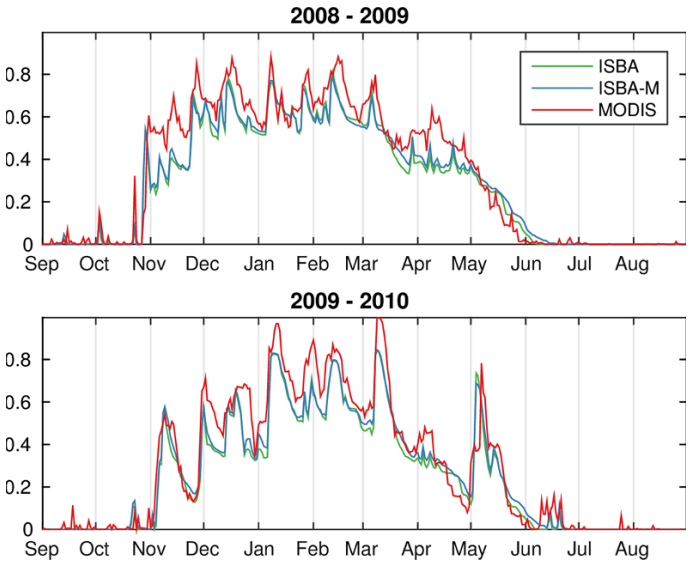


**Fig. 4** Fractional snow cover extent for the Ariège catchment at Foix: comparison of the snow cover extent simulated by the standard version of ISBA (ISBA) and the version accounting for elevation bands in mountain regions (ISBA-M) with the MODIS-derived climatology for two winters

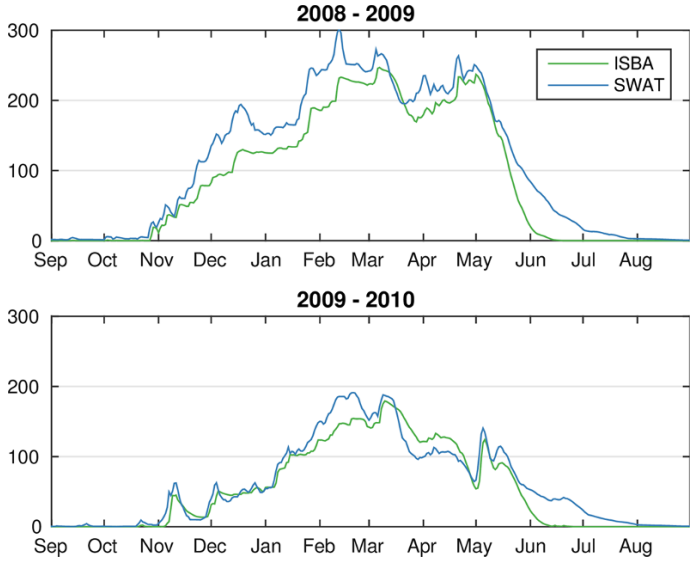


**Fig. 5** Snow water equivalent for the Ariège catchment at Foix: comparison of the snow water equivalent (mm) simulated by ISBA and SWAT over 2 years

Logically, it is necessary to pay great attention to the spring season in the evaluation of the snow cover extent. In our case, the large differences between the simulations appeared during this period. The use of space-based snow cover extent may be a good alternative for the validation of snow cover simulations in the absence of natural river discharge estimates.

### 3.2 Crop Sowing Date

The water balance of crop areas is highly influenced by the precise timing of operations such as sowing and harvesting, as well as irrigation for some crops. Hydrology and crop models have been coupled to take into account the influences of both hydrological settings and of agricultural practices on the water and nutrient cycles at the agricultural catchment scale. Most of these applications require spatially distributed models, where information on soil–crop location within the slopes as well as on hydrological settings (i.e., topography, groundwater storage, reservoir location or irrigation pumping) is included to provide spatially explicit information on water uses (Ferrant et al. 2014a; Perrin et al. 2012) and nutrient transfer and transformation within the catchment (Beaujouan et al. 2002; Ferrant et al. 2011).

Uncertainties raised by these modeling approaches at the watershed level are mainly related to the lack of agronomical observations in all soil–climatic situations encountered within the catchment and to the lack of spatial a priori knowledge on physical processes, such as soil organic matter transformations, saturated area extent and dynamics after rainfall events which influence both runoff and crop growth. Senthilkumar et al. (2015) highlighted the link between sowing, harvesting dates and water scarcity. Hutchings et al. (2012) demonstrated the importance of the timing of field operations for complex dynamic carbon and nitrogen models. However, the timing of operations is often derived from rough regional estimates or from farmers' enquiries further extrapolated to cover the whole

catchment. The use of high-resolution remotely sensed data is a promising way to improve our knowledge of some operations, in particular for winter crops.

Ferrant et al. (2014a) have explored the potential of satellite remote sensing to gain information on the crop sowing date in the cultivated hydrological catchment of Auradé (320 ha) in the Garonne basin. They used a series of 105 LAI maps derived from high-resolution Formosat-2 images acquired from 2006 to 2010 to calibrate the sowing date of sunflower and winter wheat crops at the crop field level in the agro-hydrological model TNT2 (Beaujouan et al. 2002). This model shares the same modeling objectives as the SWAT model (a comparison between both models is reported in Ferrant et al. 2011). An optimization process of the sowing date was done by matching the early variations in simulated LAI with the LAI derived from Formosat-2 images at crop field scale. The results showed a large impact on in-stream nitrogen fluxes, but a limited impact on the mean annual discharge.

However, at shorter time scales, the impact was larger. The optimization process based on the sowing date significantly improved the temporal growth dynamic simulated for the winter wheat, whereas that for sunflower was not much impacted. A delay of a few weeks in the sowing date of winter wheat (from October to November) postponed the emergence date by a few months (by 3 months in the case of the year 2010), while the emergence date of sunflower directly followed the sowing dates in spring (indeed in this season the cumulative daily temperature threshold was reached in a few days). The winter wheat growth and biomass were then highly impacted by the optimization process, which led to a modification of the nitrogen and water cycles between a priori and optimized situations.

We provide here the analysis of the water budget at a monthly time step. In Fig. 6, we represent the differences between both simulations in % for the discharge and the simulated actual evapotranspiration (AET). It appears that the crop growth optimization highly impacts the monthly AET, from −17 to +8 %. The differences are bigger in 2010 for which the use of satellite LAI leads to earlier sowing dates and wheat emergence dates for most of the fields. An increase in AET fluxes associated with this earlier development is simulated from March to June, followed by a relative decrease at the end of the growth period. This decrease is explained by a drop of soil water content due to an earlier root water uptake during spring. Monthly discharges are decreasing with the increase in AET at the end of winter and spring and remain lower than a priori simulations because of drier soils.

This type of approach can be implemented at the scale of the Garonne, with either the SWAT or SIM models, when the Sentinel-2 data will be available. The optimization process requires running the model not more than six times. Depending on how fast a model runs, the process at the crop field level can be considered not to consume too much computer time. The satellite derived information can be used at the crop field level or at the

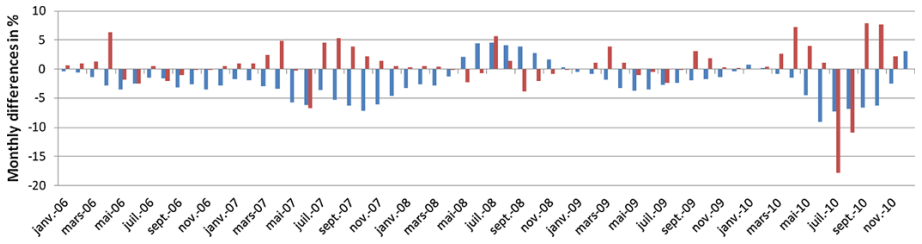


**Fig. 6** Monthly discharge (*blue*) and evapotranspiration (*red*) simulated by the TNT2 model: differences between "optimized sowing date" and "a priori sowing dates"

finer spatial scale needed by the models, the hydrological response unit (HRU) for SWAT. This is defined mainly by the land use spatial resolution, which can be either at the crop field level or at the computation square grid for SIM (8 × 8 km). The need for spatial aggregation of the satellite information depends also on the agricultural context. In this example, sunflower and winter wheat crop succession implies that both crops are spatially mixed in the studied area and should not be aggregated at the sub-basin scale. Indeed, it is crucial to differentiate between winter and spring crops as the winter crops induce larger uncertainties in the simulations. The added value of the Formosat-2 high resolution (which will be provided with Sentinel-2) is that it can explicitly provide spatial information on the intercrop field heterogeneity, to study its impact on the global water cycle.

## 4 Explicit Modeling of Human Activities at the Scale of the Basin Using a Multi-agent Simulation Platform

### 4.1 MAELIA: A Multi-agent Platform of Social–Ecological Systems

Water resource management problems arise from interactions within socio-hydrology systems, a particular type of human-nature systems. Classically these systems are conceptualized as being composed of four main core sub-systems (McGinnis and Ostrom 2014): (a) resource systems (e.g., hydrological systems), (b) resource units (e.g., water volume and flow), (c) governance systems (e.g., which regulate uses and manage water resources) and (d) users (e.g., individuals and groups who use water). Anderies et al. (2004) highlighted the role of their infrastructure (e.g., dams, water distribution networks) in the functioning of these systems.

Therond et al. (2014) developed the Multi-Agent for Environmental Norms Impact Assessment (MAELIA) platform to perform an integrated assessment of the impacts of endogenous and exogenous changes on the functioning of socio-hydrology systems. MAELIA focuses on water deficit issues and was applied in two rivers sub-basins of the Garonne basin: the Aveyron basin (a sub-basin of the Tarn basin) and the upstream part of the Garonne basin itself (upstream of the confluence with the Ariège). Originally, it allows simulating the key interactions between and within the four core sub-systems. Thanks to its multi-agent architecture, it represents the decision-making process of water users (including irrigators), dam managers and state services regarding water use restrictions. In this platform, hydrology is modeled through the use of formalisms of the Soil and Water Assessment Tool (SWAT) model (Arnold et al. 1993), which is fully coupled with human processes such as irrigation. Spatial delineation of farms' islets (a set of contiguous fields) and the annual crop pattern of each farm of the investigated river basin are provided by the French Land Parcel Identification System (LPIS) dataset (Inan et al. 2010). The analysis of different annual LPIS values allowed the reconstitution of the crop rotations of the different fields of the different farms' islets (Murgue et al. 2014, 2015). According to local databases, expert knowledge and geographic information system (GIS) treatments, each irrigated islet was connected with one or several water resources (river, small dam or groundwater). Climate data used with MAELIA came from the Safran analysis system on an 8 × 8 km grid (see Sect. 2.3).

Table 1 shows the main processes represented and the nature of the models used in MAELIA. All these intertwined processes interact at different spatial levels and at daily time steps in the platform, including feedbacks. For example, the crop water requirement at

**Table 1** Key processes of socio-hydrology systems represented in the MAELIA multi-agent platform

| Processes | Nature of the model | Spatial and temporal resolutions |
|---|---|---|
| *Ecological* | | |
| Hydrology (surface and groundwater) | Land and routing phases of SWAT (Arnold et al. 1993) | Reference watershed/day |
| Crop growth | AqYield: empirical generic crop model (Constantin et al. 2015) | Field/day |
| Other plant growth | Simplified version of SWAT formalisms | $HRU^4$/day |
| *Socioeconomic* | | |
| Land cover change | Statistical and probabilistic model based on the analysis of the Corine Land Cover database (http://www.eea.europa.eu/data-and-maps/data/corine-land-cover-2006-raster-3) | HRU/year |
| Demography | Statistic model based on French national data | District/year |
| Domestic consumption | Econometric model (Reynaud and Leenhardt 2008) | Withdrawal and reject points/day |
| Industrial consumption | Statistical model | Withdrawal and reject points/day |
| *Decision-making* | | |
| Crop allocation (cropping plan) | Multi-criteria decision based on Dempster–Shafer belief theory integrated into a Belief–Desire–Intention architecture (Taillandier et al. 2013) | Farm/year |
| Crop management | Nested decision rules (IF–THEN–ELSE) | Field/day |
| Dam management | Nested decision rules (IF–THEN–ELSE) | Dam and supplied river section/day |
| Water use restriction | Nested decision rules (IF–THEN–ELSE) | RESTRICTION ZONE/DAY |

Note that "Reference watershed" in the table corresponds to the finest watershed used by French administration to manage water. HRU stands for "hydrological response unit" (with homogenous soil, slope and land cover)

field level determines the farmer's decision and thus irrigation water withdrawals in the different resources. This decision impacts river flows that determine other decisions for water releases and/or withdrawal restrictions. In return, the resulting hydrology determines the water available for irrigation and so the farmers' capacity to irrigate and therefore the crop growth. Modeling methods for these key processes are briefly described below.

### *4.1.1 Agricultural Processes*

MAELIA simulates the spatiotemporal dynamics of crop management operations and their impacts on crop growth. The crop model AqYield (Constantin et al. 2015) simulates plant growth, soil water dynamics, and crop yield in each field. It is a simple empirical model that proved its robustness under the pedoclimatic (soil temperature and moisture) conditions and the crop irrigation strategies of the Garonne basin (Constantin et al. 2015; Murgue et al. 2014). AqYield allows the simulation of 17 crops/cultivars, including 12 species that cover 100 % of the irrigated areas of the Garonne basin: sunflower, wheat,

barley, peas, rapeseed, sorghum, soya, temporary and permanent meadows, apple, plum and maize. Maize being locally the most intensively irrigated specie, it is considered under eight crops/cultivars: one for seed, one for forage and six for grain production ranging in six earliness categories: very late (VL), late (L), semi-late (SL), semi-early (SE), early (E), very early (VE). AqYield provides soil and plant indicators to the farmer agents and hydrological information (drainage and runoff) to the MAELIA hydrological module.

The use of MAELIA in a river basin requires the description of crop management strategies (CMS) by production situation type (e.g., a combination of pedoclimatic conditions and farm type). A CMS must be defined for each crop of each crop rotation affecting each field. A CMS is coded as a set of decision rules (DRs) using the typical syntax: "IF INDICATOR OPERATOR THRESHOLD AND INDICATOR OPERATOR […] THEN ACTION (ELSE ACTION)." Such a set of DRs should be seen as a pre-established strategy that defines the conditions to trigger various sequences of technical operations depending on soil, plant, climate, water resources conditions at field level or socioeconomic conditions at farm level (e.g., workforce availability). There are about 30 individual rules per CMS (for up to 8 technical operations; Murgue et al. 2014). At the farm level, farmer agents manage the concurrence between technical operations considering pre-defined priorities. At the field level, farmer agents decide to withdraw water from a given resource, according to a priority rule between the various possible resources and accounting for how full they are.

### *4.1.2 Hydrological Processes*

The hydrological module in MAELIA uses the formalisms of the SWAT model to simulate hydrological fluxes at the sub-watershed level (25 $km^2$ in average). In MAELIA, the SWAT algorithms were implemented for both (a) the "land phase" of the hydrological cycle that controls the water loads to the main channel of each sub-watersheds (snowmelt, runoff, infiltration, redistribution in soil profile, evapotranspiration for non-crop plants, lateral subsurface flow and percolation into shallow and deep aquifers) and (b) the "routing phase" of the hydrological cycle that controls the water flows to the outlet of the watershed through the channel network (water routing through the channel, transfers to and from the shallow aquifer, evaporation).

### *4.1.3 Water Management*

Regarding water management, decision-making processes of dam manager and state services, respectively, for water releases and withdrawal restrictions, are also coded as a set of IF–THEN decision rules. These decision rules must be parameterized locally by eliciting dam managers' and state services' current practices. In MAELIA each dam manager agent seeks to optimize releases according to objectives of sustaining targeted river flows and specific constraints of its dam(s): (a) reserved flow (minimum water flow at the exit of the dam), maximum flow due to dam and river characteristics, (b) period of release (e.g., for tourism), (c) transfer time between the dam and the targeted monitoring points and (d) emptying curve of the reservoir (statistical curve used to help present releases without compromising late season ones). When it is not possible or sufficient to sustain water flow through water releases (no dams in the sub-watershed, no more available water in the dam), the state services might issue drought decrees that prohibit the withdrawal of water in some areas and for some days. Three levels of withdrawal restrictions can be launched: 1 or 2 days a week (level 1), 3 or 4 days a week (level 2) or 7 days a week (i.e., permanent

prohibition, level 3). Each drought decree concerns one or several pre-defined "drought zones." For level 1 or 2, these drought zones are divided in sectors (sub areas) so that each day of the week a different sector is successively concerned with the prohibition. Additionally, the decision to apply this restriction is constrained by principles regarding the progressiveness of regulations (i.e., withdrawal restrictions must be progressive) and down- and upstream solidarity (upstream area of a given drought zone must be in a restriction level that is greater or equal). Restriction decisions are taken once every week. The modeling of dams and regulation management is detailed in Mayor et al. (2012).

#### *4.1.4 Other Socioeconomic Processes*

Regarding other socioeconomic processes, such as domestic and industrial water demands and non-agricultural land cover evolutions, MAELIA uses statistical and econometric formalisms either tailored (e.g., industrial demand) or existing (e.g., Reynaud and Leenhardt 2008, for an econometric model of domestic demand according to the water price, principal residence rate, household income, summer maximum temperature and population density).

#### *4.1.5 Calibration of the Model*

When applying MAELIA to a river basin, the calibration of the MAELIA platform is performed module by module, combining quantitative and qualitative approaches. Many parameters can influence the model outputs, with a high level of interactions. In order to get an overview of the model behavior and to screen influential parameters, multiple sensitivity analyses are performed, while considering some subsets of processes or not. These step-by-step sensitivity analyses enabled the different influences and interactions to be disentangled and are a preliminary step to the calibration process. The calibration process is multi-objective (e.g., reproducing water flows and anthropogenic dynamics). It uses a multi-point approximation method (Lardy et al. 2012). The principle of this method is to replace the original optimization problem by a succession of simpler and time-independent problems. This approximation is achieved thanks to meta-models for a limited part of the parameter space.

### 4.2 Evaluation and Impact of Changes in the Spatial Allocation of Cropping Systems in the Aveyron Sub-basin

#### *4.2.1 Studied Area and Methodology*

Through a participatory design methodology, Murgue et al. (2015) identified with stakeholders from the Aveyron sub-basin different types of changes in the socio-hydrology system that may limit the recurrent water deficits experienced. These deficits correspond to the annual water quantities necessary to maintain river flows above the regulatory minimum thresholds, i.e., the minimum flow that ensures the proper functioning of aquatic environment locally (for details see Mazzega et al. 2014). The methodology was implemented on an 800 $km^2$ irrigated landscape located in the lower reaches of the Aveyron sub-basin. The mean annual volume withdrawn for irrigation is around 18 $hm^3$. Feedstock cereals and maize cropping dominate the area, with numerous patches of fruit and high-income seed-production fields. The utilized agricultural area is 40,000 ha. There are about 1150 farms, of which 43 % are irrigated.

During the design process, agricultural land stakeholders as well as water management and environment authorities were asked to specify and quantify as precisely as possible the nature of the changes (e.g., crop rotation, crop management practices) and their location (e.g., in which soil, farm type or pedoclimatic area), including farm level acceptability thresholds (e.g., which area in a farm can support changes). The geographic information system included in MAELIA acted as a hub during the design process, providing information to ease the elicitation of participants' visions and enabling the formalization of the proposals into spatially explicit alternatives.

Information on the current spatial distribution of cropping systems and the designed alternatives were used as inputs to the MAELIA platform. It was run on a 10 years climatic series (2001–2010) to assess effects of alternative spatial allocations of cropping systems on daily river flows and water management (e.g., dam releases of water).

#### *4.2.2 Evaluation of the MAELIA Instance*

As suggested by Bergez et al. (2010) regarding evaluation of integrated modeling tools, we articulated quantitative and qualitative approaches for the evaluation of the MAELIA usage in the Aveyron sub-basin. For this, we organized workshops with local agricultural and water management experts and presented them with outputs of simulations using the current cropping system spatial distribution, and dams and restriction management strategies as input. During these workshops, the analyses of the simulations were focused on key outputs that were representative of the socio-hydrology system behavior; e.g., annual irrigation withdrawals, dynamics of crop management operations (per CMS pedoclimatic conditions) and simulated stream flow for the main rivers. We provided local experts with the quantitative data when available, mainly the regional water agency data on annual withdrawal levels (based on farmer annual declarations), daily measurements of the river flows at river basin outlet, daily dam water releases, etc.

Outcomes of the quantitative and qualitative assessments showed that our use of the MAELIA platform allowed the current intra- and interannual withdrawal dynamics from the field to the sub-basin scale to be reproduced (for details see Murgue et al. 2014). Local experts compared simulation outputs with the data from the regional water agency and concluded that the simulations were very satisfactory (Fig. 7). They also validated the simulated dynamics of crop management operations (e.g., sowing dates, first and last irrigation dates). We also observed that MAELIA reproduced with a good accuracy the observed flow dynamic during the low-flow season (results not shown here). However, even if simulated dam water releases and restriction days were considered as being quite consistent in their patterns, they did not match with the observed daily data. The detailed analysis of these results with local experts showed that, actually, the decision process of releasing dam water and setting withdrawal restrictions does not follow the rules determined by the local authorities. The actual process is the outcome of a social negotiation where "the negotiation ingredients may include the development of conflicts among the stakeholders, breaches of discussions, the game of political influences, issue linking, electoral considerations and the preservation of the social peace, etc." (Mazzega et al. 2014). Even if the outcomes of such a negotiation process cannot be simulated with a modeling platform like MAELIA, this method can be used to assess ex ante (based on forecasts) theoretical impacts of changes in agricultural activities or water resources management under the ceteris paribus (all other things being equal) hypothesis (Mazzega et al. 2014).

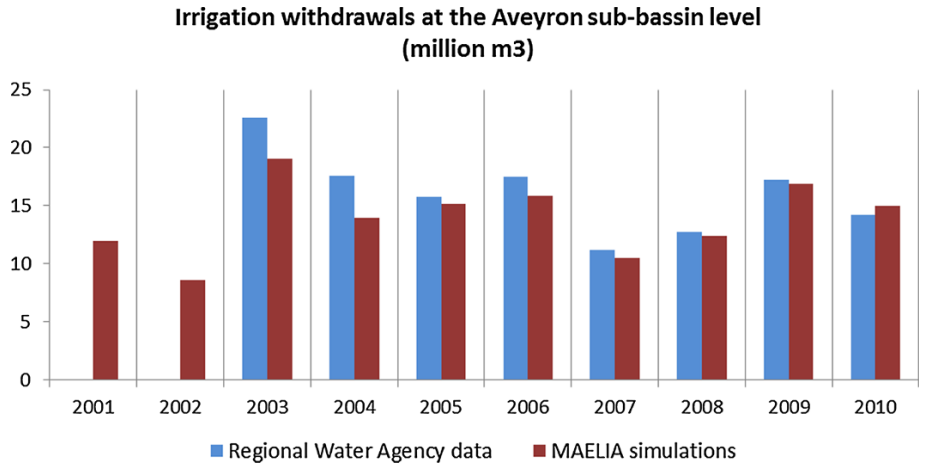


**Fig. 7** Annual withdrawal volumes (in million $m^3$) estimated by the regional water agency through aggregation of annual irrigator declarations (2003–2010, *blue*) and estimated with the MAELIA modeling platform through simulation of irrigation management strategies at the field level (2001–2010, *red*). For the MAELIA simulations, in 2003, 2004 and 2005, the crop patterns of farms in the sub-basin were estimated while for the other years observed data from the French Land Parcel Identification System were used. This may explain the underestimation of water withdrawals by MAELIA for 2003 and 2004

### *4.2.3 Impact Assessment of Crop Rotation Changes*

Here, we present the assessment of one key co-designed alternative aiming at reducing the overall irrigation demand and so reduce the global water deficit of the Aveyron sub-basin. It corresponds to the replacement of irrigated maize mono-cropping by a maize–wheat rotation. The wheat crops are irrigated if necessary since they are cropped on fields where irrigation is possible. When designing this alternative, farmers specified that for economic reasons the maize–wheat rotation should be only implemented on 40 % of farms' maize mono-cropping area (i.e., in a particular year, the wheat crop would replace maize on only 20 % of the maize mono-cropping area). This alternative resulted in changing maize rotation practices in 100 ha on about 3000 ha of maize mono-cropping. As a test, we also assessed the potential impact on river flow of this type of alternative if they were implemented on 100 % of the farms' maize mono-cropping area. These two different simulations are called AltRot40% and AltRot100%, respectively.

Table 2 summarizes the impact on the reduction in annual withdrawals in the study area and the potential reduction in the estimated deficit during the two driest summers in the 10-year study period. AltRot40% allows for an average 4.2 % reduction in annual

**Table 2** Impact of the alternate scenarios AltRot40% (replacement of irrigated maize mono-cropping by a maize–wheat rotation over 40 % of the present maize fields) and AltRot100% (same as Alt40%, but over 100 % of the irrigated maize mono-cropping) on the water withdrawn and the water deficit, expressed in %

| | Water withdrawn (%) 2000–2010 | Water deficit (%) 2003 | Water deficit (%) 2009 |
|---|---|---|---|
| AltRot40% | −4.2 | −11 | −14 |
| AltRot100% | −10.5 | −27 | −39 |

withdrawals from the watershed. For the years 2003 and 2009 (the two driest summers in the 10 years climatic series), the change triggers a reduction of about 0.8 and 1.0 $hm^3$, respectively, 11 and 14 % of the estimated water deficit of the basin. AltRot100% has a more significant impact, allowing a reduction in the withdrawals by about a half of the estimated deficit in the driest years.

The analysis of simulated discharges showed that AltRot40% and AltRot100% have different effects depending on the sub-watershed. In watershed, where river flows are driven by dam releases (e.g., the Aveyron river), these alternatives have a low impact on the river flow itself. They allow the saving of water in dams at the beginning of the irrigation season and therefore to secure the possibility of replenishing the flows with water releases at the end of the season. In catchments where water releases from the dam have no (significant) impacts, the simulations showed that the implementation of these alternatives variously raises and lowers the discharge, through the cropping season, and has a tendency to reduce the river discharge at the end of the season (Fig. 8). For the Aveyron river, AltRot100% significantly raises the flow level during the low-flow season. For the Lère sub-watershed, the impact can be either positive or negative; however, it is always negative toward the end of the season (October and November).

This occurrence is explained by the fact that replacing maize by wheat, while it reduces irrigation withdrawals, also induces less drainage and runoff from the fields to the surrounding rivers. Indeed, as wheat evapotranspiration is higher than that for maize in spring, the soil moisture level is lower: The spring rainfall almost entirely goes into the soil under wheat and evapotranspirates during May and June. Conversely, in a maize field, with the later development of the crop, the soil is kept moist and the rainfall is drained to the aquifers or runs off to the adjacent rivers. As the growing season progresses, the soil

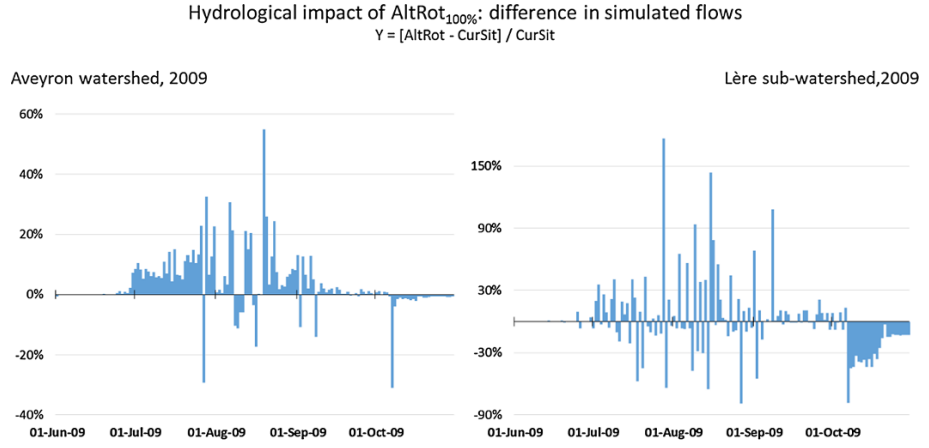


| % of days simulated over/under the flow level in Current Situation [May - September, 2000-2010] | | |
|---|---|---|
| watershed | *Over* | *Under* |
| *Aveyron* | 10.6% | 1.9% |
| *Lère* | 18.1% | 10.7% |

**Fig. 8** Difference (in %) in the simulated outflows between AltRot100% and the current situation [(AltRot − CurSit)/CurSit] for the Aveyron river (strongly supported by water releases from dams) and the Lère river (with only a few water releases from dams)

moisture under wheat is lower due to evapotranspiration. As a consequence, the summer rain has to replace the water in the soil before the adjacent rivers are fed. In contrast, as maize is intensively irrigated during low-flow season, the soil is kept moist, and the summer rain is drained or runs off to adjacent water bodies.

In conclusion, neither AltRot40% nor AltRot100% can meet the expectations of local water managers to suppress the annual water deficits, but, of course, AltRot100% has a stronger impact than AltRot40%. However, as this alternative is far beyond that designed by local stakeholders, its acceptability by farmers seems to be difficult. The MAELIA simulations showed that in situations where water is not available from reservoirs to replenish the river flow and irrigation water is abstracted directly from the rivers, these alternatives may have negative effects all through the season, especially at the end of the growing season. Even if the evaluation of the MAELIA simulations gave satisfactory results, these scenarios are subject to model errors. The figures provided by MAELIA must be used with caution; they must be further confirmed by sensitivity studies to individual processes or by the use of different models.

## 5 Conclusions

The Garonne river area has been subjected to significant climate change over the past 50 years. Both ISBA–MODCOU and SWAT hydrological models highlight trends toward less water resources being available from year to year. This negative trend of the Garonne river flow is mainly due to the increasing simulated evapotranspiration.

There are now more high-resolution space-based data providing useful information on both natural and anthropogenic processes. Two examples have been considered in this paper. In the case of snow, MODIS data were successfully used to validate the snow cover extent of the Ariège at Foix, a mountainous sub-catchment. However, some difficulties may arise when converting the snow cover extent to snow water equivalent, as the relation between these two quantities may be complex. The results over the Garonne basin derived from the ISBA–MODCOU model, which is able to simulate both the snow cover extent and discharge, are in good agreement with both the MODIS and the natural discharge of the Ariège river at Foix. The explicit treatment of elevation bands significantly improved the score of the discharge in ISBA–MODCOU and SWAT (Grusson et al. 2015), while the differences are small concerning the snow cover extent. The MODIS snow cover extent validation may then be extended to the whole mountain range, in order to complement existing in situ snow cover measurements and discharge data.

Concerning the vegetation growth, the use of realistic sowing dates modified the AET and discharge, with a contrasted impact depending on the year. This pilot study was limited to a small watershed in the Garonne river basin because (a) the agro-hydrological model used requires calibration of water cycle using discharge and runs at the spatial resolution of the high-resolution satellite images (8 m) and (b) these satellite data with a short revisit time were only available within a narrow swath (Formosat-2). However, a simplified crop growth modeling approach based on satellite images (Duchemin et al. 2008) can be adapted to larger study areas, and the upcoming Sentinel satellite missions will provide similar imagery at the global scale from 2016. In particular, the Sentinel-2 multispectral imagery (Drusch et al. 2012) will enable LAI maps to be generated at 20 m resolution every 5 days for all land areas. Such a high spatial resolution is necessary in areas such as the Garonne river basin because the cultivated fields are often smaller than 10 ha. With

current midresolution sensors such as MODIS (500 m), there is a risk of mixing the signal from winter and summer crops which are often cultivated in adjacent fields. Shorter revisit times (e.g., in comparison with the 16 days for the Landsat mission) are also needed to capture the crop growth and the date of the harvest. We expect that these remote sensing data will enable land surface models to be better constrained so that the hydrological modeling at the catchment scale may be improved. Concerning the impact of human activities, the multi-agent simulation platform MAELIA is able to simulate the impact of realistic agricultural scenarios discussed with local stakeholders on the river flows and water management (i.e., dam releases). The scenario tested in this paper showed that substantial hydrological impacts may only be caused by very significant changes in the crops being grown.

The aim of the work described here is to build a coherent framework representing the socio-hydrology system at the scale of the Garonne catchment. The work must be completed to cover the whole basin, accounting for additional human processes, such as large reservoir management for hydropower and agriculture, and develop the validation using additional data. First, there is a need to develop methods to aggregate the information from the field to relevant hydrological components (sub-basins, irrigated areas, local aquifers, administrative areas, etc.). Secondly, present and future high-resolution satellite information should be used to calibrate, constrain or validate the modeling. In addition to information on sowing dates, data from Sentinel-2 will provide information on vegetation development and proxies for the soil water holding capacity. The SWOT mission (to be launched in 2020, Biancamaria et al. 2015) is designed to observe the surface water elevation in rivers wider than 100 m and water bodies (lakes, reservoirs, ponds, continuous wetlands) with an area greater than 250 m $\times$ 250 m. In the Garonne catchment, it will provide information on the main rivers and on the actual water storage in the largest reservoirs. It is hoped that the construction of this modeling framework of the Garonne socio-hydrology system will provide valuable information for (1) the operational management of the low-water flow period, (2) the evaluation of scenarios for the development of agriculture and (3) the adaptation to climate change.

**Acknowledgments** This work was carried out within the framework of the project REGARD funded by the STAE foundation (Toulouse, France). Discharge observations were provided by the French Hydro database (Ministère de l'Ecologie, du Développement durable et de l'Energie, http://www.eaufrance.fr), which gathers data from many observers. The authors thank Eric Sauquet and Frédérick Hendrickx for fruitful discussions on the Garonne river and for making available the natural river flows at Foix, and the Editor in Chief for suggesting linguistic changes. This paper arises from the International Space Science Institute (ISSI) workshop "Remote sensing and water resources", held at ISSI, Bern, Switzerland, from October 6, 2014, to October 10, 2014.

## References

Alcamo J, Döll P, Henrichs T, Kaspar F, Lehner B, Rosh T, Siebert S (2003) Development and testing of the WaterGAP 2 global model of water use and availability. Hydrol Sci J 48(317):337

Anderies JM, Janssen MA, Ostrom E (2004) A framework to analyze the robustness of social-ecological systems from an institutional perspective. Ecol Soc 9(1):18

Arnold JG, Allen PM, Bernhardt G (1993) A comprehensive surface-groundwater flow model. J Hydrol 142:47–69

Artinyan E, Habets F, Noilhan J, Ledoux E, Dimitrov D, Martin E, Le Moigne P (2008) Modelling the water budget and the riverflows of the Maritsa basin in Bulgaria. Hydrol Earth Syst Sci 12:21–37

Asokan S, Destouni G (2014) Irrigation effects on hydro-climatic change: basin-wise water balance-constrained quantification and cross-regional comparison. Surv Geophys 35:879–895

Bardeau M, Bouardaa S (2010) Gestion des systèmes aquifères alluviaux dans le bassin Adour-Garonne - Modélisation de la nappe alluviale de la Garonne en Haute-Garonne – Année 3. BRGM/RP-58063-FR. Rapport final. http://sigesmpy.brgm.fr/IMG/pdf/mod31_annee3_final_rp-58063-fr.pdf. Accessed 27 Jan 2016

Beaujouan V, Durand P, Ruiz L, Aurousseau P, Cotteret G (2002) A hydrological model dedicated to topography-based simulation of nitrogen transfer and transformation: rationale and application to the geomorphology—denitrification relationship. Hydrol Process 16:493–507

Bergez J-E, Kuiper M, Therond O, Taverne M, Belhouchette H, Wery J (2010) Evaluating integrated assessment tools for policy support. In: Brouwer FM, Ittersum MK (eds) Environmental and agricultural modelling: Integrated approaches for policy impact assessment. Springer, Netherlands, pp. 237–256

Biancamaria S, Lettenmaier DP, Pavelsky TM (2015) The SWOT mission and its capabilities for land hydrology. Surv Geophys. doi:10.1007/s10712-015-9346-y

Boé J, Habets F (2014) Multi-decadal river flow variations in France. Hydrol Earth Syst Sci 18:691–708

Boone A, Etchevers P (2001) An intercomparison of three snow schemes of varying complexity coupled to the same land surface model: local-scale evaluation at an Alpine site. J Hydrometeorol 2:374–394

Caballero Y, Voirin-Morel S, Habets F, Noilhan J, LeMoigne P, Lehenaff A, Boone A (2007) Hydrological sensitivity of the Adour-Garonne river basin to climate change. Water Resour Res. doi:10.1029/2005WR004192

Claverie M (2012) Estimation spatialisée de la biomasse et des besoins en eau des cultures à l'aide de données satellitales à hautes résolutions spatiale et temporelle: application aux agrosystèmes du sud-ouest de la France. PhD Thesis, University of Toulouse

Constantin J, Willaume M, Murgue C, Lacroix B, Therond O (2015) The soil–crop models STICS and AqYield predict yield and soil water content for irrigated crops equally well with limited data. Agric For Meteorol 206:55–68

Courault D, Hadria R, Ruget F, Olioso A, Duchemin B, Hagolle O, Dedieu G (2010) Combined use of FORMOSAT-2 images with a crop model for biomass and water monitoring of permanent grassland in Mediterranean region. Hydrol Earth Syst Sci 14:1731–1744

Decharme B, Martin E, Faroux S (2013) Reconciling soil thermal and hydrological lower boundary conditions in land surface models. J Geophys Res Atmos 118:7819–7834

Destouni G, Jaramillo F, Prieto C (2013) Hydroclimatic shifts driven by human water use for food and energy production. Nat Clim Change 3:213–217

Döll P (2009) Vulnerability to the impact of climate change on renewable groundwater resources: a global-scale assessment. Environ Res Lett. doi:10.1088/1748-9326/4/3/035006

Döll P, Kaspar F, Lehner B (2003) A global hydrological model for deriving water availability indicators: model tuning and validation. J Hydrol 270:105–134

Döll P, Hoffmann-Dobrev H, Portmann F, Siebert S, Eicker A, Rodell M, Strassberg G, Scanlon B (2012) Impact of water withdrawals from groundwater and surface water on continental water storage variations. J Geodyn 59–60:143–156

Döll P, Müller Schmied H, Schuh C, Portmann FT, Eicker A (2014) Global-scale assessment of groundwater depletion and related groundwater abstractions: combining hydrological modeling with information from well observations and GRACE satellites. Water Resour Res 50:5698–5720

Donohue RJ, Roderick ML, McVicar TR (2007) On the importance of including vegetation dynamics in Budyko's hydrological model. Hydrol Earth Syst Sci 11:983–995

Douglas-Mankin KR, Srinivasan R, Arnold JG (2010) Soil and Water Assessment Tool (SWAT) model: current developments and applications. Trans ASABE 53:1423–1431

Drusch M, Bello UD, Carlier S, Colin O, Fernandez V, Gascon F, Hoersch B, Isola C, Laberinti P, Martimort P, Meygret A, Spoto F, Sy O, Marchese F, Bargellini P (2012) Sentinel-2: ESA's optical high-resolution mission for GMES operational services. Remote Sens Environ 120:25–36

Duchemin B, Maisongrande P, Boulet G, Benhadj I (2008) A simple algorithm for yield estimates; evaluation for semi-arid irrigated winter wheat monitored with green leaf area index. Environ Model Softw 23:876–892

Durand M, Neal J, Rodriguez E, Andreadis KM, Smith LC, Yoon Y (2014) Estimating reach-averaged discharge for the River Severn from measurements of river water surface elevation and slope. J Hydrol 511:92–104

ESDB (2006) European soil data base v2.0, 1 km × 1 km "dominant value and dominant STU" Rasters. http://eusoils.jrc.ec.europa.eu/ESDB_Archive/ESDB_data_1k_raster_intro/ESDB_1k_raster_data_intro.html. Accessed 20 Apr 2015

Faroux S, Kaptué Tchuenté AT, Roujean J-L, Masson V, Martin E, Le Moigne P (2013) ECOCLIMAP-II/Europe: a twofold database of ecosystems and surface parameters at 1 km resolution based on satellite information for use in land surface, meteorological and climate models. Geosci Model Dev 6:563–582

Ferrant S, Oehler F, Durand P, Ruiz L, Salmon-Monviola J, Justes E, Dugast P, Probst A, Probst J-L, Sanchez-Perez J-M (2011) Understanding nitrogen transfer dynamics in a small agricultural catchment: comparison of a distributed (TNT2) and a semi distributed (SWAT) modeling approaches. J Hydrol 406:1–15

Ferrant S, Gascoin S, Veloso A, Salmon-Monviola J, Claverie M, Rivalland V, Dedieu G, Demarez V, Ceschia E, Probst J-L, Durand P, Bustillo V (2014a) Agro-hydrology and multi-temporal high-resolution remote sensing: toward an explicit spatial processes calibration. Hydrol Earth Syst Sci 18:5219–5237

Ferrant S, Caballero Y, Dewandel B, Perrin J, Dazin F, Aulong S, Ahmed S, Maréchal JC (2014b) Projected impacts of climate change on farmers' extraction of groundwater from crystalline aquifers in South India. Sci Rep. doi:10.1038/srep03697

Foley JA, DeFries R, Asner GP, Barford C, Bonan G, Carpenter SR, Chapin FS, Coe MT, Daily GC, Gibbs HK, Helkowski JH, Holloway T, Howard EA, Kucharik CJ, Monfreda C, Patz JA, Prentice IC, Ramankutty N, Snyder PK (2005) Global consequences of land use. Science 309:570–574

Frans C, Istanbulluoglu E, Mishra V, Munoz-Arriola F, Lettenmaier DP (2013) Are climatic or land cover changes the dominant cause of runoff trends in the Upper Mississippi River Basin? Geophys Res Lett 40:1104–1110

Gascoin S, Hagolle O, Huc M, Jarlan L, Dejoux J-F, Szczypta C, Marti R, Sánchez R (2015) A snow cover climatology for the Pyrenees from MODIS snow products. Hydrol Earth Syst Sci 19:2337–2351

Gassman PW, Reyes MR, Green CH, Arnold JG (2007) The soil and water assessment tool: historical development, applications, and future research directions. Trans ASABE 50:1211–1250

Gaudou B, Sibertin-Blanc C, Therond O, Amblard F, Auda Y, Arcangeli J-P, Balestrat M, Charron-Moirez M-H, Gondet E, Hong Y, Lardy R, Louail T, Mayor E, Panzoli D, Sauvage S, Sánchez-Pérez J-M, Taillandier P, Van Bai N, Vavasseur M, Mazzega P (2014) The MAELIA multi-agent platform for integrated analysis of interactions between agricultural land-use and low-water management strategies. In: Alam SJ, Parunak HVD (eds) Multi-agent-based simulation XI. Springer, Berlin, pp 85–100

Goderniaux P, Brouyère S, Fowler HJ, Blenkinsop S, Therrien R, Orban P, Dassargue A (2009) Large-scale surface–subsurface hydrological model to assess climate change impacts on groundwater reserves. J Hydrol 373:122–138

Green TR, Bates BC, Charles SP, Fleming PM (2007) Physically based simulation of potential effects of carbon dioxide-altered climates on groundwater recharge. Vadose Zone J 6:597–609

Grouillet B, Fabre J, Ruelland D, Dezetter A (2015) Historical reconstruction and 2050 projections of water demand under anthropogenic and climate changes in two contrasted Mediterranean catchments. J Hydrol 522:684–696

Grusson Y, Xiaoling S, Gascoin S, Sauvage S, Raghavan S, Anctil F, Sánchez Pérez JM (2015) Exploring snow and streamflow dynamics in an alpine watershed using the semi-distributed hydrological model SWAT. J Hydrol 531:574–588

Gurdak JJ, Roe CD (2010) Review: recharge rates and chemistry beneath playas of the High Plains aquifer, USA. Hydrogeol J 18:1747–1772

Habets F, Boone A, Champeaux JL, Etchevers P, Franchistéguy L, Leblois E, Ledoux E, Le Moigne P, Martin E, Morel S, Noilhan J, Seguí PQ, Rousset-Regimbeau F, Viennot P (2008) The SAFRAN–ISBA–MODCOU hydrometeorological model applied over France. J Geophys Res. doi:10.1029/2007JD008548

Habets F, Philippe E, Martin E, David CH, Leseur F (2014) Small farm dams: impact on river flows and sustainability in a context of climate change. Hydrol Earth Syst Sci 18:4207–4222

Hall D, Riggs G (2007) Accuracy assessment of the MODIS snow products. Hydrol Process 21:1534–1547

Hendrickx F, Sauquet E (2013) Impact of warming climate on water management for the Ariège River basin (France). Hydrol Sci J 58:976–993

Holman IP, Tascone D, Hess TM (2009) A comparison of stochastic and deterministic downscaling methods for modelling potential groundwater recharge under climate change in East Anglia, UK: implication for groundwater resource management. Hydrogeol J 17:1629–1641

Hutchings NJ, Reinds GJ, Leip A, Wattenbach M, Bienkowski JF, Dalgaard T, Dragosits U, Drouet JL, Durand P, Maury O, de Vries W (2012) A model for simulating the timelines of field operations at a European scale for use in complex dynamic models. Biogeosciences 9:4487–4496

Inan HI, Sagris V, Devos W, Milenov P, van Oosterom P, Zevenbergen J (2010) Data model for the collaboration between land administration systems and agricultural land parcel identification systems. J Environ Manag 91:2440–2454

Jyrkama MI, Sykes JF (2007) The impact of climate change on spatially varying groundwater recharge in the Grand River watershed (Ontario). J Hydrol 338:237–250
Kandasamy J, Sounthararajah D, Sivabalan P, Chanan A, Vigneswaran S, Sivapalan M (2014) Socio-hydrologic drivers of the pendulum swing between agricultural development and environmental health: a case study from Murrumbidgee River basin, Australia. Hydrol Earth Syst Sci 18:1027–1041
Kovalevskii VS (2007) Effect of climate changes on groundwater. Water Resour 34:140–152
Lardy R, Mazzega P, Sibertin-Blanc C, Aud Y, Sánchez Pérez JM, Sauvage S, Therond O (2012) Calibration of simulation platforms including highly interweaved processes: the MAELIA multi-agent platform. In: Ames DP, Quinn N, Rizzoli A (eds) 7th International Congress on Environmental Modelling and Software (iEMSs), pp 1–8
Lehner B, Liermann CR, Revenga C, Vörösmarty C, Fekete B, Crouzet P, Döll P, Endejan M, Frenken K, Magome J, Nilsson C, Robertson JC, Rödel R, Sindorf N, Wisser D (2011) High-resolution mapping of the world's reservoirs and dams for sustainable river-flow management. Front Ecol Environ 9:494–502
Lobell D, Bala G, Mirin A, Phillips T, Maxwell R, Rotman D (2009) Regional differences in the influence of irrigation on climate. J Climate 22:2248–2255
Magand C, Ducharne A, Le Moine N, Gascoin S (2013) Introducing hysteresis in snow depletion curves to improve the water budget of a land surface model in an alpine catchment. J Hydrometeorol 15:631–649
Mayor E, Mazzega P, Panzoli D, Sibertin-Blanc C, Therond O, Vavasseur M (2012) Formal representation of water withdrawal policies for integrated assessment. In: Gilbert T, Kirkilionis M, Nicolis G (eds) Proceedings of the European conference on complex systems, pp 1–15
Mazzega P, Therond O, Debril T, March H, Sibertin-Blanc C, Lardy R, Sant'ana D (2014) Critical multi-level governance issues of integrated modelling: an example of low-water management in the Adour-Garonne basin (France). J Hydrol 519(Part C):2515–2526
McGinnis MD, Ostrom E (2014) Social-ecological system framework: initial changes and continuing challenges. Ecol Soc. doi:10.5751/ES-06387-190230
Mishra AK, Singh VP (2010) A review of drought concepts. J Hydrol 391:202–216
Moisselin JM, Schneider M, Canellas C, Mestre O (2002) Les changements climatiques en France au 20ème siècle. Etude des longues séries homogénéisées de données de température et de précipitations. La Météorol 38:45–56
Moss RH, Edmonds JA, Hibbard KA, Manning MR, Rose SK, van Vuuren DP, Carter TR, Emori S, Kainuma M, Kram T, Meehl GA, Mitchell JFB, Nakicenovic N, Riahi K, Smith SJ, Stouffer RJ, Thomson AM, Weyant JP, Wilbanks TJ (2010) The next generation of scenarios for climate change research and assessment. Nature 463:747–756
Murgue C, Lardy R, Vavasseur M, Leenhardt D, Therond O (2014) Fine spatio-temporal simulation of crop and farming systems effects on irrigation withdrawal dynamics within a river basin. In: Ames DP, Quinn N, Rizzoli A (eds) 7th International Congress on Environmental Modelling and Software, iEMSs, pp 1784–1791
Murgue C, Therond O, Leenhardt D (2015) Toward integrated water and agricultural land management: participatory design of agricultural landscapes. Land Use Policy 45:52–63
Nash J, Sutcliffe J (1970) River flow forecasting through conceptual models. Part I A discussion of principles. J Hydrol 10:282–290
Parajuli P, Jayakody P, Sassenrath G, Ouyang Y, Pote J (2013) Assessing the impacts of crop-rotation and tillage on crop yields and sediment yield using a modeling approach. Agric Water Manag 119:32–42
Perrin J, Ferrant S, Massuel S, Dewandel B, Maréchal J, Aulong S, Ahmed S (2012) Assessing water availability in a semi-arid watershed of southern India using a semi-distributed model. J Hydrol 460–461:143–155
Probst JL (1983) Hydrologie du bassin de la Garonne: Modèles de Mélange, Bilan de l'Erosion, Exportation des Nitrates et des Phosphates. PhD thesis, Univ. Toulouse
Qiu GY, Yin J, Tian F, Geng S (2011) Effects of the "Conversion of Cropland to Forest and Grassland Program" on the Water Budget of the Jinghe River Catchment in China. J Environ Qual 40:1745–1755
Reynaud A, Leenhardt D (2008) MoGIRE: a model for integrated water management. In: Sànchez-Marrè M, Béjar J, Comas J, Rizzoli AE, Guariso G (eds) Proceedings of the 2008 International Congress on Environmental Modelling and Software, iEMSs, pp 576–583
Sauquet E, Dupeyrat A, Hendrickx F, Perrin C, Samie R, Vidal J-P (2009) IMAGINE 2030, climate and water management: uncertainties on water resources for the Garonne river basin in 2030? http://cemadoc.irstea.fr/oa/PUB00028876-imagine-2030-climat-amenagements-garonne-quelles-i.html. Accessed 20 Apr 2015
Scibeck J, Allen DM (2006) Modeled impacts of predicted climate change on recharge and groundwater levels. Water Resour. doi:10.1029/2005WR004742

Senthilkumar K, Bergez J-E, Leenhardt D (2015) Can farmers use maize earliness choice and sowing dates to cope with future water scarcity? A modelling approach applied to south-western France. Agric Water Manag 152:125–134

Sivapalan M, Savenije HHG, Blöschl G (2012) Socio-hydrology: a new science of people and water. Hydrol Process 26:1270–1276

Szczypta C, Gascoin S, Houet T, Hagolle O, Dejoux JF, Vigneau C, Fanise P (2015) Impact of climate and land cover changes on snow cover in a small Pyrenean catchment. J Hydrol 521:84–99

Taillandier P, Therond O, Gaudou B (2013) A new BDI agent architecture based on the belief theory. Application to the modeling of cropping plan decision-making. In: Seppelt R, Voinov AA, Lange S, Bankamp D (eds) Managing resources of a limited planet, proceedings of the sixth biennial meeting of the International Environmental Modelling and Software Society, iEMSs, pp 2463–2470

Therond O, Sibertin-Blanc C, Lardy R, Gaudou B, Ballestrat M, Hong Y, Louail T, Mayor E, Nguyen VB, Taillandier V, Vavasseur M, Mazzega P (2014) Integrated modelling of social-ecological systems: the MAELIA high-resolution multi-agent platform to deal with water scarcity problems. In: Ames DP, Quinn NWT, Rizzoli AE (eds) 7th International Congress on Environmental Modelling and Software, iEMSs, pp 1833–1840

van Emmerik THM, Li Z, Sivapalan M, Pande S, Kandasamy J, Savenije HHG, Chanan A, Vigneswaran S (2014) Socio-hydrologic modeling to understand and mediate the competition for water between agriculture development and environmental health: Murrumbidgee River basin, Australia. Hydrol Earth Syst Sci 18:4239–4259

Vidal J-P, Martin E, Franchistéguy L, Baillon M, Soubeyroux J-M (2010) A 50-year high-resolution atmospheric reanalysis over France with the Safran system. Int J Climatol 30:1627–1644

Vörösmarty CJ, Green P, Salisbury J, Lammers RB (2000) Global water resources: vulnerability from climate change and population growth. Science 289:284–288

Wada Y, van Beek LPH, van Kempen CM, Reckman JWTM, Vasak S, Bierkens MFP (2010) Global depletion of groundwater resources. Geophys Res Lett. doi:10.1029/2010GL044571

DOI 10.1007/978-3-319-32449-4_4
Reprinted from *Surveys in Geophysics* Journal, DOI 10.1007/s10712-015-9354-y

# On Creating Global Gridded Terrestrial Water Budget Estimates from Satellite Remote Sensing

**Yu Zhang[1] · Ming Pan[1] · Eric F. Wood[1]**

Received: 16 March 2015 / Accepted: 12 December 2015 / Published online: 4 January 2016


**Abstract** The increasing availability and reliability of satellite remote sensing products [e.g., precipitation (*P*), evapotranspiration (*ET*), and the total water storage change (*TWSC*)] make it feasible to estimate the global terrestrial water budget at fine spatial resolution. In this study, we start from a reference water budget dataset that combines all available data sources, including satellite remote sensing, land surface model (LSM) and reanalysis, and investigate the roles of different non-satellite remote sensing products in closing the terrestrial water budget through a sensitivity analysis by removing/replacing one or more categories of products during the budget estimation. We also study the differences made by various satellite products for the same budget variable. We find that the gradual removal of non-satellite data sources will generally worsen the closure errors in the budget estimates, and remote sensing retrievals of *P*, *ET*, and *TWSC* together with runoff (*R*) from LSM give the worst closure errors. The gauge-corrected satellite precipitation helps to improve the budget closure (4.2–9 % non-closure errors of annual mean precipitation) against using the non-gauge-corrected precipitation (7.6–10.4 % non-closure errors). At last, a data assimilation technique, the constrained Kalman filter, is applied to enforce the water balance, and it is found that the satellite remote sensing products, though with worst closure, yield comparable budget estimates in the constrained system to the reference data. Overall, this study provides a first comparison between the water budget closure using the satellite remote sensing products and a full combination of remote sensing, LSM, and reanalysis products on a quasi-global basis. This study showcases the capability and potential of the satellite remote sensing in closing the terrestrial water budget at fine spatial resolution if properly constrained.

**Keywords** Global terrestrial water budget · Satellite remote sensing · CKF · Constraint

✉ Yu Zhang
yz5@Princeton.EDU

[1] Department of Civil and Environmental Engineering, Princeton University, E-208 E-Quad, Princeton, NJ 08544, USA

## 1 Introduction

The evolution and shift of the terrestrial water cycle pose a significant impact on the climate system, the availability of water resources, the occurrence of hydrological extremes, etc. The global terrestrial water cycle is also key in understanding the complex interactive feedbacks and mechanisms among the land surface, ocean and the atmosphere. Better understanding of the global water cycle can be enabled by accurate and reliable estimation of the global terrestrial water budget that is continuous in time and space from various data sources such as traditional in situ observations, advanced satellite remote sensing, land surface model (LSM), and reanalysis. Though in situ observations always serve as the "truth", their limited spatial fetch and high cost make them less economical. By contrast, satellite remote sensing, with its mission in observing Earth at a fine spatial resolution with temporal continuity, makes it possible to estimate the water budget in less developed regions where the in situ gauge stations are sparse or non-existent. In addition, satellite remote sensing products are also always used as the forcing (e.g., precipitation) or the basic setups (e.g., land cover, topography) for land surface, weather, and climate models, which can also provide water budget estimates such as evapotranspiration and runoff at large scales that supplement the point scale in situ measurement. However, the accuracy and reliability of the budget estimates from these models highly depend on factors like the parameterization, initial condition, forcing, and calibration/validation.

Terrestrial water budget consists of four major components: the precipitation ($P$), evapotranspiration ($ET$), runoff ($R$), and total water storage change ($TWSC$), and the mass balance of water requires that:

$$TWSC = P - ET - R \tag{1}$$

With the development and improvement in satellite remote sensing techniques, all the components of the terrestrial water budget can be estimated from the space-borne remote sensing, though the accuracy and resolution vary across the different water budget components due to varying sensor characteristics. For example, precipitation can be estimated by merging microwave and infrared information, such as with the Tropical Rainfall Measuring Mission (TRMM) Multi-satellite Precipitation Analysis (TMPA: Huffman et al. 2007, 2010), the Precipitation Estimation from Remotely Sensed Information using Artificial Neural Networks-Cloud Classification System (PERSIANN-CCS: Hong et al. 2007), and the Climate Prediction Center morphing method (CMORPH: Joyce et al. 2004). Global estimations of evapotranspiration can be derived from satellite surface radiation budget, surface meteorology, and vegetation cover (e.g., Fisher et al. 2008; Mu et al. 2007; Vinukollu et al. 2011). Potentially runoff can be retrieved from satellite altimetry. The Surface Water Ocean Topography (SWOT: Durand et al. 2010) mission, which is expected to be launched in 2020, will play a leading role in surface hydrological observations by providing information for major rivers and water bodies at near global coverage with a repeating period of 21 days. SWOT will use the Ka-band radar and provide sea surface height and terrestrial water heights at 120-km-wide swath. The radar measurements will also be processed for measuring rivers with widths larger than 100 meters width and lakes with areas larger than $(250\ \text{m})^2$. SWOT will provide river elevation (with an accuracy of 10 cm), slope (with an accuracy of 1 cm/1 km) and width which can be used in estimating river discharge (Paiva et al. 2015; Pavelsky et al. 2014). The surface and subsurface total water storage ($TWS$) can be measured by the NASA Gravity Recovery And Climate Experiment (GRACE) twin satellites (Landerer and Swenson 2012; Tapley et al. 2004;

Wahr et al. 2004), which were launched on March 17, 2002, at the coarse spatial resolution of ~220 km and monthly timescale. Then the measurements of micro-gravity at their original resolution are processed onto 1° spatial resolution and monthly timescale by three centers, Geoforschungs Zentrum Potsdam (GFZ), Center for Space Research at University of Texas, Austin (CSR), and Jet Propulsion Laboratory (JPL), with the gravity anomalies attributed to changes in total water storage. GRACE has been widely used in water budget estimation (e.g., Gao et al. 2010; Pan et al. 2012; Sahoo et al. 2011; Sheffield et al. 2009; Wang et al. 2014) as well as drought analysis (e.g., Famiglietti 2014; Thomas et al. 2014). As a successor to the original GRACE mission, a GRACE Follow-on (GRACE-FO, http://grace.jpl.nasa.gov/mission/grace-fo/) is planned for launch in 2017 to continue measuring the Total Water Storage (*TWS*).

At regional scales where in situ observations are available, Pan et al. (2012) estimated the errors in each water budget component against the in situ observations and then merged those products based on their error information. In addition, earlier studies (Gao et al. 2010; Sahoo et al. 2011; Sheffield et al. 2009; Troy et al. 2011; Vinukollu et al. 2011) attempted to close the water budget at the basin scale by using satellite remote sensing. However, the closure cannot be achieved without enforcing the water balance through approaches such as data assimilation. Sahoo et al. (2011) applied a constrained Kalman filter (CKF) to close the water budget using satellite remote sensing and provided balance-constrained best estimates of the water budget for ten major basins.

At the global scale, previous studies (e.g., Dirmeyer et al. 2006; Haddeland et al. 2011; Oki et al. 1995; Trenberth et al. 2007; Weedon et al. 2011) estimated the terrestrial water budget from either single or multiple land surface and/or hydrologic models for limited periods mostly during the 1990s. A recent study (Rodell et al. 2015) blended multiple sourced datasets into a "best guess" by utilizing the standard deviation/spread of the uncertainties for each component and estimated the global terrestrial water budget for 2000–2010. But none of these studies provides a multi-decadal global terrestrial water budget record covering most of the satellite era. Currently the authors are carrying out an additional analysis for estimating and closing the global terrestrial water budget that combine multiple data sources (Table 1) that include in situ observations, satellite remote sensing, and LSM outputs and reanalysis, at 0.5° spatial resolution and monthly timescale for the period of 1984–2010. A subset of these data records (2004–2007) is used in this paper as the reference data to evaluate the water budget estimation using different combinations of remote sensing data sources.

Though current satellite remote sensing offers the potential to estimate gridded terrestrial water budget over the globe, which is especially of significant importance for ungauged and sparsely gauged regions, challenges exist in quantifying the errors in each satellite remote sensing products when reliable in situ observations are lacking—and even when they are available. This study aims at creating a global terrestrial gridded (0.5°) monthly water budget from satellite remote sensing that has budget closure by applying a CKF algorithm. The period of 2004–2007 is selected based on the common availability of all the datasets listed in Table 1. This paper is organized as follows: Sect. 2 introduces the datasets, the methodology in estimating and closing water budget, and the experiments used to assess the impact of the data sources on the water budget; Sect. 3 presents the results from using data products that range from all available products to remotely sensed products along on estimating and closing water budget; and Sect. 4 presents the conclusions and findings from the study.

**Table 1** Data summary

| Dataset | Period | Spatial resolution | Temporal resolution | References |
|---|---|---|---|---|
| *Precipitation* | | | | |
| CSU | 1998–2010 | 0.25° | 3 h | (Bytheway and Kummerow 2013) |
| PGF | 1948–2010 | 0.25° | 3 h | (Sheffield et al. 2006) |
| CHIRPS | 1981–present | 0.5° | Monthly | (Funk et al. 2014) |
| GPCC(v6) | 1901–2010 | 0.5° | Monthly | (Schneider et al. 2014) |
| TMPA-RT | 2001–present | 0.25° | 3 h | (Huffman et al. 2007, 2010) |
| *Evapotranspiration* | | | | |
| SRB–PGF–PM | 1984–2007 | 0.5° | 3 h | (Vinukollu et al. 2011) |
| VIC | 1948–2010 | 0.25° | 3 h | (Sheffield and Wood 2007) |
| ERA-interim | 1979–present | T255 | – | (Simmons et al. 2006) |
| MERRA | 1979–present | 2/3 × 1/2 H grids | – | (Rienecker et al. 2011) |
| GLEAM | 1984–2007 | 0.5° | Daily | (Miralles et al. 2011) |
| SRB-CFSR-SEBS | 1984–2007 | 0.5° | Daily | (Vinukollu et al. 2011) |
| SRB-CFSR-PM | | | | |
| SRB-CFSR-PT | | | | |
| *Runoff* | | | | |
| VIC | 1948–2010 | 0.25° | 3 h | (Sheffield and Wood 2007) |
| *Total water storage (TWS)* | | | | |
| VIC | 1948–2010 | 0.25° | 3 h | (Sheffield and Wood 2007) |
| GRACE | 2002–present | 1° | Monthly | (Landerer and Swenson 2012) |

The Princeton Global Forcing (PGF) dataset used in this study, which is an updated version of the PGF described in (Sheffield et al. 2006), provides near-surface meteorological data for driving land surface models and other terrestrial modeling systems. All other acronyms are defined Sect. 2.1

Forced by the near-surface meteorological variables from PGF listed above, VIC model simulates evapotranspiration and runoff at 0.25°, 3 h over the land from 1948 to 2010 as an updated version of (Sheffield and Wood 2007)

## 2 Data and Methodology

### 2.1 Utilized Data

Three satellite precipitation products used in this study. Two are the Colorado State University (CSU) and the Real Time product of TRMM Multi-satellite Precipitation Analysis (TMPA-RT). The CSU product (Bytheway and Kummerow 2013) is the TMPA (Huffman et al. 2007, 2010) accumulated rainfall with uncertainty estimates and is a 3-h, 0.25° spatial resolution gridded product available between 50°N and 50°S. Different from the standard TMPA products, the TMPA-RT product provides the precipitation estimation at near real time over 50°N– 50°S, but without rain gauge adjustment. The difference between TMPA-RT and CSU reveals the role of correcting the satellite retrievals using ground gauges. The third satellite product is from the Climate Hazard group InfraRed Precipitation with Stations (CHIRPS, Funk et al. 2014) product. In addition, the in situ based Global Precipitation Climate Center (GPCC) product (Schneider et al. 2014) and the multi-source merged product of Princeton Global Forcing (PGF, Sheffield et al. 2006)

dataset that is based on in situ, satellite and reanalysis model precipitation are also used in our study.

Five satellite remote sensing products are used for global evapotranspiration (*ET*) estimation. The products are various combinations of data sources and *ET* algorithms (radiation–surface meteorology–*ET* algorithm). The algorithms are run at a daily time step and then aggregated to monthly totals. The products are: (1) SRB–PGF–PM: Surface Radiation Budget–Princeton Global Forcing–Penman–Monteith; (2) SRB–CFSR–PM: Surface Radiation Budget–Climate Forecast System Reanalysis–Penman–Monteith; (3) SRB–CFSR–PT: Surface Radiation Budget–Climate Forecast System Reanalysis–Priestly-Taylor; (4) SRB–CFSR–SEBS: (the Surface Radiation Budget–Climate Forecast System Reanalysis–Surface Energy Balance System (SEBS); and (5) GLEAM: the Global Land-surface Evaporation: the Amsterdam Methodology, (Miralles et al. 2011). The algorithms for models (1)–(4) are described in Vinukollu et al. (2011). Three *ET* models (2)–(4) use CFSR meteorology and CFSR surface radiation that has been adjusted to match the monthly SRB surface radiation. Additionally, two reanalysis *ET* products from ERA-interim (Simmons et al. 2006) and NASA's Modern-Era Retrospective Analysis for Research and Application (MERRA, Rienecker et al. 2011), as well as one *ET* from the Variable Infiltration Capacity (VIC) land surface model (LSM), forced by an updated version of PGF (Sheffield and Wood 2007), are also used.

The runoff is generated at 0.25° spatial resolution and 3 h, from the same VIC LSM (Sheffield and Wood 2007). For the runoff fields used in here, VIC was calibrated over 43 globally well-distributed river basins.

The terrestrial Total Water Storage Change (*TWSC*) is estimated from both the VIC LSM and GRACE (Landerer and Swenson 2012) ReLease05 (RL05) (http://grace.jpl.nasa.gov/data/get-data/monthly-mass-grids-land/). Since most of the soil water dynamics occur in the upper portion of the column, it was decided to use both a LSM and GRACE retrievals as *TWSC* estimates even though it is recognized that GRACE should be a more inclusive product. The GRACE gravity anomaly retrievals are post-processed onto 1° spatial resolution and monthly timescale by GFZ, CSR, and JPL, as discussed earlier. The provided scaling grid was then multiplied to the 1° GRACE land data in order to reduce the attenuation of the surface mass variations at small spatial scales due to the sampling and post-processing (e.g., the de-stripping filter and the 300-km Gaussian Filter). It is noted that the current 1° GRACE land data cannot accurately observe ice mass changes over Greenland and Antarctica, or glacier and ice caps (Jacob et al. 2012). The ensemble mean (equal weighting of JPL, CSR, GFZ products) is calculated as the *TWSC* from GRACE. Sakumura et al. (2014) points out that this is the most appropriate method in reducing the noise in the gravity field solutions within the available scatter of the solutions.

All the products in Table 1 are either aggregated or disaggregated onto 0.5° spatial resolution and the monthly timescale. The reader is referred to the references in Table 1 for detailed information for each product. In addition, monthly streamflow observations from Global Runoff Data Center (GRDC) are also used in this study, as well as for validation.

## 2.2 Product Merging and Water Budget Closure

There are insufficient in situ observations, especially for *ET*, *R*, and *TWSC*, to estimate the errors and/or biases for each water budget component at the grid scale over the globe. Therefore, in this study, the deviations from the ensemble mean of all the data sources for the same budget variable is used as a proxy of the uncertainty/error in the individual products. The merging procedure for each budget component is a weighted averaging,

where the optimal merging weight $w_i$ is given by the following equation (Luo et al. 2007; Sahoo et al. 2011):

$$w_i = \frac{1}{\sigma_i^2} \Big/ \sum_{i=1}^{n} \frac{1}{\sigma_i^2} \tag{2}$$

in which $w_i$ is the merging weight for product $i$, $\sigma_i^2$ is the error variance of product $i$ calculated against the ensemble mean, and $n$ is the total number of the products. Note that $\sum w_i$ equals to 1. The larger the error variance of product $i$, the lower is its merging weight. The merging process is conducted in the unconstrained system.

In the constrained system, the CKF algorithm (Sahoo et al. 2011) is applied that assures budget closure at each grid cell over the globe. In short, CKF redistributes the non-closure errors back onto the different water budget components according to their error levels and correlations. The water balance residual is defined as $r = P - ET - R - TWSC$. The budget components can be written as the column vector $x$, $x = [P, ET, R, TWSC]^T$, and then the residual of the water balance can be expressed as a linear function of the vector, $r = G\,x$, where $G = [1, -1, -1, -1]$. The error covariance matrix of $x$ is calculated as $\varepsilon_{xx} = \overline{(\hat{x} - x)(\hat{x} - x)^T}$, where $\hat{x}$ is an estimate of $x$, its "true value" and the overbar represents expectation over the time series. In this study, $(\hat{x} - x)$ is replaced with the spread of the ensemble in each water budget component. This uncertainty estimation method was first proposed by Adler et al. (2001) and then applied in Tian and Peters-Lidard (2010) to generate a global precipitation uncertainty map for a variety of satellite remote sensing products. $\varepsilon_{xx}$ has the dimension $4 \times 4$ since $x$ consists of four budget variables. Then the balance-constrained estimate is calculated via $\hat{x}' = \hat{x} - \varepsilon_{xx} G^T (G \varepsilon_{xx} G^T)^{-1} \hat{r}$. The residual term $\hat{r}$ is redistributed back into different water budget components through the above equation. Mathematically, the CKF algorithm mimics assimilating a zero-error observation of $r$ (i.e., $r = 0$).

### 2.3 Design of the Budget Closure Experiments

Five experiments listed in Table 2 are carried out in terms of a sensitivity analysis to understand how datasets from different sources affect the estimation and closure of the terrestrial water budget. Starting with the complete suite of measurements and products [experiment (a)], referred to here as the reference dataset, and removing from the reference data, one at a time, in situ observations [experiment (b)], reanalysis products [experiment (c)], in situ and reanalysis products together [experiment (d)], it is possible to determine the impact of including various data sources in the global water budget estimates and its closure. The five experiments are conducted in both unconstrained (that is without applying the CKF algorithm) and the constrained (with CKF) systems.

## 3 Results and Discussion

### 3.1 Roles of Non-satellite Sources in Closing the Water Budget

To assess the contribution from non-satellite data sources to the non-closure/imbalance, an error sensitivity analysis, in terms of experiment (a–e), is conducted by removing/replacing datasets with ground observations, or reanalysis, one category at a time, and then all

**Table 2** Data sources used in each sensitivity experiment

| Experiment | (a) | (b) | (c) | (d) | (e) |
|---|---|---|---|---|---|
| **P** | | | | | |
| PGF | ✔ | | ✔ | | |
| CSU | ✔ | | ✔ | | |
| GPCC | ✔ | | ✔ | | |
| CHIRPS | ✔ | | ✔ | | |
| TMPA-RT | | ✔ | | ✔ | ✔ |
| **ET** | | | | | |
| PGF–PM | ✔ | ✔ | ✔ | ✔ | ✔ |
| VIC | ✔ | ✔ | ✔ | ✔ | |
| ERA | ✔ | ✔ | | | |
| MERRA | ✔ | ✔ | | | |
| GLEAM | ✔ | ✔ | ✔ | ✔ | ✔ |
| SRB–CFSR–SEBS | ✔ | ✔ | ✔ | ✔ | ✔ |
| SRB–CFSR–PM | ✔ | ✔ | ✔ | ✔ | ✔ |
| SRB–CFSR–PT | ✔ | ✔ | ✔ | ✔ | ✔ |
| **TWSC** | | | | | |
| VIC | ✔ | ✔ | ✔ | ✔ | |
| GRACE–CSR | ✔ | ✔ | ✔ | ✔ | ✔ |
| GRACE–GFZ | ✔ | ✔ | ✔ | ✔ | ✔ |
| GRACE–JPL | ✔ | ✔ | ✔ | ✔ | ✔ |
| **R** | | | | | |
| VIC | ✔ | ✔ | ✔ | ✔ | ✔ |

The data in use in experiment (a) reference; (b) remove gauge; (c) remove reanalysis; (d) remove gauge and reanalysis; (e) remote sensing only, are checked in the table above; the experiments listed above are corresponding to the experiment (a–e) shown in Fig. 1, Fig. 2 in the unconstrained system and Fig. 7 in the constrained system

together, in the unconstrained system. Figure 1a shows the average monthly non-closure estimated from the reference data [experiment (a)]. Figure 1b–e shows the monthly average non-closure estimated by replacing the gauge-adjusted precipitation products with satellite-only product [experiment (b)], removing two reanalysis *ET* products [experiment (c)], removing both gauge-adjusted precipitation and reanalysis *ET* products [experiment (d)], and removing all gauge corrections, reanalysis, and LSM outputs [experiment (e)]. Figure 2 further shows the impact of removing/replacing different category/categories of the datasets from the reference dataset in terms of the mean absolute error (MAE, mm/yr) of the imbalance as a function of mean annual precipitation. It is noticed that the reference data give the best water budget closure across different climate regimes within different mean annual precipitation bins (dark line in Fig. 2). Only removing the reanalysis *ET* products [purple line in Fig. 2, experiment (c)] gives a better budget closure than the other three cases [red, blue and orange lines in Fig. 2, experiments (b), (d) and (e)] when the mean annual precipitation is higher than 30 mm; it gives a poorer closure than the cases with gauge removal [red line in Fig. 2, experiment (b)] and both gauge and reanalysis removal [blue line in Fig. 2, experiment (d)] when the mean annual precipitation is below 30 mm. As the area fraction of mean annual precipitation that is under 30 mm maintains a small portion (<5 %) in which only removing reanalysis gives worse closure, the spatial map of averaged imbalance also shows generally better closure estimates when only the reanalysis *ET* is removed [Fig. 1c, experiment (c)] than the other three cases in which the gauge-adjusted precipitation products are replaced with only using remote sensing products [Fig. 1b, d, e, experiments (b), (d) and (e)]. This indicates the critical role of gauge

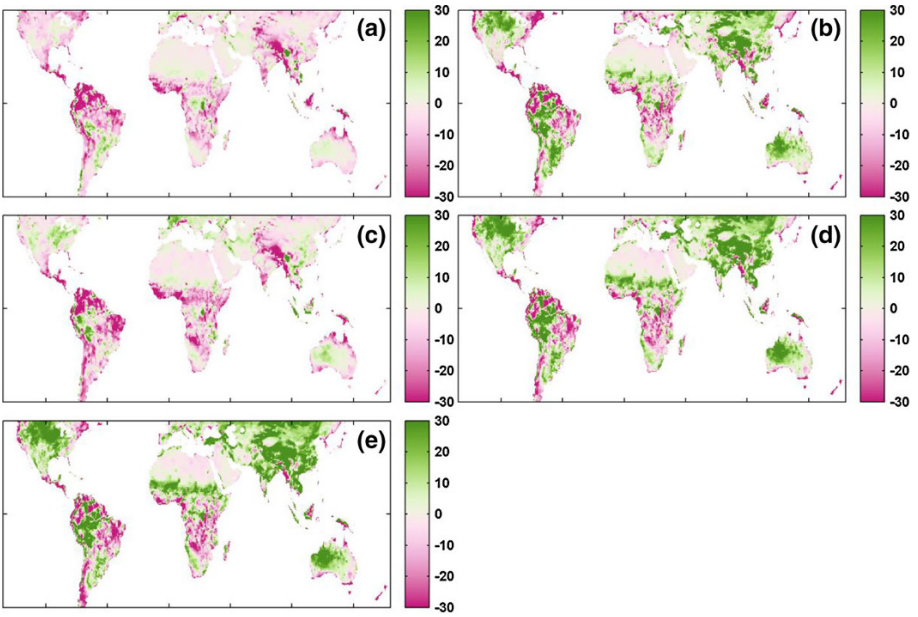


**Fig. 1** Sensitivity analysis according to experiments **a**–**e** in terms of the average monthly water budget closure (*P*–*ET*–*R*–*TWSC*, mm/month) during 2004–2007 in the unconstrained system for c **a** reference dataset; **b** in situ precipitation gauge products removed from the reference; **c** reanalysis removed from the reference; **d** both in situ precipitation gauge products and reanalysis removed from the reference; **e** replace the reference data with satellite-only remote sensing products and runoff from VIC

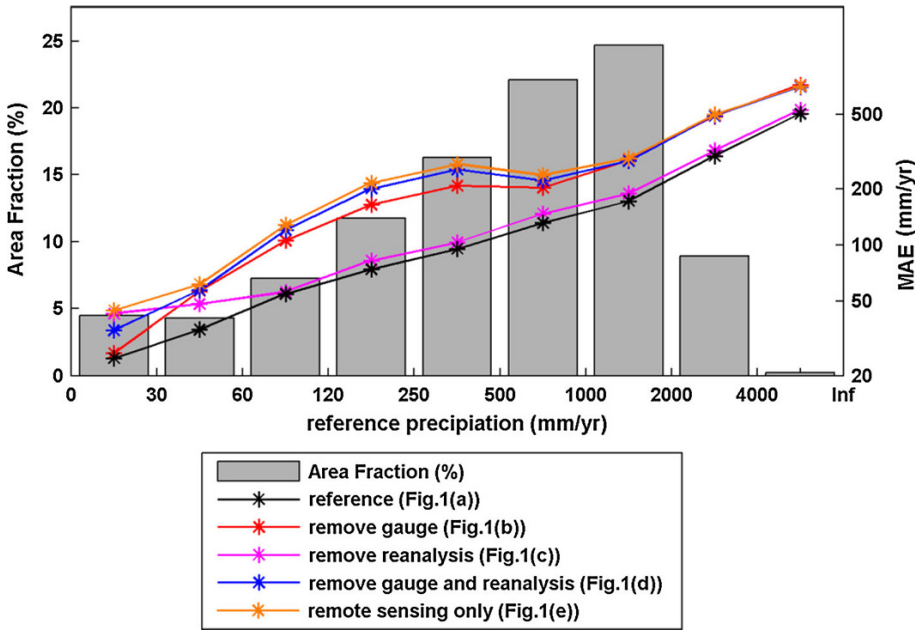


**Fig. 2** Mean absolute error (MAE, mm/yr) of the non-closure as a function of the amount of the mean annual precipitation from the reference for experiments **a**–**e** in the unconstrained system. *MAE is in log scale

correction in closing the water budget. The slight difference between Fig. 1b and d reveals the negative impact of further removing reanalysis *ET* products when the gauge-involved precipitation products are replaced with satellite remote sensing only product when the mean annual precipitation is smaller than 1000 mm [red line vs. blue line in Fig. 2, experiment (b) vs. (d)]; meanwhile, the difference between Fig. 1d and e suggests that the further removal of the *TWSC* and *ET* from LSM VIC has a slightly negative impact in the budget closure when the mean annual precipitation is lower than 1000 mm [blue line vs. orange line in Fig. 2, experiment (d) vs. (e)]. However, the three cases in which the gauge-adjusted precipitation products are replaced with remote sensing only product (red, blue, and orange lines in Fig. 2) show very similar performance in closing the budget when the precipitation is larger than 1000 mm/yr.

### 3.2 Roles of In Situ Precipitation Observations in Water Budget Closure

The role of in situ precipitation observations are investigated by comparing the water budget estimates between gauge-corrected satellite precipitation CSU and the TMPA-RT precipitation estimated solely from satellite observations, together with various remote sensing *ET* products, runoff from VIC, and *TWSC* from GRACE, at multiple temporal scales. In general, at the annual scale, the water budget is more balanced when the gauge-corrected CSU is combined with different remote sensing *ET* products than TMPA-RT as the markers are more aligned with the diagonal lines in Fig. 3**a1**–**e1**. The exceptions are South America, which shows an obvious balance deterioration when combined with *ET* products from SRB–PGF–PM, GLEAM and SRB–CFSR–PM, and Europe which shows a balanced deterioration as well when combined with *ET*s from SRB–CSFR–SEB and SRB–CFSR–PM. Similar to what is revealed by Fig. 3, Fig. 4 also shows improvement in budget estimation, represented by a general better agreement between $P - ET$ ($y$ axis) and VIC-simulated runoff ($x$ axis), from gauge-corrected CSU rather than using the non-gauge-corrected TMPA-RT at basin scales. Both Figs. 3 and 4 show a downshift of $P - ET$

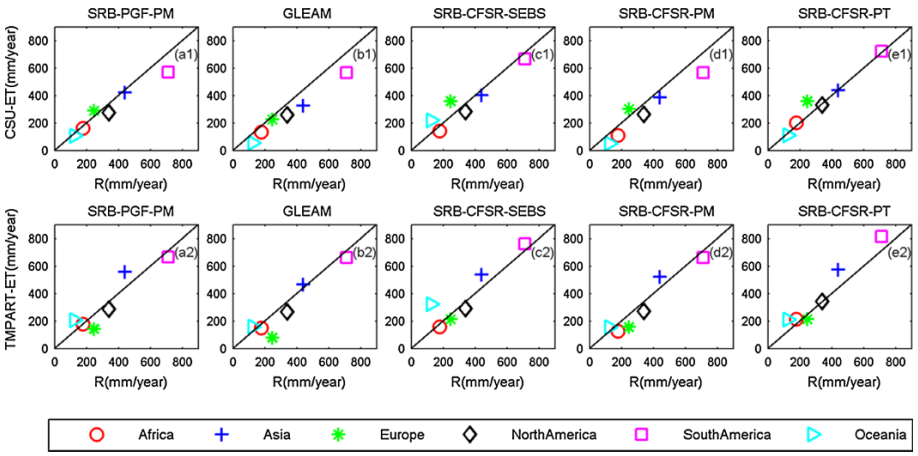


**Fig. 3** Comparison of the average annual runoff (mm/year) between the satellite inferred runoff ($y$ axis) from different *ET* products subtracted from ground rain gauge-corrected (CSU, **a1**–**e1**) and non-gauge-corrected (TMPA-RT, **a2**–**e2**) satellite precipitation, and land surface model simulated runoff (R, $x$ axis) during 2004–2007 at continental scales

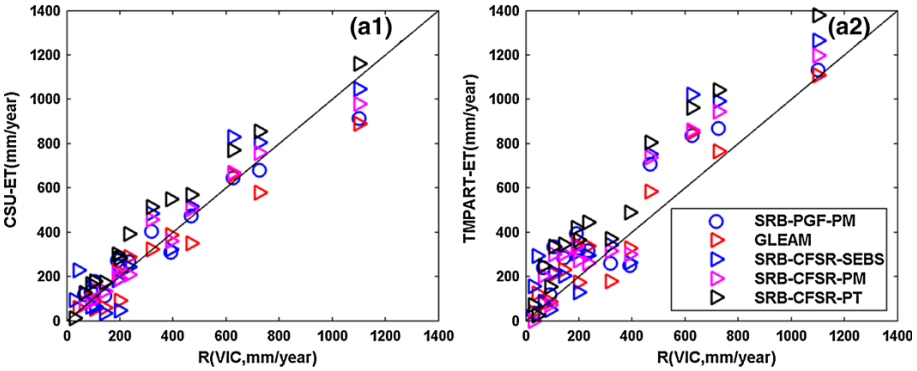


**Fig. 4** Comparison of the average annual runoff (mm/year) between the satellite inferred runoff (*y* axis) from different *ET* products subtracted from ground rain gauge-corrected (CSU, **a1**) and non-gauge-corrected (TMPA-RT, **a2**) satellite precipitation, and land surface model simulated runoff (R, *x* axis) during 2004–2007 at basin scales

(*y* axis) calculated from CSU to TMPA-RT at both continental and basin scales, which suggests an overall overestimation in TMPA-RT with respect to gauge observations.

The seasonal cycle of non-closure error estimated by CSU (Figs. 5**a1–f1**, 6**a1–f1**) and TMPA-RT (Figs. 5**a2–f2**, 6**a2–f2**) combined with different remote sensing *ET* products at both continental and basin scales are illustrated in Figs. 5 and 6, respectively. The spread of the non-closure error is relatively higher in South America in both cases when CSU (Fig. 5**e1**) and TMPA-RT (Fig. 5**e2**) are used for water budget estimation, and this indicates high uncertainties among different remote sensing *ET*s exist in South America. In general, the rain gauge-adjusted CSU precipitation products improve the water budget closure at both continental and basin scales relative to the remote sensing only TMPA-RT product, except in South America where the improvements are minimal compared to other continents (Fig. 5). The same happens for the Amazon and Murray Darling basins (Fig. 6).

The non-closure error ratio (%) is calculated as the absolute value of the non-closure divided by the precipitation and then aggregated over space and time at both annual and monthly scales as shown in Table 2. In general, CSU shows lower non-closure ratio than TMPA-RT when combining with most of the *ET* products. However, it shows higher non-closure when CSU is combined with GLEAM *ET* at annual scale, and SRB–CFSR–PM *ET* at both annual and monthly scales.

### 3.3 Effects of Different Remote Sensing *ET* Products in the Water Budget Closure

Five remote sensing *ET* products are evaluated in terms of non-closure ratio over land at multiple temporal scales when combined with CSU and TMPA-RT in estimating the budgets as listed in Table 3. Globally, SRB–CSFR–PT reaches the minimal non-closure ratio when combined with CSU at both annual (4.2 %) and monthly (8 %) scales. TMPA-RT shows the best estimation of the water budget when they are combined with SRB–CSFR–PM at the annual scale (7.6 %) and with the SRB–CSFR–PT at the monthly scale (9.3 %). Note that such an "optimal" combination of *P* and *ET* (in terms of budget closure) will depend on time and location.

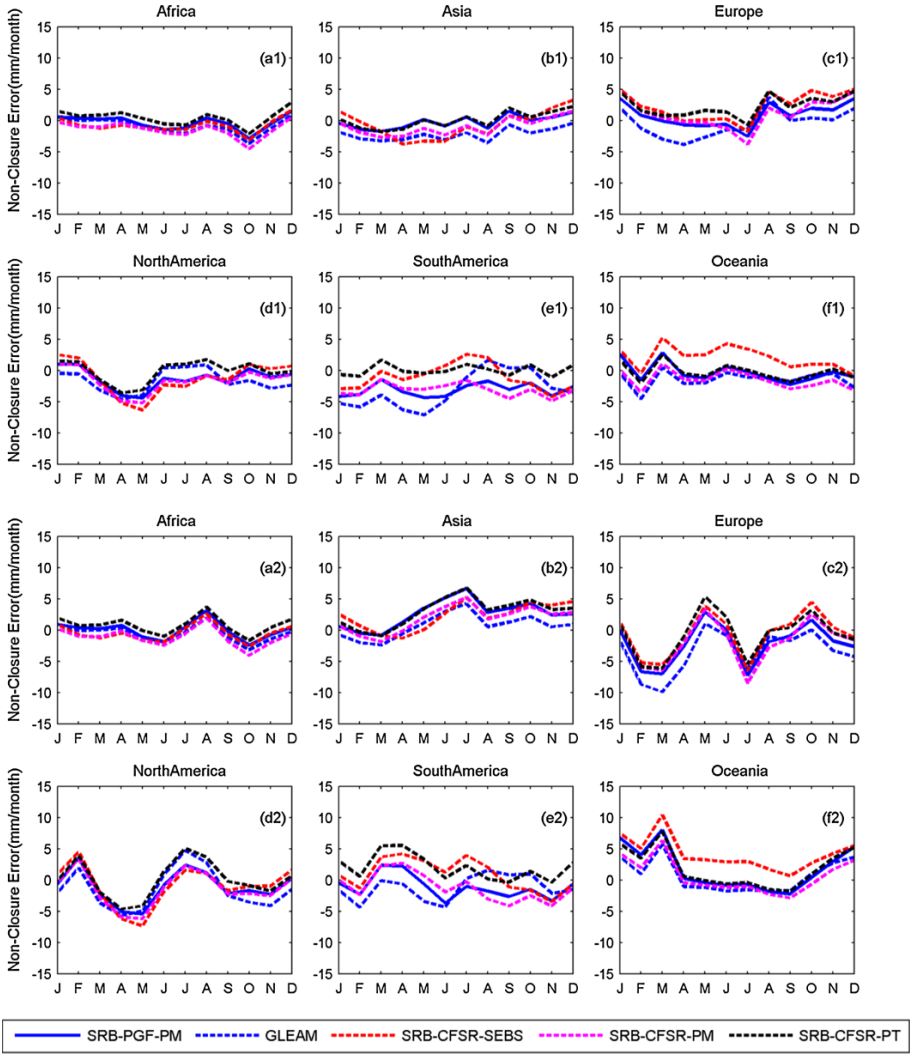


**Fig. 5** Comparison of the seasonal cycle of non-closure error estimated by ground rain gauge-corrected (CSU, **a1**–**e1**) and non-gauge-corrected (TMPA-RT, **a2**–**e2**) satellite precipitation, together with different *ET* products, *TWSC* from GRACE, and runoff simulated from VIC during 2004–2007 at continental scales

### 3.4 Roles of CKF in Constraining the Water Balance

Though the gauge-adjusted CSU product gives better water budget closure than the non-gauge-adjusted product TMPA-RT, neither exactly closes the water budget in the unconstrained system. In order to enforce the water balance, the CKF algorithm is applied, which assures closure of the budget at each global grid cell for experiments (a–e) in the constrained system. The precipitation and *ET* from the reference data [experiment (a)] in the constrained system are considered as one benchmark here to evaluate the performance of experiments (b–e). The relative root-mean-square error [RMSE (%)] of the constrained

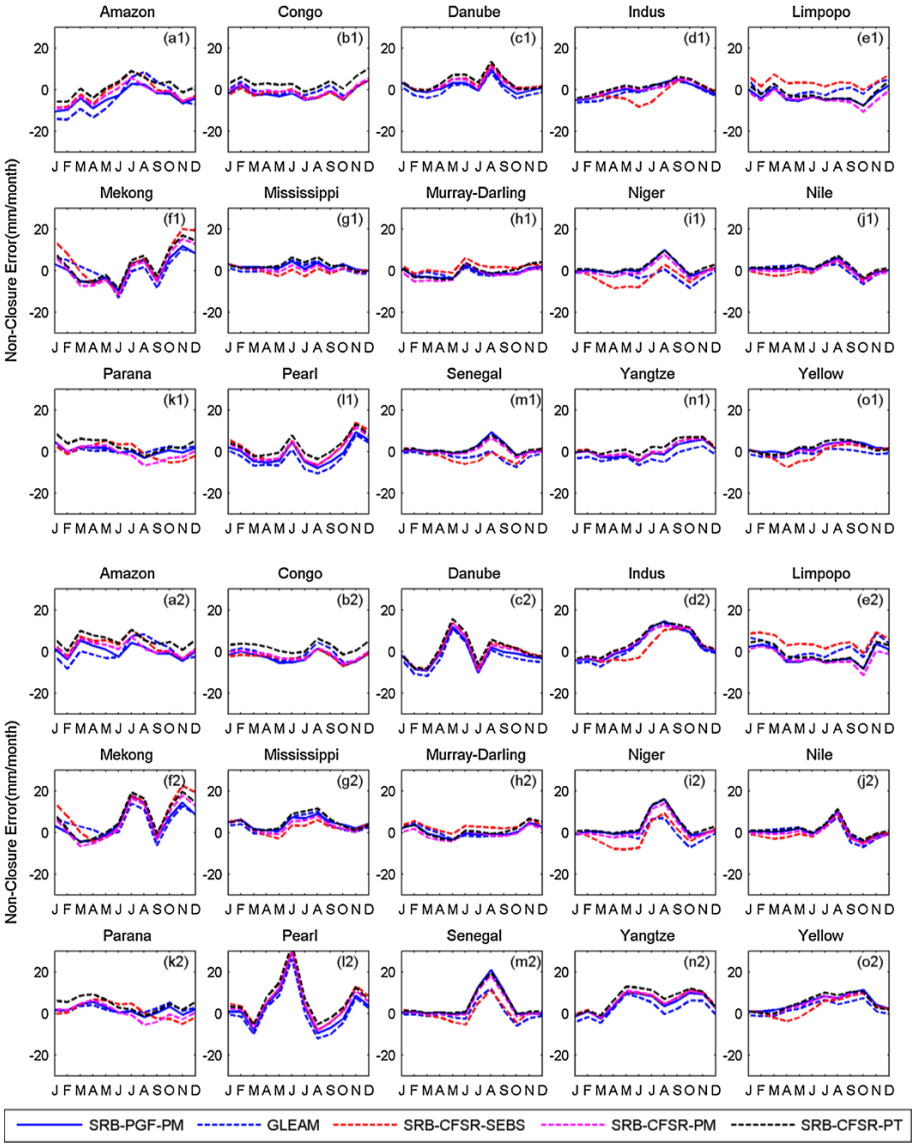


**Fig. 6** Comparison of the seasonal cycle of non-closure error estimated by ground rain gauge-corrected (CSU, **a1**–**o1**) and non-gauge-corrected (TMPA-RT, **a2**–**o2**) satellite precipitation, together with different *ET* products, *TWSC* from GRACE, and runoff simulated from VIC during 2004–2007 at basin scales

precipitation and *ET* estimates from experiments (b–e) is calculated against the reference dataset [experiment (a)]. In general, it shows that the closest *P* and *ET* estimates to the budget estimates, from the reference in the constrained system, when only the reanalysis is removed [purple line in Fig. 7, experiment (c)], while the poorest estimates are when all possible non-satellite sources are removed [orange line in Fig. 7, experiment (e)]. It is also found that removing the reanalysis causes less impact to the precipitation estimate (top

**Table 3** Non-closure ratio (%, non-closure/precipitation) at multiple temporal scales over land

| | | Annual | Monthly |
|---|---|---|---|
| CSU | SRB–PGF–PM | 4.9 | 9.4 |
| | GLEAM | 8.6 | 9.6 |
| | SRB–CFSR–SEBS | 8.7 | 10.7 |
| | SRB–CFSR–PM | 9.0 | 11.6 |
| | SRB–CFSR–PT | **4.2** | **8.0** |
| TMPA-RT | SRB–PGF–PM | 8.7 | 10.4 |
| | GLEAM | 8.3 | 10.0 |
| | SRB–CFSR–SEBS | 10.4 | 11.2 |
| | SRB–CFSR–PM | **7.6** | 10.3 |
| | SRB–CFSR–PT | 7.7 | **9.3** |

The numbers in bold indicate the best water budget estimates (with the least non-closure) that are optimally combined of *P* and *ET* from different products

panel in Fig. 7) than to the *ET* estimate (bottom panel in Fig. 7), especially when the reference annual precipitation and *ET* are relatively low.

This study aims at exploring the potential of the satellite remote sensing in replacing the reference data for budget estimation, which corresponds to experiment (e). Figure 8 shows an example of the water budget components (*P*, *ET* and *R* in Fig. 8a–c, and *TWSC* in Fig. 8d–f); water budget closure in the unconstrained system (Fig. 8g); the average attribution of each component with the remote sensing products [Fig. 8h corresponding to experiment (e)]; and the reference data [Fig. 8i corresponding to experiment (a)] are used to estimate the water budget throughout 2004–2007 for the unconstrained (first column) and constrained (second and third columns) systems for the Amazon River basin. Over the Amazon basin where the rainfall is heavy and the gauges are relatively sparse, the uncertainties in rainfall are higher, making precipitation the major recipient of the budget error attribution (Fig. 8h–i). The constrained water budget fluxes (*P*, *ET* and *R*) and *TWSC* estimated from remote sensing are similar to that estimated from the reference data. This suggests that though the reference data seem to close better the water budget (Fig. 1a) compared to the remote sensing data (Fig. 1e) in the unconstrained system, the budget estimates in the constrained system via CKF data assimilation approach are quite comparable between the remote sensing (Fig. 8b, e) and the reference data (Fig. 8c, f).

Further comparison of the monthly average terrestrial water budget estimates in both the unconstrained and constrained systems during 2004–2007 is shown in Fig. 9. The differences between the water budget components estimated from remote sensing and the reference data in both unconstrained system and constrained system are shown in Fig. 9**f1–l1** and **f2–l2**, respectively. There is no difference in runoff between reference and remote sensing in the unconstrained system (Fig. 9k1) as VIC runoff is the only source for both experiments. In the constrained system, such differences show up as the CKF redistributes budget errors. For precipitation, the difference between reference and remote sensing drops from the unconstrained system to the constrained system (Fig. 9**i1** vs. **i2** with the bias (%) dropping from 232 to −2 %, RMSE (%) dropping from 548 to 45 % and the correlation coefficient (CC) increasing from 0.43 to 0.94). Decreases in the differences between *ET*/*TWSC* estimated from the reference and remote sensing are also found when the constraint is enforced (Fig. 9**j1** vs. **j2** and **l1** vs. **l2**). The estimates from the reference data and the remote sensing in the constrained system are quite comparable, and this suggests good

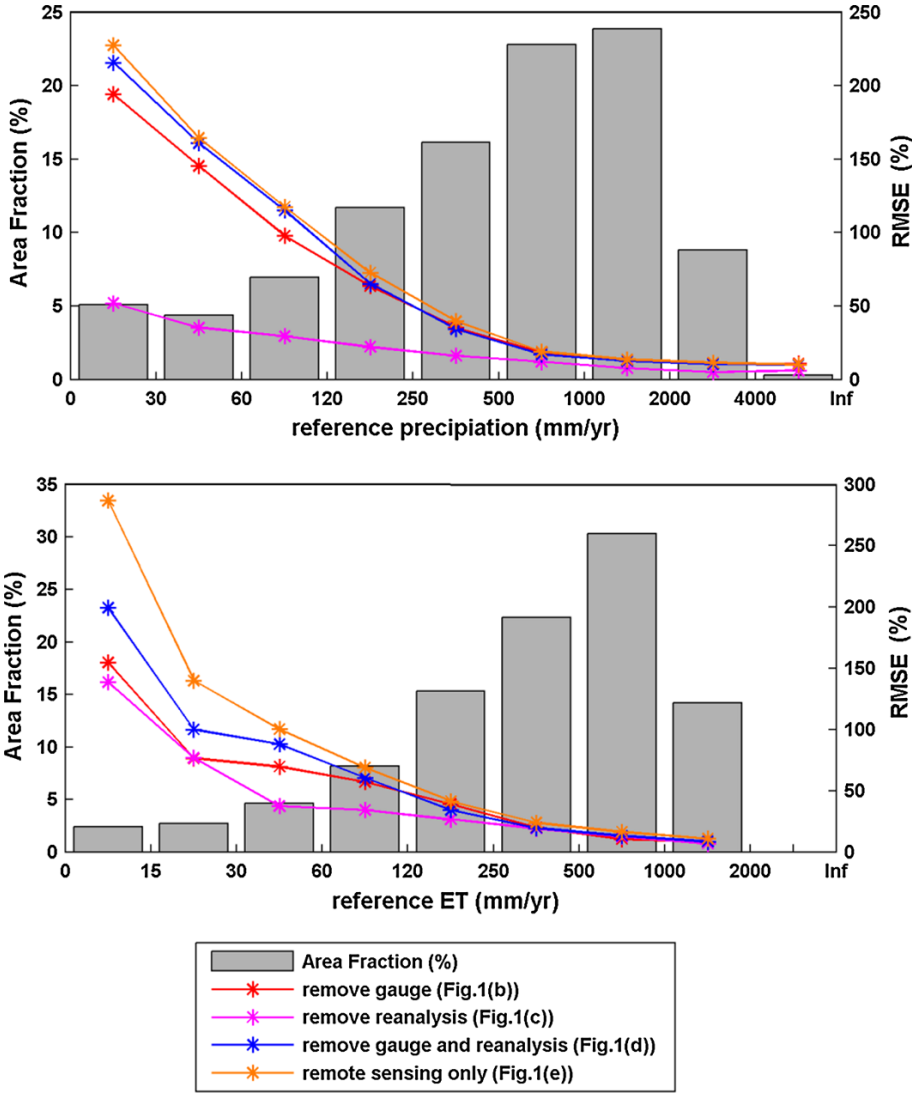


**Fig. 7** RMSE (%) of the non-closure as a function of mean annual precipitation and ET from the reference budget estimates for experiments (*b–e*) in the constrained system

potential of satellite remote sensing to provide a very good estimate of the global water budget if properly constrained.

### 3.5 Runoff Validation Against GRDC Data at the Basin Scale

In situ observational runoff data for 32 large basins as used in Pan et al. (2012) and 331 medium-sized basins (with sizes no larger than $10^4$ km$^2$) were collected from Global Runoff Data Centre (GRDC). The data availabilities vary from basin to basin. By filtering

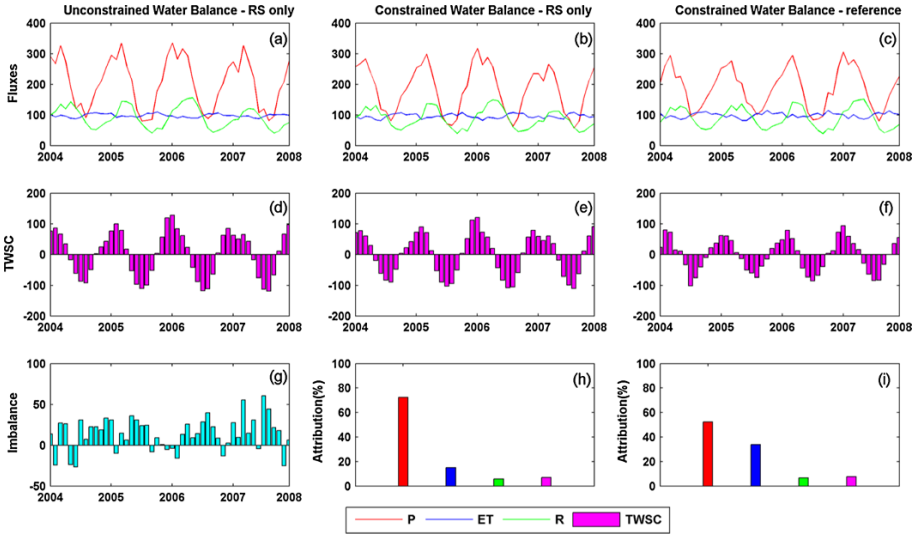


**Fig. 8** Unconstrained water budget (*P*, *ET* and *R* in **a**, *TWSC* in **d**) estimated from satellite remote sensing, constrained water budget estimated from satellite remote sensing (*P*, *ET* and *R* in **b**, *TWSC* in **e**) and the reference data (*P*, *ET* and *R* in **c**, *TWSC* in **f**) over the Amazon River basin. **g** is the imbalance before the water budget constraint. The imbalance after the water budget constraint equals to zero and the attribution from each water budget components are shown in **h**, **i** for unconstrained and constrained system, respectively

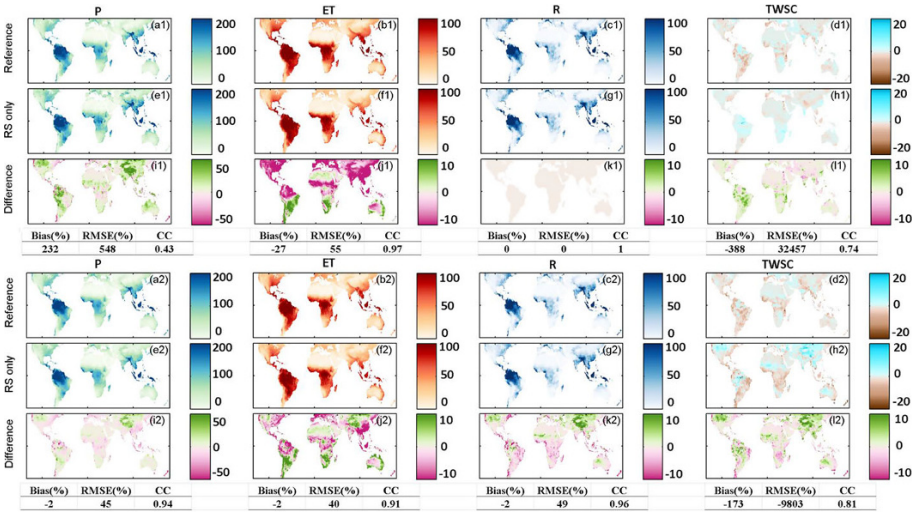


**Fig. 9** Comparison of the average monthly water budgets (mm/month) estimated from the reference data (**a1**–**d1**) and (**a2**–**d2**), the satellite remote sensing data (**e1**–**h1**) and (**e2**–**h2**), and the differences between the reference data and the remote sensing products in estimating the water budgets in the unconstrained (**i1**–**l1**) and constrained systems (**i2**–**l2**). *The corresponding statistic indices of water budgets estimated from remote sensing relative to the reference data are listed under each budget terms for both unconstrained and constrained system

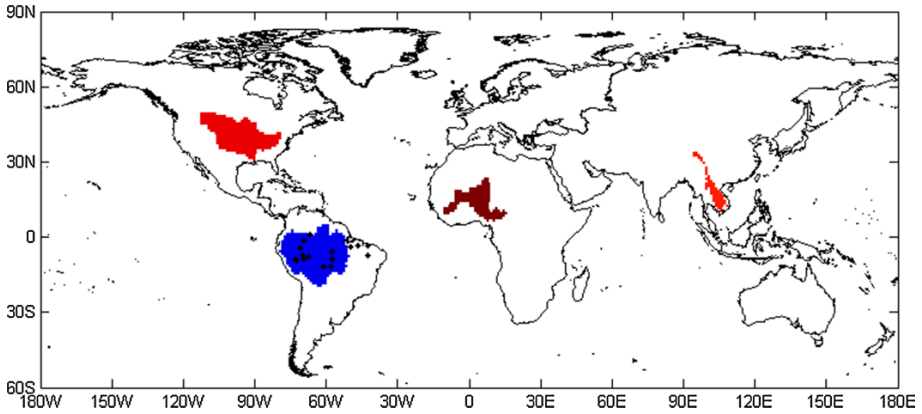


**Fig. 10** Locations of the four large river basins and the outlets of the 16 medium river basins for validation which are shown as + symbols

out those gauge observations with data availability that cover our research period 2004–2007, only four large basins and 16 medium-sized basins are left for validation (Fig. 10). This illustrates the challenge of identifying in situ runoff data for validating Earth observations. The basin sizes of the 16 medium basins are ranging from 10,400 to 363,000 $km^2$. The four large basins are evenly distributed in different continents, but all of the 16 medium-sized basins are located in South America. Figure 11 illustrated the monthly runoff time series estimated from a combination of different data sources, which correspond to experiments (a–e) in the constrained system, compared against the GRDC observation. The runoffs estimated and constrained from different data sources from experiments (a–e) align well with each other for those four large river basins except for Mississippi river basin, which has the densest in situ observations that may lead to large variations among different data sources for the same water budget component (particularly precipitation during the summer season). The larger variation in any of the budget component will impact the budgets estimated and constrained from the constrained system. The poor estimates of runoff in Niger River basin might be caused by the precipitation error over that region due to limited in situ observation of precipitation in Africa that would impact the data quality of precipitation products from different sources, or features like wetlands that are not well represented in VIC.

Figure 12 further provides the comparison of monthly mean runoff estimated from the five experiments with different data sources against GRDC observations for the sixteen medium-sized river basins. Similar to what is shown in Fig. 11, the runoff estimated and constrained from different data sources from experiments (a–e) are in general agreement, which demonstrate that using satellite remote sensing only data sources [experiment (e)] together with the CKF in the constrained system can achieve similar budget estimates (e.g., for runoff) to other experiments (a–d) with different data sources. However, some of the runoff estimated from the experiments does not align well with GRDC observations. This is possibly due to the coarse spatial resolution (0.5°) of the estimated budgets from the experiments. Uncertainties exist in the basin mask files for extracting the monthly runoff

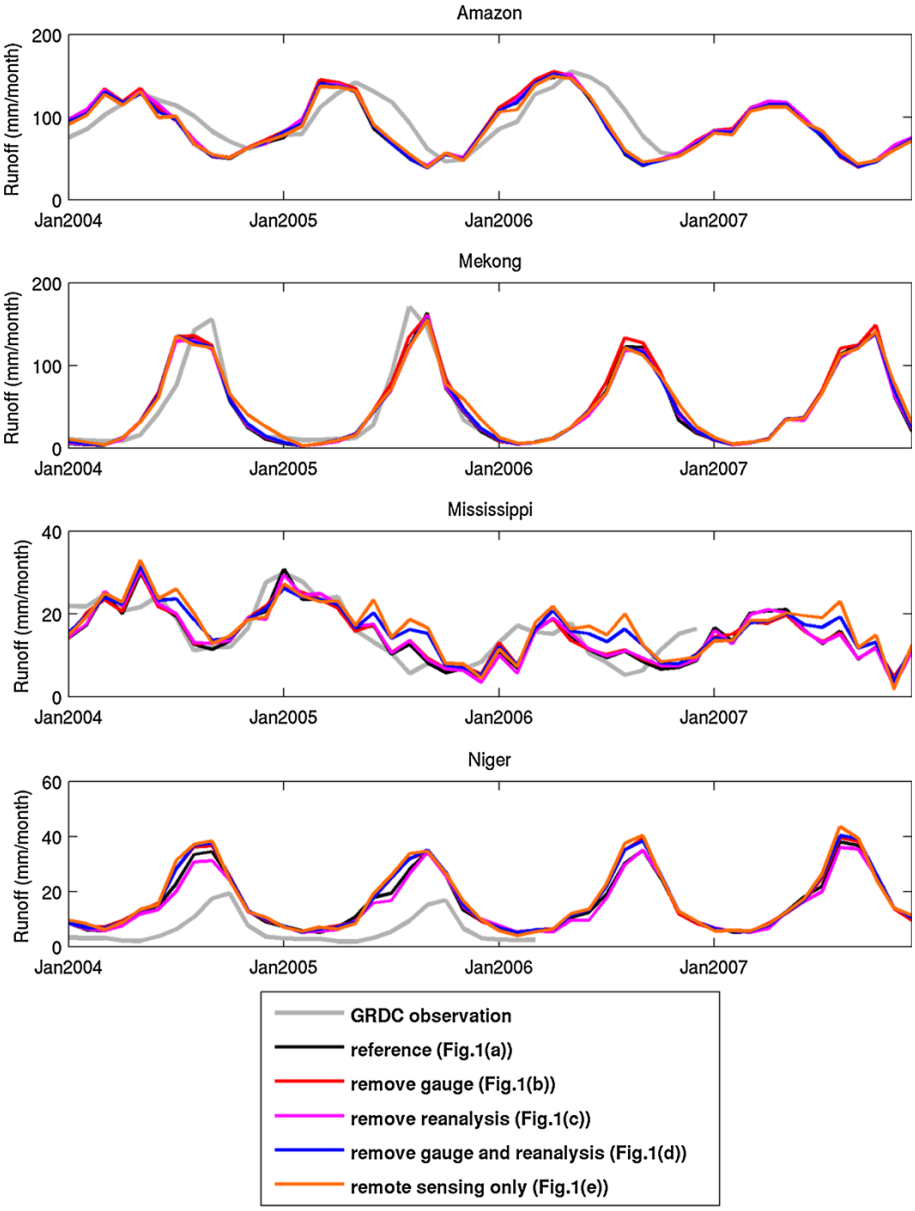


**Fig. 11** Comparison of monthly time series of runoff estimated from experiments (*a–e*) from the constrained system over the four large river basins against GRDC observation

from the global datasets, and these uncertainties would be particular large for those basins which only cover a limited number of pixels, though we have assigned a fraction to those boundary pixels in our basin mask extraction algorithm.

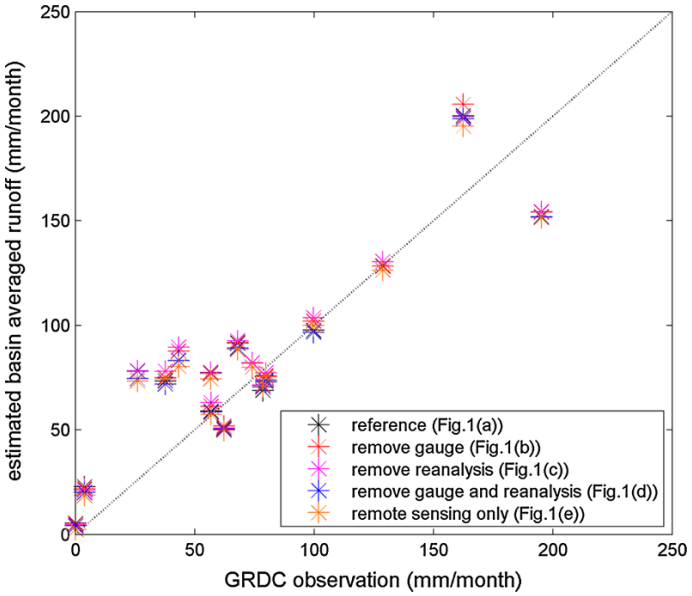


**Fig. 12** Comparison of monthly mean runoff estimated from experiments (*a*–*e*) from the constrained system over the 16 medium-sized river basins against GRDC observation

## 4 Conclusions

This study creates closed terrestrial, global water budget estimates using satellite remote sensing at a 0.5° spatial resolution and monthly timescale for the period of 2004–2007. We also investigate the roles of data from different sources in estimating and closing the budget, and particularly assess the capability of the satellite remote sensing in closing the terrestrial water budget at the 0.5° spatial resolution through constrained data assimilation.

The water budget closure is sensitive to the gauge-adjusted precipitation but is less sensitive to reanalysis *ET* products in the unconstrained system. Comparison among the water budget closure datasets that were estimated by removing/replacing one or more categories of data from the reference set shows that non-satellite data sources can help to reduce the non-closure errors significantly. Particularly, replacing the gauge-corrected precipitation datasets with satellite-only TMPA-RT for the budget estimation leads to larger non-closure errors, which reflects a high bias in TMPA-RT.

The rain gauge-corrected CSU precipitation product, when combined with different remote sensing *ET* products, *TWSC* from GRACE and runoff from VIC, outperforms the non-gauge-corrected TMPA-RT precipitation at multiple spatial and temporal scales in the water budget closure. The discrepancy between the non-closure errors based on using CSU or TMPA-RT precipitation demonstrates the need of a rain gauge adjustment for global gridded satellite-based water budget estimates.

As neither the reference data [experiment (a)] nor the remote sensing data [experiment (e)] can exactly close the water budget in the unconstrained system, the CKF data assimilation approach is applied to constrain the budget closure. Once constrained, the differences between budget estimates from the reference data and from satellite-only remote sensing become fairly small, suggesting a good potential for being able to use remote sensing alone to reasonably reproduce the water budgets.

Runoff estimated from experiments (a–e) with constraints is validated against GRDC observations. A limited number of basins are applied for validation due to the limited data availability for the study period. The validation results show that the runoff estimated from remote sensing only in experiment (e) can achieve very similar runoff estimates from other experiments (a–d) with more categories of data sources, and meanwhile is lined up fairly well with GRDC runoff expect for those smaller basins with mask uncertainties for the coarse spatial resolution at 0.5°.

As we demonstrate the potential for remote sensing in water budget studies, further efforts are still needed to understand the discrepancies among different data sources such as in situ observations, satellite remote sensing, land surface models, and reanalysis data products in closing the water budget. With the current satellite missions such as the Global Precipitation Mission (GPM) and Soil Moisture Active Passive (SMAP) mission, and future missions such as Surface Water Ocean Topography (SWOT) mission for global surface elevations and river stage and discharge, it is very promising that the community can retrieve accurate depiction of the global water budget at fine resolutions and over a longer time period.

**Acknowledgments** This paper is part of the special issue of the ISSI workshop on remote sensing and water resources. This work is supported by NASA research grants NNX08AN40A "Developing Consistent Earth System Data Records for the Global Terrestrial Water Cycle" and NNX09AK35G "Development and diagnostic analysis of a multi-decadal global evaporation product for NEWS"

## References

Adler RF, Kidd C, Petty G, Morissey M, Goodman HM (2001) Intercomparison of global precipitation products: the third Precipitation Intercomparison Project (PIP-3). Bull Am Meteorol Soc 82:1377–1396

Bytheway JL, Kummerow CD (2013) Inferring the uncertainty of satellite precipitation estimates in data-sparse regions over land. J Geophys Res Atmos 118:9524–9533. doi:10.1002/jgrd.50607

Dirmeyer PA, Gao X, Zhao M, Guo Z, Oki T, Hanasaki N (2006) GSWP-2: multimodel analysis and implications for our perception of the land surface. Bull Am Meteorol Soc 87:1381–1397. doi:10.1175/BAMS-87-10-1381

Durand M, Fu L-L, Lettenmaier DP, Alsdorf DE, Rodriguez E, Esteban-Fernandez D (2010) The surface water and ocean topography mission: observing terrestrial surface water and oceanic submesoscale eddies. Proc IEEE 98:766–779

Famiglietti JS (2014) The global groundwater crisis. Nat Clim Change 4:945–948. doi:10.1038/nclimate2425

Fisher JB, Tu KP, Baldocchi DD (2008) Global estimates of the land–atmosphere water flux based on monthly AVHRR and ISLSCP-II data, validated at 16 FLUXNET sites. Remote Sens Environ 112:901–919

Funk CC et al (2014) A quasi-global precipitation time series for drought monitoring. US Geol Surv Data Ser. doi:10.3133/ds832

Gao H, Tang Q, Ferguson CR, Wood EF, Lettenmaier DP (2010) Estimating the water budget of major US river basins via remote sensing. Int J Remote Sens 31:3955–3978

Haddeland I et al (2011) Multimodel estimate of the global terrestrial water balance: setup and first results. J Hydrometeorol 12:869–884

Hong Y, Gochis D, Cheng J-T, Hsu K-L, Sorooshian S (2007) Evaluation of PERSIANN-CCS rainfall measurement using the NAME event rain gauge network. J Hydrometeorol 8:469–482

Huffman GJ et al (2007) The TRMM multisatellite precipitation analysis (TMPA): quasi-global, multiyear, combined-sensor precipitation estimates at fine scales. J Hydrometeorol 8:38–55

Huffman GJ, Adler RF, Bolvin DT, Nelkin EJ (2010) The TRMM multi-satellite precipitation analysis (TMPA). Springer, Satellite rainfall applications for surface hydrology, pp 3–22

Jacob T, Wahr J, Pfeffer WT, Swenson S (2012) Recent contributions of glaciers and ice caps to sea level rise. Nature 482:514–518

Joyce RJ, Janowiak JE, Arkin PA, Xie P (2004) CMORPH: a method that produces global precipitation estimates from passive microwave and infrared data at high spatial and temporal resolution. J Hydrometeorol 5:487–503
Landerer FW, Swenson SC (2012) Accuracy of scaled GRACE terrestrial water storage estimates. Water Resour Res 48(4)
Luo L, Wood EF, Pan M (2007) Bayesian merging of multiple climate model forecasts for seasonal hydrological predictions. J Geophys Res Atmos 1984–2012:112
Miralles DG, Holmes TRH, De Jeu RAM, Gash JH, Meesters AGCA, Dolman AJ (2011) Global land-surface evaporation estimated from satellite-based observations. Hydrol Earth Syst Sci 15:453–469. doi:10.5194/hess-15-453-2011
Mu Q, Heinsch FA, Zhao M, Running SW (2007) Development of a global evapotranspiration algorithm based on MODIS and global meteorology data. Remote Sens Environ 111:519–536
Oki T, Musiake K, Matsuyama H, Masuda K (1995) Global atmospheric water balance and runoff from large river basins. Hydrol Process 9:655–678
Paiva RCD, Durand MT, Hossain F (2015) Spatiotemporal interpolation of discharge across a river network by using synthetic SWOT satellite data. Water Resour Res 51:430–449
Pan M, Sahoo AK, Troy TJ, Vinukollu RK, Sheffield J, Wood EF (2012) Multisource estimation of long-term terrestrial water budget for major global river basins. J Clim 25:3191–3206
Pavelsky TM, Durand MT, Andreadis KM, Beighley RE, Paiva RCD, Allen GH, Miller ZF (2014) Assessing the potential global extent of SWOT river discharge observations. J Hydrol 519:1516–1525
Rienecker MM et al (2011) MERRA: NASA's modern-era retrospective analysis for research and applications. J Clim 24:3624–3648. doi:10.1175/JCLI-D-11-00015.1
Rodell M et al (2015) The observed state of the water cycle in the early 21st century. J Clim. doi:10.1175/JCLI-D-14-00555.1
Sahoo AK, Pan M, Troy TJ, Vinukollu RK, Sheffield J, Wood EF (2011) Reconciling the global terrestrial water budget using satellite remote sensing. Remote Sens Environ 115:1850–1865
Sakumura C, Bettadpur S, Bruinsma S (2014) Ensemble prediction and intercomparison analysis of GRACE time-variable gravity field models. Geophys Res Lett 41:1389–1397
Schneider U, Becker A, Finger P, Meyer-Christoffer A, Ziese M, Rudolf B (2014) GPCC's new land surface precipitation climatology based on quality-controlled in situ data and its role in quantifying the global water cycle. Theor Appl Climatol 115:15–40. doi:10.1007/s00704-013-0860-x
Sheffield J, Wood EF (2007) Characteristics of global and regional drought, 1950–2000: analysis of soil moisture data from off-line simulation of the terrestrial hydrologic cycle. J Geophys Res Atmos 112:D17115. doi:10.1029/2006JD008288
Sheffield J, Goteti G, Wood EF (2006) Development of a 50-year high-resolution global dataset of meteorological forcings for land surface modeling. J Clim 19:3088–3111
Sheffield J, Ferguson CR, Troy TJ, Wood EF, McCabe MF (2009) Closing the terrestrial water budget from satellite remote sensing. Geophys Res Lett 36(7)
Simmons A, Uppala S, Dee D, Kobayashi S (2006) ERA-interim: new ECMWF reanalysis products from 1989 onwards. ECMWF Newsl 110:26–35
Tapley BD, Bettadpur S, Ries JC, Thompson PF, Watkins MM (2004) GRACE measurements of mass variability in the Earth system. Science 305:503–505
Thomas AC, Reager JT, Famiglietti JS, Rodell M (2014) A GRACE-based water storage deficit approach for hydrological drought characterization. Geophys Res Lett 41:1537–1545
Tian Y, Peters-Lidard CD (2010) A global map of uncertainties in satellite-based precipitation measurements. Geophys Res Lett 37(24)
Trenberth KE, Smith L, Qian T, Dai A, Fasullo J (2007) Estimates of the global water budget and its annual cycle using observational and model data. J Hydrometeorol 8:758–769
Troy TJ, Sheffield J, Wood EF (2011) Estimation of the terrestrial water budget over northern eurasia through the use of multiple data sources. J Clim 24:3272–3293. doi:10.1175/2011JCLI3936.1
Vinukollu RK, Meynadier R, Sheffield J, Wood EF (2011) Multi-model, multi-sensor estimates of global evapotranspiration: climatology, uncertainties and trends. Hydrol Process 25:3993–4010. doi:10.1002/hyp.8393
Wahr J, Swenson S, Zlotnicki V, Velicogna I (2004) Time-variable gravity from GRACE: first results. Geophys Res Lett 31(11)
Wang S, Huang J, Li J, Rivera A, McKenney DW, Sheffield J (2014) Assessment of water budget for sixteen large drainage basins in Canada. J Hydrol 512:1–15
Weedon GP et al (2011) Creation of the WATCH forcing data and its use to assess global and regional reference crop evaporation over land during the twentieth century. J Hydrometeorol 12:823–848

DOI 10.1007/978-3-319-32449-4_5
Reprinted from *Surveys in Geophysics* Journal, DOI 10.1007/s10712-016-9362-6

# Lake Volume Monitoring from Space

**J.-F. Crétaux[1] · R. Abarca-del-Río[2] · M. Bergé-Nguyen[1] · A. Arsen[3] · V. Drolon[3] · G. Clos[1] · P. Maisongrande[1]**

Received: 11 September 2015 / Accepted: 20 January 2016 / Published online: 8 February 2016


**Abstract** Lakes are integrators of environmental change occurring at both the regional and global scale. They present a wide range of behavior on a variety of timescales (cyclic and secular) depending on their morphology and climate conditions. Lakes play a crucial role in retaining and stocking water, and because of the significant global environmental changes occurring at several anthropocentric levels, the necessity to monitor all morpho-dynamic characteristics [e.g., water level, surface (water contour) and volume] has increased substantially. Satellite altimetry and imagery are now widely used together to calculate lake and reservoir water storage changes worldwide. However, strategies and algorithms to calculate these characteristics are not straightforward, and specific approaches need to be developed. We present a review of some of these methodologies by using lakes over the Tibetan Plateau to illustrate some critical aspects and issues (technical and scientific) linked to the observation of climate change impact on surface waters from remote sensing data. Many authors have measured water variation using the limited remote sensing measurements available over short time periods, even though the time series are probably too short to directly link these results with climate change. Indeed, there are many processes and factors, like the influence of lake morphology, that are beyond observation and are still uncertain. The time response for lakes to reach a new state of equilibrium is a key aspect that is often neglected in current literature. Observations over a long period of time, including maintaining a constellation of comprehensive and complementary satellite missions with service continuity over decades, are therefore necessary especially when the ground gauge network is too limited. In addition, the design of future satellite missions with new instrumental concepts (e.g., SAR, SARin, Ka band altimetry, Ka interferometry) will also be suitable for complete monitoring of continental waters.

✉ J.-F. Crétaux
jean-francois.cretaux@legos.obs-mip.fr

[1] Legos/CNES, 14 Avenue Edouard Belin, 31400 Toulouse, France

[2] Departamento de Geofísica (DGEO), Universidad de Concepción (UDEC), 160-C, Concepción, Chile

[3] Legos/CNRS, 14 Avenue Edouard Belin, 31400 Toulouse, France

**Keywords** Satellite altimetry and imagery · Lakes · Climate change · Tibetan Plateau

## 1 Introduction

Water is an unavoidable need for all life on Earth. An adequate supply of clean, safe, freshwater is a basic prerequisite for human survival and the economic development of regions and nations. However, water is unevenly distributed in space or in time and does not always coincide with our consumption needs and wants (domestic, agricultural or industrial). On a global scale, water runoff is largely concentrated in the temperate climatic zones and equatorial regions. The general geographical distribution of the world's lakes is also very irregular with most of them being located over the Northern Hemisphere and at higher latitudes in glaciated areas (Downing et al. 2006). Lakes and reservoirs constitute essential elements of the hydrological and biogeochemical water cycles due to their basic ability to store, retain, clean, and provide water consistently. They influence many facets of ecology, biodiversity (Dudgeon et al. 2006), the economy, and human welfare (Rast and Straskraba 2000). It therefore follows that lakes are important modifiers of many biochemical and hydrological processes. Lakes vary physically in terms of illumination levels (incoming radiation), temperature, and water currents and also have chemical variations in terms of nutrients, major ions, and contaminants. Biological variations can be noted in terms of structure and function as well as static versus dynamic variables, such as biomass, population numbers, and growth rates. All these variables present spatial and temporal variability, the latter going from minutes to geological times (see Rast and Straskraba 2000). Lake, reservoir, and wetland distribution is of great interest in many scientific disciplines. Besides their regional significance, global distribution is of special interest for large-scale studies of environment, biodiversity, health (spread of waterborne diseases), agricultural suitability, climate change modeling, and for assessments of present and future water resources (Williamson et al. 2009). Despite their importance, many considered continental waters to be a minor part of the biosphere, and therefore, until very recently, the activity of inland waters was ignored in global estimates of ecosystem processes (see Downing 2010). Now it is recognized that freshwater ecosystems play a substantial role in many key processes, such as within anthropogenic gases flux exchanges (Tranvik et al. 2009; Raymond et al. 2013; Seekel et al. 2014). It was only until very recently that there were still major uncertainties in these global estimates because many key processes (physical, chemical, and biological) scale with lake size and the total area and distribution of lentic ecosystems were not well reported.

There are a limited number of comprehensive worldwide lake datasets (Halbfass 1914; Meybeck 1995; Lehner and Döll 2004; Downing et al. 2006; McDonald et al. 2012) that contain information on location, extent, and other basic characteristics of open water bodies and wetland areas on a global scale. The recent developments in the field of remote sensing have improved these datasets and promise global land cover images of increasing quality and resolution, including the possibility to monitor spatiotemporal changes in lake and wetland extents. Verpoorter et al. (2014) made a recent inventory of global lakes using satellite imagery with production of contours for all lakes that are greater than 0.002 $km^2$, which is currently the most complete existing database. They counted more than 117 million lakes for a total surface area of 5,000,000 $km^2$.

Since the middle of the 1990's, satellite radar altimetry has been a successful technique for monitoring height variations of continental surface water, such as lakes and rivers (Morris and Gill 1994; Alsdorf et al. 2001; Calmant et al. 2008; Abarca-del-Rio et al. 2012; Sima et al. 2013; Yi et al. 2013; Silva et al. 2014; Pandey et al. 2014; Tarpanelli et al. 2015 and many others). The surface water level is measured within a terrestrial reference frame with repeatability varying from 10 to 35 days depending on the orbit cycle of the satellite. Although data acquisition is independent from weather conditions, radar altimetry can have a few limitations; i.e., lake-shore topography may affect elevation calculations from the altimeter. In some extreme cases of mountain lakes, echoes can be foreseen and tracked several kilometers before and after the satellite passes causing slant range estimation (Arsen et al. 2015). Many measurements can be lost due to the presence of other small water bodies at different altitudes in the vicinity of the main target. Accuracy of elevation retrieval is also dependent on lake or river size and also on surface roughness. Finally, an altimeter is a nadir pointing system and therefore does not have a global view of the planet. However, the altimetry technique permits systematic continental-scale lake and river monitoring and can provide water level estimations in remote areas where in situ data are not available. Another advantage of satellite altimetry is its ability to monitor lakes and rivers over decades with a revisit on each target ranging from a few days to a few months depending on the orbit. For example, the TOPEX/Poseidon or Jason-1 and Jason-2 satellites have a cycle of 10 days, while for CryoSat-2 the revisit cycle is 369 days allowing a very dense coverage of the Earth's surface. For large lakes, many satellites can pass over them providing continuous surveillance over decades.

A lake acts as an integrator of climate change (Adrian et al. 2009; Schindler 2009), from seasonal to inter-annual and secular scales, with different response times depending on its morphology (Mason et al. 1994). The water stored in lakes responds (directly and indirectly) to any changes in precipitation and air temperature (Robertson and Ragotzkie 1990; De Wit and Stankiewicz 2006).

Climate change impacts lakes in many different ways. For example, increasing air temperature in mountain areas accelerates glacial thawing leading to a dramatic increase in surface runoff like over the Tibetan Plateau (Wang et al. 2012; Gao et al. 2015) or the Andean chain (Bliss et al. 2014; López-Moreno et al. 2014). Meanwhile, the increasing air temperature also enhances evapotranspiration over the lake's watershed, therefore leading to diminished runoff. It is clear that mountain lakes are also directly influenced by changes in precipitation (Kang et al. 2010; Lei et al. 2014). In tropical regions, the exchange of water between ocean and atmosphere has a direct impact on continental waters at seasonal and inter-annual timescales. The lakes in eastern Africa are a case in point. Many authors have investigated these links, especially between large lakes like Victoria, Malawi or Tanganyika, and the Indian Ocean. They have shown that the role of the Indian Ocean in the water level time series is significantly correlated with El-Niño (Nicholson and Yi 2002) or with the Indian Ocean Dipole (Tierney et al. 2013). In arid regions the impact of climate change may also be very significant, although it can be masked by human use of water resources. This is the case in Central Asia for example, where the Aral Sea started to shrink in the 1960's due to irrigation of the central Asian steppes for agricultural development, but this shrinkage has also been enhanced by climate warming (Aus Der Beck et al. 2011; Cretaux et al. 2013b). Lakes also play a major role in the water cycle processes of the boreal regions. These regions (like Siberia or Canada) are characterized by the presence of large flooded areas and a very dense network of hundreds of lakes. This includes a mix of both permanent and temporary lakes. The result is a high rate of evaporation in summertime, while in winter most of these lakes are covered with ice (Kouraev et al. 2007).

For example, inter-annual changes of lake areas in the Yukon Valley (Alaska) were quantified over the period 1954–2000 by Altmann et al. (2010) who found that 2300 lakes increased, 430 shrank, and only 200 remained unchanged. Moreover, the role of lakes and reservoirs in the prediction of future climate impact on water resources is now taken into account in hydrological and atmospheric models (Bowling and Lettenmaier 2010; Balsamo et al. 2012).

It is therefore essential to measure their elevation changes over very long time periods, which will reinforce interest in multi-satellite constellations. As a final point on large lakes, depending on size and wind conditions accuracy is relatively good compared with in situ measurements as it may reach down to a few centimeters (e.g., the Great Lakes of North America, large lakes in East Africa or in Central Asia, Cretaux et al. 2011; Cheng et al. 2010; Ričko et al. 2012). For smaller lakes, accuracy of satellite altimetry is reduced but generally kept lower than the amplitude of inter-annual variability of the lake level (it may reach several meters or decameters for some artificial reservoirs), which in the absence of other measurements (e.g., in situ) remains a useful source of information for different purposes ranging from science to operational (Cretaux et al. 2015). It is impossible to measure lake and reservoir level variations globally from ground measurements. Furthermore, satellite radar altimetry techniques have moved from being experimental to fully operational under space agencies' program frameworks from many parts of the world (Europe, USA, China, and India) allowing continuity of service.

Lake surveying is an important objective for WMO (World Meteorological Organization) and GCOS (Global Climate Observing System) as lakes are potential proxies within the framework of global climate variability. In actual fact, the volume of water in a surface storage unit at any time is an integrator variable, reflecting both atmospheric (precipitation, evaporation energy) and hydrological (surface water recharge, discharge and ground water tables) conditions. Thus, within the few Essential Climate Variables (ECVs) (see http://www.gosic.org/ios/MATRICES/ECV/ECV-matrix.htm and http://www.fao.org/gtos/doc/pub52.pdf) defined to support the work of the United Nations Framework Convention on Climate Change (UNFCCC) and the Intergovernmental Panel on Climate Change (IPCC), one of these variables refers to water level changes and 79 lakes worldwide have been selected by the Global Terrestrial Network for Lakes (GTN-L) for monitoring (see http://www.gosic.org/content/gcos-terrestrial-ecv-lakes and http://www.gosic.org/sites/default/files/ECVT4-Lakes.pdf). For that reason, a data collection center (called Hydrolare, see http://hydrolare.net/database.php) has been created under the sponsorship of GCOS and GTOS (Global Terrestrial Observing System) and is hosted by the State Hydrological Institute of St Petersburg in Russia. Its function is to maintain a Web database for delivery of the ECVs of the lakes in the GTN-L list (see http://www.wmo.int/pages/prog/gcos/documents/GTN-L_List.pdf) based on synergy of in situ gauges (working with national hydrological services and other institutions and agencies providing and holding data on lakes and reservoirs) and remote sensing data, principally satellite altimeter measurements.

The Hydroweb database (http://www.legos.obs-mip.fr/en/soa/hydrologie/hydroweb/) was created by Legos (Toulouse, France) in 2003, and delivers the water level of 230 lakes and volume of about 100 lakes and is officially associated with Hydrolare. Hydroweb products are completely based on satellite altimetry and imagery.

In Sect. 2 of this paper, we provide a general introduction to satellite altimetry. In Sect. 3 we concentrate on satellite imagery, and in Sect. 4 we demonstrate how to calculate lake water storage changes by a combination of both these techniques, and the Hydroweb database is briefly presented. In Sect. 5 we illustrate how to apply these techniques to a regional case study of lakes covering the Tibetan Plateau (TP).

## 2 Satellite Altimetry

### 2.1 Introduction

The first satellite altimeter to be launched was GEOS-III in 1975, followed in 1978 by Seasat. The first use of satellite altimetry for hydrology was with GEOSAT launched in 1985 (Koblinsky et al. 1993). However, thanks to substantial progress in orbit determination from geodetic systems such as Doris, the use of GPS and laser started with the launch of the US/French TOPEX/Poseidon (T/P) satellite in 1992. Two pioneering papers published by same author in the 1990's using satellite altimetry are still considered 20 years later as basic references for lakes (Birkett 1995) and for rivers (Birkett 1998).

Since then, many studies have illustrated certain case studies using satellite altimetry for lake surveys (Birkett et al. 1999; Aladin et al. 2005; Coe and Birkett 2005; Hwang et al. 2005; Medina et al. 2008; Lee et al. 2011; Singh et al. 2012; Kleinherenbrink et al. 2015 and many others). The information obtained by this technique is the average water level above a reference surface for a set of lakes once they are overpassed by the satellite. Indeed, current satellite altimeter missions were all based on the measurements made by the altimeter at the nadir of the satellite. Therefore, only a constellation of several satellites may allow monitoring a large number of lakes and reservoirs. For example, Cretaux et al. (2015) have shown that, over the Syr Darya river in Central Asia, all the small reservoirs located within its watershed will be monitored with a constellation of Sentinel-3A (hereinafter S3A), Sentinel-3B (hereinafter S3B), Jason-3, Jason-CS/Sentinel-6, and SARAL/AltiKa.

### 2.2 Basics of Satellite Altimetry

Satellite altimeters are designed to measure the two-way travel time of short radar (or laser) pulses reflected from the Earth's surface which gives the distance between the satellite and the reflected surface, called "*range*." The shape of the reflected signal, known as the "waveform," represents the power distribution of accumulated echoes as the radar pulse hits the surface. The waveforms that are acquired using a tracking system placed onboard the satellite are called "trackers" and can be modeled by a theoretical shape from which the time for the signal to be bounced back can be determined. The travel time is calculated using a predefined analytic function, which fits the time distribution of the reflected energy. The first altimetry missions were designed for the ocean domain. Therefore, the algorithm elaborated to process the waveform were fitted to classic ocean surfaces described in Brown (1977) where it is considered that thermal noise is followed by a rapid rise of the returned power called 'leading edge', and a gentle end sloping plateau known as 'trailing edge.' However, over the continents the waveforms are generally contaminated by noise resulting from multiple land returns such as vegetation, bare sands, or steep shorelines. Consequently, the shape of the echoes reflected by continental waters is often very different from that reflected by the ocean surface. It can thus become difficult, if not impossible, to calculate a river or small lake's water level using the classic "Brown" analytic function.

One way of working around this is to use alternative and more suitable retracking functions of the waveforms. With the Envisat mission launched by ESA in 2002, it was decided to provide the users the measurement ranges using four different retracking algorithms: The OCOG/ICE-1 (Wingham et al. 1986) and ICE-2 (Legresy and Remy 1997) retrackers have been developed to recover heights over ice sheets, and the SEA-ICE (Laxon 1994) to recover

heights over sea ice. In general, for large lakes the ocean tracker is well suited, but for rivers and small lakes the OCOG/ICE1 retracking algorithm is the preferred one as it has proven to be more accurate over this type of surface than the other three (Frappart et al. 2006). Other retracking algorithms designed for hydrological waveform analysis have been developed. Berry et al. (2005) proposed to classify the waveform by their typology and to apply a different algorithm for each class. This has been applied within the automatic near-real-time altimetry data processing to all flying altimetry missions and delivered through the "River&lake" Website (http://www.tethys.eaprs.cse.dmu.ac.uk/RiverLake), as well as to the historical missions. Another algorithm was developed for automatic calculation of lake and river time series of the *DAHITI* database (http://www.dahiti.dgfi.tum.de: Schwatke et al. 2015). All retracking algorithms are potentially affected by biases because they do not measure the same physical quantity (some track the very nadir point, others process spatial average within the footprint). Taking into account these biases is essential when combining ranges from different trackers of a mission, or when comparisons between different products are made (Cretaux et al. 2011a).

The water height calculation ($H$) of a lake or river using satellite altimetry is based on the following equation:

$$H = Alt - R - T_E \tag{1}$$

where $H$ is considered with respect to a geoid, $Alt$ is the altitude of the satellite above an ellipsoid, $R$ is the measured range, and $T_E$ is the sum of different corrections that take into account atmospheric refraction (propagation in the ionosphere and the troposphere), tidal effects (solid Earth and polar), and geoid height above the ellipsoid. For readers who need more detailed information, a full discussion of the computation of lake height and associated errors can be found in Birkett and Beckley (2010) and Cretaux et al. (2013a). Nevertheless, it is necessary here to provide some information on the specific issue of orthometric height correction due to geoid gradient along the tracks of the satellites. For propagation and tidal correction, altitude of the satellite and range measurements, these variables are provided by space agencies to the users through the *Geophysical Data Records* (GDRs). They also provide geoid correction; however, current products delivered in the GDRs are not accurate enough at short wavelengths for lakes. In Birkett (1995) and Crétaux and Birkett (2006) it has been shown that a specific computation must be performed to correctly account for the slope of the geoid over a distance of several hundred meters, which is far lower than the current geoid model resolution. The "repeat track technique" is used to solve this problem. The geoid slope is recalculated for each of the tracks of the satellite and then is averaged using all cycles. The result of this calculation is a mean vertical profile along the track which serves as correction for geoid in Eq. 1. Below are two examples: a mean lake profile along an ICESat track over Lake Issykkul (Fig. 1) and four individual passes over a track on Lake Ziling (Fig. 2).

### 2.3 Past, Present, and Future Satellite Altimetry

The past satellite altimeters of the class of T/P, Envisat, and Jason-2 were operating in low-resolution mode (LRM) in Ku Band (13.6 GHz). Despite it not being optimal for hydrology, many studies have been based on this technique, and it has progressively led spatial agencies to include hydrological objectives in the definition of new missions. The SARAL/AltiKa mission from CNES and ISRO (French and Indian space agencies) were the first to operate in Ka band (35.75 GHz) allowing a reduction in the footprint size by a

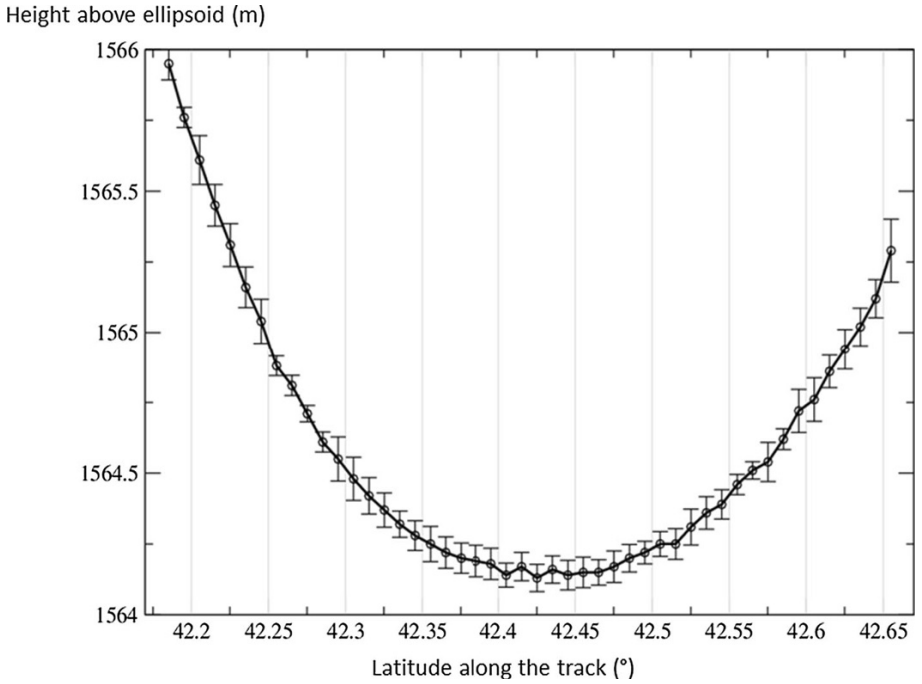


**Fig. 1** Vertical mean lake profile along an ICESat track over Lake Issykkul in Central Asia

factor 2–3 and of the ionospheric effect. The hydrological interest is that the water height of many narrow rivers or reservoirs has been measured with decimeter accuracy which was not possible with past altimeters (Arsen et al. 2015). On January 17, 2016, the Jason-3 mission (same instrumental and orbital characteristics as Jason-1 and Jason-2 satellites) was launched.

On January 12, 2003, the first and only laser altimetry instrument GLAS was launched by NASA (Zwally et al. 2003). It emitted at a wavelength of 1064 and 532 nm on the orbiting ICESat and had a near polar, near circular orbit of 91-day repeat cycle at an altitude of 590 km. GLAS provides laser footprint geolocation and surface elevation above ellipsoid with a dedicated algorithm after corrections for tides and atmospheric effects (Brenner et al. 2000). Altimetry from GLAS is derived from the 1064-nm beam measurement. The laser footprint is $\sim$70 m and the data spacing is $\sim$170 m. Because the laser beam suffered from technical problems, it was only turned on for short periods (typically 2-month windows twice a year). It was designed to study polar ice sheets but has also been used for lake level measurements. Thus, many authors have used ICESat products, particularly over the Tibetan Plateau. Although the satellite's repeat cycle and longevity were was not optimal for hydrology, spatial coverage was very high and had the potential to measure water level over a large set of lakes, as shown over the Tibetan Plateau where more than 100 lakes have been studied (Zhang et al. 2013; Phan et al. 2011; Kropáček et al. 2012; Song et al. 2013; Wang et al. 2013). It was also used to monitor river water level variations (Baghdadi et al. 2011; Jarihani et al. 2013). Furthermore, it ensured accuracy of up to a few centimeters due to the signal's very small footprint, and data provided by the National Snow and Ice Data Center (NSIDC) needed no additional corrections. The only

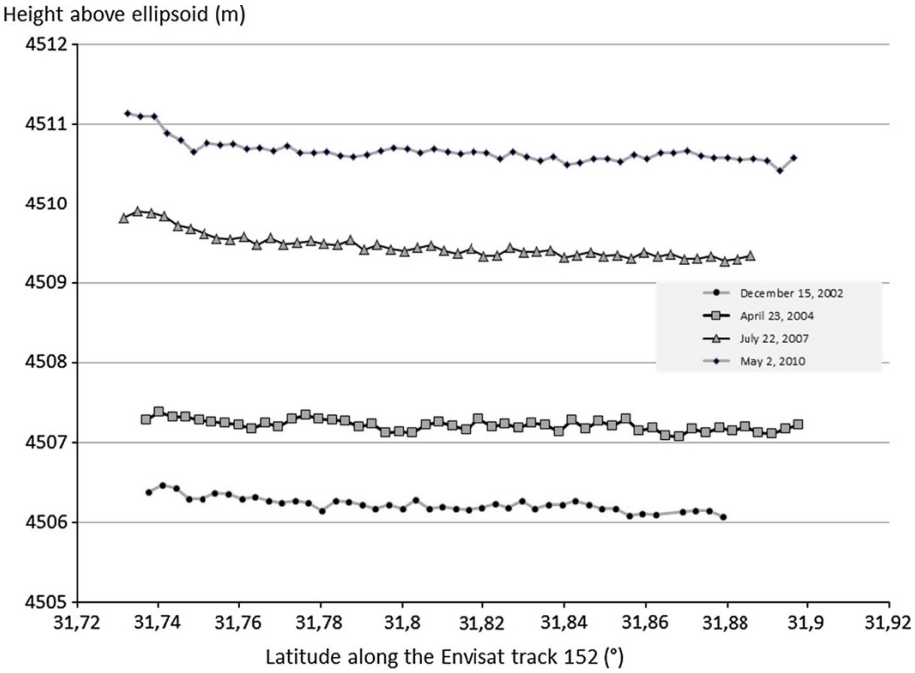


**Fig. 2** Water height above the ellipsoid of reference is calculated for each individual measurement along the track at different epoch (orbital cycle). The slope along the track is calculated and used to correct each measurement in order to calculate water altitude above the geoid cycle by cycle. We used the example of Lake Ziling with Envisat track number 152 at four different dates

correction necessary was for the vertical gradients and undulations of the geoid using the same method as that described in Sect. 2.2. Launched on April 8, 2010, by ESA, the Cryosat-2 satellite was primarily designed to study sea ice and polar ice caps. Cryosat-2 has a 369-day repeat orbit (5344 revolutions) with an inter-track at the equator of 7.5 km. This orbital characteristic is a real limitation for river studies, but it has some significance for lakes. First, Cryosat-2 is the first altimeter which has two antennas: an altimeter in Ku band which can work in LRM or SAR mode, and a second antenna which can turn the instrument to an interferometric mode called SARin. It allows precise determination of the reflecting point's geolocation within the radar footprint. Second, Cryosat-2 is of interest due to its very long repeat cycle, leading to a very short inter-track ($\sim$7 km at the equator and less than 6 km over 40° latitude), and it can cover a huge number of water bodies on the Earth's surface and has the potential to measure water level changes for thousands of lakes and reservoirs worldwide. ESA provides classic GDRs of Cryosat-2 instruments for all modes of tracking (LRM, SAR, and SARin), and some authors have developed specific algorithms for them to be used over lakes (Kleinherenbrink et al. 2014) including geoid slope errors. One interest of using Cryosat-2 for lake surveys is that it also offers the possibility to fill the gap between Envisat and SARAL/AltiKa (between 2011 and 2013) and hence allows lake level variations to be calculated from the launch date of ERS2 in 1994 to the present day (see Sect. 2.4).

A new generation of altimeters has been developed by the European Space Agency and missions are being prepared for launch: Sentinel 3A for early 2016, followed by Sentinel-3B scheduled for launch within the following 18 months. The altimeters onboard Sentinel-

3A and Sentinel-3B are designed to operate in SAR mode on Ku band frequency. SAR mode will improve the ability of the altimeters to measure water level. This is particularly significant for small water bodies: straits of water like rivers, pools, artificial lakes, or reservoirs. The footprint areal extent will be reduced by a factor ranging from 10 to 50 with respect to the classical LRM altimetry mode ($\sim$300 km$^2$ with Jason2). Furthermore, the SAR mode will be able to redirect the measurement target point on the route. This will allow a better selection of the water body and reduce pollution from the surrounding ground signal. Therefore, it will increase the signal-to-noise ratio with regard to the LRM. In addition, the S3B/S3A tandem orbit configuration (they are operated as a couple of satellites in interleaved orbit) is particularly promising as it will allow densification of the Earth's coverage and therefore target a large number of lakes. At Legos (Biancamaria, personal communication), it has been calculated that a constellation of Jason-2, Jason-3, SARAL/AltiKa, S3A and S3B would be capable of measuring the water level for 98 % of the 3720 lakes on the Earth that have an area larger than 50 km$^2$ and 71 % of the 14,411 lakes with an area larger than 10 km$^2$. This corresponds to approximately 40 % of total water storage content in lakes worldwide. This new configuration of orbit and measurement systems will significantly improve the survey of narrow tanks both quantitatively and qualitatively.

In 2020, another mission called "Jason Continuity of Service" (Jason-Cs/Sentinel-6, with the same footprint as Jason-3's (300 km$^2$)) will be set up in the same orbit. If Jason-3 is still functioning at that time, it would then be located in a different orbit, known as interleaved orbit (ground track shifted in longitude by half of its initial orbit equatorial ground track distance), resulting in double spatial coverage for each satellite. It has still not been decided whether the altimeter will be switched to SAR mode over the continent. This satellite constellation will provide a dense survey network with increased sampling time of lakes and reservoirs. Moreover, some of these instruments are now designed to survey continental water. Having different satellites will also preclude erroneous measurements from any single one of them.

However, over the next few years, the main development in this area has been the Surface Water and Ocean Topography (SWOT) which is currently under development by the National Aeronautics and Space Administration (NASA), the Centre National d'Études Spatiales (CNES), the Canadian Space Agency (CSA), and the UK Space Agency (UKSA). SWOT will carry an interferometer in Ka band that provides water elevation images for two 50 km swaths on either side of the satellite. Its objective is to measure water level and contour of all lakes with an area bigger than 250 m $\times$ 250 m every 10 days (with a goal of 100 m $\times$ 100 m). The two swaths are separated by a band of 20 km without observation except along track using an additional nadir altimeter (Rodriguez 2015). The satellite will have an inclination of 77.6 degrees, and the entire emerged surface can be covered. These orbital and instrumental characteristics will allow, for example, total coverage of the Tibetan Plateau's (TP's) 1000 lakes that have an area greater than 1 km$^2$, whereas at present the altimeters in LRM or SAR mode cover only a small proportion of them. It will also provide delineation of rivers that are broader than 100 m (with a goal of 50 m).

The expected precision from the SWOT mission (Rodriguez 2015) is that river slope will be measured over each 10 km length of the rivers larger than 100 meters to 1.7 cm/km of accuracy allowing monitoring of river discharge. Water height of lakes, reservoirs, and floodplains will be measured with 10 cm accuracy for 1000 mm $\times$ 1000 m areas (1 km$^2$ area), 20 cm accuracy for 250 m $\times$ 250 m areas (0.0625 km$^2$) and 45 cm for 100 mm $\times$ 100 m areas (0.01 km$^2$).

The mission will provide a large range of applications for water management and the scientific study of hydrology and once the majority of the Earth's lakes, reservoirs, and rivers have been mapped every 10 days by SWOT many components of the water cycle can be measured, for example, global discharge of rivers to the ocean, water storage changes in natural and artificial reservoirs, and floodplain dynamics. When the 3-year mission is completed, the seasonal global water cycle can then be measured by SWOT and the data assimilated into models. Our knowledge gap regarding lakes and reservoirs in particular is expected to be vast (Biancamaria et al. 2010; Lee et al. 2010; Bates et al. 2014). For example, the mission will allow us to control inflow and outflow discharge for each reservoir (worldwide). Thus, the major advantage of this unique and dedicated mission will be the possibility to propose an independent, reliable, and accurate measurement system of diverse parameters to water management authorities and scientists. This could allow greater control over flow, use, and water storage availability over an entire basin (Cretaux et al. 2015).

### 2.4 Combination of Multi-Satellite Data

In many cases a lake can be covered by the tracks of different satellites, sometimes with overlapping periods and sometimes without a common period of observation. The main advantage of this is the possibility to perform a multi-satellite data processing approach for a lake's water height variations over a long period of time. For example, Lake Ziling was observed by ERS2, Envisat, SARAL/AltiKa, ICESat, and Cryosat-2 satellites from 1994 until 2015. In this framework, the use of ICESat and Cryosat-2 data was fundamental since they allow calculating relative biases between each of the missions. The calculated water level time series from each satellite are biased for two main reasons: First, there is an instrumental bias of each altimeter: This is well documented in the literature (Bonnefond et al. 2010; Mertikas et al. 2010). The second reason is that the geoid variations over a lake are not precisely known on a short wavelength of several kilometers, and as the tracks are not located exactly over the same region of a given lake, it adds a relative bias between each time series obtained from individual altimeter (Cretaux et al. 2013a; Cheng et al. 2010).

Both errors are added together, which requires some a priori adjustment of inter-track and inter-satellite biases. When only one satellite crosses a lake, even with several tracks, the geoid slope is calculated using all existing data along the track one by one and are then averaged. As tracks do not pass at the same date over the lake, the date of reference of each lake level product in Hydroweb is calculated as the barycenter of the time of each pass.

If the lake is below the orbit of several satellites, it is therefore necessary to adapt the data processing to determine the relative biases over each lake in order to calculate water level variations from multi-satellite data sources. The calculation is done in Hydroweb in a three-step process.

- Time series of each satellite is calculated independently as described above in Sect. 2.2
- Relative bias is calculated during the overlapping period
- Each bias is then removed to the individual time series, and the long-term time series is calculated at the last step.

An example is given in the figures below. For Lake Ziling (Fig. 3, 4) we can see that from the first measurements obtained with ERS-2 data to the last measurements obtained with Saral-AltiKa, the use of ICESat and Cryosat-2 has allowed us to link each of the five time series obtained independently, and to fill the gap between two alike missions such as

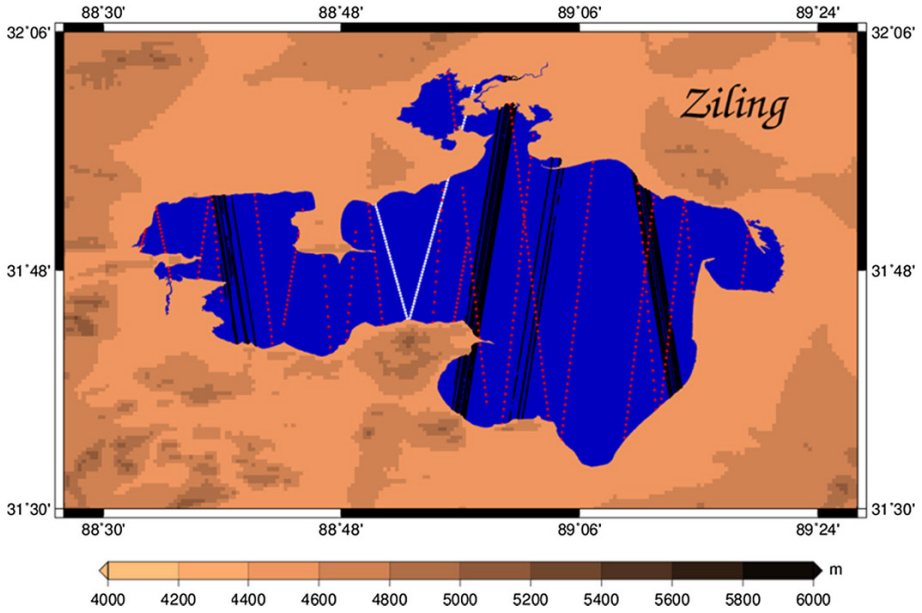


**Fig. 3** Map of Lake Ziling. White lines represent the ERS2, Envisat, and SARAL/AltiKa tracks, red lines the Cryosat-2 tracks and black lines the ICESat tracks

Envisat and SARAL/AltiKa. ICESat data used for this computation was the GLA06 v33 global elevation product distributed by the NSIDC, and the Cryosat-2 data over the Tibetan plateau was turned to SARin mode. The relative biases range from a few meters to a few centimeters. The resulting 20-year time series of Lake Ziling is given in Fig. 15e.

In the next example, we present the results of calculations over Lake Ngoring-co. For this lake, seven satellites were used: T/P, Jason-1, Jason-2, ERS2, Envisat, SARAL/AltiKa, and Cryosat-2 (Fig. 5). Using all of them after relative biases correction allows us to determine lake level variations over the period 1993–2015, hence more than 20 years. This is the only way that we can examine the impact of climate change on lakes like this. Note that none of the satellites could individually capture the complex inter-annual variability of this lake. This is important to note because it is not characterized by a long-term trend but by abrupt changes followed or preceded by relatively stable lake level change or a slight trend over a few years (Fig. 6).

## 2.5 Accuracy of Satellite Altimetry Over Lakes

Over the Great Lakes (area >100 $km^2$), it has been shown (Ričko et al. 2012) that the accuracy of satellite altimetry can reach values as low as 5 cm. However, pertaining to narrow reservoirs that accuracy may vary from 10 s cm to 1 m. For example, comparisons of altimetry products with in situ daily gauge data show that the RMS accuracy ranges from a minimum of 3 cm for Lake Issykkul, 5–10 cm for the Great Lakes (Superior and Erie), to a maximum of 80 cm for the smaller Lake Powell (Ričko et al. 2012). The results of these analyses demonstrate the absolute need to make careful comparisons between the lake levels inferred from in situ and satellite altimetry. However, it is difficult to determine the direct relationship between lake size and the accuracy of altimetry products.

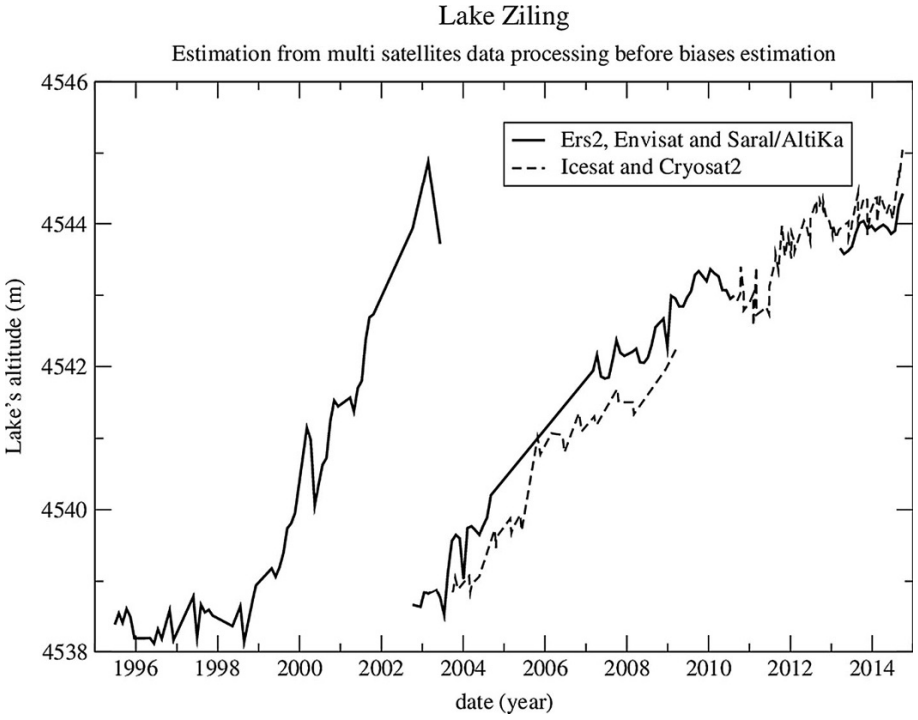


**Fig. 4** Satellite altimeters over Lake Ziling from different satellites before adjusting for relative biases

The accuracy of lake height measurement depends on several factors: range, orbit, and correction errors. Range errors result from surface roughness and quality of the retracking of the altimeter waveform. It is also important to emphasize that the altimeter measurement is an average over the footprint which intrinsically differs from a single-point measurement of a ground gauge and which is furthermore generally done along the coast line (Table 1).

Table 2 summarizes the measurement accuracy for a set of 24 lakes of various sizes and located in different regions. We have compiled some published results with new calculations using in situ measurements collected either on the web, or from direct collaboration. The idea was to address the recurrent question concerning accuracy of altimetry for lakes and rivers and its dependency on the size of the water bodies. Is there a minimum size and anything under which the altimeter does not provide valid water levels? The results given in Table 2 clearly show that for big lakes the accuracy is largely subdecimeter and that lake size influences the quality of the results. But the results show that accuracy is also dependent on the lake's environment: mountain lakes (Argentino, General de Carrera), or those with ice and snow in winter (Onega, Athabasca); obviously, large but narrow reservoirs (Mead, Powell) have degraded accuracy. For Lake Onega, for example, we calculated the accuracy in all but the winter season, and the RMS was twice as good as that over the whole year.

In a recent study (Arsen et al. 2015) the authors quantified the improvement in accuracy when using the SARAL/AltiKa measurements over mountain lakes in regard to the results

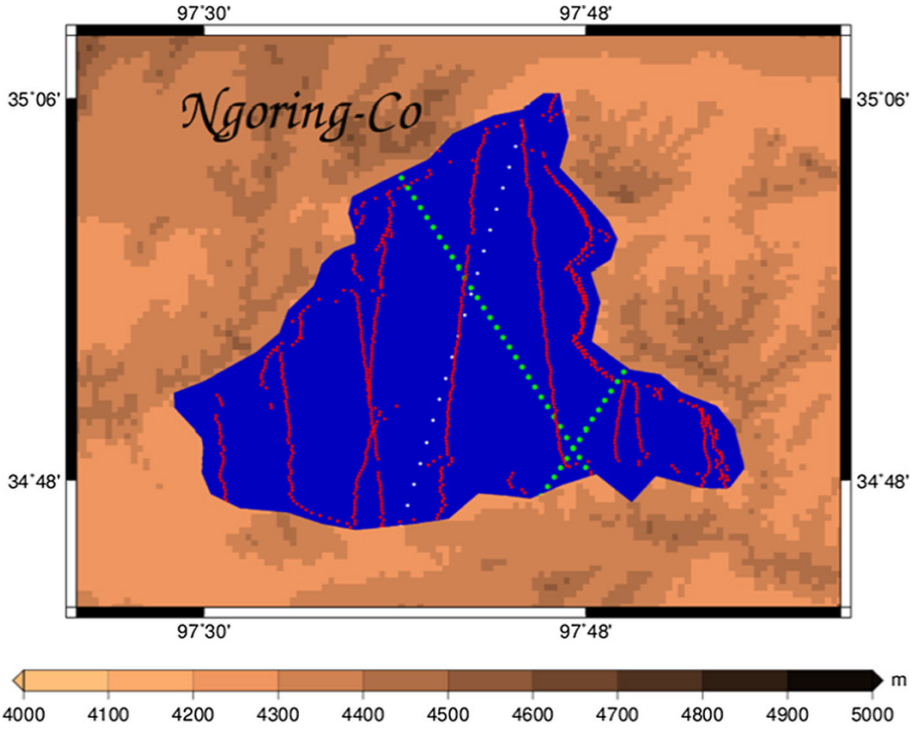


**Fig. 5** Map of Lake Ngoring-co. White lines represent the ERS2, Envisat and SARAL/AltiKa tracks, red lines the Cryosat-2 tracks and black lines the ICESat tracks. Cryosat-2 measurements, in contrast to other missions, do not follow a straight line along the track of the satellite since the SARin measurements are selected for the TP. The SARin mode which uses Cryosat-2 two antennas to form a cross-track interferometer allows precise determination of the reflecting point within the footprint

obtained with Envisat. Their results were classified with respect to the length of the effective track over a given lake instead of using lake size as comparison criteria. The study was performed for 15 lakes in the Andean chain and results show that with Envisat there is a clear dependency of the RMS in terms of length of the effective track over the lake, while it was unquestionably not the case with SARAL/AltiKa. An order of magnitude of accuracy improvement with SARAL/AltiKa was calculated: For the 15 lakes, the RMS had an approximate average of 10 cm, while it was 1 meter or sometimes more with Envisat. With its smaller footprint than Envisat, the SARAL/AltiKa measurements still had an RMS of 10–12 cm (Arsen et al. 2015).

## 3 Satellite Imagery

Satellite altimetry is used to calculate water height variations over a lake. However, this is not sufficient when the goal is to establish water balance of a lake which is preferentially represented by the water storage changes. To determine the absolute water volume of a lake is impossible without precise bathymetry (Crétaux et al. 2005; Lei et al. 2014; Song et al. 2014a, c). However, the determination of absolute water volume of a lake is not

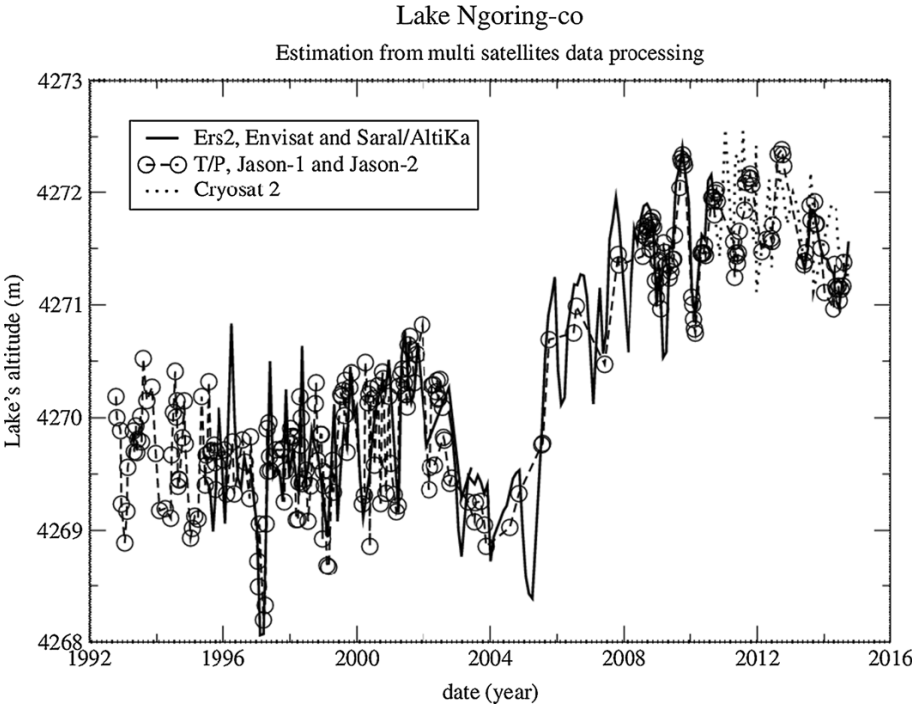


**Fig. 6** Combination of data from several satellite altimeters over Lake Ngoring-Co after the adjustment of relative biases

fundamental when it is easier to calculate volume variations. To perform this variable, we can use a combination of a lake's water height and water surface extent at different dates and then establish a relationship between these variables and water volume changes. This calculation has been used in many published studies (for an example see Gao et al. 2012; Duan and Bastiaanssen 2013; Arsen et al. 2014). The first step relates to using satellite imagery to compute several lakes' water mask therein corresponding to concomitant water heights. However, the methodology to extract water mask from satellite imagery is not straightforward and is why there is a description below. The Hydroweb database uses this approach to determine the water surface of Tibetan lakes and other lakes throughout the world.

Many methods exist for the extraction of water surface from satellite imagery, which, according to the number of bands used, are generally divided into single-band and multi-band methods. Using the simplest approach, a single band is selected from a multi-spectral image and used to extract water surface information. In practice, both the surface reflectance and satellite digital numbers are used to calculate vegetation cover or water extent (Crétaux et al. 2011b). The second category takes advantage of reflective difference in each multi-spectral band. Spectral signature analysis of water among different bands can be made, and tree methods can be used to delineate water surface or other features. Commonly used methods are based on an index, which combines a multi-band ratio of visible red/green and near-infrared (NIR)/short-wave infrared (SWIR) bands. Then, the water mask is derived from thresholding the chosen index (regions with an index above the given

**Table 1** List of past and future missions used in Hydroweb with their general characteristics

| Mission | Agency | Frequency | Mode | Time (year) | Cycle (day) |
|---|---|---|---|---|---|
| T/P | NASA/CNES | Ku | LRM | 1992–2005 | 10 |
| Jason-1 | NASA/CNES | Ku | LRM | 2002–2011 | 10 |
| Jason-2 | NASA/CNES | Ku | LRM | 2008-present | 10 |
| Jason-3 | NASA/CNES/EUMETSAT/NOAA | Ku | LRM | 2015 | 10 |
| Jason-Cs | NASA/CNES/EUMETSAT/NOAA/ESA | Ku | Not decided yet | 2017 | 10 |
| GFO | NRL | Ku | LRM | 2002–2008 | 17 |
| ERS-2 | ESA | Ku | LRM | 1995–2002 | 35 |
| Envisat | ESA | Ku | LRM | 2002–2011 | 35 |
| SARAL/AltiKa | CNES/ISRO | Ka | LRM | 2013-present | 35 |
| Sentinel-3A | ESA | Ku | SAR | 2015 | 27 |
| Sentinel-3B | ESA | Ku | SAR | 2016 | 27 |
| CryoSat-2 | ESA | Ku | LRM/SAR/SARin | 2010-present | 369 |
| ICESat-1 | NASA | Laser | LRM | 2003–2009 | 91 |
| ICESat-2 | NASA | Laser | LRM | 2017 | 91 |
| SWOT | NASA/CNES/CSA/UKSA | Ka | SAR | 2020 | 21 |

threshold are classified as water). Different indexes have been proposed in the literature. The Normalized Difference Water Index (NDWI) was first introduced by McFeeters (1996) and expressed as the band ratio:

$$\mathrm{NDWI} = \frac{-\mathrm{NIR}}{\mathrm{Green} + \mathrm{NIR}} \tag{2}$$

Xu (2006) proposed Modified Normalized Difference Water Index (MNDWI) expressed as the band ratio:

$$\mathrm{MNDWI} = \frac{-\mathrm{MIR}}{\mathrm{Green} + \mathrm{MIR}} \tag{3}$$

For convenience, we label indexes that use green and NIR as $\mathrm{NDWI}_{\mathrm{L/M:\ Green,\ NIR}}$ and indexes that uses green and SWIR as $\mathrm{MNDWI}_{\mathrm{L/M:\ Green,\ SWIR}}$ (L = Landsat, M = MODIS), where Green can be the Landsat TM/ETM + band 2 (520–600 nm) or MODIS band 4 (545–565 nm), and NIR as Landsat TM/ETM + band 4 (750–900 nm) or MODIS band 5 (1230–1250 nm). Similarly, MIR (or SWIR) can be mid (short)-infrared bands such as Landsat TM/ETM + band 5 (1550–1750 nm) or MODIS band 6 (1628–1652 nm). Many other formulations of spectral band ratios can also be found in different combinations of visible or infrared bands (Ji et al. 2009). Boschetti et al. (2014) provide a useful and coherent review of existing water indices and their application for water detection. From band ratio histograms, different objects can be separated from their background with a simple threshold method (Otsu 1979). Computing the previously described indexes is relatively easy. However, choosing the adequate threshold value to compute the water mask can be very tricky because of two major issues. First, band ratios calculated from different band combinations necessarily have different threshold values for

**Table 2** Comparison (RMS and $R^2$) of average water level from satellite altimetry (available on Hydroweb database) for a set of 24 lakes of various location and size where in situ measurements are available from different sources

| Lake name | Continent | Area (km$^2$) | Period | RMS (cm) | $R^2$ |
|---|---|---|---|---|---|
| Argentino[1] | South Am | 1466 | 1992–2011 | 22 | 0.96 |
| Athabasca[2] | North Am | 7900 | 1992–2009 | 28 | 0.91 |
| Aydarkul[3] | Asia | 3000 | 2002–2010 | 12 | 0.95 |
| Baikal[4] | Asia | 31,500 | 1992–2009 | 11 | 0.94 |
| Bratsk[4] | Asia | 3100 | 1992–2009 | 41 | 0.98 |
| Erie[2] | North Am | 25,800 | 1992–2011 | 10 | 0.95 |
| Guri[2] | South Am | 3500 | 2002–2010 | 82 | 0.99 |
| General Carrera[1] | South Am | 1850 | 2002–2010 | 22 | 0.90 |
| Huron[2] | North Am | 59,570 | 1992–2011 | 8 | 0.99 |
| Issykkul[6] | Asia | 6000 | 2002–2014 | 3 | 0.99 |
| Khanka[4] | Asia | 4400 | 2000–2010 | 13 | 0.6 |
| Ladoga[4] | Europe | 18,135 | 1992–2010 | 8 | 0.98 |
| Mead[5] | North Am | 350 | 2001–2010 | 64 | 0.99 |
| Michigan[2] | North Am | 58,000 | 1992–2011 | 11 | 0.98 |
| Oahe[6] | North Am | 700 | 2002–2010 | 45 | 0.99 |
| Onega[4] | Europe | 18,200 | 1992–2010 | 15 | 0.88 |
| Ontario[2] | North Am | 19,000 | 1992–2011 | 6 | 0.98 |
| Powell[5] | North Am | 400 | 1992–2010 | 85 | 0.99 |
| Superior[2] | North Am | 82,200 | 1992–2011 | 6 | 0.97 |
| Tana[2] | Africa | 3000 | 1992–2006 | 17 | 0.97 |
| Tchad[2] | Africa | 1540 | 1992–2008 | 28 | 0.91 |
| Titicaca[7] | South Am | 7800 | 2000–2005 | 7 | 0.99 |
| Volta[2] | Africa | 8500 | 1999–2010 | 53 | 0.98 |
| Woods[2] | North Am | 4350 | 1992–2011 | 27 | 0.81 |

[1] Subsecretaría de Recursos Hídricos (www.hidricosargentina.gov.ar)

[2] From Ričko et al. 2012

[3] From www.cawater-info.net

[4] In situ data from State Institute of Hydrology of St Petersburg, Russia

[5] United States Bureau of Reclamation

[6] In situ data from the Institute of Water Problems, Bishkek

[7] Personal communication from J-L Guyot (*source*: Institute of Hydrology, Peru)

the same feature. Thus, a unique threshold cannot be applied to a multi-satellite study. Additionally, optical properties of surface objects vary with time due to factors such as varying Sun–target–satellite geometry, atmospheric or soil conditions, water turbidity, sediment load, and sensor degradations. Liu et al. (2012) have proved that small threshold variations can occur even on a daily basis. Secondly, band ratio threshold varies depending on the proportion of sub-pixel water/land/vegetation components. Mixed pixels are especially important for coarse resolution satellite images [SPOT VEGETATION (1 km), and MODIS (250/500 m)] because large pixels usually have complex combinations of water/land cover types within the pixel area. Several studies investigated the issue of the

optimal band combination to best delineate water features. Xu (2006) found that the $NDWI_{L2,4}$ (McFeeters 1996) was unable to completely discriminate buildup from water features and have proposed $MNDWI_{L2,5}$. Ji et al. (2009) evaluate mixture pixel impacts on simulated spectral bands of Landsat ETM+, SPOT, ASTER, and MODIS and recommend $MNDWI_{M4,5}$ and $MNDWI_{L2,5}$ for use in mapping surface as the less affected by sub-pixel vegetation components. Ouma and Tateishi (2006) tested five different forms of band ratios for water body delineation including $NDWI_{L2,4}$ and $MNDWI_{L2,5}$. They ranked $NDWI_{L2,4}$ as second and $MNDWI_{L2,5}$ as third in order of best performance. In a more recent study Boschetti et al. (2014) compared performances of several MODIS band ratios and recommended the combination of $MNDWI_{M4,6}$ as the best for pure water pixel detection. These studies show that, depending on the instrument used and specific conditions of the study zone (water turbidity/depth, percentage of water present in the pixel), one combination of bands can outperform another. Therefore, it is necessary to validate the results with ground observations if available, but even then, final conclusions will depend on the methodology employed and the study zone delineation. Although interesting conclusions can be found among previously cited publications, only a few of them offer real examples of band ratio thresholds (e.g., Sakamoto et al. 2007). The subjective selection of the threshold value may lead to an over- or underestimation of open water area. We use one example to illustrate the difficulties in threshold selection. In Fig. 7, several grounds to water intersection profiles are shown for Lake Zhari Namco in the Tibetan Plateau (30°55′N 85°38′E). They represent $NDWI_{L2,4}$/$MNDWI_{L2,5}$ values calculated with Landsat 5TM, 7ETM+, and Landsat 8 OLI at different dates. The profiles start over a small 2- to 3-pixel-wide water pond and pass over the lake's surface. We can see on MNDWI profiles

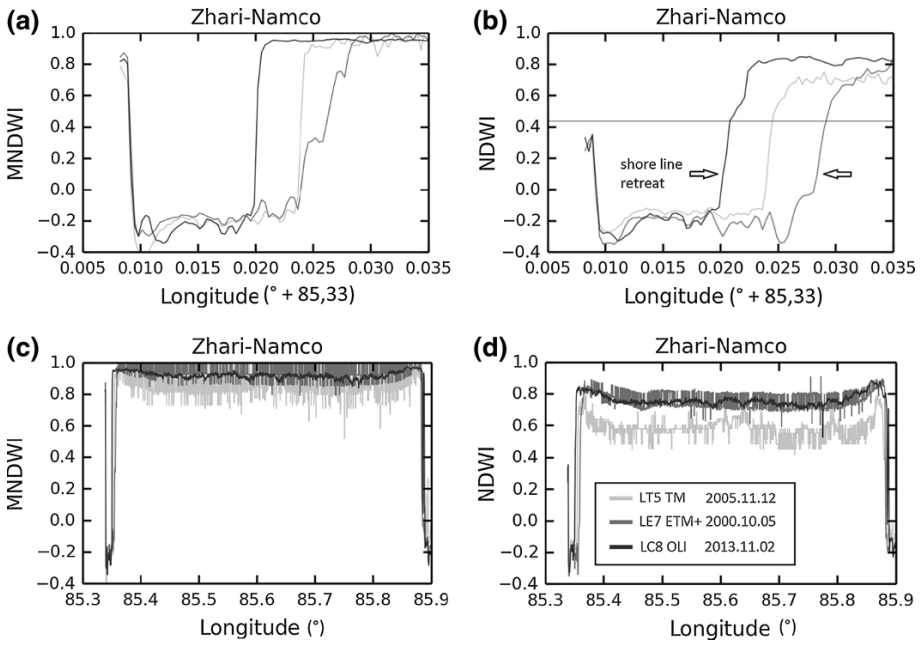


**Fig. 7** Methods of water pixel mapping with MNDWI for the Lake Zhari Namco near the shoreline using Landsat images (**a**), with NDWI (**b**), and longitudinal profiles across the entire lake for MNDWI (**c**) and for NDWI (**d**)

(Fig. 7a) that the land/water crossing has very strong signatures for both the lake and the water pond. The small water pond composed of mixed pixels has a much weaker response on NDWI (Fig. 7b). Indeed, Xu (2006) has proved that the detection of mixed pixels is easier with MNDWI. However, the strong response of mixed pixels reduces the gap between maximal values and makes the differentiation between open water and mixed pixels more difficult. The land/water crossings of NDWI profiles are composed of several lines with different slopes. A particular region can be located around 0.42 on LC8 OLI 2013.11.02 profile (Fig. 7b). The value 0.42 NDWI (0.44 MNDWI) has been calculated by Xu (2006) as the mean value which characterizes the open water surface of Lake Bayi. We can see the same transition on two others profiles. Figure 7c, d represents longitudinal profiles of MNDWI/NDWI across the entire Lake Zhari Namco. One can immediately notice that NDWI/MNDWI values in the middle of the lake have lower values than near shore, which is due to partial transparency of water near shore. We also notice a high-frequency noise from artifacts on Landsat 5 TM and 7ETM+ images owing to sensor degradation. The mean values of MNDWI and NDWI vary in time and are the lowest for the 2001 image. The 2006 profile has much higher mean value, and thus we can attribute these changes to temporal variations in air aerosols and water turbidity rather than sensor degradation. A fixed threshold of 0.9 on the MNDWI deduced from near shore values could simply be used if the objective is to map only water pixels (Fig. 7a).

However, in this case, taking a lower MNDWI threshold will automatically include all mixed pixels in our estimations. With a fixed threshold of 0.4 NDWI, it can then be possible to map open water pixels of Lake Zhari Namco in all three cases. From our experience, the use of MNDWI or NDWI clearly depends of the study zone. Most of the lakes can be accurately mapped with NDWI. In some cases the use of MNDWI may be also interesting. Within the Hydroweb database, the areal extent, i.e., surface time series, may vary slightly from other studies. This situation is perfectly understandable. As there is no clear definition of where a lake starts or ends, each author is able to perform their own delineation. However, the discrepancy between results may increase due to low-resolution bias. Low-resolution bias is the inaccuracy introduced by the differences in spatial resolution between high and low-resolution data (Boschetti et al. 2014). This surface bias must be estimated in order to properly translate results obtained with one resolution to another (e.g., Arsen et al. 2014). For the Hydroweb database, the hypsometry of lakes is estimated with no more than 10–15 images (information given).

In the frame of Hydroweb, the following steps are used in Landsat image processing:

- Overview of study zone before delineation. Several factors should be estimated: minimum and maximum water extent, appearing/disappearing islands, flooding areas, the presence of vegetation/aquatic vegetation components, and in situ data availability.
- Image selection. If possible strictly limited to cloud free, ice-free and inundation-free scenes in order to reduce difficulties in interpretation.
- Definition of region of interest (ROI) based on maximum and minimum water extension, cutoff of unnecessary parts (mountains, rivers) to reduce difficulties in interpretation, and safety margin for water rise.
- For each image: conversion of digital number (DN) in each spectral band to surface reflectance using the calibration coefficients provided in the image's metadata including latest sensor degradation studies. Atmospheric corrections such as dark object subtraction (Chavez 1989, 1996) are optional and mostly required for vegetation change mapping (Song et al. 2011).
- For each image: MNDWI and NDWI generation.

- The water surface is calculated for all open water pixels starting from an initial value of NDWI $\geq$ 0.4. Statistical study of histogram profiles at ground/water intersection can be used for manual adjustments of the threshold to ensure a coherent and well distinguished shoreline. Water class is constant during the study. This guarantees that mixed pixels are selected in exactly the same manner. Underestimations of NDWI will be corrected with supervised methods.
- For each image: thresholding of NDWI or MNDWI, generation of snapshots, subsets, and ROI files. Overview of results and supervised corrections of: extra thin cloud strips, inclusions (ice or clouds), sensor artifacts, algae or vegetation blooms, and other underestimations.

For more information about satellite image data processing, we recommend the processing guideline proposed by Ji et al. 2009.

Consequently, in Hydroweb we first use the water level time series inferred from satellite altimetry in order to determine some key periods when the lake was at extreme height and some intermediate values in order to select satellite imagery at those dates. It is not realistic to determine water extent of a lake for each measurement of its water level, especially when a lake is too large and is not covered by only one image.

We used Landsat 7 ETM+ and Landsat 5 TM images (available on the USGS GLOVIS image archive (http://www.gloviusgs.gov/) and when the spatial resolution was not necessarily high MODIS images (500 m of resolution, MOD09GHK products) were also selected. In general, we try to select between 10 and 15 images at different dates and calculate the hypsometry relationship (dA/dH), where A is the lake area (in km$^2$) and H is the height of the water surface above the geoid (in m), which is then applied to determine surface extent of the lakes each time a water level is calculated using satellite altimetry. The hypsometry is expressed as a polynomial of degree 1, 2 or 3 depending on the linearity of the couples of water level and surface extent of the lake. In such processing, we do not need to process a large amount of satellite images, and this is a practical way to deliver through Hydroweb time series of lake surface extent together with height time series.

## 4 Storage Change Calculation

The determination of volume variations is done under the hypothesis that between two successive measurements (at date $T_0$ and $T_1$) of the couple, $A$ and $H$, the morphology of the lake is regular and has a pyramidal shape (Abileah et al. 2011), and we can therefore derive the water volume changes from the following equation:

$$\Delta V = \frac{(H1 - H0) \times (A1 + A0 + \sqrt{A1 \times A0})}{3} \tag{4}$$

where **V** represents the volume variation between two consecutive measurements, ***H1, H0*** and ***A1, A0*** are levels and areal extents at date $\boldsymbol{T_1/T_0}$, respectively. Figure 8 gives an example on Lake Ayakkum located in the northern part of the TP with a two-order polynomial fit of area versus height of the lake.

From Fig. 9 above it is interesting to note that the hypsometry of a lake is not always linear. This implies that, in Hydroweb, we consider the polynomial coefficient to determine surface variation from height variations only in the domain of validity of the hypsometry, so we don't extrapolate the water surface for water height outside of the maximum and minimum values used to determine polynomial coefficients. As a comparison, in Song et al. (2013) the same

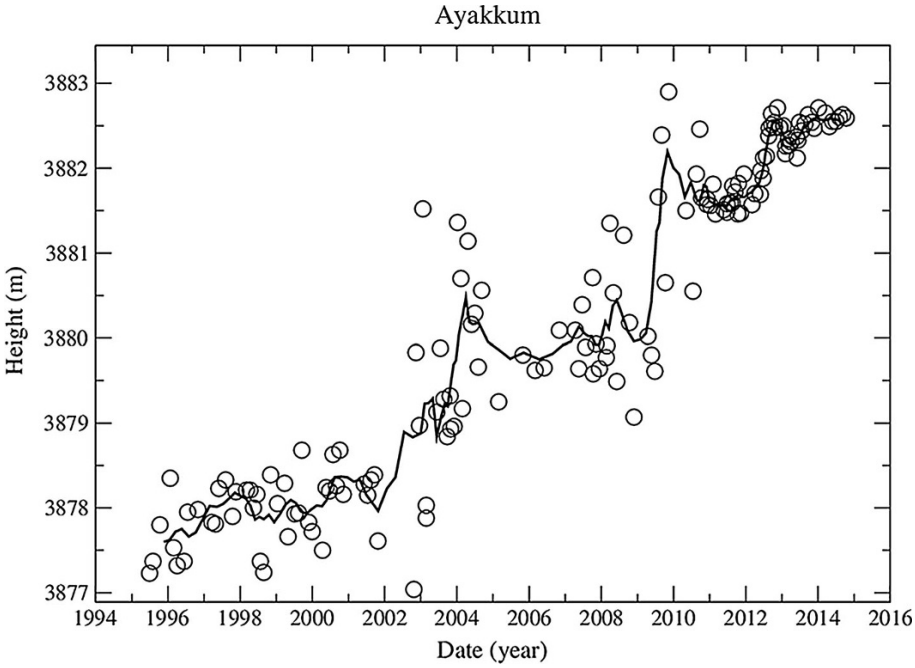


**Fig. 8** Lake Ayakkum's height from multi-satellite altimetry (ERS2, Envisat, CryoSat-2, and SARAL/AltiKa). The circles represent individual measurements and the black line a moving average done over every six individual measurements

calculation was made for a set of 12 Tibetan lakes, and we see that for Lake Ayakkum *they established a linear functio*n of area versus height (Area = 89.2857 × height – 345602) because only ICESat data from 2003 to 2009 was used, which could lead to some errors in water surface extrapolation for similar cases. Indeed, for a low lake water height of 3880 m, the two sets of polynomial coefficients both give an area of about 820–830 $km^2$. In contrast, for a high lake water height of 3882 m (reached in 2011–2012), the second-order polynomial development leads to 896 $km^2$, while in Song et al. (2013) with a one-order polynomial development, it reaches more than 1000 $km^2$.

In Hydroweb, the time series for about 20 lakes of the Tibetan Plateau are given for these three variables, H, A, and dV over at least one decade. We use the multi-satellite approach which is described in Sect. 2.4. The data from ERS2, T/P, Jason-2, Envisat, ICESat, Cryosat-2, and SARAL/AltiKa have been used to perform the calculation of water level variations of these lakes. We therefore provide long decadal time series for some of these lakes, and we show in the next section the results obtained for a list of 11 large lakes in the southern TP, with the majority of them having more than 20 years' worth of data.

## 5 Case Study: The Tibetan Plateau

The Tibetan Plateau is the largest and highest region on Earth and the source of 10 major river systems that provide irrigation, power and drinking water for over 1.3 billion people—nearly 20 % of the world's population—and is known as the "water tower of Asia."

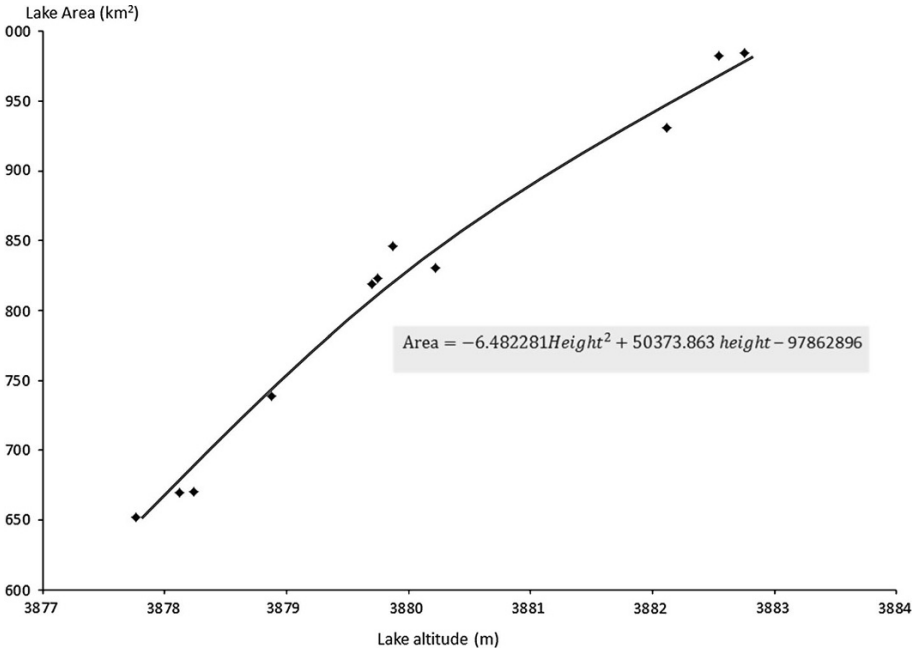


**Fig. 9** Hypsometry polynomial of Lake Ayakkum (within the hypsometry equation, height is expressed in meters and area in $km^2$)

The TP is considered as one of the most sensitive regions on Earth to global warming (Yao et al. 2012) and therefore plays a key role on both hydrology and climate for southern and eastern Asia. Its ice fields contain the largest reserve of fresh water outside the polar regions. It has been named The Third Pole. It has an average altitude of 4000 m a.s.l and is covered by mountains, glaciers, high altitude plateaus, permafrost, and hundreds of lakes (Liu and Chen 2000; Liu et al. 2009a; Huang et al. 2011; Wan et al. 2014; Zhang et al. 2015).

Its climate is very dry in the northwest (50 mm/year of rainfall) and more humid in the Southwest (700 mm/year) with more than 60 % of its precipitation falling during the summertime (Kang et al. 2010). It is under the influence of the Indian and East Asian monsoon and of the westerlies (Li et al. 2007). The TP has been warming over the last 50 years at a rate of 0.36°/decade (Wang et al. 2008) which doubles previous estimates made by Liu and Chen (2000). This phenomenon has been more pronounced over the last 30 years, particularly in winter (Kang et al. 2010; Huang et al. 2011). Precipitation changes have strong regional patterns and high inter-annual variability. It has become wetter in the East and central part (Kang et al. 2010; Xu et al. 2008) and dryer in the Northeast and West (Huang et al. 2011; Kang et al. 2010; Xu et al. 2008).

The consequences of these climate change geographical patterns are visible on lake water balance. Some are declining, for example in the far south of the TP or near the source of the Yellow River (Huang et al. 2011). Many of the lakes in the western regions and central part of the TP and in the North are, in contrast, expanding due to the accelerated melting of glaciers and permafrost (Liu et al. 2009a; Huang et al. 2011). However, there is not always a direct relation between long-term precipitation changes and lake level

variations (Huang et al. 2011; Zhang et al. 2011a; Liu et al. 2009a). In general, the magnitude of precipitation changes is too low to explain water level increasing a few decimeters per year as noted by Zhang et al. (2011a). The impact of climate change on water resources over the TP is therefore very complex: a mix not only of direct precipitation changes and evaporation increase under a warming climate, but also of glaciers, snow, and thickening of the active layer of the permafrost, which increase surface and underground inflow to the lakes (Ma et al. 2010; Liu et al. 2009a; Kang et al. 2010; Huang et al. 2011; Zhang et al. 2011a; Li et al. 2014; Song et al. 2014c; Zhang et al. 2015). The decrease in the frozen duration due to warming, which is very pronounced in winter time, also increases the potential contribution of permafrost to lake storage changes (Huang et al. 2011; Li et al. 2008; Liao et al. 2013). It has been observed that in some regions of the TP, the lower limit of the permafrost has risen by more than 80 m, and the active layer has grown by a few decimeters since 1970 (Li et al. 2008), and the total permafrost extent over the TP has declined by 100,000 $km^2$ (Kang et al. 2010). In addition, melting of massive ground ice has resulted in thermokarst ponds which, as a major heat source, speeds up the moisture change, and enhances degradation of its surrounding permafrost (Li et al. 2014). This could explain the geographical disparity of lake storage changes over the TP.

There are 37,000 glaciers covering the TP, and most of them have retreated since the end of the 20th century (Neckel et al. 2014; Wei et al. 2014), directly increasing the surface water recharge to lakes and downstream rivers. The area of the TP glaciers has decreased by 7 % over the last 40 years (Krause et al. 2010) and will probably continue to shrink in the future (Solomon et al. 2007). If this increases the surface water runoff at short timescale, at longer timescale a significant reduction of stream flow resulting from glaciers melting is predicted (Eriksson et al. 2009).

Many studies are now investigating the impact of melting glaciers on the water balance of lakes by using satellite remote sensing and/or models (Kang et al. 2010; Ye et al. 2007; Liao et al. 2013; Song et al. 2014c). For example, Wu and Zhu (2008) and Yao et al. (2007) explored links between area changes of glaciers in Lake Namco's watershed and its expansion in size over recent years. Ye et al. (2007) have estimated the contribution of glaciers in the water balance of Lake Yamzhog Yumco in South Tibet under expansion at the end of the last century. Phan et al. (2013) have shown that glacier melting has become an important factor of water storage change for a large number of lakes over the TP.

As essential natural resources for many different uses, lakes over the TP are therefore under increasing climate stress which needs to be quantified and understood. However, there are only a few gauging instruments (meteorological and hydrological) installed on the TP, and the monitoring of glaciers, permafrost, regional climate change, runoff, and lake level is performed very sparsely and only in recent years. This is why the majority of studies are now based on remote sensing data, and satellite altimetry application for lakes over the TP has been widely adopted by hydrologists and climatologists.

Indeed, satellite altimetry (radar and laser) has been used to calculate water level changes of lakes over the TP. It could be focused on a specific subregion of the TP concerning an individual or limited number of lakes such as lakes Namco and Ziling that were studied in Wang et al. (2013), Li et al. (2014), Song et al. (2015), Ngoring-co by Lee et al. (2011), Liao et al. (2013), Ngangze and La'anga from Hwang et al. (2005) and many others (along with references in the papers cited before). Since 2010 several authors have studied lake level changes and their connection to climate change using satellite altimetry and/or satellite imagery as a principal source of information for the whole TP (Liu et al. 2009a; Zhang et al. 2011a; Phan et al. 2011; Huang et al. 2011; Song et al. 2014b; Kleinherenbrink et al. 2015). They generally try to describe the water level or storage

changes of the lakes in terms of global warming and to determine which component of the water balance is the most influential.

However, nothing regarding the potential use of lakes as a climatic index at the global scale has been published so far. Many studies have investigated the correlation of lakes (mainly at local or regional scale) with climate indexes like the El Niño Southern Oscillation (ENSO), Pacific Decadal Oscillation (PDO) or North Atlantic Oscillation (NAO), but the strong potential of lakes to be considered as a proxy which may be quantified as climatic index has not yet been considered in the literature. However, Street-Perrott et al. (1986) and Mason et al. (1994) have established that lakes react as a low-pass filter to any changes in one of the components of their water budget and have defined associated equations. We will show in the following that this theory could help to interpret the water level and storage changes by using examples of lakes in the TP.

The theory of lake water balance states that a lake always evolves in a way to reach an equilibrium state where water input is equal to water output. We have calculated that Lake Namco has an equilibrium response time of 160 years, Lake Ziling 100 years, Lake Tangra Yumco more than 500 years, and Lake Ayyakum only 24 years (using equations given in Mason et al. 1994). This means that two lakes, for example, lakes Ziling and Tangra Yumco that are in close proximity to each other and with approximately the same net evaporation rate (E–P), will not react with the same temporal patterns to any changes of the evaporation rate E or the precipitation rate P. It should be noted that the equilibrium response may also change if the bathymetry of a lake at different altitudes moves from a steep to shallow shoreline (or the opposite).

We calculated the equilibrium response type for different values of E–P and for different types of lakes (Mason et al. 1994). For lakes with a steep bathymetry (left part of the figure), this time is rather long and is amplified for arid lakes. For shallow lakes (right part of the figure), the relative dependency on E–P diminishes and equilibrium response time is very rapid (a few years). Thus, for a large majority of lakes on the Tibetan Plateau the time to reach equilibrium can take centuries (Figs. 10, 11, 12, 13, 14, 15).

## 6 Results

A large number of recent studies have assumed that the lakes of the TP are globally in a phase of expansion as a consequence of marked climate change observed over many years. However, the majority of these studies were based on a short time period of a few years at the beginning of the twenty-first century (Zhang et al. 2011a; Phan et al. 2011; Song et al. 2013; Wu et al. 2014). The authors have shown that between 2003 and 2009 (using ICESat data) from about 100 lakes monitored, the water height of a large proportion of them increased on average by about 20 cm/year. In Song et al. (2013), the authors also calculated water storage changes for a large number of lakes of the TP, but they only used ICESat data to determine the hypsometry. Their study only covered the period up to 2011. They show a general increase in water storage over the decade 2000–2011 of about 6.79 $km^3$/year. Although these observations are not doubted, it is premature to draw conclusions on the impact of climate warming over so short a period of time. One of the most interesting cases is regarding Lake Namco, the subject of many recent publications.

Lake Namco is located in southeastern Tibet and is one of the largest lakes of the TP with an area of approximately 2000 $km^2$, a catchment area of 11,000 $km^2$, and an altitude of about 4725 m. Krause et al. (2010) calculated the water balance changes of this lake

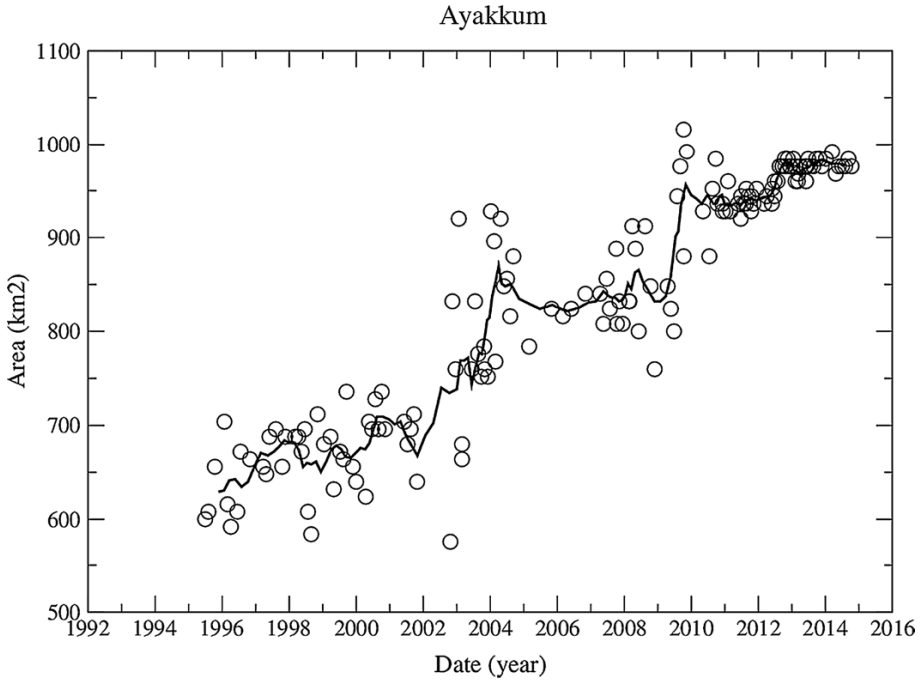


**Fig. 10** Calculation of Lake Ayakkum areal extent from a combination of satellite altimetry and satellite imagery (using the hypsometry polynomial given in Fig. 9)

over the previous 50 years and have shown that it is controlled by snow and glacier melt and inter-annual precipitation variability (between 300 and 500 mm/year). They calculated that glacier melting increased the lake level by 17.5 m and the volume by 33.5 $km^3$. They also compared and validated their model's results to altimetry data for the period 2005–2009. Liu et al. (2009b) used satellite imagery (Landsat and CBERS) to measure areal extent variations of this lake since 1976. They tried to link these changes to variations of E, P, and R. They revealed that the wetter and warmer winter climate since the late 1980's and mid-1990's has increased the ground temperature which has in turn enhanced spring surface runoff and glacier melting. Meanwhile, it has decreased the seasonal underground frost (from 2.35 to 1.93 m on average) leading to acceleration of the permafrost contribution to the lake's water balance. Liu et al. (2009b) also detected the years when abrupt changes were observed in different climate variables (E, P, R, air temperature) in the watershed of Lake Namco. Results from their analysis show that 1996 was a key year for runoff changes, with a 20 % increase in annual discharge, leading the lake to expand.

In another study, Kropáček et al. (2012) processed the satellite altimetry data from Geosat Follow On (GFO), Envisat and ICESat, from 2000 to 2009, and satellite images from Landsat satellites over the period 1976–2009. They observed an expansion of the lake of 82 $km^2$ (also confirmed in Zhang et al. (2011b)) and an increase in the water level of 0.31 m/year during the period of measurements. This coincides quite well with the results obtained by Krause et al. (2010), although they mentioned stabilization of the lake level after 2005.

Zhang et al. (2011b) estimated Lake Namco water storage changes and its link with climate change using different sources of information: meteorological data from 1976 to 2009, satellite images, and lake bathymetry. They estimated the total water storage

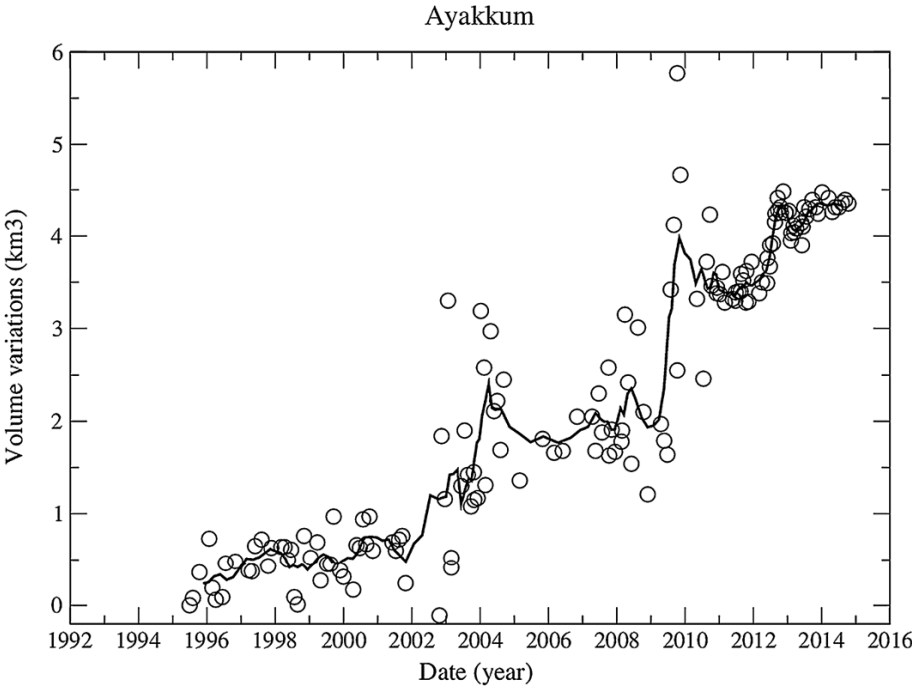


**Fig. 11** Volume variations for Lake Ayakkum using variations of altitude and areal extent given in Figs. 8 and 10

increase over the period of study of 9 $km^3$ and an area growth of 88 $km^2$ in good agreement with work obtained by Kropáček et al. (2012). From Fig. 16, we can see that this exactly corresponds to the lake volume change inferred from altimetry and imagery from 1996 to 2005. They concluded that the main origin of lake growth is rising temperature which yields to increasing discharge from glacier thawing. Wu et al. (2014) have developed a model which tends to demonstrate that this lake is in constant expansion, and they validate their model using 2003–2009 ICESat data. However, they noted a diminishing rate of lake level rising at the end of the study period.

Figure 15a shows the water level variations of this lake inferred from 20 years of multi-satellite altimetry missions (ERS2, Envisat, ICESat, Cryosat-2, and SARAL/AltiKa). We clearly see that it has increased relatively continuously from 1995 to 2005 and has now reached a stable level (until end of 2014) of about 4725 m a.s.l. Has the lake reached a new equilibrium surface? This would mean that with an equilibrium response time of 160 years, if recent evolution of this lake is due to climate warming and started around the year 1996 as shown in Liu et al. (2009b), then lake level stabilization around the years 2005–2006 is an indication that climate conditions have changed again: It could be due to deceleration of glaciers melting in the watershed of Lake Namco following a decade of acceleration. It could also be due to a large decrease in precipitation in the watershed. In either case, it must be confronted and assimilated into lake models. This unique example shows that recent research that tries to explain the expansion of Lake Namco in the light of glacier acceleration and permafrost melting should take into account this lake's new state.

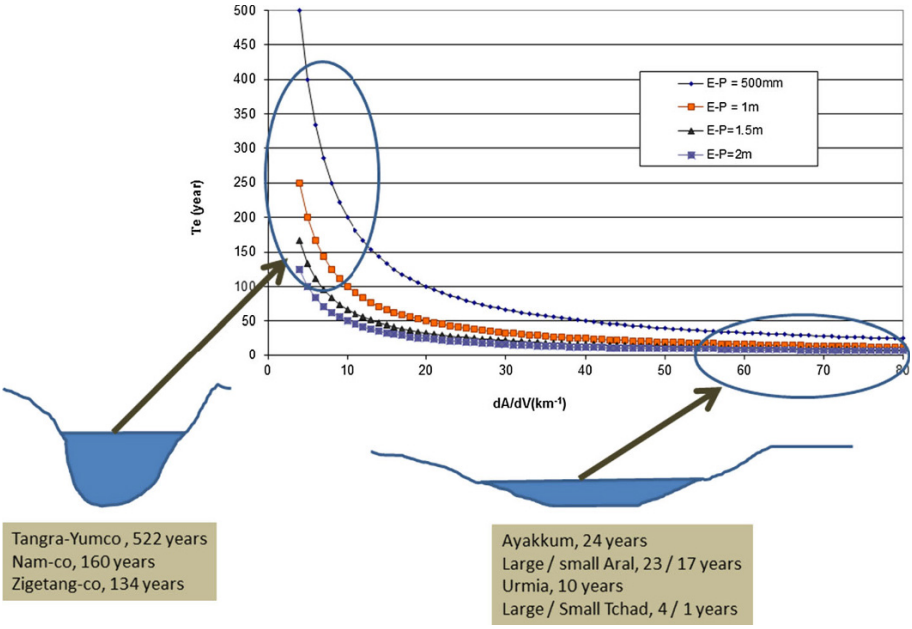


**Fig. 12** Simulation of the equilibrium response time for lakes with various types of morphologies: from steep bathymetry to shallow lakes based on the equations given in Mason et al. (1994)

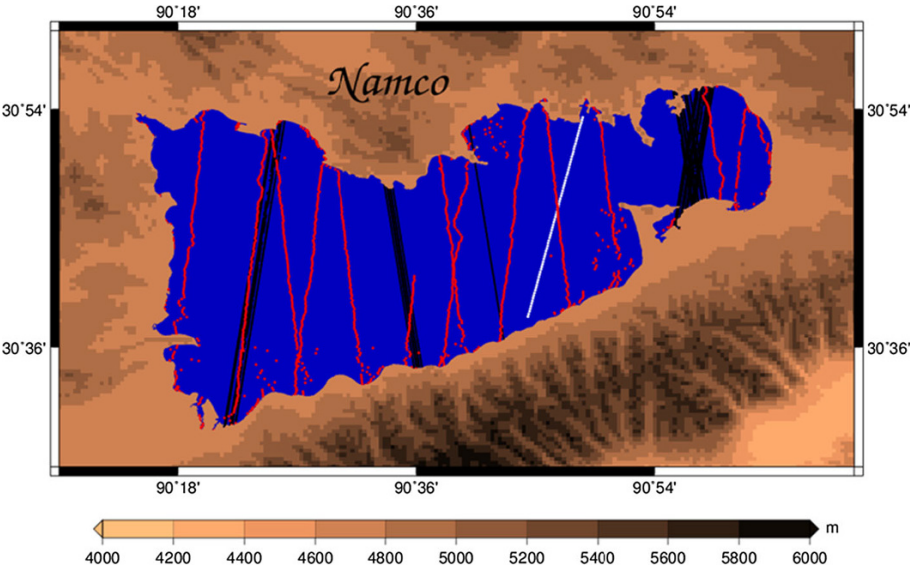


**Fig. 13** Map of Lake Namco. White lines represent the ERS2, Envisat and SARAL/AltiKa tracks, red lines the Cryosat-2 tracks and black lines the ICESat tracks

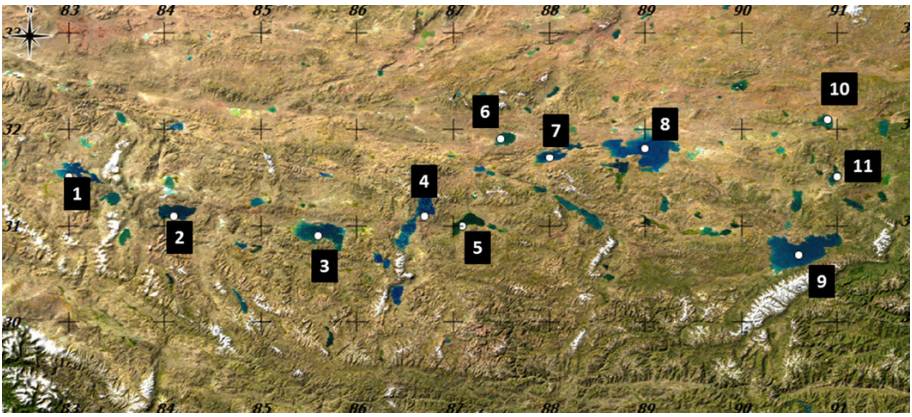


**Fig. 14** Map of the 11 large lakes of the southern part of the TP. 1: Ngangla Ringco, 2: Taro Co, 3: Zhari Namco, 4: Tangra Yumco, 5: Ngangze, 6: Dagze Co, 7: Urru Co, 8: Ziling, 9: Namco, 10: Zigetangco, 11: Pung Co

We shall now look at a set of large lakes located in the southern part of the TP with longitudinal distribution around latitude 31°–32° North (Fig. 14). It includes the TP's two main lakes: Lake Ziling and Lake Namco. We chose only lakes with a minimum of 10 years of observation. In fact, the majority of them benefit from more than 20 years of multi-satellite data. What can be learnt from the water level time series of these lakes in terms of climate change? In another words, can the time series of these lakes be used to indicate and quantify climate change impact on the lakes of the TP?

Among these lakes, six of them clearly present a similar increase in their water level that started in 1997–1998: Ziling, Nganze, Zhari Namco, Dagze co, Zigetangco, and Tangra Yumco (Fig. 15c–g, k). The Dagze Co (Fig. 15f) and Zigetangco (Fig. 15d) continue to expand at the same high rate in 2014, while Ziling (Fig. 15e) and Ngangze (Fig. 15c) started to increase at a lower rate after 2006, and the Zhari Namco (Fig. 15k) started to shrink in 2009–2010. For the Zhari Namco (Fig. 15k), there is a clear oscillation at decadal timescale which can only be seen with 20 years' worth of data. For the four others, it is difficult to detect whether the trend observed after 1998 will continue or whether we can only observe a portion of longer time scale fluctuations. In contrast to this, Namco (Fig. 15a) and Pung Co (Fig. 15b), lake water levels that increased continuously until 2006 have now stabilized to a constant value. The water level of Lake Urru Co (Fig. 15h) seemed to stabilize earlier (in 2002). Taro Co (Fig. 15i) and Ngangla Ringco (Fig. 15j) started to shrink after 2010, significantly for the former, and slightly for the latter.

Lei et al. (2013a, b) analyzed the water storage and water balance variations of lakes Ziling, Namco, Pung Co and Zigetangco from 1976 to 2010 using a combination of satellite imagery and bathymetry of these lakes. Their results are in very good agreement with the water volume calculated in the Hydroweb database and reproduced in Fig. 16. However, time sampling of the water volume variations in Lei et al. (2013a, b) is rather irregular. This can be refined using satellite altimetry results which provide quite interesting results between 1994 and 2000 for these four lakes. It was mentioned above that lakes Namco and Pung Co (for example) grew at a reasonably steady rate from 1996 to 2005, while Lake Zigetangco started to grow around 1997–1998. The results for Lake

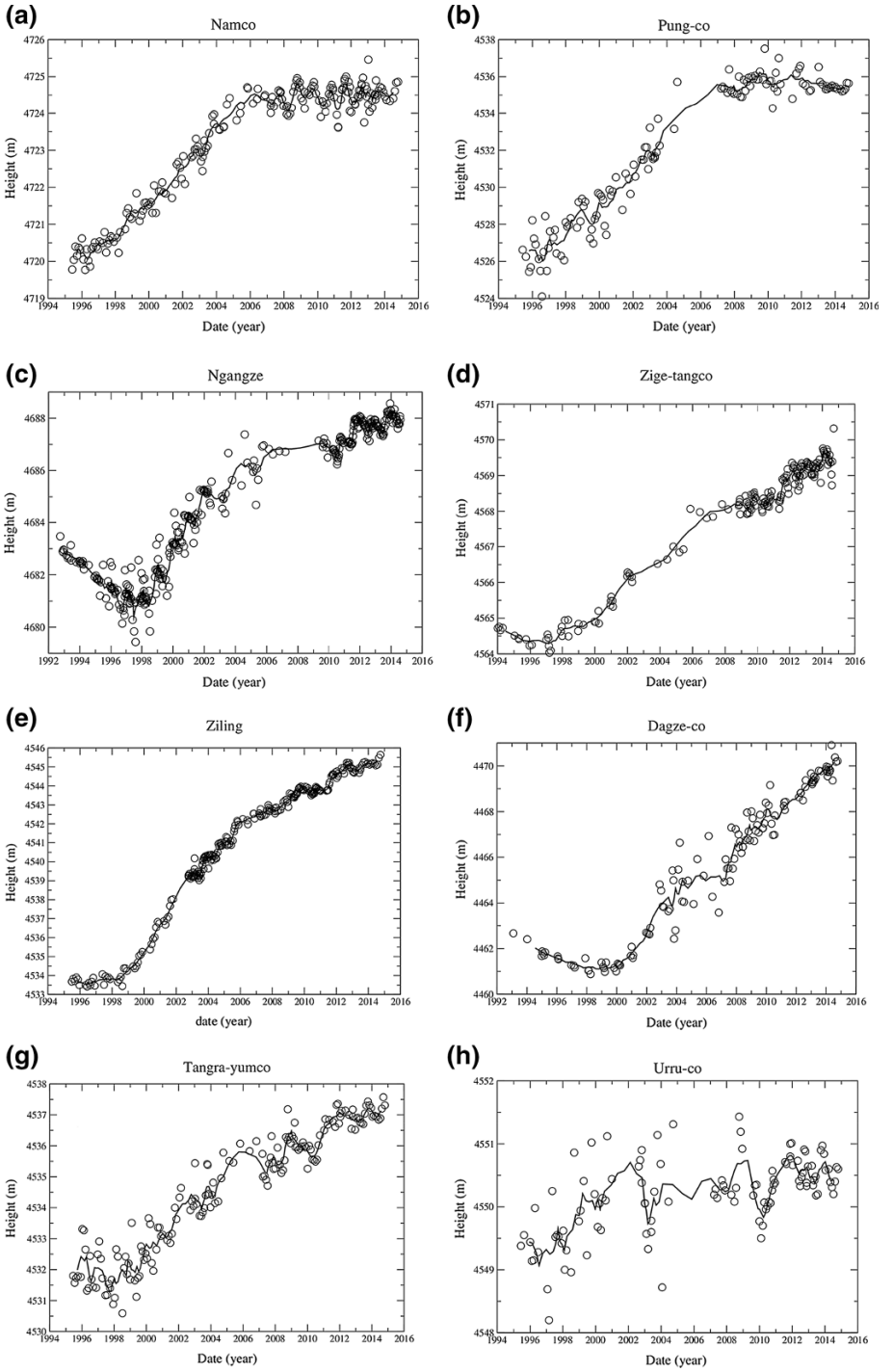


**Fig. 15** Water height of 11 large lakes of the Tibetan Plateau from satellite altimetry

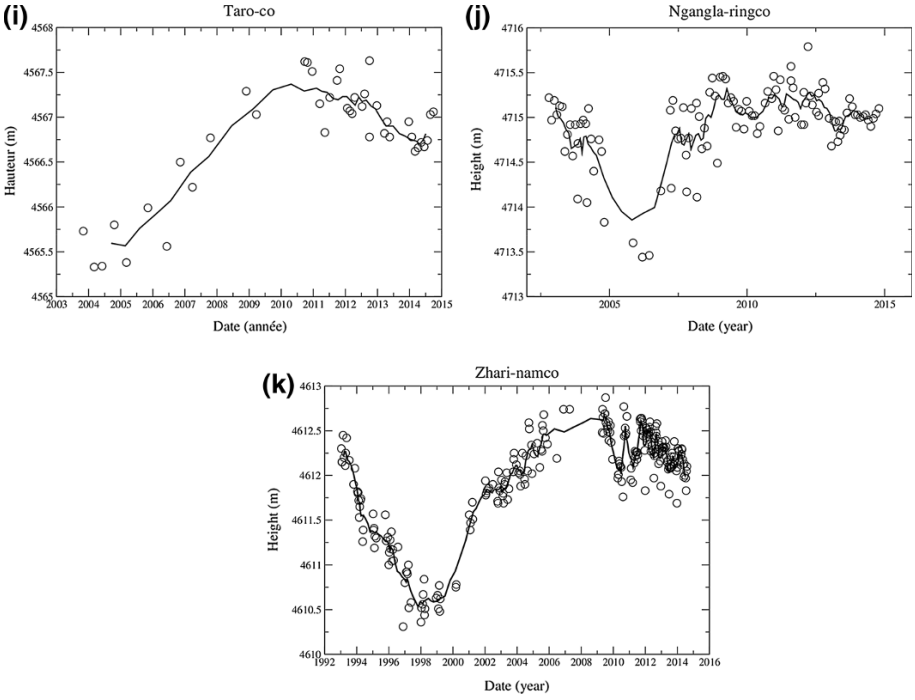


**Fig. 15** continued

Ziling are in very good agreement with the results of Lei et al. (2013a, b). They also modeled the water balance from meteorological data and concluded that lake storage changes were due to an increase in precipitation and runoff and a decrease in evaporation. They also concluded that for Lake Namco the melting glaciers had a higher impact on lake storage change, which was less true for the other lakes. Unfortunately, their model was valid only until 2006 and did not allow them to detect the stabilization of lakes Namco and Pung Co after this date. Results of Liu et al. (2009b) were in better agreement with satellite altimetry for the period 1994–2000 as they clearly revealed an abrupt change in 1996 for Lake Namco. In Hwang et al. (2005) water level variations of Lake Ngangze were analyzed, and they concluded that this lake was under the influence of the South Indian Monsoon correlated with El Nino. Air moisture in the region has increased causing (in particular) the abrupt change of the lake level in 1998 (Fig. 15c). What can be observed using altimetry for lakes such as Lakes Ziling (Fig. 15e), Dagze Co (Fig. 15f), Ngangze (Fig. 15c) or Zhari Namco (Fig. 15k) is an abrupt change in water level from 1998 to 1999 that could be a result of the same phenomenon. However, in such cases, it does not explain why other lakes under the same climatic conditions (Tangra Yumco (Fig. 15g), Pung Co (Fig. 15b) or Namco (Fig. 15a)) present rather different behavior (changes that occurred 2–3 years earlier). Instead, we think that the differences observed between these lakes are more likely due to a conjunction of different causes: glaciers and permafrost melting, P and E changes, and long decadal climate fluctuations with inter-annual responses controlled by their morphology.

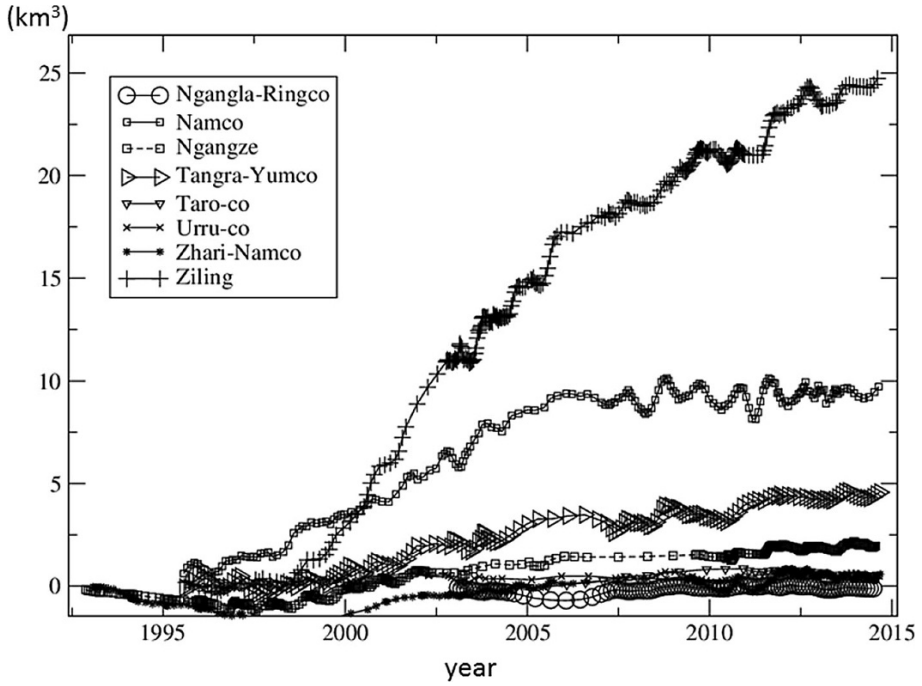


**Fig. 16** Water volume changes for the 11 big lakes of South Tibet inferred from satellite altimetry combined with satellite imagery

The equations of the water budget of a lake, as defined by Mason et al. (1994) show that it is often necessary to observe water level and surface variations over decades in order to analyze the evolution of a lake. It is easy to discern (Fig. 15a–k) that although all of the large lakes of South Tibet [apart from Lake Ngangla Ringco (Fig. 15j)] grew in height and size very significantly between 2003 and 2009, at least half of them (Namco, Urru Co, Taro Co, Pung Co, Zhari Namco: Fig. 15a, b, h, i, k, respectively) reached apparent equilibrium or have even shrunk since the end of the year 2000. Many possibilities can be supposed: the lakes (Namco, Pung Co, Urru Co: Fig. 15a, b, h, respectively) have or have not yet (Ziling, Ngangze, Tangra Yumco, Zigetangco, Dagze Co: Fig. 15c, e, f, g, k respectively) reached a new equilibrium, or they follow a pluri annual cycle as seems to be the case for Lake Zhari Namco (Fig. 15k) or Lake Taro Co (Fig. 15i).

For all of these lakes, we have also calculated area and volume variations. We can see that the main part of total volume changes for the 11 lakes chosen here results from three lakes: Lake Ziling with 25 $km^3$ during the 20 years of measurements, Lake Namco with 9 $km^3$ between 1996 and 2005 and Lake Tangra Yumco with 5 $km^3$ over the last 20 years. For the other lakes the contribution is much lower (Fig. 16).

## 7 Conclusions

Analyzing the causes of water height variations of lakes and understanding the processes involved in their water level and storage variations depends on the availability of observations over long periods of time. In many regions, the network of ground gauges is absent

or too limited. This requires maintaining a constellation of satellites with continuity, overlap, and service over decades. However, the main reason the space agencies have been driven to continue developing altimetry missions in the future is principally due to the operational and research applications for oceanography. Within the past 20 years the use of satellite altimetry for hydrology has emerged and influenced future missions by employing new instrumental concepts (SAR, SARin, Ka band Altimetry, Ka interferometry) which are more suitable for continental waters.

Methodologies for calculating water level and volume variations using satellite data are not straightforward and require the development of specific approaches in order to correct the measurements for some effects like geoid slope errors. Satellite imagery processing also leads to algorithm development to extract the water contour of lakes that are mostly based on normalized indexes. The Hydroweb database provides the water level for about 230 lakes worldwide to scientists who do not want to process the altimetry data themselves. For some specific regions or individual lakes, the Hydroweb also produces areal extent and volume variations of lakes, as is done for many lakes over the Tibetan Plateau. The accuracy of satellite altimetry can be calculated using in situ measurements as ground truth. It generally ranges from a few centimeters for large lakes to a few decimeters for narrow reservoirs or rivers. However, it is often the only tool to measure water level and to analyze the impact of climate variability over continental waters. Many missions have been launched since 1992 with T/P, SARAL/AltiKa, Cryosat-2 and Jason-2 still in orbit, while Jason-3 has just been launched and Sentinel-3 will soon be launched. Methods to combine the products of each of these missions with past ones like ERS2, Envisat, GFO, T/P or Jason-1 can be developed in order to produce decadal water level time series.

Satellite altimetry and satellite imagery together are now widely used for the calculation of lake and reservoir water storage changes worldwide in order to study their inter-annual variability. By using the lakes over the TP we have illustrated some key aspects and issues (technical and scientific) linked with the survey of climate change impacts on surface waters from remote sensing data.

- The lakes respond to climate change (cyclic and secular) occurring at regional to global scale.
- They present a high variety of behavior depending on climate conditions and on their morphology.
- In contrast to general observations for rivers, the temporal variability of lake water height is dominated by large temporal scales as seen in the Tibetan Plateau.

We have seen that for the big lakes over the Central TP the water levels respond to climate change and may vary a lot from one lake to another. Many authors have measured water level variations of Tibetan lakes using short periods of altimetry measurements and tried to analyze their results within the framework of climate change using model or some climate variables. The link with glaciers and permafrost melt or precipitation changes are likely to be the origin of many of the observed changes, but the time series used are certainly too short to lead to definitive conclusions, and processes beyond observation are still uncertain. For example, in 2005 and 2006 lakes Namco and Pung Co reached an equilibrium value which was not the case for other lakes in the vicinity like lakes Ziling or Tangra Yumco. Other lakes like the Zhari Namco or Taro Co seem to be dominated by cyclic variations. The influence of a lake's morphology enters into the calculation of the time response for a lake to reach a new state of equilibrium, and is a key aspect often neglected in the current literature.

**Acknowledgments** The authors acknowledge the Centre National d'Etudes Spatiales (CNES) for financing our project through the TOSCA project. The authors are also grateful to the Centre for Topographic Studies of the Oceans and Hydrosphere (CTOH, www.legos.obs-mip.fr/observations/ctoh) at LEGOS (Toulouse, France) for providing altimetry data in a standard and useful form. The Landsat data have been downloaded from the Earth explorer system of United States Geological Survey (USGS) from their web site: http://earthexplorer.usgs.gov/. We are grateful for this service.



## References

Abarca-del-Rio R, Crétaux J-F, Berge-Nguyen M, Maisongrande P (2012) Does the Titicaca Lake still control the Poopo lake water levels? An investigation using satellite altimetry, and MODIS data (2000–2009). Remote Sens Lett 3(8):707–714

Abileah R, Vignudelli S, Scozzari A (2011) A completely remote sensing approach to monitoring reservoirs water volume. Int Water Technol J 1:63–77

Adrian R, O'Reilly CM, Zagarese H et al (2009) Lakes as sentinels of climate change. Limnol Oceanogr 54(6):2283–2297

Aladin NV, Crétaux J-F, Plotnikov IS, Kouraev AV, Smurov AO, Cazenave A, Egorov AN, Papa F (2005) Modern hydro-biological state of the Small Aral Sea. Environmetrics 16:1–18. doi:10.1002/env.709

Alsdorf DE, Birkett CM, Dunne T, Melack J, Hess L (2001) Water level changes in a large Amazon lake measured with spaceborne radar interferometry and altimetry. Geophys Res Lett 28(14):2671–2674

Altmann G, Rowland JC, Wilson CJ, Verbyla D, Charsley-Groffman L (2010) Quantification of inter-annual and inter-seasonal variability of lake areas within discontinuous permafrost of the Yukon Flats, Alaska. Abstract H41B-1090 presented at 2010 Fall Meeting, AGU, San Francisco, California, 13–17 December

Arsen A, Crétaux J-F, Berge-Nguyen M, Abarca del Rio R (2014) Remote sensing derived bathymetry of Lake Poopó. Remote Sens 6(1):407–420

Arsen A, Cretaux J-F, Abarca Del Rio R (2015) Use of SARAL/AltiKa over mountainous lakes, intercomparison with Envisat mission. Mar Geodes 38(1):534–548. doi:10.1080/01490419.2014.1002590

Aus Der Beck T, Voss F, Flörke M (2011) Modelling the impact of global change on the hydrological system of the Aral Sea basin. Phys Chem Earth 36(13):684–695. doi:10.1016/j.pce.2011.O3.004

Baghdadi N, Lemarquand N, Abdallah H, Bailly JS (2011) The relevance of GLAS/ICESat elevation data for the monitoring of river networks. Remote Sens 3:708–720

Balsamo G, Saigao R, Dutra E, Boussetta S, Stockdale T, Potes M (2012) On the contribution of lakes in predicting near-surface temperature in a global weather forecasting model. Tellus Ser A Meteorol Oceanogr 9:15829. doi:10.3402/tellusa.v64i0.15829

Bates PD, Neal JC, Alsdorf D, Schumann GJP (2014) Observing global surface water flood dynamics. Surv Geophys 35(3):839–852

Berry PAM, Garlick JD, Freeman JA, Mathers EL (2005) Global inland water monitoring from multimission altimetry. Geophys Res Lett 32:L16401. doi:10.1029/2005GL022814

Biancamaria S, Andreadis KM, Durand M, Clark EA, Rodriguez E, Mognard NM, Alsdorf DE, Lettenmaier DP, Oudin Y (2010) Preliminary characterization of SWOT hydrology error budget and global capabilities. IEEE J Special Issue Microw Remote Sens Land Hydrol Res Appl 3(1):6–19. doi:10.1109/JSTARS.2009.2034614

Birkett CM (1995) Contribution of TOPEX/POSEIDON to the global monitoring of climatically sensitive lakes. J Geophys Res 100(C12):25179–25204

Birkett CM (1998) Contribution of the Topex NASA radar altimeter to the global monitoring of large rivers and wetlands. Water Resour Res 34(5):1223–1239

Birkett CM, Beckley B (2010) Investigating the Performance of the JASON-2/OSTM Radar Altimeter over Lakes and Reservoirs. Mar Geodesy 33(1):204–238

Birkett CM, Murtugudde R, Allan T (1999) Indian Ocean climate event brings floods to East Africa's lakes and the Sudd Marsh. Geophys Res Lett 26:1031–1034

Bliss A, Hock R, Radić V (2014) Global response of glacier runoff to twenty-first century climate change. J Geophys Res Earth Surf 119(4):717–730

Bonnefond P, Exertier P, Laurain O et al (2010) Absolute calibration of Jason-1 and JASON-2Altimeters in Corsica during the formation flight phase. Mar Geod 33(S1):80–90
Boschetti M, Nutini F, Manfron G, Brivio PA, Nelson A (2014) Comparative analysis of normalised difference spectral indices derived from MODIS for detecting surface water in flooded rice cropping systems. PLoS ONE 9(2):e88741. doi:10.1371/journal.pone.0088741
Bowling LC, Lettenmaier DP (2010) Modeling the effects of lakes and wetlands on the water balance of Arctic environments. J Hydrometeorol 11(2):276–295. doi:10.1175/2009JHM1084.1
Brenner AC, Bentley CR, Csatho BM, Harding DJ, Hofton MA, Minster J, Roberts L, Saba JL, Schutz R, Thomas RH, Yi D, Zwally HJ (2000) Derivation of range and range distributions from laser pulse waveform analysis for surface elevations, roughness, slope, and vegetation heights. Algorithm theoretical basis document. Version 3.0. Greenbelt, MD, USA
Brown GS (1977) The average impulse response of a rough surface and its applications. IEEE Trans Antennas Propag 25:67–74. doi:10.1109/TAP.1977.1141536
Calmant S, Seyler F, Cretaux J-F (2008) Monitoring continental surface waters by satellite altimetry. Surv Geophys 29(4–5):247–269. doi:10.1007/s10712-008-9051-1
Chavez PS Jr (1989) Radiometric calibration of landsat thematic mapper multispectral images. Photogramm Eng Remote Sens 55:1285–1294
Chavez PS Jr (1996) Image-based atmospheric corrections-revisited and improved. Photogramm Eng Remote Sens 62:1025–1036
Cheng K-C, Kuo C-Y, Tseng H-Z et al (2010) Lake surface height Calibration of Jason-1 and Jason-2 over the Great Lakes. Mar Geod 33(S1):186–203
Coe MT, Birkett CM (2005) Water resources in the Lake Chad basin: prediction of river discharge and lake height from satellite radar altimetry. Water Resour Res. doi:10.1029/2003WR002543
Crétaux J-F, Birkett CM (2006) lake studies from satellite altimetry. C R Geosci. doi:10.1016/J.crte.2006.08.002
Cretaux J-F, Jelinski W, Calmant S, Kouraev AV, Vuglinski VV, Bergé Nguyen M, Gennero M-C, Nino F, Abarca-Del-Rio R, Cazenave A, Maisongrande P (2011) SOLS: a lake database to monitor in Near Real Time water level and storage variations from remote sensing data. J Adv Space Res 47(9):1497–1507. doi:10.1016/j.asr.2011.01.004
Cretaux J-F, Letolle R, Bergé-Nguyen M (2013) History of Aral Sea level variability and current scientific debates. Glob Planet Changes 11:99–113
Cretaux J-F, Biancamaria S, Arsen A, Bergé-Nguyen M, Becker M (2015) Global surveys of reservoirs and lakes from satellites and regional application to the Syrdarya river basin. Environ Res Lett 10(1):015002. doi:10.1088/1748-9326/10/1/015002
Crétaux J-F, Kouraev AV, Papa F, Bergé Nguyen M, Cazenave A, Aladin NV, Plotnikov IS (2005) Water balance of the Big Aral sea from satellite remote sensing and in situ observations. J Great Lakes Res 31(4):520–534
Crétaux J-F, Calmant S, Romanovski V, Perosanz F, Tashbaeva S, Bonnefond P, Moreira D, Shum CK, Nino F, Bergé-Nguyen M, Fleury S, Gegout P, Abarca Del Rio R, Maisongrande P (2011) Absolute calibration of Jason radar altimeters from GPS kinematic campaigns over Lake Issykkul. Mar Geod 34(3–4):291–318. doi:10.1080/01490419.2011.585110
Crétaux J-F, Bergé-Nguyen M, Calmant S, Romanovski VV, Meyssignac B, Perosanz F, Tashbaeva S, Arsen A, Fund F, Martignago N, Bonnefond P, Laurain O, Morrow R, Maisongrande P (2013) Calibration of Envisat radar altimeter over Lake Issykkul. J Adv Space Res 51(8):1523–1541. doi:10.1016/j.asr.2012.06.039
De Wit M, Stankiewicz J (2006) Changes in surface water supply across Africa with predicted climate change. Science 311(5769):1917–1921
Downing JA (2010) Emerging global role of small lakes and ponds: little things mean a lot. Limnetica 29(1):9–24
Downing JA, Prairie YT, Cole JJ, Duarte CM, Tranvik LJ, Striegl RG, McDowell WH, Kortelainen P, Caraco NF, Melack JM, Middelburg J (2006) The global abundance and size distribution of lakes, ponds, and impoundments. Limnol Oceanogr 51:2388–2397. doi:10.4319/lo.2006.51.5.2388
Duan Z, Bastiaanssen WGM (2013) Estimating water volume variations in lakes and reservoirs from four operational satellite altimetry databases and satellite imagery data. Remote Sens Environ 134:403–416
Dudgeon D, Arthington AH, Gessner MO, Kawabata Z-I, Knowler DJ, Lévêque C, Naiman RJ, Prieur-Richard A-H, Soto D, Stiassny MLJ, Sullivan CA (2006) Freshwater biodiversity: importance, threats, status and conservation challenges. Biol Rev 81:163–182. doi:10.1017/S1464793105006950
Eriksson M, Jianshu X, Shrestha AB, Vaidya RA, Nepal S, Sandstrom K (2009) The changing Himalayas: impact of climate change on water resources and livelihoods in the greater Himalayas. ICIMOD, Kathmandu

Frappart F, Calmant S, Cauhopé M, Seyler F, Cazenave A (2006) Results of ENVISAT RA-2 derived levels, validation over the Amazon basin. Remote Sens Environ 100:252–264
Gao H, Birkett CM, Lettenmeir DP (2012) Global monitoring of large reservoir storage from satellite remote sensing. Water Resour Res 48:W09504. doi:10.1029/2012WR012063
Gao T, Kang S, Cuo L, Zhang T, Zhang G, Zhang Y, Sillanpaa M (2015) Simulation and analysis of glacier runoff and mass balance in the Nam Co basin, southern Tibetan Plateau. J Glaciol 61(227):447
Halbfass W (1914) Das Süsswasser der Erde (The freshwater of the Earth). Druch und Verlag von Philipp Reclam jun, Leipzig, p 189
Huang L, Liu J, Shao Q, Liu R (2011) Changing inland lakes responding to climate warming in northern Tibetan Plateau. Clim Change 24:479–502. doi:10.1007/s10584-011-0032-x
Hwang C, Peng M-F, Ning J, Luo J, Sui C-H (2005) Lake level variations in China from TOPEX/Poseidon altimetry: data quality assessment and links to precipitation and ENSO. Geophys J Int 161:1–11
Jarihani AA, Callow JN, Johansen K, Gouweleeuw B (2013) Evaluation of multiple satellite altimetry data for studying inland water bodies and river floods. J Hydrol 505: 78–90. ISSN 0022-1694. Doi:10.1016/j.jhydrol.2013.09.010
Ji L, Zhang L, Wylie B (2009) Analysis of dynamic thresholds for the normalized difference water index. Photogramm Eng Remote Sens 75:1307–1317
Kang S, Xu Y, You Q, Flügel W, Pepin N, Yao T (2010) Review of climate and cryospheric change in the Tibetan Plateau. Environ Res Lett 5:8. doi:10.1088/1748-9326/5/1/015101
Kleinherenbrink M, Ditmar PG, Lindenbergh RC (2014) Retracking Cryosat data in the SARIn mode and robust lake level extraction. Remote Sens Environ 152:38–50
Kleinherenbrink M, Lindenbergh RC, Ditmar PG (2015) Monitoring of lake level changes on the Tibetan Plateau and Tian Shan by retracking Cryosat SARIn waveforms. J Hydrol 521:119–131
Koblinsky CJ, Clarke RT, Brenner AC, Frey H (1993) Measurement of river level variations with satellite altimetry. Water Resour Res 29(6):1839–1848. doi:10.1029/93WR00542
Kouraev AV, Semovski SV, Shimaraev MN, Mognard NM, Legresy B, Remy F (2007) Ice regime of lake Baikal from historical and satellite data: influence of thermal and dynamic factors. Limnol Oceanogr 52(3):1268–1286
Krause P, Biskop S, Helmschrot J, Flügel W-A, Kang S, Gao T (2010) Hydrological system analysis and modeling of tha Nam-Co basin in Tibet. Adv. Geosci 27:29–36. doi:10.5194/adgeo-27-29-2010
Kropáček J, Braun A, Kang S, Feng C, Ye Q, Hochschild V (2012) Analysis of lake level changes in Nam Co in central Tibet utilizing synergistic satellite altimetry and optical imagery. Int J Appl Earth Obs Geoinf 17:3–11. doi:10.1016/j.jag.2011.10.001
Laxon S (1994) Sea ice altimeter processing scheme at the EODC. Int J Remote Sens 15(4):915–924
Lee H, Durand M, Jung HC, Alsdorf D, Shum CK, Sheng T (2010) Characterization of surface water storage changes in Arctic lakes using simulated SWOT measurements. Int J Remote Sens 31(14):3931–3953. doi:10.1080/01431161.2010.483494
Lee H, Shum C-K, Tseng K-H, Guo J-Y, Kuo C-Y (2011) Present day lake level variation from Envisat altimetry over the North eastern Qinghai-Tibetan plateau: links with precipitation and temperature. Terr Atmos Ocean Sci 22(2):169–175. doi:10.3319/TAO.2010.08.09.01(TibXS)
Legresy B, Remy F (1997) Surface characteristics of the Antartic ice sheet and altimetric observations. J Glaciol 43(144):197–206
Lehner B, Döll P (2004) Development and validation of a global database of lakes, reservoirs and wetlands. J Hydrol 296:1–22. doi:10.1016/j.jhydrol.2004.03.028
Lei Y, Yao T, Bird BW, Yang K, Zhai J, Sheng Y (2013a) Coherent lake growth on the central Tibetan Plateau since the 1970s: characterization and attribution. J Hydrol 483:61–67
Lei Y, Yao T, Bird BW, Yang K, Zhai J, Sheng Y (2013b) Coherent lake growth on the central Tibetan Plateau since the 1970s: characterization and attribution. J Hydrol 483:61–67
Lei Y, Yang K, Wang B, Sheng Y, Bird BW, Zhang G, Tian L (2014) Response of inland lake dynamics over the Tibetan Plateau to climate change. Clim Change 125(2):281–290. doi:10.1007/s10584-014-1175-3
Li XY, Xu HY, Sun YL, Zhang DS, Yang ZP (2007) Lake-level change and water balance analysis at Lake Qinghai, West China during recent decades. Water Resour Manag 21:1505–1516. doi:10.1007/s11269-006-9096-1
Li X, Cheng G, Jin H, Kang E, Che T, Jin R, Wu L, Nan Z, Wang J, Shen Y (2008) Cryosphere change in China. Glob Planet Change 62:210–218
Li S, Zhan H, Lai Y, Sun Z, Pei W (2014) The coupled moisture-heat process of permafrost around a thermokarst pond in Qinghai-Tibet Plateau under global warming. J Geophys Res Earth Surf 119(4):836–853

Liao J, Shen G, Li Y (2013) Lake variations in response to climate change in the Tibetan Plateau in the past 40 years. Int J Digit Earth 6(6):534–549
Liu XD, Chen BD (2000) Climatic warming in the Tibetan Plateau during recent decades. Int J Climatol 20(14):1729–1742
Liu J, Wang S, Yu S, Yang D, Zhang L (2009a) Climate warming and growth of high-elevation inland lakes on the Tibetan Plateau. Global Planet Change 67:209–217
Liu J, Kang S, Gong T, Lu A (2009b) Growth of a high-elevation large inland lake, associated with climate change and permafrost degradation in Tibet. Hydrol Earth Syst Sci Discuss 6:5445–5469
Liu J, Wang Z, Gong T, Uygen T (2012) Comparative analysis of hydroclimatic changes in glacier-fed rivers in the Tibet and Bhutan-Himalayas. Quat Int 282:104–112
López-Moreno JI, Fontaneda S, Bazo J et al (2014) Recent glacier retreat and climate trends in Cordillera Huaytapallana, Peru. Glob Planet Change 112:1–11
Ma R, Duan H, Hu C, Feng X, Li A, Ju W, Jiang J, Yang G (2010) A half-century of changes in China's lakes: global warming or human influence? Geophys Res Lett 37:L24106. doi:10.1029/2010GL045514
Mason IM, Guzkowska MAJ, Rapley CG, Street-Perrot FA (1994) The response of lake levels and areas to climate change. Clim Change 27:161–197
McDonald CP, Rover JA, Stets EG, Striegl RG (2012) The regional abundance and size distribution of lakes and reservoirs in the United States and implications for estimates of the global lake extent. Limnol Oceanogr 57:597–606. doi:10.4319/lo.2012.57.2.0597
McFeeters SK (1996) The use of Normalized Difference Water Index (NDWI) in the delineation of open water features. Int J Remote Sens 17(7):1425–1432
Medina C, Gomez-Enri J, Alonso J, Villares P (2008) Water level fluctuations derived from Envisat Radar altimetry (RA-2) and in situ measurements in a subtropical water body: lake Izabal (Guatemala). RSE. doi:10.1016/J.rse.2008.05.001
Mertikas SP, Ioannides RT, Tziavos IN et al (2010) Statistical models and latest results in the determination of the absolute bias for the radar altimeters of Jason satellites using the Gavdos facility. Mar Geod 33(S1):114–149
Meybeck M (1995) Global distribution of lakes. In: Lerman A, Imboden DM, Gat JR (eds) Physics and chemistry of lakes. Springer, Berlin, pp 1–36
Morris CS, Gill SK (1994) Evaluation of the Topex/Poseidon altimeter system over the great Lakes. J Geophys Res 99(C12):24527–24539
Neckel N, Kropáček J, Bolch T, Hochschil V (2014) Glacier mass changes on the Tibetan Plateau 2003–2009 derived from ICESat laser altimetry measurements. Environ Res Lett 9(1):014009
Nicholson SE, Yin X (2002) Mesoscale patterns of rainfall, cloudiness and evaporation over the Great lakes of East Africa, Kluwer Academic Publishers, The East African great lakes: limnology, paleolimnology and biodiversity, Advance in global change research, vol 12
Otsu N (1979) A threshold selection method from gray-level histograms. IEEE Syst Man Cybern 9(1):62–66
Ouma YO, Tateishi R (2006) A water index for rapid mapping of shoreline changes of five East African Rift Valley lakes: an empirical analysis using Landsat TM and ETM data. Int J Remote Sens 27(15):3153–3181
Pandey RK, Crétaux J-F, Bergé-Nguyen M, Mani Tiwari V, Drolon V, Papa F, Calmant S (2014) Water level estimation by remote sensing for 2008 flooding of the Kosi river. Int J Remote Sens 35(2):424–440. doi:10.1080/01431161.2013.870678
Phan VH, Lindenbergh R, Menenti M (2011) ICESat derived elevation changes of Tibetan lakes between 2003 and 2009. Int J Appl Earth Observ Geoinf. doi:10.1016/j.jag.2011.09.015
Phan VH, Lindenbergh RC, Menenti M (2013) Geometric dependency of Tibetan lakes on glacial runoff. Hydrol Earth Syst Sci Discuss 10:729–768. doi:10.5194/hessd-10-729-2013
Rast W, Straskraba M (2000) Lakes and reservoirs, similarities, differences and importance. Short series on planning and management of lakes and reservoirs, UNEP-IETC (International Environment Technological Center)/ILEC (International Lake Environment Committee Foundation), vol 1, 24 p, ISBN: 4-906356-27-3 (available at http://www.ilec.or.jp/en/pubs/p2/lake-resvr)
Raymond PA, Hartmann J, Lauerwald R et al (2013) Global carbon dioxide emissions from inland waters. Nature 503(7476):355–359
Ričko M, Birkett CM, Carton JA, Cretaux J-F (2012) Intercomparison and validation of continental water level products derived from satellite radar altimetry. J Appl Remote Sens 6:061710. doi:10.1117/1.JRS.6.061710
Robertson DM, Ragotzkie RA (1990) Changes in the thermal structure of moderate to large sized lakes in response to changes in air temperature. Aquat Sci 52(4):360–380
Rodriguez E (2015) Surface Water and Ocean Topography project, science requirement document, release February 2015, JPL D-61923

Sakamoto T, Nguyen NV, Kotera A, Ohno H, Ishitsuka N, Yokozawa M (2007) Detecting temporal changes in the extent of annual flooding within the Cambodia and the Vietnamese Mekong Delta from MODIS time-series imagery. Remote Sens Environ 109(3):295–313

Schindler DW (2009) Lakes as sentinels and integrators for the effects of climate change on watersheds, airsheds, and landscapes. Limnol Oceanogr 54(6):2349–2358

Schwatke C, Dettmering D, Bosch W, Seitz F (2015) Kalman filter approach for estimating water level time series over inland waters using multi-mission satellite altimetry. HESS Discuss 12:4813–4855. doi:10.5194/hessd-12-4813-2015

Seekell DA, Carr JA, Gudasz C, Karlsson J (2014) Upscaling carbon dioxide emissions from lakes. Geophys Res Lett 41(21):7555

Silva JS, Calmant S, Seyler F, Moreira DM, Oliveira D, Monteiro A (2014) Radar altimetry aids managing gauge networks. Water Resour Manag 28–3:587–603. doi:10.1007/s11269-013-0484-z

Sima S, Tajrishy M (2013) Using satellite data to extract volume-area elevation relationships for Urmia Lake, Iran. J Great Lakes Res 39(1):90–99. doi:10.1016/j.jglr.2012.2.013

Singh A, Seitz F, Schwatke C (2012) Inter-annual water storage changes in the Aral Sea from multi-mission satellite altimetry, optical remote sensing, and GRACE satellite gravimetry. Remote Sens Environ 123:187–195

Solomon S, Qin D, Manning M, Chen Z, Marquis M, Averyt K, Tignor M, Miller H (eds) (2007) The physical science basis. In: Contribution of working group I to the fourth assessment report of the intergovernmental panel on climate change, IPCC. Cambridge University Press: Cambridge

Song X, Huang C, Sexton JO, Feng M, Narasimhan R, Channan S, Townshend JR (2011) An assessment of global forest cover maps using regional higher-resolution reference datasets. In: Proceedings of IEEE international geoscience and remote sensing symposium, 752–755

Song C, Huang B, Ke L (2013) Modeling and analysis of lake water storage changes on the Tibetan Plateau using multi-mission satellite data. Remote Sens Environ 135:25–35

Song C, Huang B, Ke L, Richards KS (2014a) Seasonal and abrupt changes in the water level of closed lakes on the Tibetan Plateau and implications for climate impacts. J Hydrol 514:131–144

Song C, Huang B, Ke L (2014b) Inter-annual changes of alpine inland lake water storage on the Tibetan Plateau: detection and analysis by integrating satellite altimetry and optical imagery. Hydrol Process 28(4):2411–2418

Song C, Huang B, Richards K, Ke L, Hien Phan V (2014c) Accelerated lake expansion on the Tibetan Plateau in the 2000s: induced by glacial melting or other processes? Water Resour Res 50(4):3170–3186

Song C, Ye Q, Cheng X (2015) Shifts in water-level variation of Namco in the central Tibetan Plateau from ICESat and CryoSat-2 altimetry and station observations. Sci Bull 60(14):1287–1297

Street-Perrott FA, Guzkowska MAJ, Mason IM, Rapley CG (1986) Response of lake levels to climatic change—past, present and future. In: Titus JG (ed) Effects of changes in stratospheric ozone and global climate, vol. 3 Climate Change, Proceedings of the United Nations/Environmental Protection Agency International Conference on Health and Environmental Effects of Ozone Modification and Climate Change, Washington DC, USA, 16-20 June 1986, EPA/UNEP, 211–216

Tarpanelli A, Brocca L, Barbetta S, Faruolo M et al (2015) Coupling MODIS and radar altimetry data for discharge estimation in poorly gauged river basins. IEEE Trans Geosci Remote Sens 8(1):141–148. doi:10.1109/JSTARS.2014.2320582

Tierney JE, Smerdon JE, Anchukaitis KJ, Seager R (2013) Multidecadal variability in East African hydroclimate controlled by the Indian Ocean. Nature 493(7432):389–392

Tranvik LJ, Downing JA, Cotner JB et al (2009) Lakes and reservoirs as regulators of carbon cycling and climate. Limnol Oceanogr 54(6part2):2298–2314

Verpoorter C, Kutser T, Seekell DA, Tranvik LJ (2014) A global inventory of lakes based on high-resolution satellite imagery. Geophys Res Lett 41:6396–6402. doi:10.1002/2014GL060641

Wan W, Xiao P, Feng X, Li H, Ma R, Duan H, Zhao L (2014) Monitoring lake changes of Qinghai-Tibetan Plateau over the past 30 years using satellite remote sensing data. Chin Sci Bull 59(10):1021–1035

Wang B, Bao Q, Hoskins B, Wu G, Liu Y (2008) Tibetan Plateau warming and precipitation change in East Asia. Geophys Res Lett 35:L14702. doi:10.1029/2008GL034330

Wang G, Liu G, Liu LA (2012) Spatial scale effect on seasonal streamflows in permafrost catchments on the Qinghai–Tibet Plateau. Hydrol Process 26(7):973–984

Wang X, Gong P, Zhao Y et al (2013) Water-level changes in China's large lakes determined from ICESat/GLAS data. Remote Sens Environ 132:131–144

Wei J, Liu S, Guo W, Yao X, Xu J, Bao W, Jiang Z (2014) Surface-area changes of glaciers in the Tibetan Plateau interior area since the 1970s using recent Landsat images and historical maps. Ann Glaciol 55(66):213–222

Williamson CE, Saros JE, Vincent WF, Smol JP (2009) Lakes and reservoirs as sentinels, integrators, and regulators of climate change. Limnol Oceanogr 54(6):2273
Wingham DJ, Rapley CG, Griffiths H (1986) New techniques in satellite altimeter tracking systems. In: Proceedings of IGARSS'86 Symposium, Zürich, 8–11 Sept 1986, ESA SP-254 (pp 1339–1344)
Wu Y, Zhu L (2008) The response of lake-glacier variations to climate change inNam Co Catchment, central Tibetan Plateau, during 1970–2000. J Geogr Sci 18:177–189
Wu Y, Zheng H, Zhang B, Chien D, Lei L (2014) Long-term changes of lake level and water budget in the Nam Co Lake basin, Central Tibetan Plateau. J Hydrometeorol 15:1312–1322
Xu HQ (2006) Modification of normalised difference water index (NDWI) to enhance open water features in remotely sensed imagery. Int J Remote Sens 27:3025–3033
Xu ZX, Gong TL, Li JY (2008) Decadal trend of climate in the Tibetan Plateau regional temperature and precipitation. Hydrol Process 22:3056–3065
Yao T, Pu J, Lu A, Wang Y, Yu W (2007) Recent glacial retreat and its impact on hydrological processes on the Tibetan Plateau, China, and surrounding regions. Arct Antarct Alp Res 39(4):642–650
Yao T, Thompson LG, Mosbrugger V, Zhang F et al (2012) Third pole environment (TPE). Environ Dev 3:52–64
Ye Q, Zhu L, Zheng H, Naruse R, Zhang X, Kang S (2007) Glacier and lake variations in the YamzhogYumco basin, southern Tibetan Plateau, from 1980 to 2000 using remote-sensing and GIS technologies. J Glaciol 53(183):673–676
Yi Y, Kouraev AV, Shum CK, Vuglinsky VS, Cretaux J-F, Calmant S (2013) The performance of altimeter waveform retrackers at lake Baikal. Terr. Atmos Sci 24(4I):513–519. doi:10.3319/TAO.2012.10.09.01
Zhang G, Xie H, Kang S, Yi D, Ackley S (2011a) Monitoring lake level changes on the Tibetan Plateau using ICESat altimetry. RSE 115:1733–1742. doi:10.1016/j.rse.2011.03.005
Zhang B, Wu Y, Zhu L, Wang J, Li J, Chen D (2011b) Estimation and trend of water storage at Nam Co Lake, central Tibetan Plateau. J Hydrol 405:161–170
Zhang G, Yao T, Xie H, Kang S, Lei Y (2013) Increased mass over the Tibetan Plateau: from lakes or glaciers? Geophys Res Lett 40(10):2125–2130
Zhang G, Yao T, Xie H, Wang W, Yang W (2015) An inventory of glacial lakes in the Third Pole region and their changes in response to global warming. Glob Planet Change 131:148–157
Zwally HJR, Schutz C, Bentley J, Bufton T, Herring J, Minster J, Spinhirne RT (2003) GLAS/ICESat L1B global elevation data, version 33: GLA 06. Boulder, Colorado, USA

DOI 10.1007/978-3-319-32449-4_6
Reprinted from *Surveys in Geophysics* Journal, DOI 10.1007/s10712-015-9346-y

# The SWOT Mission and Its Capabilities for Land Hydrology

**Sylvain Biancamaria[1] · Dennis P. Lettenmaier[2] · Tamlin M. Pavelsky[3]**

Received: 16 March 2015 / Accepted: 6 October 2015 / Published online: 27 October 2015


**Abstract** Surface water storage and fluxes in rivers, lakes, reservoirs and wetlands are currently poorly observed at the global scale, even though they represent major components of the water cycle and deeply impact human societies. In situ networks are heterogeneously distributed in space, and many river basins and most lakes—especially in the developing world and in sparsely populated regions—remain unmonitored. Satellite remote sensing has provided useful complementary observations, but no past or current satellite mission has yet been specifically designed to observe, at the global scale, surface water storage change and fluxes. This is the purpose of the planned Surface Water and Ocean Topography (SWOT) satellite mission. SWOT is a collaboration between the (US) National Aeronautics and Space Administration, Centre National d'Études Spatiales (the French Spatial Agency), the Canadian Space Agency and the United Kingdom Space Agency, with launch planned in late 2020. SWOT is both a continental hydrology and oceanography mission. However, only the hydrology capabilities of SWOT are discussed here. After a description of the SWOT mission requirements and measurement capabilities, we review the SWOT-related studies concerning land hydrology published to date. Beginning in 2007, studies demonstrated the benefits of SWOT data for river hydrology, both through discharge estimation directly from SWOT measurements and through assimilation of SWOT data into hydrodynamic and hydrology models. A smaller number of studies have also addressed methods for computation of lake and reservoir storage

✉ Sylvain Biancamaria
sylvain.biancamaria@legos.obs-mip.fr

[1] LEGOS, Université de Toulouse, CNES, CNRS, IRD, UPS, 14 Avenue Edouard Belin, 31400 Toulouse, France

[2] Department of Geography, University of California - Los Angeles, 1145 Bunche Hall, Los Angeles, CA 90095-1524, USA

[3] Department of Geological Sciences, University of North Carolina, 104 South Rd., CB #3315, Chapel Hill, NC 27599-3315, USA

change or have quantified improvements expected from SWOT compared with current knowledge of lake water storage variability. We also briefly review other land hydrology capabilities of SWOT, including those related to transboundary river basins, human water withdrawals and wetland environments. Finally, we discuss additional studies needed before and after the launch of the mission, along with perspectives on a potential successor to SWOT.

**Keywords** Surface Water and Ocean Topography (SWOT) satellite mission · Continental surface waters · Lakes · Reservoirs · Rivers

## 1 SWOT Mission Overview

### 1.1 The Needs for a Global Water Surface Mission and Its Requirements

In the late 1990s and early 2000s, the crucial need for more quantitative data on spatiotemporal dynamics of surface waters at a global scale became clear in context of a declining in situ gage network and increasing need to observe and model the global water cycle (Alsdorf et al. 2003). To address this challenge, Alsdorf and Lettenmaier (2003) advocated development of a "topographic imager" satellite mission with $\sim$100 m spatial resolution (to observe main channels, floodplains and lakes), temporal resolution on the order of a few days (to sample flood waves and river dynamic at basin scale) and capability to measure height changes that characterize variations in river discharge and lake water storage. Alsdorf et al. (2007) provided a more in-depth study showing that "spatial and temporal dynamics of surface freshwater discharge and changes in storage globally" are poorly known because:

- in situ networks are very heterogeneous (some countries have dense networks, whereas others have only a few measurements points),
- these data are not always shared at the international level,
- current satellite missions do not provide measurements adequate to observe global spatiotemporal dynamics of continental water surface.

For that reason, Alsdorf et al. (2007) proposed a new satellite mission based on synthetic aperture radar (SAR) interferometry, called Water and Terrestrial Elevation Recovery (WATER). The concept of this satellite mission is built on the legacy of the Shuttle Radar Topography Mission (SRTM) and the Wide Swath Ocean Altimeter (WSOA). SRTM (Farr et al. 2007) was a SAR interferometer in C- and X-bands that flew in February 2000 on the NASA Space Shuttle Endeavour. SRTM provided a near-global digital elevation model (DEM) at 90-m spatial resolution between 60°S and 60°N, but because of the specular returns characteristic of its oblique look angles (between 30° and 60°) it provided poor measurements of surface water. Because the two interferometric antennas were separated by a 60-m mast, construction of an SRTM-like system on a satellite platform would be problematic. A similar concept, WSOA, was envisioned as an additional payload to the altimetry Jason-2 satellite mission with the aim of imaging ocean topography. The distance between the two Ku-band antennas was set to 6.4 m to facilitate inclusion on a satellite platform (resulting in kilometric pixel resolution), and a near-nadir look angle was chosen to better observe the ocean surface (Fu and Rodríguez 2004).

WSOA was definitely withdrawn in 2004 and never flown. To adapt this concept to the needs of continental water surface observation, Alsdorf et al. (2007) proposed to use Ka-band instead of Ku-band, allowing better spatial resolution (see Sect. 1.2). In 2007, in its Decadal Survey (NRC 2007), the National Research Council recommended to NASA this new satellite mission, under the name Surface Water and Ocean Topography (SWOT, https://swot.jpl.nasa.gov/), to measure both the ocean and land water surface topography. Since then, SWOT has been collaboratively developed by NASA, the Centre National d'Etudes Spatiales (CNES, the French space agency) and more recently the Canadian Space Agency (CSA/ASC) and the United Kingdom Space Agency (UKSA). Currently, SWOT is planned for launch in late 2020. It will observe the whole continental waters–estuaries–ocean continuum and therefore link the ocean and hydrology scientific communities. However, in this paper, the ocean component of the mission will not be addressed.

Figure 1 shows an overview of the main spatiotemporal physical processes related to the land hydrologic cycle and the SWOT observation window. SWOT is designed to observe a large fraction of rivers and lakes globally and will provide robust observations of their seasonal cycles. However, at least by itself, it is not conceived to observe climate-scale variability (and especially climate change) and will not be able (except on rare occasions) to monitor flash floods. As stated by Rodríguez (2015), SWOT aims to address the following hydrologic science questions:

- What are the temporal and spatial scales of the hydrologic processes controlling surface water storage and transport across the world's continents?
- What are the spatially distributed impacts of humans on surface water, for example through water impoundment behind dams, withdrawals and releases to rivers and lakes, transboundary water sharing agreements, diversions, levees and other structures?
- What are the regional- to global-scale sensitivities of surface water storages and transport to climate, antecedent floodplain conditions, land cover, extreme droughts and cryosphere?
- Can regional and global extents of floodable land be quantified through combining remotely sensed river surface heights, widths, slopes and inundation edge with coordinated flood modeling?
- What are the hydraulic geometries and three-dimensional spatial structures of rivers globally, knowledge of which will improve our understanding of water flow?

The scientific rationales for these questions and the measurement needs are presented in the SWOT Mission Science Document (Fu et al. 2012). Based on these needs, the SWOT Science Requirements (Rodríguez 2015, summed up in Table 1), have been derived to design the SWOT mission, which is presented in Sects. 1.2 to 1.4 (Sect. 1.2 for the main payload, Sect. 1.3 concerning SWOT products over land and Sect. 1.4 for its spatiotemporal sampling). Then, Sects. 2 and 3 present the benefits of SWOT for measurement of rivers and other water bodies, respectively.

### 1.2 Characteristics of the KaRIn Instrument

To meet the SWOT science requirements (Table 1), a Ka-band radar interferometer (KaRIn) has been designed as the mission main payload. KaRIn will be a SAR interferometer in Ka-band (35.75 GHz frequency or 8.6 mm wavelength), with near-nadir incidence angles (between 0.6° and 3.9°, Fjørtoft et al. 2014). Figure 2 shows a conceptual view of the KaRIn operating system and ground coverage. It will provide images of water

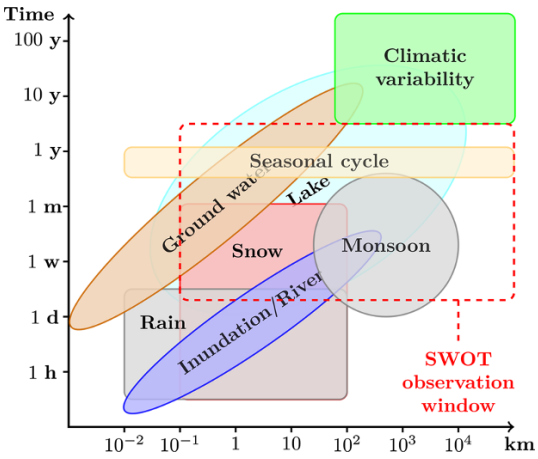


**Fig. 1** Time–space diagram of continental water surface processes and SWOT observation window. Inspired from Blöschl and Sivapalan (1995) and Skøien et al. (2003)

elevations within two swaths, one on each side of the satellite. These two swaths (each 50 km wide) will be separated by a 20-km gap at the satellite nadir (Fig. 2). KaRIn will operate in bistatic mode: one antenna emits the electromagnetic signal toward the closest swath and the two antennas (10 m apart) receive the backscattered signal in their respective directions. Interferometry effectively involves a triangulation: each point in the swath will be observed from two different positions (the antennas positions), which will allow precise estimation of the location of each point. More precisely, the phase difference between the backscattered signals received by the two antennas (the so-called interferogram) will be used to invert water elevations. More details of SAR interferometry and the KaRIn measurements are provided in chapters 6 and 7 in Fu et al. (2012) and by Fjørtoft et al. (2014). Table 2 summarizes the main characteristics of the KaRIn instrument.

KaRIn will provide images of water surface elevation with pixel sizes ~6 m in the azimuth direction (direction of the satellite orbit) and from 60 m (near range, see Fig. 2) to 10 m (far range) in the range direction (perpendicular to the azimuth), as also indicated in

**Table 1** SWOT mission science requirements and goals (Rodríguez 2015)

| | |
|---|---|
| Observed areas | All observed water areas detected by SWOT will be provided to end users, but:<br>errors will be *evaluated* for (250 m)$^2$ (= 62,500 m$^2$) water bodies and 100 m (width) × 10 km (long) river reaches or higher<br>errors will be *characterized* for (100 m)$^2$ to (250 m)$^2$ water bodies and 50 m to 100 m (width) × 10 km (long) river reaches |
| Height accuracy | <10 cm when averaging over water area >1 km$^2$<br><25 cm when averaging over (250 m)$^2$ <water area <1 km$^2$ |
| Slope accuracy | 1.7 cm/km for evaluated river reaches when averaging over water area >1 km$^2$ |
| Relative errors on water areas | <15 % for evaluated water body and river reaches<br><25 % of total characterized water body and river reaches |
| Mission lifetime | 3 months of fast sampling calibration orbit + 3 years of nominal orbit |
| Rain/layover/frozen water flag | 68 % or more of the contaminated data should be correctly flagged |
| Data collection | >90 % of all ocean/continents within the orbit during 90 % of operational time |

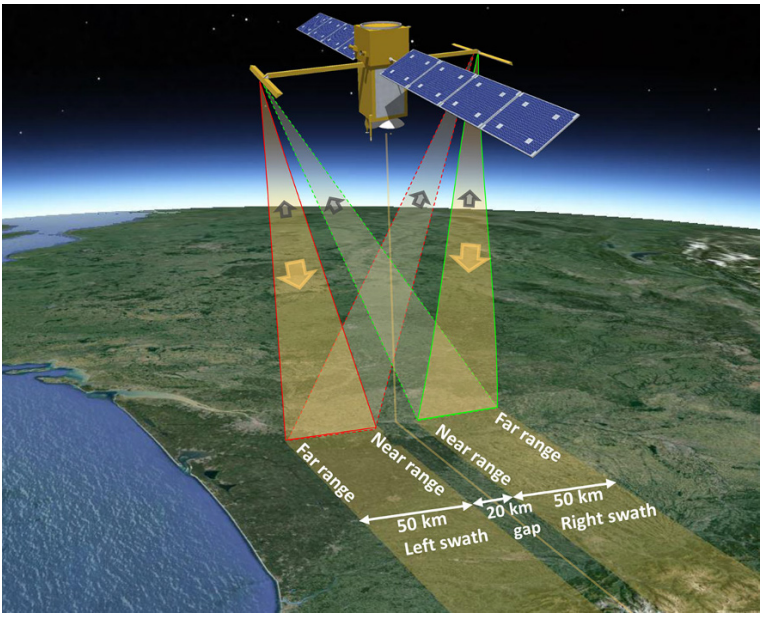


**Fig. 2** Conceptual view of the future SWOT mission with its principal payloads: the Ka-band radar interferometer (KaRIn, with the observed swaths shown by the *yellow polygons*) and a Ku-band nadir altimeter (*yellow line*). Satellite size and altitude are not to scale compared with the Google Earth background image (South West of France), but the ground swaths are to scale (*background image* Google Earth, Landsat image, data SIO, NOAA, US Navy, NGA, GEBCO)

Table 2 (Fu et al. 2012; Fjørtoft et al. 2014; Biancamaria et al. 2010). However, it should be clearly understood that this image is obtained in "radar projection" and not in a geolocated projection. Indeed, the radar instrument measures the distance between the observed point and the antenna. Therefore, in radar images, two consecutive pixels in the range direction correspond to points on the ground that have a similar distance from the satellite. For that reason, when pixels are geolocated, they are more scattered, they do not correspond to a regular grid, and their shape becomes distorted. For example, a hill, which is a few kilometers away from a river, could have a distance to the satellite similar to that of the center of the river and therefore could be located close to the river center in a SAR image. However, in this example, the river banks will have a different distance from the satellite and could be several pixels distant from the river center pixel. Therefore, the top of the hill will be closer to the river center than the river banks. This effect, hereafter referred to as "layover," occurs when surrounding topography or vegetation is at the same distance from the satellite as the water surface (land over water layover). Furthermore, pixels with large vertical errors will also have high geolocation error (vertical and horizontal accuracies are functions of the phase interferogram accuracy). For that reason, the most basic geolocated SWOT products will likely be delivered as point cloud products that can more accurately take into account these geolocation inversion effects (Rodríguez 2015). The 10 m to 60 m $\times$ 6 m intrinsic pixel size also can be somewhat misleading, as a SWOT measurement requirement (Table 2) is not given for this spatial resolution. While these pixels represent the basic unit of SWOT measurement, in fact, water elevations measured by the KaRIn instrument at this native pixel size will be metric if not decametric in

**Table 2** SWOT mission characteristics

| | |
|---|---|
| Orbit | |
| Altitude | 890.5 km |
| Inclination | 77.6° |
| Repeat period | 20.86 days |
| KaRIn (core payload) | |
| One swath extent (total swaths: 2) | 50 km |
| Distance between the two swaths outer edges | 120 km |
| Distance between the two swaths inner edges ("nadir gap") | 20 km |
| Radar frequency/wavelength | 35.75 GHz/8.6 mm (Ka-band) |
| Distance between the two antennas (baseline) | 10 m |
| Instrument azimuth pixel size (radar projection) | 6–7 m |
| Instrument range pixel size (radar projection) | From 60 m (near range, incidence angle $\sim$0.6°) to 10 m (far range, $\sim$3.9°) |
| Additional science payload | |
| Nadir altimeter | Similar to the dual-frequency (Ku/C) Poseidon-3 nadir altimeter on Jason-2 |
| Precise orbit determination system | Laser retroreflector<br>DORIS receiver<br>GPS receiver |
| Radiometer (usable only over oceans) | Three-frequency (18, 23 and 34 GHz) radiometer, similar to advanced microwave radiometer on Jason-2 |

accuracy. Achieving the decimetric accuracy that is a stated requirement in Rodríguez (2015) and Table 2 will require averaging over many such pixels. This issue is discussed in more detail in Sect. 1.3.

In Ka-band, water is more or less a specular reflector, whereas land is rougher. KaRIn near-nadir incidence angles are particularly suited to monitor water bodies, as water will backscatter most of the emitted energy toward the satellite nadir (because of its specular behavior and the near-nadir look angle), whereas land will backscatter energy in all directions and therefore less in the antenna direction. Because of this different energy scattering between water and land, the difference in amplitude of the received electromagnetic wave between water and non-water pixels should be quite high and will be used to compute the water mask. However, because SWOT look angles are close to the nadir, but not exactly at the nadir, some water surface roughness is still needed to get sufficient energy. Thus, when the water surface becomes extremely flat, typically for wind speed $\ll$1 m s$^{-1}$, there could be some loss of data in the far swath where the look angle is close to 3.9° (Enjolras and Rodríguez 2009; Moller and Esteban-Fernandez 2015). This issue is currently under investigation using measurements from the AirSWOT platform, an airborne SWOT analogue (Rodríguez et al. 2010), obtained during campaigns conducted in 2014 and 2015. It will allow better quantification of the frequency and magnitude of layover effects.

Very few satellite missions have used Ka-band, which is therefore not as well understood as lower frequency bands. For example, most current nadir altimeters use Ku- or C-bands, whereas SAR imaging missions are in L-, C- or X-bands. Additionally, these

current sensors have lower (nadir altimeters) or higher (SAR imagery missions) observation incidence angles than SWOT. However, using Ka-band instead of higher wavelength bands has several advantages: first, it allows a finer spatial resolution (which is dependent on the electromagnetic wavelength) from the SAR processing and, second, it facilitates a shorter baseline (distance between the two antennas) for a given targeted instrumental vertical accuracy, for the interferometry processing (a shorter baseline corresponds to a shorter mast between the two antennas, which is easier to construct). Shorter wavelengths also result in less penetration into soil, snow and vegetation (Fjørtoft et al. 2014), which should allow better estimation of wetland and saturated soil surface elevation and snow volume variations, if interferograms can be computed.

A drawback of Ka-band is its sensitivity to rain rates above about 3 mm/h (Rodríguez 2015). The only altimetry satellite mission in Ka-band preceding SWOT is the Satellite with Argos and ALtiKa (SARAL) mission with the AltiKa nadir altimeter, launched only recently (February 2013). Measurements obtained from this new instrument will help to better understand backscattering in Ka-band over different surfaces (water, bare soil, vegetation, snow, etc.). However, AltiKa, as a nadir altimeter, does not have exactly SWOT look angles; its measurements integrate all the energy backscattered in a cone covering angles between $-0.3°$ and $0.3°$ to the nadir (AltiKa half antenna aperture is $0.3°$, Steunou et al. 2015). The Global Precipitation Measurement (GPM) Mission Core Observatory, launched in February 2014, carries the dual-frequency precipitation radar (DPR) in Ku- and Ka-bands (http://pmm.nasa.gov/GPM/flight-project/DPR). In Ka-band, DPR scans across a 125-km swath ($\pm 8.5°$ across track) with a 5-km footprint. Analyzing DPR measurements will provide useful information on backscatter properties in Ka-band; however, the GPM observation angle covers a wider range than SWOT with a much coarser spatial resolution.

For those reasons, airborne and field campaigns have been organized by the Jet Propulsion Laboratory (JPL) (Moller and Esteban-Fernandez 2015) and CNES (Fjørtoft et al. 2014) to better understand Ka-band backscattering at SWOT-like incidence angles. These campaigns have confirmed the decrease in the backscatter coefficient with the incidence angle and a water/land backscatter coefficient contrast of around 10 dB, except when the water surface is very flat (low wind speed and hence extremely low surface roughness). Moller and Esteban-Fernandez (2015) have also reported the impact of decorrelation time (and therefore wind speed and water surface turbulence) on pixel azimuth size, which could become higher than expected based on the instrument characteristics (Table 2). In addition to KaRIn, SWOT will carry additional scientific payload (Table 2), including a dual-frequency (Ku- and C-bands) nadir altimeter, similar to the Poseidon-3 instrument on-board Jason-2 (Desjonquères et al. 2010). It will provide water elevation measurements in the middle of the 20-km gap between the two KaRIn swaths. A radiometer will also facilitate, over the oceans, corrections to path delay due to wet tropospheric effects. However, it will not be used over land because land emissivity dominates the radiometric signal (Fu et al. 2012). Wet troposphere corrections over land will be computed using an atmospheric model, one effect of which will be that the residual tropospheric error will likely be larger over land than over the ocean and should be on the order of 4 cm (Fu et al. 2012).

### 1.3 SWOT Measurements over Terrestrial Surface Waters

SWOT will provide measurements of surface water elevation, slope and water mask. In this paper, water elevation ($H$) corresponds to the distance between the top of the water surface and a given reference surface (geoid or ellipsoid), whereas water depth

($d$) corresponds to the distance between the water surface and the water body (e.g., river) bottom. It is important to note that SWOT will not measure water depth. SWOT level-2 data products (i.e., the highest level of processed data delivered by NASA and CNES to end users) are currently being defined. There remains, therefore, some uncertainty as to their specific nature. However, some characteristics of SWOT level-2 data product over land are provided in the science requirements document (Rodríguez 2015), which is the basis for the discussion in this section. As outlined in Rodríguez (2015), these products will likely include:

- For each pass, a water mask consisting of a geolocated point cloud product with all KaRIn pixels that are identified as water, with the finest spatial resolution to meet appropriate geolocation accuracy (i.e., 10 % of the pixel size in any direction). Surface water elevation corresponding to the provided pixel size (with an estimation of the surface water elevation uncertainty) will be associated with each point within the water mask.
- At least once every repeat cycle, a global water mask following the shorelines of all observed water bodies will be provided in vector format, with one water elevation for each individual water body, along with other information (such as area within the water body and its slope). Water storage within each such water body will be easily derived from this product.
- A global one-dimensional vector product that will include estimated discharge along river reaches at each observation time, for all river reaches wider than 50 m.
- A cross-sectional map of all observed water bodies will be derived from time-varying water elevations along the shores of each water body. This map will be updated yearly.

As SWOT will observe almost all continental surfaces every 21 days, it will provide a tremendous amount of data in the point cloud product, which includes the KaRIn pixels resolution stated in Table 2 (as a reminder, vertical accuracy at such spatial resolution is very low). It will therefore be very difficult for end users to use so much data in a non-gridded format at global, regional or even basin scales. For that reason, vector products providing height-integrated measurements for entire lakes and for discrete river reaches have been defined.

The SWOT mission is designed to observe all rivers wider than 100 m and water bodies (lakes, reservoirs, ponds, continuous wetlands) with an area greater than 250 m $\times$ 250 m (i.e., 62,500 $m^2$) that lie within the swath coverage. Moreover, NASA and CNES teams will strive to design an instrument and processing methods that will be able to observe rivers wider than 50 m and water bodies with an area above 100 m $\times$ 100 m. If SWOT is able to observe smaller rivers or water bodies, the measured data will be provided. Besides, lower-level product (SAR amplitude and phase images, interferograms) will be provided on demand and could be used to reprocess data a posteriori, which might help to improve products resolution if feasible. The main sources of errors that will affect KaRIn measurements are instrument thermal noise (white noise), differences in the return signal speckle, error in the interferometric baseline roll angle, wet and dry tropospheric effects, ionospheric effects, topographic layover and vegetation layover and attenuation (see chapter 6 in Fu et al. 2012). Thermal noise and speckle dominate the error budget at the KaRIn pixel level (10 m to 60 m $\times$ 6 m, Table 2), leading to multi-meter vertical errors. These errors are random for one pixel, but their standard deviations tend to increase in the far range of the measurement swath (Enjolras and Rodríguez 2009). Fortunately, these random errors can be reduced, by averaging over water pixels, by the square root of the number of pixels averaged. For this reason, the science requirements (Table 1) are

provided for water areas much larger than a single pixel. However, the other sources of error will not be reduced by the averaging process. Over 1 $km^2$ (e.g., a 10 km reach for a river of 100 m width), SWOT water elevation will have a 10-cm ($1\sigma$) accuracy. For this averaging area, random errors and wet tropospheric effects are the main error sources. Locally, especially near the water bodies margins, topographic and vegetation layover can be a source of large errors, especially given the near-nadir incidence angles used by KaRIn. Therefore, the received energy by the antenna will be a mixture of the energy backscattered by water and topography or vegetation, leading to potentially large errors in retrieved water elevation, geolocation and water extent. SWOT performance will be evaluated for water bodies meeting the observation requirement (lakes, reservoirs and wetlands with area greater than 250 m $\times$ 250 m and rivers wider than 100 m), in order to validate that the instrument meets the accuracies provided in Table 1. Furthermore, SWOT performance will be characterized for the observational goals (100 m $\times$ 100 m to 250 m $\times$ 250 m water bodies and 50- to 100-m-wide rivers). Estimates of measurement accuracy will be provided with SWOT data products.

There is currently no near-real-time consideration for provision of SWOT data products, consistent with the scientific rather than operational nature of the mission. However, derived products are expected to be provided within 60 days of their collection (requirement). There is also a goal to provide water elevations for a select number of reservoirs ($<$1000) within 30 days of collection. Finally, it is worth noting that an on-board averaged ocean water elevation product computed over a regular grid will also be provided over continents (all observed pixels will be available, not just the ones that are entirely covered by water). This ocean product will have a spatial resolution between 250 m and 1 km (the grid size has not yet been finalized). However, while the elevation accuracy over oceans will be centimetric, the accuracy of this product over continents is not defined and has not yet been evaluated, in part because SAR interferometry processing over land is much more complex than over oceans.

### 1.4 SWOT Spatiotemporal Coverage

There will be an initial calibration phase for the SWOT mission with a fast sampling orbit (1-day repeat period), but reduced spatial coverage relative to the subsequent orbit. The objective of this fast sampling phase of the mission is to obtain frequent overpasses of the satellite over specific ocean/land hydrology targets that will allow calibration of radar system parameters. For open oceans, it will also help to characterize water elevation temporal decorrelation times. This initial calibration phase will last 3 months, which is expected to be sufficient to obtain a fully calibrated system for the nominal phase (Rodríguez 2015). The nominal phase of the mission (also termed the science phase) will have a non-Sun synchronous, 890.5 km altitude, 20.86-day repeat period and 77.6° inclination orbit (Table 2) and will last at least 3 years. The remainder of this section is applicable only to this nominal orbit.

SWOT spatial coverage and revisit times per orbit repeat period (i.e., $\sim$21 days) depend on orbit characteristics, instrument swath width (2 $\times$ 50 km), nadir gap width (20 km) and a function of latitude as well. Figure 3 shows a map of the number of SWOT revisits per orbit repeat period ($\sim$21 days) over the continents between 78°S and 78°N (a). To improve figure readability and given the scope of this paper, oceans have been masked in blue. However, oceans and continents will have the same sampling pattern. Figure 3b shows the lower Amazon basin, which illustrates the extent of locations that will never be sampled by SWOT (white diamonds). Tropical regions will be sampled less frequently

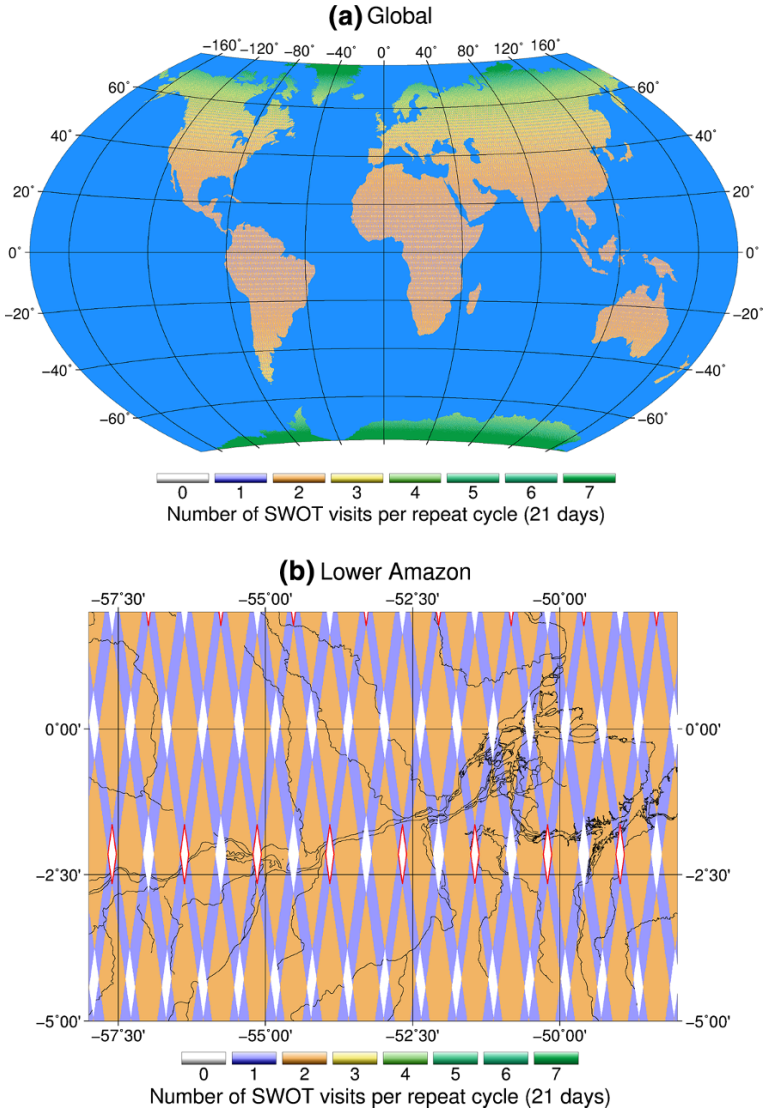


**Fig. 3** Number of SWOT revisits per orbit repeat period (21 days) over the continents (oceans have been masked, but ocean data will also be provided) in between 78°S and 78°N (**a**) and a zoom over the Lower Amazon (**b**). Over the lower Amazon, *white diamonds* with *magenta* boundaries correspond to observation gaps due to the orbit intertrack distance

than higher latitudes; the number of revisits per repeat period ranges from a maximum of two at the equator to more than ten above 70°N/S. Few regions will never be observed (white in Fig. 3a, b); however, much of the equatorial regions will be seen only once per repeat period.

Figure 3 also shows that the mission will observe almost all continental surfaces from 78°S to 78°N, which will be a tremendous improvement compared with nadir altimeters, which miss many water bodies. Regions not observed by SWOT are the results of the

20-km nadir gap between the two swaths (white diamonds without magenta boundaries on Fig. 3b) and the orbit intertrack distance, which does not always allow for adjacent swaths to overlap at the lowest latitudes (white diamonds with magenta boundaries on Fig. 3b). Gaps due to orbit intertrack distance are only present in the 25°S–25°N latitude band, with their largest extent between 10°S and 10°N. Coverage gaps resulting from the nadir gap cover a much broader latitude band (60°S–60°N) and are the main source of observation gaps. The total gap area over all latitudes between 78°S and 78°N is about 3.55 % of the whole land area (or $4.90 \times 10^6$ km$^2$). This is consistent with the SWOT science requirement (Rodríguez 2015), which states: "SWOT shall collect data over a minimum of 90 % of all ocean and land areas covered by the orbit inclination for 90 % of the operation time" (Table 2). The coverage gap can, however, be locally higher than 10 % between 10°S and 10°N. On average over this band of latitudes, 7 % of land is unobserved and the maximum coverage gap is 14 % over a 1° latitude band centered on 4.5°N.

Satellite nadir altimeters measure water elevation along the satellite tracks and, therefore, most sampled river reaches are observed only once per repeat period (except for the few locations where ascending and descending tracks cross). Thus, temporal sampling of rivers by nadir altimeters is essentially equal to the orbit repeat period. Large lakes may be sampled more than once during a repeat cycle by altimeters, but uncertainties in the geoid when different parts of a lake are sampled must be corrected for (Crétaux et al. 2011). These difficulties will be overcome for SWOT, as for most locations in both rivers and lakes there will be more than one observation per repeat period for the reasons indicated above. The number of revisits is, however, unevenly distributed in time during the repeat period. This is illustrated in Fig. 4, which shows the SWOT observation mask (black bars correspond to observation dates) for all latitudes along the 30°E meridian versus days during a repeat period. For example, at the equator and at 30°E, there will be two observations: one at day 15 and one at day 20, but no observations for 16 consecutive days. The distribution of revisit times during a repeat period is not monotonically controlled by latitude, which makes it difficult to infer directly how errors from temporal sampling vary as a function of latitude. SWOT products that will be used for seasonal studies may require computing monthly time series.

The uneven SWOT temporal sampling will be a source of error in the computation of monthly means. Computing cycle-based averaged (i.e., 21 days average) might be a viable alternative for SWOT, but this option requires additional study. The impacts of these

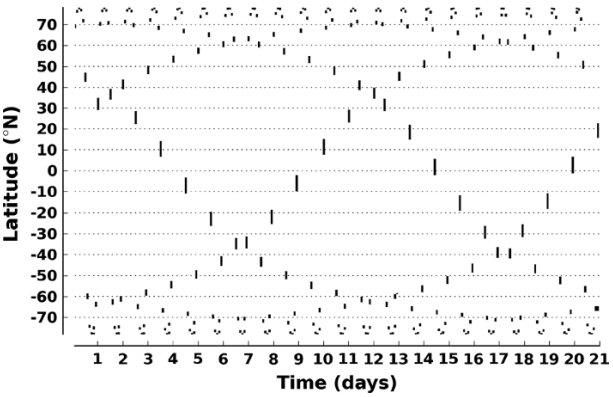


**Fig. 4** SWOT observations mask (*black bars* correspond to an observation) along 30°E meridian versus days (during an orbit repeat period)

variations in temporal sampling depend on the nature of the water body sampled. For example, the water surface elevation of some lakes may not vary significantly except on monthly or longer timescales, while many rivers exhibit changes in discharge on daily or even hourly timescales. In rivers, errors associated with gaps in temporal sampling result from missed local maximum/minimum flows (Biancamaria et al. 2010; Papa et al. 2012), the importance of which depends on the flashiness of the river. To estimate error in monthly averages due only to the SWOT uneven temporal sampling, Biancamaria et al. (2010) proposed a method that used daily in situ discharge time series from 216 gages for a previously proposed SWOT orbit (970 km, 22-day repeat period and 78° inclination orbit with two 60-km swaths). For simplicity and solely for the purpose of estimating the impact of temporal sampling error, the Biancamaria et al. (2010) method assumed that SWOT measurements have already been converted to discharge. Furthermore, errors due to instantaneous estimation of discharge were not considered, though in reality they may be a significant component of the error budget. In situ discharge time series were used because they are much more readily available than water height. Since the errors in monthly discharge are expressed as percentages, the results should be somewhat similar to those for water height.

Updated for the current orbit, the method of Biancamaria et al. (2010) gives a mean temporal sampling error for all 216 gages of 8.1 %. On average, monthly mean temporal sampling errors decreased with increasing latitude, ranging from 10.0 % around the equator to 6.1 % above 60°N. For 11 large rivers distributed from the equator to the high latitudes, Papa et al. (2012) showed that insufficiently frequent temporal sampling around the seasonal peak discharge can lead to substantial errors in mean river discharge computed over a satellite repeat period. For boreal rivers, nadir altimetry sampling with a repeat period longer than 20 days leads to errors $\gg$20 % due to the relatively large fraction of the annual discharge of boreal rivers that occurs over relatively short periods following ice breakup. Errors are much smaller using SWOT temporal sampling. Furthermore, considering the 11 rivers, SWOT temporal sampling errors are correlated with the discharge temporal variance contained in all frequencies above 1/(20 days) ($R^2 = 0.87$) rather than drainage area ($R^2 = 0.18$), at least for the few number of tested large rivers.

Unlike for rivers, there are not yet comprehensive studies estimating the impact of SWOT temporal sampling on the measurement of variations in lake storage. However, given the fact that storage change in the large majority of global lakes remains entirely unobserved and that storage change in many observed lakes varies on seasonal or annual timescales (Crétaux et al. 2015), it is expected that the impacts of limited temporal sampling will be smaller than in the case of rivers.

In summary, despite the uneven time sampling and the limited regions that will not be sampled, SWOT will provide unprecedented observations of continental surface waters at global scale. The next sections review in more detail published studies that have explored, for different science questions, the benefits of the SWOT mission for land hydrology (Sect. 2 for rivers, Sect. 3.1 for lakes and reservoirs and Sect. 3.2 for other water bodies and specific applications).

## 2 River Studies

### 2.1 Rivers Seen by SWOT

SWOT will monitor the spatial and temporal dynamics of surface water globally, especially rivers. At a specific location, river stage, width and velocity variations and therefore

discharge depend on many local factors such as soil characteristics, bedrock characteristics, topographic variability, channel density, vegetation characteristics, and the space–time variability of precipitation, and drainage area, among other characteristics. SWOT will provide the first globally consistent and coherent images of river storage and discharge variations. Over the last two decades, optical imagery and digital elevation data have helped to map medium to large rivers, whereas airborne and local measurements have provided valuable information for smaller rivers (Lehner et al. 2008; Allen and Pavelsky 2015). SWOT will provide consistent and coherent information about the spatial distribution of river storage and discharge, which will especially improve the availability of information about rivers that are not well monitored because in situ observations are not collected or because they are not shared across political boundaries. In addition, SWOT will provide critical information about the impact of river discharge characteristics and variations on human societies. This includes the nature of floods and droughts in poorly monitored river basins and the characteristics of discharge in rivers that cross international boundaries (transboundary basins).

Notwithstanding the profound improvement that SWOT will provide in the availability of information about rivers globally, SWOT does not have the objective of and cannot be an in situ gage network replacement. In most circumstances, in situ gages will be, by far, more precise than any remote sensing discharge estimates. This is especially important for applications such as water management, where highly accurate and precise information is required for legally significant purposes. For example, data from the gauge on the Colorado River at Lees Ferry, AZ, are used to determine the allocation of water to surrounding states. SWOT will likely not be sufficiently accurate for this purpose. On the other hand, stream gage information is by its nature local and does not provide a full view of the spatial variations of streamflow. Moreover, some types of rivers such as highly braided channels and rivers with poorly defined banks are not well suited to in situ gauge measurements. The main benefit of SWOT in this respect will be to provide new and complementary 2D observations for a wide range of different river planforms. Clearly, SWOT will not observe full river networks because it will be limited to measuring rivers 50–100 m in width.

Therefore, a key question is: What portions of the global river network SWOT will observe and what improvement will it represent compared to current capabilities? Pavelsky et al. (2014) have addressed these questions. Using river networks from Hydro1k (Verdin and Greenlee 1998) and HydroSHEDS (Lehner et al. 2008), the global in situ gage discharge time-series database from the Global Runoff Data center (GRDC, http://www.bafg.de/GRDC/EN/Home/homepage_node.html) and downstream hydraulic geometry (power law relationships between drainage area, mean annual discharge and river width at sub-basin scales), they have quantified the fraction of global river basins that SWOT would observe given river observability thresholds of 100 and 50 m. They found that SWOT would observe more than 60 % of the global sub-basins with an area of 50,000 $km^2$ given the ability to observe rivers wider than 100 m. If SWOT can meet the goal of observing 50-m-wide rivers, more than 60 % of sub-basins with an area of 10,000 $km^2$ would be observed. For the smallest river basins observed, only the mainstem river will likely be measured by SWOT.

For SWOT-observable rivers, a number of studies have investigated the potential to produce river discharge estimates directly from SWOT water level, surface slope and inundation extent observations. We review these studies in Sect. 2.2. In Sect. 2.3, we review studies that have pursued an alternate pathway of combining SWOT observations with hydrologic and river hydrodynamic modeling to produce river discharge estimates.

### 2.2 Instantaneous Direct River Discharge Estimations

Space-based observations of discharge began nearly two decades ago with the observation that variations in river width, observable from satellites, can be used along with limited in situ discharge data to develop rating curves (Smith et al. 1995, 1996; Smith 1997; Smith and Pavelsky 2008). A few years later, the first attempts were made to use nadir altimetry in conjunction with in situ observations to derive river discharge from altimetry-based water elevation data using rating curves (e.g., Kouraev et al. 2004). An alternative strategy of estimating discharge using water elevation, width, slope and velocity observed by or derived from spaceborne sensors was pursued in studies by Bjerklie et al. (2003) and Bjerklie et al. (2005) at about the same time. These attempts were specific to individual study reaches, were highly parametrized and required ancillary in situ data in addition to altimetry-based variables. It was recognized that the next logical step was to develop discharge algorithms that could take advantage of all the information provided by SWOT (water elevations, slopes and inundation extent) so as to produce river discharge estimates at the scale of large river basins or even globally.

Following the analysis by Pavelsky and Durand (2012) that new discharge algorithms specifically tuned for SWOT data need to be developed, four different discharge algorithms have been proposed to derive river discharge from SWOT. Characteristics of these algorithms are summarized in Table 3 and are briefly presented in the next paragraph. Gleason and Smith (2014) and Gleason et al. (2014) have pursued an approach that they termed at-many-stations hydraulic geometry (AMHG hereafter). Bjerklie (2007) describes an approach (B2007 hereafter) that is based on an equation similar to the Manning equation with tuned power law coefficients. Garambois and Monnier (2015), hereafter GM2015, propose a method based on physical and numerical approximations of the Saint-Venant equations to invert the unobserved equivalent bathymetry and friction coefficient and then derive discharge. Durand et al. (2014) also use physical and numerical approximations (different from GM2015) of the Saint-Venant equations. This algorithm is referred to hereafter as "MetroMan," because it uses the Manning equation along with the continuity equation and a Metropolis algorithm to invert bathymetry, friction and discharge. We discuss each of these algorithms, including hypotheses and limitations, briefly below. Additionally, these algorithms are summarized in Table 3.

The AMHG algorithm will use the intensive SWOT observations of river width to derive discharge using the well-known geomorphologic relationship between river width ($w$) and discharge ($Q$) at a specific location: $w = aQ^{b}$. The $a$ and $b$ coefficients are considered constant in time but vary along a given river. The innovation of the AMHG algorithm is based on the important fact (reported for the first time in Gleason and Smith 2014) that $a$ and $b$ at cross sections within the same river reach commonly exhibit a well-defined log-linear relationship. Therefore, by considering width variations at many cross sections along a river in combination, the number of unknowns is decreased, allowing $a$, $b$ and $Q$ to be estimated using a genetic algorithm requiring only multi-temporal width observations at many river reaches (Gleason et al. 2014). A global parametrization is proposed by Gleason et al. (2014) when no a priori information is available. In this paper, the authors highlight a series of cases for which the algorithm will not work (corresponding to rivers that do not verify the conditions listed in column "Tested river types" for this algorithm in Table 3). When these cases (types of rivers) are excluded, the relative root mean square error (RMSE) between AMHG and in situ discharge ranges from 26 to 41 % for instantaneous discharge.

**Table 3** Current discharge algorithms designed to use SWOT data ($n$ means Manning coefficient, $w$ river width, $S$ river surface slope, $H$ river elevation, $A_0$ unobserved cross-sectional flow area and $Q$ discharge)

| Discharge algorithm | Algorithm basis | Tested river types | SWOT variables used | First guess/ancillary data | Output(s) |
|---|---|---|---|---|---|
| AMHG (Gleason and Smith 2014; Gleason et al. 2014) | $w/Q$ geomorphic scaling relationship along river reach | Single channel and width variability and no lateral in/outflows and no several order magnitude variation and $b > 0.1$ (in $w = aQ^b$) | $w$ | – | $Q$ |
| B2007 (Bjerklie et al. 2003, 2005; Bjerklie 2007) | Manning-like equation with calibrated exponent and time-varying Manning coefficient | Single channel | $H$, $w$, constant $S$ | Mean annual $n$ and $Q$ | $Q$, time varying $n$ |
| GM2015 (Garambois and Monnier 2015) | Shallow water equations (low Froude) | Single channel and no in/outflows | $\delta H$, $w$, $S$ | $n$, $A_0$, baseflow $Q$ | $Q$, corrected $n$, corrected $A_0$ |
| MetroMan (Durand et al. 2014) | Diffusive approximation of shallow water equations | Single channel | $\delta H$, $w$, $S$ | $n$, $A_0$, baseflow $Q$ | $Q$, corrected $n$, corrected $A_0$ |

Bjerklie's algorithm (Bjerklie 2007) is based on a tuned Manning equation, using a constant river slope and parameterized Manning coefficient ($n$) varying in time and taking into account idealized channel shape. It requires as ancillary parameters the mean annual discharge (required because SWOT will provide surface water elevation and not river water depth). This method is robust if there are no floods and if the mean annual discharge is accurately known.

The GM2015 algorithm is a forward and inverse model based on the 1D Saint-Venant's equations applied to river reaches and rewritten to take into account SWOT measurements of water surface elevation, width and slope. It assumes no lateral inflows, steady-state flows at observation times, low Froude number (<0.5, corresponding to neglecting the inertia term in the momentum equation), trapezoidal cross section and constant friction coefficient in time. The inverse model allows retrieval of discharge and an effective friction coefficient (Strickler or Manning coefficient) and cross-sectional geometry for the lowest observed level (i.e., the low flow bathymetry), for a given set of observations. The identified coefficients (friction and cross-sectional geometry) can then be used to compute discharge for other SWOT observations using the forward model. Garambois and Monnier (2015) tested the GM2015 algorithm on more than 90 synthetic rivers covering a wide range of conditions (width, depth, discharge) that will be observed by SWOT. They reported RMSE of discharge below 15 % for first guess error exceeding 50 % and a very robust estimation of discharge, as measurements errors and errors due to physical approximation are included in the estimated bathymetry and friction coefficient errors. Even if some equifinality (Beven 2006) exists between friction coefficients and bathymetry, the GM2015 algorithm seems to provide accurate estimates of equivalent bathymetry and friction in the range of tested discharge.

The MetroMan algorithm, like GM2015, uses an approximation (the diffusive wave approximation) of the 1D Saint-Venant equations. However, the mathematical implementation of the forward and inverse models is different, and it also takes into account unknown lateral inflows. It has been evaluated using a 22.4 km river reach of the Severn River (river width $\sim$60 m) in the UK and one of its tributaries for an in-bank flow event (duration 5 days) and an out-of-bank flood event (duration 15 days). For the in-bank event, when lateral inflows from tributaries were known, discharge was retrieved with 10 % RMSE, whereas when lateral inflows were unknown, the discharge RMSE went up to 36 %. For the out-of-bank flood event with unknown lateral inflows, the RMSE was 19 %. Both the GM2015 and MetroMan algorithms required multiple observations (at different times) of water surface height, width and slope (average over 1–10 km river reaches) and require substantial variability in water elevation and discharge across the observations. Bathymetry and friction affect river flows at different spatial scales. It worth noting that MetroMan and GM2015 retrieve these river parameters at the kilometer river reach scale and might therefore be slightly different from the ones estimated at the local scale.

Results from these investigations are encouraging and demonstrate the feasibility of retrieving river discharge from SWOT observations alone. Although these four algorithms were developed by different teams, their development was not independent as all author groups are members of the SWOT Science Definition Team (SDT) Discharge Algorithms Working Group. Intercomparison studies are currently being performed over different types of rivers, and the relative strengths and weaknesses of each algorithm are being evaluated. Pending the results of these ongoing comparisons, the potential for implementation and performance of the algorithms at global scales is still an open question. Furthermore, at this point they have only been tested over non-braided rivers, whereas many large rivers (e.g., the Amazon, Ganges/Brahmaputra and Ob') and many smaller

rivers are at least partially braided. The precise river reaches to which the algorithms can be applied globally remain undefined but most likely will have lengths ranging from a few kilometers to a few tens of kilometers. For those algorithms that require ancillary information and/or a first guess (see "first guess/ancillary data" column in Table 3), this information will be defined and provided globally before launch. Finally, testing of algorithms with real SWOT data and realistic errors will be crucial for fully assessing the suitability of these algorithms.

### 2.3 Data Assimilation and Optimal Interpolation

An alternate strategy for estimation of discharge and other water surface variables is the use of indirect and/or statistical methods. Work in this area falls into two categories: optimal interpolation (OI) to improve spatial/temporal coverage of SWOT water elevation and discharge estimates (Yoon et al. 2013; Paiva et al. 2015) and data assimilation (DA), which uses SWOT data to correct hydraulic/hydrologic model parameters or state vectors (Andreadis et al. 2007; Durand et al. 2008; Biancamaria et al. 2011; Yoon et al. 2012; Andreadis and Schumann 2014; Pedinotti et al. 2014; Munier et al. 2015). Table 4 summarizes all these studies. All of the nine studies summarized were designed in the context of observing system simulation experiments (OSSE), a methodology designed to assess the potential of a new type of measurements before it is built or deployed. Figure 5 shows the conceptual framework of an OSSE in the context of SWOT studies using optimal interpolation (a) and data assimilation (b). Among these nine studies, the OSSE consisted of first computing time series of realistic states (water elevations and discharges) over a specified study domain with a hydraulic or hydrologic model. This simulation is considered to be the "truth" in the context of the OSSE (Fig. 5). Then, a SWOT simulator is run to provide what the algorithm treats as SWOT measurements. These so-called virtual or synthetic SWOT observations are then used with OI or DA methods to improve the SWOT estimate of river discharge and/or related variables. Comparison of these derived values to the "truth" allows quantification of the benefits of SWOT data coupled with the dynamic model. In all studies included here, synthetic SWOT data have been simulated with simple methods: SWOT spatiotemporal sampling is computed using SWOT orbit and swath extents to sample "true" water elevations (or discharge for Paiva et al. 2015), to which white noise (corresponding to instrument noise only) has been added. As the SWOT mission has evolved through different design stages between 2007 and 2015, different orbits and swath extents (e.g., no nadir gap) have been considered (see Table 4). Only Munier et al.'s (2015) study is recent enough to consider the final SWOT nominal orbit presented in Sect. 1.4. Furthermore, all of the studies have been performed as twin experiments in which the same model has been used for computing the "true" states and the "corrupted" ones (Fig. 5).

Among the OI studies, Yoon et al. (2013) used local space–time ordinary kriging to estimate water height between SWOT observation times over the Tennessee River. Their method used hydrodynamic model outputs to compute the true heights. They obtained mean spatial and temporal RMSE of 11 and 12 cm, respectively. However, when they used in situ gage time series as the truth, the temporal RMSE increased to 32 cm. This difference is apparently due in part to effects of water management, which are not taken into account in the hydrodynamic model. Paiva et al. (2015) also used spatiotemporal OI but applied it to estimate discharge rather than water height. They developed an innovative method termed River Kriging (RK), which analytically derives space–time discharge covariance using the diffusive wave approximation to the Saint-Venant equations. They

**Table 4** Published SWOT-related studies using data assimilation (DA) or optimal interpolation (OI) to correct/optimize different variables (*d* means water depth, *H* water elevation, *w* width, *S* water surface slope, *Q* discharge, $A_i$ inundation area, *Z* bathymetric elevation, $S_z$ bathymetric slope, *n* Manning coefficient)

| References | DA/OI schemes | Model(s) + error | SWOT observations used + error | Corrected/optimized variable(s)/parameter(s) | Study domain |
|---|---|---|---|---|---|
| Andreadis et al. (2007) | EnKF | Hydrodynamic model + inflows errors | *d* (140 km swath, 8-day/16-day/32-day orbit) + white noise | *d* | Ohio River (50 km reach) |
| Durand et al. (2008) | EnKF | Hydrodynamic model + $S_z$ and *n* errors | *H* (140-km swath, 16-day orbit) + white noise | $\underline{Z}$, $\underline{S_z}$ | Amazon River (240 km reach) |
| Biancamaria et al. (2011) | LEnKF + LEnKS | Hydrodynamic model + precip. errors | *d* (140-km swath, 22-day orbit) + white noise | *d* | Ob River (1120 km) |
| Yoon et al. (2012) | EnKF + LEnKS | Hydrodynamic model + precip. errors/*z* errors/*z* spatial autocorrelation | *H*, *S*, *w* (140-km swath, 22-day orbit) + white noise | *Z*, *d* | Ohio basin river system |
| Yoon et al. (2013) | LSTOK | – | *d* (140-km swath, 22-day orbit) + white noise | *d* at times with no SWOT obs. | Tennessee River (1050 km) |
| Andreadis and Schumann (2014) | LEnTKF | Hydrodynamic model + sampling historical simulation | *H*, *w*, $A_i$ (multi-sat missions) + white noise | Initial condition to forecast model | Ohio River (500 km reach) |
| Pedinotti et al. (2014) | EKF | Hydrologic model (0.5° × 0.5° pixels) + *n* errors | *d* (140 km swath, 22-day orbit) + white noise | *n* | Whole Niger basin |
| Paiva et al. (2015) | RK | Space–time *Q* covariance from diffusive wave approx. Saint-Venant equation | *d*, *S*, *w*, *Q* (140-km swath, 22-day orbit) + white noise | *Q* at times with no SWOT obs. | Ganges–Brahmaputra–Meghna river system in Bangladesh |
| Munier et al. (2015) | LEnKS + MPC | Hydrodynamic model and reservoir model + precip. errors | *d* (120-km swath, 21-day orbit) + white noise | *d* + optimized reservoir release | Upper Niger basin and Selingue reservoir |

*(L)EnKF/S* (local) ensemble Kalman filter/smoother, *LSTOK* local space–time ordinary kriging, *LEnTKF* local ensemble transform Kalman filter, *EKF* extended Kalman filter, *RK* river kriging, *MPC* model predictive control

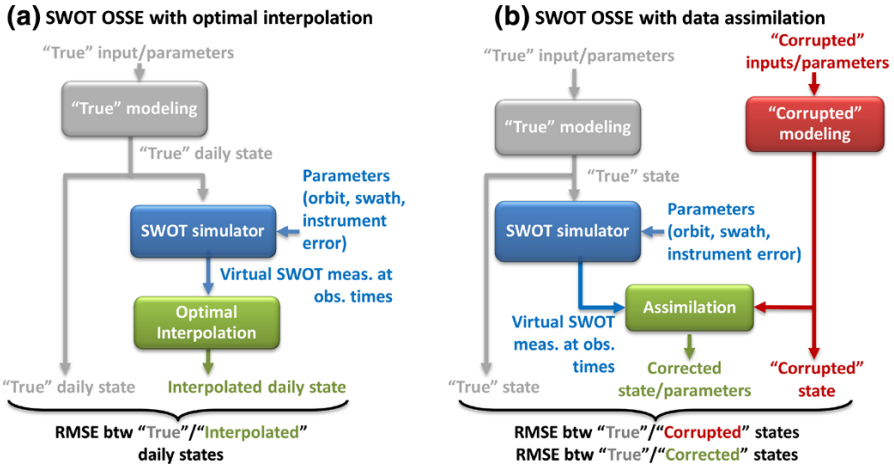


**Fig. 5** Conceptual sketches of SWOT observing system simulation experiments (OSSE) using optimal interpolation (**a**) or data assimilation (**b**)

showed, using the Ganges–Brahmaputra–Meghna rivers system in Bangladesh, that the RK method out-performed linear interpolation, simple kriging and ordinary kriging. Furthermore, RK-interpolated daily discharge had accuracy similar to that of the initial SWOT discharge time series. However, the method did not perform well when tidal forcing dominated the discharge signal. Taken together, the Yoon et al. (2013) and Paiva et al. (2015) studies show the potential to interpolate SWOT observations at daily timescales. However, they have been applied to a very limited set of rivers to date.

DA techniques are increasingly being used in the framework of real-time operations to forecast water levels in the context of flooding (Bates et al. 2014), for real-time reservoir operations (Munier et al. 2015), for model calibration and parameter estimation (Bates et al. 2014) or for the purpose of reconstructing the history of some components of the continental water cycle (Reichle et al. 2014). All of these themes have been addressed by one or more of the SWOT DA studies referenced in Table 4. Andreadis et al. (2007) and Biancamaria et al. (2011) used virtual SWOT water depth measurements to correct water depth from river hydrodynamics models applied to the Ohio and Ob' Rivers, respectively. Assumptions included well-known bathymetry and no bias in water elevation measurements. They showed that in these two applications, model errors dominated and therefore assimilating SWOT (synthetic) data helped to decrease water depth error and consequently discharge estimates. These studies demonstrated the potential of SWOT data to improve forecasting of streamflow. Keeping in mind that the SWOT mission will probably not produce near-real-time products, these approaches nonetheless can be applied to producing discharge and water level products retrospectively once the SWOT data become available, especially with the use of a DA smoother (Biancamaria et al. 2011) that tends to smooth discontinuities before and after the assimilation time of an observation with a DA filter.

Flood forecasting is an area of hydrology particularly suited to the use of DA techniques. In these applications, model initial conditions are critical to producing accurate forecasts. This was the motivation for the work of Andreadis and Schumann (2014) who developed methods of using satellite water elevation and water area (from nadir altimetry, LiDAR, SAR imagery and SWOT) to correct initial conditions in an application of a

hydrodynamic model to the Ohio River. They showed that using satellite observations improved water elevation and flood extent forecasts with lead times up to ten days. For some flood events, however, model errors exceeded errors due to initial conditions after a few days, and the benefits of the assimilation dissipated. Additionally, it has recently been shown that assimilating flood water level derived from SAR images combined with floodplain topography into a hydrodynamic modeling helps to improve flood forecasts (García-Pintado et al. 2013, 2015).

Other studies have demonstrated the capability of using SWOT data to correct hydraulic model parameters (especially bathymetry, elevation and slope; see Durand et al. 2008 and Yoon et al. 2012) or hydrologic model parameters (friction coefficients; see Pedinotti et al. 2014). Errors in the corrected parameters have decreased in some cases by more than 50 % via DA. Of course, these results have to be interpreted carefully, as they are dependent on the model/observation errors used and the fact that they have been done in the context of model twin experiments, which often result in a benefit to DA-based methods in comparison with "real" applications. Nonetheless, these studies are promising and clearly show the potential benefits of SWOT data in conjunction with river hydrodynamic modeling even if the SWOT data are not delivered in near real time.

Finally, Munier et al. (2015), using DA in conjunction with an automatic control algorithm, showed the potential of SWOT to improve management of the Selingue Reservoir in the upper Niger River basin by optimizing reservoir releases to meet a minimum low flow requirement upstream of the Niger Inner Delta. Their algorithm made use of SWOT data both for estimation of reservoir storage and for discharge computation using a simplified river hydrodynamics model applied to the reach downstream of the reservoir.

It should be highlighted that all the teams involved in the studies reported here are collaborating at different levels. Members of the author groups that produced the papers reviewed in this section met during the "Hydrologic Data Assimilation for the SWOT Mission" meeting, held on November 12–13, 2013 (Biancamaria et al. 2014), and further DA work in the next few years leading up to launch of the SWOT mission is promising.

The studies reviewed in Sects. 2.1–2.3 show the benefits that can be expected from SWOT measurements for better understanding river flow dynamics, from the river reach scale to the river basin scale. New and innovative techniques have already been developed that can exploit SWOT data, and these methods will be available from the beginning of the mission to ensure quick use and science return of SWOT data. However, more work is still needed, especially to explore the implications of SWOT errors, which have been represented to date using highly simplifying assumptions. SWOT errors will be much more complex than white noise. In particular, the impacts of layover, water classification errors, wet troposphere effects and correlated instrument error along the swath are topics of immediate relevance that currently are being investigated.

## 3 Lake/Reservoir Studies and Other Land Hydrology Applications

Section 2 summarized SWOT river-related studies with a focus on river discharge estimation (both directly and through data assimilation). Lakes and reservoirs have been somewhat less studied as shown in Table 5, which summarizes SWOT-related lake and reservoir studies. Compared with the five SWOT discharge algorithms papers and nine DA/OI papers, there are only three papers that consider lakes and/or reservoirs in the

**Table 5** Published SWOT-related studies on lakes and reservoirs

| Reference | Method | SWOT observations | Study domain |
|---|---|---|---|
| Biancamaria et al. (2010) | Parametrization of global annual storage variation | Lakes area >(250 m)$^2$ and height variations >SWOT height accuracy | Extrapolation of global lakes distribution |
| Lee et al. (2010) | Lake storage change from optical image, satellite altimetry, in situ gage and parametrization | $\delta H$ with white noise function of lake area (140-km swath, 3-day and 22-day orbit) | Multiple Arctic lakes |
| Munier et al. (2015) | Hydrologic model, hydrodynamic model + DA of SWOT observations, reservoir model + release optimization | $d$ (120-km swath, 21-day orbit) + white noise | Upper Niger basin and Selingue reservoir |

context of SWOT. This is in part due to the fact that the main SWOT lake/reservoir product, storage change estimation of all observed lakes and reservoirs, is more easily derived from SWOT direct measurements (maps of water elevations and water surface extent), than is river discharge. Nonetheless, SWOT has important implications for understanding the dynamics of individual lakes and reservoirs and their part in the land surface water budget. The mission is expected to lead to a major leap in our understanding of these water bodies. For instance, storage variations in reservoirs globally, which have been estimated to have produced a "drag" on sea-level rise of about 0.5 mm/yr or around 1/6 of observed sea-level rise, are so poorly estimated that the sign of this term is no longer known due to slowing of global reservoir construction and filling of existing reservoirs with sediment (Lettenmaier and Milly 2009).

Furthermore, SWOT will not only observe rivers and lakes/reservoirs, but also all other water bodies on the continents and at their interfaces with the oceans: wetlands, stream–aquifer interfaces, estuaries and ice sheets. In particular, it will be a tremendous source of information for transboundary river basins, which are a challenge for water managing between upstream and downstream countries. More generally, SWOT will observe the direct human impact on the continental water cycle and therefore will have not only scientific but also societal and political implications.

### 3.1 Lakes and Reservoirs

There is currently large uncertainty concerning the global distribution of lakes (Downing et al. 2006; Verpoorter et al. 2014) and the variations of water stored in them. The locations of largest lakes are, of course, well known and monitored. It is also well known that the majority of lakes are located at high latitudes (above 50°N; Lehner and Döll 2004). However, there is still considerable uncertainty concerning the number of medium and small lakes, even aside from their spatial and temporal dynamics. For example, according to Downing et al. (2006), based on multiple databases and extrapolation for smaller lakes, there are slightly more than 300 million lakes globally with a surface area exceeding 0.001 km$^2$, most of which (99.87 % in number and 43 % in area) have surface areas less than 1 km$^2$. However, the numbers of small lakes in Downing et al. (2006) are inferred from the distribution of larger lakes rather than being directly observed, so this estimate is

highly uncertain. In contrast, Verpoorter et al. (2014) report, using Landsat imagery, about 117 million lakes with surface areas that exceed 0.002 $km^2$, a predominance of which have areas between 0.1 and 1 $km^2$. However, the use of Landsat imagery (which has a pixel size of 30 m) tends to underestimate small water bodies, especially those that cover less than about 10 Landsat pixels, or about 0.01 $km^2$. Furthermore, it is difficult to classify water surfaces at the global scale automatically because of clouds, cloud shadow, the use of images acquired at different dates, differences in lake turbidity and other factors, all of which add uncertainty to current estimates of the global distribution of lakes by area. In addition, it is very difficult to automatically differentiate the smallest lakes observable in Landsat imagery from segments of partially detected rivers. Finally, all of the current global lakes databases (e.g., Lehner and Döll 2004; Verpoorter et al. 2014) are static and do not provide any information about spatiotemporal dynamics, notwithstanding well-known studies of long-term variations in the surface areas of both large (e.g., Gao et al. 2012) and small (e.g., Smith et al. 2005) lakes. SWOT will provide revolutionary information concerning lake extent and water storage, which will be beneficial not just for a better understanding of the continental hydrologic cycle but also for the carbon (Cole et al. 1994) and methane (Walter et al. 2007) cycles at continental and global scales.

If the global distribution of lakes is subject to large uncertainties, their water elevation changes are even less well known. Therefore, estimating total water storage change in all lakes remains a challenge. Biancamaria et al. (2010) have provided early estimates. Using annual water level amplitudes from 224 lakes worldwide, they found no clear correlation between annual water level variations and lake area or lake drainage area. Rather, it seemed that inter-annual water surface amplitudes followed a log-normal distribution, which they used to estimate water level variations for all lakes globally. They used a power law relationship between the number of lakes and lake area derived by Downing et al. (2006) to compute the number of all lakes and their size. By performing a very rough approximation of cylindrical lake bathymetry, using the previously mentioned lake log-normal water level distribution, the Downing et al. (2006) lake numbers versus lake areas relationship, they were able to compute cumulative lake storage change as a function of lake area and, ultimately, the total annual lake storage change (about 9000 $km^3$). Their computation was based on just one realization of the log-normal water level distribution for each lake area bin and did not consider uncertainty due to the random distribution. In order to take this uncertainty into account, 100 realizations of the log-normal water level distribution have been generated for each lake area bin. For each realization, the same methodology of Biancamaria et al. (2010), previously described, has been applied. Figure 6 shows the updated results with the ensemble of 100 realizations (gray curves). The mean of this ensemble, which is likely a better approximation of the cumulative annual lake storage change than a single realization of the log-normal distribution, is represented by the green curve on Fig. 6. The ensemble mean is close to the cumulative storage change published by Biancamaria et al. (2010), while the ensemble spread clearly shows the uncertainty associated with the log-normal water level distribution approximation. Of course, there are also errors from the number of lakes versus lake area power law and the cylindrical bathymetry approximation, which add (unrepresented) errors to the annual storage change estimates at global scale. It should be noted that these errors are extremely difficult to estimate and have yet to be modeled.

Currently, storage change can be computed for the small number of lakes for which in situ data are freely available. The alternative is to use satellite data to derive water elevation (from nadir altimeters or Lidar) and surface extent (from optical or SAR sensors) (Gao et al. 2012; Zhang et al. 2014; Arsen et al. 2014; Baup et al. 2014; Crétaux et al.

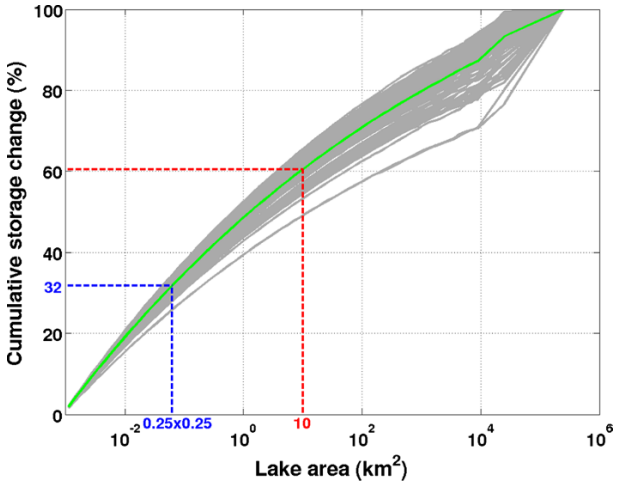


**Fig. 6** Cumulative lake storage change (in % of the total lake storage change in the ensemble mean) versus lake area for 100 realizations of the log-normal random distribution of the annual water level variation estimated by Biancamaria et al. (2010). The ensemble mean corresponds to the *green curve*

2015). However, these approaches require data from at least two different satellites, nearly always at different observation times, with different space–time resolutions. As such, they require significant manual editing of the time series (especially for water elevation) and are challenging to apply automatically at large scales. The resolution of current nadir altimeters also limits the application of these methods. Satellite capability to monitor specific lakes depends on not just the radar footprint on the ground but also the lake shape. Current results (e.g., from the Hydroweb database, http://www.legos.obs-mip.fr/en/soa/hydrologie/hydroweb/) show that 10 $km^2$ lake area (dashed red line on Fig. 6) is, on average, a good guess for the minimum lake extent that nadir altimeters can observe, though some results can be obtained for smaller lakes (Baup et al. 2014). Considering the constellation of satellites that are the most likely to operate in the near future (AltiKa, Jason-3, Sentinel-3A and Sentinel-3B), based on the distribution shown in Fig. 6 (green curve) and assuming that these satellites will sample all lakes above 10 $km^2$ area that are intersected by their nadir ground tracks (which is a very optimistic hypothesis), then only 36 % of the total annual storage change can be measured (as not all lakes above 10 $km^2$ will be observed).

By way of contrast, SWOT should be able to monitor about 65 % of total annual storage change (Biancamaria et al. 2010). In Fig. 6, all lakes above 250 m × 250 m or about 0.06 $km^2$ (blue dashed line) account for 68 % of the total annual storage change, but SWOT will miss a small fraction of these lakes. This is due to measurement errors that could be higher than the annual water level amplitude for some lakes in between 0.06 and 1 $km^2$. However, SWOT should overcome most of the uncertainty in the lake spatial distribution (gray curves in Fig. 6), at least for lakes with an area above 0.06 $km^2$. To assess the accuracy that could be expected from SWOT-derived lake storage changes, Lee et al. (2010) performed an OSSE for Arctic lakes, using a methodology similar to the one presented in Sect. 2.3 for optimal interpolation and shown in Fig. 5a. Based on daily interpolated lake level variations from altimetry, satellite optical images and parameterizations, daily water level variations for several thousands of lakes in the Peace-Athabasca Delta (Canada), Northern Alaska (US) and West Siberia (Russia) were derived and used as

the "truth." With this dataset, they estimated that, at high latitudes, SWOT lake storage change measurements will probably have errors lower than 5 % for lakes larger than 1 $km^2$, whereas errors for lakes with areas of 0.01 $km^2$ should be around 20 %, confirming the relatively high accuracy that is expected from SWOT data. However, this study did not consider measurements errors due to layover, water classification, wet troposphere, etc. (see Sect. 1.3). Work on a more limited number of lakes in the Peace–Athabasca Delta suggests that errors in water surface elevation will dominate the calculation of storage change measurements in comparatively large lakes, while errors in inundated area will play a more important role for storage change calculations in small lakes (Smith and Pavelsky 2009).

Reservoirs also play an important role in the continental water cycle. Zhou et al. (2015) showed, using a large-scale water management model, that 166 of the world's largest reservoirs, which have a total storage capacity of 3900 $km^3$ ($\sim$60 % of all reservoirs storage), could have almost 700 $km^3$ seasonal storage variation ($\sim$10 % of the total reservoirs storage). Despite this significant variability, there is only the study of Munier et al. (2015) that has investigated the potential of SWOT for reservoirs monitoring (see Sect. 2.3). This study showed the potential use of SWOT reservoir measurements to optimize reservoir operations. Gao et al. (2012) and Crétaux et al. (2015) have shown the feasibility of computing storage change for large reservoirs using nadir altimetry, which is very promising for SWOT. The lack of knowledge of the distribution of small lakes is also true for reservoirs. Even with global datasets for reservoirs, like the one compiled by the International Commission on Large Dams (ICOLD) or the Global Reservoir and Dam (GRanD) database (Lehner et al. 2011), there is little information for intermediate and small reservoirs. Given gaps in current understanding of the number and area distribution of lakes and reservoirs, SWOT will provide a major improvement in the ability to observe the dynamics of these water bodies directly. In particular, it will help to better characterize the role of small lakes and reservoirs at global scales, which are mostly ignored in current estimates of the dynamics of land water storage (Zhou et al. 2015).

### 3.2 Other Land Hydrology Applications and Synergistic Land Sciences

To date, published studies concerning SWOT have been mostly focused on understanding and assessing benefits of the new type of measurements that will be produced for river and lakes dynamics. This focus was essential as the mission was in an early stage of definition. Nonetheless, a number of other applications of SWOT data are expected in the land hydrology arena (Durand et al. 2010; Fu et al. 2012; Rodríguez 2015). One of these is the management of water in transboundary river basins. These basins cross one or more international boundaries and imply sharing of water, which in many cases can lead to tensions between upstream and downstream countries. Transboundary river basins are important globally, as they cover around 45 % of the global land area and involve 145 countries and 40 % of the total human population (Wolf et al. 1999). Clark et al. (2015, accepted) have reviewed studies using nadir altimetry for three transboundary basins (the Brahmaputra–Ganges–Meghna, the Indus and the Niger basins) and highlighted the importance of upcoming SWOT data for providing freely available observations of storage change, water level and discharge over the entire basin areas (not including the minor observations gaps discussed in Sect. 1.4) repetitively and independently from national networks.

Another field that will greatly benefit from SWOT data will be the study of the direct impact of human activities (like water management infrastructures and water withdrawals)

on the land hydrologic cycle. For example, reservoirs (Shiklomanov and Lammers 2009) and soil changes and erosion (Descroix et al. 2012) can have important impacts on downstream river discharge, and these impacts will be observed and may be quantifiable by SWOT. SWOT will also provide valuable information to model development and validation, especially for land surface models used in numerical weather prediction and climate models. Most such models at present only represent natural rivers. SWOT observations may also have application to studies of stream–aquifer exchanges at basin and continental scales, filling a current observation gap (Flipo et al. 2014).

SWOT will also provide useful data in wetland environments, although the range of observable wetlands remains uncertain. In wetlands with sparse vegetation and large extents of open water, it is likely that SWOT will provide useful measures of water surface elevation and inundation extent. Where vegetation is denser, it remains unclear to what extent SWOT will be affected by scattering and layover caused by the vegetation. However, given difficulties in measuring the hydrology of large wetlands in situ and their importance in the global carbon and methane cycles, SWOT measurements may provide substantial benefits even if sampling under dense vegetation proves limited. Experiments to better define the opportunities and constraints of SWOT wetland measurements are, as of this writing, in the final planning stages. They will use measurements from AirSWOT (Rodríguez et al. 2010), to better understand SWOT returns from inundated vegetation.

Complementary to land hydrology, some additional science objectives for SWOT, referred to as synergistic sciences (Fu et al. 2012; Rodríguez 2015), have been identified, including:

- Freshwater/marine interfaces, especially in estuaries. This issue bridges ocean and continental hydrology and, while it is a key component of the hydrologic cycle, it is just beginning to be addressed in the context of SWOT.
- Antarctic and Greenland ice sheet topographic variability. As shown in Fig. 3, most of Greenland (which extends up to 82°N) and a substantial portion of Antarctica (and all its coastal regions) will be sampled and at the highest time sampling frequency. However, it should be noted that SWOT performance over ice and snow is not yet well characterized (Fjørtoft et al. 2014). In addition, it is likely that SWOT data for many portions of these ice sheets will be available only at the lower resolution used for SWOT ocean products.
- Helping to characterize snow cover variability and, perhaps, helping to characterize land cover variability.
- Estimation of vertical deflection due to gravity changes over large lakes.

These are just some of the anticipated SWOT scientific applications that have yet to be investigated in any substantial detail. Because most of these applications are synergistic to SWOT's principal scientific goals and because SWOT observing technology is not optimized for them, more investigations are needed to determine how useful SWOT data will be. For example, better characterization of Ka-band backscatter over snow and ice is needed (this also has implications for observations of high-latitude rivers during ice breakup). In addition, for most new satellite technologies like SWOT, applications not yet anticipated will emerge once the data become available.

## 4 Conclusions and Perspectives

We have described the characteristics of the upcoming wide swath altimetry satellite mission, SWOT, and have reviewed recent published papers that have evaluated key scientific hydrology uses of SWOT data. We argue that SWOT will be transformational for land hydrology in providing fundamental information about rivers, lakes and wetlands that has never before been available directly from observations. The SWOT mission will provide, for instance, maps of surface water elevation and their temporal evolution, therefore providing for the first time estimates of surface water storage and fluxes at global scale for rivers wider than 50–100 m.

It will also characterize spatiotemporal variability of lakes and reservoirs with areas larger than $\sim 0.06$ km$^2$, implying direct estimates of about two-thirds of global lake and reservoir storage variations (current nadir altimeters provide estimates in both cases that represent less than 20 percent of the total). Some of the types of studies for which SWOT data will be especially well suited are:

- global water balance studies,
- flood dynamics for medium to large rivers, especially those that persist for multiple SWOT revisits,
- studies of surface water in the global carbon and methane cycles,
- documentation and quantification, of direct human impacts on the hydrologic cycle.

With respect to Earth system modeling, it will provide constraints and diagnostics that will allow better representation of processes such as flood dynamics and human influence on the water cycle, which at present are poorly quantified in global coupled land–atmosphere–ocean models. For example, most such models do not represent the storage of water in man-made reservoirs, or its effect on river discharge (Wood et al. 2011). SWOT will also have important societal impacts on understanding of transboundary river basins; in many such cases, data about river discharge and reservoir storage are not shared among upstream and downstream countries, and in this respect, the SWOT data, which will be freely available, will be transformational.

However, there is still much to be learned before the planned launch of the mission some 5 years from the time of this writing. One priority must be to strengthen the results of studies performed to date, especially by taking into account more realistic quantifications of the magnitudes and types of SWOT measurement errors (e.g., spatially correlated instrumental noise, error due to the roll of the satellite, wet troposphere errors, water classification errors, topography and vegetation errors). These errors will be chiefly explored using two complementary tools: an increasingly sophisticated high-resolution SWOT simulator and AirSWOT airborne campaigns, which will provide SWOT-like measurements that can be compared to simultaneous ground validation data. To compute river discharge, four algorithms have been proposed, and they need to be investigated on diverse real cases, especially braided rivers. They also require a priori information such as river bathymetry and friction coefficients. The sensitivity of discharge estimates to the accuracy of these a priori parameters should be estimated, and they should be computed at a global scale prior to launch.

Furthermore, synergies with other satellite missions observing different component of the water cycle that are likely to collect data simultaneously with SWOT should be investigated, to improve understanding of the water cycle as a whole. Results from discussion of the SWOT Science Definition Team to date suggest that data assimilation

approaches are not yet mature enough for global application. For this reason, studies like those reviewed in Sect. 2.2 are based on the need for simple algorithms, which can be applied more or less directly to SWOT observations of river water levels, slopes and widths to estimate discharge. However, some recent studies (Yamazaki et al. 2011; Neal et al. 2012; Schumann et al. 2013; Bates et al. 2014) suggest that application of river hydrodynamics models has advanced to the point that applications of these models (which would be the physics core for data assimilation algorithms) may now be feasible at continental and global scales (Wood et al. 2011; Schumann et al. 2014; Bierkens et al. 2015). Thus, the role of data assimilation in SWOT river discharge and related variables may need to be revisited.

Finally, some thinking about the successor of SWOT is now appropriate. If SWOT is successful, it almost certainly will motivate demand for continuing observations, in the same way that the first ocean altimeter, TOPEX/Poseidon, did for ocean sciences. With the launch date of SWOT approaching quickly, it is not too early to think about how a future mission might extend and improve on results from SWOT.

**Acknowledgments** S.B. acknowledges funding from the CNES Terre–Océan–Surfaces Continentales–Atmosphère (TOSCA) committee for the SWOT Science Definition Team. D.L. acknowledges funding from NASA Earth Sciences, Grant No. NNX15AF01G. T.P.'s work on this paper was supported by NASA Terrestrial Hydrology Program Grant No. NNX13AD05G and by funding from the SWOT Project at the NASA/Caltech Jet Propulsion Lab. We thank two anonymous reviewers and Pierre-Andre Garambois for their comments, which we believe have improved the manuscript.This paper originated with presentations at the International Space Science Institute (ISSI) *Workshop on Remote Sensing and Water Resources*, held in Bern (Switzerland), October 6–10, 2014.

## References

Allen GF, Pavelsky TM (2015) Patterns of river width and surface area revealed by satellite-derived North American River Width data set. Geophys Res Lett 42(2):295–402. doi:10.1002/2014GL062764

Alsdorf DE, Lettenmaier DP (2003) Tracking fresh water from space. Science 301:1485–1488

Alsdorf DE, Lettenmaier DP, Vörösmarty C (2003) The need for global, satellite-based observations of terrestrial surface waters. EOS Trans Am Geophys Union 84(29):269–276. doi:10.1029/2003EO290001

Alsdorf DE, Rodríguez E, Lettenmaier DP (2007) Measuring surface water from space. Rev Geophys 45(2):RG2002. doi:10.1029/2006RG000197

Andreadis KM, Schumann GJP (2014) Estimating the impact of satellite observations on the predictability of large-scale hydraulic models. Adv Water Resour 73:44–54. doi:10.1016/j.advwatres.2014.06.006

Andreadis KM, Clark EA, Lettenmaier DP, Alsdorf DE (2007) Prospects for river discharge and depth estimation through assimilation of swath-altimetry into a raster-based hydrodynamics model. Geophys Res Lett 34:L10403

Arsen A, Crétaux JF, Berge-Nguyen M (2014) Remote sensing-derived bathymetry of lake Poopo. Remote Sens 6(1):407–420. doi:10.3390/rs6010407

Bates PD, Neal JC, Alsdorf DE, Schumann GJP (2014) Observing global surface water flood dynamics. Surv Geophys 35(3):839–852. doi:10.1007/s10712-013-9269-4

Baup F, Frappart F, Maubant J (2014) Combining high-resolution satellite images and altimetry to estimate the volume of small lakes. Hydrol Earth Syst Sci 18:2007–2020. doi:10.5194/hess-18-2007-2014

Beven K (2006) A manifesto for the equifinality thesis. J Hydrol 320(1–2):18–36. doi:10.1016/j.jhydrol.2005.07.007

Biancamaria S, Andreadis KM, Durand MT, Clark EA, Rodriguez E, Mognard NM, Alsdorf DE, Lettenmaier DP, Oudin Y (2010) Preliminary characterization of SWOT hydrology error budget and global capabilities. IEEE J Sel Top Appl Earth Obs Remote Sens 3(1):6–19. doi:10.1109/JSTARS.2009.2034614

Biancamaria S, Durand MT, Andreadis K, Bates PD, Boone A, Mognard NM, Rodriguez E, Alsdorf DE, Lettenmaier DP, Clark EA (2011) Assimilation of virtual wide swath altimetry to improve Arctic river modelling. Remote Sens Environ 115(2):373–381. doi:10.1016/j.rse.2010.09.008

Biancamaria S, Andreadis K, Ricci S (2014) Using images of continental water surface elevations from upcoming satellite mission. EOS Trans Am Geophys Union 95(12):105. doi:10.1002/2014EO120004

Bierkens MFP, Bell VA, Burek P, Chaney N, Condon LE, David CH, de Roo A, Döll P, Drost N, Famiglietti JS, Flörke M, Gochis DJ, Houser P, Hut R, Keune J, Kollet S, Maxwell RM, Reager JT, Samaniego L, Sudicky E, Sutanudjaja EH, van de Giesen N, Winsemius H, Wood EF (2015) Hyper-resolution global hydrological modelling: what is next? Everywhere and locally relevant. Hydrol Process 29(2):310–320. doi:10.1002/hyp.10391

Bjerklie DM (2007) Estimating the bankfull velocity and discharge for rivers using remotely sensed river morphology information. J Hydrol 341(3–4):144–155. doi:10.1016/j.jhydrol.2007.04.011

Bjerklie DM, Dingman SL, Vörosmarty CJ, Bolster CH, Congalton R (2003) Evaluating the potential for measuring river discharge from space. J Hydrol 278(1):17–38. doi:10.1016/S0022-1694(03)00129-X

Bjerklie DM, Moller D, Smith LC, Dingman SL (2005) Estimating discharge in rivers using remotely sensed hydraulic information. J Hydrol 309(1–4):191–209. doi:10.1016/j.jhydrol.2004.11.022

Blöschl G, Sivapalan M (1995) Scale issues in hydrological modelling: a review. Hydrol Process 9(3–4):251–290. doi:10.1002/hyp.3360090305

Clark EA, Biancamaria S, Hossain F, Crétaux JF, Lettenmaier DP (2015) Current and future application for altimetry in trans-boundary river management. In: Benveniste J, Vignudelli S, Kostianov AG (eds) Inland water altimetry. Springer, Berlin. ISBN 978-3-642-22678-6 (should be published in 2015, accepted)

Cole JJ, Caraco NF, Kling GW, Kratz TK (1994) Carbon-dioxide supersaturation in the surface waters of lakes. Science 265(5178):1568–1570. doi:10.1126/science.265.5178.1568

Crétaux JF, Jelinski W, Calmant S, Kouraev A, Vuglinski V, Berge-Nguyen M, Gennero M-C, Abarca Del Rio R, Cazenave A, Maisongrande P (2011) SOLS: a lake database to monitor in the Near Real Time water level and storage variations from remote sensing data. Adv Space Res 47(9):1497–1507. doi:10.1016/j.asr.2011.01.004

Crétaux JF, Biancamaria S, Arsen A, Bergé-Nguyen M, Becker M (2015) Global surveys of reservoirs and lakes from satellites and regional application to the Syrdarya river basin. Environ Res Lett 10(1):015002. doi:10.1088/1748-9326/10/1/015002

Descroix L, Genthon P, Amogu O, Rajot JL, Sighomnou D, Vauclin M (2012) Change in Sahelian Rivers hydrograph: the case of the recent red floods of the Niger River in the Niamey region. Glob Planet Change 98–99:18–30. doi:10.1016/j.gloplacha.2012.07.009

Desjonquères JD, Carayon G, Steunou N, Lambin J (2010) Poseidon-3 radar altimeter: new modes and in-flight performances. Mar Geod 33(S1):53–79. doi:10.1080/01490419.2010.488970

Downing JA, Prairie YT, Cole JJ, Duarte CM, Tranvik LJ, Striegl RG, McDowell WH, Kortelainen P, Caraco NF, Melack JM, Middelburg JJ (2006) The global abundance and size distribution of lakes, ponds, and impoundments. Limnol Oceanogr 51(5):2388–2397. doi:10.4319/lo.2006.51.5.2388

Durand MT, Andreadis KM, Alsdorf DE, Lettenmaier DP, Moller D, Wilson M (2008) Estimation of bathymetric depth and slope from data assimilation of swath altimetry into a hydrodynamic model. Geophys Res Lett 35:L20401. doi:10.1029/2008GL034150

Durand MT, Fu LL, Lettenmaier DP, Alsdorf DE, Rodríguez E, Esteban-Fernandez D (2010) The Surface Water and Ocean Topography mission: observing terrestrial surface water and oceanic submesoscale eddies. Proc IEEE 98(5):766–779. doi:10.1109/JPROC.2010.2043031

Durand MT, Neal J, Rodríguez E, Andreadis K, Smith L, Yoon Y (2014) Estimating reach-averaged discharge for the River Severn from measurements of river water surface elevation and slope. J Hydrol 511:92–104. doi:10.1016/j.jhydrol.2013.12.050

Enjolras VM, Rodríguez E (2009) An assessment of a Ka-band radar interferometer mission accuracy over Eurasian Rivers. IEEE Trans Geosci Remote Sens 47(6):1752–1765. doi:10.1109/TGRS.2008.2006370

Farr TG, Rosen PA, Caro E, Crippen R, Duren R, Hensley S, Kobrick M, Paller M, Rodríguez E, Roth L, Seal D, Shaffer S, Shimada J, Umland J, Werner M, Oskin M, Burbank D, Alsdorf D (2007) The shuttle radar topography mission. Rev Geophys 45(2):R2004. doi:10.1029/2005RG000183

Fjørtoft R, Gaudin JM, Pourthié N, Lalaurie JC, Mallet A, Nouvel JF, Martinot-Lagarde J, Oriot H, Borderies P, Ruiz C, Daniel S (2014) KaRIn on SWOT: characteristics of near-nadir Ka-band interferometric SAR imagery. IEEE Trans Geosci Remote Sens 52(4):2172–2185. doi:10.1109/TGRS.2013.2258402

Flipo N, Mouhri A, Labarthe B, Biancamaria S, Rivière A, Weill P (2014) Continental hydrosystem modelling: the concept of nested stream–aquifer interfaces. Hydrol Earth Syst Sci 18(8):3121–3149. doi:10.5194/hess18-3121-2014

Fu LL, Rodríguez E (2004) High-resolution measurement of ocean surface topography by radar interferometry for oceanographic and geophysical applications. In: Sparks RSJ, Hawkesworth CJ (eds) The state of the planet: frontiers and challenges in geophysics. Geophysical Monograph 150, AGU, Washington, pp 209–224

Fu LL, Alsdorf DE, Morrow R, Rodríguez E, Mognard NM (2012) SWOT: the Surface Water and Ocean Topography mission. JPL Publication 12-05. http://swot.jpl.nasa.gov/files/swot/SWOT_MSD_1202012.pdf. Accessed 20 Feb 2015

Gao H, Birkett C, Lettenmaier DP (2012) Global monitoring of large reservoir storage from satellite remote sensing. Water Resour Res 48(9):W09504. doi:10.1029/2012WR012063

Garambois PA, Monnier J (2015) Inference of effective river properties from remotely sensed observations of water surface. Adv Water Resour 79:103–120. doi:10.1016/j.advwatres.2015.02.007

García-Pintado J, Neal JC, Mason DC, Dance S, Bates PD (2013) Scheduling satellite-based SAR acquisition for sequential assimilation of water level observations into flood modelling. J Hydrol 495:252–266. doi:10.1016/j.jhydrol.2013.03.050

García-Pintado J, Mason DC, Dance SL, Cloke HL, Neal JC, Freer J, Bates PD (2015) Satellite-supported flood forecasting in river networks: a real case study. J Hydrol 523:706–724. doi:10.1016/j.jhydrol.2015.01.084

Gleason CJ, Smith LC (2014) Toward global mapping of river discharge using satellite images and at-many-stations hydraulic geometry. PNAS 111(13):4788–4791

Gleason CJ, Smith LC, Lee J (2014) Retrieval of river discharge solely from satellite imagery and at-many-stations hydraulic geometry: sensitivity to river form and optimization parameters. Water Resour Res 50(12):9604–9619. doi:10.1002/2014WR016109

Kouraev AV, Zakharova EA, Samain O, Mognard NM, Cazenave A (2004) Ob' river discharge from TOPEX/Poseidon satellite altimetry (1992–2002). Remote Sens Environ 93(1–2):238–245. doi:10.1016/j.rse.2004.07.007

Lee H, Durand MT, Jung HC, Alsdorf D, Shum CK, Sheng Y (2010) Characterization of surface water storage changes in Arctic lakes using simulated SWOT measurements. Int J Remote Sens 31(14):3931–3953. doi:10.1080/01431161.2010.483494

Lehner B, Döll P (2004) Development and validation of a global database of lakes, reservoirs and wetlands. J Hydrol 296:1–22. doi:10.1016/j.jhydrol.2004.03.028

Lehner B, Verdin K, Jarvis A (2008) New global hydrography derived from spaceborne elevation data. EOS Trans Am Geophys Union 89(10):93–94. doi:10.1029/2008EO100001

Lehner B, Reidy Liermann C, Revenga C, Vörösmarty C, Fekete B, Crouzet P, Döll P, Endejan M, Frenken K, Magome J, Nilsson C, Robertson JC, Rödel R, Sindorf N, Wisser D (2011) High-resolution mapping of the world's reservoirs and dams for sustainable river-flow management. Front Ecol Environ 9(9):494–502. doi:10.1890/100125

Lettenmaier DP, Milly PCD (2009) Land waters and sea level. Nat Geosci 2(7):452–454. doi:10.1038/ngeo567

Moller D, Esteban-Fernandez D (2015) Near-nadir Ka-band field observations of fresh water bodies. In: Lakshmi V, Alsdorf D, Anderson M, Biancamaria S, Cosh M, Entin J, Huffman G, Kustas W, van Oevelen P, Painter T, Parajka J, Rodell M, Rüdiger C (eds) Remote sensing of the water cycle. AGU Geophysical Monograph, 206, Wiley, New York, pp 143–155

Munier S, Polebistki A, Brown C, Belaud G, Lettenmaier DP (2015) SWOT data assimilation for operational reservoir management on the upper Niger River Basin. Water Resour Res. doi:10.1002/2014WR016157

National Research Council (2007) Earth science and applications from space: national imperatives for the next decade and beyond. National Academies Press, Washington

Neal JC, Schumann GJP, Bates PD (2012) A subgrid channel model for simulating river hydraulics and floodplain inundation over large and data sparse areas. Water Resour Res 48:W11506. doi:10.1029/2012WR012514

Paiva RCD, Durand MT, Hossain F (2015) Spatiotemporal interpolation of discharge across a river network by using synthetic SWOT satellite data. Water Resour Res. doi:10.1002/2014WR015618

Papa F, Biancamaria S, Lion C, Rossow WB (2012) Uncertainties in mean river discharge estimates associated with satellite altimeters temporal sampling intervals: a case study for the annual peak flow in the context of the future SWOT hydrology mission. IEEE Geosci Remote Sens Lett 9(4):569–573. doi:10.1109/LGRS.2011.2174958

Pavelsky TM, Durand MT (2012) Developing new algorithms for estimating river discharge from space. EOS Trans Am Geophys Union 93(45):457. doi:10.1029/2012EO450006

Pavelsky TM, Durand MT, Andreadis KM, Beighley RE, Paiva RCD, Allen GH, Miller ZF (2014) Assessing the potential global extent of SWOT river discharge observations. J Hydrol 519:1516–1525. doi:10.1016/j.jhydrol.2014.08.044

Pedinotti V, Boone A, Ricci S, Biancamaria S, Mognard NM (2014) Assimilation of satellite data to optimize large-scale hydrological model parameters: a case study for the SWOT mission. Hydrol Earth Syst Sci 18(11):4485–4507. doi:10.5194/hess-18-4485-2014

Reichle RH, De Lannoy GJM, Forman BA, Drapper CS, Liu Q (2014) Connecting satellite observations with water cycle variables through land data assimilation: examples using the NASA GEOS-5 LDAS. Surv Geophys 35:577–606. doi:10.1007/s10712-013-9220-8

Rodríguez E (2015) Surface Water and Ocean Topography mission (SWOT), Science Requirements Document. JPL document D-61923. https://swot.jpl.nasa.gov/files/swot/SRD_021215.pdf. Accessed 20 Feb 2015

Rodríguez E, Moller D, Smith LC, Pavelsky TM, Alsdorf DE (2010) AirSWOT: an airborne monitoring platform for surface water monitoring. AGU Fall Meeting Abstract #H32D-06

Schumann GJP, Neal JC, Voisin N, Andreadis KM, Pappenberger F, Phanthuwongpakdee N, Hall AC, Bates PD (2013) A first large-scale flood inundation forecasting model. Water Resour Res 49(10):6248–6257. doi:10.1002/wrcr.20521

Schumann GJP, Bates PD, Neal JC, Andreadis KM (2014) Fight floods on a global scale. Nature 507(7491):169

Shiklomanov AI, Lammers RB (2009) Record Russian river discharge in 2007 and the limits of analysis. Environ Res Lett 4(4):045015. doi:10.1088/1748-9326/4/4/045015

Skøien JO, Blöschl G, Western AW (2003) Characteristic space scales and timescales in hydrology. Water Resour Res 39(10):1304. doi:10.1029/2002WR001736

Smith LC (1997) Satellite remote sensing of river inundated area, stage, and discharge: a review. Hydrol Process 11:1427–1439

Smith LC, Pavelsky TM (2008) Estimation of river discharge, propagation speed, and hydraulic geometry from space: Lena River, Siberia. Water Resour Res 44:W03427. doi:10.1029/2008GL033268

Smith LC, Pavelsky TM (2009) Remote sensing of volumetric storage change in lakes. Earth Surf Process Landf 34:1353–1358

Smith LC, Isacks BL, Forster RR, Bloom AL, Preuss I (1995) Estimation of discharge from braided glacial rivers using ERS-1 SAR: first results. Water Resour Res 31(5):1325–1329

Smith LC, Isacks BL, Bloom AL, Murray AB (1996) Estimation of discharge from three braided rivers using synthetic aperture radar (SAR) satellite imagery: potential application to ungaged basins. Water Resour Res 32(7):2021–2034

Smith LC, Sheng Y, MacDonald GM, Hinzman LD (2005) Disappearing Arctic lakes. Science 308(5727):1429. doi:10.1126/science.1108142

Steunou N, Desjonquères JD, Picot N, Sengenes P, Noubel J, Poisson JC (2015) AltiKa altimeter: instrument description and in flight performance. Mar Geod 38(Suppl 1):22–42. doi:10.1080/01490419.2014.988835

Verdin KL, Greenlee SK (1998) HYDRO1k documentation, US Geological Survey. https://lta.cr.usgs.gov/HYDRO1KReadMe. Accessed 24 Feb 2015

Verpoorter C, Kutser T, Seekell DA, Tranvik LJ (2014) A global inventory of lakes based on high resolution satellite imagery. Geophys Res Lett 41(18):6396–6402. doi:10.1002/2014GL060641

Walter KM, Smith LC, Chapin FS (2007) Methane bubbling from northern lakes: present and future contributions to the global methane budget. Philos Trans R Soc A Math Phys Eng Sci 365(1856):1657–1676. doi:10.1098/rsta.2007.2036

Wolf AT, Natharius JA, Danielson JJ, Ward BS, Pender JK (1999) International river basins of the world. Int J Water Resour Dev 15(4):387–427

Wood EF, Roundy JK, Troy TJ, van Beek LPH, Bierkens MFP, Blyth E, de Roo A, Döll P, Ek M, Famiglietti J, Gochis D, van de Giesen N, Houser P, Jaffé PR, Kollet S, Lehner B, Lettenmaier DP, Peters-Lidard C, Sivapalan M, Sheffield J, Wade A, Whitehead P (2011) Hyperresolution global land surface modeling: meeting a grand challenge for monitoring Earth's terrestrial water. Water Resour Res 47(5):W05301. doi:10.1029/2010WR010090

Yamazaki D, Kanae S, Kim H, Oki T (2011) A physically based description of floodplain inundation dynamics in a global river routing model. Water Resour Res 47(4):W04501. doi:10.1029/2010WR009726

Yoon Y, Durand MT, Merry CJ, Clark EA, Andreadis KM, Alsdorf DE (2012) Estimating river bathymetry from data assimilation of synthetic SWOT measurements. J Hydrol 464:363–375. doi:10.1016/j.jhydrol.2012.07.028

Yoon Y, Durand MT, Merry CJ, Rodríguez E (2013) Improving temporal coverage of the SWOT mission using spatiotemporal kriging. IEEE IEEE J Sel Top Appl Earth Obs Remote Sens 6(3):1719–1729. doi:10.1109/JSTARS.2013.2257697

Zhang S, Gao H, Naz BS (2014) Monitoring storage in South Asia from multisatellite remote sensing. Water Resour Res 50(11):8927–8943. doi:10.1002/2014WR015829

Zhou T, Nijssen B, Gao H, Lettenmaier DP (2015) The contribution of reservoirs to global land surface water storage variations. J Hydrometeor. doi:10.1175/JHM-D-15-0002.1

DOI 10.1007/978-3-319-32449-4_7
Reprinted from *Surveys in Geophysics* Journal, DOI 10.1007/s10712-015-9339-x

# Toward a High-Resolution Monitoring of Continental Surface Water Extent and Dynamics, at Global Scale: from GIEMS (Global Inundation Extent from Multi-Satellites) to SWOT (Surface Water Ocean Topography)

**Catherine Prigent[1] · Dennis P. Lettenmaier[2] · Filipe Aires[1,3] · Fabrice Papa[4,5]**

Received: 24 April 2015 / Accepted: 28 August 2015 / Published online: 12 October 2015


**Abstract** Up to now, high-resolution mapping of surface water extent from satellites has only been available for a few regions, over limited time periods. The extension of the temporal and spatial coverage was difficult, due to the limitation of the remote sensing technique [e.g., the interaction of the radiation with vegetation or cloud for visible observations or the temporal sampling with the synthetic aperture radar (SAR)]. The advantages and the limitations of the various satellite techniques are reviewed. The need to have a global and consistent estimate of the water surfaces over long time periods triggered the development of a multi-satellite methodology to obtain consistent surface water all over the globe, regardless of the environments. The Global Inundation Extent from Multi-satellites (GIEMS) combines the complementary strengths of satellite observations from the visible to the microwave, to produce a low-resolution monthly dataset ($0.25^\circ \times 0.25^\circ$) of surface water extent and dynamics. Downscaling algorithms are now developed and applied to GIEMS, using high-spatial-resolution information from visible, near-infrared, and synthetic aperture radar (SAR) satellite images, or from digital elevation models. Preliminary products are available down to 500-m spatial resolution. This work bridges the gaps and prepares for the future NASA/CNES Surface Water Ocean Topography (SWOT) mission to be launched in 2020. SWOT will delineate surface water extent estimates and their water storage with an unprecedented spatial resolution and accuracy, thanks to a SAR

✉ Catherine Prigent
catherine.prigent@obspm.fr

[1] CNRS, Laboratoire d'Etude du Rayonnement et de la Matière en Astrophysique et Atmosphères (LERMA), Observatoire de Paris, 61, avenue de l'Observatoire, 75014 Paris, France

[2] Department of Geography, University of California, 1255 Bunche Hall, Box 951524, Los Angeles, CA 90095, USA

[3] Estellus, 93, Boulevard de Sébastopol, 75002 Paris, France

[4] Laboratoire d'Etude en Géophysique et Océanographie Spatiales, IRD, 18, avenue Edouard Belin, 31401 Toulouse, France

[5] Indo-French Cell for Water Sciences, IRD-IISc Joint International Laboratory, Indian Institute of Science, C V Raman Ave, Bangaluru, Karnataka 560012, India

in an interferometry mode. When available, the SWOT data will be adopted to downscale GIEMS, to produce a long time series of water surfaces at global scale, consistent with the SWOT observations.

**Keywords** Satellite remote sensing · Wetland · Hydrology

## 1 Introduction

Terrestrial surface waters amount to less than 1 % of the total Earth water and cover less than 6 % of the ice-free continents at any time (Shiklomanov 1993). However, they are the source of most ($\sim$2/3) of water consumed by humans (UN-Water 2007) and have a large impact on the biodiversity and on the biogeochemical and hydrological cycles, along with a key role on the climate variability. Continental surface waters encompass a very large variety of environments and circumstances, from exceptionally flooded populated areas and their related human loss, to strategic rice paddies to feed the populations, tropical wetlands very rich in biodiversity, or climate-sensitive boreal peat land with their large methane emission. The definition of wetlands varies according to research foci, and no overall consensus on the subject exists.

Despite their importance, there is a lack of reliable, continuous, and consistent information on the inundation extent and dynamics, at both global and regional scales, to satisfy a large and diverse community of users. Mapping of surface waters involves a wide range of users, practitioners, and stakeholders. These include water and disaster managers, insurance companies, hydrologists, ecologists, weather forecasters, or climate modelers. Some applications require high spatial resolution and temporal sampling with almost real-time observations, and others will favor global low spatial resolution with long-term objectives.

The potential role of satellite Earth observations for the mapping of surface waters has been stressed on many occasions, for different applications (e.g., Committee on Earth Observation Satellites 2013; Global Earth Observations 2013; Convention on Biological Diversity 2014). There are ongoing efforts to promote the satellite Earth observations for surface water mapping in these fields (e.g., the Global Monitoring of Environment and Security project DISASTER or the European Space Agency project GlobWetland I–III), but all user needs are still far from being satisfied.

Current satellite remote sensing techniques can produce seamless global land cover maps and distinguish many terrestrial environments, but still struggle to generate accurate high-spatial-resolution representations of surface water extents. There is some agreement on the surface area of the permanent open water bodies from satellite. With approximately 60 % of the floodplains and wetlands inundated during only some time of the year, the knowledge of the extent and large variability of the land surface waters at regional-to-global scales is still incomplete, even with the satellite observations.

The US–French Surface Water and Ocean Topography (SWOT) mission, to be launched in 2020, will provide the community with high spatial resolution and temporal sampling of the continental surface waters, thanks to a synthetic aperture radar (SAR) in an interferometry mode. However, what can be done meanwhile, with the current satellite observations, to support user needs and prepare for the SWOT mission?

We will first briefly review the satellite observation techniques that are commonly used to estimate the continental surface waters, including the advantages and limitation of each

technique (Sect. 2). Some examples will be given. The need to have a global and consistent estimate of the water surfaces over long time periods triggered the development of a multi-satellite methodology to obtain consistent surface water all over the globe, regardless of the environments. This method, first developed at low spatial resolution ( ~25 km), is now downscaled down to 100 m, for a consistent estimation of the surface water extent across spatial scales. These efforts will be described in Sect. 3. The potential of the SWOT mission to map the surface water will be presented in Sect. 4. We will conclude on the interest in the combination of the multiple sources of surface water estimates (Sect. 5).

## 2 The Potential and Limitation of Satellite Techniques for Surface Water Estimation

The detection and quantification of surface water extent from satellite sensors rely on the differences between the reflection and emission properties of water and land surfaces, due to differences in the refractive index of the medium or/and in its surface state (roughness/flatness). Remote sensing techniques employing visible, infrared, and microwave observations offer varying degrees of success in detecting the wetland extent and in quantifying its dynamics. Some recent examples of visible and near-infrared estimates are presented, as well as passive and active microwave results.

Table 1 summarizes the different satellite techniques to map water surfaces, along with their key characteristics.

### 2.1 Visible (VIS) and Near-Infrared (NIR) Observations

Optical and near-infrared satellite observations provide good spatial resolution but are limited by their inability to penetrate clouds and dense vegetation.

Using the NOAA advanced very-high-resolution radiometer (AVHRR), inundated surfaces in herbaceous environments have been estimated with a ~1 km resolution, such as in the Okavango delta (McCarthy et al. 2005) or in the Brahmaputra region (Jain et al. 2006). Since the advent of the moderate-resolution imaging spectroradiometer (MODIS) observations, it is possible to monitor continental-scale inundated areas with a 250- to 500-m spatial resolution, with freely and globally available data. Bergé-Nguyen and Crétaux (2015) showed the potential of MODIS data to monitor temporal changes in flooding in semiarid regions such as the Inner Niger Delta. Xiao et al. (2005, 2006) analyzed paddy fields in China by identifying the flooded pixels from the difference between the Land Surface Water Index (LSWI) and Vegetation Indexes (NDVI or EVI).

**Table 1** Satellite techniques to map water surfaces and their main characteristics

| Technique | Spatial resolution | Temporal sampling | Contamination | Remarks |
|---|---|---|---|---|
| VIS/NIR | Down to ~30 m | Down to daily if cloud free | Clouds, vegetation | Open water only at global scale |
| Active microwave SAR | Down to ~20 m | Up to 6 days with Sentinel 1 | Vegetation to some extent | Regional applications mostly so far |
| Passive microwave | ~10 km | Daily | Vegetation to some extent | Detection of open water as well as wetlands |

Sakamoto et al. (2007) described the multi-year surface hydrology in the Mekong Delta using the MODIS reflectances. They develop a wavelet-based filter to limit the impact of the cloud cover during the monsoon season.

Nakaegawa (2012) compared water-related cover types in six 1-km global land cover datasets. They include the Global Lakes and Wetlands Database (GLWD) (Lehner and Doll 2004) based essentially on inventories and five estimates from visible imagery such as a MODIS classification and a SPOT-derived estimate. The global total open water areas are similar for all datasets. However, the agreement is mediocre for wetlands, with the visible and near-infrared satellite estimate of the total wetland surface of the order of 10 times lower than the GLWD surface. There is only a 5 % chance that a wetland pixel in GLWD corresponds to one in the other five datasets. This is partly due to the difficulty of detecting water under a vegetation canopy and to the period of reference selected in the different datasets. It is noted that the GLWD can be considered to be the best 1-km global static water-related land cover dataset currently available.

We tested two MODIS-derived wetland detection methods over the Mekong Delta region, based on the work of Sakamoto et al. (2007) and Bergé-Nguyen and Crétaux (2015) (Fig. 1). With the Sakamoto et al. (2007) method, we tested two cloud filters. The water extents at the maximum are comparable, with similar seasonality. However, the estimates show significant differences, especially for the detection of the mixed pixels. The methods are quite sensitive to the different thresholds adopted in the algorithms, and their sensitivity to cloud is critical to the results.

A water detection methodology initially developed for MODIS has recently been applied to the entire Landsat archive over 30 years at 30-m resolution, exploiting the processing power of the Google Earth Engine platform (Pekel et al. 2015). A global validation exercise showed an accuracy of 90 % with respect to local estimates. Changes in lakes, river courses, and dams are documented, as well as coastal modifications. The potential of the methodology for open water detection appears very attractive, but it has not been evaluated yet for wetland characterization.

The method is sensor-neutral and can be applied to other optical instruments. The Sentinel 2 mission is designed to provide a global coverage of the Earth's land surface every 10 days with one satellite and 5 days with two satellites. The first satellite has been launched recently (June 2015). Among many other objectives, Sentinel 2 will contribute to the mapping of water surfaces. It is expected that methods already developed for MODIS and Landsat will be applied to the observations, with possible adaptation to the Sentinel 2 specificities.

### 2.2 Active Microwave Observations

Synthetic aperture radar (SAR) and altimeters are active microwave instruments that measure the backscattering coefficient of observed surfaces. Microwaves have the ability to penetrate clouds and, to a certain extent, vegetation. When observed off-nadir (as with the SAR), open water surfaces are characterized by low backscattering coefficients. The presence of vegetation can scatter the signal and increase the backscattering, making the detection of wetland site specific. The longer the wavelength, the less sensitive it is to the presence of vegetation. The SAR observations can provide very high spatial resolution (below 50 m), but until recently the spatiotemporal coverage was limited, with only a few mosaics available per year in some areas, preventing systematic, long-term assessments of inundation dynamics. The ENVISAT SAR instrument, for instance, operated between 2002 and 2012 and imaged the Earth with a large swath at C band (5.3 GHz). For the

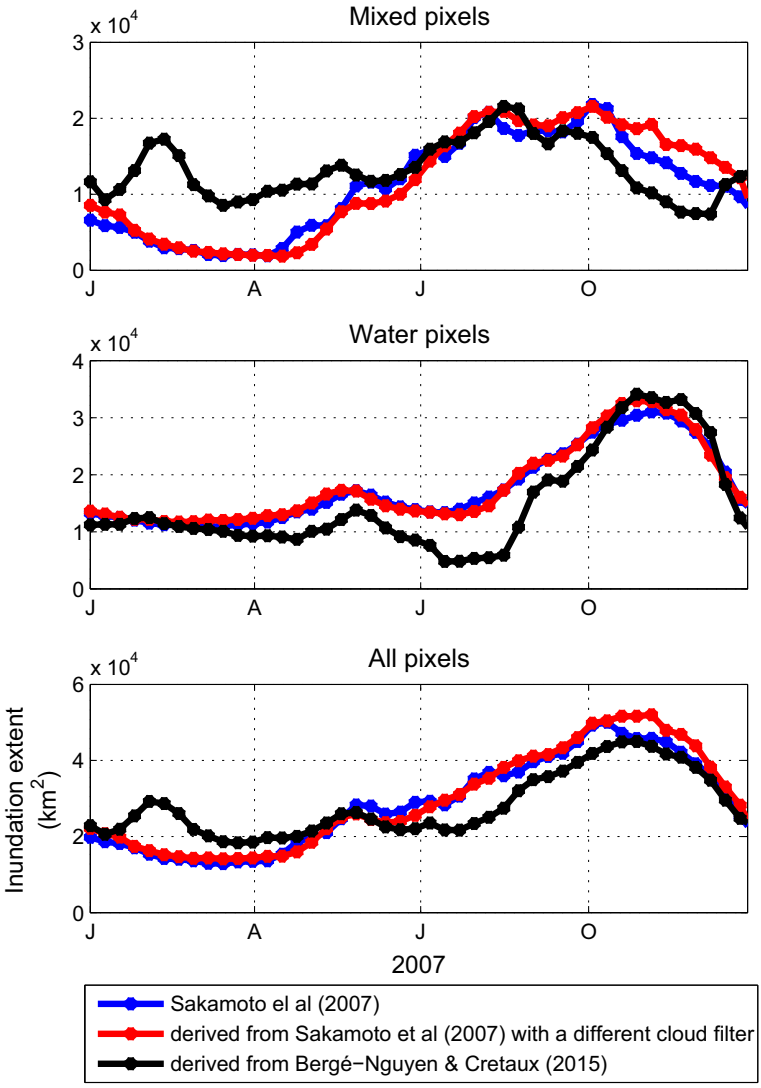


**Fig. 1** Inundation extent over the Mekong Delta, as estimated by different methods, on a monthly mean basis, for 2007

northernmost latitudes, almost daily observations were available, but some other areas were hardly covered such as South America or Australia.

Henderson and Lewis (2008) reviewed the literature on the detection of wetland ecosystems with SAR, including the optimum wavelength and polarization. A large range of observation configurations and analysis methodologies have been tested, with different efficiencies depending on the type of environment. They conclude that it is difficult to select a unique methodology for systematic global application and that a combination with visible / near-infrared observations is always very efficient.

Using long-wavelength SAR observations (L-band, 1.4 GHz), Hess et al. (2003) produced detailed maps of the low and high water stages in the Amazon basin, despite the dense tropical forest. With ENVISAT SAR data, Bartsch et al. (2012) detected the open water dynamics at high latitudes, but showed difficulties in delineating the vegetated wetlands. Kuenzer et al. (2013) derived inundated images of the Mekong basin for 2007–2011 from ENVISAT SAR, with a spatial resolution of $\sim$90 m. The inundation cycle is described, thanks to a reasonable revisit time in the region over several years. A preprocessing step filters the image and reduces the speckle. Then, a series of thresholds is carefully applied on the backscatter to isolate the water surfaces, before applying a morphological image processing. Bouvet and Toan (2011) analyzed the rice paddies in South Asia with success, using ENVISAT SAR observations.

The extensive archive of ENVISAT SAR images has not been analyzed much for large-scale water mapping. Nevertheless, a global map of permanent and open water bodies has been obtained recently by Santoro and Wegmuller (2014), exploiting the temporal variability of the observations. At least 10 images are required for a reliable estimate, which is not always obtained over the ENVISAT SAR life time (Santoro and Wegmuller 2014). There is no evaluation yet of this method for wetland mapping, at global scale.

Similar techniques are currently adjusted to be applied to the recently launched Sentinel 1 SAR (April 2015). Sentinel 1 will provide an improved coverage and temporal sampling, especially over Europe. The mission will image the entire Earth every six days when the two satellites have been launched. With the most promising methods to detect water surface based on the temporal variability of the signal, the high temporal sampling of the Sentinel SAR is expected to revolutionize the mapping of water surfaces with high spatial resolution, high temporal sampling, even under cloudy regions.

Satellite altimeters are also active microwave instruments. They observe at nadir to measure surface topography and were originally designed for ocean surfaces. Techniques have been developed to obtain accurate measurements of water height in rivers, lakes, and wetlands from these satellite-borne instruments (e.g., Birkett 1998; Fu and Cazenave 2001). Altimeters are very sensitive to the presence of water, with a significant increase in the backscattering over water surfaces (Papa et al. 2003). However, current altimeters have very narrow surface tracks and do not provide sufficient spatial coverage to analyze the horizontal structure of water bodies, except over boreal regions where their polar orbits offer better spatial coverage. Papa et al. (2006) quantified the extent and seasonality of boreal inundation using observations from the Topex–Poseïdon dual-frequency satellite altimeter and evidenced the high potential of the altimeters for surface extent estimations.

### 2.3 Passive Microwave Observations

Passive microwave observations have long been used to detect surface water extents (e.g., Giddings and Choudhury 1989). Inundation decreases emissivity in both linear polarizations, especially at lower frequencies, due to differences in dielectric properties of water and soil or vegetation. In addition, inundation can also increase the polarization difference with the roughness change related to the presence of water. However, the spatial resolution of current passive microwave observations is of the order of 10–50 km, limiting their potential use for a large range of applications.

Most passive microwave studies are based solely on simple analyses of the raw passive microwave observations. The study of the Amazon basin by Sippel et al. (1998) or the analysis of the boreal regions by Mialon et al. (2005) is one such example, at regional scale. Schroeder et al. (2010) also rely mainly on the passive microwave observations from

AMSR-E to estimate the North Eurasian inundation dynamics. However, the passive microwave signal is strongly modulated by the surface temperature and, above 10 GHz, it can be contaminated by the atmosphere (water vapor), clouds, and rain. These factors, especially surface temperature, can seriously distort time-series estimates of surface water variations.

## 3 A Multi-satellite Methodology for Global Surface Water Estimation

These considerations lead to the conclusion that there is not today a unique and exclusive technique for detecting surface water, including open water and wetlands. A multi-satellite technique has been derived for the retrieval of surface water extent and dynamics at the global scale. It capitalizes on the complementary strengths of the satellite observations to extract maximum information about inundation characteristics and to minimize problems related to analysis of measurements by one instrument only (Prigent et al. 2001, 2007, 2012; Papa et al. 2010).

### 3.1 The Global Inundation Extent from Multi-satellites (GIEMS)

Satellite data have different sensitivities to surface properties (e.g., vegetation, topography, and soil properties), making it possible to disentangle the contributions of the various factors on the observations. Passive microwave observations are particularly sensitive to the presence of the surface water, even under vegetation canopy, and the inundation detection will primarily rely on the passive microwave signal. Passive microwave observations have limited spatial resolution (of the order of 20 km, depending on the frequency), but can provide frequent global coverage over a long time period (more than 20 consistent years of data available).

The following satellite observations are used: (1) passive microwaves from the special sensor microwave/imager (SSM/I) measurements between 19 and 85 GHz; (2) active microwave backscattering coefficients at 5.25 GHz from scatterometers; and (3) visible and near-infrared reflectances and the derived NDVI. Preprocessing is applied to the passive microwave observations to suppress the modulation by the surface temperature and by the atmospheric effects. In vegetated areas, the vegetation contribution to the passive microwave is estimated with information from the active microwave and NDVI observations. An unsupervised clustering algorithm merges the three sets of satellite observations and identifies the inundated pixels. A mixture model based on the statistical relationship between the passive polarization differences and the active microwave backscatter quantifies the fractional inundation of each pixel identified in the previous step. The technique is globally applicable without tuning for specific environments. The availability and reliability of the active microwaves and the visible/near-infrared observations imposed some fine-tuning of the initial methodology (details are provided in Papa et al. 2010).

Fifteen years of global monthly water surface extents 1993–2007 are available, on an equal-area grid of $0.25^\circ \times 0.25^\circ$ at the equator (each pixel covers 773 $km^2$) (http://lerma.obspm.fr/spip.php?article91&lang=en). Figure 2 shows the averaged yearly maximum inundation from GIEMS, from 1993 to 2007. The water surfaces are realistically detected under all environments. See the boreal floodplains around the Ob or the Yenisei, the Inner Niger Delta in Mali, or the Pantanal and riverine wetlands along the Amazon in South

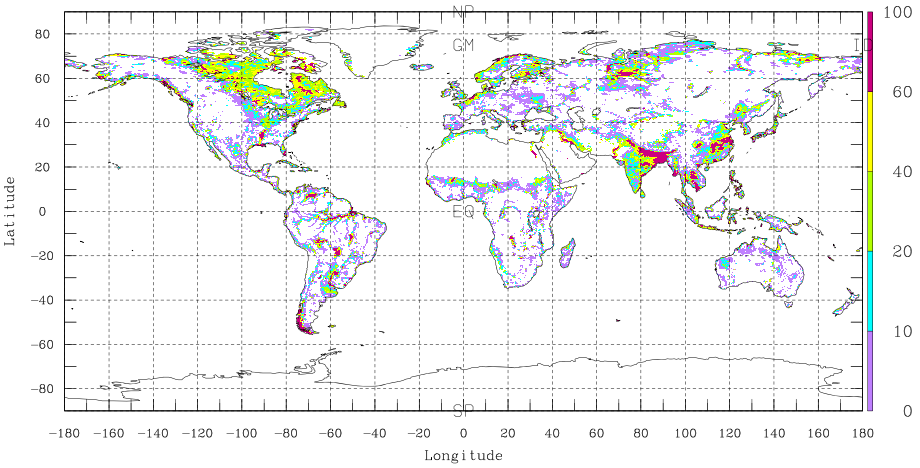


**Fig. 2** The averaged yearly maximum inundation at the global scale from GIEMS, in terms of percentage of inundation for each pixel, from 1993 to 2007. Each pixel is 773 $km^2$

America. Note that the GIEMS estimates include all surface waters such as the Asian rice paddies, as well as river and lakes.

GIEMS, with its long time series, provides key information on the seasonal and inter-annual variability of the inundation, even at regional scale. As an example, a major flood occurred in the American Midwest, along the Mississippi and Missouri rivers and their tributaries, from April to October 1993, causing terrible devastation and flooding up to 80,000 $km^2$. Figure 3 presents the mean surface water extent in August over the Midwest in the USA between 1993 and 2007 (top), as compared to its value in August 1993 (bottom). The maximum inundated surface in the region calculated by GIEMS is very close to the official number, and its spatial pattern follows closely the expected hydrological structures.

Regional assessment of this database using SAR data indicates that the approach realistically captures wetland complexes but can underestimate small wetlands comprising less than 10 % fractional coverage of a grid cell ($<80\,km^2$). The dataset has been extensively evaluated at the global scale (Prigent et al. 2007; Papa et al. 2010) and for a wide range of environments, including boreal (Papa et al. 2007, 2008) and tropical regions (Papa et al. 2006; Frappart et al. 2008).

The availability of this consistent and carefully evaluated dataset at a global scale and over a long period of time makes it possible to perform climatological analysis. We observed a decline of the wetland extent of $\sim$6 % over the globe between 1993 and 2008. The largest declines of open water are found where large increases in population have occurred over the last two decades, suggesting a global scale effect of human activities on continental surface freshwater (Prigent et al. 2012).

GIEMS has also been used for biogeochemical and hydrological analyses, such as the evaluation of methane surface emissions models (Bousquet et al. 2006; Ringeval et al. 2010; Melton et al. 2013; Wania et al. 2013) and the validation of the river flooding schemes coupled with land surface models (Decharme et al. 2008, 2011; Ringeval 2012; Pedinotti et al. 2012).

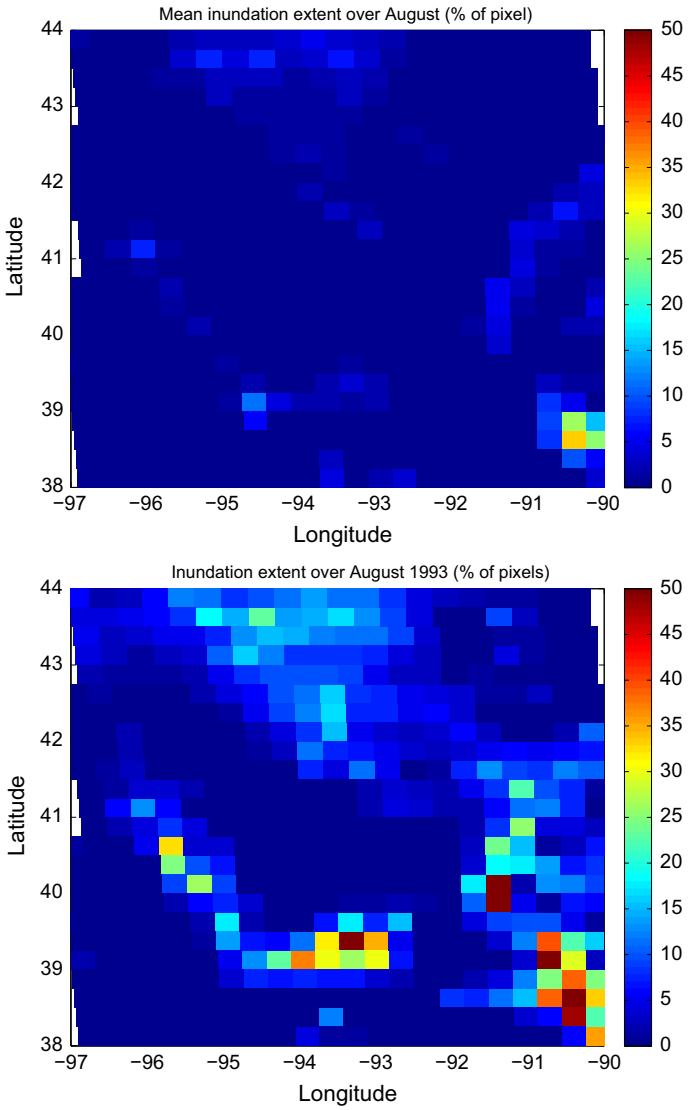


**Fig. 3** Mean surface water extent in August over the Midwest in the USA between 1993 and 2007 (*top*), and its value in August 1993 (*bottom*)

## 3.2 Downscaling of GIEMS

With a $0.25^\circ \times 0.25^\circ$ spatial resolution, the initial GIEMS dataset is clearly not adequate for all applications. Would it be possible to develop downscaling methodologies to derive high-resolution surface water extent from the existing GIEMS low-resolution dataset? Since GIEMS has global coverage, the ideal situation would be to develop a downscaling technique general enough to work in all environments. However, each hydrological basin has its own characteristics such as its topography, vegetation, or space–time variability.

The downscaling algorithm needs to take into account these specificities and the availability of the a priori high-spatial-resolution information for a particular basin. The high-spatial-resolution information can come from satellite observations such as visible /near-infrared images or SAR measurements, or it can be extracted from static topography information. Methodologies have been explored, using these different types of high-spatial-resolution sources. They are described here.

### *3.2.1 Downscaling Based on High-Resolution Satellite Observations*

Two downscaling methodologies based on high-resolution satellite observations have been developed and evaluated, with very encouraging results. These two methods require inundation information at high spatial resolution, at least for some time steps, in coincidence with the coarse spatial resolution dataset.

The first methodology is based on image processing techniques and can be applied with a limited number of high-spatial-resolution information (Aires et al. 2013). It has been applied and evaluated over the Amazon basin, using the SAR-derived observations of Hess et al. (2003) to calibrate the method, at only two time steps, for low and high waters. The probability of a high-spatial-resolution pixel to be inundated depends on the status of its neighboring pixels, and this probability is derived from the SAR images. The inundation then fluctuates between the low and high water stages for each month, based on the GIEMS monthly dynamics, using a dilatation factor driven by the inundation probability. Following this methodology, 15 years of monthly mean inundation extent for the Amazon basin have been produced at 500-m spatial resolution (Aires et al. 2013). Figure 4 shows an example of the downscaling of GIEMS with the SAR observations, over the Amazon

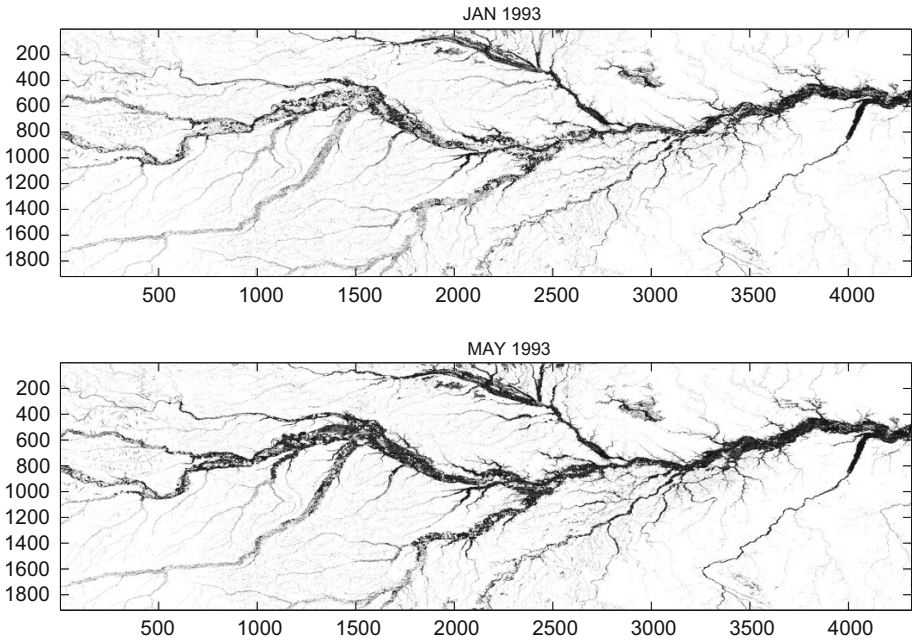


**Fig. 4** Inundation extent from the downscaling of GIEMS, for two contrasted months in 1993, over the Amazon Basin

basin, in 1993, from two contrasted months. The hydrological structures are very realistic: The results benefit from the spatial structure of the SAR data coupled to the temporal dynamics of GIEMS. With the advent of the recently available Sentinel 1 SAR data, it is expected to have soon a global coverage of the inundated surfaces derived from the high-resolution observations, at different periods of the year at global scale. The downscaling method will be trained on this SAR-derived dataset and propagated backward in time, as for the Amazon case.

The second solution requires the availability of more information on the dynamics of the inundation at high resolution. It uses the empirical orthogonal function (EOF) representation of the space–time variability of the high-resolution inundation extent, and to be efficient, a reasonable representation of the inundation dynamics has to be provided over a year. It has been applied to the Inner Niger Delta, using MODIS-derived inundation extent (Bergé-Nguyen and Crétaux 2015), to produce a long time series (1993–2011) of high-resolution inundation extent. This technique makes possible not only the downscaling of low-spatial-resolution information but also the temporal and spatial interpolation of high-resolution dataset (Aires et al. 2014).

### *3.2.2 Downscaling Based on Topography Information*

Topography information at high spatial resolution can also provide the basic information to derive an inundation probability to determine from GIEMS where inundation is spatially more likely at high resolution. Digital elevation models (DEM) can describe the topography with the necessary accuracy at a global scale, making this methodology globally applicable.

Fluet-Chouinard et al. (2015) adopt the Shuttle radar topography mission (SRTM)-derived HydroSHED topographic information trained on a global land cover map (GLC2000 Bartholomé and Belward 2005) to produce an inundation probability map based only on topography information. The downscaled inundation map is then generated from the inundation probability map by distributing the inundated area of the coarse pixels among the fine-resolution pixels having the highest probabilities of inundation. The technique is applied to GIEMS to produce a 15 arc-s ($\sim$500 m) map of the mean annual minimum, mean annual maximum, and long-term maximum (GIEMS-D15). Comparison with independent regional maps shows reasonable agreement, with some variation depending on the environments. This database is available under request at http://www.estellus.fr/index.php?static13/giems-d15. Work is underway to produce a monthly mean dynamic dataset at 90-m resolution from GIEMS.

## 4 The Future with SWOT

As noted above, the altimeter observations are very sensitive to the presence of water, but their current ability to see freshwater bodies is severely limited by the fact that all present and past altimeters are nadir pointing, that is, they produce information only for the water surfaces that their thin track crosses. This has the effect that water bodies with surface areas less than about 10 $km^2$ generally are not resolvable by nadir altimeters (Biancamaria et al. 2015). Furthermore, it is difficult to obtain estimates of the temporal variations of water bodies much smaller than this threshold.

The joint US–French Surface Water and Ocean Topography (SWOT) mission is intended to provide a major improvement in the availability of surface extent and storage

change for surface bodies such as lakes, reservoirs, wetlands, and rivers. The revolutionary aspect of SWOT compared to former altimeters is that it will provide swath, rather than track, data; hence, the size of water bodies for which surface and storage change estimates can be retrieved is dictated by factors other than the distance between altimeter satellite tracks. SWOT's primary instrument will be a Ka-band radar interferometer (KaRIn), which is a SAR interferometer in the Ka-band (37 GHz), with near nadir incidence angles (between 0.6° and 3.9°, Fjrtoft et al. 2014). SWOT will provide images of water surface and elevation in swaths on both sides of the satellite track, each of which will be 50 km wide. Because interferometry effectively involves a triangulation, each point in the swath will be observed from two different (antenna) positions, which will allow precise estimation of the location of each point. More details of SAR interferometry and the KaRIn measurements are provided by Biancamaria et al. (2015) and references therein. KaRIn will provide images of water surface elevations for pixels with sizes $\sim$6 m in the direction of the satellite orbit and from 10 to 60 m in the direction perpendicular to the satellite orbit (the smallest dimension is for pixels far off-nadir in the swath; the largest dimension is for those closest to nadir). The instrument concept is presented in Fig. 5.

SWOT will extract a dynamic water surface mask (i.e., that identifies open water as contrasted with other land cover) for each satellite overpass. The SWOT Science Requirements Document (Rodríguez 2015) indicates that the SWOT requirement is to estimate surface water areas for water bodies larger than 250 $m^2$ to an accuracy (one standard deviation) of better than 15 %, and the goal is for one standard deviation error for smaller water bodies (between 100 and 250 $m^2$) of no more than 25 %. The SWOT pixel size is expected to be from 50 to 300 $m^2$. The requirement and goal are based on discretization errors presuming adequate radiometric contrast between land and water pixels. Fjrtoft et al. (2014) show that the contrast at the SWOT KaRIn instrument frequency can

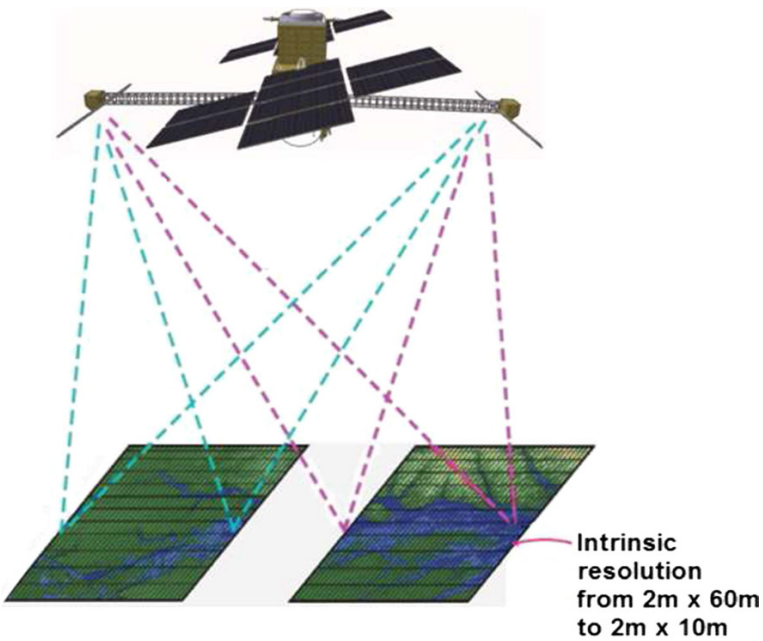


**Fig. 5** SWOT instrument concept. Courtesy of Lee et al. (2010)

be as high as 20 dB. However, they also point out that the ability to discriminate between land and water pixels is complicated for the KaRIn instrument by the fact that its incidence angle (0.6°–3.9°) is small relative to most existing SARs and Ka-band has backscatter characteristics at small incidence angles that are not well documented. They further note that the layover effect at these small incidence angles (which occurs when the slope of surrounding topography exceeds the incidence angle) are prevalent at much smaller surface slopes than for larger incidence angles. However, layover is mitigated by the backscatter contrast between water and surrounding topography, and this in turn is affected by surface roughness and other factors. The combined effect of these various factors is not well understood at this point; however, ongoing testing with an aircraft version of the KaRIn instrument is expected to much better define these interactions.

The water surface elevation estimates for these pixels are approximately statistically independent with error standard deviations of around 1 m; hence, errors are reduced (by averaging) by approximately 1/sqrt(n), where n is the number of pixels. Accordingly, by averaging the number of pixels in a water body of area 1 $km^2$, the vertical error estimates become less than 10 cm (see Fu et al. 2012 for details). The actual error budget of course is much more complicated (due to other sources of errors, like the effects of surrounding topography and wet tropospheric delay), but the goal of SWOT is to obtain vertical errors less than 10 cm for water bodies with areas greater than 1 $km^2$ (Rodríguez 2015).

Lee et al. (2010) in a study of Arctic lakes estimated that SWOT surface extent errors should be less than about 5 % for lakes with surface areas greater than 1 $km^2$ and less than about 20 % for lakes with surface areas of 1 ha. Downing et al. (2006) estimated that there are about 300 million lakes globally with surface area exceeding 0.001 $km^2$, of which 99.87 % in number and 43 % in area have surface areas less than 1 $km^2$. Verpoorter et al. (2014) estimated about 117 million lakes with surface areas that exceed 0.002 $km^2$, most of which have areas between 0.1 and 1 $km^2$. Both studies have important caveats, and there remains considerable uncertainty as to the distribution of lakes at the global scale. Based on Downing et al. (2006) and other estimates, Biancamaria et al. (2015) concluded that SWOT should be able to see the dynamics of surface area and height for a total of about 65 % of global lake storage globally. The approximately 1/3 that will not be seen will mostly be in small lakes and ponds with surface areas less than about 6 ha. One should keep in mind that there are certain caveats, not all of which are considered in any but the most recent studies. For instance, the ability to recover storage change in some lakes will be compromised by layover effects, which essentially result from confounding of the surface elevation retrieval with surrounding topography. This is mostly a potential problem in topographically complex regions (e.g., mountains), and there are in fact some opportunities for mitigating this issue, at least for larger lakes. Furthermore, there are other aspects of the SWOT error budget that continue to be studied and will likely affect the above estimates.

The current generation of nadir altimeters, along with visible band instruments such as MODIS with overpass intervals short enough to produce time series of surface extent, only sees about 15 % of total lake surface and storage. Increasing this number to around 65 % represents a huge improvement.

## 5 Conclusions and Perspective

Up to now, high-resolution mapping of surface water extent from satellites has only been available for a few regions, over limited time periods. The extension of the temporal and spatial coverage of these maps was not possible, due to the lack of necessary satellite observations (e.g., poor time sampling for the SAR), or to physical limitation of the remote sensing technique (e.g., the interaction of the radiation with vegetation or cloud for visible observations).

Satellite-derived maps of open water bodies at high spatial resolution are now emerging, over long time series, with the systematic processing of a large volume of satellite data [e.g., Pekel et al. (2015) with Landsat or Santoro and Wegmuller (2014) with the ENVISAT SAR]. However, these estimates only cover open water bodies and exclude the wetlands, despite their interest for a large range of environmental applications.

GIEMS provides the only global monthly surface water extent database, thoroughly evaluated and available over a long period of time (15 years). Its extension in time up to the present is underway. GIEMS comprises all surface waters, including open water, wetlands, or rice paddies. Its original spatial resolution is $\sim$25 km, but downscaling methodologies have been developed to provide the user community with down to 100-m resolution estimates. Some methods involve the use of high-spatial-resolution satellite data from visible/infrared observations or from SAR measurements, to train the downscaling algorithms. Other methods require topography information from digital elevation models. A first version of GIEMS at 500-m spatial resolution is available, based on this methodology (GIEMS-D15). Work is underway to produce a 90-m spatial resolution data base, with a monthly mean temporal resolution.

The downscaling of GIEMS provides a global consistent reference dataset on water surfaces, at high spatial resolution. It can complement the local independent current estimates, with a reference that is suitable at large scale, for applications such as risk management or pricing of insurance policies.

The advent of the SWOT mission will be transformational for the hydrology field, with its capacity to delineate surface water extent (lakes, rivers, wetlands during seasons of inundation, and reservoirs) and to estimate their water storage with an unprecedented spatial resolution and accuracy.

To provide the scientific community with a very long time record of surface water extent with a high spatial resolution and accuracy, the SWOT data, when available, can be adopted to downscale GIEMS over a common period of observations. The downscaling methodology trained on the SWOT dataset can then be applied back in time to produce a long time series of water surfaces at global scale, with a high spatial resolution, and consistent with the SWOT database. This will provide the hydrology and climate communities with an exceptional database that will be continuously extended in time during the SWOT lifetime.

**Acknowledgments** We are grateful to Bill Rossow and Elaine Matthews for their involvement at the origin of the work on GIEMS. We like to thank Etienne Fluet-Chouinard and Bernhard Lehner for their contribution to the GIEMS downscaling. We are also grateful to Sylvain Biancamaria for providing details for the SWOT description and to Pham Duc Binh for the comparisons of the surface water extents over the Mekong Delta. The downscaling of GIEMS has been partly financed by CNES, in the framework of the SWOT mission preparation, with the support of Selma Cherchali and Jean-Francois Crétaux.

## References

Aires F, Papa F, Prigent C (2013) A long-term, high-resolution wetland dataset over the Amazon basin, downscaled from a multi-wavelength retrieval using SAR. J Hydrometeorol 14:594–6007

Aires F, Papa F, Prigent C, Crétaux JF, Bergé-Nguyen M (2014) Characterization and downscaling of the inundation extent over the Inner Niger delta using a multi-wavelength retrievals and Modis data. J Hydrometeorol 27:1958–1979. doi:10.1175/JCLI-D-13-00161.1

Bartsch A, Trofaier A, Hayman G, Sabel D, Schlaffer S, Clark D, Blyth E (2012) Detection of open water dynamics with ENVISAT ASAR in support of land surface modelling at high latitudes. Biogeosciences 9:703–714. doi:10.5194/bg-9-703-2012

Bartholomé E, Belward AS (2005) GLC2000: a new approach to global land cover mapping from earth observation data. Int J Remote Sens 26:1959–1977

Bergé-Nguyen M, Crétaux J-F (2015) Inundations in the inner Niger delta: monitoring and analysis using MODIS and global precipitation datasets. Remote Sens. doi:10.3390/rs70x000x

Biancamaria S, Lettenmaier DP, Pavelsky TM (2015) The SWOT mission and capabilities for land hydrology. Surv Geophys (in press)

Birkett CM (1998) Contribution of the TOPEX NASA radar altimeter to the global monitoring of large rivers and wetlands. Water Resour Res 34. doi:10.1029/98WR00124

Bouvet A, Le Toan T (2011) Use of ENVISAT/ASAR wide-swath data for timely rice fields mapping in the Mekong River delta. Remote Sens Environ 115(4):1090–1101. doi:10.1016/j.rse.2010.12.014

Bousquet P et al (2006) Contribution of anthropogenic and natural sources to atmospheric methane variability. Nature 443:439–443. doi:10.1038/nature05132

Committee on Earth Observation Satellites (CEOS) (2013) Ad-hoc Disasters Team, CEOS disaster risk management observation strategy, Issue 2.1

Convention on Biological Diversity (2014) Earth Observation for biodiversity monitoring: a review of current approaches and future opportunities for tracking progress towards the Aichi Biodiversity Targets, CBD Technical Series No. 72. http://www.cbd.int/doc/publications/cbd-ts-72-en

Decharme B, Douville H, Prigent C, Papa F, Aires F (2008) A new river flooding scheme for global climate applications: offline validation over South America. J Geophys Res 113:D11110. doi:10.1029/2007JD009376

Decharme B, Alkama R, Papa F, Faroux S, Douville, Prigent C (2011) Global off−line evaluation of the ISBA−TRIP flood model. Clim Dyn 38:1389–1412. doi:10.1007/s00382-011-1054-9

Downing JA, Prairie YT, Cole JJ, Duarte CM, Tranvik LJ, Striegl RG, McDowell WH, Kortelainen P, Caraco NF, Melack JM, Middelburg JJ (2006) The global abundance and size distribution of lakes, ponds, and impoundments. Limnol Oceanogr 51(5):2388–2397. doi:10.4319/lo.2006.51.5.2388

Fjrtoft R, Gaudin JM, Pourthié N, Lalaurie JC, Mallet A, Nouvel JF, Martinot-Lagarde J, Oriot H, Borderies P, Ruiz C, Daniel D (2014) KaRIn on SWOT: characteristics of near-nadir Ka-band interferometric SAR imagery. IEEE Trans Geosci Remote Sens 52(4):2172–2185. doi:10.1109/TGRS.2013.2258402

Fluet-Chouinard E, Lehner B, Rebelo L-M, Papa F, Hamilton SK (2015) Development of a global inundation map at high spatial resolution from topographic downscaling of coarse-scale remote sensing data. Rem Sens Environ 158:348–361

Frappart F, Papa F, Famiglietti SJ, Prigent C, Rossow WB, Seyler F (2008) Interannual variations of river water storage from a multiple satellite approach: a case study for the Rio Negro River basin. J Geophys Res 113. doi:10.1029/2007JD009438

Fu LL, Cazenave A (2001) Satellite altimetry and earth science. A handbook of techniques and application. Academic Press, London

Fu LL, Alsdorf DE, Morrow R, Rodríguez E, Mognard NM (2012) SWOT: the surface water and ocean topography mission. JPL publication 12-05

Giddings L, Choudhury BJ (1989) Observation of hydrological feature with Nimbus-7 37 GHz data applied to South America. Int J Remote Sens 10:1673–1686

Global Earth Observations (2013) The GEOSS water strategy, from observations to decision, executive summary and full report. ftp://ftp.earthobservations.org/TEMP/Water/

Henderson FM, Lewis AJ (2008) Radar detection of wetland ecosystems: a review. Int J Remote Sens 29(20):5809–5835. doi:10.1080/01431160801958405

Hess LL, Melack JM, Novob EMLM, Barbosac CCF, Gastil M (2003) Dualseason mapping of wetland inundation and vegetation for the central Amazon basin. Remote Sens Environ 87:404–428

Jain SK, Saraf AK, Goswami A, Ahmad T (2006) Flood inundation mapping using NOAA AVHRR data. Water Resour Manag 20(6):949–959

Kuenzer C, Gue H, Huth J, Leinenkugel P, Li X, Cech S (2013) Flood mapping and flood dynamic of the Mekong delta: ENVISAT ASAR- WSM based time series analyses. Remote Sens 5:687–715. doi:10.3390/rs5020687

Lee H, Durand MT, Jung HC, Alsdorf D, Shum CK, Sheng Y (2010) Characterization of surface water storage changes in Arctic lakes using simulated SWOT measurements. Int J Remote Sens 31(14):3931–3953. doi:10.1080/01431161.2010.483494

Lehner B, Doll P (2004) Development and validation of a global database of lakes, reservoirs and wetlands. J Hydrol 296:1–22

Melton JR et al (2013) Present state of global wetland extent and wetland methane modelling: conclusions from a model inter- comparison project (WETCHIMP). Biogeosciences 10:753–788. doi:10.5194/bg-10-753-2013

Mialon A, Royer A, Fily M (2005) Wetland seasonal dynamics and interannual variability over northern high latitudes derived from microwave satellite data. J Geophys Res 110. doi:10.1029/2004JD005697

McCarthy J, Gumbricht T, McCarthy TS (2005) Ecoregion classification in the Okavango Delta, Botswana from multitemporal remote sensing. Int J Remote Sens 26:43394357

Nakaegawa T (2012) Comparison of water-related land cover types in six 1-km global land cover dataset. J Hydro Meteorol. doi:10.1175/JHM-D-10-05036.1

Papa F, Legresy B, Remy F (2003) Use of the Topex-Poseidon dual-frequency radar altimeter over land surfaces. Remote Sens Environ 87:136–147. doi:10.1016/S0034-4257(03)00136-6

Papa F, Prigent C, Rossow WB, Legresy B, Remy F (2006a) Inundated wetland dynamics over boreal regions from remote sensing: the use of TopexPoseidon dualfrequency radar altimeter observations. Int J Remote Sens 27:4847–4866. doi:10.1080/01431160600675887

Papa F, Prigent C, Durand F, Rossow WB (2006b) Wetland dynamics using a suite of satellite observations: a case study of application and evaluation for the Indian Subcontinent. Geophys Res Lett 33:L08401. doi:10.1029/2006GL025767

Papa F, Prigent C, Rossow WB (2007) Ob River flood inundations from satellite observations: a relationship with winter snow parameters and river runoff. J Geophys Res 112. doi:10.1029/2007JD008451

Papa F, Prigent C, Rossow WB (2008) Monitoring flood and discharge variations in the large Siberian Rivers from a multi-satellite technique. Surv Geophys. doi:10.1007/s10712-008-9036-0

Papa F, Prigent C, Jimenez C, Aires T, Rossow WB (2010) Interannual variability of surface water extent at global scale, 1993–2004. J Geophys Res 115. doi:10.1029/2009JD012674

Pekel JF, Cottam A, Gorelick N, Belward A (2015) 30 Years global scale mappingof surface water dynamics at 30 m resolution. Mapping water bodies from space conference Frascati Italy. http://www.conftool.pro/mwbs2015/sessions.php

Pedinotti V, Boone A, Decharme B, Cretaux JF, Mognard N, Panthou G, Papa F, Tanimoun BA (2012) Evaluation of the ISBA-TRIP continental hydrologic system over the Niger basin using in situ and satellite derived datasets. Hydrol Earth Syst Sci 16:1745–1773. doi:10.5194/hess-16-1745-2012

Prigent C, Matthews E, Aires F, Rossow WB (2001) Remote sensing of global wetland dynamics with multiple satellite data sets. Geophys Res Lett 28:4631–4634

Prigent C, Papa F, Aires F, Rossow WB, Matthews E (2007) Global inundation dynamics inferred from multiple satellite observations. J Geophys Res 1993–2000:112. doi:10.1029/2006JD00784

Prigent C, Papa F, Aires F, Jimenez C, Rossow WB, Matthews E (2012) Changes in land surface water dynamics since the 1990s and relation to population pressure. Geophys Res Lett 39:5. doi:10.1029/2012GL051276

Ringeval B, de NobletDucoudré N, Ciais P, Bousquet P, Prigent P, Papa F, Rossow WB (2010) An attempt to quantify the impact of changes in wetland extent on methane emissions on the seasonal and interannual time scales. Global Biogeochem Cycles 24:GB2003. doi:10.1029/2008GB003354

Ringeval B et al (2012) Modelling subgrid wetland in the ORCHIDEE global land surface model: evaluation against rive discharges and remotely sensed data. Geosci Model Dev Discuss 5:683–735

Rodríguez E (2015) Surface water and ocean topography mission (SWOT), science requirements document. JPL document D-61923. JPL D-61923, Feb. 12, 2015, retrieved from https://swot.jpl.nasa.gov/files/swot/SRD021215 Aug 24, (2015)

Sakamoto T, Nguyen NV, Kotera A, Ohno H, Ishitsuka N, Yokozawa M (2007) Detecting temporal changes in the extent of annual flooding within the Cambodia and the Vietnamese Mekong delta from MoDIS time-series imagery. Remote Sens Environ 109:295–313

Santoro M, Wegmuller U (2014) Multi-temporal synthetic aperture radar metrics applied to map open water bodies. IEEE J Sel Top Appl Earth Obs Remote Sens 7:3225–3238. doi:10.1109/JSTARS.2013.2289301

Sippel SJ, Hamilton SK, Melack JM, Novo EMM (1998) Passive microwave observations of inundation area and the area/stage relation in the Amazon river floodplain. Int J Remote Sens 19:3055–3074

Schroeder R, Rawlins MA, McDonald KC, Podest E, Zimmermann R, Kueppers M (2010) Satellite microwave remote sensing of North Eurasian inundation dynamics: development of coarse-resolution products and comparison with high-resolution synthetic aperture radar data. Environ Res Lett 5:015003. doi:10.1088/1748-9326/5/1/015003

Shiklomanov I (1993) World fresh water resources. In: Gleick Peter H (ed) Water in crisis: a guide to the world's fresh water resource. Oxford University Press, New York

United Nations—Water (2007) Coping with water scarcity. Challenge of the twenty-first century (http://www.fao.org/nr/water/docs/escarcity)

Verpoorter C, Kutser T, Seekell DA, Tranvik LJ (2014) A global inventory of lakes based on high-resolution satellite imagery. Geophys Res Lett 41:6396–6402. doi:10.1002/2014GL060641

Wania R et al (2013) Present state of global wetland extent and wetland methane modelling: methodology of a model intercomparison project (WETCHIMP). Geosci Model Dev 6:617–641. doi:10.5194/gmd66172013

Xiao X et al (2005) Mapping paddy rice agriculture in South and Southeast Asia using multi-temporal MODIS images. Remote Sens Environ 100:95–113

Xiao X et al (2006) Mapping paddy rice agriculture in southern China using multi-temporal MODIS images. Remote Sens Environ 95:480–492

DOI 10.1007/978-3-319-32449-4_8
Reprinted from *Surveys in Geophysics* Journal, DOI 10.1007/s10712-016-9367-1

# Assessing Global Water Storage Variability from GRACE: Trends, Seasonal Cycle, Subseasonal Anomalies and Extremes

**Vincent Humphrey**[1] · **Lukas Gudmundsson**[1] · **Sonia I. Seneviratne**[1]

Received: 11 August 2015 / Accepted: 29 January 2016 / Published online: 26 February 2016


**Abstract** Throughout the past decade, the Gravity Recovery and Climate Experiment (GRACE) has given an unprecedented view on global variations in terrestrial water storage. While an increasing number of case studies have provided a rich overview on regional analyses, a global assessment on the dominant features of GRACE variability is still lacking. To address this, we survey key features of temporal variability in the GRACE record by decomposing gridded time series of monthly equivalent water height into linear trends, inter-annual, seasonal, and subseasonal (intra-annual) components. We provide an overview of the relative importance and spatial distribution of these components globally. A correlation analysis with precipitation and temperature reveals that both the inter-annual and subseasonal anomalies are tightly related to fluctuations in the atmospheric forcing. As a novelty, we show that for large regions of the world high-frequency anomalies in the monthly GRACE signal, which have been partly interpreted as noise, can be statistically reconstructed from daily precipitation once an adequate averaging filter is applied. This filter integrates the temporally decaying contribution of precipitation to the storage changes in any given month, including earlier precipitation. Finally, we also survey extreme dry anomalies in the GRACE record and relate them to documented drought events. This global assessment sets regional studies in a broader context and reveals phenomena that had not been documented so far.

**Keywords** GRACE · Water storage · Precipitation · Temperature · Drought · Signal decomposition

✉ Vincent Humphrey
vincent.humphrey@env.ethz.ch

[1] Institute for Atmospheric and Climate Science, ETH Zurich, Universitaetstrasse 16, 8092 Zurich, Switzerland

## 1 Introduction

Land water resources are essential for human society and are affected by climate variability and human water use (Jiménez Cisneros et al. 2014). It is thus important to monitor changes in land water storage, as well as the underlying processes leading to their variations in space and time. The Gravity Recovery and Climate Experiment (GRACE), launched in 2002, constitutes an essential tool for such analyses, as was demonstrated in a wealth of studies (Tapley et al. 2004a; Wahr et al. 2004; Rodell et al. 2004; Andersen et al. 2005; Velicogna and Wahr 2006; Güntner et al. 2007a; Ramillien et al. 2008; Zaitchik et al. 2008; Rodell et al. 2009; Chen et al. 2010a; Houborg et al. 2012; Sasgen et al. 2012; Gardner et al. 2013; Wouters et al. 2014; Reager et al. 2014; Famiglietti 2014; Chen et al. 2015; Wahr 2015). After more than a decade of observations, the GRACE mission has resulted in an unprecedented view on global water storage variability, with a great diversity in terms of temporal scales, ranging from long-term trends to short-lived deviations from the seasonal cycle. These different scales of temporal variability often constitute a common denominator between GRACE studies, either implicitly—as when the discussion focuses on specific aspects like the seasonal cycle, trends or extremes—or explicitly—as when water storage time series are decomposed into subseries. Since the earliest GRACE studies, it has been, for instance, very common to refer to the phasing and amplitude of the seasonal cycle when comparing GRACE terrestrial water storage with other datasets such as model simulations (e.g., Tapley et al. 2004b; Wahr et al. 2004). As the temporal coverage of the GRACE record extended, more comprehensive studies also identified secular trends and inter-annual anomalies by separating the GRACE signal into long-term trends, periodical components and residual noise (Ramillien et al. 2005; Schmidt et al. 2008b; Steffen et al. 2009). However, there is still no global overview on the relative magnitude and distribution of these features of temporal variability. In addition, while certain of these features (e.g., seasonal cycles and trends) are relatively well described, others (e.g., high-frequency residuals and extremes) have typically attracted much less attention so far and remain more difficult to interpret.

From a global perspective, terrestrial water storage anomalies derived from GRACE are dominated by a seasonal signal in most parts of the world. Consequently, the earliest studies comparing GRACE with hydrological models have primarily focused on the seasonal component. Most often, the seasonal cycle in GRACE was shown to compare relatively well with model simulations, both with respect to the signal's amplitude and phase (Wahr et al. 2004; Swenson and Milly 2006; Syed et al. 2008; Schmidt et al. 2008b; Döll et al. 2014a). Reviews (Ramillien et al. 2008; Güntner 2008; Schmidt et al. 2008a) showed that seasonal disagreement between GRACE and model data was usually attributed to deficiencies in the modelling of water storage compartments and to errors in the precipitation forcing, but also to signal leakage and inaccuracies of the GRACE data. Multiple studies have shown that long-term variability in the GRACE record over land can be related to long-term trends in groundwater (Rodell et al. 2009; Voss et al. 2013; Döll et al. 2014b; Chen et al. 2015; Richey et al. 2015a, b) and surface water (Swenson and Wahr 2009; Singh et al. 2012), teleconnections (Phillips et al. 2012) and mass variations in the cryosphere (Sasgen et al. 2012; Velicogna and Wahr 2013). The hydrological signal extracted from GRACE can also be contaminated by glacial isostatic adjustment (Wu et al. 2010) and crustal deformations caused by major earthquakes (Han et al. 2006, 2011, 2013). While the seasonal cycle, long-term anomalies and secular trends are arguably well documented, fewer studies have focused on subseasonal variability and extreme events at a

global scale. So far only case studies have shown that major drought and flood events can be observed in the GRACE record (e.g., Andersen et al. 2005; Seitz et al. 2008; Frappart et al. 2012; Long et al. 2013; Abelen et al. 2015). Only recently, the potential of GRACE for monitoring drought conditions (Houborg et al. 2012; Thomas et al. 2014) and predicting flood potential (Reager et al. 2014) was investigated globally. However, large challenges remain since month-to-month variability in GRACE is highly contaminated with outliers, measurement errors and uncertainties arising from data processing (Bonin et al. 2012).

The overarching goal of this study is to provide a global and comprehensive survey of the dominant features of temporal variability in terrestrial water storage observed from GRACE. Our approach is to decompose the total signal at each grid point into (1) *linear trends*, (2) *inter-annual variability*, (3) *seasonal cycle* and (4) *subseasonal variability*. We first assess the contribution of each component to the total signal at the global scale (Sect. 4.1). In Sect. 4.2, the magnitude and significance of the linear trends are discussed in the context of previous regional studies. Subsequently, the decomposed subseries of terrestrial water storage are compared with decomposed precipitation and temperature fields. Starting with the inter-annual anomalies, regions of high correlation between GRACE and these atmospheric drivers are identified (Sect. 4.3). Section 4.4 provides global maps of the maximum and minimum seasonal water storage and identifies phase shifts with respect to the seasonal cycles of both precipitation and temperature (Sect. 4.4). In Sect. 4.5, we focus on the subseasonal residuals and show that a careful averaging of the daily atmospheric data to the monthly resolution reveals excellent correlations with the high-frequency component of the GRACE signal. Finally, we use the decomposition approach to identify and analyse drought events in the GRACE record (Sect. 4.6).

## 2 Data

### 2.1 GRACE Data

Monthly grids of terrestrial water storage anomalies used in this study are based on the spherical harmonic coefficients (Release 05) provided by the Center for Space Research (CSR), the Jet Propulsion Laboratory (JPL) and the GeoForschungsZentrum Potsdam (GFZ) for the period April 2002–August 2015. For more information on the GRACE mission, the gravity recovery process and the derivation of water storage anomalies from the spherical harmonic coefficients, we refer the reader to the reviews from Wouters et al. (2014) or Wahr (2015) and the references therein. The gridded product used in this study is the GRACE Tellus dataset (available at http://grace.jpl.nasa.gov). This dataset provides mass grids in units of equivalent water height for the three different sets of harmonic coefficients mentioned above, at a temporal resolution of approximately 1 month and with a grid resolution of 1°. It is worth noting that although 1° (or even finer) grids are commonly used in global analyses of terrestrial water storage anomalies, this does not reflect the actual spatial resolution of the GRACE measurements. Due to the truncation of spherical harmonics, the effective spatial resolution is by construction limited to a few hundreds of kilometres (Landerer and Swenson 2012). Additionally, postprocessing filters that are used to reduce spatially correlated errors further degrade the spatial resolution of the GRACE signal (Swenson and Wahr 2006; Duan et al. 2009; Longuevergne et al. 2010; Frappart et al. 2011b; Wouters et al. 2014). This causes spatial autocorrelation in the

gridded dataset, as can be seen in Fig. 1, which also provides a general overview of the regions where hydrological variability, as detected by GRACE, has the largest magnitude.

At the time of writing, the GRACE Tellus product is obtained through the following processing: the degree one harmonic coefficients (Earth's geocenter) are estimated from Swenson et al. (2008), the coefficients of degree-order 2–0 (related to Earth oblateness) are replaced with more reliable solutions from Satellite Laser Ranging (Cheng et al. 2011) and correction for glacial isostatic adjustment is applied following Geruo et al. (2013). A known issue is that GRACE maps are heavily contaminated with correlated noise; hence, several spatial filtering techniques have been proposed that aim at restoring the geophysical signal (Kusche 2007; Ramillien et al. 2008; Werth et al. 2009; Frappart and Ramillien 2012). In the Tellus product, the destriping filter of Swenson and Wahr (2006) is applied to correct for North–South oriented stripes in GRACE maps and a 300 km Gaussian filter is additionally applied to the data to reduce residual noise. Finally, it is worth mentioning that GRACE time series are not evenly spaced in time. GRACE "months" most often do not correspond to calendar months due to instrument issues and solutions for several months can be missing, in particular after 2011. Instead, GRACE months represent approximately 1 month long periods with varying numbers of days.

Sources of errors in GRACE include measurement errors, aliasing errors originating from the inaccurate correction of atmospheric and oceanic mass redistribution, and spatial leakage (Seo et al. 2006). Spatial leakage is caused both by the truncation of spherical harmonics and the postprocessing filters applied to the data (Chen et al. 2007a; Landerer and Swenson 2012). Since there are no other large-scale observations of terrestrial water storage that could be used as ground truth, estimating errors and confidence intervals for GRACE data is a major challenge (Güntner 2008). One possibility to reduce uncertainty in the GRACE data is to use the ensemble mean of the solutions obtained by different processing centres (Werth et al. 2009; Sakumura et al. 2014). In this study, we use the mean of the three solutions from CSR, JPL and GFZ provided in the GRACE Tellus dataset.

In order to correct for the amplitude attenuation caused by the postprocessing filters applied to the GRACE data, the Tellus dataset also provides the scaling factors proposed

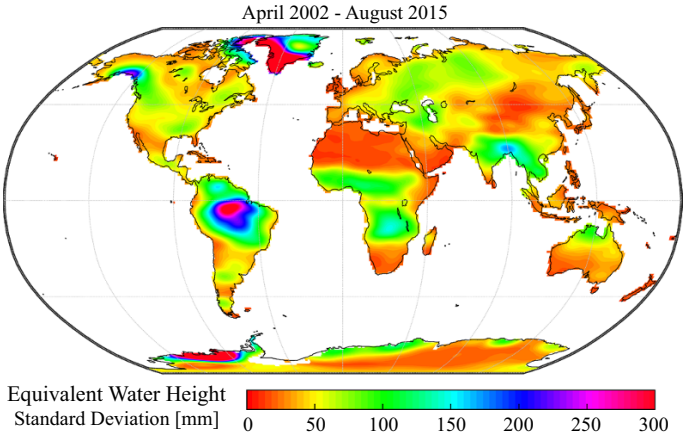


**Fig. 1** Standard deviation of equivalent water height from the ensemble mean of GRACE Tellus CSR, JPL and GFZ solutions (mm)

by Landerer and Swenson (2012). These scaling factors are derived by first applying the complete GRACE processing to modelled estimates of terrestrial water storage and subsequently comparing the agreement between the original and processed model data. A disadvantage of these scaling factors is that they can depend on the hydrological model used as a reference, especially in semi-arid and arid regions as well as over irrigated areas (Long et al. 2015). Long et al. (2015) also mention that scaling factors found in some regions should be interpreted carefully. For these reasons, scaling factors were not applied to the GRACE data in this study.

### 2.2 Filtered Grids of Atmospheric Reanalysis

The atmospheric reanalysis ERA-Interim, from the European Centre for Medium-Range Weather Forecasts (ECMWF), is used to derive daily fields of mean 2 m air temperature and precipitation totals (Dee et al. 2011; available at http://apps.ecmwf.int/datasets/data/interim-full-daily/). This dataset is obtained at a 0.25° resolution and averaged to the 1° resolution of the GRACE Tellus dataset. However, the effective spatial resolution of the hydrological signal observed in GRACE is still coarser than 1°, due to the resolution of the GRACE measurements (see Sect. 2.1). For the Tellus product, this effective spatial resolution is approximately 300 km (3° at the equator). In order to make the atmospheric data comparable with GRACE, we apply a 300 km Gaussian filter to the atmospheric grids. Without this filter, the atmospheric fields would show much more detailed patterns than the GRACE data. It is important to note that when GRACE solutions are compared with modelled estimates of terrestrial water storage, a common practice is to apply the whole GRACE processing to the model data, including an expansion of the modelled mass distribution into spherical harmonics and the subsequent postprocessing (e.g., Wahr et al. 2004; Schmidt et al. 2006; Swenson and Milly 2006; Syed et al. 2008). However, this latter approach cannot be applied to global fields of temperature and precipitation, which is why we only apply a Gaussian filter. We also note that the correlations between GRACE and filtered atmospheric fields are expected to increase as a consequence of this filtering. This effect has already been documented in a similar setting by Abelen and Seitz (2013) when comparing GRACE results with both modelled and remotely sensed soil moisture.

## 3 Methods

### 3.1 Signal Decomposition

#### *3.1.1 Background and Previous Approaches*

Decomposition of the GRACE hydrological signal is common practice in the recent literature, and different methods have been used to address different objectives. One possibility is to aim at isolating the contribution of specific water storage compartments such as groundwater, soil moisture or snow mass to the total GRACE signal. This leads to highly underdetermined inversion problems of blind signal separation and gives rise to non-unique solutions as the contributing geophysical signals are most often not statistically independent. To account for this, inversion methods have been proposed that can use higher-order statistical information derived from model data to decompose the total signal (Ramillien et al. 2004, 2005; Frappart et al. 2006; Schmeer et al. 2012). Assimilation of

GRACE data into a land surface scheme could also be seen as another approach relating GRACE variability to water storage compartments that are already partitioned in a model structure (Zaitchik et al. 2008; Eicker et al. 2014). In groundwater studies, a common strategy is to directly subtract model estimates of snow storage, soil moisture and surface water from the total GRACE signal and use the remainder as an estimate of groundwater changes (Rodell and Famiglietti 2002; Rodell et al. 2007, 2009; Chen et al. 2015). Another decomposition approach is based on extracting the dominant *spatio-temporal* patterns of long-term trends and periodic GRACE signals by means of dimensionality reduction methods. This has been done, for instance, with principal component analysis (Schrama et al. 2007; Rangelova et al. 2007; Schmidt et al. 2008b), independent component analysis (Forootan and Kusche 2012; Frappart et al. 2011b) or multichannel singular spectrum analysis (Rangelova et al. 2010). A last option is based on extracting *temporal* components (i.e. at each grid cell) using time series decomposition techniques. This approach has been used to assess the properties and the relative importance of the resulting features of temporal variability (Barletta et al. 2012; Frappart et al. 2013). Occasionally, the employed decomposition also assumes that the data follows a predefined pattern, as, for instance, when the seasonal cycle is represented by fitted harmonic functions (Steffen et al. 2009). In this paper, we aim at a temporal decomposition of the time series, making as few assumptions as possible and accounting for the irregular spacing of the GRACE "months". This additive decomposition is summarized in Eq. 1, where the original signal ($X_{\text{tot}}$) is represented as the sum of a *long-term component* ($X_{\text{long}}$), a *seasonal cycle* ($X_{\text{seas}}$) and the remaining *subseasonal residuals* ($X_{\text{sub}}$). These high-frequency residuals are expected to be a combination of both a real signal representing subseasonal water storage variability and the noise that is present in the GRACE data. The *long-term component* ($X_{\text{long}}$) is further divided into *linear trends* ($X_{\text{lin}}$) and the anomalies with respect to this linear trend, being here referred to as *inter-annual variability* ($X_{\text{inter}}$).

$$X_{\text{tot}} = \underbrace{X_{\text{long}}}_{X_{\text{lin}}+X_{\text{inter}}} + X_{\text{seas}} + X_{\text{sub}} \tag{1}$$

### 3.1.2 Seasonal Trend Decomposition Using Loess (STL)

The Seasonal Trend Decomposition using Loess procedure (STL) introduced by Cleveland et al. (1990) is a robust decomposition method that is used to extract the mean seasonal cycle and to separate the remaining deseasonalized signal into a low- and a high-frequency component, where the low-frequency component should contain only periodicities larger than 12 months. This procedure was already used with GRACE data by Baur (2012) and Hassan and Jin (2014) as a method to derive the long-term component, in Bergmann et al. (2012) to robustly deseasonalize GRACE time series, and in Frappart et al. (2013) to compare terrestrial water storage with monthly rainfall time series in the Amazon basin. It has also been successfully applied, for instance, in a hydro-climatological setting (Gudmundsson et al. 2011) or to extract temperature trends (Dufresne et al. 2013). The STL procedure is based on locally weighted smoothing of the deseasonalized time series in which the smoothing parameters are analytically optimized to minimize spectral leakage between the high- and the low-frequency components. We introduce here an adaptation of the original algorithm allowing us to apply this method to unevenly spaced time series, accounting for the irregular temporal spacing of the GRACE data. The STL procedure consists of passes of different smoothing filters and includes the calculation of robustness

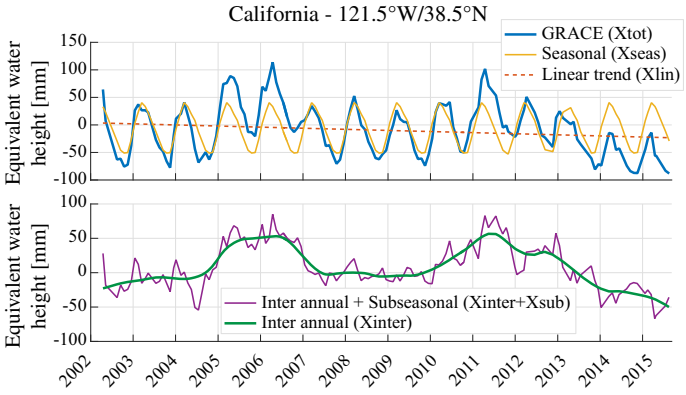


**Fig. 2** Example of signal decomposition (see Eq. 1) at a grid cell located in California

weights in order to account for the possible influence of outliers in the time series. A detailed description of the modified algorithm is presented in Appendix 1.

The STL procedure decomposes the time series into the three components: $X_{\text{seas}}$, $X_{\text{sub}}$ and $X_{\text{long}}$ (Eq. 1). The latter component $X_{\text{long}}$ is the long-term (or low-frequency) component of the time series and is further decomposed into the components $X_{\text{lin}}$ and $X_{\text{inter}}$ (Eq. 1). The linear trend $X_{\text{lin}}$ is first estimated from the long-term component ($X_{\text{long}}$) using the Theil–Sen estimator (Sen 1968), and $X_{\text{inter}}$ is computed as the deviation from this linear trend ($X_{\text{inter}} = X_{\text{long}} - X_{\text{lin}}$). Compared to classical linear regression, using the Theil–Sen slope provides an estimate of the trend that is more robust and less sensitive to large anomalies occurring near the beginning or the end of the time series. This procedure is applied to each grid cell of both the *monthly* GRACE data and the *daily* atmospheric forcing so that we obtain decomposed time series for each of these datasets. In Fig. 2, we illustrate how the presented approach decomposes the GRACE signal into the different subcomponents for the case of a specific grid cell located in California.

## 3.2 Monthly Averaging of the Daily Decomposed Forcing Time Series

The decomposed daily atmospheric forcing data need to be averaged to monthly values in order to enable a comparison with the GRACE time series. The common approach for this is to use the monthly arithmetic mean (e.g., Frappart et al. 2013; Forootan et al. 2014a; Ahmed et al. 2014). As a reference method, we use the arithmetic mean of the days exactly covered by each GRACE monthly solution. We thus obtain monthly series for each component of the atmospheric daily series. In addition, we present hereafter a more sophisticated averaging method that accounts for storage processes that specifically influence the high-frequency component ($X_{\text{sub}}$).

### *3.2.1 Limitations of the Arithmetic Mean for the Comparison of High-Frequency Anomalies*

When comparing averaged time series of water storage with precipitation, some systematic errors are introduced simply because of the arbitrarily chosen averaging intervals (e.g., monthly intervals in the present case). As water storage is a state and precipitation a flux

variable, temporal averages can at times cause a mismatch of the two monthly time series, especially in the case of high-frequency anomalies. A typical example is when a very large precipitation event occurs just at the end of a given month: this extreme event will have a large effect on the precipitation average of the given month but its influence on water storage will be most relevant for the subsequent months. Such artefacts are often falsely attributed to observational errors. In order to address this issue, we propose an alternative to the arithmetic mean that takes the effect of earlier precipitation into account.

### 3.2.2 Comparing Flux and State Variables at Different Temporal Resolutions

Hereafter, precipitation anomalies correspond to a time-dependent *flux* variable, denoted $f(t)$ where $t = \{t_1, \ldots, t_i, \ldots, t_n\}$ is an evenly spaced time vector of length $n$, with units of days. Similarly, daily water storage anomalies correspond to a time-dependent *state* variable denoted $s(t)$. In our case, the *state* variable $s(t)$ is not observed at the daily time scale; however, the GRACE product provides *average values* of $s(t)$ for arbitrary time intervals which approximately correspond to a month. We define this new averaged time series as $s^*(t^*)$, where $t^* = \left\{t_1^*, \ldots, t_j^*, \ldots, t_m^*\right\}$ is an unevenly spaced time vector of length $m$ corresponding to the GRACE "months". The relation between $s(t)$ and $s^*(t^*)$ can be represented by the arithmetic mean (see Fig. 3 for a schematic illustration of the presented relations):

$$s^*\left(t_j^*\right) = \frac{1}{n_j} \sum_{t_i \in [a_j, b_j]} s(t_i) \tag{2}$$

where $a_j$ and $b_j$ correspond to the edges of the $j$th time interval (e.g., of the $j$th GRACE month) and $n_j$ is the number of days falling within this interval ($n_j = b_j - a_j$).

Our main concern is now to determine the relation between $f(t)$ and $f^*(t^*)$. As mentioned above, a common approach is to compute the mean of the daily values over the given time intervals. Analogously to Eq. 2, this simply corresponds to:

$$f^*\left(t_j^*\right) = \frac{1}{n_j} \sum_{t_i \in [a_j, b_j]} f(t_i) \tag{3}$$

Here, we suggest the use of a weighted mean of $f(t)$ as an alternative approach:

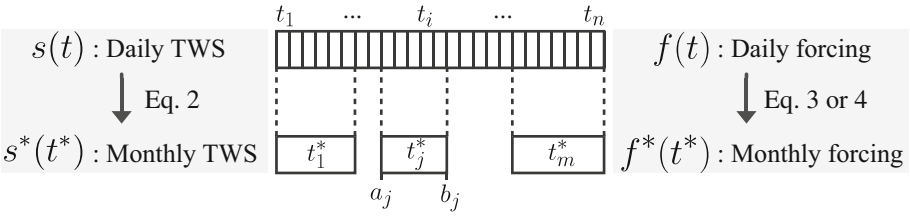


**Fig. 3** Schematic representation of the correspondence between daily time series and the irregular—quasi-monthly—temporal resolution of the GRACE time series. For daily time steps, $t = \{t_1, \ldots, t_i, \ldots, t_n\}$ going from the 1st to the $n$th day. For quasi-monthly time steps, $t^* = \left\{t_1^*, \ldots, t_j^*, \ldots, t_m^*\right\}$ going from the 1st to the $m$th month, $a_j$ and $b_j$ denoting the first and last days of a given month

$$f^*\left(t_j^*\right) = \sum_{i=1}^{n} \hat{W}\left(t_j^*, t_i\right) \cdot f(t_i) \tag{4}$$

where the normalized weights $\hat{W}\left(t_j^*, t_i\right)$, which will be defined in the next section, depend both on $t_j^*$ and $t_i$ and have the property that:

$$\sum_{i=1}^{n} \hat{W}\left(t_j^*, t_i\right) = 1 \tag{5}$$

### 3.2.3 Weights Based on Integrated Exponential Decay Functions

A simple way to represent the effect of a short-term precipitation anomaly (e.g., a daily precipitation event) on the subsequent state of water storage is the exponential decay function. This is equivalent to assuming linear storage components (bucket models), which is common practice in conceptual hydrological modelling (Beven 2012). Here, we assume that the influence of a flux anomaly (e.g., a precipitation event) on the state variable (e.g., water storage) will decrease exponentially with time. Formally, we define $w(t, t_i)$ as the influence of a given flux anomaly $f(t_i)$ observed at time $t_i$ on the subsequent values of the state variable $s(t)$ at time $t > t_i$.

$$w(t, t_i) = \begin{cases} 0, & \text{if} \quad t < t_i \\ \mathrm{e}^{-\frac{1}{\tau}(t - t_i)}, & \text{if} \quad t \geq t_i \end{cases} \tag{6}$$

where $\tau$ is a free parameter controlling the rate of exponential decay and is expressed in units of time (e.g., in days). The influence of the given flux anomaly $f(t_i)$ on the earlier values of the state variable (i.e. when $t < t_i$) is of course zero.

However, $w(t, t_i)$ only represents the influence of $f(t_i)$ on the subsequent daily values of $s(t)$, but we are in fact interested in the influence of $f(t_i)$ on the values of $s^*(t^*)$—the monthly values. For a given $t_j^*$, summing $w(t, t_i)$ over the corresponding time interval $t \in \left[a_j, b_j\right]$ yields:

$$W\left(t_j^*, t_i\right) = \sum_{t \in \left[a_j, b_j\right]} w(t, t_i) \tag{7}$$

For illustrative purposes, this summation is shown in Fig. 4. The two examples correspond to the case of a flux anomaly $f(t_i)$ occurring either before (Fig. 4a) or during (Fig. 4b) the given time interval $\left[a_j, b_j\right]$. The last step is to ensure that the property set by Eq. 5 is fulfilled by normalizing the weights (Eq. 8):

$$\hat{W}\left(t_j^*, t_i\right) = \frac{W\left(t_j^*, t_i\right)}{\sum_{i=1}^{n} W\left(t_j^*, t_i\right)} \tag{8}$$

When this is done with a fixed $t_j^*$ and for all values of $t_i$, we obtain the averaging filter illustrated in Fig. 5 for different values of $\tau$—the free parameter controlling the rate of the exponential decay. From this figure, we see that weights are assigned to flux anomalies including to those occurring before the time interval $t_j^*$. Additionally, we provide a more

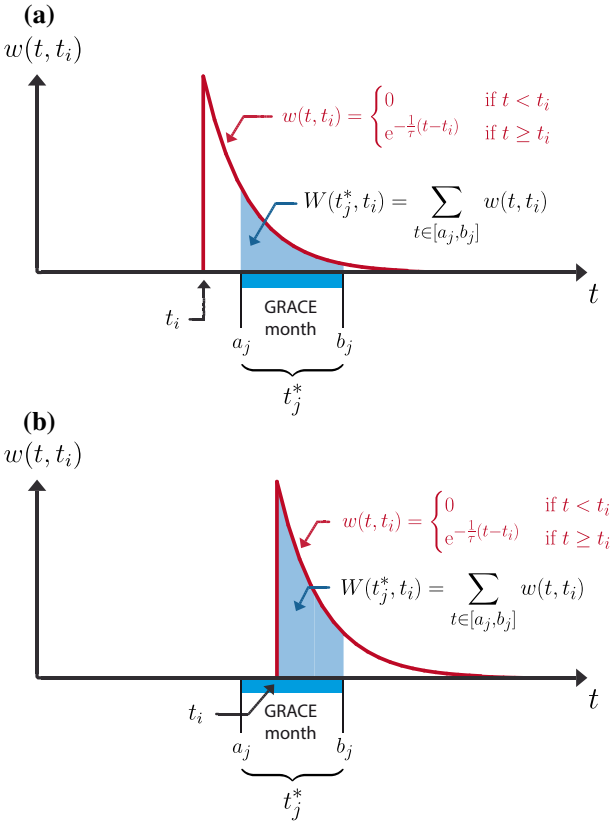


**Fig. 4** Illustration of Eqs. 6 (*red*) and 7 (*blue*). The red curve depicts the exponentially decaying influence of a given daily flux anomaly (precipitation) occurring at time $t_i$ on the state variable (water storage) at subsequent time steps. The summation of this influence over the interval covered by a given GRACE month corresponds to the relative weight (*blue area*) assigned to the flux at time $t_i$. See the text for a description of the different symbols

practical formulation of this weighting function obtained after integrating and normalizing Eq. 6 analytically (Appendix 2):

$$\hat{W}\left(t_j^*, t_i\right) = \begin{cases} \dfrac{e^{\frac{1}{\tau}(t_i-a)} - e^{\frac{1}{\tau}(t_i-b)}}{b-a} & \text{if} \quad a \geq t_i \\ \dfrac{1 - e^{\frac{1}{\tau}(t_i-b)}}{b-a} & \text{if} \quad a < t_i \leq b \\ 0 & \text{if} \quad b < t_i \end{cases} . \tag{9}$$

### 3.2.4 Shape and Properties of the Weighting Function

The parameter $\tau$ controls the rate of exponential decay and will hereafter be referred to as the *decay time scale* of the weighting function. Inverting Eq. 6 for $\tau$ shows that $\tau$ corresponds to the number of time steps (e.g., days) after which the influence of a given flux anomaly $f(t_i)$ will have reduced to 1/e $\approx$ 37 % of its initial influence at time $t_i$.

An interesting property is that when $\tau$ tends to small values (see Fig. 5 for $\tau = 1$), $\hat{W}\left(t_j^*, t_i\right)$ converges very quickly to a weighting function that is almost equivalent to the arithmetic mean performed over the interval $\left[a_j, b_j\right]$ (i.e. Eq. 3). Small values of $\tau$

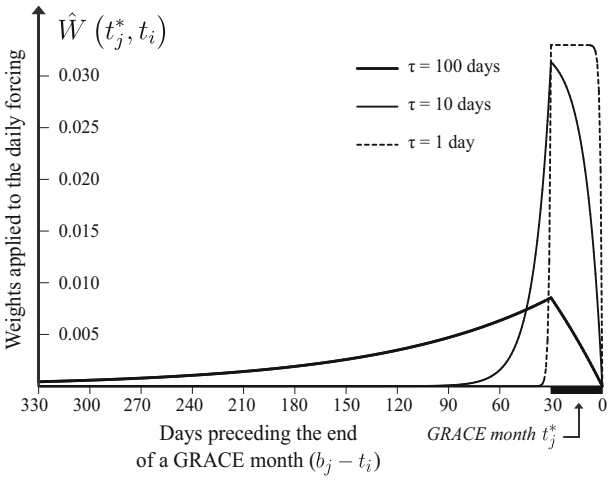


**Fig. 5** Illustration of the shape of the weighting function (Eq. 9) for different values of the decay time scale $\tau$. The $y$-axis corresponds to the normalized weight ($\hat{W}$) that is applied to the daily flux time series when it is averaged to the approximately monthly GRACE resolution

correspond to small decay time scales, indicating that a single flux anomaly will not have a prolonged effect on the state variable. A hydrological interpretation of this feature suggests a short mean residence time of the water store. Inversely, large values of $\tau$ imply longer residence times and, therefore, more weight is given to anomalies occurring before the time interval of interest. In such a case, it is interesting to note that anomalies occurring near the end of the given time interval are assigned small weights. Hence, the difference between the presented weighting scheme and an arithmetic mean becomes more important for larger $\tau$. Since the value of $\tau$ at each grid cell is unknown in our application, it needs to be estimated from the data. Here, we optimize the agreement between the monthly averaged subseasonal forcing (i.e. $X_{\text{sub}}$ of $f(t)$) and the subseasonal monthly GRACE (i.e. $X_{\text{sub}}$ of $s^*(t^*)$) by maximizing the squared product–moment correlation coefficient. In the presented study, this weighting function is used for the analysis of the subseasonal component only (Sect. 4.5).

## 3.3 Significance Testing and Correlation Analysis

### *3.3.1 Linear Trends*

A common nonparametric test for detecting monotonic trends in hydro-meteorological time series is the Mann–Kendall rank-based test. However, serial correlation (autocorrelation) in time series has been shown to heavily influence the power of this test (Yue et al. 2002), and several methods have been proposed to address this issue (Hamed and Rao 1998; Yue and Wang 2004; Hamed 2009). Here, we use the modified Mann–Kendall trend test described by Yue and Wang (2004) on deseasonalized GRACE time series ($X_{\text{tot}} - X_{\text{seas}}$). In this test, the autocorrelation estimated from the deseasonalized and detrended time series is used to compute an effective sample size, which is then used to correct the Mann–Kendall statistic. In addition, as the trend test is performed locally (i.e. at each grid cell) and due to the high spatial autocorrelation of the GRACE data, there is an increased probability that the null hypothesis is falsely rejected (Wilks 2011). Hence, we additionally control this false discovery rate (FDR) using the approach described by Benjamini and Hochberg (1995), which has shown good performance when applied to climate data (Ventura et al. 2004; Wilks 2006; Gudmundsson and Seneviratne 2015). The

trends are considered statistically significant when the $p$ value falls below a critical value ($p < 0.01$).

### 3.3.2 Inter-Annual Anomalies

Regarding the inter-annual anomalies ($X_{\text{inter}}$), the degree of linear association between GRACE and the atmospheric forcing is quantified with the product–moment correlation coefficient. As the inter-annual anomalies correspond to the low-frequency component of the GRACE signal, they exhibit important serial correlation, which prevents the use of conventional hypothesis testing techniques (e.g., $t$ test). Here, we use moving block bootstrapping in order to estimate the null distribution of the correlation coefficient at each grid point (Mudelsee 2014). Although there is no standard recommendation on the selection of an optimal block length, a good starting point is to use a block length larger than the decorrelation time (i.e. the number of time steps after which the serial correlation is not significant anymore). Based on this criterion, we find that a block length of 20 months is sufficient for our application. We perform 10,000 bootstrap replications at each grid point and estimate the 95 % confidence intervals from this null distribution. A correlation coefficient is declared significant when it does not belong to the range of the local confidence interval.

### 3.3.3 Seasonal Cycle

Previous studies have shown that there is often a temporal lag between the seasonal cycle of precipitation and terrestrial water storage (e.g., Papa et al. 2008; Ahmed et al. 2011; Frappart et al. 2013). It is also known that water storage and surface temperature are related through evapotranspiration and snow melt; however, differences in the phasing of GRACE versus these atmospheric variables were, to our knowledge, never surveyed at a global scale. We define the phase shift as the lag (in months) minimizing the residual sum of squares between the standardized seasonal cycles of both GRACE and the atmospheric forcing. When these paired seasonal cycles strongly differ in shape, this procedure can sometimes lead to meaningless lag values. A t-test of the Pearson product–moment correlation between the time–lagged seasonal cycles is used to filter out these potentially misleading values ($p < 0.01$). We additionally control the FDR following Benjamini and Hochberg (1995).

### 3.3.4 Subseasonal Residuals

Similarly as for the inter-annual anomalies, the product–moment correlation coefficient is used to quantify the degree of linear association between GRACE and the atmospheric forcing data. The subseasonal residuals ($X_{\text{sub}}$) correspond to the high-frequency component and are thus the least affected by serial correlation. However, we found that these time series still contain minor but significant serial correlation (not shown). For consistency, we thus use an identical significance testing setting as for the inter-annual anomalies (i.e. a moving block bootstrapping).

## 3.4 Identifying Droughts in the GRACE Record

Here we investigate the *average storage deficit* during drought events identified using an approach based on Thomas et al. (2014). This approach defines 1) storage deficit as a

negative departure (in mm) from the seasonal cycle and 2) drought duration as the number of months with continuous deficits. The *average storage deficit* simply corresponds to the arithmetic mean of the storage deficit observed during a given drought event and is used as a measure of average drought intensity. Here two differences compared to Thomas et al. (2014) are introduced.

First, we remove the linear trends from the time series prior to drought identification. The reason is that strong linear trends can result in one end of the time series being systematically above/below the seasonal cycle. In such a case, the proposed method would have a tendency to underestimate/overestimate the magnitude of dry events. Hence for the purpose of this study, linear trends are removed prior to the analysis and potential decadal drying trends are discussed in a separate section. Our analysis is thus based on the sum of the inter-annual and subseasonal components only ($X_{\text{inter}} + X_{\text{sub}}$, also see Fig. 2). Occasionally, drought events occurring at the end or the beginning of the time series can be large enough to influence the trend estimate itself, even when using the Theil–Senn slope to reduce this effect. Hence, it is important to note that, in some cases, removing the linear trends may cause an underestimation of the drought intensity.

Second, the minimum duration for considering a drought event is defined as a period of three consecutive months with water storage deficit. Unlike Thomas et al. (2014), we apply this criterion only to the inter-annual component $X_{\text{inter}}$ (see Fig. 2) and not to the sum of the inter-annual and subseasonal components ($X_{\text{inter}} + X_{\text{sub}}$). The reason is that, compared to the basin-scale assessment of Thomas et al. (2014), subseasonal variability ($X_{\text{sub}}$) is larger at the grid level and including it would otherwise considerably reduce the probability of observing long periods with consecutive deficits.

## 4 Global Hydrological Variability in the GRACE Data

### 4.1 Distribution of GRACE Variance Among Temporal Components

The relative magnitude of the three components extracted from the STL procedure ($X_{\text{long}}$, $X_{\text{seas}}$ and $X_{\text{sub}}$) can be evaluated by comparing each component's variance to that of the total signal. As shown in Fig. 6, the relative magnitude of each of the different components

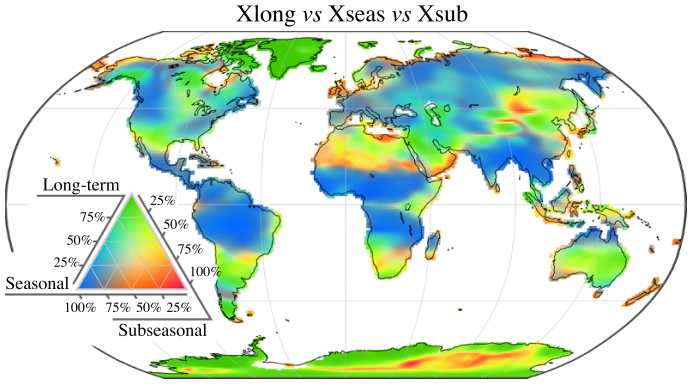


**Fig. 6** Distribution of the total GRACE variance among the long-term (*green*), seasonal (*blue*) and subseasonal (*red*) components, expressed in per cent of the total variance, indicating the dominant modes of temporal variability in terrestrial water storage for different regions

is subject to high spatial variability across the world. To ease the interpretation, Fig. 6 can also be compared to the standard deviation of the total signal in Fig. 1. As already identified in early studies (Wahr et al. 2004), the seasonal cycle is dominant in many tropical regions like the Amazon basin, Central Africa and India. A notable exception is the Indo-Australian archipelago where the GRACE signal is heavily perturbed by signal leakage from the ocean as well as gravity anomalies consecutive to the 2004 Sumatra earthquake. The seasonal cycle is also dominant at higher latitudes, particularly in Siberia and in north-western America, although these regions do not have the largest variance in absolute terms.

Subseasonal variability ($X_{\text{sub}}$) is dominant in regions where the GRACE signal has already a relatively low variance (Fig. 1) and is most likely dominated by noise such as in the Sahara desert. Although we do not further investigate this matter, it is interesting to note that Arctic coastal regions such as the coasts of Northeast Siberia and Canada seem to be mostly affected by subseasonal variability.

We also observe that many regions of the world are dominated by inter-annual variability ($X_{\text{long}}$). The signal found in Greenland and Antarctica, parts of Alaska and the Hudson Bay is the result of the interplay between ice mass loss, other water storage changes and glacial isostatic adjustment. As a result, these regions require a specific treatment before conclusions can be drawn concerning the dominant features of hydrological variability (Velicogna et al. 2014). Other regions particularly dominated by long-term variability include the south-western Central USA as well as the Middle East, some of which are already documented in the literature as being influenced by decadal droughts and long-term trends in groundwater storage (Long et al. 2013; Voss et al. 2013; Forootan et al. 2014b). Other interesting features include the Lake Victoria and the Aral Sea where long-term surface water variations can be related to both human activities and climate variability (Swenson and Wahr 2009; Singh et al. 2012). Finally, some regions in the southern hemisphere like Australia and Argentina were also shown to exhibit an important inter-annual variability that can be related to the El-Niño Southern Oscillation (ENSO) (García-García et al. 2011; Abelen et al. 2015).

### 4.2 Linear Trends

In this section, we will assess in further detail the relative importance of linear trends ($X_{\text{lin}}$) versus nonlinear inter-annual variability ($X_{\text{inter}}$) by looking at the magnitude of each of these two components in the long-term variability ($X_{\text{long}}$):

$$R_{\text{lin/long}} = \frac{\sigma^2_{\text{lin}}}{\sigma^2_{\text{long}}} = 1 - \frac{\sigma^2_{\text{inter}}}{\sigma^2_{\text{long}}} \tag{10}$$

This formulation is also equivalent to the coefficient of determination of the linear trend as estimated by the Theil–Sen slope with respect to the long-term component. The colour scale in Fig. 7a represents the ratio of the linear trend variance to that of the whole long-term component (Eq. 10) and shows how the long-term component ($X_{\text{long}}$) variance is partitioned between linear ($X_{\text{lin}}$) and nonlinear trends ($X_{\text{inter}}$). The sign, magnitude and significance ($p < 0.01$) of the linear trends are shown in Fig. 7b. Note the truncated colour scale for negative trends beyond $-30$ mm/year.

We observe that the long-term variability in large areas of Greenland and Antarctica is dominated by a linear trend. This can be related to ice mass loss once glacial isostatic adjustment has been accounted for (Ramillien et al. 2006; Velicogna and Wahr 2006; Chen et al. 2006b; Wouters et al. 2008; Velicogna 2009; Velicogna and Wahr 2013). Examples

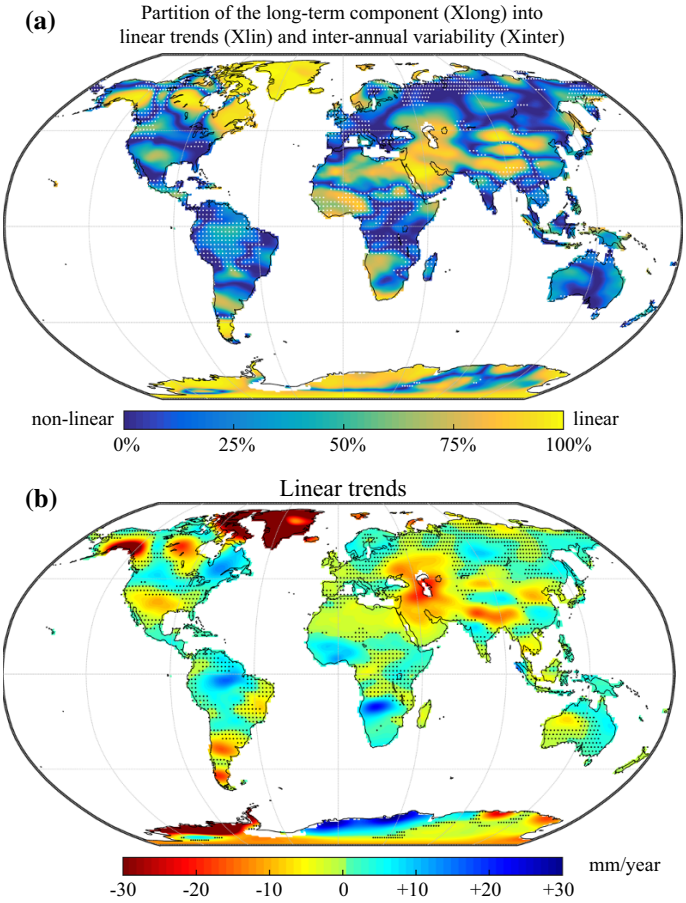


**Fig. 7** **a** Fraction of the long-term variability that corresponds to a linear trend, expressed in per cent of the long-term variance. Large values (*yellow*) indicate that most of the long-term variability corresponds to a linear trend. Small values (*blue*) indicate that (non-linear) inter-annual variability is dominating. Stippling indicates regions where the long-term variability represents less than 20 % of the total GRACE variance (see also Fig. 6). **b** Magnitude of linear trends in the GRACE signal (expressed in mm/year). Stippling indicates regions with non-significant trends ($p < 0.01$). Note that the colour scale is truncated for negative trends beyond −30 mm/year

of other regions of the cryosphere concerned with documented linear trends include Alaskan mountain glacier melting (Chen et al. 2006a; Arendt et al. 2013; Larsen et al. 2015) and icefield melting in Patagonia (Chen et al. 2007b; Ivins et al. 2011). Strong linear trends located close to the Hudson Bay have been related to glacial isostatic adjustment (Tamisiea et al. 2007), and recent studies focusing on Arctic regions showed that both isostatic and hydrological trends contribute to the observed signals (Frappart et al. 2011a; Wang et al. 2013).

Many pronounced negative trends can also be observed in other regions of the world. One of the most recognized drying trends occurs in north-west India and is related to groundwater depletion (Rodell et al. 2009; Chen et al. 2014). Most of the long-term signal

that is dominating GRACE variability over the Middle East, the Caspian Sea and the Aral Sea can be attributed to a drying trend partly due to anthropogenic water abstraction (Singh et al. 2012; Voss et al. 2013; Joodaki et al. 2014; Forootan et al. 2014a). On the contrary, the region of Lake Victoria is dominated by nonlinear variations in the long-term component, which have been related to hydropower dam operations, precipitation anomalies and ENSO (Awange et al. 2008; Swenson and Wahr 2009; Becker et al. 2010; Hassan and Jin 2014). Another important drying trend can be found in Argentina, especially in the southern part of the La Plata basin (Chen et al. 2010b; Abelen et al. 2015). Finally, the drying trend documented by Crowley et al. (2006) in the Congo river basin for the period 2002–2006 is found to be insignificant based on the current analysis.

The significance analysis also identified regions with trends which have not been identified yet or have only drawn little attention so far. For instance, the extended drying trends located to the North of both the Black Sea and the Caspian Sea could be potentially investigated in more detail. Interestingly, small but statistically significant drying trends ($-3$ mm/year) can also be found over large portions of the Sahara desert. So far, little attention has been devoted to GRACE variability in this region as most of the signal is contaminated by noise. Nevertheless, these drying trends have been partly documented (Ahmed et al. 2014; Ramillien et al. 2014) and to some extent attributed to groundwater extraction from fossil aquifers in the Sahara region.

Significant positive trends can also be found in southern Africa, near the Upper Zambezi and Okavango river basins as well as in the Sahel and the Niger basin, and these trends have already been well documented (Ramillien et al. 2014). In a comparison with rainfall observations from different sources, Ahmed et al. (2014) have found that the increasing trend in the Niger basin could be related to an increase in precipitation; however, this was not the case for the Upper Zambezi and the Okavango basins. Although Ahmed et al. (2014) suggest that this could be due to longer residence times in these watersheds, we feel that more investigation is still required to explain the very strong positive trend in this region. A positive trend is also found in the Amazon basin and has been described, for instance, in Chen et al. (2010a) and could, to a certain extent, be related to precipitation anomalies based on an analysis of the period 2003–2008 by Xavier et al. (2010).

The linear trends derived over north-western China raise some concerns with respect to a possibly spurious origin. The alternating bipolar patterns of positive and negative trends, oriented along the meridian 100°E, could be due to some accidental disturbance originating in the processing of the GRACE data. A very similar pattern could already be found in Fig. 8 of Frappart et al. (2011b), which compared trends derived after different postprocessing methods for the period 2003–2008. It is possible that these trends found over China are specific to the destriping algorithm of Swenson and Wahr (2006) since they are not reproduced by the other postprocessing methods investigated by Frappart et al. (2011b). However, Feng et al. (2013) were also able to relate drying trends in the Beijing region to groundwater observations. Consequently, special care should be taken when interpreting trends from the current GRACE Tellus estimates in that region.

### 4.3 Inter-Annual Anomalies

The inter-annual anomalies correspond to the nonlinear part of the long-term component (Eq. 1). In this section, we assess the degree to which the inter-annual anomalies derived from the GRACE time series can be correlated with the inter-annual anomalies of the atmospheric forcing. Figure 8a depicts the correlation between the inter-annual water storage and precipitation anomalies. We observe moderately high positive correlations

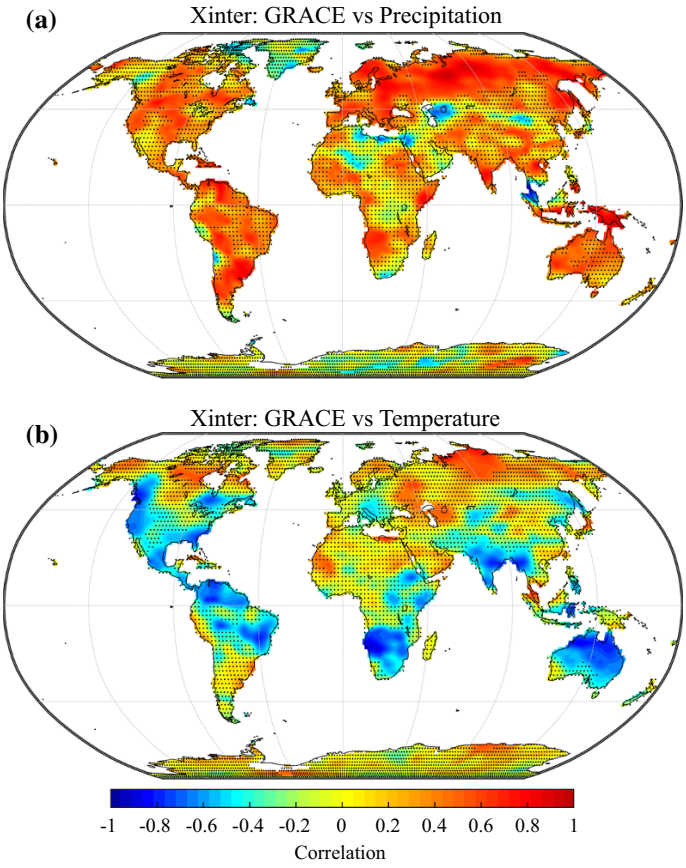


**Fig. 8** Correlation between the inter-annual variability of water storage and **a** precipitation, **b** temperature. Stippling indicates regions with non-significant correlation coefficients ($p < 0.05$)

(>0.6) between these two components for parts of Europe, Russia and North America, which indicate a positive effect of precipitation on terrestrial water storage. Correlations are more erratic over subtropical and equatorial regions, possibly resulting from deficiencies in the ERA-Interim precipitation forcing, which are known to be more pronounced, for instance, over Africa and South America (Simmons et al. 2010). In these regions, other precipitation datasets based either on ground measurements or satellite observations may give different results. For example, we find relatively low correlations between inter-annual water storage and precipitation over the region of the African Great Lakes; however, Becker et al. (2010) found a seemingly good agreement with GRACE when using monthly precipitation data from the Global Precipitation Climatology Project (GPCP). For Africa and South America, Morishita and Heki (2008) found that mass changes from GRACE could be related to precipitation anomaly patterns extracted from the Climate Prediction Center Merged Analysis of Precipitation (CMAP). Over the Amazon, Chen et al. (2010a) related inter-annual water storage change to precipitation anomalies (from GPCP) and ENSO indices, while Frappart et al. (2013) found that the inter-annual variability of water storage was in reasonable agreement with precipitation

from the Tropical Rainfall Measuring Mission (TRMM). Although correlation coefficients are mostly positive, significant negative correlations can occasionally be found but seem either accidentally caused by perturbations of the long-term gravimetric signal by large earthquakes (e.g., Sumatra region) or would need to be confirmed in a regional investigation (Caspian Sea area).

The same analysis was performed with ERA-Interim 2 m temperature (Fig. 8b). We find that the correlation between inter-annual water storage and temperature is negative in most cases. Correlations are moderately strong over parts of North America, South America, southern Africa, India and Australia. Such a negative relationship is usually expected not only since temperature is an important driver for evaporative demand but also because low moisture availability can result in higher temperatures (Seneviratne et al. 2010; Mueller and Seneviratne 2012). However, correlations found in the southern hemisphere could also be related to confounding factors such as atmospheric circulation patterns (e.g., ENSO) and hence do not necessarily indicate a direct link between temperature and terrestrial water storage. In addition, significant positive correlations between long-term temperature and water storage anomalies can be found over parts of Siberia. Long-term water storage anomalies in this region may be related to interactions with permafrost although such relationships are still unclear at this stage (Velicogna et al. 2012; Vey et al. 2013).

Non-significant correlations can be due either to other unidentified sources of long-term variability in the GRACE data or errors and biases in the long-term variability of the ERA-Interim atmospheric forcing. However, the absence of correlation with either precipitation or temperature in some regions could also indicate that long-term variability in the atmospheric forcing is not controlling or controlled by terrestrial water storage, i.e. that there is no obvious relationship between these variables at the inter-annual time scale. In addition, the literature covered in the section on linear trends already showed that anthropogenic groundwater withdrawal and dam operations could be responsible for long-term changes in the terrestrial water storage variations retrieved from GRACE. Finally, we note that a very large number of locations exhibit moderate correlations (between 0.3 and 0.5 in absolute value), which are actually not significant once serial correlation is taken into account in hypothesis testing (using bootstrapping). This is also an indication that analyses of the inter-annual variability of water storage would greatly benefit from the longer record length that may be provided in the future by the GRACE Follow-On mission scheduled for launch in 2017.

### 4.4 Seasonal Cycle

The STL decomposition provides a data-driven way of estimating the seasonal cycle which, in contrast to the common practice, does not rely on harmonic models (fitted sines and cosines, e.g., Wahr et al. 2004; Hinderer et al. 2006; Schmidt et al. 2008b). Here we characterize GRACE seasonality by mapping the months with the *maximum* and the *minimum* of the seasonal cycle of water storage and show that they generally follow latitudinal bands (Fig. 9a, b). In the Northern Hemisphere, the peak in terrestrial water storage generally occurs in spring for the cold and temperate regions and in autumn for the subtropical regions (and vice versa in the Southern Hemisphere). The minimum water storage occurs in autumn for the cold and temperate regions and in spring for the subtropical regions (and oppositely in the Southern Hemisphere). In subarctic regions, there is a clear latitudinal trend towards a later maximum, likely corresponding to the delayed response of snow melt to temperature at higher latitudes. Interestingly, the seasonal

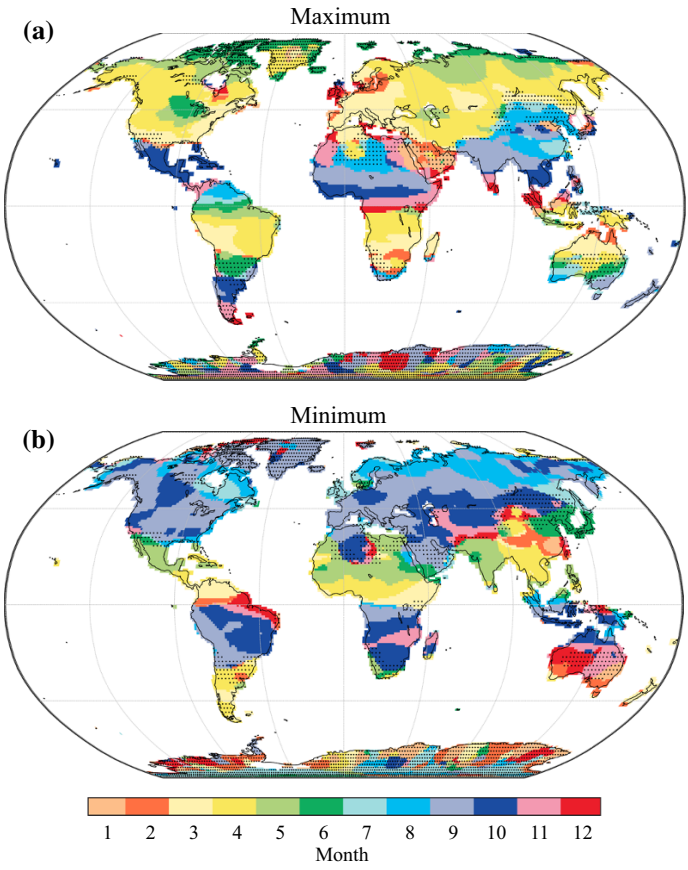


**Fig. 9** **a** Month with the maximum of the seasonal cycle of water storage. **b** Month with minimum seasonal water storage. Stippling indicates regions where the seasonal variability represents <20 % of the total GRACE variance

maximum appears to be also delayed near large inland reservoirs (e.g., the Great Lakes and the Caspian Sea), which potentially reflects the influence of run-off and storage processes and could be subject to further investigations. In most regions, the months with maximum and minimum terrestrial water storage are spaced by an interval of 6 ± 1 months. However, this is not always the case: in northern India, the maximum terrestrial water storage occurs in September and the minimum in May, which is consistent with the effect of the June–September monsoon. These maps can, for instance, be directly compared with hydrological models (see Fig. 6 in Güntner et al. 2007b for an example with a closely resembling colour scale). In addition, it is worth mentioning that the seasonal cycle of water storage over African regions located close to the equator (e.g., the Congo basin, Lake Victoria) exhibits a strong secondary peak, which likely corresponds to the oscillation of the inter-tropical convergence zone (not shown). This secondary peak is also present—although less pronounced—over Ecuador, southern India and Indonesia but is completely absent over the Amazon basin (not shown).

The phase shift between GRACE and the seasonal cycles of precipitation and temperature is shown in Fig. 10a, b. Over most tropical and subtropical regions, the seasonal

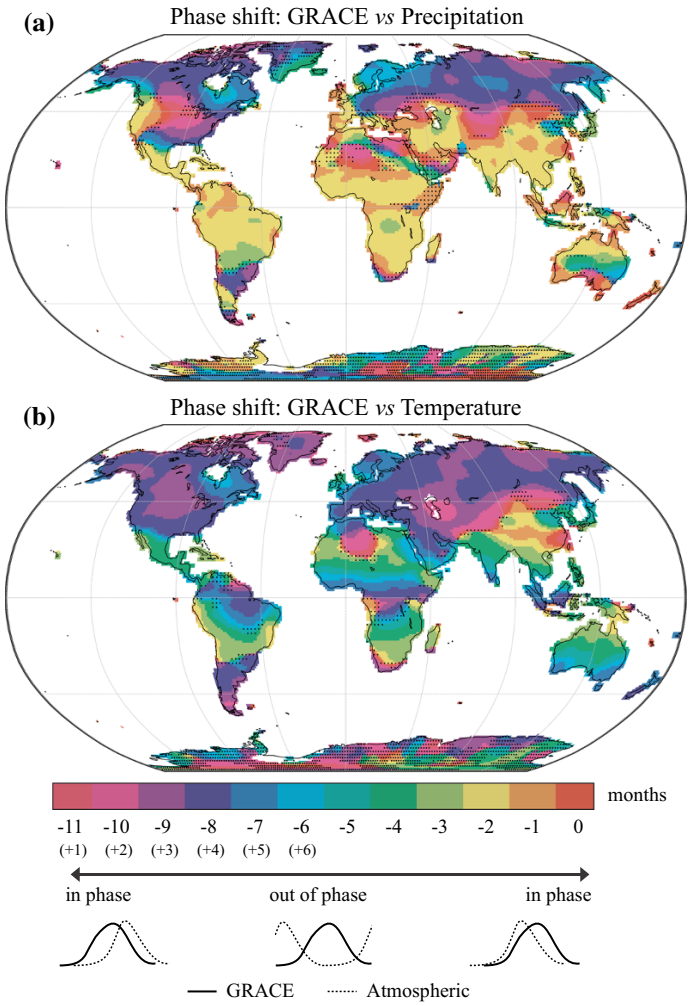


**Fig. 10** Phase shift (in months) between the seasonal cycle of water storage and the seasonal cycle of **a** precipitation and **b** temperature. Small phase shifts (−1, 0 or −11(+1) months) indicate that the atmospheric forcing is nearly in phase with water storage, whereas large phase shifts (−7, −6 or −5 months) indicate that they are out of phase. Stippling indicates regions where the correlation between optimally phase shifted seasonal cycles is not significant ($p < 0.05$)

peak of precipitation typically occurs 1–2 months *earlier* than the peak in water storage, likely due to the effect of storage processes. Very similar lags have been found for the Amazon subbasins (see Table 3 in Frappart et al. 2013), for selected regions over central Africa (see Fig. 3 in Ahmed et al. 2011) as well as by Rieser et al. (2010) over Australia (all three studies used satellite precipitation data from TRMM). On the contrary, subarctic and inland temperate regions experience the highest precipitation during the warmer summer months, approximately 3–5 months *later* than the spring maximum in water storage. For coastal subarctic areas, the precipitation maximum tends to occur in autumn due to greater temperature differences between the ocean and land, resulting in a 5- to

7-month phase shift between water storage and precipitation (e.g., Alaska, British Columbia and Scandinavia). More details concerning the phasing of GRACE with snow storage and discharge measurements can be found in Frappart et al. (2011a).

The seasonal cycle of temperature is generally out of phase with respect to the seasonal cycle of water storage (Fig. 10b). In most temperate and subarctic regions, the peak temperature typically occurs in summer, 2–3 months earlier than the autumn minimum in water storage. Over tropical regions, the seasonal cycle of temperature is completely opposed to the water storage cycle, with corresponding phase shifts of 4–7 months. This anti-phasing between water storage and temperature is likely related to the effects of both temperature and radiation on evapotranspiration. Over equatorial regions, the seasonality of temperature is much less pronounced but still lagging the water storage cycle by 3–4 months. The southern part of China exhibits a very specific pattern, with maximum temperatures occurring in summer and seasonal water storage peaking in late summer, resulting in an almost perfect phasing between water storage and temperature.

### 4.5 Subseasonal Residuals

Figure 11a shows the correlation between the high-frequency components of GRACE and precipitation averaged with the new averaging scheme presented in Sect. 3.2. Significant positive correlations are found over many regions of the world, indicating that a large fraction of high-frequency GRACE variability can be statistically related to short-term anomalies of the precipitation forcing. Interestingly, significant correlations can also be found over large portions of Indonesia, although the GRACE signal in this region is usually believed to be strongly deteriorated by signal leakage from the ocean. A possible explanation might be that short-term precipitation variability in this tropical monsoon region is large enough to overcome the higher errors associated with coastal and insular regions. A notable exception to the global pattern is the Congo river basin where no significant correlations can be found. This area corresponds to a major convective region for the global climate system which is still poorly represented by atmospheric reanalyses in comparison with other regions (Washington et al. 2013). Many extremely arid regions also show non-significant correlations (Sahara, Atacama, Taklamakan and Gobi deserts), confirming the view that high-frequency GRACE variability in these regions is dominated by noise.

In order to assess the influence of the new averaging method, we can visually compare the correlations shown in Fig. 11a to the correlations obtained with a simple monthly arithmetic mean of the daily residuals (Fig. 11b). The exponential decay approach enhances the correlations over most regions of the world, with an average increase of $+0.3$ (excluding regions which exhibit non-significant correlations in Fig. 11a). Figure 12a enables an even more direct comparison between the distributions of the correlations shown in Fig. 11a, b. This illustrates the value of the proposed weighting scheme and reveals that using monthly arithmetic averages of precipitation may have resulted in underestimating the relation with water storage on the subseasonal time scale. This finding is of particular interest for studies comparing GRACE data to monthly precipitation time series (e.g., Forootan et al. 2014a) which typically make use of monthly precipitation averages.

Values of the calibrated decay parameter $\tau$ used to compute the monthly averages from the daily precipitation data are shown in Fig. 11c. Overall, decay time scales exhibit systematic spatial variability that could potentially be related to many different factors, including climatic conditions as well as soil and vegetation characteristics. The probability

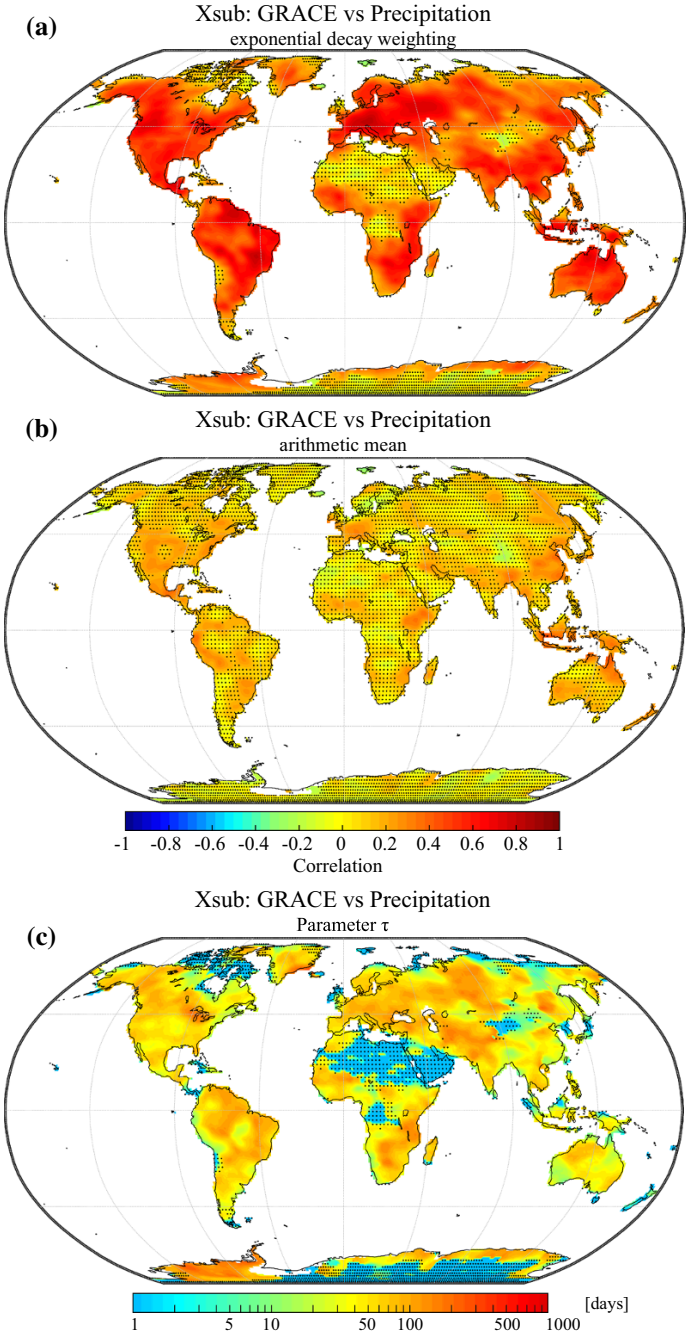


**Fig. 11** **a** Correlation between the subseasonal variability of water storage and precipitation averaged with the weighting function introduced in Sect. 3.2 (Eq. 9). **b** Correlation between the subseasonal variability of water storage and precipitation averaged using the arithmetic mean (Eq. 3). **c** Value of the calibrated decay parameter ($\tau$) with units of days. Stippling indicates regions with non-significant correlation coefficients ($p < 0.05$)

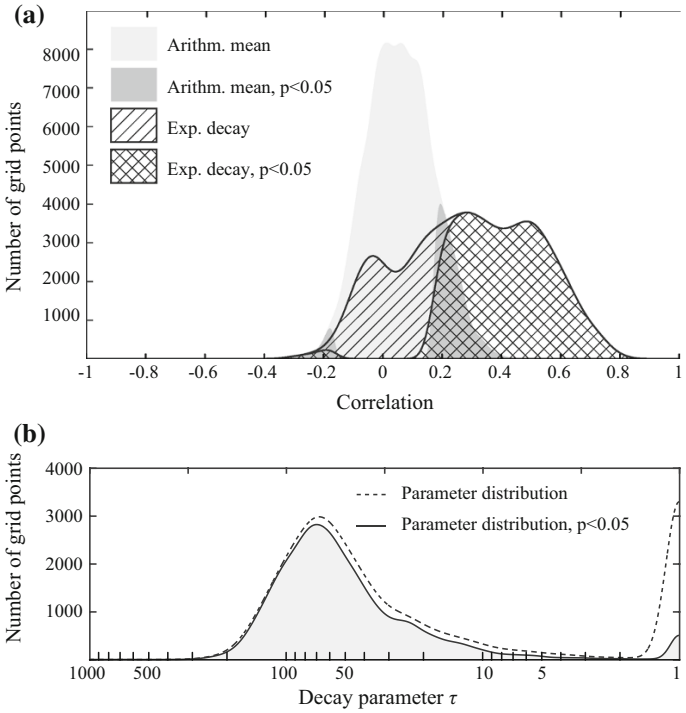


**Fig. 12** **a** Distribution of the correlation coefficients obtained with a simple average of the precipitation forcing (*grey surface*) versus the distribution of the correlation coefficients obtained with the newly introduced weighting function (*hatched surface*). The part of significant correlation coefficients ($p < 0.05$) is indicated using a darker colour or double hatching. **b** Distribution of the calibrated decay parameters used in the weighting function. Note the base 10 logarithmic scale of the *x*-axis

density distribution of this parameter is also shown in Fig. 12b, and we find that significant values generally range between 10 and 200 days with a median value of approximately 50 days. Based on the weighting function (Eq. 9), it can be calculated that for the median value of $\tau = 50$ days, the precipitation residuals of the first 100 days preceding the beginning of a GRACE month account for 65 % of the monthly average. On the contrary, days covered by the time interval of a given GRACE month account for only 25 % of the monthly average. This shows that, on the subseasonal time scale, precipitation preceding a GRACE month usually has a higher impact on correlations with terrestrial water storage than the precipitation of the coinciding month. This is due to the fact that the influence of high-frequency precipitation anomalies on regional hydrology tends to decay with time so that precipitation events occurring just before or at the very beginning of a GRACE month have a higher impact on the average water storage of a given month. Conversely, precipitation anomalies occurring during or at the very end of a GRACE month have a lower impact on the water storage anomalies, or may even occur after the latest GRACE overpass.

Figure 13a shows the results of the same analysis performed with the temperature data. It reveals regions where the integrated effect of antecedent temperatures can be statistically related to water storage anomalies. Temperature is one of the main controls for evaporative

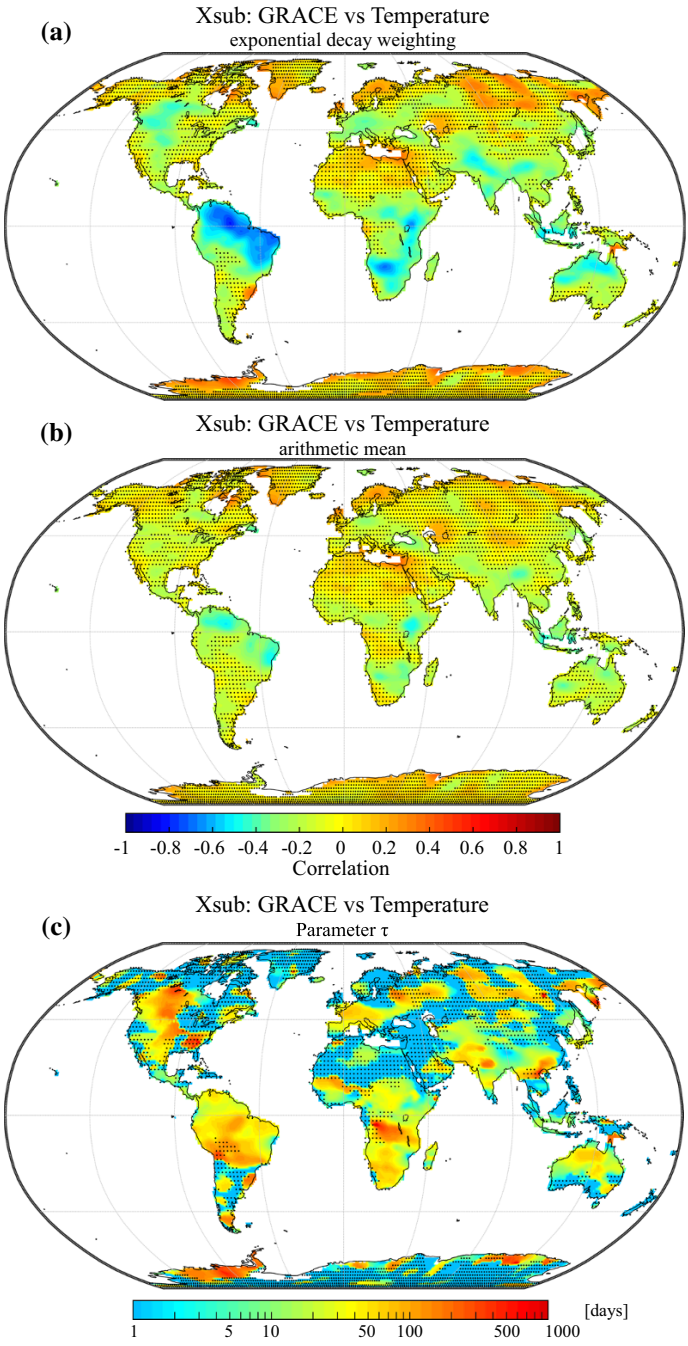


**Fig. 13** **a** Correlation between the subseasonal variability of water storage and temperature averaged with the weighting function introduced in Sect. 3.2 (Eq. 9). **b** Correlation between the subseasonal variability of water storage and temperature averaged using the arithmetic mean (Eq. 3). **c** Value of the calibrated decay parameter ($\tau$) with units of days. Stippling indicates regions with non-significant correlation coefficients ($p < 0.05$)

demand, and hence, negative correlations are expected and can indeed be found over many regions of the world, especially over South America, South Africa, the region of the African Great Lakes, India, Indonesia and northern Australia. As for precipitation, the use of the exponential decay approach leads to enhanced correlations when compared to the arithmetic mean (Fig. 13b). However, improvements are less important than for precipitation and are often concentrated in regions where a significant relationship can already be found with the simple mean. Decay time scales over these regions (Fig. 13c) generally fall between 1 to 3 months, yielding a data-driven first-order estimate of how long temperature anomalies can significantly impact the subsequent state of terrestrial water storage. Positive and significant correlations can occasionally be found over some areas, notably over Siberia, Scandinavia and Antarctica. For these regions, we hypothesize that these positive correlations could reflect the tendency of warm winters to be more humid in comparison with cold winters. On the other hand, warm summers are also expected to increase snow melt so that we cannot come to a definitive conclusion for these regions based on the presented results.

### 4.6 Droughts

In Fig. 14a, we show the maximum *average storage deficit* (see Sect. 3.4) ever observed for all drought events identified in the GRACE record. The year corresponding to this maximum is depicted in Fig. 14b for events with a magnitude larger than 30 mm. This threshold was chosen to mask out smaller features which are difficult to interpret in a global assessment but may still be relevant in a regional context. Many droughts that have previously been documented in the GRACE literature can be identified, notably the 2010 Amazon drought, which is additionally illustrated in Fig. 15a. Drought events in the Amazon basin were shown to be related to precipitation deficits and ENSO (Davidson et al. 2012; Frappart et al. 2013). A multi-year drought is also found for the period 2004–2008 (Fig. 15a) and likely corresponds to the multiple consecutive dry years identified, for instance, by Frappart et al. (2012) and Thomas et al. (2014). Note that this is related to the chosen drought metric, which might not capture all relevant aspects. The ongoing drought in the Central Valley of California is also identified in Fig. 14b, and the time series of the average storage deficit (Fig. 15b) shows that this region also suffered from multiple dry episodes in previous years. This was already identified in previous studies which related these recurrent drought events to severe groundwater depletion (Famiglietti et al. 2011; Famiglietti 2014; Chen et al. 2015). Other documented events identified in Fig. 14b include the 2008–2009 drought in the La Plata basin (Abelen et al. 2015), the 2010–2013 drought in Texas (Long et al. 2013), the 2007–2009 drought in the south-eastern USA (Houborg et al. 2012) and the 2012–2015 North American drought (Chew and Small 2014; Hoerling et al. 2013). We also identify the 2006–2007 dry conditions over Lake Victoria (Swenson and Wahr 2009) and the African Great lakes (Becker et al. 2010) and the 2006–2008 drought in the Zambezi basin (Thomas et al. 2014), which are, in this analysis, captured together as a large-scale and spatially contiguous event. Drought conditions can also be found in northern India for the period 2009–2010 even though the linear trend due to groundwater depletion has been removed from the data prior to drought identification. The year 2009 was indeed shown to be the driest year of the decade for this region in terms of precipitation (Chen et al. 2014) and resulted in higher groundwater abstraction rates. Our analysis shows that the average storage deficit was consecutively maximal in 2010.

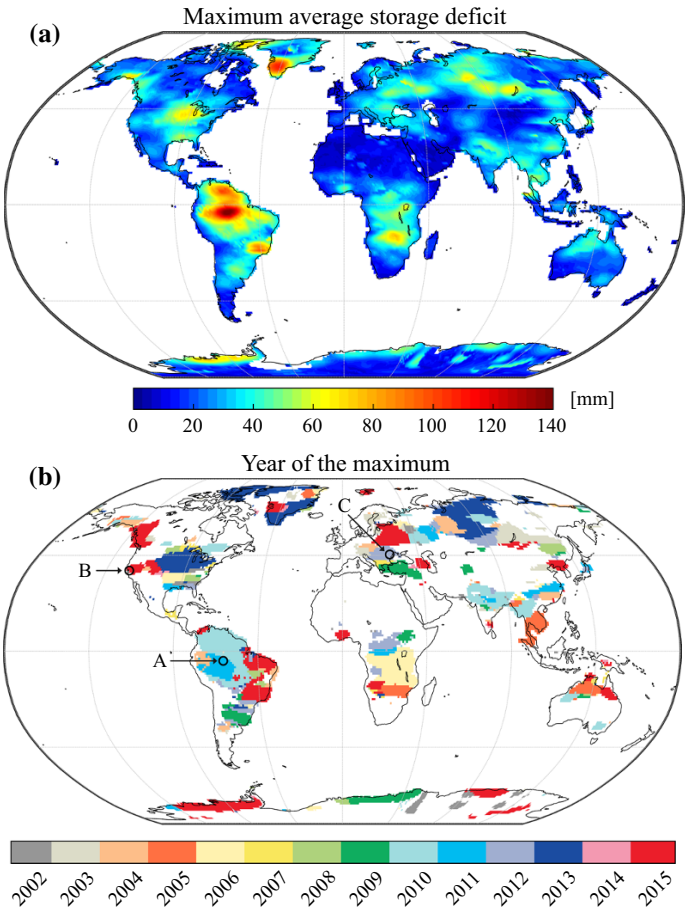


**Fig. 14** **a** Maximum value of the average storage deficit observed in the period April 2002–August 2015, expressed in mm of equivalent water height. **b** Year corresponding to the maximum value of the average storage deficit, showing only regions with a deficit larger than 30 mm. Letters *A*–*C* correspond to the location of the time series in Fig. 15

The Sumatra region also exhibits an important "deficit" which, as confirmed by a local investigation, is probably an artefact caused by the 2004 earthquake. In Australia, multi-year droughts have been related to precipitation deficits (García-García et al. 2011). However, due to the long duration of these decadal drought events, the average storage deficit is lower. Our results also reveal undocumented features found in the GRACE record, such as a dry event from 2012 to 2014 over south-eastern Europe (Figs. 14b, 15c) as well as a severe drought in the Sao Paulo region and a moderate drought over North Korea in 2015 (both still ongoing at the time of writing). A dry period can also be identified during 2010–2011 to the North of the Caspian Sea and is likely associated with the 2010 Russian heatwave. Many other events can also be found over central Russia and were, to our knowledge, never identified using GRACE data.

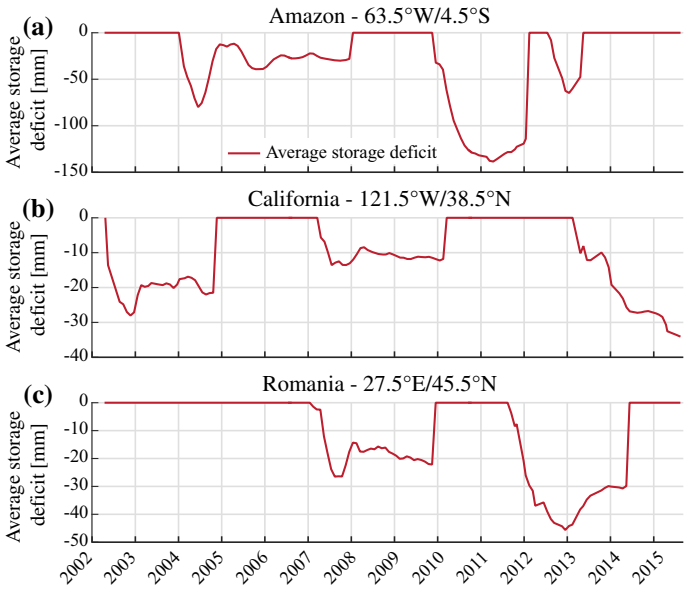


**Fig. 15** Time series of average water storage deficit for grid cells (see location in Fig. 14b) in **a** Amazon (63.5°W/4.5°S), **b** California (121.5°W/38.5°N), **c** Romania (27.5°E/45.5°N)

## 5 Conclusions

In this study, we have decomposed the GRACE time series into (1) linear trends, (2) nonlinear inter-annual anomalies, (3) seasonal cycles and (4) subseasonal residuals. The relative importance of each of these components with respect to the original GRACE signal has been evaluated, allowing for a global assessment of the dominant features of temporal variability in terrestrial water storage. In most cases, the GRACE signal is dominated by seasonal or/and long-term variability, while subseasonal variability generally accounts for a small fraction of the total signal variance. Partitioning the long-term variability into linear trends and nonlinear components reveals that some regions are dominated by linear trends, while nonlinear inter-annual variability is prevalent in others. The magnitudes of the linear trends have been quantified using the robust Theil–Sen estimator, reproducing many already documented trends but also revealing some features that had not been identified previously. In addition, the significance of the trends was evaluated using statistical hypothesis testing techniques which take serial correlation (autocorrelation) into account, contrasting the common practice in the GRACE literature.

In a more detailed analysis, each component of temporal variability (except linear trends) has been compared with equivalent components extracted from daily precipitation and temperature time series of the atmospheric reanalysis ERA-Interim:

- *Inter-annual variability* We have found that the inter-annual variability of GRACE can be only partly related to anomalies in precipitation and temperature, confirming the results of previous regional studies. Although limitations of the considered atmospheric reanalysis may alter the results at the regional level, this suggests that the inter-annual

variability of GRACE is only partly related to the investigated atmospheric drivers, potentially highlighting the role of human water use as additional driver.

- *Seasonal variability* We have provided a comprehensive overview on the seasonality of terrestrial water storage and related it to the seasonal cycles of both precipitation and temperature. In tropical and equatorial regions, the seasonal cycle of precipitation was generally found to precede terrestrial water storage with a temporal lag of one to 2 months, while the seasonal cycle of temperature would typically be phase shifted by 6 months with respect to water storage. However, this was clearly not the case in temperate and cold regions, which is probably due to the more complex interplay between precipitation, storage processes, snow dynamics and temperature.
- *Subseasonal variability* We have shown that high-frequency variability of the GRACE record can be reconstructed from precipitation anomalies once an adequate averaging filter is applied to the daily precipitation forcing. This filter was designed to explicitly take the effect of earlier precipitation into account when comparing daily precipitation series with monthly GRACE data. This new method yields substantially better results compared to the classical approach based on monthly arithmetic means, providing a new perspective on the hydrological value of subseasonal (month to month) fluctuations of the GRACE signal, which have partly been interpreted as noise in previous studies.
- *Droughts* Finally, we have surveyed extreme dry events in the GRACE time series. The most important anomalies in terms of water storage deficits were documented on a global scale and related to droughts already described in the existing literature. Undocumented features were also identified using this global approach and will be subject to further investigation.

In summary, we have surveyed key features of temporal variability in the GRACE record and related them to the dominant atmospheric drivers, in contrast to the common practice of comparing GRACE terrestrial water storage to hydrological model simulations. We have related our results to physical interpretations from the rich body of regional GRACE studies, resulting in a comprehensive overview which will both contribute to a general understanding of terrestrial water storage and provide a global observation-based reference for hydrologists and climate scientists. As a novelty, we have shown that high-frequency (month to month) fluctuations of the GRACE signal contain a meaningful hydrological signal, which can be reconstructed from daily precipitation forcing. These findings have important implications for the assessment of GRACE uncertainties as well as for comparisons with hydrological model simulations.

**Acknowledgments** This research was funded by the ERC DROUGHT-HEAT project (Contract No. 617518). GRACE land mass grids were processed by the Jet Propulsion Laboratory (JPL) GRACE Team and are available at http://grace.jpl.nasa.gov, supported by the NASA MEaSUREs Program. The European Centre for Medium-Range Weather Forecasts (ECMWF) and ERA-Interim teams are gratefully acknowledged for providing the atmospheric reanalyses. We also thank the two anonymous reviewers whose comments and suggestions helped improve and clarify this manuscript.

## Appendix 1: STL for Unevenly Spaced Time Series

STL was introduced by Cleveland et al. (1990) for evenly spaced time series. In this appendix, we present a summary of a simplified STL procedure that includes a modification of the original algorithm for unevenly spaced time series. An important difference with the original STL authored by Cleveland et al. is that the seasonal cycle is defined as constant, i.e. it is not allowed to vary in shape or amplitude over time. We also introduce a modification in the computation of robustness weights that accounts for time series exhibiting large differences in variance (heteroskedasticity) between seasons.

Our focus is to decompose the total signal of a given time series $\mathbf{X} = \{x_1, \ldots, x_i, \ldots, x_n\}$ associated with a time vector $\mathbf{T} = \{t_1, \ldots, t_i, \ldots, t_n\}$ into a constantly repeating seasonal component $X_{\text{seas}}$, a long-term trend component $X_{\text{long}}$ and the remaining subseasonal residuals $X_{\text{sub}}$.

The STL procedure consists of an inner loop and an outer loop. In the inner loop, seasonal and trend components are estimated from the time series using several passes of smoothing filters. In the outer loop, robustness weights are estimated to reduce the influence of outliers in the time series and are used in the next iteration of the inner loop. This procedure stops once some user-defined stability criterion has been reached.

### Locally Weighted Regression (Loess)

Since the algorithm involves multiple passes of a smoothing filter based on locally weighted regression (Loess), we first present a generic formulation for this smoothing filter. The Loess estimator of $x$ at time $t_z$ is denoted $g(t_z)$ and is given by a weighted polynomial fit of degree $d$ to the values of $\mathbf{X}$ that are in the vicinity of $t_z$ and are given some weights $w$. This vicinity is restricted in time by a maximum time-lag parameter $\lambda$. The weights $w_i$ associated with each values of $\mathbf{X}$ that are in the vicinity of $t_z$ are given by the tricube function (Eq. 11).

$$w_i = \begin{cases} 0, & \text{if} \quad |D(t_i, t_z)| > \lambda \\ \left[1 - \left(\dfrac{|D(t_i, t_z)|}{\lambda}\right)^3\right]^3, & \text{if} \quad |D(t_i, t_z)| \leq \lambda \end{cases} \tag{11}$$

where $D(t_i, t_z)$ is a function of the distance in time between the two points. The values of $\mathbf{X}$ closest to $t_z$ will thus have the highest weights. Hence, for each prediction point $t_z$, $\mathbf{X}$ is associated with a vector of weights $\mathbf{W}$ that depends on $t_z$, $\lambda$ and the nature of the distance function $D$:

$$\mathbf{W}(t_z, \lambda, D) = \{w_i, \ldots, w_n\} \tag{12}$$

The degree of the polynomial fit $g(t_z)$ that is fitted at each $t_z$ has to be chosen by the user depending on the application (usually a degree 1 or 2 polynomial is sufficient). Once this is performed for every time step in $\mathbf{T}$, we obtain $\mathbf{G} = \{g(t_1), \ldots, g(t_n)\}$, the so-called *local regression* of the original time series.

We introduce two different metrics for the distance $D(t_i, t_z)$ between two points in time. The first one is simply an *absolute distance* in time and is given by:

$$D_{\text{abs}}(t_i, t_z) = t_i - t_z \tag{13}$$

The second one is the *periodic distance* and depends on the length $p$ of the chosen periodicity, for instance, suppose the time vector $\mathbf{T}$ is in units of days, then $p$ will be equal to 365.25 days for a seasonal periodicity. The periodic distance is given by:

$$D_{\text{per}}(t_i, t_z) = \left[\left(t_i - t_z + \frac{p}{2}\right) \bmod p\right] - \frac{p}{2} \tag{14}$$

where mod is the modulo operator. Thus, time points spaced from $t_z$ by multiples of exactly $p$ days are assigned a null distance, and then, the distance linearly increases until the time points spaced by multiples of $p/2$ days are assigned the maximum distance. Note that these distance metrics are used not only for the calculation of weights but also as the input vector of the polynomial fit $g(t_z)$ to the values of $\mathbf{X}$.

## Inner Loop

The inner loop of the STL procedure aims at estimating the seasonal and long-term components of the time series $\mathbf{X}$ through the following steps.

*Step 1 Compute the detrended time series* $\boldsymbol{X}$* On the very first pass of the inner loop, the long-term trend $\boldsymbol{X}_{\text{long}}$ will not be known yet so that $\mathbf{X}$* is simply the original time series $\mathbf{X}$. Otherwise, $\boldsymbol{X}_{\text{long}}$ is subtracted from $\mathbf{X}$, yielding the detrended time series $\mathbf{X}$*.

*Step 2 Compute the seasonal cycle* $\mathbf{X}_{\text{seas}}$ The seasonal cycle is estimated at all points in $\mathbf{T}$ from $\mathbf{X}$* using Loess with $D_{\text{per}}$ and a free parameter $\lambda_{\text{per}}$ that defines the vicinity in terms of periodic distance. The weight vector used in the local polynomial regression is denoted $W_{\text{per}}$:

$$W_{\text{per}}(t_z) = W\left(t_z, \lambda_{\text{per}}, D_{\text{per}}\right) \tag{15}$$

Note: after the first iteration of the inner and outer loops, $W_{\text{per}}$ is used in combination with the robustness weights $W_{\text{robust}}$. The weights simply correspond to the product of $W_{\text{per}}$ and $W_{\text{robust}}$.

*Step 3 Compute deseasonalized time series* $\boldsymbol{X}^{\text{D}}$ A deseasonalized time series $\mathbf{X}^{\text{D}}$ is obtained by subtracting the seasonal cycle $\boldsymbol{X}_{\text{seas}}$ from the original time series $\mathbf{X}$.

*Step 4 Compute the long-term trend* $X_{\text{long}}$ The long-term trend is estimated after applying Loess to the deseasonalized time series $\mathbf{X}^{\text{D}}$ with the distance function $D_{\text{abs}}$ and parameter $\lambda_{\text{long}}$ which defines the associated weight vector $W_{\text{long}}$.

$$W_{\text{long}}(t_z) = W\left(t_z, \lambda_{\text{long}}, D_{\text{abs}}\right) \tag{16}$$

As in step 2, these weights are used in combination with the robustness weights $W_{\text{robust}}$ after the first iteration of the inner and the outer loop.

## Outer Loop

Once an initial run of the inner loop has been carried out, the original time series can be decomposed into $\mathbf{X} = \boldsymbol{X}_{\text{long}} + \boldsymbol{X}_{\text{seas}} + \mathbf{X}_{\text{resid}}$, where $\mathbf{X}_{\text{resid}}$ corresponds to the residuals. Following Cleveland et al. (1990), extremely large residuals are assumed to correspond to outliers and are assigned a small or a zero weight. These weights are defined using the bisquare function:

$$w_{\text{robust}} = \begin{cases} 0, & \text{if} \quad |x_{\text{resid}}| > h \\ \left[1 - \left(\frac{|x_{\text{resid}}|}{h}\right)^2\right]^2, & \text{if} \quad |x_{\text{resid}}| \leq h \end{cases} \tag{17}$$

where $h$ is:

$$h = 6 \cdot \text{median}(|\mathbf{X}_{\text{resid}}|) \tag{18}$$

However, a problem arises when time series exhibit seasonal heteroskedasticity because the value of $h$ would change when different seasons of the time series are considered. A typical case of seasonal heteroskedasticity is when precipitation totals are very low during the dry season but exhibit high variability during the wet season. If we followed the approach of Cleveland et al., relatively small outliers in the dry season would be unlikely detected, whereas large but still realistic variations during the wet season would be more likely detected as outliers. This problem can be avoided by introducing seasonally varying estimates of $h$. This is done by calculating $h$ at each prediction point $t_z$ using a weighted median with the weights $W_{\text{per}}$ computed from the periodic distance (step 2):

$$h(t_z) = 6 \cdot \text{median}\big(|\mathbf{X}_{\text{resid}}|, W_{\text{per}}(t_z)\big) \tag{19}$$

## Choosing the Parameters

The following parameters need to be defined: $p$ the length of each cycle of the seasonal component; $d$ the degree of the weighted polynomial regression; $\text{n}_{\text{inner}}$ the number of passes through the inner loop; $\text{n}_{\text{outer}}$ the number of iterations of the outer loop; $\lambda_{\text{per}}$ the maximum time lag for the computation of the seasonal component; $\lambda_{\text{long}}$ the maximum time lag for the computation of the long-term component

Parameter $p$ is obviously determined by the nature of the investigated time series (here, $p = 365.25$). We chose a polynomial of degree $d = 2$ in order to hinder smoothing of the low and high peaks of the seasonal cycle. For the trend component, a polynomial of degree $d = 1$ is sufficient. The number of passes and iterations was chosen so that the resulting decomposition reaches stability. For the number of passes of the inner loop, Cleveland et al. recommend $n_{\text{inner}} = 2$. Regarding $n_{\text{outer}}$, we experimentally determined that $n_{\text{outer}} = 3$ was sufficient for our application.

The parameter $\lambda_{\text{per}}$ determines the smoothness of the seasonal cycle, with larger values, resulting in a smoother estimate of the seasonal cycle. On the other hand, smaller values of $\lambda_{\text{per}}$ will reduce the number of points actually used in the local regression so that the resulting seasonal cycle is more likely to be affected by outliers or sudden changes arising from the uneven spacing of the time series. Hence, the choice of $\lambda_{\text{per}}$ is a balanced consideration between accuracy and robustness in the representation of the seasonal cycle. In this paper, a good compromise was experimentally found with $\lambda_{\text{per}} = 60$ days.

The parameter $\lambda_{\text{long}}$ controls the degree of leakage of the long-term component into the residuals. Larger values of the parameter will result in a smoother estimate of the trend but also cause some of the long-term signal to be incorporated into the residuals. Vice versa, smaller values of this parameter will make the long-term component more sensitive to high-frequency variability. In this application, we followed the recommendations from Cleveland et al. who showed that $\lambda_{\text{long}} = 1.5 \times p$ provides a good compromise in most cases.

## Appendix 2

### Analytical Integration of the Weighting Function

Integrating Eq. 6 over the interval $\left[a_j, b_j\right]$ associated with the monthly interval $t_j^*$ must be done with care since the function $w(t, t_i)$ is discontinuous. In total, three cases can be considered: (1) the continuous case where $a_j \geq t_i$ (Fig. 4a), (2) the discontinuous case where $a_j < t_i \leq b_j$ (Fig. 4b) and (3) the continuous case where $b_j < t_i$. For convenience, we note $a_j = a$ and $b_j = b$:

$$\begin{aligned} W\left(t_j^*, t_i\right) &= \int_a^b w(t, t_i)\mathrm{d}t \\ &= \begin{cases} \int_a^b w(t, t_i)\mathrm{d}t & \text{if} \quad a \geq t_i \\ \int_a^{t_i} w(t, t_i)\mathrm{d}t + \int_{t_i}^b w(t, t_i)\mathrm{d}t & \text{if} \quad a < t_i \leq b \\ \int_a^b w(t, t_i)\mathrm{d}t & \text{if} \quad b < t_i \end{cases} \\ &= \begin{cases} -\tau \mathrm{e}^{-\frac{1}{\tau}(b-t_i)} + \tau \mathrm{e}^{-\frac{1}{\tau}(a-t_i)} & \text{if} \quad a \geq t_i \\ -\tau \mathrm{e}^{-\frac{1}{\tau}(b-t_i)} + \tau & \text{if} \quad a < t_i \leq b \\ 0 & \text{if} \quad b < t_i \end{cases} \end{aligned} \tag{20}$$

The normalized version of $W\left(t_j^*, t_i\right)$ is given by (equivalently to Eq. 8):

$$\hat{W}\left(t_j^*, t_i\right) = \frac{W\left(t_j^*, t_i\right)}{\int_{-\infty}^{+\infty} W\left(t_j^*, t_i\right)\mathrm{d}t_i} \tag{21}$$

The denominator has to be decomposed into three continuous parts:

$$\int_{-\infty}^{+\infty} W\left(t_j^*, t_i\right)\mathrm{d}t_i = \int_{-\infty}^{a} W\left(t_j^*, t_i\right)\mathrm{d}t_i + \int_a^b W\left(t_j^*, t_i\right)\mathrm{d}t_i + \int_b^{+\infty} W\left(t_j^*, t_i\right)\mathrm{d}t_i \tag{22}$$

The first part yields:

$$\begin{aligned} \int_{-\infty}^{a} W\left(t_j^*, t_i\right)\mathrm{d}t_i &= \left(\tau^2 \mathrm{e}^{-\frac{1}{\tau}(b-a)} - \tau^2 \mathrm{e}^{-\frac{1}{\tau}(a-a)}\right) - \left(\tau^2 \mathrm{e}^{-\frac{1}{\tau}(b+\infty)} - \tau^2 \mathrm{e}^{-\frac{1}{\tau}(a+\infty)}\right) \\ &= \tau^2 \mathrm{e}^{-\frac{1}{\tau}(b-a)} - \tau^2 \end{aligned} \tag{23}$$

The second part yields:

$$\int_a^b W\left(t_j^*, t_i\right)\mathrm{d}t_i = \left(\tau^2 \mathrm{e}^{-\frac{1}{\tau}(b-b)} + \tau b\right) - \left(\tau^2 \mathrm{e}^{-\frac{1}{\tau}(b-a)} + \tau a\right) = \tau^2 + \tau b - \tau^2 \mathrm{e}^{-\frac{1}{\tau}(b-a)} - \tau a \tag{24}$$

And the third part is:

$$\int_b^{+\infty} W\left(t_j^*, t_i\right)\mathrm{d}t_i = 0 \tag{25}$$

Thus after combining equations 23, 24 and 25, equation 22 can be rewritten as:

$$\int_{-\infty}^{+\infty} W\left(t_j^*, t_i\right)\mathrm{d}t_i = \tau^2 \mathrm{e}^{-\frac{1}{\tau}(b-a)} - \tau^2 + \tau^2 + \tau b - \tau^2 \mathrm{e}^{-\frac{1}{\tau}(b-a)} - \tau a + 0 = \tau(b-a) \tag{26}$$

which is then injected in Eq. 21, yielding the normalized weighting function (Eq. 9):

$$\hat{W}\left(t_j^*, t_i\right) = \frac{W\left(t_j^*, t_i\right)}{\int_{-\infty}^{+\infty} W\left(t_j^*, t_i\right)\mathrm{d}t_i} = \begin{cases} \dfrac{\mathrm{e}^{-\frac{1}{\tau}(b-t_i)} + e^{-\frac{1}{\tau}(a-t_i)}}{b-a} & \text{if} \quad a \geq t_i \\ \dfrac{\mathrm{e}^{-\frac{1}{\tau}(b-t_i)} + 1}{b-a} & \text{if} \quad a < t_i \leq b \\ 0 & \text{if} \quad b < t_i \end{cases} = \begin{cases} \dfrac{\mathrm{e}^{\frac{1}{\tau}(t_i-a)} - e^{\frac{1}{\tau}(t_i-b)}}{b-a} & \text{if} \quad a \geq t_i \\ \dfrac{1 - \mathrm{e}^{\frac{1}{\tau}(t_i-b)}}{b-a} & \text{if} \quad a < t_i \leq b \\ 0 & \text{if} \quad b < t_i \end{cases} \tag{27}$$

## References


Abelen S, Seitz F (2013) Relating satellite gravimetry data to global soil moisture products via data harmonization and correlation analysis. Remote Sens Environ 136:89–98. doi:10.1016/j.rse.2013.04.012

Abelen S, Seitz F, Abarca-del-Rio R, Güntner A (2015) Droughts and floods in the La Plata basin in soil moisture data and GRACE. Remote Sens 7:7324–7349. doi:10.3390/rs70607324

Ahmed M et al (2011) Integration of GRACE (gravity recovery and climate experiment) data with traditional data sets for a better understanding of the time-dependent water partitioning in African watersheds. Geology 39:479–482. doi:10.1130/G31812.1

Ahmed M, Sultan M, Wahr J, Yan E (2014) The use of GRACE data to monitor natural and anthropogenic induced variations in water availability across Africa. Earth-Sci Rev 136:289–300. doi:10.1016/j.earscirev.2014.05.009

Andersen OB, Seneviratne SI, Hinderer J, Viterbo P (2005) GRACE-derived terrestrial water storage depletion associated with the 2003 European heat wave. Geophys Res Lett 32:L18405. doi:10.1029/2005GL023574

Arendt A, Luthcke S, Gardner A, O'Neel S, Hill D, Moholdt G, Abdalati W (2013) Analysis of a GRACE global mascon solution for Gulf of Alaska glaciers. J Glaciol 59:913–924. doi:10.3189/2013JoG12J197

Awange JL, Sharifi MA, Ogonda G, Wickert J, Grafarend EW, Omulo MA (2008) The falling Lake Victoria water level: GRACE, TRIMM and CHAMP satellite analysis of the lake basin. Water Resour Manag 22:775–796. doi:10.1007/s11269-007-9191-y

Barletta V, Bordoni A, Aoudia A, Sabadini R (2012) Squeezing more information out of time variable gravity data with a temporal decomposition approach. Global Planet Change 82–83:51–64. doi:10.1016/j.gloplacha.2011.11.010

Baur O (2012) On the computation of mass-change trends from GRACE gravity field time-series. J Geodyn 61:120–128. doi:10.1016/j.jog.2012.03.007

Becker M, Llovel W, Cazenave A, Güntner A, Crétaux J-F (2010) Recent hydrological behavior of the East African great lakes region inferred from GRACE, satellite altimetry and rainfall observations. C R Geosci 342:223–233. doi:10.1016/j.crte.2009.12.010

Benjamini Y, Hochberg Y (1995) Controlling the false discovery rate: a practical and powerful approach to multiple testing. J R Stat Soc B Methodol 57:289–300

Bergmann I, Ramillien G, Frappart F (2012) Climate-driven interannual ice mass evolution in Greenland. Global Planet Change 82–83:1–11. doi:10.1016/j.gloplacha.2011.11.005

Beven KJ (2012) Rainfall-runoff modelling: the primer, 2nd edn. Wiley, Chichester. doi:10.1002/9781119951001

Bonin JA, Bettadpur S, Tapley BD (2012) High-frequency signal and noise estimates of CSR GRACE RL04. J Geodesy 86:1165–1177. doi:10.1007/s00190-012-0572-5

Chen JL, Tapley BD, Wilson CR (2006a) Alaskan mountain glacial melting observed by satellite gravimetry. Earth Planet Sci Lett 248:368–378. doi:10.1016/j.epsl.2006.05.039

Chen JL, Wilson CR, Tapley BD (2006b) Satellite gravity measurements confirm accelerated melting of Greenland ice sheet. Science 313:1958–1960. doi:10.1126/science.1129007

Chen JL, Wilson CR, Famiglietti JS, Rodell M (2007a) Attenuation effect on seasonal basin-scale water storage changes from GRACE time-variable gravity. J Geodesy 81:237–245. doi:10.1007/s00190-006-0104-2

Chen JL, Wilson CR, Tapley BD, Blankenship DD, Ivins ER (2007b) Patagonia icefield melting observed by gravity recovery and climate experiment (GRACE). Geophys Res Lett 34:L22501. doi:10.1029/2007GL031871

Chen JL, Wilson CR, Tapley BD (2010a) The 2009 exceptional Amazon flood and interannual terrestrial water storage change observed by GRACE. Water Resour Res 46:W12526. doi:10.1029/2010WR009383

Chen JL, Wilson CR, Tapley BD, Longuevergne L, Yang ZL, Scanlon BR (2010b) Recent La Plata basin drought conditions observed by satellite gravimetry. J Geophys Res-Atmos 115:D22108. doi:10.1029/2010JD014689

Chen J, Li J, Zhang Z, Ni S (2014) Long-term groundwater variations in Northwest India from satellite gravity measurements. Global Planet Change 116:130–138. doi:10.1016/j.gloplacha.2014.02.007

Chen J, Famiglietti JS, Scanlon BR, Rodell M (2015) Groundwater storage changes: present status from GRACE observations. Surv Geophys. doi:10.1007/s10712-015-9332-4

Cheng M, Ries J, Tapley B (2011) Variations of the Earth's figure axis from satellite laser ranging and GRACE. J Geophys Res-Solid Earth 116:B01409. doi:10.1029/2010JB000850

Chew CC, Small EE (2014) Terrestrial water storage response to the 2012 drought estimated from GPS vertical position anomalies. Geophys Res Lett 41:6145–6151. doi:10.1002/2014GL061206

Cleveland RB, Cleveland WS, McRae JE, Terpenning I (1990) STL: a seasonal-trend decomposition procedure based on loess. J Off Stat 6:3–73

Crowley JW, Mitrovica JX, Bailey RC, Tamisiea ME, Davis JL (2006) Land water storage within the Congo Basin inferred from GRACE satellite gravity data. Geophys Res Lett 33:L19402. doi:10.1029/2006GL027070

Davidson EA et al (2012) The Amazon basin in transition. Nature 481:321–328. doi:10.1038/nature10717

Dee DP et al (2011) The ERA-interim reanalysis: configuration and performance of the data assimilation system. Q J R Meteorol Soc 137:553–597. doi:10.1002/qj.828

Döll P, Fritsche M, Eicker A, Müller Schmied H (2014a) Seasonal water storage variations as impacted by water abstractions: comparing the output of a global hydrological model with GRACE and GPS observations. Surv Geophys 35:1311–1331. doi:10.1007/s10712-014-9282-2

Döll P, Müller Schmied H, Schuh C, Portmann FT, Eicker A (2014b) Global-scale assessment of groundwater depletion and related groundwater abstractions: combining hydrological modeling with information from well observations and GRACE satellites. Water Resour Res 50:5698–5720. doi:10.1002/2014WR015595

Duan X, Guo J, Shum C, van der Wal W (2009) On the postprocessing removal of correlated errors in GRACE temporal gravity field solutions. J Geodesy 83:1095–1106. doi:10.1007/s00190-009-0327-0

Dufresne JL et al (2013) Climate change projections using the IPSL-CM5 earth system model: from CMIP3 to CMIP5. Climate Dyn 40:2123–2165. doi:10.1007/s00382-012-1636-1
Eicker A, Schumacher M, Kusche J, Doll P, Muller Schmied H (2014) Calibration/data assimilation approach for integrating GRACE data into the water GAP global hydrology model (WGHM) using an ensemble Kalman filter: first results. Surv Geophys 35:1285–1309. doi:10.1007/s10712-014-9309-8
Famiglietti JS (2014) The global groundwater crisis. Nat Climate Change 4:945–948. doi:10.1038/nclimate2425
Famiglietti JS et al (2011) Satellites measure recent rates of groundwater depletion in California's Central Valley. Geophys Res Lett 38:L03403. doi:10.1029/2010GL046442
Feng W, Zhong M, Lemoine J-M, Biancale R, Hsu H-T, Xia J (2013) Evaluation of groundwater depletion in North China using the gravity recovery and climate experiment (GRACE) data and ground-based measurements. Water Resour Res 49:2110–2118. doi:10.1002/wrcr.20192
Forootan E, Kusche J (2012) Separation of global time-variable gravity signals into maximally independent components. J Geodesy 86:477–497. doi:10.1007/s00190-011-0532-5
Forootan E et al (2014a) Multivariate prediction of total water storage changes over West Africa from multi-satellite data. Surv Geophys 35:913–940. doi:10.1007/s10712-014-9292-0
Forootan E et al (2014b) Separation of large scale water storage patterns over Iran using GRACE, altimetry and hydrological data. Remote Sens Environ 140:580–595. doi:10.1016/j.rse.2013.09.025
Frappart F, Ramillien G (2012) Contribution of GRACE satellite gravimetry in global and regional hydrology, and in ice sheets mass balance, water resources management and modeling. In: Purna N (ed) Water resources management and modeling. InTech, p 322. doi:10.5772/34212
Frappart F, Ramillien G, Biancamaria S, Mognard NM, Cazenave A (2006) Evolution of high-latitude snow mass derived from the GRACE gravimetry mission (2002–2004). Geophys Res Lett 33:L02501. doi:10.1029/2005GL024778
Frappart F, Ramillien G, Famiglietti JS (2011a) Water balance of the Arctic drainage system using GRACE gravimetry products. Int J Remote Sens 32:431–453. doi:10.1080/01431160903474954
Frappart F, Ramillien G, Leblanc M, Tweed SO, Bonnet M-P, Maisongrande P (2011b) An independent component analysis filtering approach for estimating continental hydrology in the GRACE gravity data. Remote Sens Environ 115:187–204. doi:10.1016/j.rse.2010.08.017
Frappart F, Papa F, da Silva JS, Ramillien G, Prigent C, Seyler F, Calmant S (2012) Surface freshwater storage and dynamics in the Amazon basin during the 2005 exceptional drought. Environ Res Lett 7:044010. doi:10.1088/1748-9326/7/4/044010
Frappart F, Ramillien G, Ronchail J (2013) Changes in terrestrial water storage versus rainfall and discharges in the Amazon basin. Int J Climatol 33:3029–3046. doi:10.1002/joc.3647
García-García D, Ummenhofer CC, Zlotnicki V (2011) Australian water mass variations from GRACE data linked to Indo-Pacific climate variability. Remote Sens Environ 115:2175–2183. doi:10.1016/j.rse.2011.04.007
Gardner A et al (2013) A reconciled estimate of glacier contributions to Sea level rise: 2003 to 2009. Science 340:852–857. doi:10.1126/science.1234532
Geruo A, Wahr J, Zhong S (2013) Computations of the viscoelastic response of a 3-D compressible Earth to surface loading: an application to glacial isostatic adjustment in Antarctica and Canada. Geophys J Int 192:557–572. doi:10.1093/gji/ggs030
Gudmundsson L, Seneviratne SI (2015) European drought trends. Proc Int Assoc Hydrol Sci 369:75–79. doi:10.5194/piahs-369-75-2015
Gudmundsson L, Tallaksen LM, Stahl K, Fleig AK (2011) Low-frequency variability of European runoff. Hydrol Earth Syst Sci 15:2853–2869. doi:10.5194/hess-15-2853-2011
Güntner A (2008) Improvement of global hydrological models using GRACE data. Surv Geophys 29:375–397. doi:10.1007/s10712-008-9038-y
Güntner A, Schmidt R, Döll P (2007a) Supporting large-scale hydrogeological monitoring and modelling by time-variable gravity data. Hydrogeol J 15:167–170. doi:10.1007/s10040-006-0089-1
Güntner A, Stuck J, Werth S, Döll P, Verzano K, Merz B (2007b) A global analysis of temporal and spatial variations in continental water storage. Water Resour Res 43:W05416. doi:10.1029/2006WR005247
Hamed KH (2009) Exact distribution of the Mann-Kendall trend test statistic for persistent data. J Hydrol 365:86–94. doi:10.1016/j.jhydrol.2008.11.024
Hamed KH, Rao AR (1998) A modified Mann–Kendall trend test for autocorrelated data. J Hydrol 204:182–196. doi:10.1016/S0022-1694(97)00125-X
Han S-C, Shum CK, Bevis M, Ji C, Kuo C-Y (2006) Crustal dilatation observed by GRACE after the 2004 Sumatra–Andaman earthquake. Science 313:658–662. doi:10.1126/science.1128661
Han S-C, Sauber J, Riva R (2011) Contribution of satellite gravimetry to understanding seismic source processes of the 2011 Tohoku-Oki earthquake. Geophys Res Lett 38:L24312. doi:10.1029/2011GL049975

Han S-C, Riva R, Sauber J, Okal E (2013) Source parameter inversion for recent great earthquakes from a decade-long observation of global gravity fields. J Geophys Res-Solid Earth 118:1240–1267. doi:10.1002/jgrb.50116

Hassan AA, Jin S (2014) Lake level change and total water discharge in East Africa Rift Valley from satellite-based observations. Global Planet Change 117:79–90. doi:10.1016/j.gloplacha.2014.03.005

Hinderer J, Andersen O, Lemoine F, Crossley D, Boy J-P (2006) Seasonal changes in the European gravity field from GRACE: a comparison with superconducting gravimeters and hydrology model predictions. J Geodyn 41:59–68. doi:10.1016/j.jog.2005.08.037

Hoerling M et al (2013) Causes and predictability of the 2012 Great Plains drought. B Am Meteorol Soc 95:269–282. doi:10.1175/BAMS-D-13-00055.1

Houborg R, Rodell M, Li B, Reichle R, Zaitchik BF (2012) Drought indicators based on model-assimilated gravity recovery and climate experiment (GRACE) terrestrial water storage observations. Water Resour Res 48:W07525. doi:10.1029/2011WR011291

Ivins ER, Watkins MM, Yuan D-N, Dietrich R, Casassa G, Rülke A (2011) On-land ice loss and glacial isostatic adjustment at the Drake passage: 2003–2009. J Geophys Res Solid Earth 116:B02403. doi:10.1029/2010JB007607

Jiménez Cisneros BE et al. (2014) Freshwater resources. In: Field CB et al. (eds) Climate change 2014: impacts, adaptation, and vulnerability. Part A: global and sectoral aspects. Contribution of working group II to the fifth assessment report of the intergovernmental panel on climate change. Cambridge University Press, pp 229–269. doi:10.1017/cbo9781107415379.008

Joodaki G, Wahr J, Swenson S (2014) Estimating the human contribution to groundwater depletion in the Middle East, from GRACE data, land surface models, and well observations. Water Resour Res 50:2679–2692. doi:10.1002/2013WR014633

Kusche J (2007) Approximate decorrelation and non-isotropic smoothing of time-variable GRACE-type gravity field models. J Geodesy 81:733–749. doi:10.1007/s00190-007-0143-3

Landerer FW, Swenson SC (2012) Accuracy of scaled GRACE terrestrial water storage estimates. Water Resour Res 48:W04531. doi:10.1029/2011WR011453

Larsen CF, Burgess E, Arendt AA, O'Neel S, Johnson AJ, Kienholz C (2015) Surface melt dominates Alaska glacier mass balance. Geophys Res Lett 42:5902–5908. doi:10.1002/2015GL064349

Long D, Scanlon BR, Longuevergne L, Sun AY, Fernando DN, Save H (2013) GRACE satellite monitoring of large depletion in water storage in response to the 2011 drought in Texas. Geophys Res Lett 40:3395–3401. doi:10.1002/grl.50655

Long D, Longuevergne L, Scanlon BR (2015) Global analysis of approaches for deriving total water storage changes from GRACE satellites. Water Resour Res 51:2574–2594. doi:10.1002/2014WR016853

Longuevergne L, Scanlon B, Wilson C (2010) GRACE hydrological estimates for small basins: evaluating processing approaches on the High Plains Aquifer, USA. Water Resour Res 46:W11517. doi:10.1029/2009WR008564

Morishita Y, Heki K (2008) Characteristic precipitation patterns of El Niño/La Niña in time-variable gravity fields by GRACE. Earth Planet Sci Lett 272:677–682. doi:10.1016/j.epsl.2008.06.003

Mudelsee M (2014) Climate time series analysis: classical statistical and bootstrap methods. Atmospheric and oceanographic sciences library, vol 51, 2nd edn. Springer, New York. doi:10.1007/978-90-481-9482-7

Mueller B, Seneviratne SI (2012) Hot days induced by precipitation deficits at the global scale. Proc Natl Acad Sci 109:12398–12403. doi:10.1073/pnas.1204330109

Papa F, Güntner A, Frappart F, Prigent C, Rossow WB (2008) Variations of surface water extent and water storage in large river basins: a comparison of different global data sources. Geophys Res Lett 35:L11401. doi:10.1029/2008GL033857

Phillips T, Nerem RS, Fox-Kemper B, Famiglietti JS, Rajagopalan B (2012) The influence of ENSO on global terrestrial water storage using GRACE. Geophys Res Lett 39:L16705. doi:10.1029/2012GL052495

Ramillien G, Cazenave A, Brunau O (2004) Global time variations of hydrological signals from GRACE satellite gravimetry. Geophys J Int 158:813–826. doi:10.1111/j.1365-246X.2004.02328.x

Ramillien G, Frappart F, Cazenave A, Güntner A (2005) Time variations of land water storage from an inversion of 2 years of GRACE geoids. Earth Planet Sci Lett 235:283–301. doi:10.1016/j.epsl.2005.04.005

Ramillien G, Lombard A, Cazenave A, Ivins ER, Llubes M, Remy F, Biancale R (2006) Interannual variations of the mass balance of the Antarctica and Greenland ice sheets from GRACE. Global Planet Change 53:198–208. doi:10.1016/j.gloplacha.2006.06.003

Ramillien G, Famiglietti JS, Wahr J (2008) Detection of continental hydrology and glaciology signals from GRACE: a review. Surv Geophys 29:361–374. doi:10.1007/s10712-008-9048-9

Ramillien G, Frappart F, Seoane L (2014) Application of the regional water mass variations from GRACE satellite gravimetry to large-scale water management in Africa. Remote Sens 6:7379–7405. doi:10.3390/rs6087379

Rangelova E, van der Wal W, Braun A, Sideris MG, Wu P (2007) Analysis of gravity recovery and climate experiment time-variable mass redistribution signals over North America by means of principal component analysis. J Geophys Res-Earth 112:F03002. doi:10.1029/2006JF000615

Rangelova E, van der Wal W, Sideris MG, Wu P (2010) Spatiotemporal analysis of the GRACE-derived mass variations in North America by means of multi-channel singular spectrum analysis. In: Mertikas SP (ed) Gravity, geoid and earth observation, vol 135. International association of geodesy symposia. Springer Berlin Heidelberg, pp 539–546. doi:10.1007/978-3-642-10634-7_72

Reager JT, Thomas BF, Famiglietti JS (2014) River basin flood potential inferred using GRACE gravity observations at several months lead time. Nat Geosci 7:588–592. doi:10.1038/ngeo2203

Richey AS, Thomas BF, Lo M-H, Famiglietti JS, Swenson S, Rodell M (2015a) Uncertainty in global groundwater storage estimates in a total groundwater stress framework. Water Resour Res 51:5198–5216. doi:10.1002/2015WR017351

Richey AS et al (2015b) Quantifying renewable groundwater stress with GRACE. Water Resour Res 51:5217–5238. doi:10.1002/2015WR017349

Rieser D, Kuhn M, Pail R, Anjasmara IM, Awange J (2010) Relation between GRACE-derived surface mass variations and precipitation over Australia. Aust J Earth Sci 57:887–900. doi:10.1080/08120099.2010.512645

Rodell M, Famiglietti JS (2002) The potential for satellite-based monitoring of groundwater storage changes using GRACE: the High Plains aquifer, Central US. J Hydrol 263:245–256. doi:10.1016/S0022-1694(02)00060-4

Rodell M, Famiglietti JS, Chen J, Seneviratne SI, Viterbo P, Holl S, Wilson CR (2004) Basin scale estimates of evapotranspiration using GRACE and other observations. Geophys Res Lett 31:L20504. doi:10.1029/2004GL020873

Rodell M, Chen J, Kato H, Famiglietti JS, Nigro J, Wilson CR (2007) Estimating groundwater storage changes in the Mississippi River basin (USA) using GRACE. Hydrogeol J 15:159–166. doi:10.1007/s10040-006-0103-7

Rodell M, Velicogna I, Famiglietti JS (2009) Satellite-based estimates of groundwater depletion in India. Nature 460:999–1002. doi:10.1038/nature08238

Sakumura C, Bettadpur S, Bruinsma S (2014) Ensemble prediction and intercomparison analysis of GRACE time-variable gravity field models. Geophys Res Lett 41:1389–1397. doi:10.1002/2013GL058632

Sasgen I et al (2012) Timing and origin of recent regional ice-mass loss in Greenland. Earth Planet Sci Lett 333–334:293–303. doi:10.1016/j.epsl.2012.03.033

Schmeer M, Schmidt M, Bosch W, Seitz F (2012) Separation of mass signals within GRACE monthly gravity field models by means of empirical orthogonal functions. J Geodyn 59–60:124–132. doi:10.1016/j.jog.2012.03.001

Schmidt R et al (2006) GRACE observations of changes in continental water storage. Global Planet Change 50:112–126. doi:10.1016/j.gloplacha.2004.11.018

Schmidt R, Flechtner F, Meyer U, Neumayer KH, Dahle C, König R, Kusche J (2008a) Hydrological signals observed by the GRACE satellites. Surv Geophys 29:319–334. doi:10.1007/s10712-008-9033-3

Schmidt R, Petrovic S, Güntner A, Barthelmes F, Wünsch J, Kusche J (2008b) Periodic components of water storage changes from GRACE and global hydrology models. J Geophys Res-Solid Earth 113:B08419. doi:10.1029/2007JB005363

Schrama EJO, Wouters B, Lavallée DA (2007) Signal and noise in gravity recovery and climate experiment (GRACE) observed surface mass variations. J Geophys Res-Solid Earth 112:B08407. doi:10.1029/2006JB004882

Seitz F, Schmidt M, Shum CK (2008) Signals of extreme weather conditions in Central Europe in GRACE 4-D hydrological mass variations. Earth Planet Sci Lett 268:165–170. doi:10.1016/j.epsl.2008.01.001

Sen PK (1968) Estimates of the regression coefficient based on Kendall's Tau. J Am Stat Assoc 63:1379–1389. doi:10.2307/2285891

Seneviratne SI et al (2010) Investigating soil moisture–climate interactions in a changing climate: a review. Earth-Sci Rev 99:125–161. doi:10.1016/j.earscirev.2010.02.004

Seo KW, Wilson CR, Famiglietti JS, Chen JL, Rodell M (2006) Terrestrial water mass load changes from gravity recovery and climate experiment (GRACE). Water Resour Res 42:W05417. doi:10.1029/2005WR004255

Simmons AJ, Willett KM, Jones PD, Thorne PW, Dee DP (2010) Low-frequency variations in surface atmospheric humidity, temperature, and precipitation: inferences from reanalyses and monthly gridded observational data sets. J Geophys Res-Atmos 115:D01110. doi:10.1029/2009JD012442

Singh A, Seitz F, Schwatke C (2012) Inter-annual water storage changes in the Aral Sea from multi-mission satellite altimetry, optical remote sensing, and GRACE satellite gravimetry. Remote Sens Environ 123:187–195. doi:10.1016/j.rse.2012.01.001

Steffen H, Petrovic S, Müller J, Schmidt R, Wünsch J, Barthelmes F, Kusche J (2009) Significance of secular trends of mass variations determined from GRACE solutions. J Geodyn 48:157–165. doi:10.1016/j.jog.2009.09.029

Swenson SC, Milly PCD (2006) Climate model biases in seasonality of continental water storage revealed by satellite gravimetry. Water Resour Res 42:W03201. doi:10.1029/2005WR004628

Swenson S, Wahr J (2006) Post-processing removal of correlated errors in GRACE data. Geophys Res Lett 33:L08402

Swenson SC, Wahr J (2009) Monitoring the water balance of Lake Victoria, East Africa, from space. J Hydrol 370:163–176. doi:10.1016/j.jhydrol.2009.03.008

Swenson S, Chambers D, Wahr J (2008) Estimating geocenter variations from a combination of GRACE and ocean model output. J Geophys Res-Solid Ea 113:B08410. doi:10.1029/2007JB005338

Syed TH, Famiglietti JS, Rodell M, Chen J, Wilson CR (2008) Analysis of terrestrial water storage changes from GRACE and GLDAS. Water Resour Res 44:W02433. doi:10.1029/2006WR005779

Tamisiea ME, Mitrovica JX, Davis JL (2007) GRACE gravity data constrain ancient ice geometries and continental dynamics over Laurentia. Science 316:881–883. doi:10.1126/science.1137157

Tapley BD, Bettadpur S, Ries JC, Thompson PF, Watkins MM (2004a) GRACE measurements of mass variability in the Earth System. Science 305:503–505. doi:10.1126/science.1099192

Tapley BD, Bettadpur S, Watkins M, Reigber C (2004b) The gravity recovery and climate experiment: mission overview and early results. Geophys Res Lett 31:L09607. doi:10.1029/2004GL019920

Thomas AC, Reager JT, Famiglietti JS, Rodell M (2014) A GRACE-based water storage deficit approach for hydrological drought characterization. Geophys Res Lett 41:1537–1545. doi:10.1002/2014GL059323

Velicogna I (2009) Increasing rates of ice mass loss from the Greenland and Antarctic ice sheets revealed by GRACE. Geophys Res Lett 36:L19503. doi:10.1029/2009GL040222

Velicogna I, Wahr J (2006) Acceleration of Greenland ice mass loss in spring 2004. Nature 443:329–331. doi:10.1038/nature05168

Velicogna I, Wahr J (2013) Time-variable gravity observations of ice sheet mass balance: precision and limitations of the GRACE satellite data. Geophys Res Lett 40:3055–3063. doi:10.1002/grl.50527

Velicogna I, Tong J, Zhang T, Kimball J (2012) Increasing subsurface water storage in discontinuous permafrost areas of the Lena River basin, Eurasia, detected from GRACE. Geophys Res Lett 39:L09403. doi:10.1029/2012GL051623

Velicogna I, Sutterley TC, van den Broeke MR (2014) Regional acceleration in ice mass loss from Greenland and Antarctica using GRACE time-variable gravity data. Geophys Res Lett 41:8130–8137. doi:10.1002/2014GL061052

Ventura V, Paciorek CJ, Risbey JS (2004) Controlling the proportion of falsely rejected hypotheses when conducting multiple tests with climatological data. J Climate 17:4343–4356. doi:10.1175/3199.1

Vey S, Steffen H, Muller J, Boike J (2013) Inter-annual water mass variations from GRACE in central Siberia. J Geodesy 87:287–299. doi:10.1007/s00190-012-0597-9

Voss KA, Famiglietti JS, Lo M, de Linage C, Rodell M, Swenson SC (2013) Groundwater depletion in the Middle East from GRACE with implications for transboundary water management in the Tigris-Euphrates-Western Iran region. Water Resour Res 49:904–914. doi:10.1002/wrcr.20078

Wahr J (2015) Time-variable gravity from satellites. In: Schubert G (ed) Treatise on geophysics, 2nd edn. Elsevier, Oxford, pp 193–213. doi:10.1016/B978-0-444-53802-4.00065-8

Wahr J, Swenson S, Zlotnicki V, Velicogna I (2004) Time-variable gravity from GRACE: first results. Geophys Res Lett 31:L11501. doi:10.1029/2004GL019779

Wang H et al (2013) Increased water storage in North America and Scandinavia from GRACE gravity data. Nat Geosci 6:38–42. doi:10.1038/ngeo1652

Washington R, James R, Pearce H, Pokam WM, Moufouma-Okia W (2013) Congo Basin rainfall climatology: can we believe the climate models? Philos T R Soc B. doi:10.1098/rstb.2012.0296

Werth S, Güntner A, Schmidt R, Kusche J (2009) Evaluation of GRACE filter tools from a hydrological perspective. Geophys J Int 179:1499–1515. doi:10.1111/j.1365-246X.2009.04355.x

Wilks DS (2006) On "field significance" and the false discovery rate. J Appl Meteorol Clim 45:1181–1189. doi:10.1175/JAM2404.1

Wilks DS (2011) Statistical methods in the atmospheric sciences. international geophysics series, vol 100, 3rd edn. Academic Press, Amsterdam

Wouters B, Chambers D, Schrama EJO (2008) GRACE observes small-scale mass loss in Greenland. Geophys Res Lett 35:L20501. doi:10.1029/2008GL034816

Wouters B, Bonin JA, Chambers DP, Riva REM, Sasgen I, Wahr J (2014) GRACE, time-varying gravity, Earth system dynamics and climate change. Rep Prog Phys. doi:10.1088/0034-4885/77/11/116801

Wu X et al (2010) Simultaneous estimation of global present-day water transport and glacial isostatic adjustment. Nat Geosci 3:642–646. doi:10.1038/ngeo938

Xavier L, Becker M, Cazenave A, Longuevergne L, Llovel W, Filho OCR (2010) Interannual variability in water storage over 2003–2008 in the Amazon Basin from GRACE space gravimetry, in situ river level and precipitation data. Remote Sens Environ 114:1629–1637. doi:10.1016/j.rse.2010.02.005

Yue S, Wang C (2004) The Mann–Kendall test modified by effective sample size to detect trend in serially correlated hydrological series. Water Resour Manag 18:201–218. doi:10.1023/B:WARM.0000043140.61082.60

Yue S, Pilon P, Phinney B, Cavadias G (2002) The influence of autocorrelation on the ability to detect trend in hydrological series. Hydrol Process 16:1807–1829. doi:10.1002/hyp.1095

Zaitchik B, Rodell M, Reichle R (2008) Assimilation of GRACE terrestrial water storage data into a land surface model: results for the Mississippi River basin. J Hydrometeorol 9:535–548. doi:10.1175/2007JHM951.1

DOI 10.1007/978-3-319-32449-4_9
Reprinted from *Surveys in Geophysics* Journal, DOI 10.1007/s10712-015-9332-4

# Groundwater Storage Changes: Present Status from GRACE Observations

**Jianli Chen[1] · James S. Famiglietti[2,3] · Bridget R. Scanlon[4] · Matthew Rodell[5]**

Received: 25 March 2015 / Accepted: 2 July 2015 / Published online: 28 July 2015


**Abstract** Satellite gravity measurements from the Gravity Recovery and Climate Experiment (GRACE) provide quantitative measurement of terrestrial water storage (TWS) changes with unprecedented accuracy. Combining GRACE-observed TWS changes and independent estimates of water change in soil and snow and surface reservoirs offers a means for estimating groundwater storage change. Since its launch in March 2002, GRACE time-variable gravity data have been successfully used to quantify long-term groundwater storage changes in different regions over the world, including northwest India, the High Plains Aquifer and the Central Valley in the USA, the North China Plain, Middle East, and southern Murray–Darling Basin in Australia, where groundwater storage has been significantly depleted in recent years (or decades). It is difficult to rely on in situ groundwater measurements for accurate quantification of large, regional-scale groundwater storage changes, especially at long timescales due to inadequate spatial and temporal coverage of in situ data and uncertainties in storage coefficients. The now nearly 13 years of GRACE gravity data provide a successful and unique complementary tool for monitoring and measuring groundwater changes on a global and regional basis. Despite the successful applications of GRACE in studying global groundwater storage change, there are still some major challenges limiting the application and interpretation of GRACE data. In this paper, we present an overview of GRACE applications in groundwater studies and discuss if and how the main challenges to using GRACE data can be addressed.

✉ Jianli Chen
chen@csr.utexas.edu

[1] Center for Space Research, University of Texas at Austin, Texas, TX 78759, USA

[2] Jet Propulsion Laboratory, California Institute of Technology, Pasadena, CA 91109, USA

[3] Department of Earth System Science, University of California, Irvine, CA 92697, USA

[4] Bureau of Economic Geology, Jackson School of Geosciences, University of Texas at Austin, Texas, TX 78759, USA

[5] Hydrological Sciences Laboratory, NASA Goddard Space Flight Center, Greenbelt, MD 20771, USA

**Keywords** Groundwater · GRACE · Satellite gravity · Groundwater depletion · Land surface model · Well data

## 1 Introduction

Groundwater storage is a vital resource to sustain agricultural, industrial, and domestic activities both in populous countries such as China and India, and in arid regions lacking adequate alternative water resources (e.g., the Middle East and North Africa). Groundwater, as an important component of the global water cycle, also plays a key role in the global water cycle's connections with climate change. Groundwater storage change is controlled by the balance between recharge (i.e., inflow into the groundwater body, or aquifer, from the soil or surface water reservoirs) and discharge (i.e., outflow from the groundwater to surface water systems) or groundwater abstractions (Freeze and Cherry 1979). Extended drought and/or excessive groundwater abstractions can lead to groundwater depletion and regional water resource scarcity and pose significant impacts on the ecosystem and economic and social developments (Foster and Loucks 2006; Rodell et al. 2009; Gleeson et al. 2010; Famiglietti 2014).

During the past few decades, intensive groundwater pumping, especially for agricultural irrigation, has led to dramatic declines of groundwater levels in many parts of the world, which in some places can be as much as up to 100–200 m (Rodell and Famiglietti 2002; Wang et al. 2006; Scanlon et al. 2012a, b; Famiglietti 2014). Due to the extremely slow process of groundwater recharge, excessive depletion of groundwater resources in those regions will not be fully restored in the foreseeable future. Groundwater depletion not only results in insufficient water to support sustainable local economic development, but also increases energy consumption as more energy is required to pump groundwater from greater depths below the surface, increasing demand on an already constrained energy supply (Konikow and Kendy 2005). Groundwater depletion can also lead to significant land subsidence, which, in extreme cases as in the San Joaquin Valley of California, has reached values of 1.2 m, impacting pipelines and transport systems. Other regions with severe subsidence include Bangkok, Thailand (Giao and Nutalaya 2006) and Jakarta, Indonesia (Abidin et al. 2008), increasing flood risks.

Monitoring and understanding groundwater storage changes, especially the long-term variability, are critical for maintaining sustainable economic development and healthy ecosystems, and better understanding the global and regional hydrological cycles and climate change. Despite their importance to freshwater supplies, groundwater resources are often poorly monitored, and accurate quantification of groundwater storage change has been difficult due to insufficient in situ groundwater level observations (Famiglietti et al. 2011). Even though in some regions in developed countries (such as the USA and Australia) monitoring well networks can be dense, quantifying regional groundwater storage changes from well data is still complicated by uncertainties in aquifer storage coefficients to convert water level changes to storage volumes (Rodell et al. 2007). Inadequate spatial and temporal coverage of monitoring networks is also a general issue. Additional complications include data formatting and inconsistencies, and human and mechanical monitoring, and recording errors. Furthermore, restrictive data sharing policies (due to political reasons) in other parts of the world may also limit studies of groundwater storage change using in situ well data.

Uncertainties in groundwater recharge estimates from water budgets in land surface models, e.g., the WaterGAP Global Hydrology Model (WGHM) can be large, particularly in semiarid regions (Döll et al. 2012). The primary discharge mechanism is often groundwater pumpage estimates, often based on country estimates from the Food and Agricultural Organization (FAO), also highly uncertain. In addition, limited in situ observations of groundwater levels reduce the reliability of the simulated groundwater storage (GWS) changes, especially at long timescales (Döll et al. 2012). These parameters are often unknown or difficult to quantify on a large regional basis. Therefore, accurately modeling long-term GWS change or groundwater depletion is challenging.

The Gravity Recovery and Climate Experiment (GRACE) is the first dedicated satellite time-variable gravity mission and provides an alternative and unique approach for monitoring large-scale mass changes in the Earth system (Tapley et al. 2004). Since its launch in March 2002, GRACE has been measuring global gravity changes on a monthly basis, with unprecedented accuracy (Wahr et al. 2004). Earth gravity changes are caused by mass redistribution within different components of the Earth's system, including the atmosphere, ocean, hydrosphere, cryosphere, and solid Earth. GRACE-observed gravity changes can be used to infer terrestrial water storage (TWS, the sum of snow water equivalent, surface water, soil water, and groundwater storage) changes, given that other geophysical causes of gravity change can be estimated and removed (e.g., Wahr et al. 2004; Chen et al. 2009). As atmospheric and oceanic contributions to gravity change have been removed in GRACE data processing using estimates from numerical models (Bettadpur 2012), over non-glaciated land areas, GRACE-observed mass changes mostly reflect TWS changes. Therefore, when water storage changes in snow, surface water reservoirs, and soil are known, GRACE gravity measurements provide an alternative and complementary tool for quantifying GWS changes over large regions.

GRACE time-variable gravity data have been successfully used to quantify long-term GWS changes in different regions over the world, including the northwest India (NWI) (Rodell et al. 2009), the High Plains Aquifer (HPA) (Scanlon et al. 2012b) and Central Valley in the USA (Famiglietti et al. 2011), the North China Plain (NCP) (Feng et al. 2013), the Middle East (Voss et al. 2013), and southern Murray–Darling Basin (MDB) in Australia, where groundwater storages have been significantly depleted in recent years (or decades) (Leblanc et al. 2009, 2012). In a commentary article, Famiglietti (2014) discussed the groundwater crisis which many parts of the world are facing in the recent decade through GRACE-observed groundwater depletions in some major aquifers or regions in the world. In this paper, we present an overview of the present status of monitoring GWS changes using GRACE time-variable gravity measurements, outline major challenges when using GRACE data in groundwater studies, and discuss if and how these challenges can be addressed.

## 2 Groundwater Depletion from GRACE

GRACE time-variable gravity fields are represented by spherical harmonic coefficients and can be used to estimate mass redistributions. However, a major challenge in estimating mass changes using GRACE gravity solutions is the well-known non-uniqueness of gravitational inversion for a 3D Earth (Chao 2005). In most GRACE applications, people have assumed that GRACE-observed gravity changes are mostly caused by mass redistribution on the Earth's surface (or close to the surface). This assumption appears valid in

most parts of the world and over a wide range of timescales. The surface mass density change ($\Delta\sigma(\theta,\lambda)$ in kg/m$^2$) can be computed as (Wahr et al. 1998),

$$\Delta\sigma(\theta,\phi)=\frac{M_{\mathrm{E}}}{4\pi a^2}\sum_{l=2}^{N}\sum_{m=0}^{l}\frac{2l+1}{1+k_l}W_l\widetilde{P}_{lm}(\cos\theta)\times[\Delta C_{lm}\cos(m\phi)+\Delta S_{lm}\sin(m\phi)], \quad (1)$$

where $\theta$ and $\lambda$ are geocentric colatitude and longitude, respectively, $a$ is Earth's mean radius ($6.371\times10^6$ m), and $M_{\mathrm{e}}$ is the mass of the Earth ($5.97219\times10^{24}$ kg); $\widetilde{P}_{lm}$ are the fully normalized associated Legendre functions of degree $l$ and order $m$, and $\Delta C_{lm}$ and $\Delta S_{lm}$ are GRACE gravity spherical harmonics coefficient change. $W_l=W_l(r)$ is the normalized Gaussian weighting function (with a maximum weight of 1), dependent on a chosen averaging radius ($r$).

GRACE satellite gravimetry is the first satellite remote sensing technique that is directly applicable to the assessment of large-scale GWS changes (Yeh et al. 2006; Swenson and Wahr 2006; Rodell et al. 2007). Over non-glacialized land areas, GRACE observes the total water mass change within a vertical column, including the atmosphere, terrestrial water, and solid Earth. Even when mass changes in the atmosphere and solid Earth can be removed using estimates from numerical models, GRACE itself cannot separate the different components of TWS changes. Therefore, water storage changes in snow, surface water reservoirs, and soil have to be estimated from other independent data source(s), such as land surface models (LSMs) in order to use GRACE to quantify GWS change (Rodell and Famiglietti 2002).

$$\Delta\mathrm{TWS}=\Delta W_{\mathrm{soil}}+\Delta W_{\mathrm{snow}}+\Delta W_{\mathrm{surface\_reservoir}}+\Delta\mathrm{GWS} \quad (2)$$

or

$$\Delta\mathrm{GWS}=\Delta\mathrm{TWS}-(\Delta W_{\mathrm{soil}}+\Delta W_{\mathrm{snow}}+\Delta W_{\mathrm{surface\_reservoir}}) \quad (3)$$

The top panel of Fig. 1 shows the long-term TWS changes (in cm/year equivalent water height) observed by GRACE for the period January 2005 and December 2009. The reason for picking up the period of 2005–2009 is to illustrate some of the strong groundwater depletion signals during that particular period such as those in southern MDB and Central Valley. At each grid point, the TWS rate is determined by an unweighted least squares fit of GRACE TWS changes calculated from the GRACE release-5 (RL05) gravity solutions provided by the Center for Space Research (CSR), University of Texas at Austin. We selected this 5-year period to better illustrate some significant long-term regional TWS and GWS changes during this particular time span. Some of the GRACE-observed long-term TWS changes may simply reflect water storage changes in surface water reservoirs, snow, and soil (SSS). After the total SSS water storage changes (shown in the middle panel of Fig. 1) estimated from the WGHM (version 2.2) (Güntner et al. 2007) have been subtracted from GRACE TWS changes, the residual changes should represent GWS changes over non-glacial regions (Fig. 1c). Some of the prominent mass change features such as those over the Greenland, Canadian Arctic Archipelago, and southern Alaska apparently represent ice mass losses during the studied period.

As the uncertainty of model-estimated SSS water storage change is unknown, some of the derived "groundwater" changes may be introduced by errors in model SSS estimates and/or GRACE TWS estimates. However, GRACE measurements have indeed captured some interesting long-term regional groundwater changes over the world that can be verified by either in situ groundwater level data or analysis of precipitation data. GRACE-

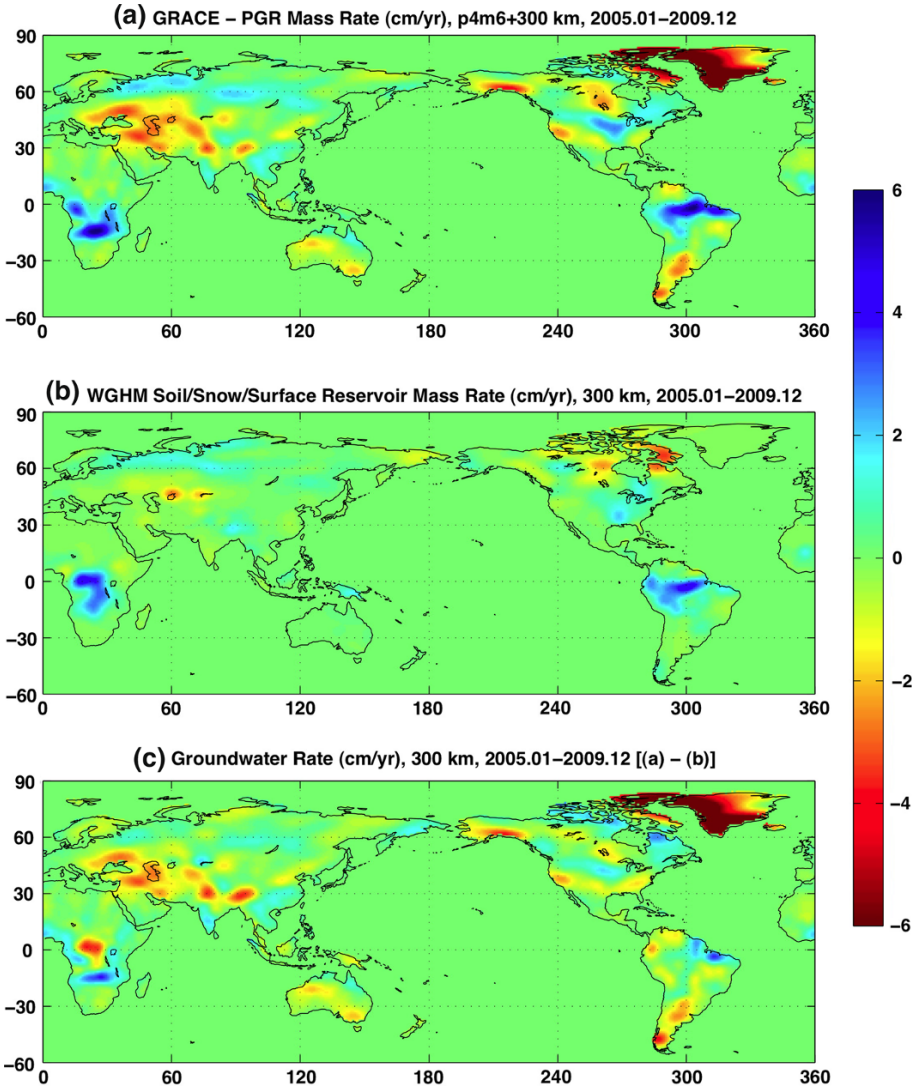


**Fig. 1** **a** GRACE-observed TWS changes (in cm/year equivalent water height) for the period January 2005–December 2009. The post-glacial rebound (PGR) effect is removed using model estimates (Geruo et al. 2013). **b** Water storage changes in soil, snow, and surface reservoirs from WGHM for the same 5-year period. **c** "Groundwater" storage changes from GRACE-WGHM, i.e. (**a**–**b**)**.** Decorrelation filter and 300 km Gaussian smoothing were applied to GRACE data, and 300 km Gaussian smoothing was applied to WGHM data

observed long-term regional groundwater changes include significant groundwater depletion in northwest and northern India (Rodell et al. 2009; Tiwari et al. 2009; Chen et al. 2014), the Middle East (Voss et al. 2013; Joodaki et al. 2014), California's Central Valley (Famiglietti et al. 2011; Scanlon et al. 2012a), and the southern MDB in Australia (Leblanc et al. 2009, 2012; Chen et al. 2015a), and lower groundwater depletions in the NCP in China (Feng et al. 2013) and HPA in the USA (Strassberg et al. 2009; Scanlon et al. 2012b; Famiglietti and Rodell 2013).

**Fig. 2** **a** GRACE-observed "groundwater" storage change rates (in cm/year of equivalent water height) for the period January 2005–December 2009, same as Fig. 1c, but enlarged for the Southeast Asia region. **b** and **c** Comparisons of GRACE-observed TWS change, WGHM model estimates of SSS water change, and GWS change from GRACE to WGHM (in cm equivalent water height) for the period January 2003–December 2012, for two points (**a**) A and (**b**) B marked by *white triangles* on Fig. 2a

An alternative to applying Eq. (3) with modeled SSS data is to incorporate GRACE TWS observations into a land surface model via data assimilation and allow the model to separate the TWS components (Zaitchik et al. 2008). This approach is only appropriate if the model explicitly represents groundwater storage. Currently, most LSMs do not. This technique has been applied successfully to isolate groundwater storage changes from soil water and snow water storage changes and to apply the results for drought monitoring in North America (Houborg et al. 2012) and Europe (Li et al. 2012), but to date it has not been used for assessing long-term groundwater trends.

## 2.1 Groundwater Depletion in North West India

Rodell et al. (2009) and Tiwari et al. (2009) combined GRACE TWS estimates and soil and snow water estimates from the Global Land Data Assimilation System (GLDAS) hydrological model (Rodell et al. 2004) and found that TWS decreased significantly in the Ganges–Brahmaputra river basins (northwest and north India) during the period August 2002–October 2008. As precipitation in the region was close to the normal level during the period, the GRACE-observed TWS decrease was not related to drought but to GWS depletion due to groundwater pumping for irrigation and domestic consumption. The estimated groundwater depletion rate averaged over the Indian states of Rajasthan, Punjab, and Haryana is 17.7 ± 4.5 $km^3$/year (4 ± 1 cm/year) over the period August 2002–October 2008 (Rodell et al. 2009), and the estimated rate for a broader region covering north India (from northwest to northeast) can be up to 54 ± 9 $km^3$/year (2 cm/year; Tiwari et al. 2009) during the same period.

Using an extended record of GRACE measurements combined with Global Land Data Assimilation System (GLDAS) snow and soil water storage estimates, and a different method for correcting leakage bias of GRACE estimates, Chen et al. (2014) reassessed the groundwater depletion rate in the NWI region. The newly estimated groundwater depletion rate is 20.4 ± 7.1 $km^3$/year (2.4 ± 0.59 cm/year) averaged over the 10-year period January 2003–December 2012. However, during the first 5 years (2003–2007), the newly estimated rate (29.4 ± 8.4 $km^3$/year; 3.5 ± 0.70 cm/year) is significantly larger than previous estimates for roughly the same period. The difference is attributed to the improved treatment of leakage effects through global forward modeling and extended studied region (which is different from the three state regions defined in Rodell et al. 2009). The groundwater depletion in NWI occurred in a broad region that includes neighboring Punjab Province of Pakistan (especially northern Punjab) (see Fig. 1 of Chen et al. 2014).

GRACE-observed groundwater depletion in the NWI region is corroborated by groundwater recharge and consumption data from the Indian government (Rodell et al. 2009). Northern India is one of the most populous regions in the world. Excessive groundwater pumping for agricultural irrigation and domestic consumption in response to the growing demand for water has exceeded the replenishable groundwater supply, causing a steady decreasing of the water table (Tiwari et al. 2009). Analyses of precipitation data and model-predicted water storage changes in surface reservoirs and subsurface soil (plus snow if applicable) indicate that annual precipitation in NWI generally has been at normal

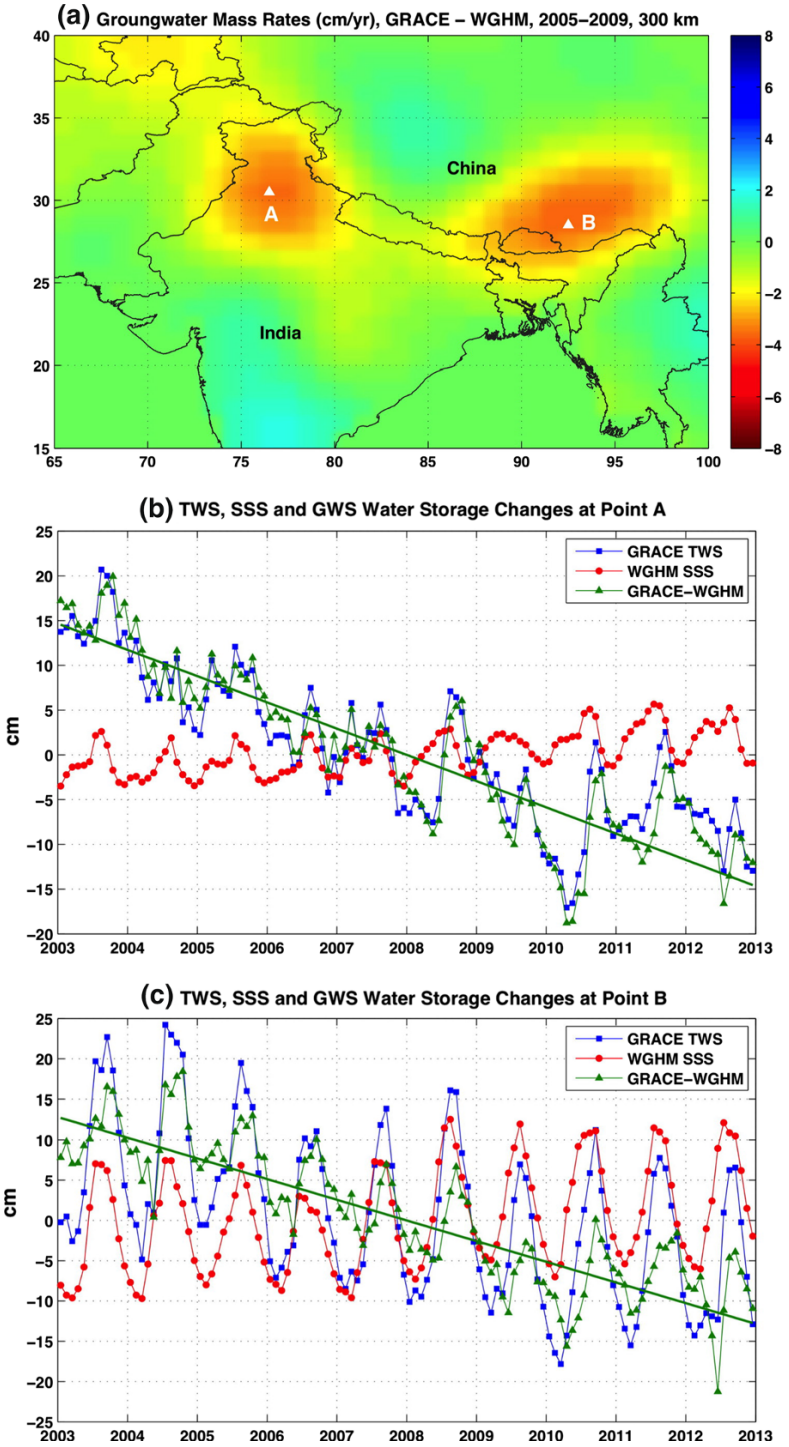
(a) Groungwater Mass Rates (cm/yr), GRACE – WGHM, 2005–2009, 300 km
China
India
A
B
(b) TWS, SSS and GWS Water Storage Changes at Point A
GRACE TWS
WGHM SSS
GRACE–WGHM
cm
(c) TWS, SSS and GWS Water Storage Changes at Point B
GRACE TWS
WGHM SSS
GRACE–WGHM
cm

levels (Rodell et al. 2009; Chen et al. 2014), and model-predicted SSS water storages have not shown any decreasing trends. This further indicates that GRACE-observed water storage decreases in the NWI region most likely (see Fig. 2) represent GWS changes. Leakage from ice melting of nearby mountain glaciers may also affect GRACE-estimated groundwater depletion in this region; however, the effect is relatively small and estimated to be $\sim -3$ km$^3$/year (Rodell et al. 2009), well within the estimated uncertainty level (Chen et al. 2014).

Interpretation of GRACE-observed mass loss in NWI may be more complicated than previously represented over the period 2005–2009; GRACE-observed mass loss extends over a broader region that covers parts of northeast India, Bangladesh, and southwest China, with the center of mass loss actually in southwest China. Furthermore, the region also covers part of the Himalayan mountain glaciers. The spatial pattern of this mass loss signal may vary when using different time spans of GRACE data, but nevertheless the contributors to this mass loss may include groundwater depletion in northeast India, northern Bangladesh, and southwest China, Himalayan mountain glaciers melting, and additional SSS water storage changes that are not correctly modeled in the WGHM. The southwest China region has experienced extended drought in the past decade, which may have contributed to GRACE-observed water storage decrease in this broad region.

### 2.2 Groundwater Depletion in the California Central Valley

Another interesting groundwater depletion signal observed by GRACE is in the Sacramento and San Joaquin River Basins in California (see Fig. 3), which encompass the Central Valley and its underlying groundwater aquifer system. The Central Valley is the most productive agricultural region in the USA, growing more than 8 % of the food produced in the USA (Faunt 2009). With limited surface water resources, groundwater has been a major water supply for agricultural activities in the Central Valley region. Excessive groundwater pumping has led to steady decreasing water tables (Faunt 2009; Famiglietti 2011; Scanlon et al. 2012a, b) and also to significant ground subsidence (Galloway et al. 1999) in the region.

Combining GRACE gravity measurements, snow water equivalent data from the National Operational Hydrologic Remote Sensing Center, in situ surface water storage estimates for the 20 largest reservoirs in the river basins, and soil moisture estimates from GLDAS (Rodell et al. 2004), Famiglietti et al. (2011) concluded that the Sacramento and San Joaquin River Basins lost water at a rate of $4.8 \pm 0.4$ km$^3$/year during the period October 2003–March 2010 and determined (based on additional observations and hydrological model information) that the majority of the water losses were due to groundwater depletion in the Central Valley. Scanlon et al. (2012a, b) extended the analysis of long-term GWS change in the Central Valley region by comparing GRACE estimates with in situ well measurements and showed that over the drought period from April 2006 through September 2009, GRACE data (minus SNODAS SWE, in situ surface water reservoir storage change, and GLDAS soil moisture estimates) indicate a groundwater depletion rate of $7.7 \pm 0.7$ km$^3$/year, agreeing very well with in situ well data estimate of $7.7 \pm 0.1$ km$^3$/year.

The significantly larger groundwater depletion rate from Scanlon et al. (2012a, b) is mostly the result of selecting a different time span (April 2006 and September 2009) from that (October 2003 to March 2010) used in Famiglietti et al. (2011). The Sacramento and San Joaquin River Basins (and the encompassed Central Valley) experienced a major

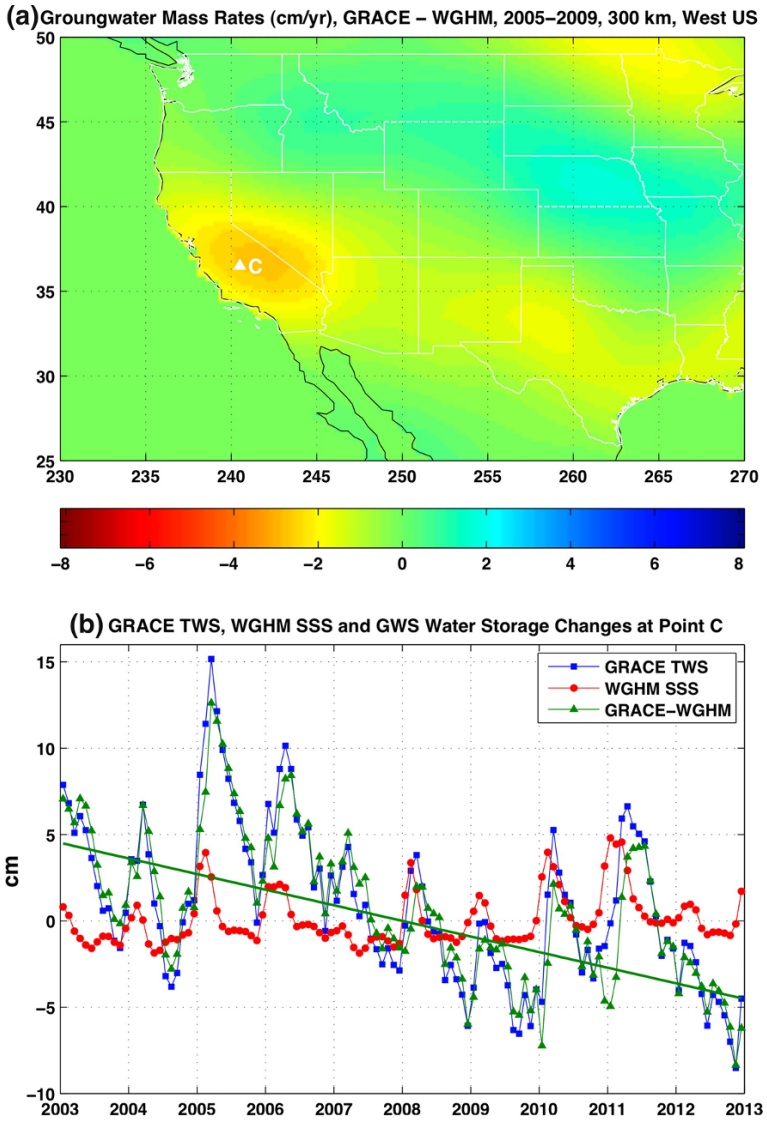


**Fig. 3** **a** Estimated GWS change from GRACE to WGHM (in cm/year of equivalent water height) over the period January 2005–December 2009, same as Fig. 1c, but enlarged for the western and mid-western USA **b** Comparison of GRACE-observed TWS change, WGHM model estimates of SSS water change, and GWS change from GRACE to WGHM (in cm equivalent water height) for January 2003 through December 2012, for point C marked by *white triangle* on Fig. 3a

drought during the period October 2006 through March 2010, which caused greater groundwater depletion than the overall average (see Fig. 3b). Using different GRACE gravity solutions and different data processing methods also contributed to the discrepancy.

The groundwater depletion in the Central Valley is expected to continue. The western USA, especially California, is experiencing one of the most severe droughts on record.

This devastating extreme drought will surely increase further groundwater demand in the Central Valley for agricultural irrigation and domestic use. Studies based on climate model predictions show clear links between this mega drought and global climate change and suggest that it may become a chronic event (Swain et al. 2014; Diffenbaugh et al. 2015).

### 2.3 Groundwater Depletion in Southern Murray–Darling Basin

The MDB is a large drainage basin (area $\sim$1.06 million km$^2$) in the interior of southeastern Australia (see Fig. 4a), covering about one-seventh of the continent. It supports almost three-quarters of the country's irrigated land and generates about 30 % of the national income derived from agriculture (van Dijk et al. 2007). Australia is the second driest continent after Antarctica, with mean annual precipitation of $\sim$450 mm (over the past century) (Lavery et al. 1997). Many parts of Australia have suffered from extended drought conditions (Leblanc et al. 2009), except for tropical northern and northeastern regions. Chronic drought conditions and excessive groundwater extraction for agricultural, industrial, and domestic consumption contribute to depletion of groundwater storage in regions such as the MDB (Tularam and Krishna 2009).

Australia is generally arid with relatively small seasonal hydrological variations (Awange et al. 2011). However, GRACE satellite gravity measurements still proved useful for estimating basin or large regional-scale TWS and GWS changes in Australia (e.g., Leblanc et al. 2009; Rieser et al. 2010; Awange et al. 2011). The MDB experienced a severe drought, termed the Millennium Drought (2001–2009; van Dijk et al. 2013), during which available in situ groundwater level measurements showed an alarming drop in groundwater storage in the southern MDB (Leblanc et al. 2012).

By analyzing in situ well data, Leblanc et al. (2009) showed that between 2001 and 2007, GWS in the MDB region lost $104 \pm 40$ km$^3$ (or $17 \pm 7$ km$^3$/year). The in situ estimates agree well with estimates from GRACE gravity measurements (combined with GLDAS snow and soil water estimates) for the period 2003–2007. Leblanc et al. (2012) extended the study to cover a longer time span and indicated that, over the period August 2002–December 2010, GRACE-estimated groundwater depletion in the southern MDB is $\sim 18 \pm 1.3$ km$^3$/year.

In a recent study, Chen et al. (2015a) carried out a new analysis of in situ groundwater level measurements (from a network of 1395 boreholes) and indicated that, over the 20-year period (1993–2012), groundwater storage in the southern MDB and adjacent coastal regions in Victoria, Australia, has been declining steadily, until a trend reversal around 2010 attributed to two wet seasons in 2010 and 2011. The average groundwater depletion rate is estimated to be $3.4 \pm 1.4$ km$^3$/year for 1993–2012 ($4.0 \pm 1.7$ km$^3$/year for 1993–2009). During the 10-year overlapping period (2003–2012) with the GRACE mission, GRACE-estimated groundwater changes (after WGHM SSS water storage estimates have been removed) agree remarkably well with in situ well data. The new GRACE estimate of groundwater depletion rate in the broad southern MDB region is $\sim 17.2 \pm 4.7$ km$^3$/year for the period 2005–2009. After groundwater recharge in the past few wet seasons, the estimated overall groundwater rate is significantly reduced. Annual GWS changes are strongly correlated with precipitation anomalies, but the magnitudes of anomalous precipitation and groundwater storage suggest that only about 20 % of anomalous precipitation contributes to groundwater recharge. The strong correlation suggests that this significant groundwater depletion is primarily related to drought plus groundwater pumping for agricultural and domestic consumption (Chen et al. 2015a).

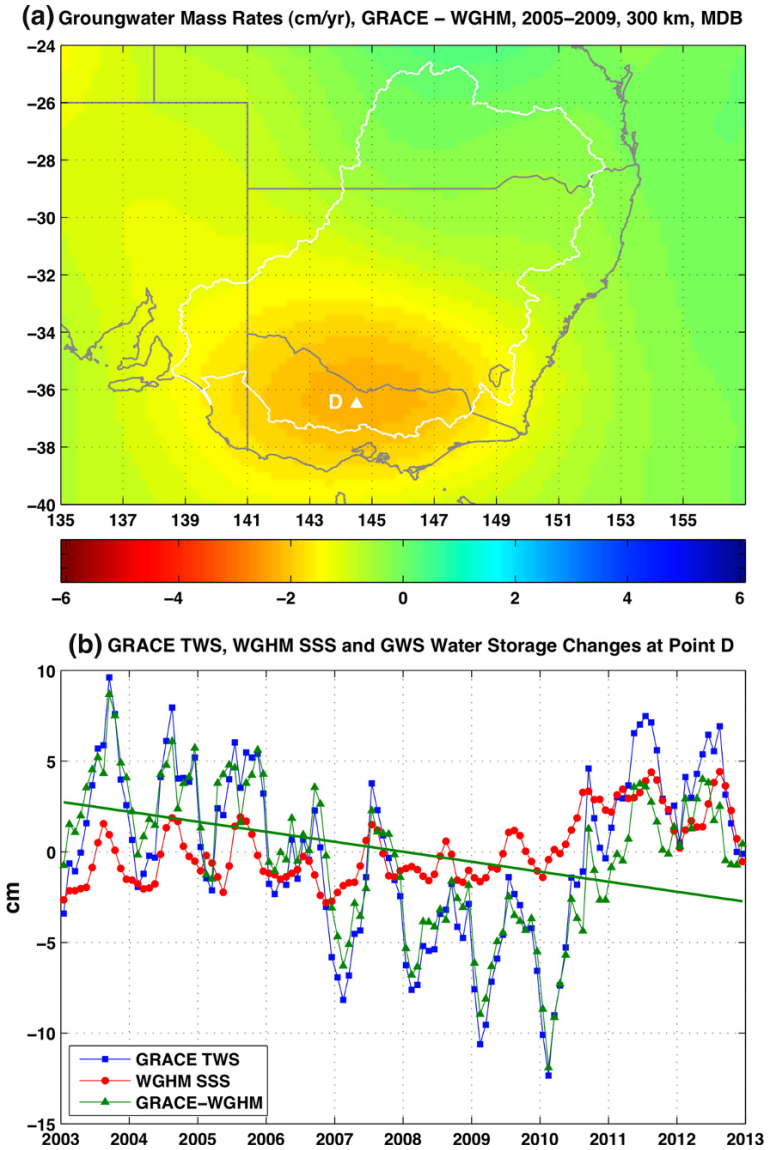


**Fig. 4** **a** GRACE-observed groundwater rates (in cm/year equivalent water height) for the period 01/2005 through 12/2009, same as Fig. 1c, but enlarged for the MDB and surrounding regions in Australia. **b** Comparisons of GRACE-observed TWS change, WGHM model estimates of SSS water change, and GWS change from GRACE to WGHM (in cm equivalent water height) for the period January 2003–December 2012, for point D marked by *white triangle* on Fig. 4a

## 2.4 Groundwater Depletions in Other Regions

GRACE also captured groundwater depletion in other regions over the world, including the Middle East, NCP in China and HPA in the USA (Fig. 1c). The groundwater

depletion signal in the Middle East appears also very significant, comparable to those in northwest and northeast India (at least over the 5-years period illustrated in Fig. 1c). After removing contributions from snow, canopy storage, and soil moisture storage using estimates from the GLDAS Variable Infiltration Capacity (VIC) model and contributions from five major surface water bodies—Lake Van, Lake Daryace (Lake Urmia), Lake Tharthar, the Assad Reservoir, and the Qadisiyah Reservoir using in situ measurements—Voss et al. (2013) show that the north-central Middle East is losing groundwater at an average rate of $13 \pm 1.5$ km$^3$/year for the period January 2003–December 2009. A similar study (Joodaki et al. 2014), using GRACE TWS estimates and the Community Land Model (CLM) 4.5 LSM estimates, shows that the largest groundwater depletion in the Middle East is occurring in Iran, with a loss rate of $25 \pm 3$ km$^3$/year during the period 2003–2012. GRACE-observed significant Iranian groundwater loss is supported by in situ well data (Joodaki et al. 2014). After the CLM4.5 model predicted natural variations in groundwater is removed from GRACE estimates, anthropogenic pumping contributions are estimated to be $14 \pm 3$ km$^3$/year, over half of the total groundwater loss. The large difference in the estimates of the two studies is due to different coverages of the studied regions, different time spans, and different LSMs used in the studies.

The NCP in North China is one of the largest irrigated areas in the world and is subjected to intensive groundwater-based irrigation. Combining GRACE gravity measurements and model estimates of snow water and soil moisture, Feng et al. (2013) showed that, over the period 2003–2010, the NCP region lost a significant amount of groundwater with an average rate of $8.3 \pm 1.1$ km$^3$/year (2 cm/year). However, other independent assessments from the Groundwater Bulletin of China Northern Plains (GBCNP) indicate that groundwater depletion rate in shallow aquifers in the plain for the same time period was only $\sim$2.5 km$^3$/year. The large discrepancy in groundwater depletion estimates may reflect contributions of groundwater depletion from deep confined aquifers in the NCP and piedmont regions of North China, which is detectable by GRACE but difficult to quantify using in situ observations (Feng et al. 2013).

The HPA (450,000 km$^2$) is ranked first among aquifers in the USA for total groundwater withdrawals (Maupin and Barber 2005). A previous assessment (McGuire 2009) based on measured groundwater data shows that high recharge in the northern HPA enables sustainable withdrawals, whereas lower recharge in the central and southern High Plains has resulted in focused depletion of groundwater. Extrapolation of the current depletion rate suggests that 35 % of the southern HPA may be unable to support irrigation within the next 30 years (Scanlon et al. 2012b). Despite the large amount of groundwater withdrawn from the HPA, quantification of long-term groundwater depletion using GRACE has been more complicated, due to the irregular shape and south–north orientation of the aquifer and difficulty in accurate separation of HPA groundwater signal from surrounding TWS changes. However, a few previous studies (Strassberg et al. 2009; Longuevergne et al. 2010) show that GRACE-estimated GWS changes are highly correlated with those from detailed groundwater level monitoring data, indicating that GRACE is capable of detecting long-term GWS in the HPA region (Rodell and Famiglietti 2002). Through analyzing GRACE data and GLDAS Noah model estimates for the period 2003–2013, a recent study (Breña-Naranjo et al. 2014) shows persistent declines in groundwater storage across the HPA at an average rate of $12.5 \pm 0.4$ km$^3$/year.

## 3 Major Challenges in Monitoring Groundwater Change Using GRACE

### 3.1 Uncertainty of SSS Water Storage Changes

As GRACE can only measure the total water mass change (assuming atmospheric and solid Earth signals have been removed using model estimates), independent determination of SSS water storage changes plays a key role in separating the GWS contribution from GRACE-observed TWS change. Any uncertainty or bias in SSS water storage estimates will directly translate into errors in GRACE GWS estimates (through Eq. 3; see Rodell and Famiglietti 2002). Although there are limited snow cover and water level measurements of surface reservoirs available, adequate in situ soil moisture (SM) measurements on large regional or basin scales are not available in most regions. Furthermore, calculations of snow water equivalent (SWE) water from remote sensing measurements of snow cover are often subject to large uncertainty. Hence, removal of SWE and SM storage changes from the GRACE TWS is generally done using output for these storage changes from LSMs or global hydrological models (Rodell et al. 2007, 2009), such as the GLDAS (Rodell et al. 2004), WGHM (Güntner et al. 2007), and the CLM (Oleson et al. 2013).

The accuracy of LSM-based estimates of SM and SWE variations depends on the quality of the input meteorological data and the ability of the model to simulate physical processes. Water storage changes in surface reservoirs (lakes, manmade reservoirs, and rivers) can be estimated from limited available in situ observations (Rodell and Famiglietti 2001; Famiglietti et al. 2011; Scanlon et al. 2012). Comparisons between estimates from two different models (e.g., GLDAS and WGHM) can provide an approximate of the level of uncertainty of model-estimated SSS variability.

Figure 5 shows the comparisons of long-term SSS trends for the 10-year period from 2003 to 2012, predicted by GLDAS Noah and WGHM. Significantly large discrepancy exists between the two model predictions (even at long-term timescales), and the magnitudes of the differences (shown in Fig. 5c) are at the same level as the signals themselves. Apparently, the large discrepancy is not due to the absence of a surface reservoir component in the GLDAS model, but mostly attributed to the uncertainty of modeled SWE and SM estimates. Much progress is required before LSMs can accurately model long-term trends in SWE and SM. Fortunately, in some of the regions studied, where groundwater storage has experienced significant depletion in recent years (e.g., NWI, HPA, Central Valley, and NCP), model-predicted SSS trends and uncertainties are relatively small and largely do not affect GRACE-estimated groundwater rates. Additionally, precipitation and other measurements can be used to help diagnose likely SSS water storage changes and the possible uncertainties of model predictions (Rodell et al. 2009; Chen et al. 2014).

### 3.2 Uncertainties in GRACE TWS Storage Changes

Limited by the coarse spatial resolution of GRACE measurements (at $\sim$200–500 km), accurate quantification of subregional TWS and/or groundwater storage changes is challenging. The spatial resolution of GRACE time-variable gravity solutions is mostly controlled by two factors: (1) the altitude of the GRACE satellites ($\sim$450 km now) and the distance ($\sim$220 km) between the twin satellites and (2) the need for spatial filtering (or smoothing) to suppress strong spatial noise in GRACE data (i.e., stripes and other residual noise) to extract reliable mass change signals. The high degree and order terms of GRACE spherical harmonic coefficients are mostly dominated by noise. Therefore, appropriate

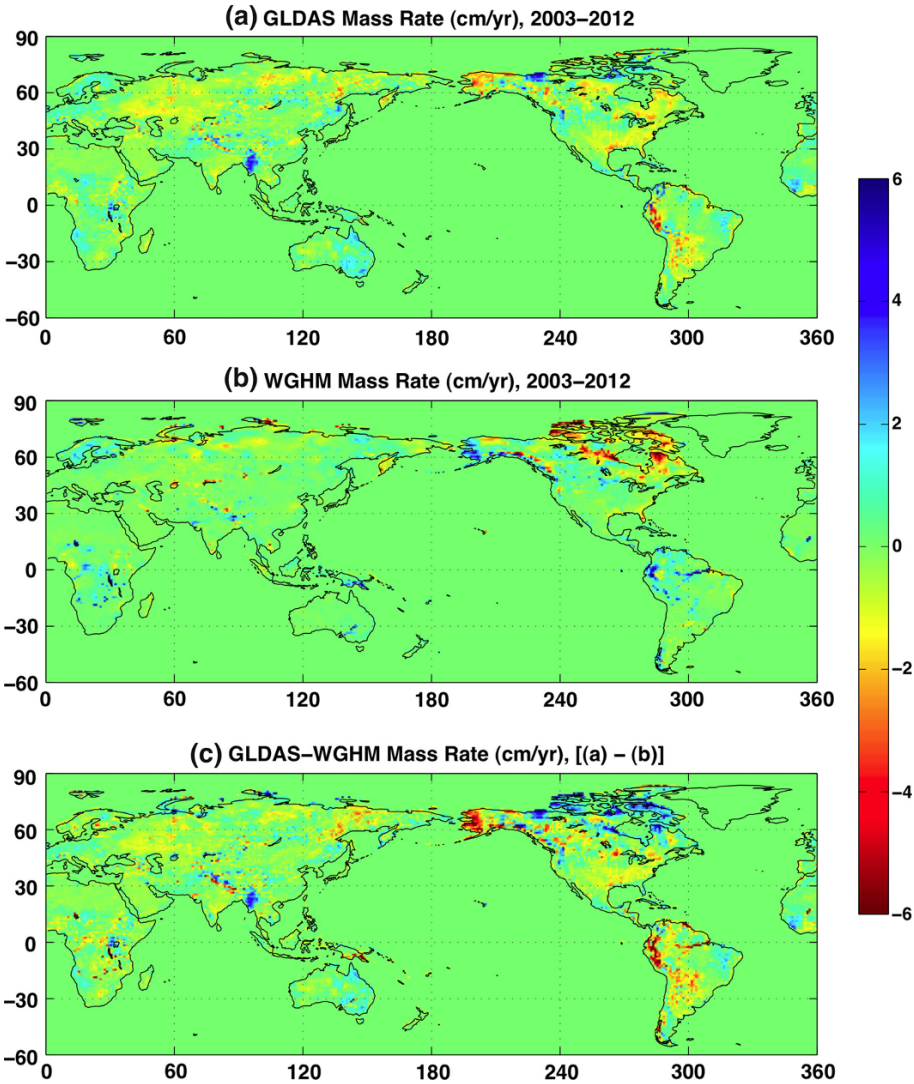


**Fig. 5** **a** GLDAS SSS rates (in cm/year equivalent water height; water in surface reservoirs, a minor component, is not included in GLDAS) over the period January 2003–December 2012. **b** WGHM SSS rates during the same 10-years period. **c** GLDAS-WGHM SSS rates, i.e. (**a**) minus (**b**). No smoothing or truncation has been applied to the model SSS data

spatial filtering, such as decorrelation filtering (Swenson and Wahr 2006) and/or Gaussian smoothing (Jekeli 1981), is needed to reduce noise.

Truncation of GRACE time-variable gravity solutions (at degree and order 60) and use of spatial filtering or smoothing degrade the spatial resolution and dampen the retrieved magnitude of GRACE-observed mass changes. Experiments shown in Fig. 6 demonstrate these effects through simulations using WGHM-simulated long-term TWS changes due to excessive groundwater withdrawal or pumping in certain regions, e.g., NWI and NCP. The

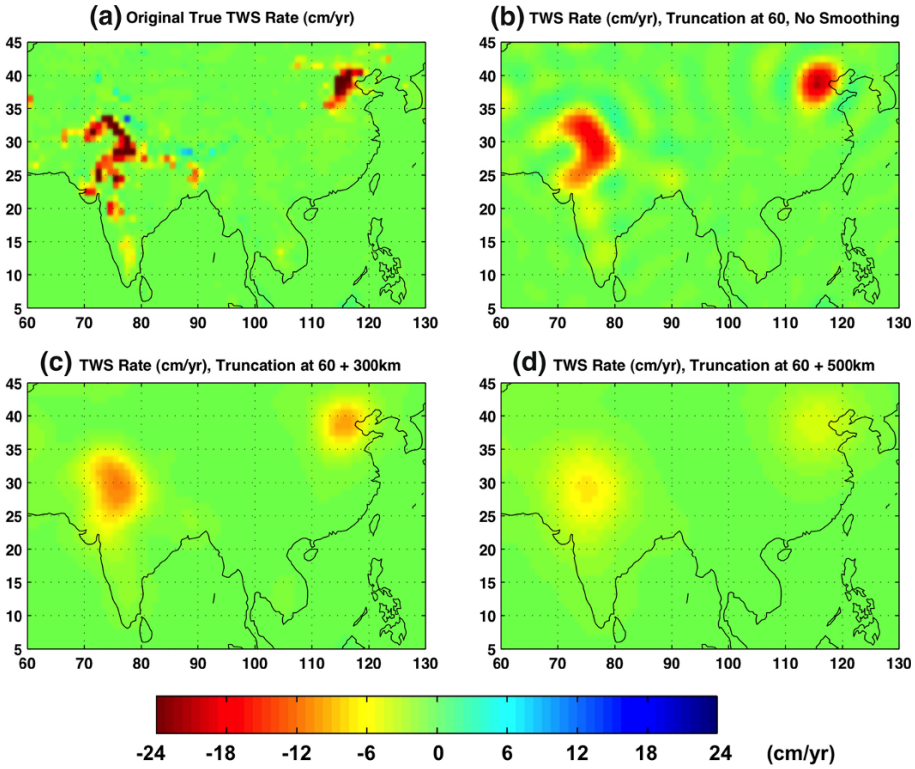


**Fig. 6** WGHM-predicted long-term TWS mass rates (in cm/year equivalent water height change) at each grid point (on 1° × 1° grids) in part of Asia in 4 different cases: **a** true model prediction from WGHM; **b** model prediction with only truncation (at degree and order 60) applied; (3) model prediction with truncation and 300 km Gaussian smoothing applied; and (4) model prediction with truncation and 500 km Gaussian smoothing applied

four panels in Fig. 6 show WGHM-predicted long-term TWS rates at each grid point (on 1° × 1° grids) in part of Asia in four different cases: (a) true model prediction; (b) model prediction with only truncation (at degree and order 60) applied; (3) model prediction with truncation and 300 km Gaussian smoothing applied; and (4) model prediction with truncation and 500 km Gaussian smoothing applied.

Truncation alone (Fig. 6b) results in significant leakage (i.e., signal spread outside original area) and attenuation of signal amplitude, relative to the original true signal (Fig. 6a). After truncation at degree and order 60 (same as used in GRACE RL05 monthly solutions) and 300 km Gaussian smoothing, the magnitudes of TWS changes in the NWI and NCP regions have been reduced to less than 50 % of the true signal. After 500 km Gaussian smoothing, the magnitudes of TWS rates are further attenuated to only ∼20–30 % of the true signal. Leakage and attenuation effects depend not only on the degree and order (60 here) of the truncation and scales of spatial filtering or smoothing, but also on the spatial pattern and distribution of the true mass change. Nevertheless, to accurately quantify long-term variations in TWS or groundwater storage using GRACE time-variable gravity data, leakage and attenuation biases in GRACE estimates have to be effectively reduced. This is a challenging task, which requires both a thorough

understanding of GRACE leakage and attenuation effects and their dependency on temporal and spatial spectra of GRACE-observed TWS changes, and accurate knowledge of how to quantify and reduce leakage and attenuation biases.

There are a number of methods that can help reduce the leakage bias. Scale factors can be used to correct the bias in GRACE values (Velicogna and Wahr 2006). Scale factors can be estimated from model-estimated TWS storage changes by comparing model-predicted TWS values with the same model estimates after truncation and filtering (Chen et al. 2005; Landerer and Swenson 2012). However, the scaling factor method may only be valid for restoring seasonal amplitude and not for restoring the amplitudes of secular trends, as it is generally believed that seasonal TWS variability (or at least its spatial patterns) can be reliably simulated by LSMs, while interannual trends are commonly not well represented. The success of this method relies on whether the model used represents well the correct spatial patterns of the signal. Long-term TWS and groundwater changes are either absent or mostly not well modeled in the hydrological models, and therefore, the scale factor method is not recommended for multi-year and long-term timescales, unless people can construct good synthetic data models that can faithfully represent long-term TWS and groundwater storage change.

Forward modeling has proved to be an effective tool for accurately quantifying leakage effects and to obtain unbiased estimates of regional mass changes using GRACE gravity data. This method has been originally developed for studying long-term ice melting rates of polar ice sheets (e.g., Chen et al. 2006, 2009; Wouters et al. 2008) and mountain glaciers (e.g., Chen et al. 2007), when the locations of ice mass changes are approximately known (which are considered constrained experiments). The forward modeling method has later been extended to global scales with no constraints in the studies of global sea level rise (e.g., Chen et al. 2013) and regional groundwater depletion (e.g., Chen et al. 2014). In the forward modeling approach, iterative numerical simulations are used to find a "true" mass change field that best matches the GRACE-observed mass change, after repeating the same data processing procedures as applied to GRACE data, which include truncation of spherical harmonics, treatment of low-degree terms, and spatial filtering. The major advantage of forward modeling is that it is solely dependent on GRACE data and is unaffected by model uncertainty as in the scale factor approach. The details of the forward modeling algorithm and procedures with and without constraint are available in a recent article (Chen et al. 2015b).

Leakage error in GRACE estimates can also be reduced by using high-resolution mascon solutions that are derived either directly from GRACE satellite range and range rate measurements (Rowlands et al. 2005; Luthcke et al. 2013) or from GRACE spherical harmonic solutions (Jacob et al. 2012; Schrama et al. 2014). Please note that forward modeling can be regarded as a mascon approach using GRACE spherical harmonic solutions and is solved in the spatial domain, as compared to the spherical harmonic domain (e.g., Jacob et al. 2012).

In addition to the leakage and attenuation effects discussed previously, other error sources also affect GRACE-observed TWS and groundwater storage change. Some low-degree spherical harmonics of GRACE gravity solutions, especially the zonal term C20, are not well determined and are recommended to be replaced by independent measurements from satellite laser ranging (Cheng and Ries 2012). The degree-1 terms ($C_{10}$, $C_{11}$, $S_{11}$), representing geocenter motion (mass center of the Earth system with respect to the origin of the reference frame) are not available in GRACE solutions. The uncertainty (or absence) of these low-degree terms on TWS and groundwater estimates may not be negligible, depending on spatial scales of the studied regions (e.g., Chen et al. 2005).

However, because groundwater depletion often occurs in relatively small confined regions (such as NWI, HPA, Central Valley, and NCP), the effects from uncertainties of those lowest degree terms (longest wavelength mass change) are expected to be small.

It is worthy of note that groundwater storage change estimates derived from GRACE observations likely have larger uncertainty in humid regions (e.g., Bangladesh) due to large seasonal water storage changes (Shamsudduha et al. 2012). This is because the uncertainty of model-estimated seasonal TWS changes in these humid regions can be translated into relatively large uncertainty of interannual or long-term TWS changes and therefore affect the estimates of long-term TWS and groundwater change. When time series are relatively short (e.g., a few to several years), the uncertainty of GRACE-estimated long-term groundwater change can be large due to strong seasonal and interannual variability. With longer records (over 13-years so far) of GRACE gravity solutions available, the associated uncertainty will become less of a concern.

## 4 Summary

The 13-year record of GRACE time-variable gravity solutions provides a revolutionary means for measuring water mass movement and redistribution in the global water cycle and offers a unique tool for monitoring long-term groundwater storage change at continental to global scales (Famiglietti 2014). GRACE measurements have captured significant groundwater depletion in many aquifers or regions globally, including NWI (and neighboring eastern Punjab Province in Pakistan), HPA, and Central Valley in the USA, the NCP in China, the Middle East, and the southern MDB in Australia. Among those, the NWI and Middle East regions show the most significant and persistent groundwater depletion over the past decade, with rates as large as $20.4 \pm 7.1$ km$^3$/year and $25 \pm 3$ km$^3$/year, respectively, for the period 2003–2012 (Chen et al. 2014; Joodaki et al. 2014). The Central Valley is also losing a large amount of groundwater with estimated depletion rates range from $4.8 \pm 0.4$ to $7.7 \pm 0.7$ km$^3$/year, depending on the time span of the studies, and GRACE estimates agree well with in situ well data (Famiglietti et al. 2011; Scanlon et al. 2012). Even though the estimated Central Valley groundwater depletion rates appear not so significant compared with those for NWI and the Middle East, the current record-breaking severe chronic drought in California is only expected to worsen the already dismal situation there.

A summary of GRACE-estimated groundwater depletion rates for regions or aquifers discussed in the present study plus some other regions compiled by Famiglietti (2014) is listed in Table 1. The definitions of aquifers or regions may be somewhat different in different studies and some of them may be overlapped. It is difficult to get an accurate estimate of the total groundwater depletion rate over the world based on these estimates due to the different time spans covered by different studies and the omission of many other aquifers or regions. However, given the significant and persistent groundwater depletions in some of the regions, the total groundwater depletion rate over the past decade in these studied regions can be easily over 100 km$^3$/year. Excessive groundwater depletions not only pose as a great threat to the sustainability of regional water resource supply and ecosystem, but also contribute to global sea level rise. The 100 km$^3$/year groundwater loss over land will contribute $\sim$0.27 mm/year to the global sea level rise. The actual total groundwater depletion rate over the world could be significantly higher than the above

**Table 1** Summary of GRACE-estimated groundwater depletion rates (in units of $km^3$/year) for selected aquifers or regions over the world discussed in the present study, plus some compiled by Famiglietti (2014)

| Aquifer or region (References) | Depletion rate ($km^3$/year) | Time period (year.month) |
|---|---|---|
| Northwestern India, Rodell et al. (2009) | 17.7 ± 4.5 | 2002.08–2008.10 |
| Northwestern India, Chen et al. (2014) | 29.4 ± 8.4 | 2003.01–2007.12 |
| Northwestern India, Chen et al. (2014) | 20.4 ± 7.1 | 2003.01–2012.12 |
| Northern India (NW + NE India), Tiwari et al. (2009) | 54 ± 9 | 2002.04–2008.06 |
| Middle East, Iran, Joodaki et al. (2014) | 25 ± 3 | 2003.01–2012.12 |
| Middle East, North-Central, Voss et al. (2013) | 13 ± 1.5 | 2003.01–2009.12 |
| Southern MDB Australia, Leblanc et al. (2012) | 18 ± 1.3 | 2002.08–2010.12 |
| Southern MDB Australia, Chen et al. (2015a, b) | 17.2 ± 4.7 | 2003.01–2010.01 |
| Central Valley USA, Famiglietti et al. (2011) | 4.8 ± 0.4 | 2003.10–2010.03 |
| Central Valley USA, Scanlon et al. (2012a, b) | 7.7 ± 0.7 | 2006.04–2009.09 |
| High Plains Aquifer, Breña-Naranjo et al. (2014) | 12.5 ± 0.4 | 2003.01–2012.12 |
| North China Plain, Feng et al. (2013) | 8.3 ± 1.1 | 2003.01–2010.12 |
| Arabian Middle East, Richey (2014) | 15.5 | 2003.01–2013.01 |
| Canning Basin Australia, Richey (2014) | 3.6 | 2003.01–2013.01 |
| Guarani South America, Richey (2014) | 1.0 | 2003.01–2013.01 |
| Northwest Sahara, Richey (2014) | 2.7 | 2003.01–2013.01 |
| Arabian Richey (2014) | 2.7 | 2003.01–2013.01 |

Please note that definitions of aquifers or regions may be different in different studies and some of them may be overlapped

estimate, as many other aquifers or regions with relatively small magnitudes of groundwater depletions are not included.

Due primarily to the sparseness of soil moisture observations, quantifying groundwater change using GRACE time-variable gravity measurements often depends on accurate removal of SSS water storage changes by subtracting modeled estimates (Rodell et al. 2007) or by assimilating GRACE TWS data into a land surface model (Zaitchik et al. 2008). This is one of the major challenges limiting effective application of GRACE data to study GWS changes. Any uncertainty in model-estimated SSS water storage changes will be reflected in the residual groundwater storage changes. Further, modeled interannual SSS trends are with significant uncertainty (as shown in Fig. 5c). GRACE-observed TWS changes are subject to large "leakage" of signals from adjacent regions, due to the truncation of GRACE gravity spherical harmonic coefficients and the spatial filtering required to suppress the dominant spatial noise in GRACE data. How to reduce leakage bias in GRACE TWS and groundwater estimates is another major challenge to overcome. The effect of uncertainty in GRACE low-degree spherical harmonic coefficients on GRACE groundwater estimates is expected to be small, due to the scales of groundwater depletion in most cases being significantly smaller than the length scales of those harmonics.

The GRACE mission is entering its 14th year, and the GRACE follow-on mission is scheduled to be launched in 2017. With the long record (now 13 years) of GRACE time series, and improvement of data quality and data processing methods, GRACE time-variable gravity measurements will continue offering great potential to improve understanding of the global water cycle and for monitoring and quantifying long-term variability in groundwater resources globally.

**Acknowledgments** This study was supported by the NASA GRACE Science Program (NNX12AJ97G), NASA ESI Program (NNX12AM86G), and NSF OPP Program (under Grants ANT-1043750).

## References

Abidin HZ, Andreas H, Djaja R, Darmawa D, Gamal M (2008) Land subsidence characteristics of Jakarta between 1997 and 2005, as estimated using GPS surveys. GPS Solut 12(1):23–32

Awange JL, Fleming KM, Kuhn M, Featherstone WE, Heck B, Anjasmara I (2011) On the suitability of the 4°×4° GRACE mascon solutions for remote sensing Australian hydrology. Remote Sens Environ 115:864–875

Bettadpur S (2012) CSR level-2 processing standards document for product release 04, GRACE 327-742, The GRACE Project, Center for Space Research, University of Texas at Austin

Breña-Naranjo JA, Kendall AD, Hyndman DW (2014) Improved methods for satellite-based groundwater storage estimates: a decade of monitoring the high plains aquifer from space and ground observations. Geophys Res Lett 41:6167–6173. doi:10.1002/2014GL061213

Chao BF (2005) On inversion for mass distribution from global (time-variable) gravity field. J Geodyn 39:223–230. doi:10.1016/j.jog.2004.11.001

Chen JL, Wilson CR, Famiglietti JS, Rodell M (2005) Spatial sensitivity of the gravity recovery and climate experiment (GRACE) time-variable gravity observations. J Geophys Res (Solid Earth) 110(B9):B8408. doi:10.1029/2004JB003536

Chen JL, Wilson CR, Tapley BD (2006) Satellite gravity measurements confirm accelerated melting of greenland ice sheet. Science 313:1958–1960. doi:10.1126/science.1129007

Chen JL, Wilson CR, Tapley BD, Blankenship DD, Ivins ER (2007) Patagonia icefield melting observed by gravity recovery and climate experiment (GRACE). Geophys Res Lett 34:L22501. doi:10.1029/2007GL031871

Chen JL, Wilson CR, Blankenship DD, Tapley BD (2009) Accelerated Antarctic ice loss from satellite gravity measurements. Nat Geosci 2:859–862. doi:10.1038/NGEO694

Chen JL, Wilson CR, Tapley BD (2013) Contribution of ice sheet and mountain glacier melt to recent sea level rise. Nat Geosci 6:549–552. doi:10.1038/NGEO1829

Chen JL, Li J, Zhang ZZ, Ni SN (2014) Long-term groundwater variations in northwest India from satellite gravity measurements. Global Planet Change 116:130–138. doi:10.1016/j.gloplacha.2014.02.007

Chen JL, Wilson CR, Tapley BD, Scanlon B, Güntner A (2015a) Long-term groundwater storage change in Victoria, Australia from satellite gravity and in situ observations. Glob Planet Change. doi:10.1016/j.gloplacha.2015.xx.xxx

Chen JL, Wilson CR, Li J, Zhang Z (2015b) Reducing leakage error in GRACE-observed long-term ice mass change: a case study in West Antarctica. J Geodesy. doi:10.1007/s00190-015-0824-2

Cheng MK, Ries JR (2012) Monthly estimates of C20 from 5 SLR satellites based on GRACE RL05 models, GRACE Technical Note 07, The GRACE Project, Center for Space Research, University of Texas at Austin (ftp://podaac.jpl.nasa.gov/allData/grace/docs/TN-07_C20_SLR.txt)

Diffenbaugh NS, Swain DL, Touma D (2015) Anthropogenic warming has increased drought risk in California. Proc Natl Acad Sci USA 112(13):3931–3936

Döll P, Hoffmann-Dobrev H, Portmann FT, Siebert S, Eicker A, Rodell M, Strassberg G, Scanlon BR (2012) Impact of water withdrawals from groundwater and surface water on continental water storage variations. J Geodyn 59:143–156. doi:10.1016/j.jog.2011.05.001

Famiglietti JS (2014) The global groundwater crisis. Nat Clim Change 4:945–948. doi:10.1038/nclimate2425

Famiglietti JS, Rodell M (2013) Water in the balance. Science 340:1300–1301. doi:10.1126/science.1236460

Famiglietti JS, Lo M, Ho SL, Bethune J, Anderson KJ, Syed TH, Swenson SC, de Linage CR, Rodell M (2011) Satellites measure recent rates of groundwater depletion in California's Central Valley. Geophys Res Lett 38:L03403. doi:10.1029/2010GL046442

Faunt CC (ed) (2009) Groundwater availability of the central valley aquifer, California, U.S. Geol. Surv. Prof. Pap., 1766, p 225

Feng W, Zhong M, Lemoine J-M, Biancale R, Hsu H-T, Xia J (2013) Evaluation of groundwater depletion in North China using the gravity recovery and climate experiment (GRACE) data and ground-based measurements. Water Resour Res 49:2110–2118. doi:10.1002/wrcr.20192

Foster SSD, Loucks DP (eds) (2006) Non-renewable groundwater resources: a guidebook on socially-sustainable management for water-policy makers. UNESCO, Paris

Freeze RA, Cherry JA (1979) Groundwater. Prentice Hall, Englewood Cliffs, p 604
Galloway D, Jones DR, Ingebritsen SE (eds) (1999) Land subsidence in the United States. U.S. Geolog. Surv., Reston **(Circular 1182)**
Geruo A, Wahr J, Zhong S (2013) Computations of the viscoelastic response of a 3-D compressible Earth to surface loading: an application to glacial isostatic adjustment in Antarctica and Canada. Geophys J Int 192:557–572. doi:10.1093/gji/ggs030
Giao PH, Nutalaya P (2006) Land subsidence in Bangkok, Thailand. Eng Geol 82(4):187–201
Gleeson T et al (2010) Groundwater sustainability strategies. Nat Geosci 3:378–379. doi:10.1038/ngeo881
Güntner A, Stuck J, Werth S, Döll P, Verzano K, Merz B (2007) A global analysis of temporal and spatial variations in continental water storage. Water Resour Res 43:W05416. doi:10.1029/2006WR005247
Houborg R, Rodell M, Li B, Reichle R, Zaitchik B (2012) Drought indicators based on model assimilated GRACE terrestrial water storage observations. Water Resour Res 48:W07525. doi:10.1029/2011WR011291
Jacob T, Wahr J, Pfeffer WT, Swenson S (2012) Recent contributions of glaciers and ice caps to sea level rise. Nature 482:514–518. doi:10.1038/nature10847
Jekeli C (1981) Alternative methods to smooth the earth's gravity field, department of geodetic science and surveying. Ohio State University, Columbus
Joodaki G, Wahr J, Swenson S (2014) Estimating the human contribution to groundwater depletion in the Middle East, from GRACE data, land surface models, and well observations. Water Resour Res 50:2679–2692. doi:10.1002/2013WR014633
Konikow LF, Kendy E (2005) Groundwater depletion: A global problem. Hydrogeol J 13:317–320
Landerer FW, Swenson SC (2012) Accuracy of scaled GRACE terrestrial water storage estimates. Water Resour Res 48:W04531. doi:10.1029/2011WR011453
Lavery B, Joung G, Nicholls N (1997) An extended high-quality historical rainfall dataset for Australia. Aust Meteorol Mag 46:27–38
Leblanc MJ, Tregoning P, Ramillien G, Tweed SO, Fakes A (2009) Basin-scale, integrated observations of the early 21st century multiyear drought in southeast Australia. Water Resour Res 45:W04408. doi:10.1029/2008WR007333
Leblanc MJ, Tweed SO, Van Dijk AIJM, Timbal B (2012) A review of historic and future hydrological changes in the Murray–Darling Basin. Glob Planet Change 80–81:226–246
Li B, Rodell M, Zaitchik BF, Reichle RH, Koster RD, van Dam TM (2012) Assimilation of GRACE terrestrial water storage into a land surface model: evaluation and potential value for drought monitoring in western and central Europe. J Hydrol 446–447:103–115. doi:10.1016/j.jhydrol.2012.04.035
Longuevergne L, Scanlon BR, Wilson CR (2010) GRACE hydrological estimates for small basins: evaluating processing approaches on the High Plains Aquifer, USA. Water Resour Res 46:11517. doi:10.1029/2009WR008564
Luthcke SB, Sabaka TJ, Loomis BD, Arendt AA, McCarthy JJ, Camp J (2013) Antarctica, Greenland and Gulf of Alaska land-ice evolution from an iterated GRACE global mascon solution. J Glaciol 59:613–631. doi:10.3189/2013JoG12J147
Maupin MA, Barber NL (2005) Estimated withdrawals from principal aquifers in the United States, 2000, U.S. Geological Survey Circular 1279
McGuire VL (2009) Changes in water levels and storage in the high plains aquifer, predevelopment to 2007: U.S. Geological Survey Fact Sheet 2009–3005, p 2. http://pubs.usgs.gov/fs/2009/3005/
Oleson K, et al (2013) Technical description of version 4.5 of the community land model (CLM), Tech. Rep. NCAR/TN-503+STR, National Center for Atmosperic Research, Boulder, CO. doi:10.5065/D6RR1W7M
Richey AS (2014) Stress and resilience in the world's largest aquifer systems: A GRACE-based methodology, PhD Dissertation, University of California, Irvine
Rieser D, Kuhn M, Pail R, Anjasmara IM, Awange J (2010) Relation between GRACE-derived surface mass variations and precipitation over Australia. Aust J Earth Sci 57:887–900. doi:10.1080/08120099.2010.512645
Rodell M, Famiglietti JS (2001) An analysis of terrestrial water storage variations in Illinois with implications for the gravity recovery and climate experiment (GRACE). Water Resour Res 37:1327–1340. doi:10.1029/2000WR900306
Rodell M, Famiglietti JS (2002) The potential for satellite-based monitoring of groundwater storage changes using GRACE: the high plains aquifer, central U.S. J Hydrol 263:245–256
Rodell M, Houser PR, Jambor U, Gottschalck J, Mitchell K, Meng C-J, Arsenault K, Cosgrove B, Radakovich J, Bosilovich M, Entin JK, Walker JP, Lohmann D, Toll D (2004) The global land data assimilation system. Bull Am Meteorol Soc 85(3):381–394
Rodell M, Chen J, Kato H, Famiglietti JS, Nigro J, Wilson CR (2007) Estimating groundwater storage changes in the Mississippi River basin (USA) using GRACE. Hydrogeol J 15:159–166. doi:10.1007/s10040-006-0103-7

Rodell M, Velicogna I, Famiglietti JS (2009) Satellite-based estimates of groundwater depletion in India. Nature 460:999–1002. doi:10.1038/nature08238

Rowlands DD et al (2005) Resolvingmassfluxathighspatialandtemporalresolution using GRACE inter-satellite measurements. Geophys Res Lett 32:L04310

Scanlon BR, Longuevergne L, Long D (2012a) Ground referencing GRACE satellite estimates of groundwater storage changes in the California central valley, USA. Water Resour Res 48:4520. doi:10.1029/2011WR011312

Scanlon BR, Faunt CC, Longuevergne L, Reedy RC, Alley WM, McGuire VL, McMahon PB (2012b) Groundwater depletion and sustainability of irrigation in the US high plains and central valley. Proc Natl Acad Sci 109(24):9320–9325. doi:10.1073/pnas.1200311109

Schrama EJO, Wouters B, Rietbroek R (2014) A mascon approach to assess ice sheet and glacier mass balances and their uncertainties from GRACE data. J Geophys Res (Solid Earth) 119:6048–6066. doi:10.1002/2013JB010923

Shamsudduha M, Taylor RG, Longuevergne L (2012) Monitoring groundwater storage changes in the highly seasonal humid tropics: validation of GRACE measurements in the Bengal Basin. Water Resour Res 48(2):W02508. doi:10.1029/2011WR010993

Strassberg G, Scanlon BR, Chambers D (2009) Evaluation of groundwater storage monitoring with the GRACE satellite: case study of the High Plains aquifer, central United States. Water Resour Res 45:W5410. doi:10.1029/2008WR006892

Swain DL, Tsiang M, Haugen M, Singh D, Charland A, Rajaratnam B, Diffenbaugh NS (2014) The extraordinary California drought of 2013/2014: character, context, and the role of climate change. Bull Am Meteorol Soc 95(9):S3–S7

Swenson S, Wahr J (2006) Post-processing removal of correlated errors in GRACE data. Geophys Res Lett 33:L08402. doi:10.1029/2005GL025285

Tapley BD, Bettadpur S, Watkins MM, Reigber C (2004) The gravity recovery and climate experiment; mission overview and early results. Geophys Res Lett 31(9):L09607. doi:10.1029/2004GL019920

Tiwari VM, Wahr J, Swenson S (2009) Dwindling groundwater resources in northern India, from satellite gravity observations. Geophys Res Lett 36:L18401. doi:10.1029/2009GL039401

Tularam GA, Krishna M (2009) Long term consequences of groundwater pumping in Australia: a review of impacts around the globe. J Appl Sci Environ Sanit, 4(2):151–166 (open access at http://www98.griffith.edu.au/dspace/handle/10072/29294).

van Dijk A, Podger G, Kirby M (2007) Integrated water resources management in the Murray-Darling Basin: Increasing demands on decreasing supplies. In: A. Schumann, M. Pahlow (eds), Reducing the vulnerability of societies to water related risks at the basin scale. IAHS Publ., 317, pp 24–30

van Dijk AIJM, Beck HE, Crosbie RS, de Jeu RAM, Liu YY, Podger GM, Timbal B, Viney NR (2013) The Millennium Drought in southeast Australia (2001–2009): natural and human causes and implications for water resources, ecosystems, economy, and society. Water Resour Res. doi:10.1002/wrcr.20123

Velicogna I, Wahr J (2006) Acceleration of greenland ice mass loss in spring 2004. Nature 443:329–331. doi:10.1038/nature.05168

Voss KA, Famiglietti JS, Lo M, Linage C, Rodell M, Swenson SC (2013) Groundwater depletion in the Middle East from GRACE with implications for transboundary water management in the Tigris–Euphrates-Western Iran region. Water Resour Res 49:904–914. doi:10.1002/wrcr.20078

Wahr J, Molenaar M, Bryan F (1998) Time variability of the Earth's gravity field: hydrological and oceanic effects and their possible detection using GRACE. J Geophys Res 103:30205–30230. doi:10.1029/98JB02844

Wahr J, Swenson S, Zlotnicki V, Velicogna I (2004) Time-variable gravity from GRACE: first results. Geophys Res Lett 31:L11501. doi:10.1029/2004GL019779

Wang J, Zhang L, Rozelle C, Blanke A, Huang Q (2006) Groundwater in China: development and response. In: Giordano M, Villholth KG (eds) The agricultural groundwater revolution: opportunities and threats to development. CABI Publishing, Wallingford

Wouters B, Chambers D, Schrama EJO (2008) GRACE observes small-scale mass loss in Greenland. Geophys Res Lett 35:L20501. doi:10.1029/2008GL034816

Yeh PJ-F, Swenson SC, Famiglietti JS, Rodell M (2006) Remote sensing of groundwater storage changes in Illinois using the gravity recovery and climate experiment (GRACE). Water Resour Res 42:W12203. doi:10.1029/2006WR005374

Zaitchik BF, Rodell M, Reichle RH (2008) Assimilation of GRACE terrestrial water storage data into a land surface model: results for the Mississippi River Basin. J Hydrometeorol 9(3):535–548. doi:10.1175/2007JHM951.1

DOI 10.1007/978-3-319-32449-4_10
Reprinted from *Surveys in Geophysics* Journal, DOI 10.1007/s10712-015-9347-x

# Modeling Groundwater Depletion at Regional and Global Scales: Present State and Future Prospects

**Yoshihide Wada**[1,2,3]

Received: 25 April 2015 / Accepted: 8 October 2015 / Published online: 20 October 2015


**Abstract** Except for frozen water in ice and glaciers, groundwater is the world's largest distributed store of freshwater and has strategic importance to global food and water security. In this paper, the most recent advances quantifying groundwater depletion (GWD) are comprehensively reviewed. This paper critically evaluates the recently advanced modeling approaches estimating GWD at regional and global scales, and the evidence of feedbacks to the Earth system including sea-level rise associated with GWD. Finally, critical challenges and opportunities in the use of groundwater are identified for the adaption to growing food demand and uncertain climate.

**Keywords** Groundwater depletion (GWD) · Climate variability · Socioeconomic development · Water scarcity · Sustainability · Projections

## 1 Introduction

Groundwater is the largest storage of freshwater available for use by humans and replenished by precipitation in a form of groundwater recharge (Fig. 1). It is estimated that there is 4.2 million km$^3$ of groundwater within 2.5 km of the Earth's surface (USGS 1999). Due to its slow response time, groundwater storage is relatively insensitive to seasonal or even multi-year climatic variation (Manga 1999; Tague et al. 2008; Taylor et al. 2013; Pokhrel et al. 2013). As a result, groundwater is generally a more reliable water resource

✉ Yoshihide Wada
y.wada@uu.nl; yoshihide.wada@nasa.gov

[1] NASA Goddard Institute for Space Studies, 2880 Broadway, New York, NY 10025, USA

[2] Center for Climate Systems Research, Columbia University, 2880 Broadway, New York, NY 10025, USA

[3] Department of Physical Geography, Faculty of Geosciences, Utrecht University, Heidelberglaan 2, 3584 CS Utrecht, The Netherlands

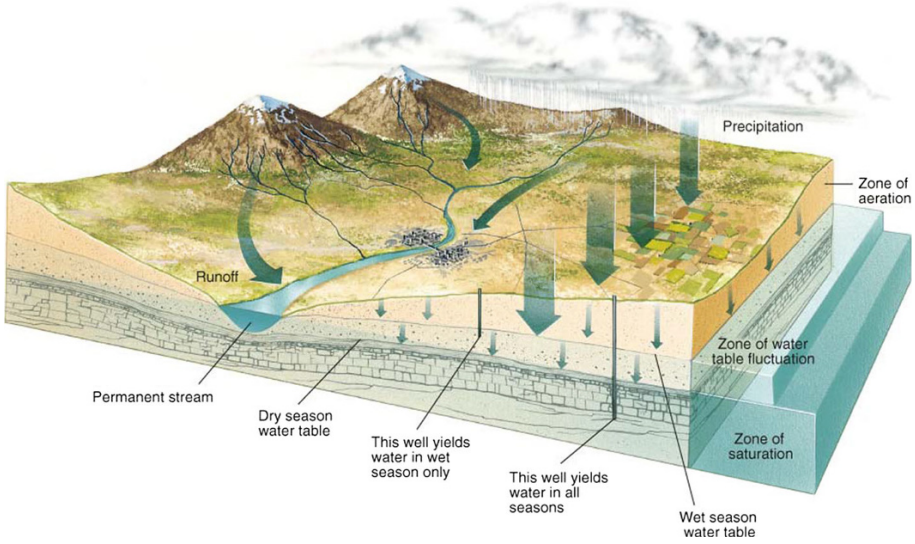


**Fig. 1** Conceptual representation of climate, groundwater, and pumping (Courtesy: Michael Dean Hitchcock)

than surface water (water in rivers, lakes, and wetlands), especially during droughts when discharge from groundwater-fed springs and shallow wells are often the only remaining sources of water (Tallaksen and van Lanen 2004; Aeschbach-Hertig and Gleeson 2012; Taylor et al. 2013). Being considered as a reliable water resource, renewal rates of groundwater are low in many regions of the world where groundwater recharge is limited due to low rainfall and high evaporation rates (Edmunds 2003; Sturchio et al. 2004; Döll and Fiedler 2008). In these parts, the risk of overexploitation is large (Konikow and Kendy 2005; Scanlon et al. 2007; Wada et al. 2010; Konikow 2011).

Many parts of the world rely heavily on groundwater for human uses, particularly areas with limited rainfall, or high water demand from irrigation and households such as India, the USA, Pakistan, China, the Middle East, and Mexico (Scanlon et al. 2010; Siebert et al. 2010; Wada et al. 2012a). For the USA, half of the population relies on groundwater for drinking water uses (USGS 1999). Irrigation involves the large-scale redistribution of freshwater from rivers, lakes, reservoirs, and groundwater, which has led to environmental flow degradation, groundwater depletion (GWD), changes in surface energy budgets associated with enhanced evapotranspiration, and eventually sea-level rise (SLR).

Except for frozen water in ice and glaciers, groundwater is the world's largest distributed store of freshwater and has strategic importance to food and water security. In this paper, the most recent advances evaluating human impacts on groundwater resources are comprehensively reviewed. This paper includes the recently advanced modeling approaches quantifying GWD and the evidence of feedbacks to the Earth system including sea-level rise associated with GWD. Critical challenges and opportunities in the use of groundwater are also identified to adapt to growing food demand and uncertain climate in the twenty-first century.

## 2 Human Water Use and Groundwater Pumping

To sustain growing food demand and increasing economic development, humans extract vast amounts of water from surface water and groundwater resources (Ramankutty and Foley 1998; Ramankutty et al. 2008; Flörke et al. 2013) (Fig. 2). Global water withdrawal has increased by 8 times from 500 to 4000 $km^3$ $year^{-1}$ since the beginning of the twentieth century with a rapid increase at a rate of 15 % per decade between 1960 and 2010 (Wada et al. 2014a). Agriculture, mostly irrigation, is the principal user of water and accounts for 70 % of the total, with the remaining part attributable to the industrial and domestic sectors (Falkenmark et al. 1997; Shiklomanov 2000a, b; Döll and Siebert 2002; Vörösmarty et al. 2005, 2010; Oki and Kanae 2006; Haddeland et al. 2006; Bondeau et al. 2007; Fischer et al. 2007; Gerten et al. 2007; Hanasaki et al. 2008a, b; Rost et al. 2008; Liu and Yang 2010; Siebert and Döll 2010; Siebert et al. 2010; Wisser et al. 2010; Biemans et al. 2011; Flörke et al. 2013; Konzmann et al. 2013; Wada et al. 2013a, b). To boost water availability, tens of thousands of reservoirs have been built in many tributaries of the major rivers and their total storage capacities exceed 8000 $km^3$ worldwide (Chao et al. 2008; Lehner et al. 2011).

Due to soaring water withdrawal, water scarcity condition is deteriorating in northwest India, northeast Pakistan, northeast China, the Middle East, and North Africa, increasing uncertainty for sustainable food production and economic development (Gleick 2000, 2003, 2010; World Water Assessment Programme 2003; Oki and Kanae 2006; Hanasaki et al. 2008a, b; Döll et al. 2009; Kummu et al. 2010; Vörösmarty et al. 2000, 2010; Wada et al. 2011a, b, 2014a, b; Gain and Wada 2014; Famiglietti 2014). The United Nations alert that in these regions, the shortage of water is beginning to constrain economic growth (World Water Assessment Programme 2009). In water-scarce regions, the water demand often exceeds the available surface water resources due to high water demand from irrigation (Siebert et al. 2010; Wisser et al. 2010; Biemans et al. 2011; Wada et al. 2013b; Haddeland et al. 2014).

Groundwater resources serve as the main source of such intense irrigation in areas overlying productive aquifers (Foster and Chilton 2003; Konikow and Kendy 2005; Siebert et al. 2010; Aeschbach-Hertig and Gleeson 2012; Wada et al. 2012a, b). Importantly, as long as groundwater abstraction is smaller than groundwater recharge, it will only reduce the groundwater discharge to surface water (base flow) (Lo et al. 2008). However, if groundwater abstraction exceeds the recharge over extensive areas for prolonged periods, persistent GWD occurs where groundwater reserves still exist, leading to falling groundwater levels (Konikow and Kendy 2005; Karami and Hayati 2005; Llamas and Martínez-Santos 2005; Shah 2005; Foster and Loucks 2006; Reilly et al. 2008; Rodell et al. 2009; Tiwari et al. 2009; McGuire 2009; Scanlon et al. 2010; Wada et al. 2010; Konikow 2011; Famiglietti et al. 2011; Döll et al. 2012, 2014; Gleeson et al. 2012a, b; Scanlon et al. 2012a, b; Taylor et al. 2013; Voss et al. 2013; Famiglietti, 2014). In that case, fossil groundwater, not being an active part of the current hydrological cycle, is used as an additional, albeit non-renewable, source of water supply that may have devastating effects on natural streamflow, groundwater-fed wetlands, and related ecosystems (Foster and Chilton 2003; Foster et al. 2004; World Water Assessment Programme 2009; Aeschbach-Hertig and Gleeson 2012). Over-pumping of groundwater can also cause extensive land subsidence due to the compaction of unconsolidated aquifer systems, being the single largest cause of subsidence. Excessive pumping has resulted in permanent subsidence and related ground

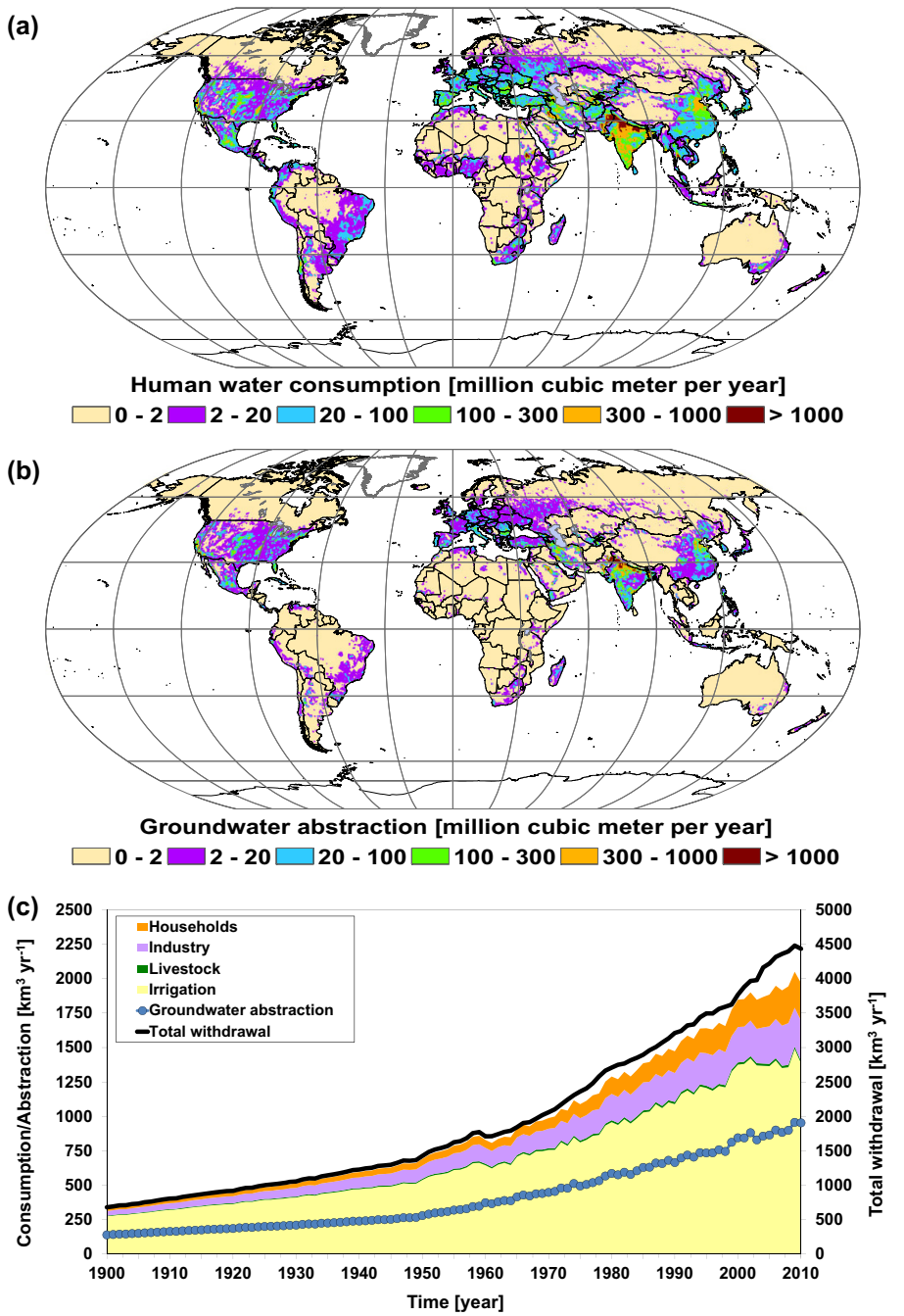


**Fig. 2** **a** Present global human water use intensity (year 2010), **b** present global groundwater abstraction rate (year 2010), and **c** historical trends of global human water use and groundwater abstraction (1900–2010). **a** and **b** are estimated at a grid scale (0.5° by 0.5°; 50 km by 50 km at the equator)

failures due to that accompanying release of water mostly non-recoverable reduction in the pore volume of the compacted soils in the aquifer system (USGS 2000).

Excessive groundwater pumping for irrigation can also perturb regional climate. Over the Ogallala Aquifer in the Great Plains (USA), groundwater-fed irrigation enhances regional precipitation by 15–30 % during July from the easternmost part of the aquifer to as far downwind as Indiana (DeAngelis et al. 2010) and a downwind precipitation by 20–30 % over the Midwest (Kustu et al. 2011). Thus, intensive groundwater irrigation causes local streamflow decrease in the Great Plains, but an increase in streamflow in the Midwest linked to the enhanced July precipitation (Kustu et al. 2010, 2011).

In order to analyze the human-induced change on water resources, a number of models that simulate the terrestrial part of the hydrological cycle on a regional to global scale (Yates 1997; Nijssen et al. 2001a, b) have been developed. These include Macro-PDM (Arnell 1999, 2004), WBM (Vörösmarty et al. 2000), VIC (Sheffield and Wood 2007), WASMOD-M (Widén-Nilsson et al. 2007), and LPJmL (Gerten et al. 2007; Konzmann et al. 2013). TRIP (Oki et al. 2001) has been used as a river routing model coupled with hydrological models. H08 (Hanasaki et al. 2008a, b, 2010), MATSIRO (Pokhrel et al. 2012a, b; Koirala et al. 2014), PCR-GLOBWB (Van Beek et al. 2011; Wada et al. 2014a), and WaterGAP (Alcamo et al. 2003a, b; Döll et al. 2003, 2009, 2014) include anthropogenic effects in global water balance simulation, considering groundwater and surface water use (water withdrawal, return flow, and consumptive water use) and reservoir regulation.

Conventionally, groundwater use is estimated from tubewell inventories or phreatic surface fluctuations; however, such information is hardly available over a large aquifer system. Table 1 shows data- and model-based estimates of the global groundwater pumping rate. The data-based estimates are primarily based on available country statistics, falling into a range of 600–800 $km^3$ $year^{-1}$. However, the model-based estimates vary substantially among the studies. Wisser et al. (2010) estimate total groundwater use to be 1700 $km^3$ $year^{-1}$. Döll (2009) estimates that to be 1100 $km^3$ $year^{-1}$ using a fraction of groundwater-to-total water withdrawals per country and WaterGAP model simulation (Alcamo et al. 2003a, b). Vörösmarty et al. (2005), Rost et al. (2008), Wisser et al. (2010), Hanasaki et al. (2010), Pokhrel et al. (2012a, b) and Yoshikawa et al. (2014) implicitly quantified unsatisfied water use (i.e., non-renewable water use), ranging from 400 to 1200 $km^3$ $year^{-1}$. The estimates vary substantially by implicitly quantifying the amounts with water demand exceeding locally accessible supplies of surface water (one grid cell) and are thus not limited to groundwater. Wada et al. (2010) combined the available global-scale information of country groundwater abstraction rate obtained from the International Groundwater Resources Assessment Centre (IGRAC; http://www.un-igrac.org/) with hydrological model simulation.

The data-based estimates contain many missing country data in Asia, Africa, South America, and Europe (e.g., Afghanistan and the Former Yugoslavia). In addition, a considerable part of groundwater pumping may remain unreported. For example, the IGRAC database reports groundwater abstraction of 190 $km^3$ (year 2000) for India, while Foster and Loucks (2006) suggest 240 $km^3$. Given extensive missing data and non-reported groundwater abstraction, the model-based estimates (e.g., Vörösmarty et al. 2005; Rost et al. 2008; Wisser et al. 2010; Hanasaki et al. 2010) have a clear advantage; however, they neglect physical, technologica,l and socioeconomic limitations in water use that exist in various countries. Potential errors in these methods can be substantial, given the considerable variation among the estimates.

**Table 1** Global estimates of groundwater pumping ($km^3$ $year^{-1}$)

| $km^3$ $year^{-1}$ | Total/Non-renewable Groundwater abstraction[a] | Year | Withdrawal/ Consumption | Runoff/ Recharge | Sources[b] |
|---|---|---|---|---|---|
| Data-based estimates | | | | | |
| Postel (1999) | –/∼200 | Contemporary | – | – | Literature and country statistics |
| IGRAC-GGIS | ∼750/– | 2000 | – | – | Literature and country statistics |
| Shah (2005) | 800–1000/– | Contemporary | – | – | FAO AQUASTAT, Llamas et al. (1992) |
| Zektser and Everett (2004) | 600–700/– | Contemporary | – | – | Country statistics |
| Model-based estimates | | | | | |
| Vörösmarty et al. (2005) | $-/389^{Irr}$–$830^{Total}$ | Average 1995–2000 | $3557^{Total}$–$1206^{Irr.}$ | 39,294/– | Simulated by WBM (0.5°) |
| Rost et al. (2008) | –/730 | Average 1971–2000 | 2534–2566/1353–1375 | 36,921/– | Simulated by LPJmL (0.5°) |
| Döll (2009) | 1100/– | 2000 | 4020/1300 | 38,800/– | IGRAC-GGIS and WaterGAP (0.5°) |
| Wisser et al. (2010) | 1708/1199 | Contemporary | 2997/– | 37,401/– | Simulated by $WBM_{plus}$ (0.5°) |
| Hanasaki et al. (2010) | –/703 | Average 1985–1999 | –/1690 | 41,820/– | Simulated by H08 (1.0°) |
| Siebert et al. (2010) | 545/– | 2000 | –/1277 | 39,549/12,600 | 15,038 national/sub-national statistics (irrigation) |
| Wada et al. (2010) | 734(±82)/283(±40) | 2000 | –/– | 36,200/15,200 | IGRAC-GGIS and PCR-GLOBWB (0.5°) |
| Pokhrel et al. (2012a,b) | –/455(±42) | 2000 | 2462(±130)/1021(±55) | –/– | Simulated by MATSIRO (1.0°) |
| Döll et al. (2012) | ∼1500/– | Average 1998–2002 | 4300/1400 | –/– | IGRAC-GGIS and WaterGAP (0.5°) |
| Yoshikawa et al. (2014) | –/510<br>–/1150 | 2000<br>2050 | $-/1358^{Irr.}$<br>$-/2355^{Irr.}$ | –/– | Simulated by H08 (1.0°) |
| Wada and Bierkens (2014) | 372/90<br>952/304<br>1621(±128)/597(±85) | 1960<br>2010<br>2099 | 1708/828<br>4436/1970<br>6223(±420)/2840(±280) | –/– | IGRAC-GGIS and PCR-GLOBWB (0.5°) |

[a] *Total* total groundwater abstraction, *Nonrenewable* non-renewable groundwater abstraction (abstraction in excess of recharge)

[b] FAO AQUASTAT: http://www.fao.org/nr/water/aquastat/main/index.stm

Estimating groundwater recharge poses an additional uncertainty since observed recharge rates are rarely available at the scale used in hydrological models. Natural replenishment of groundwater occurs predominantly from precipitation (i.e., diffuse recharge) and from surface water bodies such as ephemeral streams, wetlands or lakes (focused recharge via leakage) (Scanlon et al. 2002, 2005, 2006, 2007, 2010; Crosbie et al. 2012; Taylor et al. 2013). Therefore, recharge is strongly influenced by climate variability including climate extremes (i.e., droughts and floods) that often relate to modes of climate variability such as El Niño Southern Oscillation (ENSO) at multiyear timescales (Trenberth et al. 1988; Wilhite 2000; Seager 2007; Crosbie et al. 2012). Modeled global estimates of diffuse recharge range from 13,000 to 17,000 $km^3$ $year^{-1}$, equivalent to 30–40 % of the world's renewable freshwater resources (Döll and Fiedler 2008; Wada et al. 2010; Wada and Heinrich 2013) (Fig. 3). These modeled global recharge fluxes do not include focused recharge which, in semi-arid environments, can be substantial. Wada and Heinrich (2013) estimated additional recharge from irrigation to be 500 $km^3$ $year^{-1}$ globally, which is <5 % of the global diffuse recharge, but can be substantial over arid environments (Fig. 4).

## 3 Global and Regional Assessments of Groundwater Depletion

Large-scale assessment of GWD remains challenging. The lack of observation-based information on groundwater pumping and recharge as well as groundwater-level change hinders accurate estimates of GWD across the world (Konikow 2011; Gleeson and Wada 2013).

In order to estimate the rate of GWD at a regional- to continental- and global-scale, three different approaches have been primarily employed: (1) using ground-based measurements such as water table depth and a regional-scale (calibrated) groundwater flow model to simulate groundwater storage change due to pumping (*volume-based method*), (2) use of a large-scale hydrological and water resources model to estimate groundwater fluxes of pumping and recharge, and then resulting GWD (*flux-based method*), and (3) utilizing near in situ satellite observation such as the GRACE (Gravity Recovery and Climate Experiment) to infer groundwater storage change from total terrestrial water storage change (TWS: snow water, surface water, soil water, and groundwater storage) (*satellite-observed method*; see Chen et al. (2015) in this issue for the detailed descriptions). Table 2 summarizes recent estimates of GWD at regional and global scales using these different approaches.

Since the impact of GWD is highly localized, regional groundwater flow modeling provides accurate estimates of groundwater-level change (Aeschbach-Hertig and Gleeson 2012). Cao et al. (2013) built a multilayer, heterogeneous and anisotropic flow model using MODFLOW (Harbaugh et al. 2000) in order to simulate spatiotemporal variability in GWD across the North China Plain (NCP) (*volume-based method*). Simulated average GWD was found to be about 4 $km^3$ $year^{-1}$ from 1960s to 2008. However, GWD varied with time: 2.5 $km^3$ $year^{-1}$ in the 1970s, 4.0 $km^3$ $year^{-1}$ in the 1980s, 2.0 $km^3$ $year^{-1}$ over 1990–1996, 7.0 $km^3$ $year^{-1}$ over 1997–2001, and 4.0 $km^3$ $year^{-1}$ over 2002–2008. Using the GRACE-derived total TWS changes, Feng et al. (2013) and Huang et al. (2015) estimated GWD in the NCP to be 8.3 ($\pm$1.1) $km^3$ $year^{-1}$ over 2003–2010 and 4.0 ($\pm$0.6) $km^3$ $year^{-1}$ over 2003–2012 respectively. Hu et al. (2010) also applied a groundwater flow model over the same region and found that about 30 % reduction in irrigation could prevent GWD in the plain, and an additional 10 % reduction in irrigation pumping would induce groundwater recovery.

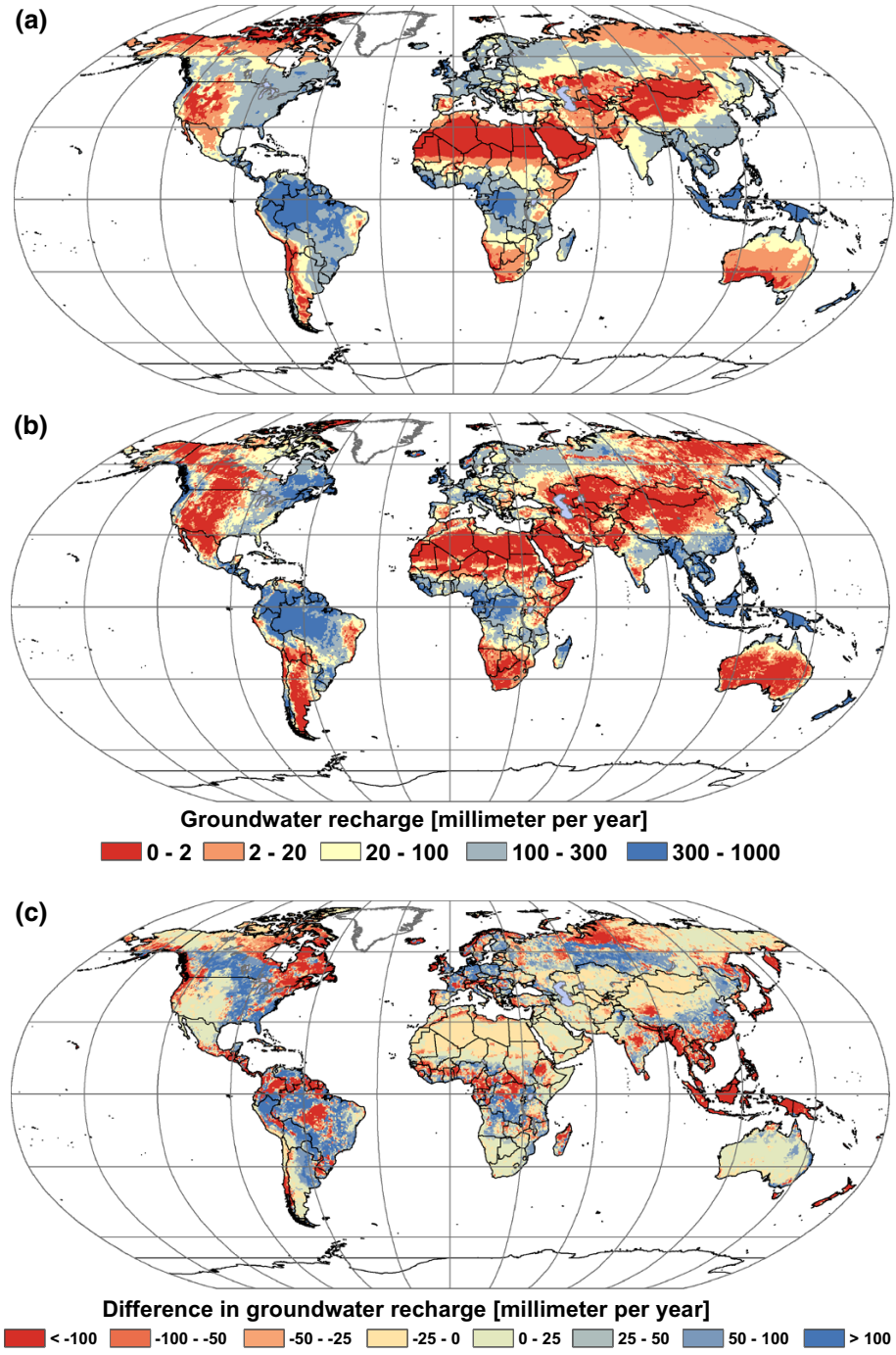


**Fig. 3** Global diffuse groundwater recharge from **a** Döll and Fiedler (2008) and **b** Wada et al. (2010), and the difference (**a**, **b**). These are estimated at a grid scale (0.5° by 0.5°; 50 km by 50 km at the equator)

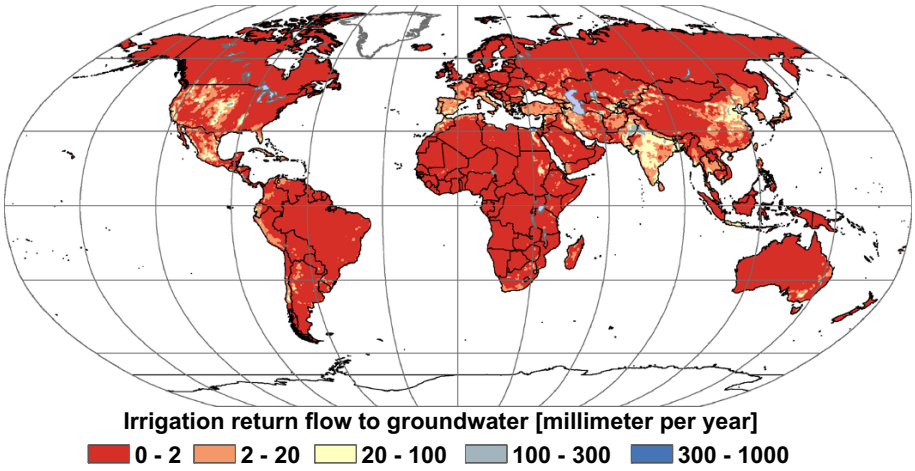


**Fig. 4** Global irrigation return flow to groundwater system estimated at a grid scale (0.5° by 0.5°; 50 km by 50 km at the equator)

Since its launch in 2002, the GRACE gravity estimation has been increasingly employed to quantify groundwater storage changes at regional scales (*satellite-observed method*). The GRACE detects changes in TWS by measuring temporal variations in the gravity field (Tapley et al. 2004). Groundwater storage changes can be assessed after subtracting remaining TWS changes from GRACE-derived total TWS changes. However, the isolation of groundwater storage change from GRACE-based TWS can cause a large difference using other water storage components derived typically from land surface or hydrological models that have different process orientations and model structure, e.g., inclusion of irrigation and reservoir operations (Rodell et al. 2009; Tiwari et al. 2009; Jacob et al. 2012; Shamsudduha et al. 2012; Voss et al. 2013). Huang et al. (2015) indicated that the shallow groundwater declines faster than the deep groundwater in the NCP, but the shallow groundwater storage recovers quickly during the recent 2008–2011 drought. In general, many large-scale models do not accurately represent surface water–groundwater interactions and simulated soil water storage may be under- or overestimated (see Döll et al. (2015) in this issue for the detailed descriptions). In addition, coarse spatial resolution and noise contamination inherent in GRACE data pose a challenge estimating GWD in small aquifers (Longuevergne et al. 2010; Famiglietti et al. 2011; Scanlon et al. 2012a, b) and subsequently global application of estimating GWD (Famiglietti 2014; Richey et al. 2015). Moreover, using in situ groundwater-level observations, Shamsudduha et al. (2012) showed that GWD estimates for the humid tropics (e.g., Bangladesh) derived from GRACE gravity estimation may be subject to large uncertainties due to highly seasonal water storage changes.

Use of a global-scale hydrological model enables to simulate the distribution of global hotspots of GWD. Wada et al. (2010) calculated GWD defined as groundwater abstraction in excess of recharge (*flux-based method*) (Fig. 5). The analysis was limited to sub-humid-to-arid climate zones to avoid overestimation arising from increased capture of discharge and enhanced recharge due to groundwater pumping (Bredehoeft 2002). The results revealed that global GWD increased from 126 (±32) to 283 (±40) $km^3$ $year^{-1}$ over 1960–2000. Wada et al. (2012a, b) applied a correction factor to constrain the original

**Table 2** Global and regional estimates of groundwater depletion (GWD) ($km^3$ $year^{-1}$)

| $km^3$ $year^{-1}$ | | GWD | Year | Notes | Sources |
|---|---|---|---|---|---|
| Global | Sahagian et al. (1994) | 86.7 | Contemporary | Limited regions (e.g., USA, India, China) | Literature<br>Country statistics |
| | Postel (1999) | 200 | Contemporary | | Literature<br>Country statistics |
| | Wada et al. (2010) | 126 (±32)<br>283 (±40) | 1960<br>2000 | Depletion equals abstraction in excess of recharge | IGRAC-GGIS<br>PCR-GLOBWB (0.5°) |
| | Konikow (2011) | 145 (±39) | 2000–2008 | Extrapolated for other than USA, north India, North China Plain, Saudi Arabia, Nubian and Sahara | In situ groundwater-level measurements, GRACE satellite observation, calibrated groundwater model, extrapolation (15.4 %; depletion to abstraction ratio of USA) |
| | Wada et al. (2012a, b) | 163 (±28)<br>204 (±30) | 1990–2000<br>2000 | Corrected against reported regional depletion estimates | IGRAC-GGIS<br>PCR-GLOBWB (0.5°) |
| | Pokhrel et al. (2012a, b) | 455 (±42) | 2000 | Depletion equals water demand in excess of water availability | MATSIRO (1.0°) |
| | Döll et al. (2014) | 113 | 2000–2009 | Application of deficit irrigation | WaterGAP (0.5°), in situ groundwater-level measurements, GRACE satellite observation |
| | Van Dijk et al. (2014) | 92 | 2003–2012 | Without data assimilation, original depletion equals 168 $km^3$ $year^{-1}$ | Data assimilation with GRACE satellite observation |
| | Famiglietti (2014) | 77.4 | 2003–2013 | Time periods vary among studies considered<br>Limited regions | Various studies using GRACE-derived total terrestrial water storage changes |
| | Pokhrel et al. (2015) | 330 | 2000 | 570 $km^3$ $year^{-1}$ for the global groundwater abstraction for 2000 | MATSIRO (1.0°) |
| Regional<br>Northwest Sahara | Richey et al. (2015) | 2.7 | 2003–2012 | Algeria, Libya, Tunisia | GRACE-derived total terrestrial water storage changes |

**Table 2** continued

| $km^3$ $year^{-1}$ | | GWD | Year | Notes | Sources |
|---|---|---|---|---|---|
| Middle East and North Africa (MENA) | Foster and Loucks (2006) | 26.8 | Contemporary | | Literature<br>Country statistics |
| | Voss et al. (2013) | 13.0 (±1.6) | 2003–2009 | Cumulative 91.3 (±10.9) $km^3$ for 2003–2009 | GRACE-derived total terrestrial water storage changes |
| Arabian | Richey et al. (2015) | 15.5 | 2003–2013 | Iraq, Jordan, Oman, Qatar, Saudi Arabia, UAE, Yemen | GRACE-derived total terrestrial water storage changes |
| Guarani | Richey et al. (2015) | 1.0 | 2003–2013 | Argentina, Brazil, Paraguay, Uruguay | GRACE-derived total terrestrial water storage changes |
| North China Plain (NCP) | Cao et al. (2013) | 4.0<br>2.5<br>4.0<br>2.0<br>7.0<br>4.0 | 1960–2008<br>1970s<br>1980s<br>1990–1996<br>1997–2001<br>2002–2008 | Cumulatively 158 $km^3$ for 1960–2008 (20 % of pumpage of 807 $km^3$) | MODFLOW |
| | Feng et al. (2013) | 8.3 (±1.1) | 2003–2010 | 2.5 $km^3$ $year^{-1}$ for shallow aquifers reported by Groundwater Bulletin of China Northern Plains | GRACE-derived total terrestrial water storage changes |
| | Huang et al. (2015) | 2.5 (±0.4)-PP<br>1.5 (±0.2)-ECP | 2003–2012 | Piedmont Plain (PP)<br>East Central Plain (ECP) | GRACE-derived total terrestrial water storage changes |
| Indus | Cheema et al. (2014) | 31 | 2007 | 68 $km^3$ of total groundwater abstraction | Remote sensing combined with a hydrological model and spatial information on canal water supplies |
| Northern India | Rodell et al. (2009) | 17.7 (±4.5) | 2002–2008 | Cumulative 109 $km^3$ for 2002–2008 | GRACE-derived total terrestrial water storage changes |
| Northern India and surrounding regions | Tiwari et al. (2009) | 54 (±9) | 2002–2008 | | GRACE-derived total terrestrial water storage changes |
| | Jacob et al. (2012) | 35 | 2003–2010 | | GRACE-derived total terrestrial water storage changes |

**Table 2** continued

| $km^3$ $year^{-1}$ | | GWD | Year | Notes | Sources |
|---|---|---|---|---|---|
| Bangladesh | Shamsudduha et al. (2012) | 0.44 (±1.24)–2.04 (±0.79)–wet seasons<br>0.52(±0.5)–2.83 (±0.42)-annual | 2003–2007 | Depletion of 0.52 (±0.30)–0.85 (±0.17) $km^3$ $year^{-1}$ from borehole hydrographs | GRACE-derived total terrestrial water storage changes |
| California's Central Valley | Famiglietti et al. (2011) | 3.1 (±0.6) | 2003–2010 | Cumulative 20.3 $km^3$ for 2003–2010 | GRACE-derived total terrestrial water storage changes |
| | Scanlon et al. (2012a) | 2.0<br>6–8 | 1962–2003<br>2006–2010 | Cumulative 24.6 $km^3$ for 1976–1977, 49.3 $km^3$ for 1987–1992, 140 $km^3$ since the 1860s, and 80 $km^3$ since the 1960s | MODFLOW |
| | Scanlon et al. (2012b) | 8.9 (± 0.9) | 2006–2010 | Cumulative 31.0 (±3.0) $km^3$ for 2006–2010 | GRACE-derived total terrestrial water storage changes |
| High Plains Aquifer | Scanlon et al. (2012a) | 5.7<br>7.0<br>12.5 | 1950–2007<br>1987–2007<br>2003–2013 | Cumulative 330 $km^3$ after pre-development in the 1950s | MODFLOW |
| Canning Basin | Richey et al. (2015) | 3.6 | 2003–2013 | Australia | GRACE-derived total terrestrial water storage changes |

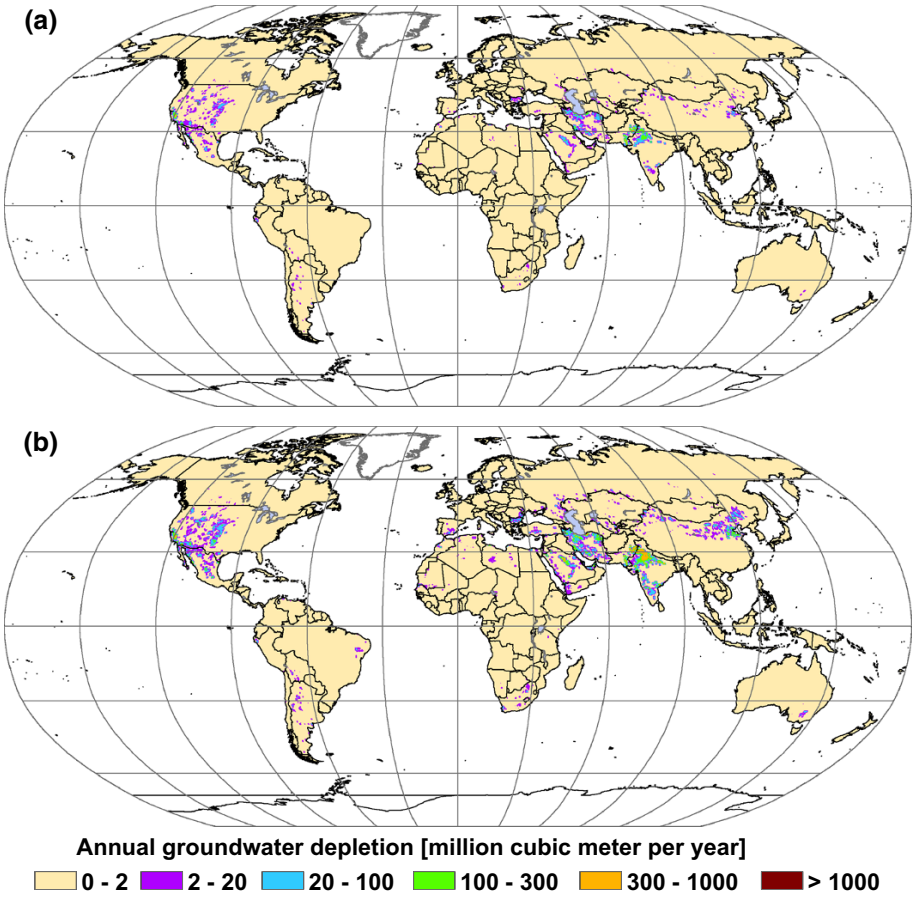


**Fig. 5** Global GWD for the year 1960 and 2010 estimated at a grid scale (0.5° by 0.5°; 50 km by 50 km at the equator)

GWD estimate (Wada et al. 2010) by regionally reported numbers, producing a 30 % lower estimate (204 ± 30 $km^3$ $year^{-1}$). The results also showed that GWD contributes nearly 20 % to global irrigation water supply. A recent study by Döll et al. (2014) combined hydrological modeling with information from well observations and GRACE satellites. They also simulated focused groundwater recharge from surface water bodies in dry regions, while Wada et al. (2010, 2012a, b) included only diffuse rain-fed recharge. Moreover, Döll et al. (2014) applied deficit irrigation (70 % of optimal water requirement) and estimated global GWD to be 113 $km^3$ $year^{-1}$ during 2000–2009 (see Table 2). Pokhrel et al. (2015) used an integrated hydrologic model, which explicitly simulates groundwater dynamics and pumping within a global land surface model. Simulated global GWD was found to be 330 $km^3$ $year^{-1}$ for 2000. Large uncertainty inherent in *flux-based method* can be largely reduced by combining hydrological model simulation with local well observations or GRACE satellite observation (Döll et al. 2014).

Recent advancement in remote sensing technique also enables to quantify GWD over a large extent. Ahmad et al. (2005) combined remote sensing and water balance approaches

and revealed large GWD in Pakistan. Cheema et al. (2014) used remotely sensed evapotranspiration and precipitation combined with a hydrological model and spatial information on canal water supplies to quantify the extent of GWD in the Indus (31 $km^3$; Table 2). Van Dijk et al. (2014) integrated water balance estimates derived from GRACE satellite observation, satellite water-level altimetry, and off-line estimates from several hydrological models, using the data assimilation framework. The data assimilation framework improved the estimate of global GWD derived from the flux-based method from 168 to 92 $km^3$ $year^{-1}$ (average 2003–2012).

Rapid advancement in large-scale hydrological modeling and increasing availability of near in situ satellite observation on groundwater storage change from the GRACE satellites provide a new opportunity to estimate the amount of GWD at a regional to global scale. This is particularly useful for areas with insufficient data and in transboundary river basins and aquifers where political conflicts sometimes hinder data sharing among sovereign countries.

## 4 Groundwater Depletion and Sea-Level Rise

Sea-level rise (SLR) is generally attributed to thermal expansion and the melt of glaciers, ice caps, and ice sheets. However, groundwater pumping for agriculture (mostly irrigation) and other uses (industry and households) contributes to SLR through the persistent removal of dormant groundwater from subsurface storage as a net transfer of freshwater to active hydrological cycle at the Earth's surface.

The rate of GWD and its contribution to SLR has been subject to much debate (Gornitz 1995; Gregory et al. 2013). In the IPCC AR4 (Solomon et al. 2007), the contribution of non-frozen terrestrial waters including GWD to sea-level variation is not included due to its perceived uncertainty. One of the earliest studies by Sahagian et al. (1994) estimated that GWD occurs at a rate of 86.7 $km^3$ $year^{-1}$ contributing 0.24 mm $year^{-1}$ to SLR, while Gornitz (2001) indicated that GWD can contribute 0.10–0.30 mm $year^{-1}$ to SLR (see also Table 2). Foster and Loucks (2006), who assessed GWD over the Middle East and North Africa, estimated 26.8 $km^3$ $year^{-1}$ equivalent to 0.075 mm $year^{-1}$ of SLR. These studies evaluate direct groundwater storage changes, but cover only limited number of aquifers and did not account some of large aquifer systems of intensive groundwater mining (e.g., Indo-Gangetic Plain and North China Plain).

More recently, based on the flux-based method Wada et al. (2010) estimated the current rate of global GWD to be 283 (±40) $km^3$ $year^{-1}$ (0.8 ± 0.1 mm $year^{-1}$), responsible for 25 (±3) % of recently observed SLR. Critical assumption is that 97 % of the GWD adds up to the ocean based on the ratio of groundwater recharge to total precipitation on Earth and assuming all other stores (atmospheric moisture and surface waters) to remain constant. Later, Wada et al. (2012b) revised their approach and estimated that the average global GWD rate amounts to 163 (±28) $km^3$ $year^{-1}$ during 1990–2000, equivalent to a SLR of 0.46 (±0.08) mm $year^{-1}$. During the twentieth century, the contribution of GWD to global sea level increased from 0.035 (±0.009) to 0.57 (±0.09) mm $year^{-1}$ (see Fig. 6).

When the contribution of global GWD to SLR is placed in context with other terrestrial water sources including reservoir impoundment, water release due to deforestation, marsh drainage, or wetland loss, and storage loss from endorheic lakes (mostly from the Aral Sea), it is important to note that reservoir impoundment due to dam building is of the opposite sign in its sea-level contribution, suggesting that the volume of water accumulated

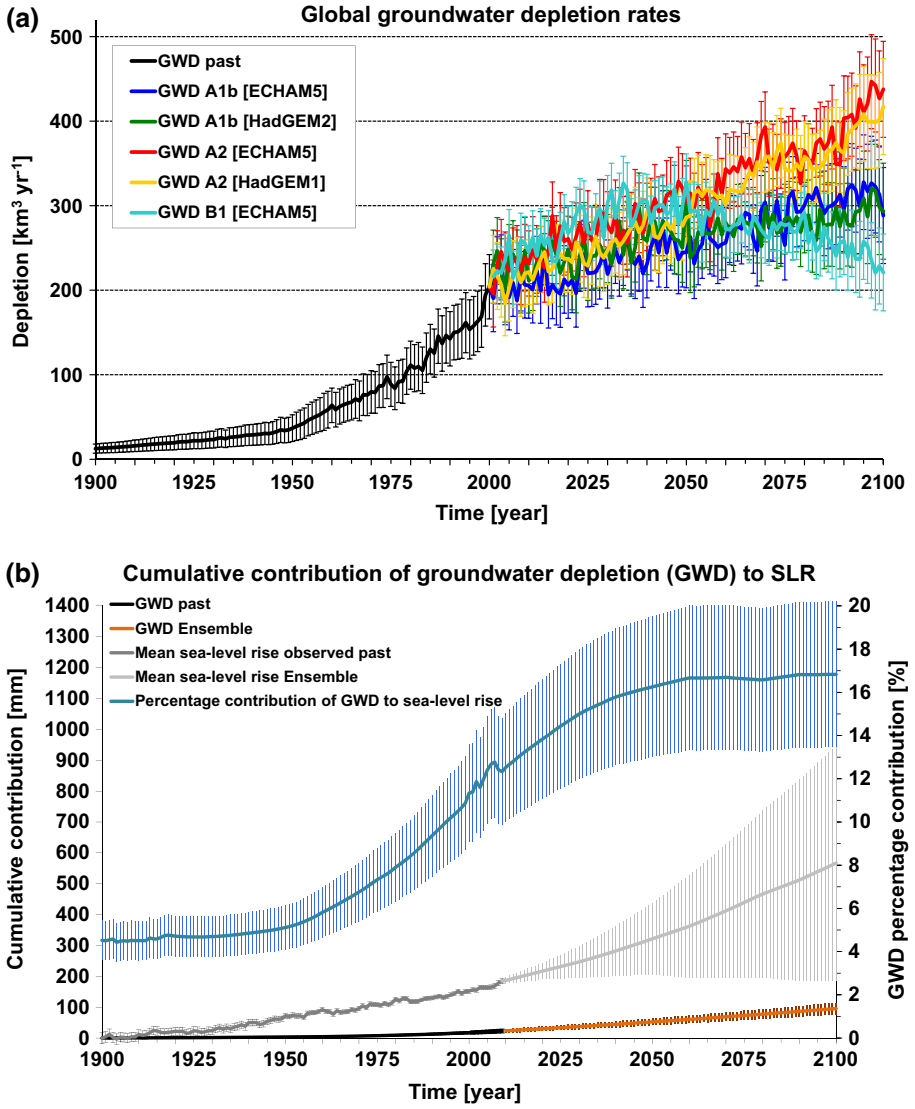


**Fig. 6** **a** Historical and future trends of global GWD rates and **b** Historical and future trends of the contribution of global GWD to sea-level rise

in reservoirs up to 2010 amounts to ~30 mm sea-level equivalent (Chao et al. 2008). However, Lettenmaier and Milly (2009) indicated that the volume of silt accumulated in reservoirs should be removed, which is equal to ~4 mm sea-level equivalent. Indeed, silting up of existing reservoirs may already be, or in coming decades may become, a larger effect on impoundment than construction of new reservoir capacity (Wisser et al. 2013).

The net contribution of terrestrial water sources to global SLR is rather small with the average rate of +0.05 (±0.016) mm year$^{-1}$ over the period 1900–1950. However, as a result of increased dam building from the mid-twentieth century, the net contribution

became consistently negative with the average rate of −0.21 (±0.08) mm year$^{-1}$ during 1950–1990, and −0.15 (±0.09) mm year$^{-1}$ during 1970–1990. Since the 1990s, dam building has been tapering off and GWD has been steadily increasing, and the net contribution became positive with the average rate of +0.25 (±0.09) mm year$^{-1}$ over the period 1990–2000. During the recent decade, GWD is fast becoming the most important positive terrestrial water contribution, and currently already outweighs the negative contribution from dam building (Wada et al. 2012b).

The flux-based method, however, overestimates GWD as it does not account for increased capture due to decreased groundwater discharge and enhanced recharge from surface waters (Bredehoeft 2002). The methods ignore the compensating changes due to pumping in other water fluxes, such as groundwater recharge and discharge. While the estimated rate by Wada et al. (2012b) is fairly well constrained, simplifying assumption may influence the results as they assumed the correction factor to be constant over time. They also assumed that groundwater is attainable throughout the projection, which may be optimistic in regions, where groundwater level may become too low for local farmers with limited technologies to extract. In addition, uncertainties arise from imposed scenarios of climate and socioeconomic development.

A subsequent volume-based study by Konikow (2011) estimated global GWD to be 145 (±39) km$^3$ year$^{-1}$ (0.41 ± 0.1 mm year$^{-1}$). This estimate used direct evidence of groundwater storage changes from groundwater-level observations, calibrated groundwater modeling, and GRACE satellite data to calculate GWD (101.6 km$^3$ year$^{-1}$; 0.29 mm year$^{-1}$) for the USA and other five aquifer systems of the world (north India, North China Plain, Saudi Arabia, Nubian and Sahara). GWD of the rest of the world (43.7 km$^3$ year$^{-1}$; 0.12 mm year$^{-1}$) was extrapolated by employing the fixed ratio of depletion to abstraction observed in the USA (15.4 %). Thus, this volume-based estimate does not account for regional variability in the relationship between GWD and abstraction. Although near-in-situ estimates of regional GWD are becoming more and more available by the benefit of the GRACE data, no global estimate of GWD based on direct groundwater observations exists.

Satellite observations open a path to monitor groundwater storage changes in data-scarce regions (Strassberg et al. 2007). Rodell et al. (2009) and Tiwari et al. (2009) report substantial GWD over north India (17.7 ± 4.5 km$^3$ year$^{-1}$; 0.05 ± 0.013 mm year$^{-1}$) and north India and adjacent regions (54 ± 9 km$^3$ year$^{-1}$; 0.15 ± 0.025 mm year$^{-1}$) (see also Table 2). Famiglietti et al. (2011) and Scanlon et al. (2012b) assessed GWD in the California's Central Valley in the USA and found substantial GWD (3.1 ± 0.6 to 8.9 ± 0.9 km$^3$ year$^{-1}$), primarily due to irrigation.

## 5 Future Projections of Groundwater Depletion

Future projections of GWD are subject to large uncertainties due to the use of climate projections from General Circulation Models (GCMs) and future scenarios of socioeconomic and land use conditions (Van Vuuren et al. 2011). Only a few studies provide future assessments of GWD worldwide.

Wada et al. (2012b) projected that the contribution of global GWD to SLR is expected to increase to 0.82 (±0.13) mm year$^{-1}$ by 2050 from 0.57 (±0.09) mm year$^{-1}$ in 2000 (Fig. 6). The increase is driven by growing water demand during the twentieth century, but is primarily affected by decreased surface water availability and groundwater recharge, and

larger evaporative demand from irrigated areas due to changes in precipitation variability and higher temperature over the twenty-first century. Due to decreasing dam building and increasing groundwater pumping, the net terrestrial water contribution to global sea level further increases to the rate of +0.84 (±0.12) mm year$^{-1}$ by 2050. The percentage contribution of GWD to global SLR will reach 17 (±3) % by 2050.

Yoshikawa et al. (2014) found that under a consistent expansion of irrigated areas, the amount of non-renewable water use is projected to reach ~1150 km$^3$ year$^{-1}$ by 2050, which will equal a quarter of the total irrigation water requirements. However, they used globally a medium population growth scenario (0.9 % year$^{-1}$) to extrapolate the future irrigated area change, which is rather high (from 2.7 in 2000 to 3.9 million km$^2$ in 2050). The expansion of irrigated areas has been slowing down in many countries. A few studies provide the future increase in irrigated areas, but their estimates are low for most parts of the world: 0.6 % year$^{-1}$ by 2030 for developing countries with 75 % of the global irrigated areas (Bruinsma 2003); from 2.87 in 2005 to 3.18 million km$^2$ in 2050 (Turral et al. 2011); global growth rates of only 0 to 0.18 % year$^{-1}$ by 2050; and then they stabilizes (Millennium Ecosystem Assessment 2005).

Wada and Bierkens (2014) quantified the fraction of the consumptive blue water use that is met from non-sustainable water resources, using the Blue Water Sustainability Index (BlWSI) (Fig. 7). The BlWSI incorporates not only GWD but also non-sustainable surface water use that compromises environmental flow requirements (Alley et al. 1999; Smakhtin 2001; Smakhtin et al. 2004; Rockström et al. 2009; Gerten et al. 2013; Pastor et al. 2013).

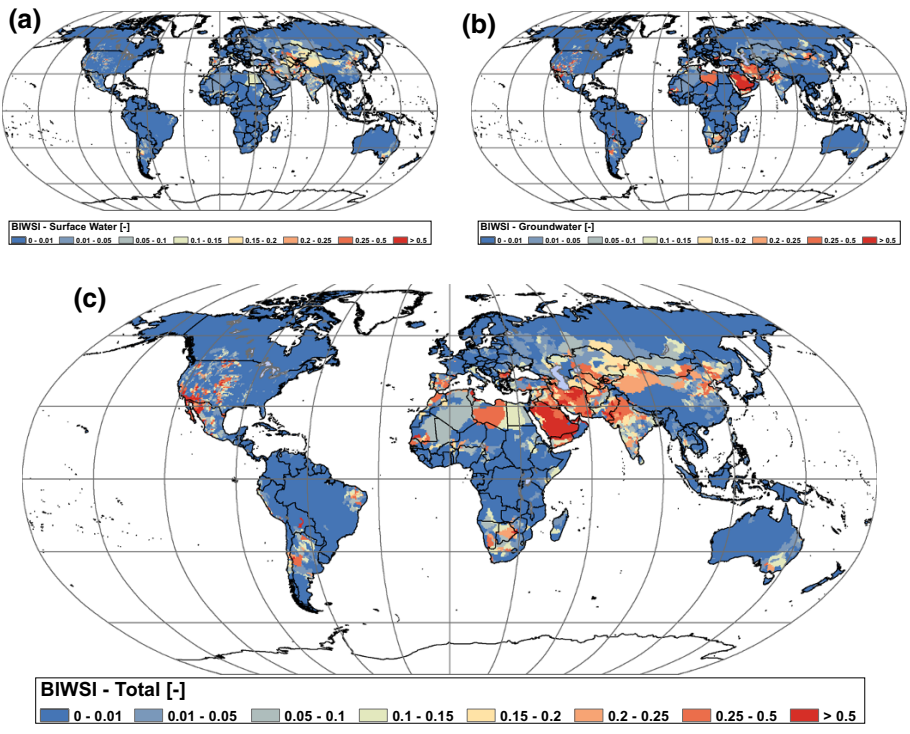


**Fig. 7** Global average non-sustainable water use (BlWSI) (dimensionless) for **a** surface water, **b** groundwater, and **c** the total at a subbasin scale (except the Antarctica and Greenland) (1960–2010)

By the end of this century, human water use is projected to rise drastically over Africa, Central, West, and South Asia, western USA, Mexico, and Central South America (the increase: >100 %), where the increase is primarily driven by rapid population growth (Fig. 8). Global water withdrawals are projected to increase to 6000 $km^3$ $year^{-1}$, while global water consumption is expected to rise to 3000 $km^3$ $year^{-1}$. As a result of rapid increase in human water use, GWD is projected to become more intense predominantly over the Indus, Saudi Arabia, Iran, Algeria, the southwestern and Central USA, and northern Mexico (Rodell et al. 2009; Tiwari et al. 2009; Famiglietti et al. 2011; Konikow 2011; Scanlon et al. 2012a, b; Cao et al. 2013; Voss et al. 2013). Over these regions, one-third of the irrigation water consumption will likely be sustained at the expense of GWD by 2050. The increase in GWD is driven by multiple factors: an increase in human water use, a decrease in surface water availability, higher low flow frequency (higher drought occurrence), or an increase in surface water over-abstraction. Highest surface water over-abstraction occurs over South, West, and Central Asia, northeastern China, Spain, and Argentina where more than a quarter of surface water consumption is non-sustainable or sustained at the expense of environmental flow. Future hotspots of non-sustainable water use from both surface water and groundwater appear over the southwestern USA, Mexico, Argentina, the Mediterranean region, the Middle East and Northern Africa region and southern Africa (Fig. 9). These regions will suffer from both increasing human water use and drier climate conditions.

Table 3 shows country estimates of total and non-renewable groundwater abstraction for major groundwater users. Over the period 1960–2010, a drastic increase in non-renewable groundwater abstraction is observed for India, Iran, and Saudi Arabia. By the end of this century, the amount of non-renewable groundwater abstraction is expected to be doubled for almost all major groundwater users. The increase is particularly pronounced for India, Pakistan, USA, and Mexico, where the regions with rising population and water use will coincide with those with decreasing surface water availability and groundwater recharge under climate change. For China, population growth is mild and climate change has a low impact on surface water availability and groundwater recharge. Over Iran and Saudi Arabia, the baseline surface water availability and groundwater recharge (for the historical period) is low and the increase in non-renewable groundwater abstraction will be driven by socioeconomic change.

The global signal suggests an increasing trend of water supplied from non-sustainable water resources especially since the late 1990s, despite larger water availability (Jung et al. 2010). By 2100, the use of non-sustainable water resources is projected to increase to 1100 (±200) $km^3$ $year^{-1}$, of which 45 (±10) % or 500 (±100) $km^3$ $year^{-1}$ and 55 (±10) % or ~600 (±100) $km^3$ $year^{-1}$ will be met from surface water over-abstraction and non-renewable groundwater abstraction, respectively, indicating that 40 % of the annual human water consumption will be non-sustainable (Fig. 10).

The estimate of non-renewable groundwater abstraction by Wada and Bierkens (2014) (~450 $km^3$ $year^{-1}$ by 2050) is less than half of that derived by Yoshikawa et al. (2014) (see Table 1 for the comparison of non-renewable groundwater abstraction among different studies). Since the change in irrigated areas is not considered, the future irrigation water use of Wada and Bierkens (2014) is ~25 % lower compared to that of Hanasaki et al. (2013a, b) and Yoshikawa et al. (2014) (see Table 4). However, the increase in irrigation intensity and water productivity, and the improvement in irrigation efficiency may substantially mitigate the rise in future irrigation water demand (Gleick 2000; Gerten et al. 2011; Elliott et al. 2014; Haddeland et al. 2014). These estimates address

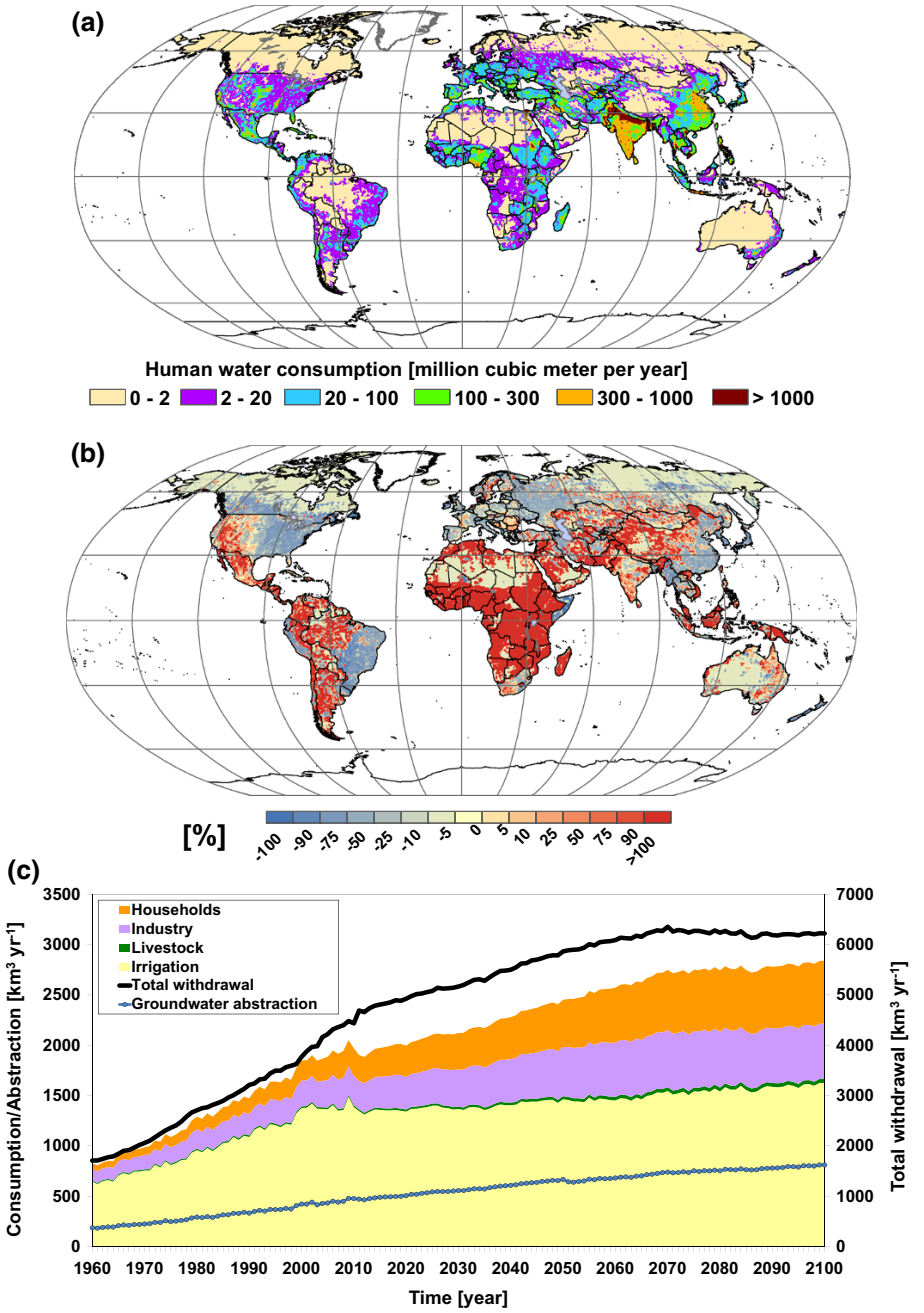


**Fig. 8** **a** Future global human water use intensity (year 2099) (million $m^3$ $year^{-1}$), **b** the relative change (%) from the present (2010) (Fig. 3) to the future **a**, **c** future trends of global human water use and groundwater abstraction

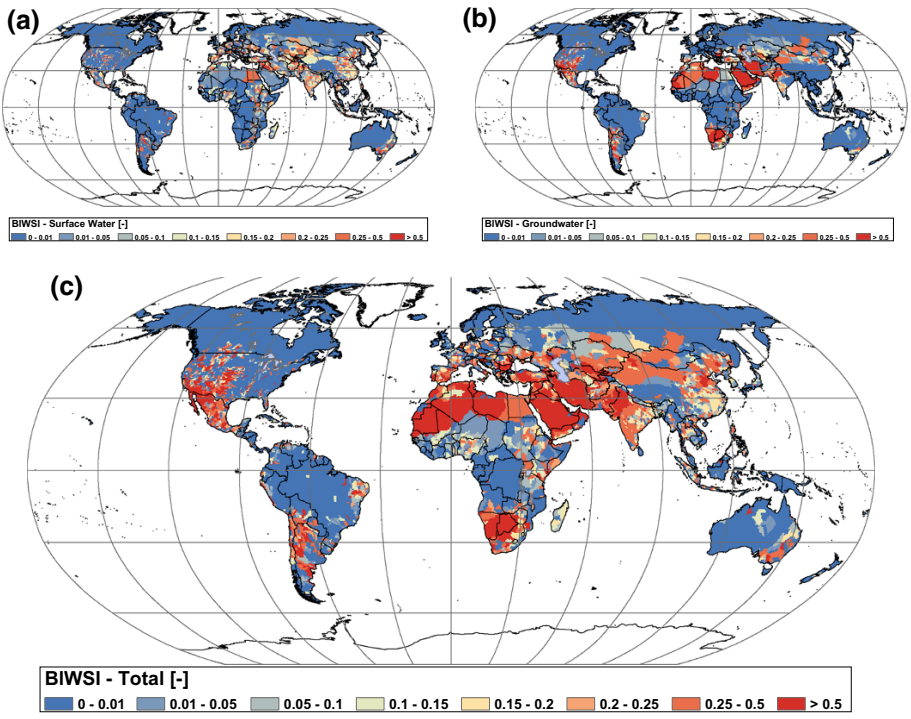


**Fig. 9** Global average non-sustainable water use (BlWSI) (dimensionless) for **a** surface water, **b** groundwater, and **c** the total at a subbasin scale (except the Antarctica and Greenland) (2069–2099)

sustainability only in terms of water quantity, but does not account for water quality, e.g., water pollution that affects the amount of readily available water over a region.

In addition to the increase in groundwater use, climate change will bring more extreme climate conditions and higher low flow frequency in many parts of the world (Lehner et al. 2006; Davie et al. 2013; Prudhomme et al. 2014; Trenberth et al. 2014; Dankers et al. 2014), which will increase our reliance of water use on groundwater resources (Famiglietti et al. 2011; Scanlon et al. 2012a, b). During prolonged drought events, groundwater pumping drastically increases, resulting in a higher groundwater dependence (Famiglietti et al. 2011; Scanlon et al. 2012a, b; Castle et al. 2014; Famiglietti 2014). A recent study of Castle et al. (2014) indicated that during a recent sustained drought, groundwater accounted nearly 80 % of freshwater loss in the Colorado River Basin, suggesting a considerable risk to the long-term ability to meet future allocations to the seven Basin states.

Changing climate will impact regional water availability and demands (Arnell 1999, 2004; Alcamo and Henrichs 2002; Alcamo et al. 2003b, 2007; Dirmeyer et al. 2006; Lehner et al. 2006; Feyen and Dankers 2009; Dai 2011, 2013; Haddeland et al. 2011; Sheffield et al. 2012; Jasechko et al. 2013; Elliott et al. 2014; Haddeland et al. 2014; Prudhomme et al. 2014; Schewe et al. 2014). Wetter conditions do not, however, always produce more groundwater recharge. During greater (> twofold) winter precipitation in the southwestern USA, enhanced evapotranspiration from desert blooms largely or entirely consumes the water surplus (Döll 2009; Portmann et al. 2013; Taylor et al. 2013). Increase

**Table 3** Total and non-renewable groundwater abstraction ($km^3\ year^{-1}$) over major groundwater users (country) for 1960, 2010 and 2099

| $km^3\ year^{-1}$ | Total (T) | | | Non-renewable (N) | | | N/T (%) | | | (N)/(T) Increase (%) | | (T) per sector for 2010 (%) | | |
|---|---|---|---|---|---|---|---|---|---|---|---|---|---|---|
| Country | 1960 | 2010 | 2099 | 1960 | 2010 | 2099 | 1960 | 2010 | 2099 | 1960–2010 | 2010–2099 | Agriculture | Domestic | Industry |
| India | 86 | 250 | 350 (±52) | 13 | 80 | 163 (±45) | 15 | 32 | 47 (±20) | 112 | 46 | 89 | 9 | 2 |
| USA | 57 | 125 | 137 (±28) | 9 | 23 | 56 (±12) | 16 | 18 | 41 (±18) | 17 | 127 | 62 | 20 | 18 |
| China | 52 | 110 | 169 (±42) | 8 | 28 | 36 (±8) | 15 | 25 | 21 (±10) | 65 | −15 | 74 | 12 | 14 |
| Pakistan | 38 | 80 | 108 (±21) | 22 | 46 | 75 (±24) | 58 | 58 | 69 (±25) | 0 | 20 | 90 | 8 | 2 |
| Iran | 34 | 72 | 98 (±18) | 18 | 47 | 65 (±11) | 53 | 65 | 66 (±24) | 23 | 2 | 90 | 6 | 4 |
| Mexico | 18 | 42 | 54 (±8) | 4 | 10 | 25 (±6) | 22 | 24 | 46 (±15) | 7 | 93 | 80 | 13 | 7 |
| Saudi Arabia | 4 | 25 | 42 (±6) | 3 | 20 | 32 (±8) | 75 | 80 | 76 (±25) | 7 | −5 | 90 | 10 | 0 |
| Globe | 372 | 952 | 1621 (±128) | 90 | 304 | 597 (±85) | 24 | 32 | 37 (±8) | 29 | 15 | 75 | 10 | 15 |

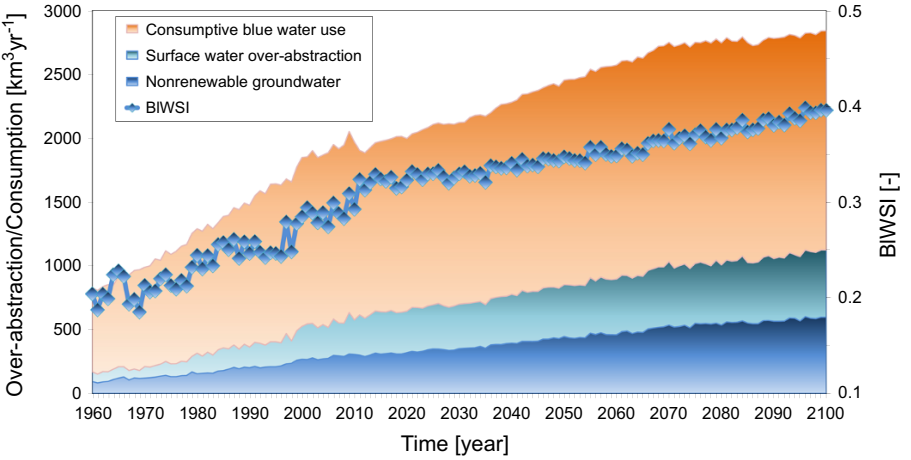


**Fig. 10** Estimated trends of consumptive blue water use, surface water over-abstraction, non-renewable groundwater abstraction (km$^3$ year$^{-1}$) (left y-coordinate), and Blue Water Sustainability Index (BlWSI) (dimensionless) (right y-coordinate) over the period 1960–2099

**Table 4** Comparison of estimated sectoral water use (withdrawal and consumption) to other estimates (km$^3$ year$^{-1}$)

| km$^3$ year$^{-1}$ | Withdrawal/ Consumption | 1960 | 2000 | 2025 | Mid-century (~2050) | End-century (~2090) |
|---|---|---|---|---|---|---|
| Agriculture (Irrigation/Livestock) | | | | | | |
| Hanasaki et al. (2013a, b) | | – | 3214/– | – | 4137/– | 4829/– |
| Yoshikawa et al. (2014) | | –/671 | –/1358 | – | –/2355 | – |
| Wada and Bierkens (2014) | | 1278/655 | 2644/1392 | 3385/1422 | 3490/1494 | 3664/1655 |
| Industry | | | | | | |
| Hanasaki et al. (2013a, b) | | – | – | 1169/– | 1437/– | 1259/– |
| Yoshikawa et al. (2014) | | – | – | – | – | – |
| Wada and Bierkens (2014) | | 356/116 | 752/257 | 1084/348 | 1443/489 | 1438/551 |
| Domestic | | | | | | |
| Hanasaki et al. (2013a, b) | | | | 598/– | 822/– | 973/– |
| Yoshikawa et al. (2014) | | – | – | – | – | – |
| Wada and Bierkens (2014) | | 85/57 | 328/199 | 609/337 | 930/470 | 1116/623 |

in irrigation water demand due to higher evapotranspiration can also affect the amount of groundwater recharge (Pfister et al. 2011a, b; Konzmann et al. 2013). Döll (2002), Fischer et al. (2007), and Wada et al. (2013b) indicated an increase in global irrigation water demand by 10–30 % by the end of this century, which is expected to induce more recharge from surface water irrigation. However, the increase varies substantially depending on the degree of global warming and associated regional precipitation changes (Alcamo et al. 2003a, b; Haddeland et al. 2014; Schewe et al. 2014).

The current degree of non-sustainable use may compromise the future livelihoods of millions of people and their living standards (Falkenmark et al. 2009; Hoekstra 2009; Hoff

et al. 2010; Fishman et al. 2011; Gleeson et al. 2012a, b; Hoekstra and Mekonnen 2012). Reliable information of readily accessible groundwater reserves in many aquifers is largely unknown (CEDARE 2001; Konikow 2011; Fan et al. 2013; De Graaf et al. 2014a, b).

## 6 A Way Forward

The sustainable use of global water resources is a key issue to economic development and food production (Postel et al. 1996; Gleick 2003, 2010; Oki and Kanae 2006; Döll et al. 2009; Rodell et al. 2009; Kummu et al. 2010, 2012, 2014; MacDonald 2010; Vörösmarty et al. 2010; Wada et al. 2010; Wisser et al. 2010; Famiglietti et al. 2011; Konikow 2011; Gleeson et al. 2012a, b; Pokhrel et al. 2012a, b; Voss et al. 2013; Gleeson and Wada 2013; Schewe et al. 2014; Hanasaki et al. 2013a, b). However, human fingerprints on Earth's water resources are being obvious from the shrunk Aral sea (Pala 2006, 2011), from rivers heavily affected by human water use such as the Colorado and the Yellow (Gleick 2003), and from dwindling groundwater resources over intense irrigated regions such as the Ogallala aquifer (Scanlon et al. 2012a, b), the California's Central Valley (Famiglietti et al. 2011), the North China Plain (Cao et al. 2013), northwest India and northeast Pakistan (Rodell et al. 2009; Tiwari et al. 2009), and the Tigris-Euphrates (Voss et al. 2013). Groundwater resources have been a reliable and readily available source of water supply, resulting in an increasing reliance on depleting groundwater resources in recent years. However, the degree of aquifer depletion is reported at an alarming rate over the Indus, Saudi Arabia, Iran, northeastern China, the southwestern and Central USA, and northern Mexico (Rodell et al. 2009; Tiwari et al. 2009; Famiglietti et al. 2011; Konikow 2011; Döll et al. 2012; Scanlon et al. 2012a, b; Cao et al. 2013; Voss et al. 2013; Famiglietti 2014).

This paper critically evaluated approaches modeling global GWD in the light of human water use. Despite model limitations and series of assumptions employed in the modeling, large-scale modeling efforts advance an important step beyond earlier work by attempting to account more realistically for the nature of groundwater pumping and associated impacts on the terrestrial water fluxes. These models have also been applied to assess future sustainability of groundwater use under envisaged population growth and socioeconomic developments. This section is dedicated to address future perspectives of sustainable groundwater management. Possible applications of the modeling framework are discussed in a wider perspective, identifying number of emerging issues for further research.

### 6.1 Quantifying the Sustainable Yield with Use of Satellite Observations and Integrated Modeling Framework

Over the last decade, GRACE satellite observations have provided an unprecedented view of the worldwide depletion of groundwater aquifers (Strassberg et al. 2007; Rodell et al. 2009; Tiwari et al. 2009). The integrated water resources modeling framework can be used to provide a reanalysis of past GWD in a data assimilation framework using both observed discharge and GRACE observations. Also, it can subsequently be used to project future GWD under scenarios as well as establishing sustainable yields for renewable groundwater reserves and the time horizon of unsustainable use for fossil reserves. However, uncertainties arising from different models are substantial and a multi-model approach is preferred (Dirmeyer et al. 2006; Gosling et al. 2010, 2011; Haddeland et al. 2011; Wada et al. 2013b).

### 6.2 Assessing Food Security

By 2050, the global population will exceed 9 billion, and a 50 % increase in annual agricultural output is expected to be required to keep up with food demand. However, available surface freshwater to meet the increase in irrigation water demand is subject to large uncertainties due to climate change (Tang and Lettenmaier 2012). As a result, one may need to rely more on groundwater being the only perennial source of freshwater in many regions (Taylor et al. 2013), contributing to regional food security. However, this will worsen progressive depletion of groundwater resources (Scanlon et al. 2012a, b) and will jeopardize a long-term sustainable water supply and associated food production.

### 6.3 Assessing Regional Mitigation Strategies on Food Security

Once groundwater resources are depleted or unavailable (e.g., economically or technologically unfeasible), irrigated crops relying on such resources will be severely impaired, which causes the loss of income for local farmers and a global decrease in crop production that may affect countries in another continent. To avoid such critical events occuring in the future, various measures can be proposed, involving innovations in water and food technology, and economic incentives (e.g., environmental tax) (Gleick et al. 2010; MacDonald 2010; Vörösmarty et al. 2010; Fader et al. 2010, 2013; Foley et al. 2011; Kummu et al. 2012; Elliott et al. 2014). However, these solutions require a substantial amount of economic investment that may not be easily realized for developing countries with limited financial and technological resources (Wada et al. 2014b). The cultural dimension then may provide another solution such that a change in diet from rice to cereals (e.g., wheat and maize) would save a large amount of water that can then be used for other crops or other water use sectors. Water management and governance also plays an important role. For instance, subsidizing electricity or diesel fuel for groundwater pumps, in order to boost food production, leads to a large increase in active irrigation wells even in areas with available surface water and during the rainy season.

Finally, large-scale modeling is essential in evaluating the mitigation and adaptation measures to ensure future water and food security in the light of groundwater resources. Assessing water resources considering GWD is critical for developing sustainable water management as policy goal and management plans, especially where and to what extent to focus limited management resources.

**Acknowledgments** The International Space Science Institute (ISSI) in Bern, Switzerland, and specifically Anny Cazenave and Nicolas Champollion, and acknowledged for hosting the ISSI Workshop on Remote Sensing and Water Resources. I wish to thank two anonymous reviewers for their constructive and thoughtful suggestions, which substantially helped to improve the quality of the manuscript. Y. Wada is supported by Japan Society for the Promotion of Science (JSPS) Overseas Research Fellowship (Grant No. JSPS-2014-878).

## References

Aeschbach-Hertig W, Gleeson T (2012) Regional strategies for the accelerating global problem of groundwater depletion. Nat Geosci 5:853–861. doi:10.1038/ngeo1617

Ahmad M-D, Bastiaanssen WGM, Feddes RA (2005) A new technique to estimate net groundwater use across large irrigated areas by combining remote sensing and water balance approaches, Rechna Doab, Pakistan. Hydrogeol J 13:653–664. doi:10.1007/s10040-004-0394-5

Alcamo J, Henrichs T (2002) Critical regions: a model-based estimation of world water resources sensitive to global changes. Aquat Sci 64:352–362. doi:10.1007/PL00012591
Alcamo J, Döll P, Henrichs T, Kaspar F, Lehner B, Rösch T, Siebert S (2003a) Development and testing of the WaterGAP 2 global model of water use and availability. Hydrol Sci J 48:317–337. doi:10.1623/hysj.48.3.317.45290
Alcamo J, Döll P, Henrichs T, Kaspar F, Lehner B, Rösch T, Siebert S (2003b) Global estimation of water withdrawals and availability under current and "business as usual" conditions. Hydrol Sci J 48:339–348. doi:10.1623/hysj.48.3.339.45278
Alcamo J, Flörke M, Märker M (2007) Future long-term changes in global water resources driven by socio-economic and climatic changes. Hydrol Sci J 52:247–275. doi:10.1623/hysj.52.2.247
Alley WM, Reilly TE, Franke OL (1999) Sustainability of ground-water resources, Circular 1186, Tech. Rep., Denver, CO, U.S. Geological Survey (USGS)
Arnell NW (1999) Climate change and global water resources. Global Environ Chang 9:31–49. doi:10.1016/S0959-3780(99)00017-5
Arnell NW (2004) Climate change and global water resources: SRES emissions and socio-economic scenarios. Global Environ Chang 14:31–52. doi:10.1016/j.gloenvcha.2003.10.006
Biemans H, Haddeland I, Kabat P, Ludwig F, Hutjes RWA, Heinke J, von Bloh W, Gerten D (2011) Impact of reservoirs on river discharge and irrigation water supply during the 20th century. Water Resour Res 47:W03509. doi:10.1029/2009WR008929
Bondeau A, Smith PC, Zaehle S, Schaphoff S, Lucht W, Cramer W, Gerten D, Reichstein M, Smith B (2007) Modelling the role of agriculture for the 20th century. Global Chang Biol 13:679–706. doi:10.1111/j.1365-2486.2006.01305.x
Bredehoeft JD (2002) The water budget myth revisited: why hydrogeologists model? Ground Water 40:340–345. doi:10.1111/j.1745-6584.2002.tb02511.x
Bruinsma J (2003) World agriculture: towards 2015/2030—an FAO perspective. Earthscan, London, p 444
Cao G, Zheng C, Scanlon BR, Liu J, Li W (2013) Use of flow modeling to assess sustainability of groundwater resources in the North China Plain. Water Resour Res. doi:10.1029/2012WR011899
Castle SL, Thomas BF, Reager JT, Rodell M, Swenson SC, Famiglietti JS (2014) Groundwater depletion during drought threatens future water security of the Colorado River Basin. Geophys Res Lett. doi:10.1002/2014GL061055
CEDARE (2001) Regional strategy for the utilisation of the nubian sandstone aquifer system volume III: ground water model, Tech. Rep., Cent. for Environ. and Dev. for the Arab Reg. and Eur., Cairo, Egypt
Chao BF, Wu YH, Li YS (2008) Impact of artificial reservoir water impoundment on global sea level. Science 320:212–214. doi:10.1126/science.1154580
Cheema MJ, Immerzeel WW, Bastiaanssen WG (2014) Spatial quantification of groundwater abstraction in the irrigated Indus basin. Ground Water 52:25–36. doi:10.1111/gwat.12027
Chen J, Famigliett JS, Scanlon BR, Rodell M (2015) Groundwater storage changes: present status from GRACE observations. Surv Geophys. doi:10.1007/s10712-015-9332-4
Crosbie RS, McCallum JL, Walker GR, Chiew FHS (2012) Episodic recharge and climate change in the Murray-Darling Basin, Australia. Hydrogeol J 20:245–261. doi:10.1007/s10040-011-0804-4
Dai A (2011) Drought under global warming: a review, WIREs Clim. Change 2:45–65. doi:10.1002/wcc.81
Dai A (2013) Increasing drought under global warming: reconciling observed and model-simulated changes. Nat Clim Change 3:52–58. doi:10.1038/nclimate1633
Dankers R, Arnell NW, Clark DB, Falloon PD, Fekete BM, Gosling SN, Heinke J, Kim H, Masaki Y, Satoh Y, Stacke T, Wada Y, Wisser D (2014) First look at changes in flood hazard in the inter-sectoral impact model intercomparison project ensemble. Proc Natl Acad Sci USA 111(9):3257–3261. doi:10.1073/pnas.1302078110
Davie JCS, Falloon PD, Kahana R, Dankers R, Betts R, Portmann FT, Wisser D, Clark DB, Itoh A, Masaki Y, Nishina K, Fekete B, Tessler Z, Wada Y, Liu X, Tang Q, Hagemann S, Stacke T, Pavlick R, Schaphoff S, Gosling SN, Franssen W, Arnell N (2013) Comparing projections of future changes in runoff from hydrological and biome models in ISI-MIP. Earth Syst Dyn 4:359–374. doi:10.5194/esd-4-359-2013
De Graaf IEM, van Beek LPH, Wada Y, Bierkens MFP (2014a) Dynamic attribution of global water demand to surface water and groundwater resources: effects of abstractions and return flows on river discharges. Adv Water Resour 64:21–33. doi:10.1016/j.advwatres.2013.12.002
De Graaf IEM, Sutanudjaja EH, van Beek LPH, Bierkens MFP (2014b) A high resolution global scale groundwater model. Hydrol Earth Syst Sci Discuss 11:5217–5250. doi:10.5194/hessd-11-5217-2014
DeAngelis A, Dominguez F, Fan Y, Robock A, Kustu MD, Robinson D (2010) Evidence of enhanced precipitation due to irrigation over the Great Plains of the United States. J Geophys Res 115:D15115. doi:10.1029/2010JD013892

Dirmeyer PA, Gao X, Guo Z, Oki T, Hanasaki N (2006) GSWP-2: multimodel analysis and implications for our perception of the land surface. Bull Am Meteor Soc 87:1381–1397. doi:10.1175/BAMS-87-10-1381

Döll P (2002) Impact of climate change and variability on irrigation requirements: a global perspective. Clim Chang 54(3):269–293. doi:10.1023/A:1016124032231

Döll P (2009) Vulnerability to the impact of climate change on renewable groundwater resources: a global-scale assessment. Environ Res Lett 4:036006. doi:10.1088/1748-9326/4/3/035006

Döll P, Fiedler F (2008) Global-scale modeling of groundwater recharge. Hydrol Earth Syst Sci 12:863–885. doi:10.5194/hess-12-863-2008

Döll P, Siebert S (2002) Global modeling of irrigation water requirements. Water Resour Res. doi:10.1029/2001WR000355

Döll P, Kaspar F, Lehner B (2003) A global hydrological model for deriving water availability indicators: model tuning and validation. J Hydrol 270:105–134. doi:10.1016/S0022-1694(02)00283-4

Döll P, Fiedler K, Zhang J (2009) Global-scale analysis of river flow alterations due to water withdrawals and reservoirs. Hydrol Earth Syst Sci 13:2413–2432. doi:10.5194/hess-13-2413-2009

Döll P, Hoffmann-Dobrev H, Portmann FT, Siebert S, Eicker A, Rodell M, Strassberg G (2012) Impact of water withdrawals from groundwater and surface water on continental water storage variations. J Geodyn 59–60:143–156. doi:10.1016/j.jog.2011.05.001

Döll P, Müller Schmied H, Schuh C, Portmann FT, Eicker A (2014) Global-scale assessment of groundwater depletion and related groundwater abstractions: combining hydrological modeling with information from well observations and GRACE satellites. Water Resour Res 50:5698–5720. doi:10.1002/2014WR015595

Döll P, Douville H, Güntner A, Müller Schmied H, Wada Y (2015) Modelling freshwater resources at the global scale: challenges and prospects. Surv Geophys. doi:10.1007/s10712-015-9343-1

Edmunds M (2003) Renewable and non-renewable groundwater in semi-arid and arid regions. In: Wood (ed) Water resources perspectives: evaluation, management and policy, developments in water science 50, Elsevier, Amsterdam, pp 265–280

Elliott J, Deryng D, Müller C, Frieler K, Konzmann M, Gerten D, Glotter M, Flörke M, Wada Y, Eisner S, Folberth C, Foster I, Gosling SN, Haddeland I, Khabarov N, Ludwig F, Masaki Y, Olin S, Rosenzweig C, Ruane AC, Satoh Y, Schmid E, Stacke T, Tang Q, Wisser D (2014) Constraints and potentials of future irrigation water availability on agricultural production under climate change. Proc Natl Acad Sci USA 111(9):3239–3244. doi:10.1073/pnas.1222474110

Fader M, Rost S, Müller C, Gerten D (2010) Virtual water content of temperate cereals and maize: present and potential future patterns. J Hydrol 384:218–231. doi:10.1016/j.jhydrol.2009.12.011

Fader M, Gerten D, Krause M, Lucht W, Cramer W (2013) Spatial decoupling of agricultural production and consumption: quantifying dependences of countries on food imports due to domestic land and water constraints. Environ Res Lett 8:014046. doi:10.1088/1748-9326/8/1/014046

Falkenmark M, Kijne JW, Taron B, Murdoch G, Sivakumar MVK, Craswell E (1997) Meeting water requirements of an expanding world population [and discussion]. Philos Trans R Soc Lond B 352:929–936. doi:10.1098/rstb.1997.0072

Falkenmark M, Rockström J, Karlberg L (2009) Present and future water requirements for feeding humanity. Food Sec 1:59–69. doi:10.1007/s12571-008-0003-x

Famiglietti JS (2014) The global groundwater crisis. Nat Clim Chang 4:945–948. doi:10.1038/nclimate2425

Famiglietti JS, Lo M, Ho SL, Bethune J, Anderson KJ, Syed TH, Swenson SC, de Linage CR, Rodell M (2011) Satellites measure recent rates of groundwater depletion in California's Central Valley. Geophys Res Lett 38:L03403. doi:10.1029/2010GL046442

Fan Y, Li H, Miguez-Macho G (2013) Global patterns of groundwater table depth. Science 339:940–943. doi:10.1126/science.122988

Feng W, Zhong M, Lemoine J-M, Biancale R, Hsu H-T, Xia J (2013) Evaluation of groundwater depletion in North China using the Gravity Recovery and Climate Experiment (GRACE) data and ground-based measurements. Water Resour Res 49:2110–2118. doi:10.1002/wrcr.20192

Feyen L, Dankers R (2009) Impact of global warming on streamflow drought in Europe. J Geophys Res 114:D17116. doi:10.1029/2008JD011438

Fischer G, Tubiello FN, van Velthuizen H, Wiberg DA (2007) Climate change impacts on irrigation water requirements: effects of mitigation, 1990–2080. Technol Forecast Soc Chang 74:1083–1107. doi:10.1016/j.techfore.2006.05.021

Fishman RM, Siegfried T, Raj P, Modi V, Lall U (2011) Over-extraction from shallow bedrock versus deep alluvial aquifers: reliability versus sustainability considerations for India's groundwater irrigation. Water Resour Res 47: W00L05. doi:10.1029/2011WR010617

Flörke M, Kynast E, Bärlund I, Eisner S, Wimmer F, Alcamo J (2013) Domestic and industrial water uses of the past 60 years as a mirror of socio-economic development: a global simulation study. Global Environ Chang 23:144–156. doi:10.1016/j.gloenvcha.2012.10.018

Foley JA, Ramankutty N, Brauman KA, Cassidy ES, Gerber JS, Johnston M, Mueller ND, O'Connell C, Ray DK, West PC, Balzer C, Bennett EM, Carpenter SR, Hill J, Monfreda C, Polasky S, Rockström J, Sheehan J, Siebert S, Tilman D, Zaks DPM (2011) Solutions for a cultivated planet. Nature 478:337–342. doi:10.1038/nature10452

Foster SSD, Chilton PJ (2003) Groundwater: the processes and global significance of aquifer degradation. Phil Trans Roy Soc Lond B Biol Sci 358:1957–1972. doi:10.1098/rstb.2003.1380

Foster S, Loucks DP (eds) (2006) Non-renewable groundwater resources: a guidebook on socially-sustainable management for water-policy makers, IHP-VI, series on Groundwater No. 10, UNESCO, Paris, France

Foster S, Garduno H, Evans R, Olson D, Tian Y, Zhang W, Han Z (2004) Quaternary aquifer of the north china plain—assessing and achieving groundwater resource sustainability. Hydrogeol J 12:81–93. doi:10.1007/s10040-003-0300-6

Gain AK, Wada Y (2014) Assessment of future water scarcity at different spatial and temporal scales of the Brahmaputra River Basin. Water Resour Manage 28:999–1012. doi:10.1007/s11269-014-0530-5

Gerten D, Schaphoff S, Lucht W (2007) Potential future changes in water limitation of the terrestrial biosphere. Clim Chang 80:277–299. doi:10.1007/s10584-006-9104-8

Gerten D, Heinke J, Hoff H, Biemans H, Fader M, Waha K (2011) Global water availability and requirements for future food production. J Hydrometeorol 12:885–899. doi:10.1175/2011JHM1328.1

Gerten D, Hoff H, Rockström J, Jägermeyr J, Kummu M, Pastor AV (2013) Towards a revised planetary boundary for consumptive freshwater use: role of environmental flow requirements. Curr Opin Environ Sustain 5:551–558. doi:10.1016/j.cosust.2013.11.001

Gleeson T, Wada Y (2013) Assessing regional groundwater stress for nations using multiple data sources with the groundwater footprint. Environ Res Lett 8:044010. doi:10.1088/1748-9326/8/4/044010

Gleeson T, Alley WM, Allen DM, Sophocleous MA, Zhou Y, Taniguchi M, Van der Steen J (2012a) Towards sustainable groundwater use: setting long-term goals, backcasting, and managing adaptively. Groundwater 50:19–26. doi:10.1111/j.1745-6584.2011.00825.x

Gleeson T, Wada Y, Bierkens MFP, van Beek LPH (2012b) Water balance of global aquifers revealed by groundwater footprint. Nature 488:197–200. doi:10.1038/nature11295

Gleick PH (2000) The changing water paradigm: a look at twenty-first century water resources development. Water Int 25:127–138. doi:10.1080/02508060008686804

Gleick PH (2003) Global freshwater resources: soft-path solutions for the 21st century. Science 302:1524–1528. doi:10.1126/science.1089967

Gleick PH (2010) Roadmap for sustainable water resources in southwestern North America. Proc Natl Acad Sci USA 107:21300–21305. doi:10.1073/pnas.1005473107

Gleick PH, Christian-Smith J, Cooley H (2010) Water-use efficiency and productivity: rethinking the basin approach. Water Int. 36:784–798. doi:10.1080/02508060.2011.631873

Gornitz V (1995) Sea-level rise: a review of recent past and near-future trends. Earth Surf Process Landforms 20:7–20. doi:10.1002/esp.3290200103

Gornitz V (2001) In: Douglas BC, Kearney MS, Leatherman SP (eds) Sea level rise: history and consequences. Academic Press, San Diego, pp 97–119

Gosling SN, Bretherton D, Haines K, Arnell NW (2010) Global hydrology modelling and uncertainty: running multiple ensembles with a campus grid. Phil Trans R Soc A 368:4005–4021. doi:10.1098/rsta.2010.0164

Gosling SN, Taylor RG, Arnell NW, Todd MC (2011) A comparative analysis of projected impacts of climate change on river runoff from global and catchment-scale hydrological models. Hydrol Earth Syst Sci 15:279–294. doi:10.5194/hess-15-279-2011

Gregory JM, White NJ, Church JA, Bierkens MFP, Box JE, van den Broeke MR, Cogley JG, Fettweis X, Hanna E, Huybrechts P, Konikow LF, Leclercq PW, Marzeion B, Oerlemans J, Tamisiea ME, Wada Y, Wake LM, van de Wal RSW (2013) Twentieth-century global-mean sea level rise: is the whole greater than the sum of the parts? J Clim 26:4476–4499. doi:10.1175/JCLI-D-12-00319.1

Haddeland I, Skaugen T, Lettenmaier DP (2006) Anthropogenic impacts on continental surface water fluxes. Geophys Res Lett 33:L08406. doi:10.1029/2006GL026047

Haddeland I, Clark D, Franssen WHP, Ludwig F, Voss F, Arnell NW, Bertrand N, Best M, Folwell S, Gerten D, Gomes S, Gosling S, Hagemann S, Hanasaki N, Harding R, Heinke J, Kabat P, Koirala S, Oki T, Polcher J, Stacke T, Viterbo P, Weedon GP, Yeh P (2011) Multimodel estimate of the global terrestrial water balance: setup and first results. J Hydrometeor 12:869–884. doi:10.1175/2011JHM1324.1

Haddeland I, Heinke J, Biemans H, Eisner S, Flörke M, Hanasaki N, Konzmann M, Ludwig F, Masaki Y, Schewe J, Stacke T, Tessler Z, Wada Y, Wisser D (2014) Global water resources affected by human interventions and climate change. Proc Natl Acad Sci USA 111(9):3251–3256. doi:10.1073/pnas.1302078110

Hanasaki N, Kanae S, Oki T, Masuda K, Motoya K, Shirakawa N, Shen Y, Tanaka K (2008a) An integrated model for the assessment of global water resources—part 1: model description and input meteorological forcing. Hydrol Earth Syst Sci 12:1007–1025. doi:10.5194/hess-12-1007-2008

Hanasaki N, Kanae S, Oki T, Masuda K, Motoya K, Shirakawa N, Shen Y, Tanaka K (2008b) An integrated model for the assessment of global water resources—part 2: applications and assessments. Hydrol Earth Syst Sci 12:1027–1037. doi:10.5194/hess-12-1027-2008

Hanasaki N, Inuzuka T, Kanae S, Oki T (2010) An estimation of global virtual water flow and sources of water withdrawal for major crops and livestock products using a global hydrological model. J Hydrol 384:232–244. doi:10.1016/j.jhydrol.2009.09.028

Hanasaki N, Fujimori S, Yamamoto T, Yoshikawa S, Masaki Y, Hijioka Y, Kainuma M, Kanamori Y, Masui T, Takahashi K, Kanae S (2013a) A global water scarcity assessment under Shared Socio-economic pathways—part 1: water use. Hydrol Earth Syst Sci 17:2375–2391. doi:10.5194/hess-17-2375-2013

Hanasaki N, Fujimori S, Yamamoto T, Yoshikawa S, Masaki Y, Hijioka Y, Kainuma M, Kanamori Y, Masui T, Takahashi K, Kanae S (2013b) A global water scarcity assessment under shared socio-economic pathways—part 2: water availability and scarcity. Hydrol Earth Syst Sci 17:2393–2413. doi:10.5194/hess-17-2393-2013

Harbaugh AW, Banta ER, Hill MC, McDonald MG (2000) MODFLOW-2000, The U. S. Geological Survey modular ground-water model-user guide to modularization concepts and the ground-water flow process. Open-File Rep. 00-92, U.S. Geol. Survey (USGS), Reston, VA

Hoekstra AY (2009) Human appropriation of natural capital: a comparison of ecological footprint and water footprint analysis. Ecol Econ 68:1963–1974. doi:10.1016/j.ecolecon.2008.06.021

Hoekstra AY, Mekonnen MM (2012) The water footprint of humanity. Proc Natl Acad Sci USA 109(9):3232–3237. doi:10.1073/pnas.1109936109

Hoff H, Falkenmark M, Gerten D, Gordon L, Karlberg L, Rockström J (2010) Greening the global water system. J Hydrol 384:177–186. doi:10.1016/j.jhydrol.2009.06.026

Hu Y, Moiwo JP, Yang Y, Han S, Yang Y (2010) Agricultural water-saving and sustainable groundwater management in Shijiazhuang Irrigation District, North China Plain. J Hydrol 393:219–232. doi:10.1016/j.jhydrol.2010.08.017

Huang Z, Pan Y, Gong H, Yeh PJ, Li X, Zhou D, Zhao W (2015) Subregional-scale groundwater depletion detected by GRACE for both shallow and deep aquifers in North China Plain. Geophys Res Lett 42:1791–1799. doi:10.1002/2014GL062498

Jacob T, Wahr J, Pfeffer WT, Swenson S (2012) Recent contributions of glaciers and ice caps to sea level rise. Nature 482:514–518. doi:10.1038/nature10847

Jasechko S, Sharp ZD, Gibson JJ, Birks SJ, Yi Y, Fawcett PJ (2013) Terrestrial water fluxes dominated by transpiration. Nature 496:347–350. doi:10.1038/nature11983

Jung M, Reichstein M, Ciais P, Seneviratne SI, Sheffield J, Goulden ML, Bonan G, Cescatti A, Chen JQ, de Jeu R, Dolman AJ, Eugster W, Gerten D, Gianelle D, Gobron N, Heinke J, Kimball J, Law BE, Montagnani L, Mu QZ, Mueller B, Oleson K, Papale D, Richardson AD, Roupsard O, Running S, Tomelleri E, Viovy N, Weber U, Williams C, Wood E, Zaehle S, Zhang K (2010) Recent decline in the global land evapotranspiration trend due to limited moisture supply. Nature 467:951–954. doi:10.1038/nature09396

Karami E, Hayati D (2005) Rural poverty and sustainability: the case of groundwater depletion in Iran. Asian J Water Environ Pollut 2:51–61

Koirala S, Yeh PJ-F, Hirabayashi Y, Kanae S, Oki T (2014) Global-scale land surface hydrologic modeling with the representation of water table dynamics. J Geophys Res Atmos 119:75–89. doi:10.1002/2013JD020398

Konikow LF (2011) Contribution of global groundwater depletion since 1900 to sea-level rise. Geophys Res Lett 38:L17401. doi:10.1029/2011GL048604

Konikow LF, Kendy E (2005) Groundwater depletion: a global problem. Hydrogeol J 13:317–320. doi:10.1007/s10040-004-0411-8

Konzmann M, Gerten D, Heinke J (2013) Climate impacts on global irrigation requirements under 19 GCMs, simulated with a vegetation and hydrology model. Hydrol Sci J 58:1–18. doi:10.1080/02626667.2013.746495

Kummu M, Ward PJ, de Moel H, Varis O (2010) Is physical water scarcity a new phenomenon? Global assessment of water shortage over the last two millennia. Environ Res Lett 5:034006. doi:10.1088/1748-9326/5/3/034006

Kummu M, de Moel H, Porkka M, Siebert S, Varis O, Ward PJ (2012) Lost food, wasted resources: global food supply chain losses and their impacts on freshwater, cropland, and fertiliser use. Sci Total Environ 438:477–489. doi:10.1016/j.scitotenv.2012.08.092

Kummu M, Gerten D, Heinke J, Konzmann M, Varis O (2014) Climate-driven interannual variability of water scarcity in food production: a global analysis. Hydrol Earth Syst Sci 18:447–461. doi:10.5194/hess-18-447-2014

Kustu M, Fan Y, Robock A (2010) Large-scale water cycle perturbation due to irrigation pumping in the US high plains: a synthesis of observed streamflow changes. J Hydrol 390:222–244. doi:10.1016/j.jhydrol.2010.06.045

Kustu MD, Fan Y, Rodell M (2011) Possible link between irrigation in the U.S. High Plains and increased summer stream flow in the Midwest. Water Resour Res 47:W03522. doi:10.1029/2010WR010046

Lehner B, Döll P, Alcamo J, Henrichs T, Kaspar F (2006) Estimating the impact of global change on flood and drought risks in Europe: a continental integrated analysis. Clim Chang 75(273–299):2006. doi:10.1007/s10584-006-6338-4

Lehner B, Reidy Liermann C, Revenga C, Vörösmarty C, Fekete B, Crouzet P, Döll P, Endejan M, Frenken K, Magome J, Nilsson C, Robertson JC, Rödel R, Sindorf N, Wisser D (2011) High-resolution mapping of the world's reservoirs and dams for sustainable river-flow management. Fron Ecol Environ 9:494–502. doi:10.1890/100125

Lettenmaier DP, Milly PCD (2009) Land waters and sea level. Nat Geosci 2:452–454. doi:10.1038/ngeo567

Liu J, Yang H (2010) Spatially explicit assessment of global consumptive water uses in cropland: green and blue water. J Hydrol 384:187–297. doi:10.1016/j.jhydrol.2009.11.024

Llamas MR, Martínez-Santos P (2005) Intensive groundwater use: a silent revolution that cannot be ignored. Water Sci Technol 51:167–174

Llamas R, Back W, Margat J (1992) Groundwater use: equilibrium between social benefits and potential environmental costs. Appl Hydrol 1:3–14. doi:10.1007/PL00010965

Lo MH, Yeh PJ-F, Famiglietti JS (2008) Using baseflow to constrain water table depth simulations in the NCAR Community Land Model (CLM). Adv Water Resour 31:1552–1564. doi:10.1016/j.advwatres.2008.06.007

Longuevergne L, Scanlon BR, Wilson CR (2010) GRACE Hydrological estimates for small basins: evaluating processing approaches on the High Plains Aquifer, USA. Water Resour Res 46:W11517. doi:10.1029/2009WR008564

MacDonald GM (2010) Water, climate change, and sustainability in the southwest. Proc Natl Acad Sci USA 107:21256–21262. doi:10.1073/pnas.0909651107

Manga M (1999) On the timescales characterizing groundwater discharge at springs. J Hydrol 219:56–69

McGuire VL (2009) Water level changes in the High Plains Aquifer, predevelopment to 2007, 2005–06, and 2006–2007, U.S. Geol. Surv. Sci. Invest. Rep., 2009-5019, U.S. Geol. Surv., Reston, Virginia. http://pubs.usgs.gov/sir/2009/5019/

Millennium Ecosystem Assessment (2005) Ecosystems and human well-being volume 2: scenarios. Island Press, Washington District of Columbia, p 515

Nijssen B, Schnur R, Lettenmaier DP (2001a) Global retrospective estimation of soil moisture using the variable infiltration capacity land surface model, 1980–93. J Clim 14:1790–1808. doi:10.1175/1520-0442(2001)014<1790:GREOSM>2.0.CO;2

Nijssen B, O'Donnell GM, Lettenmaier DP, Lohmann D, Wood EF (2001b) Predicting the discharge of global rivers. J Clim 14:3307–3323. doi:10.1175/1520-0442(2001)014<3307:PTDOGR>2.0.CO;2

Oki T, Kanae S (2006) Global hydrological cycles and world water resources. Science 313:1068–1072. doi:10.1126/science.1128845

Oki T, Agata Y, Kanae S, Saruhashi T, Yang D, Musiake K (2001) Global assessment of current water resources using total runoff-integrating pathways. Hydrol Sci J 46:983–996. doi:10.1080/02626660109492890

Pala C (2006) Once a terminal case, the north aral sea shows new signs of life. Science 312:183. doi:10.1126/science.312.5771.183

Pala C (2011) In northern aral sea, rebound comes with a big catch. Science 334:303. doi:10.1126/science.334.6054.303

Pastor AV, Ludwig F, Biemans H, Hoff H, Kabat P (2013) Accounting for environmental flow requirements in global water assessments. Hydrol Earth Syst Sci Discuss 10:14987–15032. doi:10.5194/hessd-10-14987-2013

Pfister S, Bayer P, Koehler A, Hellweg S (2011a) Environmental impacts of water use in global crop production: hotspots and trade-offs with land use. Environ Sci Technol 45:5761–5768. doi:10.1021/es1041755

Pfister S, Bayer P, Koehler A, Hellweg S (2011b) Projected water consumption in future global agriculture: scenarios and related impacts. Sci Total Environ 409:4206–4216. doi:10.1016/j.scitotenv.2011.07.019

Pokhrel Y, Hanasaki N, Koirala S, Cho J, Yeh PJ-F, Kim H, Kanae S, Oki T (2012a) Incorporating anthropogenic water regulation modules into a land surface model. J Hydrometeorol 13:255–269. doi:10.1175/JHM-D-11-013.1

Pokhrel YN, Hanasaki N, Yeh PJ-F, Yamada T, Kanae S, Oki T (2012b) Model estimates of sea level change due to anthropogenic impacts on terrestrial water storage. Nat Geosci 5:389–392. doi:10.1038/ngeo1476

Pokhrel YN, Fan Y, Miguez-Macho G, Yeh PJ-F, Han S-C (2013) The role of groundwater in the Amazon water cycle: 3. Influence on terrestrial water storage computations and comparison with GRACE. J Geophys Res Atmos 118:3233–3244. doi:10.1002/jgrd.50335

Pokhrel YN, Koirala S, Yeh PJ-F, Hanasaki N, Longuevergne L, Kanae S, Oki T (2015) Incorporation of groundwater pumping in a global land surface model with the representation of human impacts. Water Resour Res 51:78–96. doi:10.1002/2014WR015602

Portmann FT, Döll P, Eisner S, Flörke M (2013) Impact of climate change on renewable groundwater resources: assessing the benefits of avoided greenhouse gas emissions using selected CMIP5 climate projections. Environ Res Lett 8:024023. doi:10.1088/1748-9326/8/2/024023

Postel SL (1999) Pillar of sand: can the irrigation miracle last? W.W. Norton, New York

Postel SL, Daily GC, Ehrlich PR (1996) Human appropriation of renewable fresh water. Science 271:785–788. doi:10.1126/science.271.5250.785

Prudhomme C, Giuntoli I, Robinson EL, Clark DB, Arnell NW, Dankers R, Fekete B, Franssen W, Gerten D, Gosling SN, Hagemann S, Hannah DM, Kim H, Masaki Y, Satoh Y, Stacke T, Wada Y, Wisser D (2014) Drought in the 21st century: a multi-model ensemble experiment to assess global change, quantify uncertainty and identify 'hotspots', change. Proc Natl Acad Sci USA 111(9):3262–3267. doi:10.1073/pnas.1222473110

Ramankutty N, Foley JA (1998) Characterizing patterns of global land use: an analysis of global croplands data. Global Biogeochem Cycl 12(4):667–685. doi:10.1029/98GB02512

Ramankutty N, Evan AT, Monfreda C, Foley JA (2008) Farming the planet. Part 1: the geographic distribution of global agricultural lands in the year 2000. Global Biogeochem Cycles 22:GB1003 doi:10.1029/2007GB002952

Reilly TE, Dennehy KF, Alley WM, Cunningham WL (2008) Ground-water availability in the United States, U.S. Geol. Surv. Circ., p. 70. http://pubs.usgs.gov/circ/1323/

Richey AS, Thomas BF, Lo M-H, Reager JT, Famiglietti JS, Voss K, Swenson S, Rodell M (2015) Quantifying renewable groundwater stress with GRACE. Water Resour Res 51:5217–5238. doi:10.1002/2015WR017349

Rockström J, Falkenmark M, Karlberg L, Hoff H, Rost S, Gerten D (2009) Future water availability for global food production: the potential of green water for increasing resilience to global change. Water Resour Res 45:W00A12. doi:10.1029/2007WR006767

Rodell M, Velicogna I, Famiglietti JS (2009) Satellite-based estimates of groundwater depletion in India. Nature 460:999–1002. doi:10.1038/nature08238

Rost S, Gerten D, Bondeau A, Luncht W, Rohwer J, Schaphoff S (2008) Agricultural green and blue water consumption and its influence on the global water system. Water Resour Res 44:W09405. doi:10.1029/2007WR006331

Sahagian DL, Schwartz FW, Jacobs DK (1994) Direct anthropogenic contributions to sea level rise in the twentieth century. Nature 367:54–57. doi:10.1038/367054a0

Scanlon BR, Healy RW, Cook PG (2002) Choosing appropriate techniques for quantifying groundwater recharge. Hydrogeol J 10:18–39. doi:10.1007/s10040-001-0176-2

Scanlon BR, Reedy RC, Stonestrom DA, Prudic DE, Dennehy KF (2005) Impact of land use and land cover change on groundwater recharge and quality in the southwestern US. Glob Chang Biol 11:1577–1593. doi:10.1111/j.1365-2486.2005.01026.x

Scanlon BR, Keese KE, Flint AL, Flint LE, Gaye CB, Edmunds WM, Simmers I (2006) Global synthesis of groundwater recharge in semiarid and arid regions. Hydrol Process 20:3335–3370. doi:10.1002/hyp.6335

Scanlon BR, Jolly I, Sophocleous M, Zhang L (2007) Global impacts of conversions from natural to agricultural ecosystems on water resources: quantity versus quality. Water Resour Res 43:W03437. doi:10.1029/2006WR005486

Scanlon BR, Reedy RC, Gates JB (2010) Effects of irrigated agroecosystems: 1. Quantity of soil water and groundwater in the southern High Plains, Texas. Water Resour Res 46:W09537. doi:10.1029/2009WR008427

Scanlon BR, Faunt CC, Longuevergne L, Reedy RC, Alley WM, McGuire VL, McMahon PB (2012a) Groundwater depletion and sustainability of irrigation in the U.S. High Plains and Central Valley. Proc Natl Acad Sci USA 109:9320–9325. doi:10.1073/pnas.1200311109

Scanlon BR, Longuevergne L, Long D (2012b) Ground referencing GRACE satellite estimates of groundwater storage changes in the California Central Valley, USA. Water Resour Res 48:W04520. doi:10.1029/2011WR011312

Schewe J, Heinke J, Gerten D, Haddeland I, Arnell NW, Clark DB, Dankers R, Eisner S, Fekete B, Colón-González FJ, Gosling SN, Kim H, Liu X, Masaki Y, Portmann FT, Satoh Y, Stacke T, Tang Q, Wada Y, Wisser D, Albrecht T, Frieler K, Piontek F, Warszawski L, Kabat P (2014) Multi-model assessment of water scarcity under climate change. Proc Natl Acad Sci USA 111(9):3245–3250. doi:10.1073/pnas.1222460110

Seager R (2007) The turn of the century North American drought: global context, dynamics, and past analogs. J Clim 20:5527–5552. doi:10.1175/2007JCLI1529.1

Shah T (2005) Groundwater and human development: challenges and opportunities in livelihoods and environment. Water Sci Technol 51:27–37

Shamsudduha M, Taylor RG, Longuevergne L (2012) Monitoring groundwater storage changes in the highly seasonal humid tropics: validation of GRACE measurements in the Bengal Basin. Water Resour Res 48:W02508. doi:10.1029/2011WR010993

Sheffield J, Wood EF (2007) Characteristics of global and regional drought, 1950–2000: analysis of soil moisture data from off-line simulation of the terrestrial hydrologic cycle. J Geophys Res 112:D17115. doi:10.1029/2006JD008288

Sheffield J, Wood EF, Roderick ML (2012) Little change in global drought over the past 60 years. Nature 491:435–438. doi:10.1038/nature11575

Shiklomanov IA (2000a) World water scenarios analyses, chap. World water resources and water use: present assessment and outlook for 2025, Earthscan, London

Shiklomanov IA (2000b) Appraisal and assessment of world water resources. Water Int. 25:11–32. doi:10.1080/02508060008686794

Siebert S, Döll P (2010) Quantifying blue and green virtual water contents in global crop production as well as potential production losses without irrigation. J Hydrol 384:198–217. doi:10.1016/j.jhydrol.2009.07.031

Siebert S, Burke J, Faures JM, Frenken K, Hoogeveen J, Döll P, Portmann FT (2010) Groundwater use for irrigation—a global inventory. Hydrol Earth Syst Sci 14:1863–1880. doi:10.5194/hess-14-1863-2010

Smakhtin VU (2001) Low flow hydrology: a review. J Hydrol 240:147–186. doi:10.1016/S0022-1694(00)00340-1

Smakhtin VU, Revenga C, Döll P (2004) A pilot global assessment of environmental water requirements and scarcity. Wat. Int. 29:307–317. doi:10.1080/02508060408691785

Solomon S, et al (eds) (2007) Climate change 2007: the physical science basis. Contribution of working group I to the fourth assessment report of the intergovernmental panel on climate change. Cambridge University Press, Cambridge

Strassberg G, Scanlon BR, Rodell M (2007) Comparison of seasonal terrestrial water storage variations from GRACE with groundwater-level measurements from the High Plains Aquifer (USA). Geophys Res Lett 34:L14402. doi:10.1029/2007GL030139

Sturchio NC et al (2004) One million year old groundwater in the Sahara revealed by krypton-81 and chlorine-36. Geophys Res Lett 31:L05503. doi:10.1029/2003GL019234

Tague C, Grant G, Farrell M, Choate J, Jefferson A (2008) Deep groundwater mediates streamflow response to climate warming in the Oregon Cascades. Clim Change 86:189–210. doi:10.1007/s10584-007-9294-8

Tallaksen LM, van Lanen HAJ (2004) Hydrological drought. Processes and estimation for streamflow and groundwater, developments in water science, 48. Elsevier, Amsterdam, p 581

Tang Q, Lettenmaier DP (2012) 21st century runoff sensitivities of major global river basins. Geophys Res Lett 39:L06403. doi:10.1029/2011GL050834

Tapley BD, Bettadpur S, Ries JC, Thompson PF, Watkins MM (2004) GRACE measurements of mass variability in the Earth system. Science 305:503–505. doi:10.1126/science.1099192

Taylor RG, Scanlon B, Döll P, Rodell M, van Beek R, Wada Y, Longuevergne L, LeBlanc M, Famiglietti JS, Edmunds M, Konikow L, Green TR, Chen J, Taniguchi M, Bierkens MFP, MacDonald A, Fan Y, Maxwell RM, Yechieli Y, Gurdak JJ, Allen DM, Shamsudduha M, Hiscock K, Yeh PJ-F, Holman I, Treidel H (2013) Groundwater and climate change. Nat Clim Chang 3:322–329. doi:10.1038/nclimate1744

Tiwari VM, Wahr J, Swenson S (2009) Dwindling groundwater resources in northern India, from satellite gravity observations. Geophys Res Lett 36:L18401. doi:10.1029/2009GL039401

Trenberth KE, Branstator GW, Arkin PA (1988) Origins of the 1988 North American Drought. Science 242:1640–1645. doi:10.1126/science.242.4886.1640
Trenberth KE, Dai A, van der Schrier G, Jones PD, Barichivich J, Briffa KR, Sheffield J (2014) Global warming and changes in drought, Nature Clim. Change 4:17–22. doi:10.1038/nclimate2067
Turral H, Burke J, Faurès J-M (2011) Climate change, water and food security, Water Rep., 36, Food and Agric. Organ. of United Nations (FAO), Rome, Italy, p 200
U.S. Geological Survey (USGS) (1999) Ground water (general interest publication), Tech. Rep., Reston, VA. USA. http://capp.water.usgs.gov/GIP/gw_gip/
U.S. Geological Survey (USGS) (2000) Ground water resources for the future: land subsidence in the United States, USGS Fact Sheet-165-00, Tech. Rep., Reston, VA. USA. http://water.usgs.gov/ogw/pubs/fs00165/
Van Beek LPH, Wada Y, Bierkens MFP (2011) Global monthly water stress: 1. Water balance and water availability. Water Resour Res 47:W07517. doi:10.1029/2010WR009791
Van Dijk AIJM, Renzullo LJ, Wada Y, Tregoning P (2014) A global water cycle reanalysis (2003–2012) merging satellite gravimetry and altimetry observations with a hydrological multi-model ensemble. Hydrol Earth Syst Sci 18:2955–2973. doi:10.5194/hess-18-2955-2014
Van Vuuren D, Edmonds J, Kainuma M, Riahi K, Thomson A, Hibbard K, Hurtt G, Kram T, Krey V, Lamarque J-F, Masui T, Meinshausen M, Nakicenovic N, Smith S, Rose S (2011) The representative concentration pathways: an overview. Clim Chang 109:5–31. doi:10.1007/s10584-011-0148-z
Vörösmarty CJ, Green P, Salisbury J, Lammers RB (2000) Global water resources: vulnerability from climate change and population growth. Science 289:284–288. doi:10.1126/science.289.5477.284
Vörösmarty CJ, Leveque C, Revenga C (2005) Millennium ecosystem assessment volume 1: conditions and trends, chap 7: Freshwater ecosystems. Island Press, Washington, pp 165–207
Vörösmarty CJ, McIntyre P, Gessner MO, Dudgeon D, Prusevich A, Green P, Glidden S, Bunn SE, Sullivan CA, Liermann CR (2010) Global threats to human water security and river biodiversity. Nature 467:555–561. doi:10.1038/nature09440
Voss KA, Famiglietti JS, Lo M, de Linage C, Rodell M, Swenson SC (2013) Groundwater depletion in the Middle East from GRACE with implications for transboundary water management in the Tigris-Euphrates-Western Iran region. Water Resour Res. doi:10.1002/wrcr.20078
Wada Y, Bierkens MFP (2014) Sustainability of global water use: past reconstruction and future projections. Environ Res Lett 9:104003. doi:10.1088/1748-9326/9/10/104003
Wada Y, Heinrich L (2013) Assessment of transboundary aquifers of the world—vulnerability arising from human water use. Environ Res Lett 8:024003. doi:10.1088/1748-9326/8/2/024003
Wada Y, van Beek LPH, van Kempen CM, Reckman JWTM, Vasak S, Bierkens MFP (2010) Global depletion of groundwater resources. Geophys Res Lett 37:L20402. doi:10.1029/2010GL044571
Wada Y, van Beek LPH, Bierkens MFP (2011a) Modelling global water stress of the recent past: on the relative importance of trends in water demand and climate variability. Hydrol Earth Syst Sci 15:3785–3808. doi:10.5194/hess-15-3785-2011
Wada Y, van Beek LPH, Viviroli D, Dürr HH, Weingartner R, Bierkens MFP (2011b) Global monthly water stress: 2. Water demand and severity of water stress. Water Resour Res 47:W07518. doi:10.1029/2010WR009792
Wada Y, van Beek LPH, Bierkens MFP (2012a) Nonsustainable groundwater sustaining irrigation: a global assessment. Water Resour Res 48:W00L06. doi:10.1029/2011WR010562. Special Issue: Toward Sustainable Groundwater in Agriculture
Wada Y, van Beek LPH, Sperna Weiland FC, Chao BF, Wu Y-H, Bierkens MFP (2012b) Past and future contribution of global groundwater depletion to sea-level rise. Geophys Res Lett 39:L09402. doi:10.1029/2012GL051230
Wada Y, van Beek LPH, Wanders N, Bierkens MFP (2013a) Human water consumption intensifies hydrological drought worldwide. Environ Res Lett 8:034036. doi:10.1088/1748-9326/8/3/034036
Wada Y, Wisser D, Eisner S, Flörke M, Gerten D, Haddeland I, Hanasaki N, Masaki Y, Portmann FT, Stacke T, Tessler Z, Schewe J (2013b) Multimodel projections and uncertainties of irrigation water demand under climate change. Geophys Res Lett 40:4626–4632. doi:10.1002/grl.50686
Wada Y, Wisser D, Bierkens MFP (2014a) Global modeling of withdrawal, allocation and consumptive use of surface water and groundwater resources. Earth Syst Dyn 5:15–40. doi:10.5194/esd-5-15-2014
Wada Y, Gleeson T, Esnault L (2014b) Wedge approach to water stress. Nat Geosci 7:615–617. doi:10.1038/ngeo2241
Widén-Nilsson E, Halldin S, Xu C-Y (2007) Global water-balance modelling with WASMOD-M: parameter estimation and regionalization. J Hydrol 340:105–118. doi:10.1016/j.jhydrol.2007.04.002
Wilhite DA (ed) (2000) Drought: a global assessment. Routledge, London

Wisser D, Fekete BM, Vörösmarty CJ, Schumann AH (2010) Reconstructing 20th century global hydrography: a contribution to the Global Terrestrial Network-Hydrology (GTN-H). Hydrol Earth Syst Sci 14:1–24. doi:10.5194/hess-14-1-2010

Wisser D, Frolking S, Hagen S, Bierkens MFP (2013) Beyond peak reservoir storage? A global estimate of declining water storage capacity in large reservoirs. Water Resour Res 49:5732–5739. doi:10.1002/wrcr.20452

World Water Assessment Programme (WWAP) (2003) Water for people: Water for life, The United Nations World Water Development Report, United Nations Educational, Scientific and Cultural Organization (UNESCO), Paris, France

World Water Assessment Programme (WWAP) (2009) Water in a changing world, The United Nations World Water Development Report 3, United Nations Educational, Scientific and Cultural Organization (UNESCO), Paris, France

Yates DN (1997) Approaches to continental scale runoff for integrated assessment models. J Hydrol 201:289–310. doi:10.1016/S0022-1694(97)00044-9

Yoshikawa S, Cho J, Yamada HG, Hanasaki N, Khajuria A, Kanae S (2014) An assessment of global net irrigation water requirements from various water supply sources to sustain irrigation: rivers and reservoirs (1960–2000 and 2050). Hydrol Earth Syst Sci 18:4289–4310. doi:10.5194/hess-18-4289-2014

Zektser IS, Everett LG (eds) (2004) Groundwater resources of the world and their use, IHP-VI series on groundwater No. 6, United Nations Educational, Scientific and Cultural Organization (UNESCO), Paris, France

DOI 10.1007/978-3-319-32449-4_11
Reprinted from *Surveys in Geophysics* Journal, DOI 10.1007/s10712-015-9338-y

# What Can be Expected from the GRACE-FO Laser Ranging Interferometer for Earth Science Applications?

**Frank Flechtner[1] · Karl-Hans Neumayer[1] · Christoph Dahle[1] · Henryk Dobslaw[1] · Elisa Fagiolini[1] · Jean-Claude Raimondo[2] · Andreas Güntner[3]**

Received: 13 March 2015 / Accepted: 24 August 2015 / Published online: 14 September 2015


**Abstract** The primary objective of the gravity recovery and climate experiment follow-on (GRACE-FO) satellite mission, due for launch in August 2017, is to continue the GRACE time series of global monthly gravity field models. For this, evolved versions of the GRACE microwave instrument, GPS receiver, and accelerometer will be used. A secondary objective is to demonstrate the effectiveness of a laser ranging interferometer (LRI) in improving the satellite-to-satellite tracking measurement performance. In order to investigate the expected enhancement for Earth science applications, we have performed a full-scale simulation over the nominal mission lifetime of 5 years using a realistic orbit scenario and error assumptions both for instrument and background model errors. Unfiltered differences between the synthetic input and the finally recovered time-variable monthly gravity models show notable improvements with the LRI, on a global scale, of the order of 23 %. The gain is realized for wavelengths smaller than 240 km in case of Gaussian filtering but decreases to just a few percent when anisotropic filtering is applied. This is also confirmed for some typical regional Earth science applications which show randomly distributed patterns of small improvements but also degradations when using DDK4-filtered LRI-based models. Analysis of applied error models indicates that accelerometer noise followed by ocean tide and non-tidal mass variation errors are the main contributors to the overall GRACE-FO gravity model error. Improvements in these fields are therefore necessary, besides optimized constellations, to make use of the increased LRI accuracy and to significantly improve gravity field models from next-generation gravity missions.

✉ Frank Flechtner
frank.flechtner@gfz-potsdam.de

[1] Department 1 "Geodesy and Remote Sensing", GFZ German Research Center for Geosciences, Telegrafenberg, 14473 Potsdam, Germany

[2] SpaceTech GmbH, Seelbachstr. 13, 88090 Immenstaad, Germany

[3] Department 5 "Earth Surface Processes", GFZ German Research Center for Geosciences, Telegrafenberg, 14473 Potsdam, Germany

**Keywords** GRACE · GRACE-FO · Time-variable gravity modeling · Satellite-to-satellite tracking

## 1 Introduction

The GRACE (gravity recovery and climate experiment) mission (Tapley et al. 2004) launched in 2002 is the only mission capable to monitor mass variations in the Earth system. Major advances that GRACE has provided in Earth sciences have recently been summarized by Wouters et al. (2014). Prominent examples are:

- Mass balancing of the continental water content, which is ultimately a sum of precipitation, evaporation, runoff and storage, enabling us to monitor the season-dependent changes in the major river basins, as well as huge groundwater extraction due to irrigation, e.g., in India (Rodell et al. 2009) or California (Scanlon et al. 2012).
- Quantification of the increase or decrease in the ice and snow masses in the polar or large glacier areas has been achieved by scientists who were able to demonstrate a strong correlation between the climatic phenomenon ENSO/La Nina, the rainfall patterns in West Antarctica and the reduction of ice mass there (Sasgen et al. 2010).
- Monitoring of global mean eustatic sea-level variations as a consequence of mass re-distribution between continents and ocean basins for the partitioning of observed sea-level changes into mass and temperature contributions (Cazenave et al. 2009), as well as the regional re-distribution of water masses in response to time-variable surface winds that are tightly connected to time variations of hemispheric current systems such as the Antarctic Circumpolar Current (Bergmann and Dobslaw 2012).
- Observation of changes in the solid Earth following large earthquakes, such as Sumatra–Andaman (2004), Chile (2010) and Fukushima (2011, Wang et al. 2012).

These results are based on the more than 13-year long time series of monthly estimates of the global gravity field of the Earth. All GRACE instruments are still producing nominal high-quality observation data, the solar activity is still moderate, and fuel consumption is still lower than predicted. Therefore, the mission lifetime of GRACE could in principle be extended through 2018. Unfortunately, the batteries on both satellites are degrading and as a consequence the accelerometer (to observe non-gravitational forces due to atmospheric drag or solar radiation pressure), the instrument control units, and/or the microwave assembly (part of the microwave instrument (MWI) K-band inter-satellite ranging system) are powered off during the maximum eclipse season, thus interrupting the nominal science data flow every 161 days for a period of approximately 3–4 weeks (Flechtner et al. 2015). Further information on the mission status is regularly provided at http://www.csr.utexas.edu/grace/operations/mission_status.

Due to the tremendous success of GRACE data applied in many Earth science disciplines, there has been a long-standing strong request by the international user community to launch a GRACE follow-on (GRACE-FO) mission as fast as possible to extend the mass flux time series with the minimum practical data gap between both missions. GRACE-FO is, as GRACE, again implemented under US-German partnership (Flechtner et al., 2015). Overall mission management and satellite and instrument responsibility is with the Jet Propulsion Laboratory (JPL) which will procure the satellite buses and accelerometers, provide the microwave instrument, GPS receiver, and a significant portion (electronics,

laser) of a joint laser ranging interferometer (LRI). Germany will provide the launch vehicle, perform mission operations, participate in the joint science data system (SDS) and will provide major (optical) contributions to the LRI. All German contributions are managed by the GFZ German Research Centre for Geosciences. The NASA/GFZ partnership is stipulated in a memorandum of understanding (MOU), the roles and responsibilities in a cooperative project plan (CPP). GRACE-FO passed the preliminary design review (PDR) in January 2014 and entered Phase-C in March 2014. The critical design review (CDR) was successfully completed in February 2015. The system integration review (SIR) was successfully performed in July 2015. Both satellites will be launched with a Russian DNEPR in August 2017 into a circular polar orbit with an initial altitude of 490 km.

The primary objective of the GRACE-FO mission is to continue the record of climate change observations established by GRACE by extending the time series of high-resolution monthly global models of the Earth's gravity field for an additional 5-year period (Flechtner et al. 2015). For this, evolved versions of the GRACE microwave instrument (MWI), GPS receiver, and accelerometer will be used. Whenever possible, lessons learnt from GRACE will be taken into account to improve the GRACE-FO MWI-based gravity field models. For example, GRACE-FO attitude control will be based on three star camera heads instead of two in the case of GRACE. This will make attitude determination more robust (especially in phases of blinding by the Sun and/or the Moon). Also the radiator on the bottom of the GRACE-FO spacecraft will be rigid instead of using foils on GRACE to get rid of artificial signals (so-called twangs) observed in the GRACE accelerometer records (Flury et al. 2008). A secondary GRACE-FO objective is to demonstrate the effectiveness of the LRI in improving low satellite-to-satellite tracking (SST) measurement performance which is directly linked to the accuracy of the derived gravity field models (Sheard et al. 2012). The LRI will be the first ever inter-spacecraft laser interferometer and should lead to improved spatial and temporal resolution for future next-generation gravity missions (NGGM). Another secondary objective is to continue GRACE radio occultation measurements for operational provision of temperature or humidity profiles of the neutral atmosphere to numerical weather services (Wickert et al. 2009).

In a previous study, Loomis et al. (2012) investigated the accuracy and spatial resolution of monthly gravity field recovery using several possible configurations of a GRACE-FO mission by a simulation experiment covering a 25-month period. These scenarios were based on a GRACE-like orbit at 480 km altitude and 220 km separation using on-board accelerometers with the same noise characteristic as GRACE, and alternatively flying in drag-free mode at 250 km altitude at 50 km separation. They investigated the ability of these configurations to recover $1^\circ \times 1^\circ$ mascon blocks in Greenland and in the Amazon basin in the presence of instrument and background model errors. The MWI SST range-rate errors were assumed as for GRACE (0.2 μm/s), and for the Laser SST measurement performance, they assumed an optimistic (laboratory) value of 0.6 nm/s. Their main conclusion was that the increased precision of the laser link does not improve gravity estimation when flown with GRACE-like on-board accelerometers, altitude and spacecraft separation and that also only modest improvement is realized for the best-case scenario (laser, low-altitude, drag-free) primarily due to temporal aliasing errors.

As the GRACE and GRACE-FO Science Data Centers (UTCSR, JPL and GFZ) will base their monthly Level-2 gravity field model estimates on spherical harmonics, we have performed a new full-scale simulation over the nominal 5-year mission period and we have

performed a new full-scale simulation over the nominal 5-year mission period in order to investigate possible improvements by the LRI on GRACE-FO when compared to GRACE-FO MWI derived gravity models. The intention of the paper is not to compare the gain of GRACE-FO with respect to GRACE when analyzing baseline MWI data. In contrast to Loomis et al. (2012), we did not just use the difference in two atmosphere and ocean models to take into account high-frequency aliasing errors, but applied a reasonably perturbed background model of non-tidal atmosphere and ocean variability that is part of the updated ESA Earth system model specifically prepared for future gravity mission simulations (Dobslaw et al. 2015a, b). Finally, the Loomis et al. (2012) assumptions for LRI instrument noise were updated according to the actual GRACE-FO specifications (Sheard et al. 2012). The orbital decay, ground track pattern and orbital errors were simulated in order to fit to the real GRACE and expected GRACE-FO situation. In contrast to the mascon results, the GRACE spherical harmonic solutions require post-processing (filtering) in order to get rid of artificial striping due to increasing spherical harmonic errors with increasing degree and for specific orders. For this we applied and compared different isotropic and anisotropic filters with various resolutions such as Gaussian averaging (Wahr et al. 1998), the so-called DDK filtering (Kusche 2007), or the destriping method by Swenson and Wahr (2006).

Our simulation assumptions and strategy are explained in Sect. 2. The global results, when comparing the recovered GRACE-FO MWI and LRI monthly gravity model time series with the simulated "true world" input gravity signals are then described in the spectral and spatial domain (Sect. 3). Section 4 focuses on typical GRACE-FO regional results for hydrological, glaciological, oceanographic or solid Earth applications. In Sect. 5 we investigate the various contributions of instrument and background model errors to the overall MWI- and LRI-based result. A summary and our conclusions are provided in Sect. 6.

## 2 Simulation Assumptions and Strategy

The 5-year full-scale simulation is based on realistic assumptions for the upcoming GRACE-FO mission. The simulated orbits start at the target initial altitude of 490 km with an inclination of 89.0° and an eccentricity of 0.0015 and end at an altitude of about 450 km after the nominal GRACE-FO mission lifetime of 5 years. This decay of about 40 km is similar to the early GRACE mission descent. The solar activity values (necessary to simulate non-gravitational forces and accelerometer data, respectively) were taken from the period 1995–1999 which should represent similar characteristics as expected for 2018–2022. In order to maintain the inter-satellite link between 170 and 270 km, it was necessary to apply a reset of the inter-satellite distance each year (the same is done by regular orbit maintenance maneuvers during the GRACE mission lifetime). The simulated osculating altitude, satellite separation and solar activity values are shown in Fig. 1. We have not simulated any orbit maneuver to keep the ground track spacing dense throughout the complete mission period. Such kind of maneuvers are also not performed within the GRACE mission and led to temporary unfavorable repeat cycles (see http://www.gfz-potsdam.de/grace), e.g., in September 2004 (4 days) or February 2015 (2 days). Figure 2 depicts the ground track patterns for August 2019 (worst case within the 5 years, see Fig. 3), March 2021 (not optimal, but sufficient enough for nominal gravity field recovery) and May 2021 (representative month for an optimal sampling scenario).

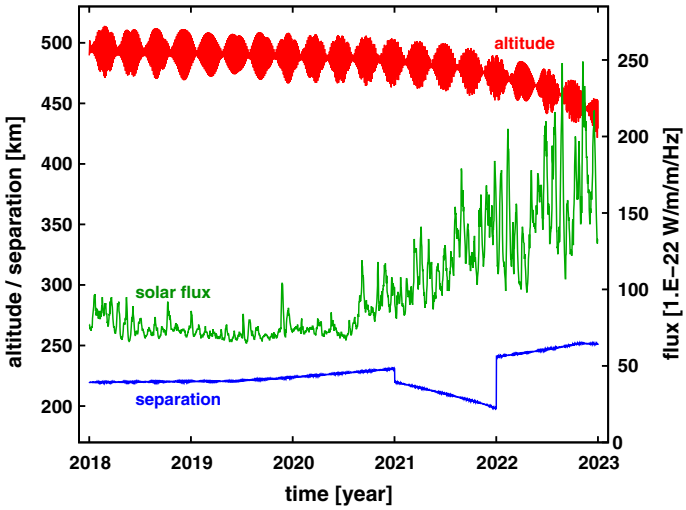


**Fig. 1** Simulated osculating altitude, minimum and maximum satellite separation and solar flux values

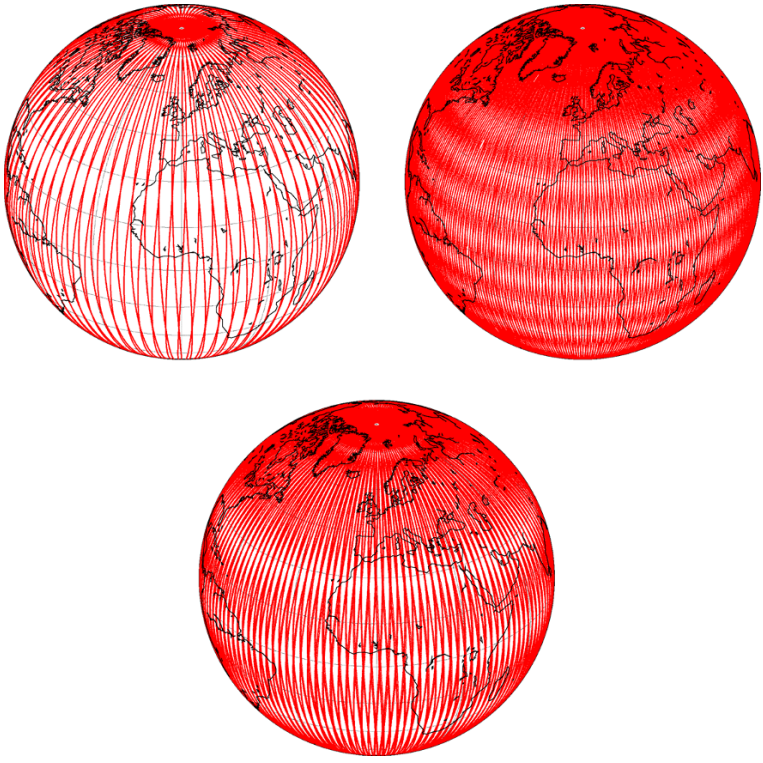

**Fig. 2** Ground track pattern for August 2019 (*left*), March 2021 (*middle*) and May 2021 (*right*)

In a first (forward simulation) step, 5-s (integration step size as for GRACE) satellite orbits and true SST observations have been simulated using GFZ's Earth parameter and orbit system (EPOS) software package which is also operationally applied for GRACE real data analysis. Non-gravitational forces have been simulated from models for atmospheric drag (MSIS86, Hedin 1987), solar radiation pressure (umbra and penumbra using solar flux values as depicted in Fig. 1), and Earth albedo and infrared (Knocke et al. 1988). The sum of these accelerations has been converted into pseudo GRACE-FO 3D accelerometer data. For nominal attitude, we assumed yaw steering. Additional background models applied during simulation included a static gravity model [EIGEN-GL04C (Förste et al. 2008, used up to degree and order 100], Sun and Moon ephemerides (DE405, Standish 1998), ocean tides (the 8 main constituents Q1, O1, P1, K1, N2, M2, S2 and K2 of EOT08a, Savcenko and Bosch 2008), and non-tidal mass variations in atmosphere, oceans, hydrology, ice, and solid Earth (called AOHIS in the following) from the updated ESA Earth system model (Dobslaw et al. 2015a, used up to degree and order 100). The high–low SST GPS phase and code observations, used to define a reference frame for LEO orbit integration (Reigber et al. 2005) have been simulated with white noise of 0.3 and 30 cm, respectively.

In the next step we have added colored noise to the simulated MWI, LRI and accelerometer data. As no realistic star camera attitude noise was available for the authors of this study (and has, probably for the same reasons, also not been treated in other GRACE-FO simulations, e.g., Loomis et al. 2012), we have referred both the simulated MWI and LRI observations to the center of mass (CoM) of the GRACE-FO spacecraft and have neglected any attitude error impact, especially on the SST data. The MWI is located about 1.4 m off from the CoM, while the LRI is virtually measuring to the CoM, thanks to its racetrack design and the triple mirror assembly (Sheard et al. 2012). Consequently, attitude errors would primarily impact the MWI-based results. Bandikova and Flury (2014) have analyzed GRACE Level-1B star camera data and reported systematically higher noise than expected. The reason was found in the incorrect implementation of algorithms for quaternion combination in the JPL processing routines. Bandikova et al. (2014) investigated the impact on gravity field determination and found that neither the Celestial Mechanics Approach nor the variational equations approach is sensitive to these noise errors. Therefore, attitude errors have not been treated in our study.

The 5-s SST noise values for MWI and LRI are modeled in terms of amplitude spectral density (ASD) as a square root of power spectrum density (PSD) with a distance-dependent factor for which we applied the average distance between the two GRACE-FO satellites (220 km). The method is described in Elsaka et al. (2014) and the values applied in our study are consistent with the expected performance of the GRACE-FO LRI (Sheard et al. 2012) and MWI (Dahle et al. 2014) SST noise: LRI 80 nm (range) resp. 9.9 nm/s (range-rate); MWI: 2.1 μm (range) resp. 0.24 μm/s (range-rate). The LRI instrument has lower errors in the high-frequency part of the spectrum (Sheard et al. 2012) which ultimately could result in improved estimation of GRACE-FO high-degree spherical harmonic coefficients (as shown in the simulation results in Fig. 10). Also, it has to be mentioned that, as for GRACE GFZ real data analysis, the MWI- and LRI-based simulations are made with range-rate SST data only. The procedure to derive accelerometer noise time series using spectral density values for a frequency ($f$) band of $10^{-4}$ to $10^{-1}$ Hz of GRACE-like accelerometer errors $[(1 + 0.005/f)^{1/2} \times 10^{-10}$ m/s$^2$/Hz$^{1/2}$ for transversal and radial direction, $(1 + 0.1/f)^{1/2} \times 10^{-9}$ m/s$^2$/Hz$^{1/2}$ for normal direction] was the same as described in Loomis et al. (2012).

In the backward simulation performed again with EPOS software, we used the simulated observations, supplemented with the colored MWI, LRI and ACC noise, to recover

the 60 monthly gravity field models up to degree and order 100. Here we also substituted the nominal background models to simulate a realistic error level in the static and time-variable gravity field. For this we used EGM96 (Lemoine et al. 1998) up to degree and order 100 as static gravity model and substituted the 8 main ocean tide constituents by GOT4.7 (Ray 2008) values.

As the a priori background model for the non-tidal mass variability in atmosphere and oceans, we employed the realistically perturbed de-aliasing model Dobslaw et al. (2015b) which is part of the updated ESA Earth system model. This perturbed background model contains (1) errors at large spatial scales that have been derived from appropriately scaled differences with the original ESA Earth system model (Gruber et al., 2011) assessed individually for periods between 10–30, 3–10, and 1–3 days, the S1 atmospheric tide, and sub-diurnal periods. Further, the model includes (2) errors at small spatial scales typically not covered by global models of atmosphere and ocean variability; and finally (3) errors due to physical processes not represented in currently available de-aliasing products as GRACE AOD1B (Flechtner et al. 2014). The updated ESA Earth system model including the perturbed background model is publicly available together with its technical documentation via doi 10.5880/GFZ.1.3.2014.001.

The gravity recovery step was performed twice: in a first run, we used explicitly the MWI data and in the second run we applied only the LRI data. All other observations (accelerometer, GPS) and background model errors were identical in both cases as this would also be the case during GRACE-FO real data analysis. Besides spherical harmonic coefficients, also arc-specific parameters such as initial orbital states and 3-hourly 3D accelerometer biases and scales have been adjusted (similar to GRACE RL05a). The resulting MWI- and LRI-based monthly gravity solutions have then been compared with the simulated ("true") gravity field time series in the spectral and spatial domain as well (if applicable) with real GRACE results to show that the simulated gravity results are as realistic as possible. For example, to check the simulated orbit accuracy, we have analyzed the satellites separation derived from GPS data only. For this we have intentionally down-weighted the MWI data (which have usually a very high weight in order to derive mid-to-short wavelength gravity coefficients). The resulting global GPS-derived range-rate residual root-mean-square (RMS) values can then be interpreted as a measure of the orbit accuracy by comparing them with the much more precise MWI observations serving as a reference. The results were typically in the order of 1.5 μm/s which is identical to GFZ GRACE RL05 real data analysis (e.g., for June 2014).

## 3 Results in the Spectral and Spatial Domain

As a measure of the true error of our simulated gravity field models, unfiltered monthly differences between the recovered and the a priori static gravity field model plus the monthly mean HIS component of the time-variable AOHIS a priori model are used. Figure 3 shows these errors in terms of latitude weighted RMS (wRMS) of equivalent water heights (EWH) for the complete simulation period of 5 years (2018–2022). The two curves depict the result obtained using the baseline MWI SST and the demonstrator LRI observations. It becomes visible that for the unfiltered case the LRI outperforms the MWI derived results for all months. The two peaks in August 2019 and November 2021 are correlated with imperfect ground track coverage compared to other months (see Fig. 2 left).

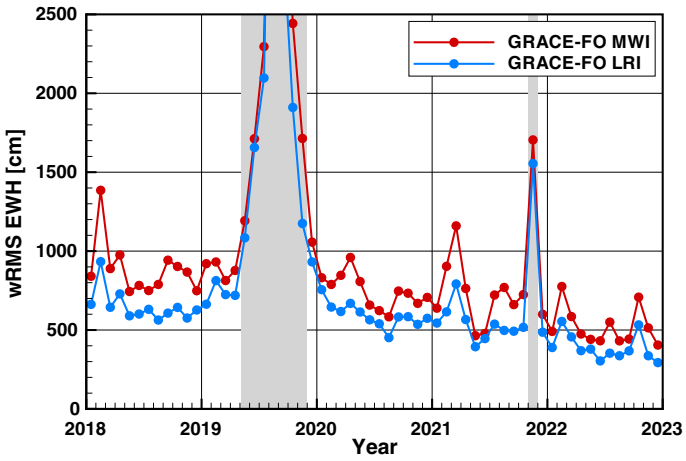


**Fig. 3** Unfiltered monthly differences between recovered and simulated gravity fields in terms of the weighted root mean square (wRMS) of equivalent water heights (EWH) for the 5-year simulation period using simulated GRACE-FO MWI (*red*) and LRI (*blue*) data. Periods with imperfect ground track pattern have been marked *gray*

**Table 1** Mean of monthly MWI- and LRI-based wRMS results in terms of EWH for the unfiltered case and after application of various filters. Note that 8 months with exceptionally large wRMS values due to repeat orbit pattern (marked with gray background color in Fig. 3) have been omitted

| Filter | MWI mean wRMS (cm) | LRI mean wRMS (cm) | Mean wRMS reduction (%) |
|---|---|---|---|
| Unfiltered | 736.64 | 564.56 | 22.9 |
| DDK1 (530 km) | 0.70 | 0.68 | 1.7 |
| DDK2 (340 km) | 1.20 | 1.19 | 1.0 |
| DDK3 (240 km) | 2.29 | 2.25 | 1.7 |
| DDK4 (220 km) | 2.73 | 2.66 | 2.6 |
| DDK5 (160 km) | 4.25 | 3.97 | 6.5 |
| Destriping and Gauss 530 km | 0.70 | 0.69 | 1.2 |
| Destriping and Gauss 340 km | 0.94 | 0.91 | 3.1 |
| Destriping and Gauss 240 km | 3.01 | 2.64 | 12.6 |
| Destriping and Gauss 220 km | 4.64 | 3.96 | 15.1 |
| Destriping and Gauss 160 km | 17.59 | 13.67 | 23.6 |
| Gauss 530 km | 1.13 | 1.15 | −1.5 |
| Gauss 340 km | 2.95 | 2.79 | 4.7 |
| Gauss 240 km | 16.23 | 13.65 | 15.1 |
| Gauss 220 km | 26.31 | 21.67 | 16.8 |
| Gauss 160 km | 110.62 | 87.23 | 20.4 |

Table 1 shows the corresponding mean wRMS values of 52 (neglecting the gray periods highlighted in Fig. 3) monthly MWI- and LRI-based models in terms of EWH for the unfiltered case and after application of various filters. Filtering is necessary to reduce degree-dependent errors for mid-to-long wavelengths resulting in a decrease in the EWH error from meter to centimeter level. It is clear that, for the unfiltered case on a global scale and on average, the LRI observations will outperform the MWI results by 23 % in terms of wRMS reduction. The corresponding gain for the anisotropic DDK filtered global results is much smaller (about 1–7 %), whereas in case of applying destriping and/or Gaussian smoothing the gain by LRI becomes again more significant (about 15–23 % depending on the Gaussian filter radius). As the Gaussian filter removes high-frequency signals, this filter is not used for regional analysis in Sect. 4. Note that typical GRACE RL05 GFZ (90°) and CSR (96°) monthly models show comparable unfiltered values, proving again that our results are realistic.

Figure 4 shows unfiltered error degree amplitudes in terms of EWH for March 2021 and May 2021. March 2021 is chosen (also for the following figures) because it represents a non-optimal, but still sufficiently dense ground track pattern for nominal gravity field recovery and May 2021 is a representative month for an optimal sampling scenario (see Fig. 2). It becomes obvious that in the first case (March 2021), the LRI slightly improves the MWI errors in the mid [below 40° (500 km)] and notable in the short wavelengths above 60° (333 km), while in the second case, no improvement is seen by the LRI.

Similar conclusions can be drawn when looking at the cumulative difference degree amplitudes for the two test months (Fig. 5). While for an optimal sampling the LRI does not improve the gravity recovery error for all wavelengths (May 2021), the March 2021 scenario with non-optimal ground track pattern shows moderate improvements by the LRI for all wavelengths above 1000 km, e.g., the error will reduce from 4 to 3 cm EWH (600 km resolution) and from 20 to 15 cm EWH (400 km), respectively.

Another way to visualize the results is shown in Fig. 6 where the unfiltered true and formal errors per degree and order for May 2021 are shown using a logarithmic scale. The formal errors are those from adjustment procedure, while the true errors are those described above. For comparison, GRACE real data errors based on the GFZ RL05a solution for May 2005 are shown as well. For the latter, the true error has been approximated by taking the

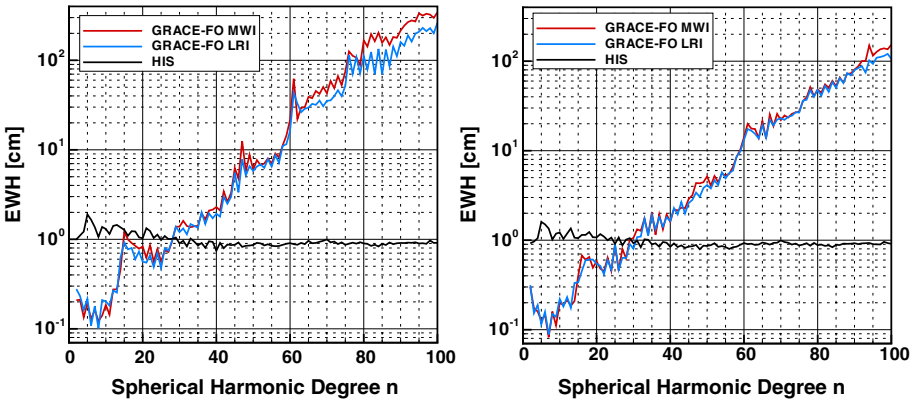


**Fig. 4** Simulated MWI (*red*) and LRI (*blue*) difference degree amplitudes with respect to the "truth" in terms of EWH for March 2021 (*left*) and May 2021 (*right*). The true signal is given by the monthly mean of the hydrology, ice and solid Earth (HIS) component of the AOHIS background model (*black*)

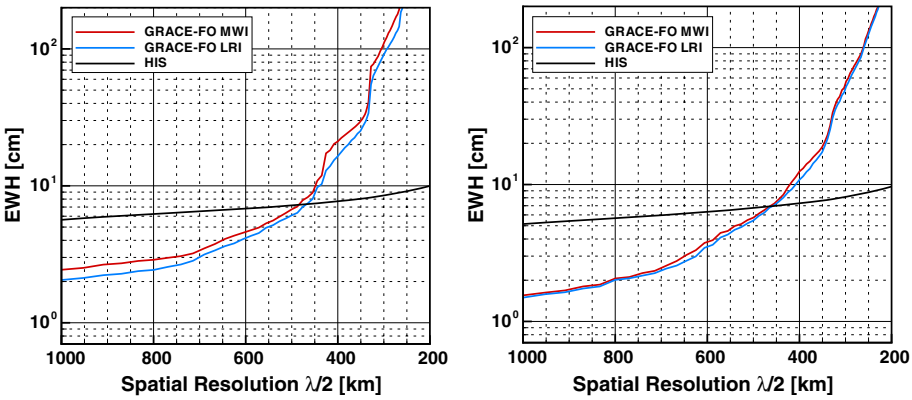


**Fig. 5** Simulated MWI (*red*) and LRI (*blue*) cumulative difference degree amplitudes w.r.t. the "truth" in terms of EWH for March 2021 (*left*) and May 2021 (*right*). The true signal is given by the monthly mean of the hydrology, ice and solid Earth (HIS) component of the AOHIS background model (*black*)

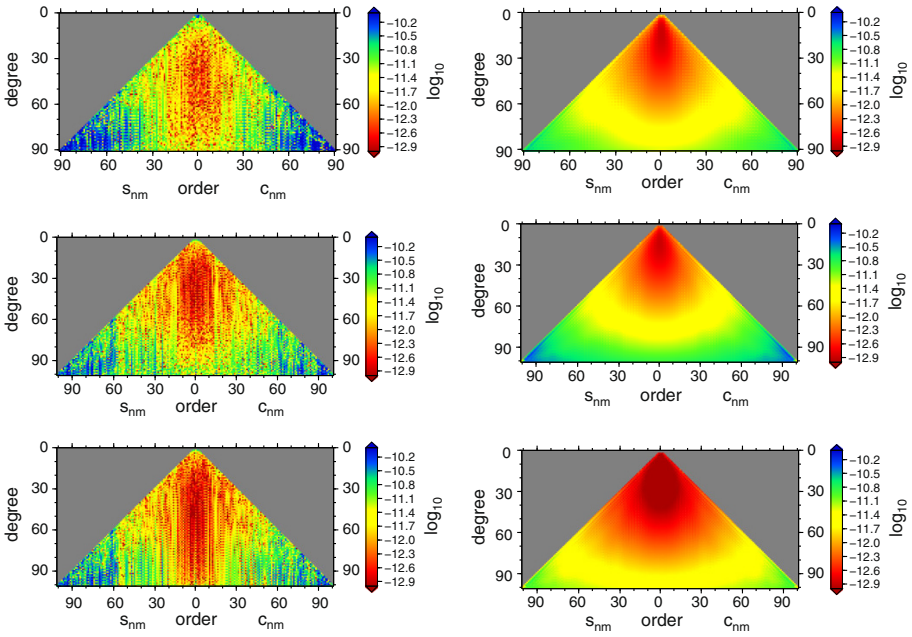


**Fig. 6** GRACE real data (*top*), simulated GRACE-FO MWI (*middle*) and LRI (*bottom*) true (*left*) and formal (*right*) errors per degree and order for May 2005 (real data) and May 2021, respectively. Note that the maximum degree and order is 100 for the simulated GRACE-FO cases, whereas it is limited to 90 for GRACE real data

difference between the solution and its static background model (EIGEN-6C, Shako et al. 2014) plus the time-variable part of EIGEN-6C (up to degree and order 50). The GRACE real and simulated MWI data show very similar error behavior, thereby verifying that the

simulations have been done realistically. In contrast, the near zonal coefficients for spherical harmonic degrees above 60 are much better determined when simulated LRI observations are used. This confirms the improvements by LRI in the short wavelengths (Fig. 4).

Figure 7 depicts the March and May 2021 unfiltered errors in the spatial domain in terms of geoid height errors. It becomes obvious that the error pattern of both months differs consistently with the ground track pattern shown in Fig. 2. In the case of a non-optimal sampling period (March 2021), the artificial spurious North–South stripes due to instrument or aliasing errors are significantly reduced by approximately 30 % when substituting MWI by LRI SST observations. In case of an optimal sampling (May 2021), the MWI errors are reduced by only about 15 %. The different contributions of instrument and background model errors to the total result are discussed in Sect. 5.

## 4 Regional Applications Using Simulated MWI and LRI Data

It has been demonstrated in the previous section that the LRI will improve the MWI-based unfiltered and filtered gravity models on a global scale only moderately and only in case of a non-optimal ground track pattern. As these globally averaged results are not meaningful for Earth system applications which have mass variation signals in defined areas such as changes in hydrological basins or melting of glaciers, we have also investigated how seasonal, sub-seasonal, trend and instantaneous (Earthquake) signals as included in the AOHIS source model are recovered when using GRACE-FO MWI or LRI data.

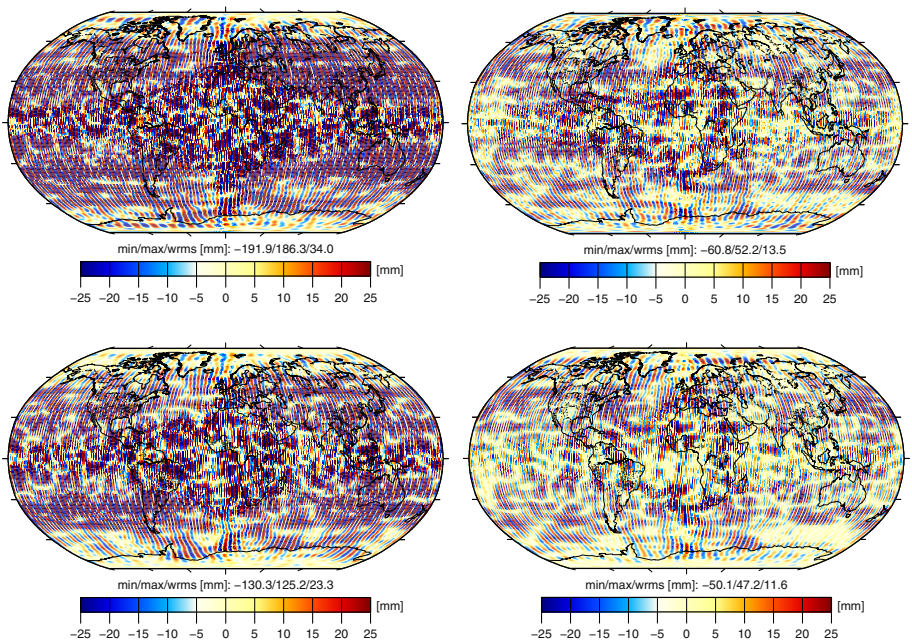


**Fig. 7** Spatial difference between simulated ("true") and recovered gravity fields in terms of unfiltered geoid heights for March 2021 (*left*) and May 2021 (*right*) for the MWI (*top*)- and LRI (*bottom*)-based results

Figure 8 left shows the RMS variability over 5 years (52 models of Table 1) of the difference between simulated ("true") and DDK4-filtered recovered gravity fields based on LRI data in terms of EWH for 1° regular grids. The corresponding plot for MWI-based gravity fields is quite similar and thus is not shown. Generally, the largest error variability (up to 150 cm EWH) is visible where ice or solid Earth signals are introduced by the AOHIS model. The difference between the RMS variability for MWI and LRI is shown in Fig. 8 right (red means LRI is closer to the truth and blue means MWI is closer to truth) and confirms that only moderate improvements up to 13 cm EWH can be expected from LRI data; however, also degradations up to 2 cm become visible.

Figure 9 shows the DDK4-filtered time series in EWH for various 2° × 2° grid boxes such as the Amazon and the Danube river basins, the Greenland and West-Antarctica ice sheet, the Bellingshausen basin in the Antarctic Circumpolar Current and the simulated Sumatra Earthquake in comparison with the corresponding components of the time-variable source model AOHIS.

Table 2 summarizes these moderate improvements of the order of 2–15 % in terms of error reduction when using LRI instead of MWI observations but also shows degradations for Amazon and Sahara (not shown in Fig. 9).

To demonstrate how realistically our simulation was performed, we have derived monthly DDK4-filtered differences between CSR RL05 and GFZ RL05a Level-2 products, both after substitution of C20 by the suggested GRACE TN07 values, for the 5-year period from 2006 to 2010 as a measure for present-day GRACE uncertainties. As can be deduced from Table 2 the average factor with respect to the simulated MWI result is, neglecting the Amazon basin, of the order of 0.86. The reasons for this are many manifold and could include either too optimistically (or neglected, see conclusion section) simulated errors or not-investigated leakage effects in the simulation.

## 5 Error Analysis

In order to find out which of the applied instrument and background model errors are the main contributors to the overall MWI- and LRI-derived global gravity model error (see Sect. 3), we have investigated the influence of the single error components [instrument noise, static gravity field error, ocean tide error, and atmosphere and ocean (AO) de-

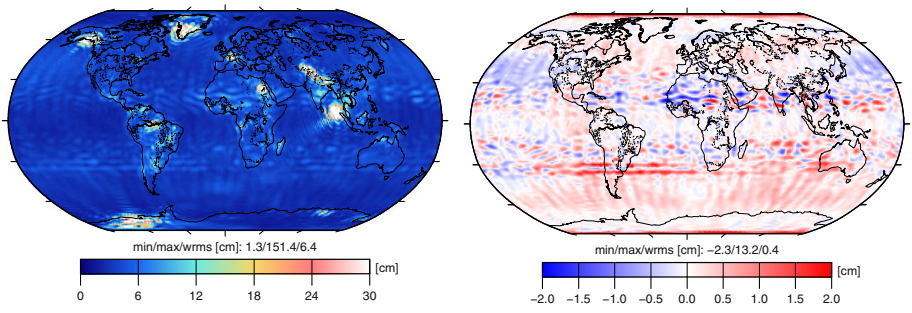


**Fig. 8** RMS variability of difference between simulated ("true") and DDK4-filtered recovered gravity fields based on LRI over the 5 years investigated in terms of EWH (*left*). The difference between the RMS variability for MWI and LRI is shown in the right figure (*red* means LRI is closer to truth, *blue* means MWI is closer to truth)

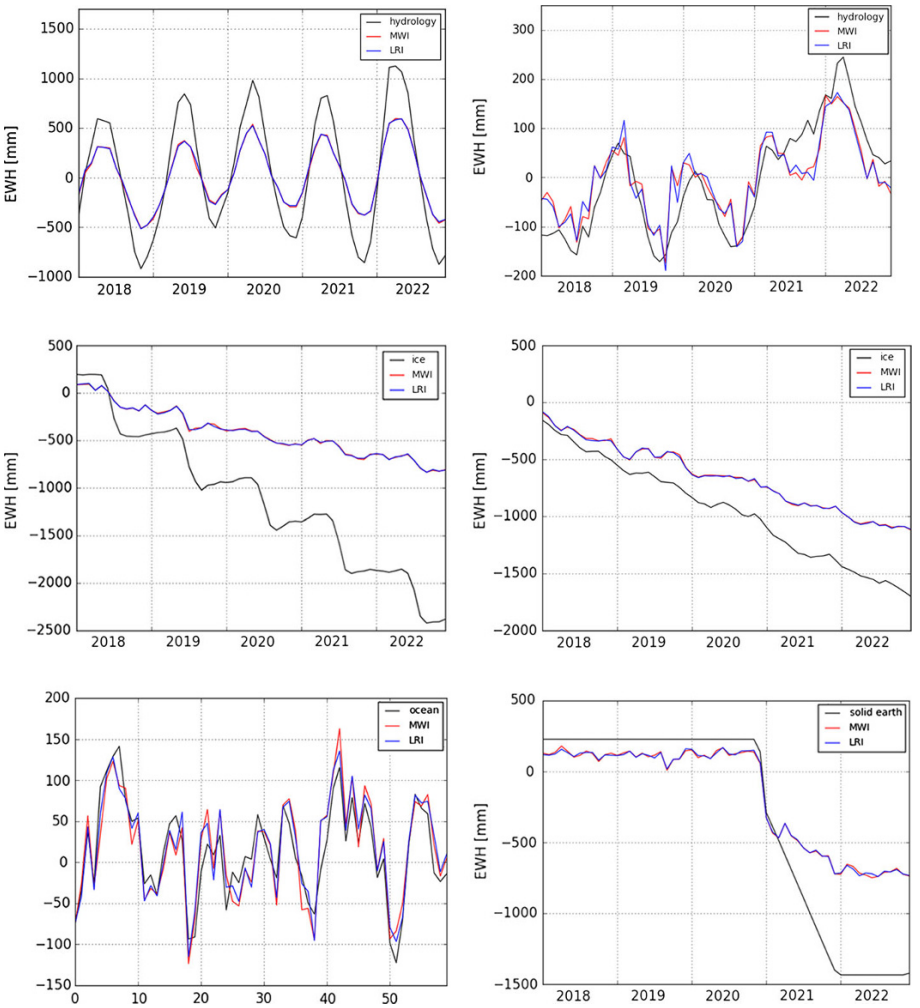


**Fig. 9** Time series for DDK4-filtered 2° × 2° grid boxes in EWH (mm) for Amazon (*top left*) and Danube (*top right*), Greenland (*middle left*) and West-Antarctica (*middle right*) and Bellingshausen (*bottom left*) and for the simulated December 2004 Sumatra earthquake (now in December 2019, *bottom right*) using MWI (*red*) or LRI (*blue*) data. The *black line* depicts the corresponding component H, I, O and S of the AOHIS model

aliasing error] on the solution from the solution for May 2021. In order to quantify a specific individual error contribution, the complete backward simulation step has been repeated with that specific error source omitted, and then the difference in that solution from the solution containing all error sources has been evaluated. Thus, the orbits are recomputed for each individual error source and not only the error propagation through the observations but also through the computed orbits is taken into account. Figure 10 shows the corresponding individual degree amplitudes in terms of geoid height error. It can be clearly seen that the impact of SST noise on gravity field recovery is significantly reduced if LRI instead of MWI observations are used. The spatial resolution where the signal-to-

**Table 2** RMS between recovered and simulated AOHIS signals (mm EWH) for various 2° × 2° grid boxes after DDK4 filtering as well as corresponding LRI gain (%) in terms of RMS reduction. Additionally, the DDK4-filtered "real data errors" (mm) derived from CSR and GFZ GRACE RL05 Level-2 data and the corresponding factor w.r.t. the simulated MWI RMS values are shown

| | MWI RMS (mm) | LRI RMS (mm) | LRI Gain (%) | RL05 CSR-GFZ RMS (mm) | Factor RL05/MWI |
|---|---|---|---|---|---|
| Sumatra | 33.58 | 31.52 | 6.5 | 30.57 | 0.91 |
| Bellingshausen | 26.44 | 22.93 | 15.3 | 21.83 | 0.83 |
| Amazon | 23.95 | 25.49 | −6.0 | 42.88 | 1.79 |
| Danube | 31.78 | 32.17 | −1.2 | 27.93 | 0.88 |
| West Antarctica | 25.60 | 25.18 | 1.7 | 23.70 | 0.93 |
| Greenland | 29.94 | 28.50 | 5.1 | 21.12 | 0.71 |
| Sahara | 37.13 | 39.65 | −6.3 | 32.30 | 0.87 |

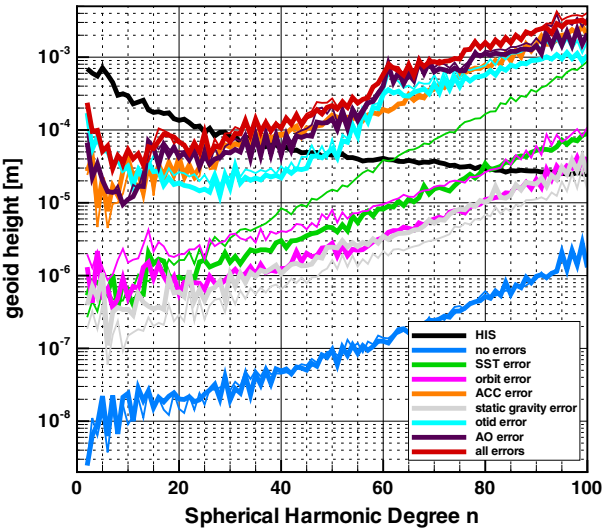


**Fig. 10** Degree amplitudes in terms of geoid height error for May 2021 for different individual instrument and model errors (see legend). The *thin* and *bold lines* show the results obtained with MWI and LRI, respectively. The *blue curve* shows the numerical accuracy of the full-scale simulations (no errors applied) which is about 3 orders of magnitude below the current GRACE-FO error level. The *black line* depicts the monthly mean HIS signal

noise ratio equals one increases from 60° (333 km) to 80° (250 km). However, it becomes also obvious that the main contributors to still existing striping (see Fig. 7 right) are the accelerometer (ACC), ocean tide (otid) and AO errors. All other errors, including the MWI and LRI SST errors, are about one order of magnitude smaller. This confirms that, on a global scale, the decreased LRI noise cannot improve the monthly gravity model for a GRACE-like constellation. Consequently, next-generation gravity missions (NGGM) which may consist of double GRACE-like pairs in a so-called Bender-constellation and which will move along much lower orbits (Elsaka et al. 2014) have to significantly reduce these errors in order to benefit from improved LRI SST measurements.

Figure 11 depicts the resulting spatial pattern for the three main error contributors. The corresponding RSS (root squared sum) gives 14.8 (MWI) and 11.8 (LRI) mm geoid height error which is consistent with the overall error of 13.5 (MWI) and 11.6 (LRI) mm of Fig. 7 right and proves that the other error sources, including SST noise, do not matter for a GRACE-like constellation.

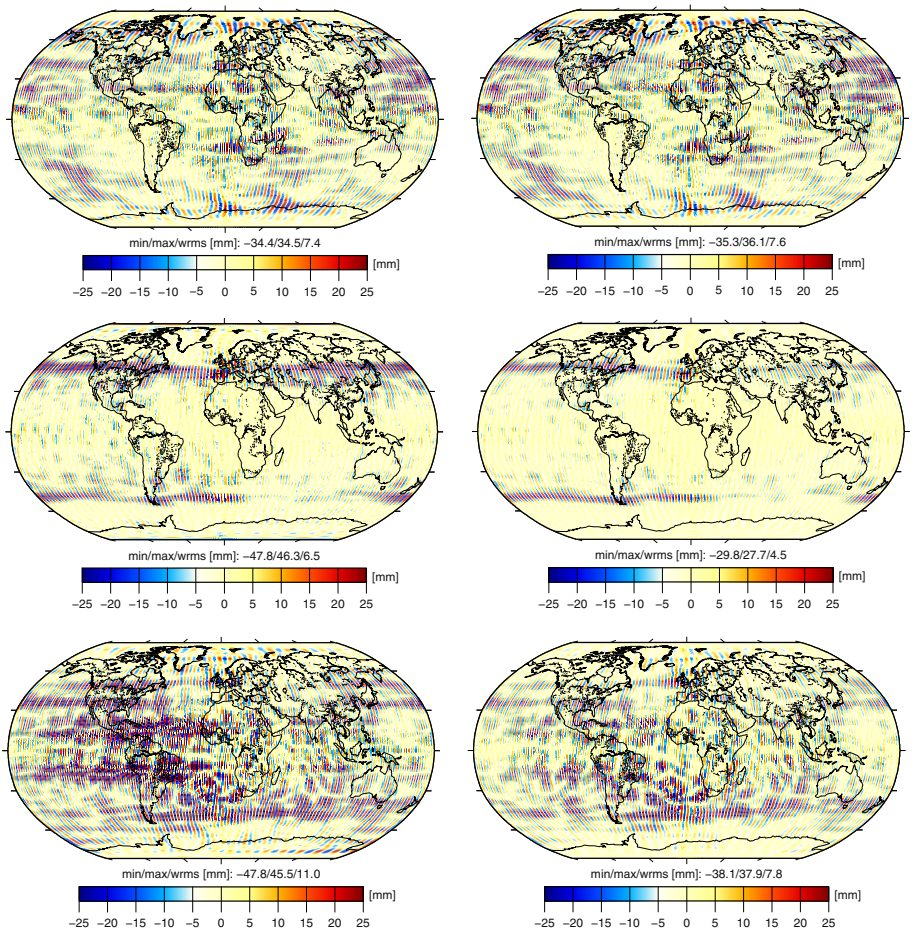


**Fig. 11** Spatial difference between simulated ("true") and recovered gravity fields in terms of unfiltered geoid heights for MWI (*left*)- and LRI (*right*)-derived gravity models for May 2021 in case of ACC errors only (*top*), ocean tide errors only (*middle*) and AO errors only (*bottom*). Statistics show minimum, maximum and wRMS of errors

## 6 Summary and Conclusions

We have performed a full-scale simulation based on realistic assumptions for the GRACE-FO orbit scenario, instrument noise for accelerometer, MWI and LRI SST observations as well as background model errors for the static gravity field and tidal and non-tidal short-term mass variations to investigate the gain in monthly gravity field determination when using the LRI SST observations instead of MWI tracking data.

The results show that the 60 unfiltered LRI-derived monthly gravity field models always outperform the corresponding MWI-based results. The corresponding time series shows an approximately 23 % smaller wRMS in terms of EWH when compared to the simulated "true world" scenario proving the expectations into the increased LRI SST accuracy. The corresponding difference degree amplitudes and cumulative degree amplitudes for two test

months March 2021 and May 2021 indicate that for non-optimal ground track pattern (March 2021) moderate improvements can be expected by the LRI for mid-to-short wavelengths. For that month also the near zonal coefficients for spherical harmonic degrees above 60 are much better determined when LRI observations are used. This is also visible in slightly less meridional striping in the spatial pattern. Applying isotropic Gaussian filtering in order to get rid of larger errors with increasing degree of spherical harmonic coefficients shows—on a global scale—also notable improvements of 13–23 % at or below 240 km spatial resolution. In contrast, anisotropic filtering (DDK) results in only minor reduction (2–7 %) of errors by the LRI instrument.

Looking into typical regional hydrological, glaciological, solid Earth and ocean applications in the Amazon or Danube basin, Greenland and West-Antarctica, the Sumatra Earth quake or the Bellingshausen basin in the Antarctic Circumpolar Current it can be concluded that the globally observed 2.6 % gain, when using DDK4-filtered LRI-derived monthly models, is not visible everywhere but shows a more or less randomly distributed pattern. There are regions like on the Southern oceans where we observe 15 % smaller errors, but in the Amazon or Sahara we also simulated 6 % larger errors when using LRI data.

The error assumptions for the accelerometer and SST data as well as for the non-tidal atmosphere and ocean mass variations have been made as realistic as possible. This is shown by comparison with real GRACE data such as GFZ RL05 orbit errors or remaining monthly gravity model errors as derived from comparison of CSR RL05 and GFZ RL05a solutions. Nevertheless, the ocean tide errors have been defined (due to lack of better knowledge) as the difference in two standard models which may not be fully realistic. Additionally, the gain which may be achieved using LRI data for GRACE-FO gravity field determination alone (neglecting the three main error contributors accelerometer noise and ocean tide and AOHIS background model errors) may be larger as we have not simulated attitude errors. This error would result in MWI phase center variations, but would not affect the LRI observations as they are already referred to the center of mass [using a triple mirror assembly, see Sheard et al. (2012)]. Both, the ocean tide and attitude error are subjects for future investigations.

As a final conclusion, it can be stated that the LRI will only moderately improve the MWI-based GRACE-FO monthly gravity model time series. Earth Science applications will benefit much more from the continued time series based on GRACE data. The main expectation in the LRI is technology demonstration for future gravity missions. Here, full advantage will be gained when a LRI will be the prime instrument on a next-generation gravity mission. This will probably be realized by the combination of a polar orbiting pair of satellites with a second pair of satellites in lower orbit and at smaller inclination, a LRI SST, plus improved accelerometers and an improved attitude and control system.

**Acknowledgments** The authors thank BMBF (German Ministry for Education and Research), BMWi (German Federal Ministry for Economics and Technology), HGF (German Helmholtz Foundation) and DLR (German Aerospace Center) for providing funding and in kind contribution for implementation of the German GRACE-FO mission elements. The paper also arises from the ISSI (International Space Science Institute, Bern, Switzerland) Workshop on Remote Sensing and Water Resources in October 2014.

**Compliance with Ethical Standard**

**Conflict of interest** The authors certify that they have NO affiliations with or involvement in any organization or entity with any financial interest (such as honoraria; educational grants; participation in speakers' bureaus; membership, employment, consultancies, stock ownership, or other equity interest; and expert testimony or patent-licensing arrangements), or non-financial interest (such as personal or professional

relationships, affiliations, knowledge or beliefs) in the subject matter or materials discussed in this manuscript.

## References


Bandikova T, Flury J (2014) Improvement of the GRACE star camera data based on the revision of the combination method. Adv Space Res 54:1818–1827. doi:10.1016/j.asr.2014.07.004

Bandikova T, Meyer U, Klinger B, Tregoning P, Flury J, Mayer-Gürr T (2014) Improved star camera attitude data and their effect on the gravity field. In: Proceedings of the GRACE science team meeting. http://www.gfz-potsdam.de/en/section/globalgeomonitoringandgravityfield/topics/development-operation-and-analysis-of-gravity-field-satellite-missions/grace/gstm/gstm-2014/meeting-program-and-abstract-list/. Last time visited August 4, 2015, German Research Centre for Geosciences, Potsdam, Germany, September 29–October 1, 2014

Bergmann I, Dobslaw H (2012) Short-term transport variability of the Antarctic Circumpolar Current from satellite gravity observations. J Geophys Res (Oceans) 117(C16):5044. doi:10.1029/2012JC007872

Cazenave A, Dominh K, Guinehut S, Berthier E, Llovel W, Ramillien G, Ablain M, Larnicol G (2009) Sea level budget over 2003–2008: a reevaluation from GRACE space gravimetry, satellite altimetry and Argo. Global Planet Change 65:83–88

Dahle C, Flechtner F, König R, Michalak G, Neumayer KH, Gruber C, König D (2014) GFZ RL05: an improved time-series of monthly GRACE gravity field solutions. In: Flechtner F, Sneeuw N, Schuh W-D (eds) Observation of the system earth from space—CHAMP, GRACE, GOCE and future missions (GEOTECHNOLOGIEN science report; 20; advanced technologies in earth sciences). Springer, Berlin, pp 29–39. doi:10.1007/978-3-642-32135-1

Dobslaw H, Bergmann I, Dill R, Forootan E, Klemann V, Kusche J, Sasgen I (2015a) The updated ESA Earth system model for future gravity mission simulation studies. J Geodesy. doi:10.1007/s00190-014-0787-8

Dobslaw H, Bergmann-Wolf I, Forootan E, Dahle C, Mayer-Gürr T, Kusche J, Flechtner F (2015b) Modeling of present-day atmosphere and ocean non-tidal de-aliasing errors for future gravity mission simulations. J Geod (submitted)

Elsaka B, Raimondo JC, Brieden P, Reubelt T, Kusche J, Flechtner F, Iran Pour S, Sneeuw N, Müller J (2014) Comparing seven candidate mission configurations for temporal gravity field retrieval through full-scale numerical simulation. J Geodesy 88:31–43. doi:10.1007/s00190-013-0665-9

Flechtner F, Dobslaw H, Fagiolini E (2014) AOD1B product description document for product release 05 (Rev. 4.2, May 20, 2014). http://www.gfz-potsdam.de/en/aod1b

Flechtner F, Morton P, Watkins M, Webb F (2015) Status of the GRACE follow-on mission. In: Proceedings of the international association of geodesy symposia gravity, geoid and height system (2012, Venice, Italy), IAGS-D-12-00141

Flury J, Bettadpur S, Tapley BD (2008) Precise accelerometry onboard the GRACE gravity field satellite mission. Adv Space Res 42:1414–1423. doi:10.1016/j.asr.2008.05.004

Förste C, Schmidt R, Stubenvoll R, Flechtner F, Meyer U, König R, Neumayer H, Biancale R, Lemoine J, Bruinsma S, Loyer S, Barthelmes F, Esselborn S (2008) The GeoForschungsZentrum Potsdam/Groupe de Recherche de Geodesie Spatiale satellite-only and combined gravity field models: EIGEN-GL04S1 and EIGENGL04C. J Geodesy 82:331–346

Gruber Th, Bamber JL, Bierkens MFP, Dobslaw H, Murböck M, Thomas M, van Beek LPH, van Dam T, Vermeersen LLA, Visser PNAM (2011) Simulation of the time-variable gravity field by means of coupled geophysical models. Earth Syst Sci Data 3(1):19–35. doi:10.5194/essd-3-19-2011

Hedin AE (1987) MSIS86 thermospheric model. J Geophys Res. doi:10.1029/JA092iA05p04649

Knocke P, Ries J, Tapley B (1988) Earth radiation pressure effects on satellites. In: Proceedings of the AIAA/AAS astrodynamics specialist conference 1988, Washington DC, USA, pp 577–586. doi:10.2514/6.1988-4292

Kusche J (2007) Approximate decorrelation and non-isotropic smoothing of time-variable GRACE-type gravity field models. J Geodesy 81:733–749. doi:10.1007/s00190-007-0143-3

Lemoine FG, Kenyon SC, Factor JK, Trimmer RG, Pavlis NK, Chinn DS, Cox CM, Klosko SM, Luthcke SB, Torrence MH, Wang YM, Williamson RG, Pavlis EC, Rapp RH, Olson TR (1998) The development of the joint NASA GSFC and the National Imagery and Mapping Agency (NIMA) Geopotential Model EGM96. NASA/TP-1998-206861, 1998

Loomis BD, Nerem RS, Luthcke SB (2012) Simulation study of a follow-on gravity mission to GRACE. J Geodesy 86:319–335. doi:10.1007/s00190-011-0521-8

Ray R (2008) GOT4.7 (private communication). Extension of Ray R (1999) A global ocean tide model from Topex/Poseidon altimetry GOT99.2. NASA technical memo 209478, Sept 1999

Reigber C, Schmidt R, Flechtner F, König R, Meyer U, Neumayer KH, Schwintzer P, Zhu SY (2005) An earth gravity field model complete to degree and order 150 from GRACE: EIGEN-GRACE02S. J Geodyn 39:1–10

Rodell M, Velicogna I, Famiglietti JS (2009) Satellite-based estimates of groundwater depletion in India. Nature 460:999–1002. doi:10.1038/nature08238

Sasgen I, Dobslaw H, Martinec Z, Thomas M (2010) Satellite gravimetry observation of Antarctic snow accumulation related to ENSO. Earth Planet Sci Lett 299:352–358. doi:10.1016/j.epsl.2010.09.015

Savcenko R, Bosch W (2008) EOT08a—empirical ocean tide model from multi-mission satellite altimetry, report no. 81. Deutsches Geodätisches Forschungsinstitut (DGFI), München

Scanlon BR, Longuevergne L, Long D (2012) Ground referencing GRACE satellite estimates of groundwater storage changes in the California Central Valley, USA. Water Resour Res 48:4520. doi:10.1029/2011WR011312

Shako R, Förste C, Abrikosov O, Bruinsma SL, Marty JC, Lemoine JM, Flechtner F, Neumayer KH, Dahle C (2014) EIGEN-6C: a high-resolution global gravity combination model including GOCE data. In: Flechtner F et al (eds) Observation of the system earth from space—CHAMP, GRACE, GOCE and future missions, advanced technologies in earth sciences. Springer, Berlin. doi:10.1007/978-3-642-32135-1_20

Sheard B, Heinzel G, Danzmann K, Shaddock D, Klipstein B, Folkner W (2012) Intersatellite laser ranging instrument for the GRACE follow-on mission. J Geodesy. doi:10.1007/s00190-012-0566-3

Standish E (1998) JPL planetary and lunar ephemerides "DE405/LE405". Interoffice memorandum IOM 312.F-98-048, JPL, Los Angeles, USA, 26 Aug 1998

Swenson S, Wahr J (2006) Post-processing removal of correlated errors in GRACE data. Geophys Res Lett 33:L08402. doi:10.1029/2005GL025285

Tapley B, Bettadpur S, Watkins M, Reigber C (2004) The gravity recovery and climate experiment: mission overview and early results. Geophys Res Lett 31:L09607. doi:10.1029/2004GL019920

Wahr J, Molenaar M, Bryan F (1998) Time variability of the Earth's gravity field: hydrological and oceanic effects and their possible detection using GRACE. J Geophys Res 103(B12):30205–30229. doi:10.1029/98JB02844

Wang L, Shum CK, Simons FJ, Tapley B, Dai C (2012) Coseismic and postseismic deformation of the 2011 Tohoku-Oki earthquake constrained by GRACE gravimetry. Geophys Res Lett 39:7301. doi:10.1029/2012GL051104

Wickert J, Michalak G, Schmidt T, Beyerle G, Cheng C, Healy S (2009) GPS radio occultation: results from CHAMP, GRACE and FORMOSAT-3/COSMIC. Terr Atmos Ocean Sci 20:35–50

Wouters B, Bonin JA, Chambers DP, Riva REM, Sasgen I, Wahr J (2014) GRACE, time-varying gravity, Earth system dynamics and climate change. Rep Prog Phys. doi:10.1088/0034-4885/77/11/116801

DOI 10.1007/978-3-319-32449-4_12
Reprinted from *Surveys in Geophysics* Journal, DOI 10.1007/s10712-016-9363-5

# Subsurface Hydrology of the Lake Chad Basin from Convection Modelling and Observations

**T. Lopez[1] · R. Antoine[2] · Y. Kerr[1] · J. Darrozes[3] · M. Rabinowicz[3] · G. Ramillien[4] · A. Cazenave[4,5] · P. Genthon[6]**

Received: 23 March 2015 / Accepted: 20 January 2016 / Published online: 2 February 2016


**Abstract** In the Lake Chad basin, the quaternary phreatic aquifer (named hereafter QPA) presents large piezometric anomalies referred to as domes and depressions whose depths are ~15 and ~60 m, respectively. A previous study (Leblanc et al. in Geophys Res Lett, 2003, doi:10.1029/2003GL018094) noticed that brightness temperatures from METEOSAT infrared images of the Lake Chad basin are correlated with the QPA piezometry. Indeed, at the same latitude, domes are ~4–5 K warmer than the depressions. Leblanc et al. (Geophys Res Lett, 2003, doi:10.1029/2003GL018094) suggested that such a thermal behaviour results from an evapotranspiration excess above the piezometric depressions, an interpretation implicitly assuming that the QPA is separated from the other aquifers by the clay-rich Pliocene formation. Based on satellite visible images, here we find evidence of giant polygons, an observation that suggests instead a local vertical connectivity between the different aquifers. We developed a numerical water convective model giving an

✉ T. Lopez
teodolina.lopez@cesbio.cnes.fr

[1] Centre d'Etudes Spatiales de la Biosphère, Unité mixte de Recherche Université Toulouse 3, Centre National d'Etudes Spatiales, Centre National de la Recherche Scientifique, Institut de Recherche pour le Développement, 31400 Toulouse, France

[2] Centre d'Etudes et d'Expertise sur les Risques, l'Environnement, la Mobilité et l'Aménagement, Laboratoire Régional de Rouen, Groupe Sciences de la Terre, CS 90245, 76121 Le Grand Quevilly, France

[3] Géosciences Environnement Toulouse, Unité mixte de Recherche Université Toulouse 3, Centre National d'Etudes Spatiales, Centre National de la Recherche Scientifique, Institut de Recherche pour le Développement, 31400 Toulouse, France

[4] Laboratoire d'Etudes en Géophysique et Océanographie Spatiales, Unité mixte de Recherche Université Toulouse 3, Centre National d'Etudes Spatiales, Centre National de la Recherche Scientifique, Institut de Recherche pour le Développement, 31400 Toulouse, France

[5] International Space Science Institute (ISSI), Bern, Switzerland

[6] Laboratoire Hydrosciences Montpellier, Unité mixte de Recherche Université Montpellier, Institut de Recherche pour le Développement, Centre National de la Recherche Scientifique, 34000 Montpellier, France

alternative explanation for the development of QPA depressions and domes. Beneath the depressions, a cold descending water convective current sucks down the overlying QPA, while, beneath the dome, a warm ascending current produces overpressure. Such a basin-wide circulation is consistent with the water geochemistry. We further propose that the thermal diurnal and evaporation/condensation cycles specific to the water ascending current explain why domes are warmer. We finally discuss the possible influence of the inferred convective circulation on the transient variations of the QPA reported from observations of piezometric levels and GRACE-based water mass change over the region.

**Keywords** Lake Chad · Piezometric anomalies · Vertical permeability · Infrared data · Convection · GRACE

## 1 Introduction

Water resource management in the Sahel regions of Africa is of prime importance. In countries such as Mali, Niger, Chad and Sudan to name just a few, water resources essentially come from groundwater reservoirs that are either weakly or even non-renewable (OSS-UNESCO 2001). In order to improve their sustainability over the medium and long term, it is important to understand their dynamics. A direct indicator of phreatic water dynamics is the variation of their piezometric level (i.e. surface level) forming piezometric anomalies. Piezometric anomalies have been reported in the phreatic aquifers of Trarza in Mauritania; Ferlo in Senegal; Gondo, Nara and Azaouad in Mali and Yaere in North Cameroon (e.g., Archambault 1960; Aranyossy and Ndiaye 1993). In the Lake Chad basin, the quaternary phreatic aquifer (named hereafter QPA) presents large piezometric anomalies extending over a few tens of km, forming domes and depressions at the piezometric surface. Their mean depth is $\sim$10 and $\sim$60 m, respectively (Schneider and Wolff 1992).

Various assumptions have been proposed to explain the origin of the piezometric depressions, e.g., groundwater overexploitation, water drainage into a deeper aquifer, geological subsidence, changes in sea level and evapotranspiration loss (Dieng et al. 1990; Aranyossy and Ndiaye 1993). The latter factor was favoured because it explains observed piezometric depressions, and the associated water deficit generated by evapotranspiration that is not compensated by lateral groundwater flow. Therefore, it became the most accepted explanation. METEOSAT images of the Lake Chad basin reveal that brightness temperatures and piezometric anomalies are correlated (Leblanc et al. 2003). These authors observed that domes are $\sim$4–5 K warmer than the depressions during wet years, suggesting that, above piezometric depressions, evapotranspiration is dominant during the temperature diurnal cycle and leads to surface cooling.

In sedimentary basins, it has been shown that, at regional scales, convective groundwater flows are usually governed by surface topography and geothermal gradients of the sediment infill (e.g., Garven 1995). In numerous cases, weakly compacted clay formations deposited in the upper part of basins may prevent interactions between superficial and deep groundwater. However, vertical permeability can be generated in weakly compacted clay formations by the development of large-scale polygonal fault systems (e.g., Cartwright and Dewhurst 1998; Neal et al. 1968).

Building on these different observations, here we suggest that evapotranspiration is coupled to the water convective circulation, explaining both the piezometric anomalies' formation and their correlation with observed surface temperature. We first describe the geological and hydrogeological setting of the Lake Chad basin. We next discuss the permeability field of the basin, taking into account potential compaction of the clay formations at depth (Sect. 3). In Sect. 4, we develop a 2D convective model simulating large-scale flow within the whole sedimentary basin. Finally, we investigate whether the modelled convective flow can explain observed bottom hole temperatures (BHT), hydrochemical data, and GRACE-based space gravity data of water storage changes.

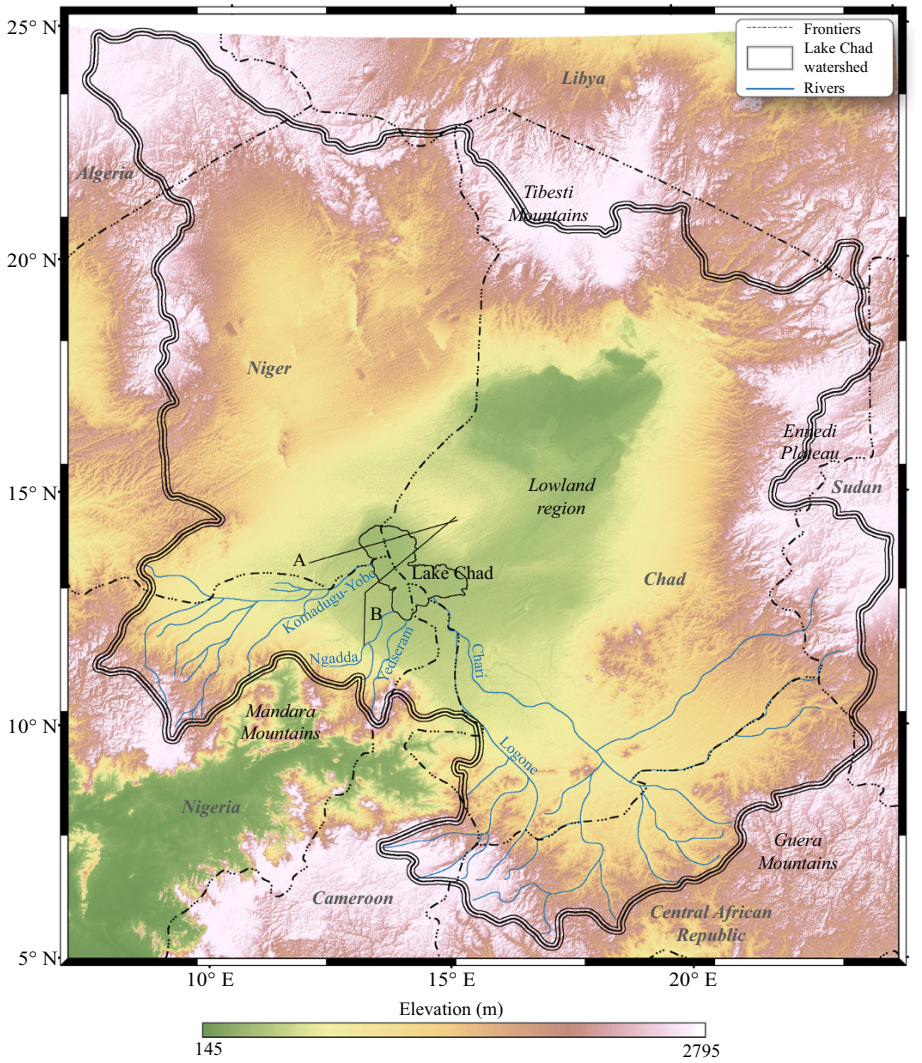


**Fig. 1** Shuttle radar topography mission (SRTM) topographic map of the Lake Chad watershed, showing its extension, its tributary rivers, the main mountains and the Lowland region. *Black lines A* and *B* represent the geological cross sections drawn in Fig. 3

## 2 Description of the Lake Chad Basin

### 2.1 Hydrology of Lake Chad

The Lake Chad watershed extends from 5°N–25.6°N to 7°E–27°E, covering 2,500,000 km$^2$ over seven countries (Algeria, Cameroon, Central African Republic, Chad, Niger, Nigeria and Sudan; Fig. 1). The central part of the basin is flat, while its surroundings consist of mountain ranges, i.e. Tibesti Mountains, Ennedi Plateau, Guera Mountains and Mandara Mountains (Fig. 1). Without any direct outlet to the sea, it is the largest endorheic watershed of the world. During the Holocene, Lake Chad extended over an area of $\sim$350,000 km$^2$ (Schuster et al. 2005; Leblanc et al. 2006) but, since the early 1980s, its size decreased to only $\sim$2500 km$^2$ (Cretaux and Birkett 2006; Bader et al. 2011). It is now named "Small Lake Chad" (Bader et al. 2011). The current hydrological active part of the lake is concentrated in its southern part. It is fed by the Chari and Logone perennial rivers as well as the seasonal Yedseram and Ngadda rivers. In the northern part, surface waters are essentially seasonal (e.g., the Komadugu-Yobe) (Fig. 1). The average rainfall above Lake Chad ranges from 200 to 400 mm year$^{-1}$, and potential evapotranspiration is on the order of 2 m year$^{-1}$ (e.g., Bader et al. 2011; Descloitres et al. 2013). Discharges from the Chari and Logone rivers represent $\sim$91 % of the fresh water supplies, while seasonal rivers bring only relatively small inputs (Roche 1980). Rainfall represents only $\sim$10 % of the total water supply. Water loss over the lake mainly results from evapotranspiration (between 80 and 90 %) and infiltration through the lake bottom ($\sim$10 %) (Roche 1980; Olivry et al. 1996; Bader et al. 2011).

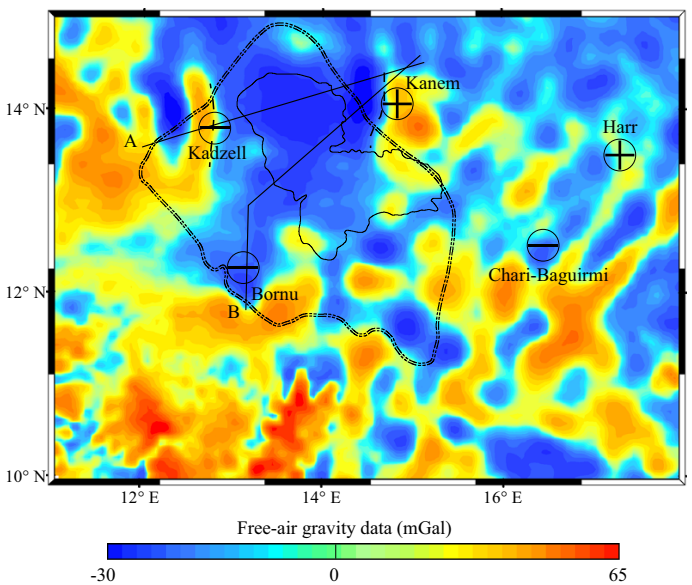


**Fig. 2** Free-air gravity map obtained from the world gravity map (WGM) of 2012. *Dashed lines* locate the presence of faults delimiting the basin. *Double dashed lines* represent the artesian limit of the Pliocene aquifer. Piezometric domes and depressions are located by the *plus* and *minus symbols*. *Black lines A* and *B* represent the geological cross sections drawn in Fig. 3

## 2.2 Geology of the Chad Basin

The Chad basin is considered as the largest intra-cratonic basin belonging to the east and central African rift system (Genik 1993; Olugbemiro and Ligouis 1999). These rifts were active from the Cretaceous to the early Palaeogene and then reactivated during the early to mid-Tertiary (Genik 1993; Griffin 2006). The free-air gravity map (Fig. 2), based on the Earth Gravitational Model EGM2012 (Balmino et al. 2011), displays gravity anomalies ranging between $\sim -30$ to $\sim 65$ mGal. Negative gravity anomalies correspond to thick sediment infill (i.e. sediment density being lower than the basement density), while positive anomalies are linked to the shallow depth basement. A large area of nearly constant gravity (e.g., the Bornu region) can be interpreted as a zone of homogeneous sediment thickness. Gravity dipoles seen in Fig. 2 (dashed lines) correspond to normal faults delimiting the Kadzell and Kanem regions (Avbovbo et al. 1986). Between the two regions, the sediment thickness increases towards the Kanem region while gravity decreases from $\sim -2$ to $\sim -30$ mGal. The SW–NE geological cross section through the Kadzell to the Kanem regions (Fig. 3a) indicates that the sediment infill is fan-shaped and oriented eastward.

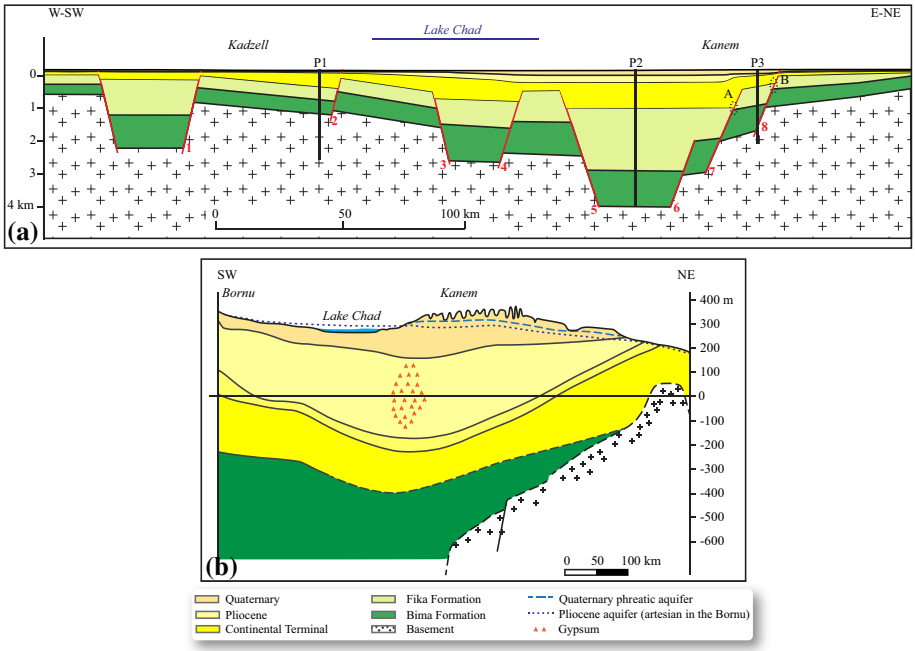


**Fig. 3** **a** Geological cross section between Kadzell and Kanem (modified from Pouclet and Durand 1983). The deposits consist of inter-bedded clay formations (Fika formation and Pliocene formation) with sandy deposits as the Quaternary formation, the Continental Terminal formation and the Bima formation. The Early Pliocene formation is integrated in the Pliocene formation. *Red lines* highlight the faults of the basin. The Lake Chad basin is controlled by an extensional tectonic of horsts (2–3 and 4–5) and grabens (1, 3–4, 5–6). *Dashed ellipses* highlight the stratigraphic throws of faults 7 and 8 that impact the Fika formation. *Vertical black lines* highlight the location of temperature profiles P1, P2, P3 displayed in Fig. 10. **b** Geological cross section of the upper part of the sedimentary infill, between Bornu and Kanem (modified from Schneider and Wolff 1992). The Early Pliocene formation has been distinguished from the Pliocene one

As indicated by the gravity map (Fig. 2), sediment thickness ranges from ∼850 m under Kadzell to ∼4000 m under Kanem. The stratigraphic sequence starts with the deposition of the Bima formation (Albian to Cenomanian) that consists of inter-bedded continental shales and sandstones. Its thickness is ∼400 and ∼1000 m below Kadzell and Kanem, respectively (e.g., Pouclet and Durand 1983; Avbovbo et al. 1986; Olugbemiro and Ligouis 1999). Then a shallow marine deposit (inter-bedded with some limestone), called Fika formation, settles from the Turonian to Santonian. Its thickness can reach up to 2 km in the deepest part of the basin (Pouclet and Durand 1983). It is followed by a sedimentation gap associated with an erosion episode that ends at the end of the Eocene–Oligocene (Pouclet and Durand 1983; Griffin 2006). The sedimentation starts again possibly during the Oligocene until the late Miocene, corresponding to the Bodele series that consist of mixed mudstone and sandstone over a thickness of ∼100 m (referred to hereafter as the Continental Terminal formation) (Schneider and Wolff 1992). During the Pliocene, deposits dated from the early Pliocene (referred hereafter as the Early Pliocene formation) consist of fluviatile sands of 10–40 m thickness (Maduabuchi et al. 2006). These are overlaid by lacustrine clays with a thickness that can reach ∼300 m (referred to hereafter as the Pliocene formation) (Schneider and Wolff 1992; Griffin 2006; Schroeter and Gear 1973). The stratigraphic sequence ends with the Quaternary formation, essentially composed of aeolian sand and fluvio-deltaic deposits (Griffin 2006). Its thickness varies from ∼15 m under Kadzell to ∼100 m under Kanem.

The eastern border of the rift is characterised by a succession of normal faults (7 and 8 on Fig. 3a) shifting the Bima formation base from 2 to 1 km in depth and the Fika formation base from 1 km to ∼500 m. *Ellipses* A and B in Fig. 3a highlight the throws generated by faults 7 and 8 at the base of the Fika formation. For example, at circle B, the throw associated with the fault 8 is ∼150 m. A detailed geological cross section of the upper part of the sediment infill from Bornu to Kanem (Schneider and Wolff 1992) is

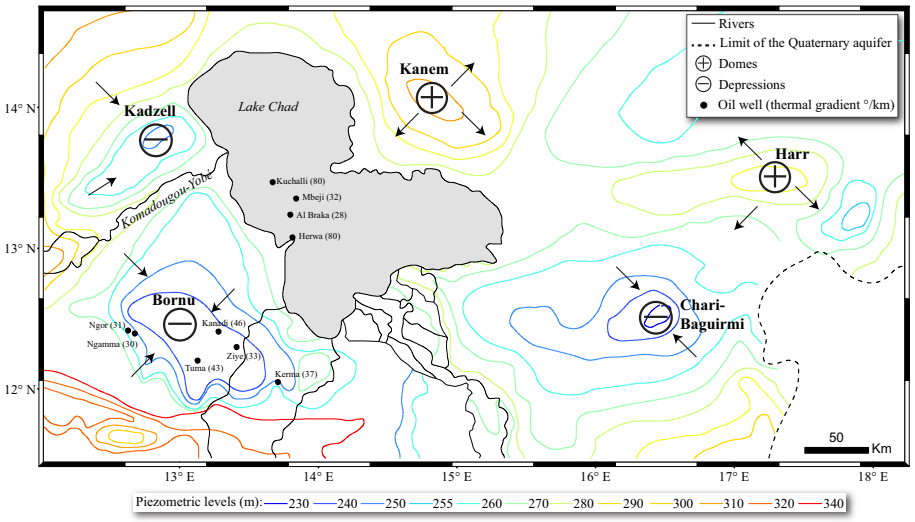


**Fig. 4** Piezometric map of the quaternary phreatic aquifer (QPA) around Lake Chad. Piezometric domes and depressions are located by the *plus* and *minus symbols*. *Arrows* highlight the flow directions in the QPA (modified from Schneider 1969). *Black dots* represent oil well locations from Nwankwo and Ekine (2010) with their thermal gradients for the first ∼300 m depth

displayed in Fig. 3b. Below Bornu, the thickness of the Pliocene and Quaternary formations is ~230 and ~70 m, respectively. Below Kanem, because of basin subsidence (Schneider and Wolff 1992), the maximum thickness of the Pliocene and Quaternary formations is 300 and 140 m, respectively.

### 2.3 Hydrogeology of the Basin

The basin comprises three main aquifers. Most of the human water use comes from the QPA. This phreatic aquifer has a continuous water table in the Quaternary formation, providing an extensive reservoir covering an area of about 500,000 $km^2$ (Eberschweiler 1993; Schroeter and Gear 1973). Hydraulic conductivity measurements indicate that this layer has a hydraulic conductivity from 1 to 100 m $day^{-1}$ (Schneider and Wolff 1992; Guideal et al. 2011; Descloitres et al. 2013). These values correspond to permeabilities ranging from $10^{-12}$ to $10^{-10}$ $m^2$. Piezometric anomalies in this aquifer have been reported by Schneider (1969) as well as by Schroeter and Gear (1973). Piezometric domes have been described in the dune field of Kanem and Harr (Fig. 4), east of Lake Chad. The Kanem dome covers approximately 17,000 $km^2$, and the highest piezometric level stands at an altitude of 310 m a.s.l. (i.e. at a depth of ~10 m below ground). In Harr, the dome area covers about 5500 $km^2$ and has an altitude of 290 m. In the western part of the QPA, three deep piezometric depressions affect the water table. The Kadzell depression area is ~4400 $km^2$, and its deepest piezometric level stands at 250 m (corresponding to a depth of ~50 m below ground). The deepest depression develops in Bornu and covers about 16,500 $km^2$. The water table falls at 240 m (i.e. at a depth of ~60 m below ground). The largest piezometric depression is the Chari-Barguimi, located at the south of the lake. It covers a surface area of 17,500 $km^2$, and its water table stands at an altitude of 230 m (i.e. at ~40 m below ground). The QPA flows from the domes towards Lake Chad and the depressions (Fig. 4). Moreover, the flow is oriented from the lake towards the depressions (e.g., Greigert 1979; Isiorho et al. 1996; Leduc 1991).

Piezometric contours superimposed on the gravity map reveal that piezometric domes and depressions are located on or nearby normal faults limiting the basin (Fig. 2). The Pliocene aquifer is confined in the Early Pliocene formation. It is of artesian type over the whole basin, except in the central and eastern part of Kanem (Figs. 2, 3b) where the water level stands a few tens of metres below the surface (Schneider and Wolff 1992) and flows from the south towards the northeast. The Continental Terminal aquifer is confined in the Continental Terminal formation. Its thickness ranges from 100 to 200 m (Eberschweiler 1993). Below Kanem, the Pliocene aquifer and the Continental Terminal merge to form a single aquifer with a thickness exceeding 275 m (Schneider and Wolff 1992; Eberschweiler 1993). During oil drilling, a deep aquifer called Continental Hammadian (~4 km deep) was discovered in the Bima formation (Schroeter and Gear 1973). However, very little is known so far about this aquifer.

### 2.4 Potential Permeability Field of the Basin

Fluid migration in clay-rich formations is extremely slow because of their small permeability ($\leq 10^{-15}$ $m^2$, e.g., Schwinka and Moertel 1999). In submarine sedimentary deposits, fractures intersecting in plan view to form polygonal patterns have been described in fine-grained sediments (e.g., Cartwright and Dewhurst 1998) and are referred as giant polygonal faults. Besides, in some oceanic basins, a regional slope of $\leq 1°$ may have a major impact on the development of giant polygons (Gay et al. 2004).

In the Lake Chad basin, the Bornu and Kadzell piezometric depressions and the Kanem dome are systematically located near to major slope breaks (Fig. 5). In the Bornu region, we discovered with satellite visible images many lineaments (Fig. 6a, b) that may be reminiscent of the giant polygons described by Gay et al. (2004). The surface topography near the slope breaks is close to 1°, a value sufficient to generate fractures in clay-rich sediment of the Pliocene formation (Gay et al. 2004). An important concentration of trees along these lineaments is observed, suggesting local access of the vegetation to the deep QPA water table. In the Kadzell region, no such giant polygonal structures are observed. However, the presence of meanders or palaeo-meanders (Fig. 6c) along the Komadugu-Yobe River (or other palaeo-rivers) is indicative of coarse deposits, locally providing a good vertical permeability down to the Continental Terminal formation (Descloitres et al. 2013). Finally, we find no surface evidence of giant polygons in Kanem, presumably a result of the thick sandy Quaternary formation. The relatively weak artesianism of the Pliocene aquifer below Kanem may indicate that the $\sim$300 m Pliocene formation is fractured. Consequently, we suggest that water exchanges indeed exist between the Quaternary and Continental Terminal aquifers on both sides of the basin.

Except in the central part of the basin, the compaction is weak as the depth of the basin is $\sim$1.5 km (Sclater and Christie 1980). Consequently, clay-rich Pliocene and Fika formations (blocks delimited by faults 1–2–3–7–8) may be overpressured (Fig. 3a) (the artesian nature of the Pliocene aquifer can be evidence of the overpressure of the Pliocene formation). At the centre of the graben, delimited by faults 5 and 6, the Fika formation lies between 1 and 3 km depth. At such depth, clays with initial fluid concentration of 60 % per volume lose up to 40 % of their volume by compaction (Sclater and Christie 1980). Such water loss induces a $\sim$800 m vertical shortening. With an initial density of 1600 kg m$^{-3}$ for the 60 % water-rich clay, this water loss may increase the clay density up to

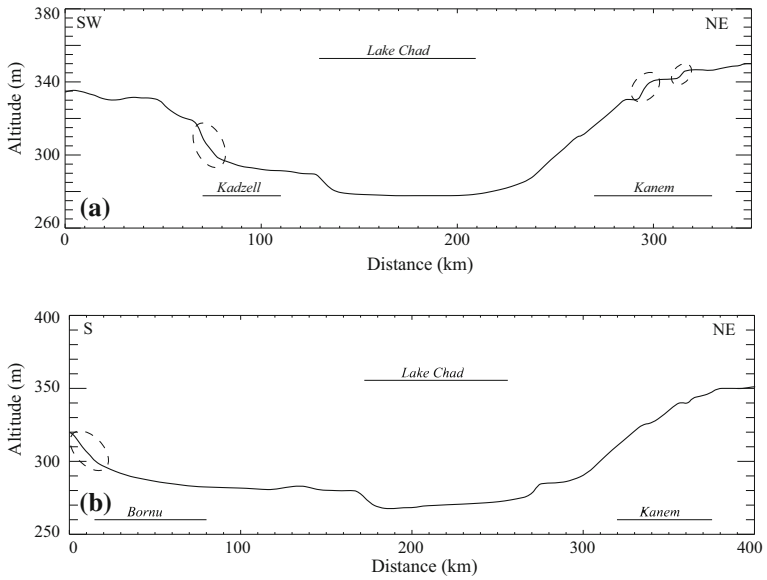


**Fig. 5** Advanced spaceborne thermal emission and reflection radiometer (ASTER) topographic profiles **a** from Kadzell to Kanem and **b** from Bornu to Kanem. *Dashed ellipses* surround slope breaks located above or close to the piezometric anomalies; their extensions are represented by the *black lines*

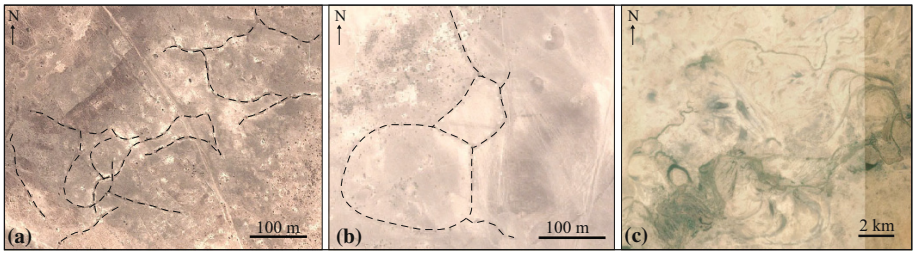


**Fig. 6** Google Earth extracts from **a** fractures (image centred at 13.78°E–11.86°N), **b** polygonal fractures (image centred at 13.70°E–12.04°N) highlighted by *black dashed lines* above the Bornu depression) and **c** palaeo-meanders of the Komadugu-Yobe river (image centred at 12.90°E–13.50°N)

2200 kg $m^{-3}$. Considering the thickness of the Fika formation and its 600 kg $m^{-3}$ extra-weight, a 12 MPa differential load may be induced by compaction. This stress level exceeds the yield strength of clays containing 24 % of water (Kopf 2002). Accordingly, compaction may produce clay fracturing in the vicinity of faults 5 and 6, causing an increase in the clay effective permeability (Luo and Vasseur 2002), and thus fluid percolation through the Fika formation and hydraulic connection between all the aquifers. Finally, in the Bima formation blocks, from faults 6–8, good hydrodynamic connectivity possibly exists. At fault 8, the throw of the Fika formation (circle B, Fig. 3a) partly inhibits vertical water circulation.

From the above discussion, we infer the following values of the horizontal permeability $K$ (Fig. 16): $10^{-18}$ $m^2$ for the substratum, with $2 \times 10^{-13}$ $m^2$ for the Bima formation, $10^{-15}$ $m^2$ for the Fika one, $10^{-13}$ $m^2$ for the Continental Terminal, $10^{-15}$ $m^2$ for the Pliocene and $10^{-12}$ $m^2$ for the Quaternary (this latter value is assumed because of computational limitations, although higher values are equally possible). Faults 5 and 6 are considered to be $\sim$10 km wide, i.e. a reasonable value for faults in a pluri-hectokilometric sedimentary basin. Their horizontal and vertical permeabilities ($K_x$ and $K_z$) are assumed to be from $10^{-15}$ to $10^{-14}$ $m^2$, respectively (Table 1). Finally, because of the vertical connectivity generated by polygonal fractures or normal faults in Kadzell and Kanem, a vertical permeability of $10^{-14}$ $m^2$ is assigned to the Pliocene formation.

## 3 2D Convective Model

In this section, we present results from a 2D convective model used to simulate the circulation of water in the Lake Chad basin. For this purpose, we build upon the numerical convection model developed by Genthon et al. (1990) for a slightly sloped (<1°) terrain. The latter study showed that large convective cells develop, with descending/ascending currents along highly permeable borders spaced a few hundred kilometres apart. Three conditions are required for this circulation to occur: (a) a minimum slope $\leq$1°, (b) an appreciable horizontal to vertical permeability ratio, and (c) the equivalent vertical Rayleigh number ($Ra$) lower than $4\pi^2$ (i.e. the threshold for the development of free porous flow convection; Eq. 7 in Appendix 1). Such conditions are fulfilled for the Lake Chad basin where the slope of the sedimentary layer is $\sim$1°, the interspersion of high permeability formations (i.e. Bima, Continental Terminal and Quaternary formations) with low permeability ones (Fika and Pliocene formations) produces a strong effective horizontal

**Table 1** Physical parameters used in the 2D convective model

| | |
|---|---|
| *Physical parameters of water* | |
| Density | 1000 kg $m^{-3}$ |
| Thermal conductivity | 0.6 W $m^{-1}$ $K^{-1}$ |
| Heat capacity | 4180 J $kg^{-1}$ $K^{-1}$ |
| *Geophysical parameters of the formations* | |
| Quaternary | |
| Density | 2650 kg $m^{-3}$ |
| Heat capacity | 900 J $kg^{-1}$ $K^{-1}$ |
| Permeability | $10^{-12}$ $m^2$ |
| Porosity | 0.4 |
| Pliocene | |
| Density | 2600 kg $m^{-3}$ |
| Heat capacity | 900 J $kg^{-1}$ $K^{-1}$ |
| Permeability | $10^{-15}$ $m^2$ |
| Porosity | 0.07 |
| Continental terminal | |
| Density | 2650 kg $m^{-3}$ |
| Heat capacity | 900 J $kg^{-1}$ $K^{-1}$ |
| Permeability | $10^{-13}$ $m^2$ |
| Porosity | 0.3 |
| Fika | |
| Density | 2600 kg $m^{-3}$ |
| Heat capacity | 900 J $kg^{-1}$ $K^{-1}$ |
| Permeability | $10^{-15}$ $m^2$ |
| Porosity | 0.07 |
| Fika faults | |
| Permeability | $K_x = 10^{-15}$ $m^2$, $K_z = 10^{-14}$ $m^2$ |
| Porosity | 0.07 |
| Bima | |
| Density | 2650 kg $m^{-3}$ |
| Heat capacity | 900 J $kg^{-1}$ $K^{-1}$ |
| Permeability | $2 \times 10^{-13}$ $m^2$ |
| Porosity | 0.4 |
| Substratum | |
| Density | 2600 kg $m^{-3}$ |
| Heat capacity | 950 J $kg^{-1}$ $K^{-1}$ |
| Permeability | $10^{-18}$ $m^2$ |
| Porosity | 0.02 |

versus vertical permeability anisotropy, and the effective vertical *Ra* number is at most equal to 31 (Eq. 7).

We performed numerical simulations in order to assess the possible hydrological regimes occurring within the Lake Chad basin. The model is built in such a way that it reproduces the detailed geological cross section of Fig. 3a. The governing equations (mass conservation, Darcy's law and heat transport), effective parameters (effective thermal conductivity and volumetric heat capacity) and boundary conditions used to describe the

circulation and the temperature distribution within the basin are detailed in Appendices 1 to 4.

We first solve the transient conductive heat equation until reaching the steady state, in order to evaluate the temperature field (Fig. 7a) when the sediment horizons are assumed to be impermeable. The time needed to reach steady state is $\sim$2 Ma, which corresponds to the conductive time of a $\sim$8-km-thick horizon. We observe that the 70 °C isotherm deepens towards the eastern border of the basin. This trend results from the increase in the thickness of the Fika formation towards the East, which acts as a thermal insulator due to its low thermal conductivity. The temperature drop is particularly strong in the 2-km-thick Fika formation between faults 5 and 6. Consequently, heat is not actively transported by conduction and the temperature rises to 173 °C within the underlying Bima formation, while at similar depths outside this domain the temperature is $\sim$150 °C. The surface conductive heat flow profile displayed by the model is represented in Fig. 8. The heat flow gradually decreases from the west to the centre of the graben located between faults 5 and 6 and then rises again when the thickness of the basin decreases eastward. The Kadzell region exhibits an important heat flow of 100 mW m$^{-2}$. This value is due to the proximity of the high conductivity substratum (5.3 W m$^{-1}$ K$^{-1}$) that lies at a depth of $\sim$1 km. Between faults 5 and 6, heat flow reaches a minimum of $\sim$65 mW m$^{-2}$ and a value of 110 mW m$^{-2}$ on the eastern part of the basin. Finally, the conductive mean heat flow at the surface is $\sim$90 mW m$^{-2}$.

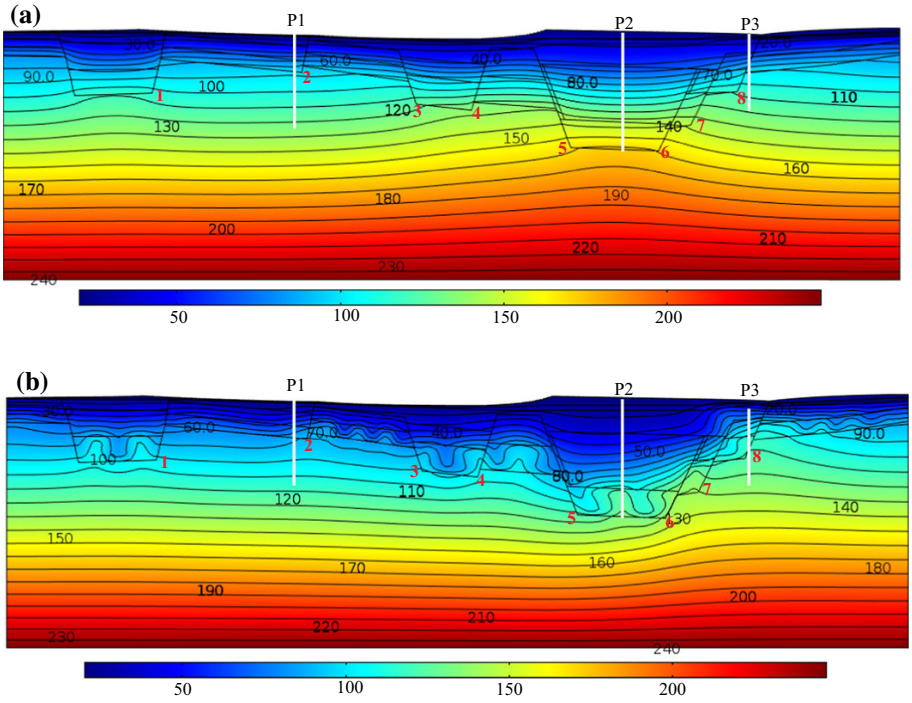


**Fig. 7** Temperature maps in °C of **a** the conductive model and **b** the convective model. The isotherms are displayed each 10 °C. *Vertical white lines* highlight the location of temperature profiles P1, P2, P3 displayed in Fig. 10

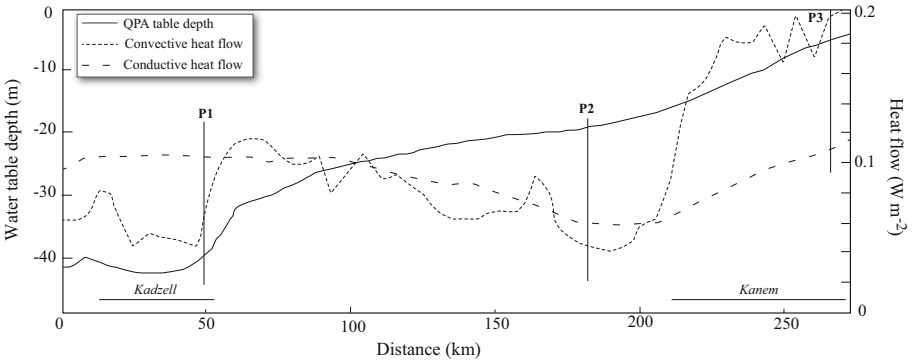


**Fig. 8** *Dotted lines* represent the convective heat flow calculated at the surface, while the *dashed lines* represent the conductive heat flow. *Continuous lines* represent the calculated piezometric level between Kadzell and Kanem derived from the pressure variations associated with the convective circulation. Profiles P1, P2, P3 are located by *vertical black lines*

Figure 7b displays the ~500,000 years snapshot of the temperature field obtained when the sedimentary horizons are permeable. Due to the large-scale slopes of the isotherms in the initial conductive temperature field, convection is triggered whatever the Rayleigh number; a basin-wide convective cell is generated. We find that a large-scale current descends along the western border of the basin, then flows towards the east in the Bima formation and finally rises up to the surface along faults 6 to 8. A cold current is located just beneath Kadzell and slightly deforms the isotherms crossing the Fika and the Bima formations. The calculated surface convective heat flow in the Kadzell region ranges from 30 to 60 mW $m^{-2}$ (Fig. 8). Between faults 2 and 8, small convective plumes develop in the thermal boundary layer within the Bima formation and are dragged along the basin-wide west–east current: this results from the fact that the vertical Rayleigh number of that layer exceeds $4\pi^2$ (Eq. 7). The convection triggered in the shallow parts of the basin (e.g., between faults 2 and 3) can induce a surface convective heat flow as high as 120 mW $m^{-2}$ (Fig. 8).

It is notable that, due to the permeability contrast between the Bima and Fika formations, small-scale convective cells remain confined within the Bima and do not enter into the quasi-impervious Fika formation. Along the eastern flank of the graben, between faults 6 to 8, a powerful 30-km-wide warm ascending current rises from the bottom of the Bima formation up to the Quaternary formation, i.e. ~100 m beneath Kanem. In the core of this current, the temperature drops from 120 to 45 °C. Such current provides a high heat flow at the surface. It ranges between 120 and 200 mW $m^{-2}$ (Fig. 8), a heat flow range also observed in other continental rift zones (e.g., Pribnow and Schellschmidt 2000). This high heat flow has two causes: (a) high conductivity of the sand at the surface (~2.1 W $m^{-1}$ $K^{-1}$) compared to the low conductivity of the clay-rich western part of the basin (~1.3 W $m^{-1}$ $K^{-1}$) and (b) isotherms rise on the eastern part of the basin. The spatial fluctuation of the heat flow visible in Fig. 8 over the Kanem causes fluctuations of the temperature field associated with the ascending current. Cold descending currents follow faults 5 and 6. These cold currents fall through the Continental Terminal, Fika and Bima formations and locally cause strong temperature drops, and the heat flow is decreased down to 40 mW $m^{-2}$. Mean surface convective heat flow amounts to 110 mW $m^{-2}$, a value corresponding to a Nusselt number of 1.2 for basin-wide convective cell. This suggests that although the local conductive heat transfer is significantly perturbed by the

convective circulation (for instance underneath Kanem), the mean heat transfer through the whole basin slightly increases due to convection. Such a phenomenon is well known in sedimentary basin modelling (Quintard and Bernard 1986; see also Appendix 4).

Figure 9a–d displays the vertical and horizontal components of the velocity. Water enters the basin in the Kadzell region with a mean Darcy velocity of 4 mm year$^{-1}$ (Fig. 9a). The fluid begins to circulate in the highly permeable ($10^{-12}$ m$^2$) Quaternary formation, then falls down into the Pliocene, Continental Terminal and Fika formations halfway between faults 1 and 2, before penetrating into the Bima formation. At the bottom of the Bima formation, the fluid circulates eastward at a mean velocity of 10 cm year$^{-1}$

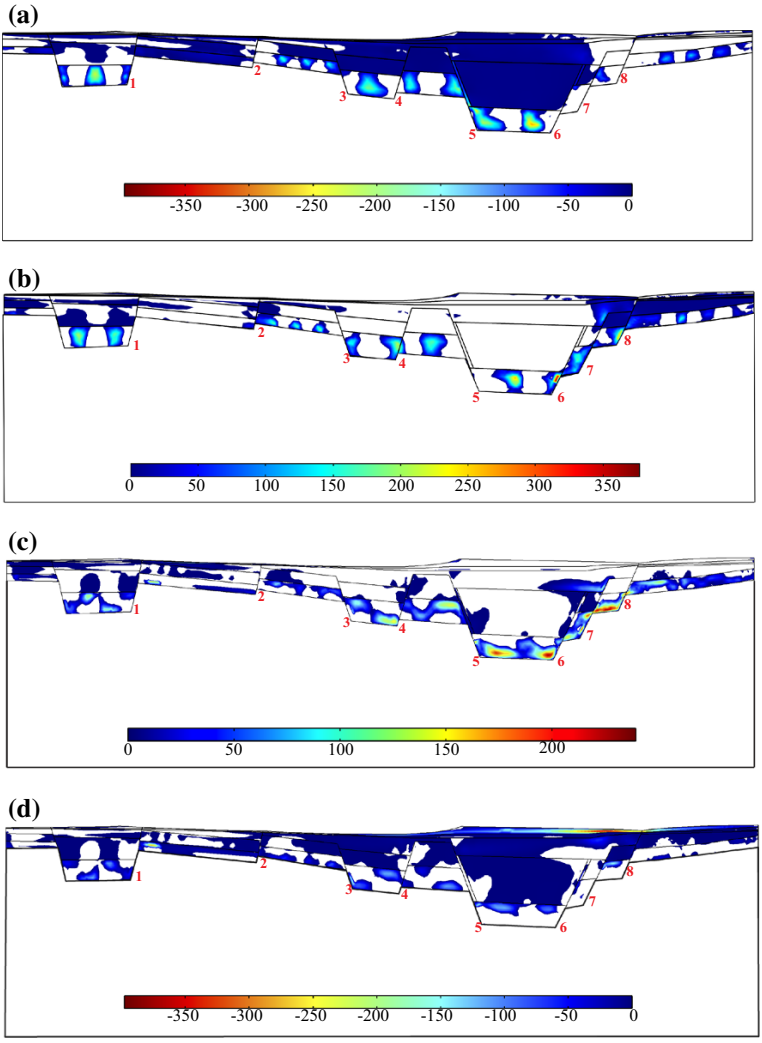


**Fig. 9** Vertical and horizontal Darcy velocities of the convective model (in mm year$^{-1}$). **a**, **b** Maps of the positive and negative *vertical* velocity fields, respectively, and **c**, **d** maps of the positive and negative *horizontal* velocity fields, respectively

(Fig. 9c) and follows the lower boundary layer of the basin-wide convective cell. Meanwhile, it is warmed by the basement and, below Kanem, rises up to the surface (Fig. 9d). Between faults 6 and 8 in the Bima formation, from a depth of 4 km up to 700 m, the mean velocity of the ascending water reaches 10 cm year$^{-1}$. The obstruction due to the presence of the throw at fault 8 in the Fika formation (circle B) decreases the mean velocity to $\sim$4 cm year$^{-1}$ from 700 m depth up to the surface (Fig. 9c; Appendix 4). Westward of Kanem, between the surface and 1.1 km depth, an important backflow is generated (Fig. 9d). The horizontal velocity within the Quaternary formation reaches a maximum of 39 cm year$^{-1}$ west of fault 8 and then progressively decreases to reach $\sim$7 cm year$^{-1}$ near fault 2. The backflow develops with a mean horizontal velocity of 3 cm year$^{-1}$ along the $\sim$600-m-thick Continental Terminal aquifer between faults 5 and 6, and to a lesser extent within the Fika formation (0.3 mm year$^{-1}$ velocity). A vertical descending current develops with velocities of 6.5 and 3 cm year$^{-1}$, within the Continental Terminal formation and faults 5 and 6, respectively, before entering inside the Bima formation (Fig. 9a). This backflow produces complex mixing of water between Kanem and Kadzell. Moreover, it cools the Fika formation and generates an asymmetric temperature field across the graben. Considering the small velocity of the basin-wide convective cell inside the Bima formation (10 cm year$^{-1}$), the overturn time of the convective flow is a few tens of Ma. This indicates that the increase in the mean geothermal heat flow due to the basin-wide convection generates transient cooling through the 4-km-thick crust and the sediment infill. Consequently, the surface heat flow progressively decreases during a few tens of Ma, then reaching the heat flow recorded at the steady-state conductive regime. It is worth noticing that the convective circulation in the basin is unsteady whatever the evolution time of the system. This results from two factors: high local *Ra* numbers in the Bima formation and along the faults 6–8 and high temperature at the bottom of the basin that drastically enhances the viscosity and coefficient of thermal expansion (see Appendix 2) (Fontaine et al. 2002).

Figure 10 shows three vertical temperature profiles derived from our model (Fig. 7b), crossing Kadzell (P1), the centre of the graben between faults 5 and 6 (P2) and Kanem (P3). For each profile, the temperatures for the conductive and convective models are shown. The temperature profiles display a linear behaviour for the conductive model. On the contrary, the convective circulation impacts the temperature by the presence of concavities. Indeed, when the profile is concave, the current is descending while, when it is

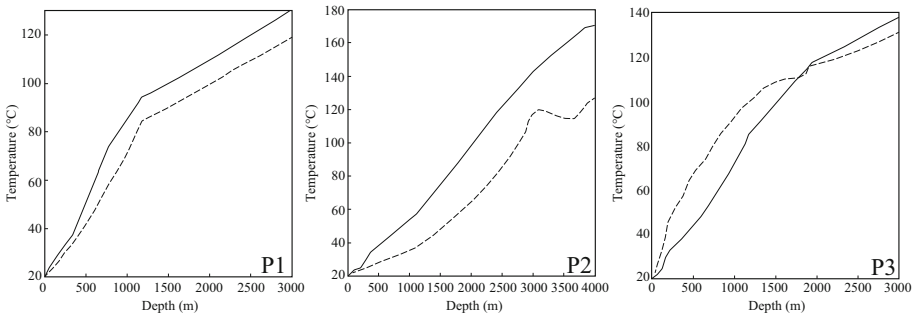


**Fig. 10** Comparison of the temperature profiles P1, P2 and P3 obtained from the convective and the conductive models. The *solid lines* represent the conductive temperatures, while the *dashed lines* represent the convective ones

convex, the current is ascending. In P1, the convective profile is located underneath the conductive one, suggesting that the layers constituting the Kadzell become colder during the convective process. The temperature difference between the two profiles reaches 15 °C at the bottom of the Bima formation (1000 m deep). The concavity of the profile down to 1 km depth is due to the cold water descending current. Nevertheless, the weak concavity of the profile is explained by the low velocity ($\sim -4$ mm year$^{-1}$) of the fluid, unable to efficiently cool the sediments. In P2, the convective profile is located beneath the conductive one. The strong concavity of this profile is explained by the presence of the intense cold descending current within fault 5. The profile is concave down to 3 km, where the temperature reaches 100 °C. Then, the profile crosses the axis of a small ascending current within the Bima formation and its temperature remains constant between 3 and 3.6 km depth. It crosses the thermal boundary layer at the bottom of the Bima formation between 3.6 and 4 km. Finally, the convective profile at P3 is typical of a warm ascending current: the convective profile is above the conductive one, and the temperature profile is convex down to 1.5–2 km. At this depth, the temperature reaches $\sim$95 °C. At larger depths, the profile crosses the substratum and reaches $\sim$110 °C at 3 km.

Garven and Freeze (1984a, b) showed that pluri-kilometric long convective circulations develop in sedimentary basins at velocity of 0.1–0.2 m year$^{-1}$. The general pattern of the circulation produced by our model (descending/ascending current from one border to the other border) is consistent with results of Garven and Freeze (1984a, b) and Gvirtzman et al. (1997). However, the conditions required to generate such cells are generally not explained in works dealing with basin-wide convection cells. It seems that two conditions are required: (a) long wavelength horizontal temperature variations in the conductive state and (b) a vertical *Ra* number less than $4\pi^2$ (otherwise the large-scale convection cells split into smaller cells). The first condition is achieved from the slope and/or thickness variations of the different formations, which have their own thermal conductivity. The second condition is fulfilled in the thickest part of the basin. Assuming an effective vertical permeability across the whole basin of $10^{-14}$ m$^2$ for the thick domain separating faults 5 and 6 (values assigned to the faults themselves), the *Ra* number is equal to 31 (Eq. 7). Alternatively, a model run with a $K_v$ of $10^{-13}$ m$^2$ in faults 5 and 6 shows splitting of the basin-wide convective cell into smaller cells. If $K_v$ equals $10^{-15}$ m$^2$, the large convective circulation is too sluggish to have any hydrodynamical and thermal impact at the surface. Our different runs lead us to conclude that the parameters considered in this study (Table 1) are optimal to obtain a wide basin convective circulation with a good fit to the observations.

Figure 11 presents the observed and model-based water table topography along the profile A. The pressure difference generated between ascending and descending currents is $\sim$0.35 MPa. It correctly reproduces the location of the observed piezometric depression and dome. The minimum pressure generated by our model is located beneath the Kadzell region, while the maximum is found below Kanem. This result can be interpreted as follows: the core of the warm current, circulating along the eastern side of the graben, presents a mean temperature excess with its surrounding of about 40 °C. Considering the thermal expansion of water ($\alpha = 3.85 \times 10^{-6}$ K$^{-1}$ at 40 °C) and current height of 4 km, we deduce that the buoyancy of the warm current induces a 0.8 MPa excess pressure. Such an excess pressure is essentially used to drive the backflow of the large convective cell in the Quaternary and Pliocene formations and eventually along the Bima formation. Assuming that half of the excess pressure is used to drive the circulation at the top and bottom cell boundaries, we estimate that the excess pressure on the horizontal interface of

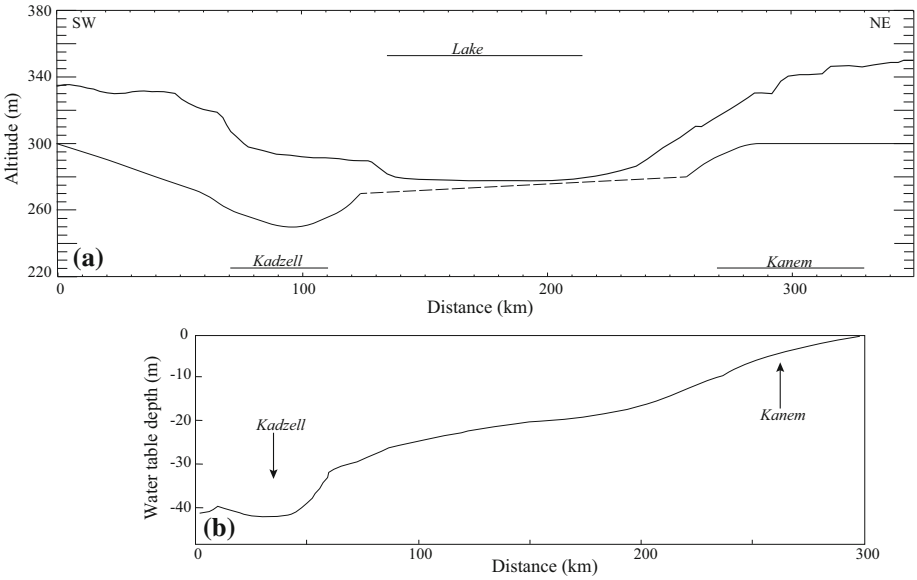


**Fig. 11** Comparison between **a** the observed water table of the QPA between Kadzell and Kanem and **b** calculated piezometric level derived from the pressure variations associated with the convective flow within the Lake Chad basin

the current below Kanem, used to drive the backflow, amounts to $\sim$0.4 MPa, in agreement with the model results.

Annual rainfall amounts to 200–400 mm over the region (e.g., Bader et al. 2011; Descloitres et al. 2013). It accumulates over the aquifer water table maintained by the large convection cell. Considering the permeability assigned to the different formations, we infer that the rain flows from Kanem to Kadzell at a velocity of 2 cm year$^{-1}$ and 2 mm year$^{-1}$ in the Quaternary and Pliocene formations, respectively. Such velocities are comparable to the backflow of the warm current in these formations. This circulation is designated as the "forced convective flow" by Gvirtzman et al. (1997). Generally, in mountainous areas, the topographic slope is a hundred times larger than the slopes generated by free convection cells. This shows that "forced convection" is the dominant transfer mode of water in mountainous areas. However, this scheme does not work in the Lake Chad basin. This does not mean that the topography at the borders does not impact the basin. The slow eastward circulation of descending cold currents observed between faults 1 and 2 (with subcritical *Ra* number) probably results from the "forced convection" at the western side of Kadzell. Such forced convection explains why the descending current of the basin-wide convective circulation does not follow fault 1 but is localised at the centre of the Kadzell area along the P1 profile (Appendix 4).

## 4 Discussion

In the previous section, we have presented results of a water convection model over the Lake Chad basin. This led us to propose a scenario describing how water circulates at depth under the basin. In this section, we examine to what extent the model results fits with

the observations. Different types of observations are considered as thermal data (subsurface and surface temperature data), hydrochemical data, piezometry evolution and water mass changes.

## 4.1 Relations Between the Deep Convective Circulation and Thermal Data

### *4.1.1 Subsurface Thermal Data*

Bottom hole temperatures profiles (referred hereafter as BHT) have been collected during the drilling of oil wells in the Nigerian sector of the basin (Nwankwo and Ekine 2010). BHT profiles are located in the northern part of Lake Chad as well as at or near the Bornu piezometric depression (Fig. 4). BHT are obtained at thermal disequilibrium and are used for internal calibration of the drills. Therefore, they are significantly affected by mud circulation during and after drilling. The data shown in Fig. 12 are corrected to first order by using American Association of Petroleum Geologists (AAPG) gradient correction factors (Nwankwo and Ekine 2010). The uncertainty of individual temperature measurements ranges from 5 to 15 °C. Each borehole temperature profile was averaged according to depth to determine the local mean temperature gradient. We observe that the mean temperature gradient substantially increases towards the north-eastern part of the basin. We also note that, in most cases, temperature profiles do not vary linearly with depth (Fig. 12). The profiles' shapes appear similar to those obtained in regions where groundwater circulation transports geothermal heat (Kilty and Chapman 1980; Pribnow and Schellschmidt 2000). In the latter studies, surface heat flow was directly linked to the temperature gradient in the first $\sim$300 m of the basin where the profile is linear and crosses the top boundary layer of the convective circulation. The profiles presented by Nwankwo and Ekine (2010) show that in the first $\sim$300 m the measured and corrected thermal gradients are similar. The thermal gradients derived from the BHT vary from 30 to 80 °C km$^{-1}$ (Fig. 4), a range consistent with model-based surface heat flow values ranging from 45 to 120 mW m$^{-2}$ (Fig. 8). Besides, whatever the error range of the BHT data, the top to bottom shapes of the Nwankwo and Ekine (2010) BTH profiles are not compatible with those expected in a medium where heat transport is conductive. Profile concavity, along ascending or descending convective currents, is also observed in our numerical model

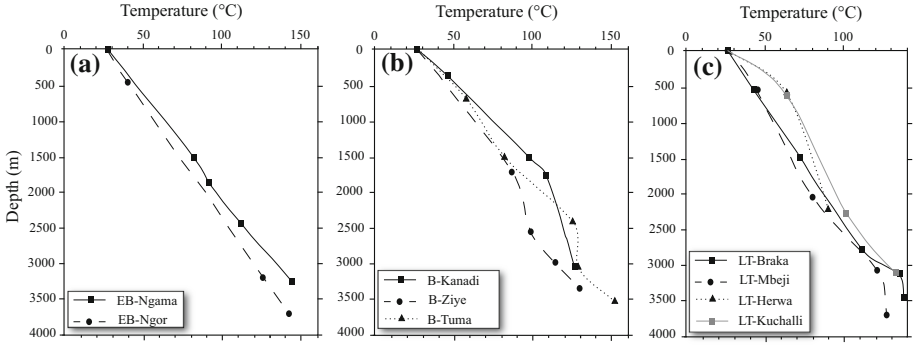


**Fig. 12** Thermal profiles obtained during oil drills (modified from Nwankwo and Ekine 2010): **a** slightly outside the Bornu depression, **b** in the Bornu depression and **c** in the ancient bed of Lake Chad (see locations in Fig. 4)

(Fig. 8). For example, between ~200 and ~1500 m, the convex shape of the LT-Herwa and LT-Kuchalli BHT profiles is similar to that of the P3 profile that crosses the warm ascending current below Kanem (Fig. 8). However, the set of boreholes is not dense enough to constrain the structure of the convective flow in a domain as large as the Lake Chad basin. In the Rhine Graben, for example, the 804 available boreholes allow characterising of the east–west convective cells, but with a very complex 3D distribution of the warm and cold currents (Pribnow and Schellschmidt 2000). By analogy, we can suspect that the real structure of the flow within the Lake Chad basin is also very complex.

#### *4.1.2 Surface Thermal Data*

According to our model (domes and depressions associated with warm and cold currents, respectively), we suggest that the brightness temperatures observed by Leblanc et al. (2003) are directly linked to the convective circulation. Leblanc et al. (2003) compared the piezometric map with monthly composite maximal brightness temperatures from the METEOSAT satellite. These data were acquired in August 1999, a period corresponding to the end of the wet season. These authors found that during wet years the piezometric domes are systematically warmer by 4–5 K than the piezometric depressions. A difference of surface heat flow by a factor of two above ascending and descending currents is predicted by our model (see Sect. 3.2). However, a heat flow difference of about ~50–100 mW $m^{-2}$ cannot maintain a surface temperature difference of 4–5 K (Sabins 1999). Only processes involving the temperature diurnal cycle can explain such a temperature contrast. Leblanc et al. (2003) explained this observation as follows: in the Kanem region, consisting of aeolian sands, rain infiltrates rapidly and deeply into the soil. Consequently, rain water does not contribute to evaporation. Thus, the observed brightness temperature reflects dry surface conditions. In the Kadzell and Bornu regions, the surface consists of a mix of fluviatile deposits (sandy clay) and aeolian deposits. In that case, the rain percolates more slowly. Thus, water evaporates, acting as a moderator of the temperature increase during the day (via latent heat).

Maximal surface temperatures obtained from 8-day composite MODIS images allow us to follow temperature seasonal variations over the year. Figure 13 shows daytime and nighttime maximal surface temperatures obtained during the year 2001, a particularly wet year (Bader et al. 2011). Temperatures data cover the Kanem, the Kadzell and the Bornu regions during the dry season (October–June, but we only focus on the January–March time span) and wet season (July–September). Whatever the season, the daytime temperature in Kanem is on average 3–4 K warmer than at Kadzell (Fig. 13a). During the nighttime, for both seasons, a similar behaviour is observed, but the temperature difference decreases to between 1 and 2 K (Fig. 13b). Usually, during the diurnal cycle, the amplitude of the surface temperature variation on dry ground is larger than on wet ground (Byrne et al. 1979; Idso et al. 1975; Sabins 1999). In the wet season, Kadzell should be warmer than Kanem during the night, in contradiction with the observations. If the Kanem soil is dry, the surrounding atmosphere is likely to be wet, because of the presence of numerous ponds which evaporate at ~2 m $year^{-1}$ (i.e. ~6 mm $day^{-1}$; Roche 1980). Besides, such ponds are not the only source of humidity. Because of the high permeability of the Kanem region, the air in the under-saturated zone circulates by convection with Darcy velocities of several cm $s^{-1}$ (Antoine et al. 2009). Such convection maintains a high water concentration in the soil. At night, when the surface temperature is cool enough, warm and humid convective air leaves the system (Antoine et al. 2009), and most of the water vapour contained in the warm convective air condenses. Consequently, it is very likely that, during

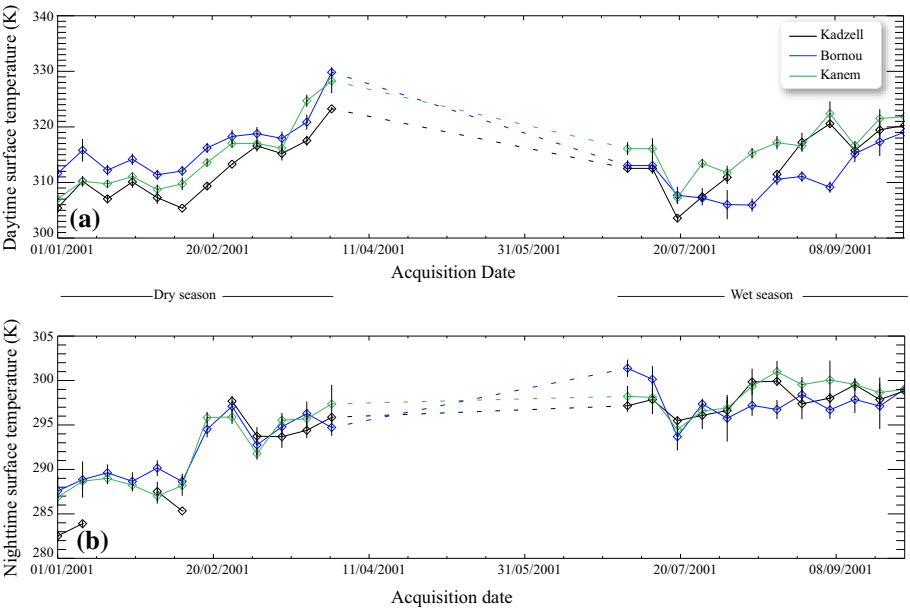


**Fig. 13** Satellite TERRA moderate resolution imaging spectroradiometer (MODIS) 8-day composite maximal surface temperature obtained during 2001 **a** by day and **b** at night, for the Kanem, Kadzell and Bornu regions. We have only considered January, February and March as representative for the dry season and July, August and September for the wet season

the night, water condensation of 1–2 mm per day heats the Kanem surface by 1–2 K. Eventually, this water infiltrates into the highly permeable sandy soil, recharges the phreatic aquifer and finally leads to drying of the surface during the day.

During the dry season, the perennial ponds in the Kanem region, linked to the piezometric dome, may be filled by the water coming from the ascending convective current. This may explain why this region remains warm as the evaporation/condensation cycle is still at work. Because of the presence of clays in the Kadzell subsurface, the diurnal temperature cycle is mainly controlled by the in situ evaporation/condensation cycle as considered by Leblanc et al. (2003). This explains why the surface temperature there is colder than in the Kanem region.

During the wet season, the temperature contrast between Bornu and Kanem evolves as in the Kadzell and Kanem regions. During the day, the Kanem region is $\sim$5 K warmer than the Bornu region, while at night the temperature difference drops to $\sim$2 K (Fig. 13a). However, during the dry season, the situation is reversed: during the day, the Bornu region is warmer than the Kanem region by $\sim$3–4 K, while at night both regions have similar temperatures (Fig. 13b). We suggest that the latter situation results from the impact of the vegetation and the proximity of the Small Lake Chad and Chari-Logone rivers. Indeed, during the dry season, soil humidity in Bornu results from water condensation and evaporation. To explain the temperature diurnal cycle, condensed water should not be available during the daytime. We propose that a significant amount of this water is absorbed by the vegetation (Gaston 1996). In Bornu, the vegetation in the dry season mainly consists of trees spaced $\sim$20 m apart, a relatively large tree density that is important for the basin's evapotranpiration/condensation cycle.

## 4.2 Relation Between Deep Convective Circulation and Hydrogeology

### *4.2.1 Evolution of the Water Composition*

In the Nigerian part of the basin, the Continental Hammadian aquifer contains mainly NaCl waters (Schneider and Wolff 1992). In the Kanem area (Table 2), Schneider and Wolff (1992) have shown that the Continental Terminal aquifer contains mainly $NaHCO_3$ waters and that the Pliocene aquifer consists mainly of $Na_2SO_4$ waters. On the contrary, the Quaternary aquifer is described by a geochemical signature of $CaHCO_3$. Chemical variation of the waters is usually interpreted to be a consequence of separate aquifers. However, our proposed convective scenario considers that all aquifers are connected by vertical drains due to the compaction of clay formations. The total dissolved solid (or TDS) of the QPA is 165 mg $L^{-1}$, while the mean TDS is 760 mg $L^{-1}$ for the Pliocene, Continental Terminal and Continental Hammadian aquifers (Schneider and Wolff 1992). Between these three aquifers, the salinity is similar except for some localised pockets of higher salinity. The apparent absence of a notable vertical salinity stratification suggests that the basin-wide convective circulation crosses the entire basin depth. In the case of a vertical salinity stratification, the convective cells are confined to layers with constant salinity and the excess pressure at the phreatic aquifer dramatically reduces the dome height.

In the Kanem region, for the deeper aquifers (i.e. the Continental Hammadian and the Continental Terminal), changes from NaCl to $NaHCO_3$ waters are interpreted as anion exchanges during the rising of waters through the Fika formation. The enrichment of the Pliocene aquifer in $SO_4^{2-}$ sulphates can be explained by the evaporitic deposit of gypsum/anhydrite during the Early Pliocene. Table 3 presents the detailed chemistry of Pliocene (in italic) and Quaternary aquifers for three regions in Kanem where the water drills were geographically close. The content (in ppm) of ions $Mg^{2+}$, $Na^+$, $K^+$ and $Cl^-$, $SO_4^{2-}$, $HCO_3^-$ decreases from one aquifer to the other. On the contrary, the calcium carbonate ($Ca^{2+}$) content increases except for the water wells of Ndelé and Rig Rig. The decrease in the $HCO_3^-$ may result from an increase in the $Ca^{2+}$ in solution, causing $CaCO_3$ precipitation. The decrease in sulphates in solution between these two aquifers may be explained

**Table 2** Concentration (in ppm) of the QPA and the Pliocene aquifer (*in italic*) of the main anions and cations (Arad and Kafri 1974; Schneider and Wolff 1992)

| | $Ca^{2+}$ | $Mg^{2+}$ | $Na^+$ | $K^+$ | $Na^+ + K^+$ | $Cl^-$ | $SO_4^{2-}$ | $HCO_3^-$ | $CaCO_3$ |
|---|---|---|---|---|---|---|---|---|---|
| Mondo | 55 | 6.5 | – | – | 83.2 | 15.9 | 103 | 116 | 190 |
| *Ngouri* | 37.1 | 14.6 | 209 | 2.65 | – | 79.8 | 271 | 311 | – |
| Boudouté | 45.2 | – | – | – | – | 11.5 | 27.2 | 130 | 212.5 |
| *Keliganga* | 1 | 4.25 | 168 | 1.37 | – | 59.9 | 62.4 | 308 | – |
| Ndelé | 23.9 | 4.6 | – | – | 37.5 | 10.7 | 49.3 | 110 | 67 |
| *Rig Rig* | 37.9 | 14.9 | 239 | 15.2 | – | 42.5 | 437 | 226 | – |

Wells had been selected by their proximity to the Kanem piezometric dome

**Table 3** Equivalent water height obtained by GRACE for the main tiles of the Lake Chad basin

| Tiles | Kadzell | Kanem | Bhar-el-Ghazal | Harr | Yobe | Bornu | Chari | Fitri |
|---|---|---|---|---|---|---|---|---|
| Trend (mm $year^{-1}$) | 0.39 | 0.11 | 0.89 | 2.0 | 1.94 | 0.48 | −0.02 | 0.50 |

by the presence of sulphate-reducing bacteria (SRB) in the Pliocene formation (Chapelle 2000) that use sulphate/sulphur as an energy source. This process is known as anaerobic respiration. Indeed, these SRB consume the dissolved sulphate and expel hydrogen sulphide and carbon dioxide (Sylvia 2004). SRB usually flourish in the warm water system, found in the ascending current below Kanem. Moreover, the remaining sulphate precipitates due to its solubility (Serafeimidis and Anagnostou 2015) in the Pliocene Formation, in agreement with the observations of gypsum deposits (Fig. 3b) (Schneider and Wolff 1992).

In the Kadzell and Bornu regions, where the convective current may locally be descending, the chemistry variation can be essentially explained by the exchanges with the clays. Indeed, the phreatic aquifer in the Niger is described as containing sodium and calcium bicarbonate and sulphate waters (Greigert 1979) associated with a relatively low water temperature. The Pliocene aquifer contains only sodium bicarbonate and sulphate waters (Arad and Kafri 1974). A hydrostatic pressure increase leads to the fluidisation of the clay-rich formation (Mainsant et al. 2012) and induces increased exchange surfaces between clay and water. Due to temperature and pressure changes, the Continental Terminal waters present sodium deficit sulphates, suggesting that the sulphate layer has been consumed by SRB. In the case of the Continental Hammadian aquifer, the presence of sodium chloride waters may involve anion exchanges of the clay-rich Fika formation (Carroll 1959).

### 4.2.2 *Comparison Between Convective Velocity and Transient Variations of the Piezometric Level: Inference on Water Mass Changes*

Piezometric levels of the QPA in the Kadzell and the Bornu regions have changed between the 1970s and the 2000s (Fig. 14) (Schneider 1969; Schroeter and Gear 1973; Zairi 2008). In the 2000s, the surface area of the Kadzell depression decreased to 3300 km$^2$ and the

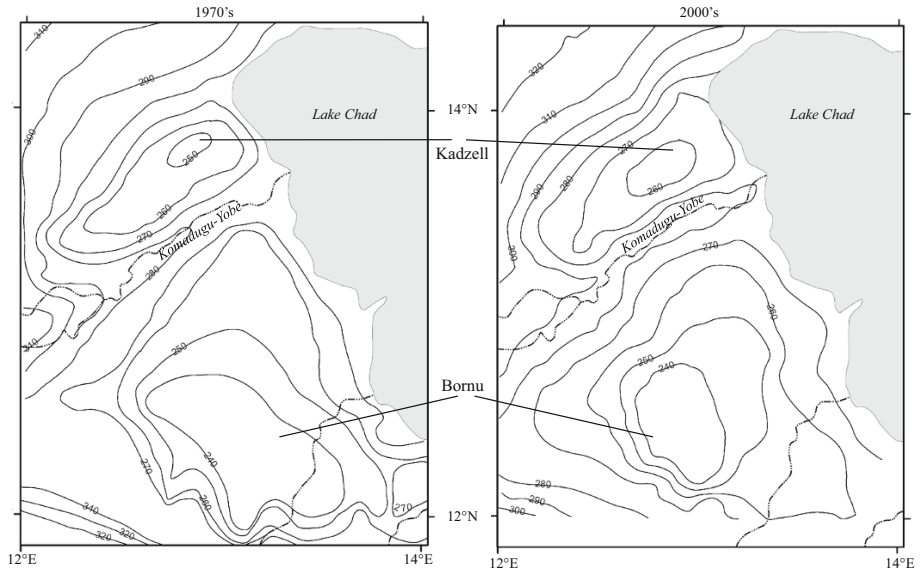


**Fig. 14** Piezometric maps of the Kadzell and Bornu depressions in **a** the 1970s (Schneider 1969) and **b** the 2000s (Zairi 2008)

maximum depth of the water table rose by ~10 m; i.e. the QPA rose in that region by ~30 cm year$^{-1}$. For the Bornu depression, the surface area decreased to 11,500 km$^2$ while the depth of the depression did not change. Considering the uncertainties in the measurements of the piezometric level during the 1970s, we consider that the 30 cm year$^{-1}$ estimate of the water table rise represents a maximum vertical Darcy velocity of ~10 cm year$^{-1}$ (considering a porosity of ~35 %). These variations observed over a 30-year time span can be explained by variations of the surface conditions (Leduc and Loireau 1997; Mahe et al. 2003). A rainfall increase can also explain this observation. Unfortunately, no recent data are available for the Kanem and Harr domes to check whether the corresponding water tables have experienced changes since the 1970s or not. The vertical Darcy velocity obtained by our model in the Quaternary formation near Kadzell is 4 mm year$^{-1}$. Thus, the velocity estimate in Kadzell does not match the 30 cm year$^{-1}$ maximal rise velocity of the piezometric level estimated above. The convective circulation has no influence on the piezometric level variations. Besides, the Darcy velocity is proportional to the pressure gradient; the water table rise requires strong modification of the hydraulic head which may be due to an important level variation of Lake Chad.

Launched in March 2002, the gravity recovery and climate experiment (GRACE) mission provides observations of the time-variable gravity field (Bruinsma et al. 2010). We analysed a new GRACE solution computed by Ramillien et al. (2014), providing regional surface water mass time series on a 2° × 2° grid (see also Ramillien et al. 2011, 2012). We derived linear trends over the Lake Chad basin (11°–17°E and 11°–20°N) for the period 2003–2012 (Fig. 15). In regions where water accumulation (provided by rainfall, rivers or

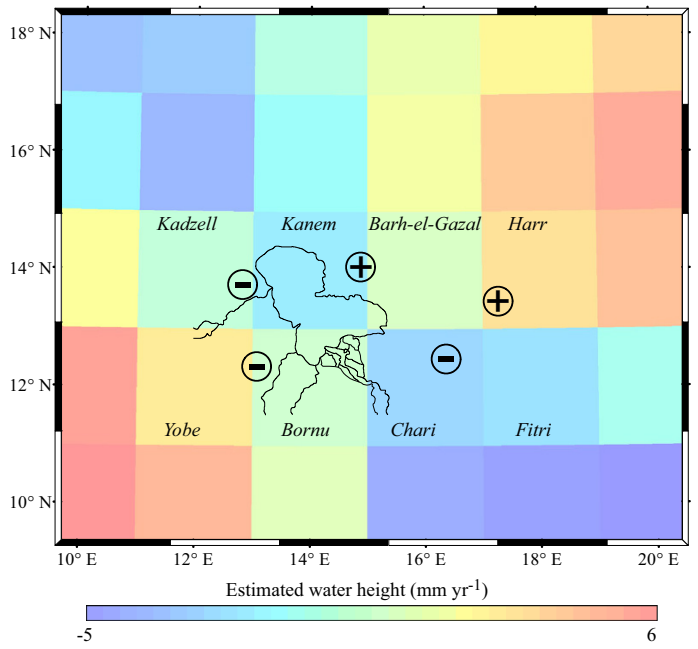


**Fig. 15** GRACE-based water surface mass trends in mm year$^{-1}$ from 2003 to 2012 (resolution of each tile is 2° × 2°). Tiles around Lake Chad have been named after the covered regions or characteristic features (Kadzell, Kanem, Barh-el-Ghazal, Harr, Yobe, Bornu, Chari and Fitri). The *symbols minus* and *plus* locate the piezometric depressions and domes, respectively

groundwater) is greater than the water deficit (the latter being mainly controlled by the evapotranspiration), the trend is positive while, if water deficit is larger, the trend is negative. The water mass trend is $\sim 1$ mm year$^{-1}$. Our results are summarised in Table 3. The trend observed in the Yobe tile is linked to water supplied by the Mandara Mountains, from both rainfall and/or river discharge. A similar explanation is valid for the Kadzell and Bornu area. The Fitri area is bordered to the south by Guera Mountains that provide water into this region. The Chari and Kanem areas display very small trends. This suggests that the water deficit is compensated by water accumulation over the 2003–2012 time span. The two last areas (Barh-el-Gazal and Harr) display a positive trend close to 2 mm year$^{-1}$. This water accumulation cannot be explained only by water supply from rainfall ($\sim 200$ mm year$^{-1}$) or rivers (there are no rivers in this area). We conclude that this water accumulation results from the ascending convective currents that develop below the Kanem and Harr domes. These regions are located very close to the zones of the maximum gravity anomalies (Fig. 2), indicating a zone of deep basement.

The GRACE-based observations are in agreement with a situation where thin sediments favour the development of zones of convective recharge, whereas the borders of thick sediments favour zones of convective discharge flows. Another result worth highlighting is the good consistency between the GRACE-based equivalent water height trend (of $\sim 2$ mm year$^{-1}$) and the transient variation of the piezometric levels (corresponding to 6 mm year$^{-1}$ elevation of the QPA for sand with a porosity of $\sim 35$ %). This is at least one order of magnitude lower than the backflow horizontal velocity of the basin-wide convection circulation. Considering that the convection is in a transient state, the 6 mm year$^{-1}$ variation of the piezometric level in a $2° \times 2°$ mesh may result from the transient modification of the top pressure field induced by the convective circulation.

## 5 Conclusions

The phreatic aquifers of the Sahelian regions have well-known surface features like depressions (with a mean depth below the surface of $\sim 60$ m) and domes (only clearly observed in the Lake Chad basin). These surface features result from evaporation/infiltration differences due to surface pedological variations between depressions and domes (Aranyossy and Ndiaye 1993; Leblanc et al. 2003). This is corroborated by the observed correlation between METEOSAT brightness temperatures and piezometric levels of the QPA in the Lake Chad basin (Leblanc et al. 2003). The results from the present study suggest that a correlation also exists between piezometric levels and sedimentary thickness in the basin. Indeed, a comparison with the free-air gravity anomalies indicates that, where the sediment infill is very thick ($\sim 4$ km), the piezometric domes develop. On the contrary, where it is thin, piezometric depressions are observed. This correlation suggests that sedimentary infill characteristics impact the brightness temperature of the surface. In order to explain the piezometric variations and the reported correlations, we propose an alternative hypothesis that combines evapotranspiration with a deep basin-wide convective circulation.

The Lake Chad basin comprises four aquifers. These are (from shallow to larger depth): the QPA, the Pliocene aquifer, the Continental Terminal aquifer and the Continental Hammadian aquifer. Each aquifer is separated by clay layers generally considered as being impervious. This statement is true when the clay layer has an extent commensurate with its thickness. In the study region, the Pliocene formation has an extent of $\sim 300$ km with a

maximum thickness of $\sim$300 m. Data from seismic prospection in oceanic margins reveal that overpressured clay layers develop giant polygonal fractures when they are submitted to horizontal tensile stresses of a few bars. We discovered the existence of such structures in the Bornu region, located close to the eastern border of the basin. By analogy, the horizontal tensile stresses applied to the Pliocene formation result from the slope break of the surface topography. Associated faults probably create a high vertical permeability connecting the phreatic aquifer with the Pliocene one. Between depths of 2 and 3 km, the compacted clay Fika formation has a maximum thickness of $\sim$2 km. The development of differential compaction in this layer may explain the formation of fractures, allowing hydrodynamical connexion between the Continental Terminal and Hammadian aquifers.

We developed a 2D numerical convective model along a cross section from the Kadzell depression (western border of the basin) to the Kanem dome (eastern border of the basin). Our model results show that a cold descending current develops below Kadzell and then is channelled in the Bima formation, along the eastern slope of the basin. Meanwhile, it is heated by about 50 °C by the basement geothermal heat. The horizontal Darcy velocity of the fluid in the Bima formation is $\sim$10 cm year$^{-1}$ that corresponds to a mean flow velocity of $\sim$1 m year$^{-1}$. Thus, it takes 1 Myr for the water to flow from the Kadzell depression to the Kanem dome. The characteristic time to heat the $\sim$4-km-thick infill by conduction is $\sim$500,000 years. These results show that the heat transport in the infill is due equally to conduction and convection. The warm current, which now has a temperature of $\sim$100 °C, rises along the permeable blocks delimiting the eastern border of the basin. The excess pressure generated by this warm ascending current at the top of the $\sim$4 km sediment infill potentially explains the piezometric level difference between Kadzell and Kanem. Moreover, our model results show that because: (a) thermal conductivity contrast between sediments and basement along the western border of the basin, (b) fracturing induced by the differential compaction, and (c) large sedimentary infill thickness, the eastern border of the basin is a zone of ascending currents.

According to GRACE space gravimetry data and the transient variation of the convective circulation, the perennial existence of water accumulation over the Kanem and Harr piezometric domes (where in both regions there are no water supplies except from rainfall during the wet season) can be explained by water supply from the convective ascending current. Finally, our model suggests that the development of piezometric domes and depressions are linked to the convective circulation and require connected aquifers, a situation which leads to water mixing. Water geochemistry variations between the aquifers are compatible with our convective model taking into account the cation exchange process in clays. Comparison of the thermal profiles obtained by our model and BHT data suggests that the thermal structure of the basin is impacted by the hydrothermal circulation that is possibly linked to a basin-wide convective circulation. The best test to check this hypothesis is to obtain BHT profiles in both the Kadzell and Kanem regions and compare them with the thermal profiles obtained by our model. Unfortunately, such information is lacking.

Heat provided by the warm ascending current below Kanem is not sufficient to explain the 1–2 K brightness temperature difference observed in Kadzell during the night. In order to explain this temperature difference, we need to consider heat provided by water condensation during the night and the possible existence of air convection in the undersaturated zone. In this case, the role of the ascending current is to deliver water to the surface in order to maintain a minimal humidity whatever the season. Finally, the detection of ascending water currents near the surface has been made possible by the combination of a highly permeable formation close to the surface and of warm zones during day and night

in all seasons, detected by space-based thermal imagers. In the future, regions of arid and/or semi-arid conditions showing this combination may indicate the existence of water close to the surface that can be linked to a deep convective circulation.

**Acknowledgments** This research has benefited from the support by the French Space Agency CNES and TOSCA (Terre, Océan, Surfaces continentales, Atmosphère) support. It has also benefited from the support of Commissariat Général au Développement Durable (CGDD) from the French Ministry of Environment, as part of the CEREMA internal research project HYDROGEO. Thanks are due to the "Bureau Gravimétrique International (BGI)/International Association of Geodesy" for providing the EGM model. We thank G. de Marsily and G. Vasseur for their constructive criticisms, and the Editor in Chief for editorial suggestions, which significantly improved the paper. This paper arises from the ISSI Workshop on Remote Sensing and Water Resources.

## Appendix 1: Governing Equations, Parameters and Equations of State

The mass conservation equation for a fluid of variable density within a fluid-saturated porous medium (rock matrix) without an internal fluid source is:

$$\frac{\partial(\varepsilon \cdot \rho_{\mathrm{f}})}{\partial t} = -\nabla \cdot (\rho_{\mathrm{f}} \cdot \vec{u}) \tag{1}$$

where $\varepsilon$ is the porosity, $\rho_{\mathrm{f}}$ the fluid density (kg m$^{-3}$), $t$ the time and $\vec{u}$ the Darcy velocity vector (m s$^{-1}$). We write $\vec{u} = (U, V)$, $U$ and $V$ being the fluid velocity component parallel to the $x$ and $z$ directions, respectively. The fluid is incompressible with a constant chemical composition, and its density is temperature dependent.

Darcy's law is used to describe the fluid velocity field $\vec{u}$:

$$\vec{u} = -\frac{K}{\mu}\left(\overrightarrow{\nabla p} - \rho\vec{g}\right), \tag{2}$$

where $K$ is the permeability, $\mu$ is the viscosity of the fluid, $\vec{g}$ is the gravity vector and $p$ is the fluid pressure. The fluid density varies linearly with temperature $T$ in °C:

$$\rho = \rho_0(1 - \alpha(T - T_0)) \tag{3}$$

where $\alpha$ is the thermal expansion coefficient and $\rho_0$ is the fluid density at $T_0 = 20$ °C, the surface temperature of the model.

Heat transport is achieved by both conduction and advection and is described for an incompressible single-phase fluid by:

$$C_{\mathrm{eq}}\left(\frac{\partial T}{\partial t}\right) = \nabla \cdot \left(\lambda_{\mathrm{eq}}\overrightarrow{\nabla T}\right) - C_{\mathrm{L}}\vec{u} \cdot \overrightarrow{\nabla} T \tag{4}$$

where $C_{\mathrm{L}}$ is the volumetric heat capacity defined by $C_{\mathrm{L}} = \rho_{\mathrm{f}}\, C_{\mathrm{P}}$, $C_{\mathrm{P}}$ is the specific heat capacity, $C_{\mathrm{eq}}$ and $\lambda_{\mathrm{eq}}$ are the weighted average volumetric heat capacity and equivalent thermal conductivity, respectively, as defined in saturated porous media of porosity $\phi$:

$$C_{\mathrm{eq}} = \phi\rho_{\mathrm{f}}C_{\mathrm{p_f}} + (1 - \phi)\rho_{\mathrm{s}}C_{\mathrm{ps}} \tag{5}$$

where f and s are subscripts for the fluid and the porous matrix, respectively. We assume that $C_{\mathrm{L}}$ remains approximately constant, a reasonable assumption since the decrease in density with temperature roughly balances the increase in the specific heat capacity with temperature. The equivalent thermal conductivity is written as:

$$\lambda_{\mathrm{eq}} = \lambda_{\mathrm{f}}^{\phi} \lambda_{\mathrm{s}}^{1-\phi} \tag{6}$$

where $\lambda_{\mathrm{f}}$ and $\lambda_{\mathrm{s}}$ are the thermal conductivities of the fluid and the porous matrix, respectively.

The vertical Rayleigh number $Ra$ characterises the vigour of the convection within the stratified porous medium and is defined as follows:

$$Ra = \frac{\alpha \rho g C_{\mathrm{L}} K_z}{\mu \lambda_{\mathrm{eq}}} \gamma h^2 \tag{7}$$

where $K_z$ represents the vertical permeability, $g$ is the acceleration due to gravity, $h$ is the height of the layer and $\gamma$ is the vertical temperature gradient.

## Appendix 2: Parameter values

In our calculations, the parameter describing the temperature dependence, $\alpha$, follows from the results obtained by Irvine and Duignan (1985). The viscosity of the fluid $\mu$ (given in units of Pa s) also varies with temperature, based on the following analytical expression (ASME 1968; Kestin et al. 1978; Rabinowicz et al. 1998a, b):

$$\mu = 0.00002414 \times 10^{\left(\frac{247.8}{T+133}\right)} \tag{8}$$

The pressure dependence of viscosity is not included, because it is small in the range of depth considered here (Norton 1984). Equation (8) shows that the fluid viscosity decreases from $17.5 \times 10^{-5}$ to $13.5 \times 10^{-5}$ Pa s in the 2–200 °C temperature interval. Above 200 °C, the viscosity remains approximately constant. In our model, the thermal conductivity $\lambda_{\mathrm{eq}}$ varies with temperature for each type of formation (crystalline rock, sandstone, shale). We used the experimental data provided by Clauser and Huenges (1995) for the thermal conductivities of sandstone, shale and quartz-rich crystalline rock between 0 and 300 °C. Finally, the other parameters such as the porosity $\phi$, the heat capacity $C$ of each phase (rock and fluid) and the density of each phase at 20 °C assigned to each geological formation are listed in Table 1.

## Appendix 3: Method and Boundary Conditions

The simulations are performed using the Comsol Multiphysics™ finite-element code, which has already been tested and successfully implemented for convective process simulations in various configurations (Holzbecher 2004; Eldursi et al. 2009; Guillou-Frottier et al. 2013). A two-dimensional grid constituted of square elements of size $d = 200$ m was considered. Thus, given the dimensions of the basin, the grid is composed of 40 elements in the z direction and 1500 elements in the x direction. The ratio $0.8d/V_{\max}$, where $V_{\max}$ represents the maximal amplitude of the Darcy velocity, determines the optimal time step at which the time evolution of the convective process can be realistically simulated.

The top of the model represents the surface topography of the Lake Chad basin, which is impermeable (the vertical velocity at the interface is zero) and maintained at a constant temperature of 20 °C. The bottom of the model consists of a quartz-rich substratum. It is maintained at a constant temperature of 247 °C and has a permeability low enough to be

considered as impermeable ($\sim 10^{-18}$ m$^2$). The flow and temperature along the lateral boundaries of the model are symmetric. All these chosen boundary conditions are the usual ones, except the flow condition along the top interface. Indeed, a real free condition would be mathematically more elegant. The latter condition is needed to adjust the depth of the piezometer (i.e. of the saturated zone) at each iteration, in order to obtain a zero pressure along that interface. That method is particularly costly and difficult to handle, because it does not necessarily ensure the incompressibility of the fluid. Besides, it is not necessarily justified as the depth of variation of the piezometer is small ($\sim 60$ m) compared to the depth of the basin. Therefore, the pressure perturbation due to convection and surface topography is small in comparison with the lithostatic pressure variations in the basin. Accordingly, in our model, the coincidence of the surface topography with the piezometer results to be an acceptable first-order approximation (McKenzie et al. 1974). Besides, it is extremely cost-effective as it does not require internal iterations between two time steps of the temperature equation. As the program retrieves the pressure after each time step, we can a posteriori compute the height of the piezometer with first-order precision. Because the topography along the borders of the basin is not flat, local flows are generated and eventually combine with those developed by convection. Actually, they have a notable impact on the circulation recovered in the model over the Kadzell and Kanem area (Sect. 2).

## Appendix 4: Evaluation of the Hydrological and Thermal Characteristics of Our Model

The maps of the fluid viscosity of the thermal expansion and of the effective thermal conductivity of the basin of our convective model are displayed in Fig. 16a–d. From these maps, we deduce that, within the Bima horizon, at the location of the P1 profile: $\gamma = 57$ °C km$^{-1}$, $K = 2 \times 10^{-13}$ m$^2$, $h = 400$ m, $\alpha = 2.9 \times 10^{-4}$ °C$^{-1}$, $\lambda_{eq} = 2.3$ - W °C$^{-1}$ m$^{-1}$, $\mu = 5 \times 10^{-4}$ Pa s, and thus, the Rayleigh number is equal to 21 (Eq. 1). Alternatively, around P2: $\gamma = 62$ °C km$^{-1}$, $h = 900$ m, $\alpha = 3.8 \times 10^{-4}$ °C$^{-1}$, and $\mu = 3 \times 10^{-4}$ Pa s, and the Rayleigh number is equal to 230. Finally, to evaluate the vertical Rayleigh number of the whole basin above faults 5 and 6, we chose the following numbers: $\gamma = 43$ °C km$^{-1}$, $K = 10^{-14}$ m$^2$, $h = 4000$ m, $\alpha = 2.6 \times 10^{-4}$ °C$^{-1}$, $k = 2$ W °C$^{-1}$ m$^{-1}$, $\mu = 10^{-3}$ Pa s, and thus, the Rayleigh number is equal to 31. These numbers indicate that (a) convection likely develops in the Bima horizon outside the block separated by faults 1 and 2, and (b) the basin-wide cell is not split into smaller ones in the graben delimited by faults 5 and 6. Below Kanem, the evaluation of the effective Rayleigh number for the entire depth of the basin is more problematic, due to the permeability variations along the trajectory of the warm current. First, at the eastern border of the basin, the permeability of the contiguous Bima blocks is $2 \times 10^{-13}$ m$^2$ in a channel extending from 4 km to $\sim 700$ m depth. In that channel, the vertical Rayleigh number is $\sim 380$ (i.e. much greater than $4\pi^2$) and the mean vertical velocity is 10 cm year$^{-1}$.

Actually, in a real 3D geometry, hydrothermal convective currents parallel to the walls of the basin may develop (Rabinowicz et al. 1998a, b). Despite the $\sim 150$-m-thick Fika formation (located eastward of fault 8, Fig. 3a), the warm current reaches the QPA through the zone of the Fika formation shift induced by throws of faults 7 and 8 (*ellipses* A and B in Fig. 3a). In the last $\sim 700$-m-thick upper sediments, the intensity of the flow remains strong as the mean vertical velocity is $\sim 4$ cm year$^{-1}$. The strength of this warm current

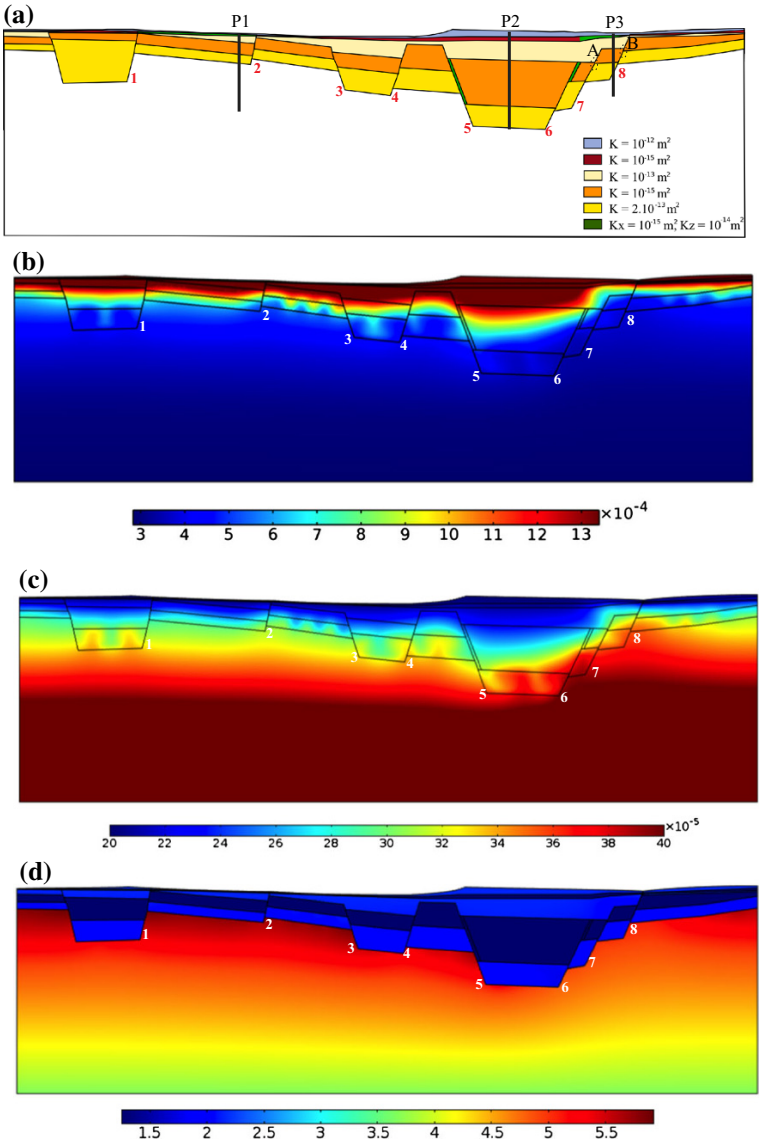


**Fig. 16** Maps of the different physical parameters used for the modelling of the convective circulation in the Lake Chad basin: **a** permeability fields assigned to the different formations of the basin. *Dashed ellipses* highlight the stratigraphic throws of faults 7 and 8 that impact the Fika formation and *vertical black lines* highlight the location of temperature profiles P1, P2, P3 displayed in Fig. 10, **b** fluid viscosity field (in Pa s), **c** variations of the thermal expansion coefficient (in $K^{-1}$) with the temperature and **d** distribution of the effective thermal conductivity (in W $m^{-1}$ $K^{-1}$) within the basin

explains the intensity of the backflow of the basin-wide convection, which reaches a horizontal velocity of 39 cm $year^{-1}$ over the Kanem, and down to $\sim$7 cm $year^{-1}$ at Kadzell. The resulting top pressure drop from Kanem to Kadzell explains the piezometric level topography.

Finally, let us suppose that the ascending and descending convective velocities along the lateral border of the basin-wide cell are constant and have an intensity equal to $V$. Then, an analytical 1D solution for the steady temperature (Eq. 4) shows that:

$$T(z) = T_{\text{bottom}} + \gamma \frac{\left(1 - \exp\left(\pm Pe \frac{z}{h}\right)\right)}{(1 - \exp(\pm Pe))} \tag{9}$$

and

$$\mathrm{d}T(z)/\partial z = - \pm Pe\,\gamma \frac{\exp\left(\pm Pe \frac{z}{h}\right)}{(1 - \exp(\pm Pe))} \tag{10}$$

where $Pe$ represents the Péclet number, which is written as:

$$Pe = \frac{C_{\text{L}} h V}{\lambda_{\text{eq}}} \tag{11}$$

In Eqs. (9) and (10), $z$ represents the height in the column of total thickness $h$, where the flow is ascending or descending, respectively. Over Kanem, $+V \sim 4$ cm year$^{-1}$, $h \sim 700$ m and $\lambda_{\text{eq}} \sim 2$ W °C$^{-1}$ m$^{-1}$ and thus $Pe \sim 1.9$. If we assume that $Pe \gg 1$, we see that:

$$\mathrm{d}T(z = h)/\partial z \approx Pe\,\gamma \approx 1.9\,\gamma \tag{12}$$

Alternatively, below Kadzel, where $V \sim -4$ mm year$^{-1}$, $h \sim 1000$ m and $\lambda_{\text{eq}} \sim 2$ - W °C$^{-1}$ m$^{-1}$, $Pe \sim 0.3$. Therefore, assuming that $Pe \ll 1$, we see that:

$$\mathrm{d}T(z = h)/\partial z = \exp(-Pe)\gamma \approx 0.75\,\gamma \tag{13}$$

For Kadzell, close to the top of P1 profile, where the axis of the descending current associated with the basin-wide cell is approximatively located, the observed conductive heat flow is $\sim$110 mW m$^{-2}$ and the convective heat flow is $\sim$70 mW m$^{-2}$. These values show that the approximation deduced from Eq. (13) is valid. Over the Kanem, close to the top of the P3 profile, the conductive heat flow is $\sim$100 mW m$^{-2}$ and the convective one is $\sim$200 mW m$^{-2}$. The approximation given by Eq. (12), which is specifically valid for a fast ascending flow, leads to a good match with this last pair of heat flow values.

In Sect. 2, we emphasise that the mean heat flows at the top of our models are not significantly different when fluids circulate by convection and when the transport of heat at the surface is purely conductive: here 110 mW m$^{-2}$, instead of 90 mW m$^{-2}$. Actually, this result can be rationalised as follows. Along the interface of the sediment and the basement, inside the Bima formation, the mean horizontal velocity $V$ of the $L \sim 240$ km basin-wide cell is $\sim$10 cm year$^{-1}$. Besides, the temperature contrast $\Delta T$ between the descending current along P1 and the basement is $\sim$30 °C (Fig. 10). For a boundary layer approximation of the mean heat flow $\phi$ along a cooling plate (Turcotte and Schubert 2002):

$$\phi = 2\lambda_{\text{eq}} \Delta T \sqrt{\frac{C_{\text{L}} V}{\pi \lambda_{\text{eq}} L}} \approx 13\,\text{mW m}^{-2} \tag{14}$$

This expression correctly accounts for the difference of heat flows between the convective and conductive models.

## References


Antoine R, Baratoux D, Rabinowicz M, Fontaine FJ, Bachèlery P, Staudacher T, Saracco G, Finizola A (2009) Thermal infrared images analysis of a quiescent cone on Piton de La Fournaise volcano: evidence for a convective air flow within an unconsolidated soil. J Volcanol Geotherm Res. doi:10.1016/j.jvolgeores.2008.12.003

Arad A, Kafri U (1974) Geochemistry of groundwaters in the Chad basin. J Hydrol 25:105–127

Archambault J (1960) L'alimentation des nappes en Afrique Occidentale. Cpt. R. de l'Hydro., Soc. Hydro. France, 383

Aranyossy J-F, Ndiaye B (1993) Formation of piezometric depressions in the Sahelian zone: study and modelling. J Water Sci. doi:10.7202/705167ar

ASME (1968) The1967 ASME steam tables. Nav Eng J. doi:10.1111/j.1559-3584.1968.tb04564.x

Avbovbo AA, Ayoola EO, Osahon GA (1986) Depositional and structural styles in Chad basin of Northeastern Nigeria. Am Assoc Petrol Geol Bull 70(12):1787–1798

Bader J-C, Lemoalle J, Leblanc M (2011) Modèle Hydrologique du Lac Tchad. Hydrol Sci J. doi:10.1080/02626667.2011.560853

Balmino G, Vales N, Bonvalot S, Briais A (2011) Spherical harmonic modeling to ultra-high degree of Bouguer and isostatic anomalies. J Geod. doi:10.1007/s00190-011-0533-4

Bruinsma S, Lemoine J-M, Biancale R, Valès N (2010) CNES/GRGS 10-day gravity field models (Release 2) and their evaluation. Adv Space Res. doi:10.1016/j.asr.2009.10.012

Byrne GF, Begg JE, Fleming PM, Dunin FX (1979) Remotely sensed land cover temperature and soil water status—a brief review. Remote Sens Environ. doi:10.1016/0034-4257(79)90029-4

Carroll D (1959) Ion exchange in clays and others minerals. Bull Geol Soc Am. doi:10.1130/0016-7606(1959)70[749:IEICAO]2.0.CO;2

Cartwright JA, Dewhurst DN (1998) Layer-bound compaction faults in fine-grained sediments. Bull Geol Soc Am. doi:10.1130/0016-7606(1998)110<1242:LBCFIF>2.3.CO;2

Chapelle FH (2000) The significance of microbial processes in hydrogeology and geochemistry. Hydrogeol J. doi:10.1007/PL00010973

Clauser C, Huenges E (1995) Thermal conductivity of rocks and minerals. In: Ahrens TJ (ed) Rock physics and phase relations: a handbook of physical constants. American Geophysical Union, Washington. doi:10.1029/RF003p0105

Cretaux J-F, Birkett C (2006) Lake studies from satellite radar altimetry. C R Geosci. doi:10.1016/j.crte.2006.08.002

Descloitres M, Chalikakis K, Legchenko A, Moussa AM, Genthon P, Favreau G, Le Coz M, Bouchera M, Oï M (2013) Investigation of groundwater resources in the Komadugu Yobe Valley (Lake Chad basin, Niger) using MRS and TDEM methods. J Afr Earth Sci 87:71–85

Dieng B, Ledoux E, de Marsily G (1990) Paleohydrogeology of the Senegal sedimentary basin: a tentative explanation of the piezometric depressions. J Hydrol 118:357–371

Eberschweiler C (1993) Monitoring and management of groundwater resources in the Lake Chad basin: mapping of aquifers water resource management—final report. R35985, CBLT-BRGM, France

Eldursi K, Branquet Y, Guillou-Frottier L, Marcoux E (2009) Numerical investigation of transient hydrothermal processes around intrusions: heat-transfer and controlled mineralization patterns. Earth Planet Sci Lett. doi:10.1016/j.epsl.2009.09.009

Fontaine FJ, Rabinowicz M, Boulègue J, Jouniaux L (2002) Constraints on hydrothermal processes on basaltic edifices: inferences on the conditions leading to hydrovolcanic eruptions at Piton de la Fournaise, Réunion Island, Indian Ocean. Earth Planet Sci Lett. doi:10.1016/S0012-821X(02)00599-X

Garven G (1995) Continental-scale groundwater flow and geologic processes. Annu Rev Earth Planet Sci 23:89–117

Garven G, Freeze A (1984a) Theoretical analysis of the role of groundwater flow in the genesis of stratabound ore deposits. 1. Mathematical and numerical model. Am J Sci 284:1085–1124

Garven G, Freeze A (1984b) Theoretical analysis of the role of groundwater flow in the genesis of stratabound ore deposits. 2. Quantitative results. Am J Sci 284:1125–1174

Gaston A (1996) The pastoral vegetation of the Lake Chad basin. In: CIRAD (ed) Livestock Atlas of the Lake Chad basin. Centre Technique de Cooperation Agricole et Rurale, Wageningen, pp 39–56

Gay A, Lopez M, Cochonat P, Sermondadaz G (2004) Polygonal faults-furrows system related to early stages of compaction—upper Miocene to recent sediments of the Lower Congo basin. Basin Res. doi:10.1111/j.1365-2117.2003.00224.x

Genik GJ (1993) Regional framework, structural and petroleum aspects of rift basins in Niger, Chad and the Central African Republic (C.A.R.). Tectonophysics. doi:10.1016/0040-1951(92)90257-7

Genthon P, Rabinowicz M, Foucher J-P, Sibuet J-C (1990) Hydrothermal circulation in an anisotropic sedimentary basin: application to the Okinawa Back Arc basin. J Geophys Res. doi:10.1029/JB095iB12p19175
Greigert J (1979) Atlas des Eaux Souterraines du Niger—Tome 1, fascicule VII: La Nappe Pliocène et le système phréatique du Manga, BGRM
Griffin DL (2006) The late Neogene Sahabi rivers of the Sahara and their climatic and environmental implications for the Chad basin. J Geol Soc. doi:10.1144/0016-76492005-049
Guideal R, Bala AE, Ikpokonte AE (2011) Preliminary estimates of the hydraulic properties of the Quaternary aquifer in N'Djaména area, Chad republic. J Appl Sci. doi:10.3923/jas.2011
Guillou-Frottier L, Carre C, Bourgine B, Bouchot V, Genter A (2013) Structure of hydrothermal convection in the Upper Rhine Graben as inferred from corrected temperature data and basin-scale numerical models. J Volcanol Geotherm Res. doi:10.1016/j.jvolgeores.2013.02.008
Gvirtzman H, Garven G, Gvirtzman G (1997) Thermal anomalies associated with forced and free groundwater convection in the Dead Sea rift valley. Geol Soc Am Bull. doi:10.1130/0016-7606(1997)109<1167:TAAWFA>2.3.CO;2
Holzbecher E (2004) Free convection in open-top enclosures filled with a porous medium heated from below. Numer Heat Transf Part A Appl. doi:10.1080/10407780490474726
Idso SB, Schmugge TJ, Jackson RD, Reginato RJ (1975) The utility of surface temperature measurements for the remote sensing of surface soil waters status. J Geophys Res. doi:10.1029/JC080i021p03044
Irvine TF, Duignan MR (1985) Isobaric thermal expansion coefficients for water over large temperature and pressure ranges. Int Commun Heat Mass. doi:10.1016/0735-1933(85)90040-5
Isiorho SA, Matisoff G, When KS (1996) Seepage relationships between Lake Chad and the Chad aquifers. Ground Water. doi:10.1111/j.1745-6584.1996.tb02076.x
Kestin J, Sokolov M, Wakeham WA (1978) Viscosity of liquid water in the range −8 °C to 150 °C. J Phys Chem. doi:10.1063/1.555581
Kilty K, Chapman DS (1980) Convective heat transfer in selected geologic situations. Ground Water. doi:10.1111/j.1745-6584.1980.tb03413.x
Kopf AJ (2002) Significance of mud volcanism. Rev Geophys. doi:10.1029/2000RG000093
Leblanc M, Razack M, Dagorne D, Mofor L, Jones C (2003) Application of Meteosat thermal data to map soil infiltrability in the central part of the Lake Chad basin, Africa. Geophys Res Lett. doi:10.1029/2003GL018094
Leblanc M, Favreau G, Maley J, Nazoumou Y, Leduc C, Stagnitti F, van Oevelen PJ, Delclaux F, Lemoalle J (2006) Reconstruction of Megalake Chad using shuttle radar topographic mission data. Palaeogeogr Palaeoclimatol. doi:10.1016/j.palaeo.2006.01.003
Leduc C (1991) Les ressources en eau du département de Diffa, Projet PNUD-DCTCDNER/86/001/. Direction Départementale de l'Hydraulique de Diffa, Diffa
Leduc C, Loireau M (1997) Fluctuations piézométriques et évolution du couvert végétal en zone sahélienne (sud-ouest du Niger). Sustainability of Water Resources under Increasing Uncertainty. In: Proceedings of the Rabat Symposium S1, IAHS, 240
Luo X, Vasseur G (2002) Natural hydraulic craking: numerical model and sensitivity study. Earth Planet Sci Lett. doi:10.1016/S0012-821X(02)00711-2
Maduabuchi C, Faye S, Maloszewski P (2006) Isotope evidence of palaeorecharge and palaeoclimate in the deep confined aquifers of the Chad basin, NE Nigeria. Sci Total Environ 370:467–479
Mahe G, Leduc C, Amani A, Paturel J-E, Girard S, Servat E, Dezetter A (2003) Augmentation récente du ruissellement de surface en region soudano-sahélienne et impact sur les ressources en eau. Hydrology of the Mediterranean and Semiarid Regions, Proceedings of an international symposium, IAHS, 278
Mainsant G, Jongmans D, Chambon G, Larose E, Baillet L (2012) Shear-wave velocity as an indicator for rheological changes in clay materials: lessons from laboratory experiments. Geophys Res Lett. doi:10.1029/2012GL053159
McKenzie DP, Roberts JM, Weiss NO (1974) Convection in the earth's mantle: towards a numerical simulation. J Fluid Mech. doi:10.1017/S0022112074000784
Neal JT, Langer AM, Kerr PF (1968) Giant desiccation polygons of Great Basin playas. Bull Geol Soc Am. doi:10.1130/0016-7606(1968)79[69:GDPOGB]2.0.CO;2
Norton DL (1984) Theory of hydrothermal systems. Annu Rev Earth Planet Sci 12:155–177
Nwankwo CN, Ekine AS (2010) Geothermal gradients in the Chad basin, Nigeria, from bottom hole temperature logs. Sci Afr 9(1):37–45
Olivry JC, Chouret A, Vuillaume G, Lemoalle J, Briquet JP (1996) Hydrologie du lac Tchad. Monogr Hydrol 12:266
Olugbemiro OR, Ligouis B (1999) Thermal maturity and hydrocarbon potential of the Cretaceous (Cenomanian-Santonian) sediments in the Bornu (Chad) basin, NE Nigeria. Bull Soc Géol France 170(5):759–772

OSS-UNESCO (2001) Les ressources en eau des pays de l'Observatoire du Sahara et du Sahel: évaluation, utilisation et gestion. Rapport UNESCO, p 88
Pouclet A, Durand A (1983) Structures cassantes Cénozoïques d'après les phénomènes volcaniques et néotectoniques au nord-ouest du lac Tcahd (Niger Oriental). Ann Soc Géol Nord CIII (France), pp 143–154
Pribnow D, Schellschmidt R (2000) Thermal tracking of upper crustal fluid flow in the Rhine Graben. Geophys Res Lett. doi:10.1029/2000GL008494
Quintard M, Bernard D (1986) Free convection in sediments. In: Burrus J (ed) Thermal modeling in sedimentary basins. Editions Technip, Paris, pp 271–286
Rabinowicz M, Boulègue J, Genthon P (1998a) Two- and three-dimensional modeling of hydrothermal convection in the sedimented Middle Valley segment, Juan de Fuca Ridge. J Geophys Res. doi:10.1029/98JB01484
Rabinowicz M, Sempéré J-C, Genthon P (1998b) Thermal convection in a vertical permeable slot: Implications for hydrothermal circulation along mid-ocean ridges. J Geophys Res. doi:10.1029/1999JB900259
Ramillien G, Biancale R, Gratton S, Vasseur X, Bourgogne S (2011) GRACE-derived surface mass anomalies by energy integral approach. Application to continental hydrology. J Geod. doi:10.1007/s00190-010-0438-7
Ramillien G, Seoane L, Frappart F, Biancale R, Gratton S, Vasseur X, Bourgogne S (2012) Constrained regional recovery of continental water mass time-variations from GRACE-based geopotential anomalies over South America. Surv Geophys. doi:10.1007/s10712-012-9177-z
Ramillien G, Frappart F, Seoane L (2014) Application of the regional water mass variations from GRACE satellite gravimetry to large-scale water management in Africa. Remote Sens. doi:10.3390/rs6087379
Roche MA (1980) Traçage naturel isotopique et salin des eaux du système hydrologique du Lac Tchad, Paris
Sabins LF (1999) Remote sensing: principles and interpretation. W. H. Freeman, San Francisco
Schneider JL (1969) Carte hydrogéologique de la République du Tchad, B.R.G.M
Schneider JL, Wolff JP (1992) Carte Géologique et Hydrogéologique à 1/1 500 000 de la république du Tchad. Mémoire explicatif, B.R.G.M
Schroeter P, Gear D (1973) Etude des ressources en eau du bassin du Lac Tchad en vue d'un programme de développement. FAO-PNUD-CBLT, Rome
Schuster M, Roquin C, Duringer P, Brunet M, Cagny M, Fontugne M, Mackaye HT, Vignaud P, Ghienne J-F (2005) Holocene Lake Mega-Chad palaeoshorelines from space. Quat Sci Rev. doi:10.1016/j.quascirev.2005.02.001
Schwinka V, Moertel H (1999) Physicochemical properties of illite suspensions after cycles of freezing and thawing. Clays Clay Miner 47:718–725
Sclater JG, Christie PAF (1980) Continental stretching: an explanation of the post-mid-Cretaceous subsidence of the central North Sea basin. J Geophys Res. doi:10.1029/JB085iB07p03711
Serafeimidis K, Anagnostou G (2015) The solubilities and thermodynamic equilibrium of anhydrite and gypsum. Rock Mech Rock Eng. doi:10.1007/s00603-014-0557-1
Sylvia DM (2004) Principles and applications of soil microbiology, 2nd edn. Pearson Prentice Hall, New Jersey
Turcotte DL, Schubert G (2002) Geodynamics, 2nd edn. Cambridge University Press, Cambridge
Zairi R (2008) Etude géochimique et hydrodynamique de la nappe libre du Bassin du Lac Tchad dans les regions de Diffa (Niger oriental) et du Bornou (nord-est du Nigeria). Ph.D. thesis

DOI 10.1007/978-3-319-32449-4_13
Reprinted from *Surveys in Geophysics* Journal, DOI 10.1007/s10712-015-9335-1

# Water and Food in the Twenty-First Century

**Ghislain de Marsily**[1,2] · **Rodrigo Abarca-del-Rio**[3]

Received: 24 March 2015 / Accepted: 4 August 2015 / Published online: 2 September 2015


**Abstract** In 2000, the World population was 6.2 billion people; it reached 7 billion in 2012 and is expected to reach 9.5 billion (±0.4) in 2050 and 11 billion (±1.5) in 2100, according to the 2012 UN projections (Gerland et al. in Science 346:234–237, 2014). The trend after 2100 is still one of the global demographic growths, but after 2060, Africa is the only continent where the population would still increase. The amount of water consumed annually to produce the food necessary to meet the needs of the populations varies greatly between countries, from about 600 to 2500 $m^3$/year per capita (Zimmer in L'empreinte eau. Les faces cachées d'une ressource vitale. Charles Léopold Meyer, Paris, 2013), depending on their wealth, their food habits, and the percentage of food waste they generate (on average, 30 % of the food produced is wasted). In 2000, the total food production was on the order of 3300 million tons (in cereal equivalents). In 2014, it is estimated that about 0.8 billion inhabitants of the planet suffer from hunger (FAO in World agriculture: towards 2030–2050. FAO, Rome, 2014. http://www.fao.org/docrep/004/Y3557E/y3557e00.HTM) and do not get the nutrition they need to be in good health or, in the case of children, to grow properly (both physically and intellectually). This food deficit was on the order of 40 million tons of cereal equivalents in 2014. The number of inhabitants with a food deficit was about 0.85 billion before the 2008 crisis and was decreasing annually, but it increased abruptly after 2008 up to 1 billion inhabitants and is slowly decreasing now. Assuming a World average water consumption for food of 1300 $m^3$/year per capita in 2000, 1400 $m^3$/year in 2050, and 1500 $m^3$/year in 2100, a volume of water of

✉ Ghislain de Marsily
gdemarsily@aol.com

Rodrigo Abarca-del-Rio
rodrigo.abarcadelrio@udec.cl

[1] Sorbonne Universités, UPMC Univ. Paris 06, CNRS, EPHE, UMR 7619 Metis, 4, place Jussieu, 75005 Paris, France

[2] French Academy of Sciences, 23 quai de Conti, 75006 Paris, France

[3] Departamento de Geofísica (DGEO), Facultad de Ciencias Físicas y Matemáticas, Universidad de Concepción, Concepción, Chile

around 8200 km$^3$/year was needed in 2000, 13,000 km$^3$/year will be needed in 2050, and 16,500 km$^3$/year in 2100 (Marsily in L'eau, un trésor en partage. Dunod, Paris, 2009). Can bioenergy be added to food production? Will that much water be available on Earth, and where will it come from? Is climate change going to modify the answers to these questions? Can severe droughts occur? Can there be conflicts related to a food deficit? Some preliminary answers and scenarios for food production will be given in this paper from a hydrologist's viewpoint.

**Keywords** World water stocks and balance · Climate change · Food supply · Bioenergy · Green and blue water · Virtual water · El Niño · Water conflicts

## 1 Where Does the Water We Use Today Come From?

Natural water on Earth has two origins: the perennial water cycle, the major one, and the stocks of freshwater. Below is an assessment of the origin and use of water for the year 2000, for which most of the data are available, but one must keep in mind that all these numbers come from different sources, may not always be consistent, and are all uncertain.

### 1.1 Freshwater Stocks

The freshwater stocks are very large (see, for example, Marsily 2009): about 28.2 million km$^3$ of ice and 15 million km$^3$ of groundwater (which may be brackish in many places), plus about 0.3 million km$^3$ in lakes, and 8500 km$^3$ in artificial reservoirs (Chao et al. 2008), plus the newly discovered 0.5 million km$^3$ of semi-freshwater stored in aquifers beneath the seabed (Post et al. 2013), whose magnitude and salinity still need to be confirmed and which may be difficult to exploit. The ice stock is decreasing because of climate change (IPCC 2014), and today the flow in the rivers from high mountains with glaciers is increased because the ice is melting.

In fact, according to Rabatel et al. (2013), the tropical Andes harbour more than 99 % of all tropical glaciers: Peru (71 %), Bolivia (20 %), Ecuador (4 %), and Colombia–Venezuela (4 %). Most of the glaciers in the Cordillera Blanca, the largest tropical glacier train in the World, are predicted to disappear, especially at lower elevations (Bradley et al. 2006; Vuille 2013) and some as soon as between 2025 and 2045 (Ramirez et al. 2007; Baraer et al. 2012). The predictions of all the different climate scenarios (IPCC 2014) are that they will melt as the warming rate has already accelerated over the last three decades and glacier loss is now occurring at an unprecedented rate (Vuille et al. 2008). In fact, glaciers all along the Andes cordillera, north to south, are reported to be retreating at varying rates and to be threatened by future climate change (Nicholson et al. 2009; Willis et al. 2012; Davies and Glasser 2012; Diaz et al. 2014). However, this retreat is particularly critical for Peru and Bolivia, as Peru's highly populated arid Pacific coast depends on water stocks from glacial melt (for drinking, irrigation, and hydroelectric power) to compensate for the lack of rainfall, especially during the May to September dry season, when nearly all of the river flow is due to glacial melt (Chevallier et al. 2011). In Bolivia, glaciers in the southern Cordillera Real supply approximately 15 % (30 % during the dry season) of the drinking water for the urban areas of La Paz and El Alto (Ramirez et al. 2007; Soruco 2012; Moya Quiroga et al. 2014).

The groundwater stocks are also decreasing, as shown in Table 1, taken from Zimmer (2013) and Wada et al. (2012).

In Table 1, the countries are listed in decreasing order of annual groundwater withdrawals for irrigation. The data are for the year 2000. The second column is the excess withdrawal, i.e. the amount of water taken from stocks. The third column is the total consumption by irrigation, from groundwater and surface water. The numbers in the line "Planet Earth" show the sum for all countries where estimates were available and not just for the first six listed. These numbers are quite uncertain; other authors reach values about half as high as these, see, for example, Konikow (2011), Döll et al. (2014, 2015, this volume). But the comparison of the withdrawals from the stocks with the total amount of irrigation water is of concern. About 10 % of the irrigation water used today is non-sustainable and comes from groundwater stocks that eventually will run out. This is of special concern at least for India and China, where the stocks will last for perhaps another 10–30 years. The annual amount taken from stocks is relatively small compared to the global stocks (256 $km^3$ compared to 15 million $km^3$), but this is a false image: what matters is the volume of residual freshwater stocks that can be exploited at the local and not at the global scale: if the stock is large, e.g., in the Sahara desert or in Siberia, is it of any use in India or China?

## 1.2 The Water Cycle

The renewable fresh water resources of Planet Earth, adapted from Shiklomanov (1999), Shiklomanov and Rodda (2003) and Trenberth et al. (2007), are estimated today at 113,000 $km^3$/year, which is the total amount of rainfall and snowfall on the continental surfaces including the Antarctic and Greenland ice sheets (but not the floating ice of the Arctic). This corresponds on average to a rain depth of 840 mm $year^{-1}$. The fate of this rainwater is as follows:

- 73,000 $km^3$/year (65 %) returns to the atmosphere, by direct evaporation and mostly by plant transpiration. This amount is partly used by rain-fed agriculture and pasture (in 2000, 6300 $km^3$/year) and sustains the needs of all terrestrial ecosystems. It is used to 100 % by nature; hence, it is by no means a "loss." It is now called "*Green Water*" (Hoekstra et al. 2011; Hoekstra and Mekonnen 2012).

**Table 1** Amount of irrigation water taken from the groundwater stocks, for the year 2000; from Zimmer (2013) and Wada et al. (2012)

| Country | Amount of groundwater pumped annually ($km^3$/year) | Amount of excess withdrawal compared to natural recharge ($km^3$/year) | Total annual consumption for irrigation ($km^3$/year) |
|---|---|---|---|
| India | 190 | 71 | 600 |
| USA | 115 | 32 | 204 |
| China | 97 | 22 | 403 |
| Pakistan | 55 | 37 | 183 |
| Iran | 53 | 27 | 59 |
| Mexico | 38 | 11 | 71 |
| Total | 548 | 200 | 1520 |
| Planet Earth | 734 | 256 | 2510 |

- 4000 km$^3$/year (3 %) represents the melting of icebergs, broken-off from the Antarctic and Greenland ice sheets, which melt in the sea and participate in the general ocean circulation.
- 36,000 km$^3$/year (32 %) is the total flow on the continents, which is called "*Blue Water*"; it consists of:
- 26,000 km$^3$/year (23 %) of direct runoff into rivers when it rains; part of which can be used directly, or stored in reservoirs for later use. This water is also used by the aquatic ecosystems, in wet zones, rivers, lakes, and coastal zones.
- 10,000 km$^3$/year (9 %) infiltrates into the ground and feed the aquifers, which in turn feed the rivers when it does not rain (7800 km$^3$/year), or flow directly into the seas or endorheic zones (2200 km$^3$/year).

A first step is to define the resource available to humans based on these numbers. In general, the volume of 73,000 km$^3$/year of evapotranspired water going back to the atmosphere (*Green Water*) is not considered a resource, which constitutes a major error since, e.g. for the year 2000, of the estimated 8200 km$^3$/year of water consumed[1] by agriculture to produce our food, about 6300 km$^3$/year is *Green Water* (5500 km$^3$/year on rain-fed farm land, over 1.34 billion ha, and 0.840 km$^3$/year on rain-fed pasture, over 3.3 billion ha), and only 1800 km$^3$/year is *Blue Water*, used for irrigation on 0.26 billion ha of irrigated land (Griffon 2006; Académie des Sciences 2006; Marsily 2009). The total surface area of the continents is 13.3 billion ha, of which (according to the FAO 2002, for 2000) approximately 1.6 is farm land, 3.7 is forest, 4.6 is grass and shrub, and 3.4 is bare land; the total area that could potentially be farmed, at the expense of forests and grass and shrub, is 4.2 billion ha. Let us assume for a moment that all the arable land on Earth was used for rain-fed agriculture. The water evapotranspired by these 4.2 billion ha would amount to approximately 23,000 km$^3$/year (assuming linearity between area and evapotranspiration), which is still larger than the estimated water needs to feed 11 billion inhabitants in 2100 (16,500 km$^3$/year).

However, the arable land that is not directly farmed by humans today, about 2.6 billion ha, is of course not bare soils: it contains all the remaining natural ecosystems, from the tropical forests to the northern forests, the grass lands, the bush land, the wetlands, etc. Transforming more land into farmland for agriculture, where this is possible, therefore, has an environmental cost, i.e. that of reducing natural ecosystems and biodiversity.

Similarly, when water is withdrawn from a river, e.g., for irrigation purposes, it is also withdrawn from the normal functioning of a natural ecosystem. In these systems, life has become adapted to making use of the resource, as efficiently as possible. The aquatic life is therefore at equilibrium with the natural flow, its seasonal variations, its floods and inundation of the plains, its droughts and their frequency, etc. Any withdrawal of water or any artificial regulation (e.g., by a dam) of the natural functioning of the system will inevitably have a negative impact on the natural ecosystems, from the source to the mouth of the river, and even on coastal areas whose ecosystems depend on the flux of freshwater into the sea for their survival. Note, however, that on average, at the global scale, one ha of irrigated land produces about three times more food than one ha of rain-fed land (Musy and Higy 2010).

Thus, the reality is as follows: the global renewable resource of freshwater on Earth (total rainfall on the continents, 113,000 km$^3$/year) is very large, and today less than 10 %

[1] The "consumed" water is that which is evaporated and returns to the atmosphere; in irrigation, it represents on average 75 % of the withdrawal; in domestic and industrial use, it represents about 15 % of the withdrawal, the rest is the return flow which goes back to the continental water cycle.

of it is used by humans, but the remaining 90 % are entirely used to sustain the natural ecosystems, and the biodiversity that makes the World what it is. Globally, it may be possible to increase the part of the resource used by humans, but only at the expense of the functioning of the natural ecosystems. The question is then: Where is the least damage done by withdrawing water from the natural systems?

The water resource is unequally distributed on Earth. At high latitudes, in the so-called cold deserts, precipitation is very low, <200 mm/year. Rainfall increases in the temperate zone, where it reaches 700–1000 mm/year and then decreases (at the latitude of the Mediterranean zone) to practically zero at the latitude of the "hot deserts," such as the Sahara, the Arabic Peninsula, the Taklimakan desert, and Mexico. It then increases again in the tropical and equatorial zone, to reach an order of 2300 mm/year. The same type of climate distribution is found for every meridian and in both hemispheres (Shelton 2009).

In Table 2, from Viviroli et al. (2007), the percentage of the World population is given as a function of the climate and vegetation zones, with the amount of direct river runoff. One can see that the World population is not distributed in accordance with the water resource. This is one reason for the local water shortages. Figure 1 gives the areas of the World where there are water shortages at present (Rijsberman 2006; IWMI 2007; WWAP 2012; WWDR 2012), based on *Blue Water* only. But two causes are outlined on this map: (1) physical water scarcity, where more than 75 % of the river flow (*Blue Water*) is withdrawn for human use, and (2) economical water scarcity, where the *Blue water* is available, but not exploited for lack of resources to finance the equipment to do so (dams, canals, irrigation systems, etc.). This zone of "economical scarcity" harbours the 0.8–1 billion undernourished inhabitants of the planet, not the "physical scarcity" zone. This is very important to realize that hunger is not, today at least, linked to a lack of water.

### 1.3 Virtual Water, Example of Tunisia

The concept of *"Virtual Water"* was introduced by Allan (1998). It represents the amount of water needed to produce the goods that are imported or exported from one country to another. In this case, the goods are agricultural products, but it could be any kind of product. To truly understand the role of *Virtual water* in the water balance of a country,

**Table 2** Climate classification adapted from Leemans (1992) and life zones from Holdridge (1967); in Viviroli et al. (2007)

| | Contains aggregated *Holdridge* life zones | *A* (%) | POP (%) | *Q* (%) | *q* (mm year$^{-1}$) |
|---|---|---|---|---|---|
| Polar and cold | Tundra and polar; cold parklands | 14.8 | 3.2 | 11.9 | 245 |
| Cool | Forest tundra; boreal forest | 11.3 | 4.0 | 11.6 | 313 |
| Temperate | Temperate forest; warm temperate forest | 9.9 | 23.3 | 15.2 | 465 |
| Steppe | Steppe; chaparral | 9.7 | 13.6 | 1.9 | 59 |
| Arid | Cool desert; hot desert | 18.5 | 7.9 | 0.3 | 5 |
| Sub-tropical | Tropical semi-arid; tropical dry forest | 18.3 | 24.8 | 8.8 | 147 |
| Humid tropical | Tropical seasonal forest; tropical rain forest | 17.5 | 23.2 | 50.3 | 872 |

*A:* Share in continental surface area (total: 133.6 million km$^2$)

POP: Share in global population (total: 6.2 billion people in 2000)

*Q*: share in global discharge (total: 36,000 km$^3$ year$^{-1}$)

*q*: Average runoff, mm year$^{-1}$; Antarctica and glaciated parts of Greenland are excluded

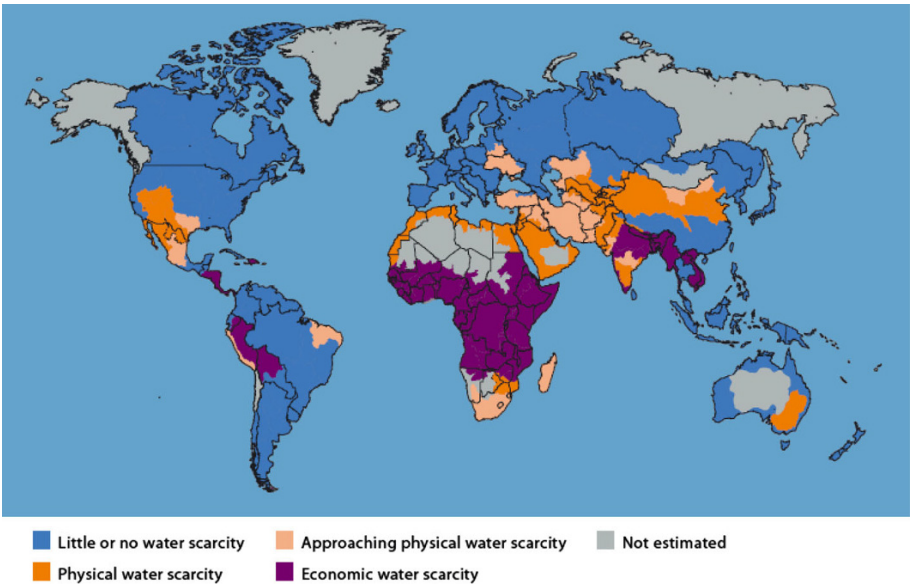


**Fig. 1** Physical and economic water scarcity (WWAP 2012)

take one example, Tunisia, a country in the arid zone where the water balance has been thoroughly studied for a long time (Chahed et al. 2008; Besbes et al. 2009, 2014). The presentation below is taken from these authors.

Tunisia is situated in North Africa and bordered by Algeria, Libya, the Mediterranean Sea, and the Sahara. The country has a surface area of 164,420 $km^2$ and had 10 million inhabitants in 2004, and 10.8 in 2013, according to the National Institute of Statistics—Tunisia. It has about 5 million ha of agricultural land, 11 % of which can be irrigated. The average rainfall is 220 mm/year, which translates into a rainfall resource of 36 $km^3$/year. Total hydraulic resources (*Blue Water*) are estimated at 5 $km^3$/year with the current climate, i.e. 3 $km^3$/year of runoff and 2 $km^3$/year of groundwater flow. It is considered that 2.1 $km^3$/year of surface water can be exploited through dam construction, and 1.8 $km^3$/year sustainably supplied by groundwater. The *Green water*, which is part of the rainfall resource infiltrated into the soil and available for evaporation and consumption by plants, is 23 $km^3$/year, of which 13 $km^3$/year refer to the whole extent of arable land (5 million ha), and 10 $km^3$/year to forest and rangeland. The remaining part of the rainfall is evaporated on bare soils and by wetlands, or transferred to the Mediterranean.

The water demand for food is estimated from the amount of water needed to produce it (Table 3). It is evident that animal products are very demanding compared to vegetal products. This is due to the fact that animals eat vegetal products (e.g., grain, soya) and to the low efficiency of vegetal-to-animal product transformation.

Based on the average diet in Tunisia, the food water demand in 2004 was about 1450 $m^3$/year per capita, while it was only 600 $m^3$/year in 1960, Fig. 2. This strong increase is due to diet changes, in particular an increase in animal product consumption. With 10 million inhabitants in 2004, the water demand for food was 14.5 $km^3$/year, when the available water resource used for agricultural production was 10 $km^3$/year (*Irrigation, Blue* 2 and *Rain-fed, Green* 8). Tunisia was therefore in theory short of about 5 $km^3$/year of

**Table 3** Water needed for food production

| Vegetal product | Water needed ($m^3$ $t^{-1}$) | Animal product | Water needed ($m^3$ $t^{-1}$) |
|---|---|---|---|
| Vegetable oil | 5000 | Beef | 13,000 |
| Rice | 1500–2000 | Poultry | 4100 |
| Wheat | 1000 | Eggs | 2700 |
| Corn | 700 | Milk | 800 |
| Citrus fruits | 400 | | |
| Vegetables | 200–400 | | |
| Potatoes | 100 | | |

Average values of water used in $m^3$/t to produce raw food (consumed fraction, not in dry matter) (Renault and Wallender 2000; Zimmer 2013)

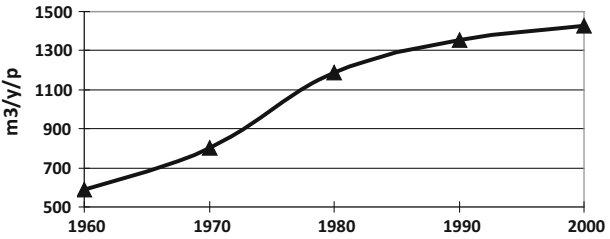


**Fig. 2** Evolution of the per capita water equivalent ($m^3$/year) of the Tunisian food demand during the last 40 years

**Table 4** Comprehensive water consumption of Tunisia (average values for the years 2000); from Besbes et al. (2009)

| Sector | Water consumption ($km^3$/year) |
|---|---|
| Irrigation | 2.1 |
| Rain-fed agriculture | 6 |
| Net imported virtual water | 3.7 |
| Urban water | 0.4 |
| Industrial water | 0.1 |
| Forests and rangelands | 5.5 |
| Water storage in dams for future droughts | 0.6 |
| Environment (conservation of wet zones) | 0.1 |
| Total water consumption | 18.5 |

water to meet its food demand and was obliged to import food (mostly cereals) as "*Virtual Water*" to balance its water budget. Table 4 gives the actual mean water consumption per type of activity for the years 1990, based on production and trade statistics of food products.

The direct water needs, which include municipalities, industry, and tourism, are small (3 %) compared to the agricultural demand. In average rainfall years, half of the water required to meet Tunisian food requirements is provided by rain-fed agriculture (*Green water*), one-sixth by irrigated agriculture (*Blue water*), and almost one-third by *Virtual water* in the form of imported food. Tunisia imports the water equivalent of 5.2 $km^3$/year, essentially in the form of cereals, and exports agricultural products such as citrus fruit, dates, olive oil, and early-season vegetables equivalent to 1.5 $km^3$/year for an average

annual net deficit of 3.7 $km^3$/year (Chahed et al. 2008). In 2025, with about 12 million inhabitants, and probably less water available because of climate change, virtual water is likely to increase to 50 % of the food demand.

Tunisia's food security goals are to satisfy, as far as possible, its basic food needs (cereals, oil, meat, milk). However, it cannot be self-sufficient in some of these products. Most importantly, climate variations cause large fluctuations in the yield from rain-fed agriculture (Besbes et al. 2009). The food trade balance of Tunisia has been negative during the last three decades, except for the rainy years of 1991, 1999, and 2004. This balance depends strongly on cereal imports, which represent close to 45 % of the total value of food commodity imports.

Large-scale hydraulic programmes to increase the *Blue Water* availability make the water cycle highly artificial, which leads to a reduction in the water feeding natural hydrologic systems, with consequences for the behaviour of continental and coastal aquatic ecosystems; a reduction in recharge to aquifers from wadis (the Arabic term for an ephemeral stream or a dry riverbed where water flows only during the rainy season) situated downstream of large dams; and a progressive salinization of soils irrigated with highly saline water. In these conditions, the protection of the environment and of the resources requires a continuous assessment of the environmental water demand, which should be included in the planning of water allowances: artificial floods for wetlands and groundwater recharge or additional irrigation share to prevent salinization of irrigated soils. Increased irrigation shares for salt leaching in soils were allocated early on, whereas the understanding of other environmental needs requiring a direct water allowance from exploited resources has been progressive and is now an essential component of water resource planning and management. On a national level, the environmental water demand remains small compared to urban and agricultural requirements, but it represents a growing concern in the planning of future hydraulic programs.

Sometime in the 1980s, by its demographic growth and food diet changes, Tunisia reached a situation where it was no longer self-sufficient in the balance of its food budget (or its water budget) and needed to import food (cereals) or "*Virtual Water*." To balance its financial budget, Tunisia needs to export products or services to raise the money needed for food import: phosphates minerals (Tunisia has no significant hydrocarbon nor coal resources), textiles, tourism, services, etc. Provided that food (cereals) is available on the international market, the real problem of Tunisia, given its demographic situation, is not water; it is how to raise the money needed to buy food in the market. In this context, the best use of the available *Blue water* may not be agriculture, but other industrial or service activities, with better water efficiency (in terms of $/$m^3$) and better job efficiency (in terms of jobs/$m^3$) than that offered by agriculture.

But is food available on the World market and likely to remain so in the future?

## 2 Scenarios for Food Production in 2050

Table 5 (part 1, situation in 2000) is an estimate for 2000 of how much food the planet produced, with a zonation taken from the Millennium Ecosystem Assessment Report (2005). Listed per zone are: its area, the area suitable for agriculture, the water resources (rain, *Green* and *Blue water*, potentially exploitable *Blue water*), the cultivated area in 2000, the percentage of cultivated arable land, the population, the food need, in million tons of cereal equivalent (i.e. each type of food is converted into cereals), the average yield

**Table 5** Estimates for the years 2000 and 2050 of the planet food production, based on the cultivated area of agricultural land, yields global amount of water *consumed (not withdrawn)* by humans from the water cycle (*Blue and Green Water*) and food needs (adapted from Griffon 2006; Marsily 2007, 2009; Agrimonde 2010; Académie des Sciences 2011; Zimmer 2013)

| Area | Asia | Latin America | West Asia and North Africa | Sub-Saharan Africa | OECD | Russia + CIS | World |
|---|---|---|---|---|---|---|---|
| Area, million ha | 2090 | 2070 | 1180 | 2430 | 3380 | 2190 | 13,340 |
| *Situation in 2000* | | | | | | | |
| Area suitable for agriculture (million ha) | 585 | 1066 | 99 | 1031 | 874 | 497 | 4152 |
| Water resources, thousands of $km^3$/year | | | | | | | |
| Rainfall | 21.6 | 30.6 | 1.8 | 19.9 | 22.4 | 9.2 | 105.5 |
| *Green water* | 11.9 | 8.3 | 1.5 | 15.5 | 14.3 | 2.5 | 54 |
| *Blue water* | 9.8 | 13.2 | 0.25 | 4.4 | 8.1 | 4 | 39.7 |
| Exploitable *Blue water* and ratio to Total *Blue water* | 9.3<br>95 % | 8.7<br>66 % | 0.24<br>96 % | 4.1<br>93 % | 5.6<br>69 % | 1.8<br>45 % | 29.7<br>75 % |
| Cultivated area, million ha (2000) | 439 | 203 | 86 | 228 | 377 | 255 | 1564 |
| % Cultivated | 75 % | 19 % | 87 % | 22 % | 43 % | 51 % | 37 % |
| Population (million) | 3322 | 538 | 372 | 706 | 987 | 279 | 6200 |
| Food need (million tons/year) | 1310 | 350 | 220 | 250 | 1020 | 190 | 3340 |
| Food production (million tons/year) | 1270 | 425 | 145 | 200 | 1070 | 190 | 3300 |
| Average yield, t/ha<br>and $m^3$/t | 2.96<br>2830 | 2.12<br>2420 | 1.71<br>1860 | 0.92<br>6150 | 2.84<br>1040 | 0.75<br>4600 | 2.11<br>2480 |
| Water consumed, thousands $km^3$/year | | | | | | | |
| *Blue + Green* | 3.6 | 1.03 | 0.27 | 1.23 | ~1.12 | 0.89 | 8.14 |
| % of rainfall | 16 % | 3.3 % | 15 % | 6 % | 5 % | 10 % | 8 % |
| % *Blue water* for irrigation | ~30 % | 11 % | 53 % | 3 % | ~17 % | 21 % | 22 % |
| % *Green water* | ~70 % | 89 % | 47 % | 97 % | ~83 % | 79 % | 78 % |
| Food Deficit/Excess million tons/year | −40 | +75 | −75 | −50 | 50 | 0 | −40 |
| Protected areas, million ha | 156 | 866 | 14 | 813 | 497 | 242 | 2588 |

**Table 5** continued

| Area | Asia | Latin America | West Asia and North Africa | Sub-Saharan Africa | OECD | Russia + CIS | World |
|---|---|---|---|---|---|---|---|
| *Situation expected in 2050* | | | | | | | |
| Variation of area suitable for agriculture due to climate change, million ha | −40 | −40 | −10 | −20 | +80 | +80 | +50 |
| Resulting area available for agriculture | 545 | 1026 | 89 | 1011 | 954 | 577 | 4202 |
| Food need, million tons/year | 2720 | 665 | 455 | 800 | 1300 | 240 | 6180 |
| *Production scenario 1, 2050* | | | | | | | |
| Variation of cultivated area, million ha | +51 | +346 | +4 | +500 | +80 | +80 | +1061 |
| Resulting cultivated area | 480 | 546 | 89 | 718 | 457 | 335 | 2625 |
| Expected yield, t/ha<br>and variation | 4,29<br>+45 % | 2,33<br>+10 % | 1,88<br>+10 % | 1,11<br>+21 % | 3,38<br>+20 % | 1<br>+33 % | 2,35<br>+12 % |
| Food production, million t/year | 2060 | 1270 | 170 | 800 | 1545 | 335 | 6180 |
| Food Deficit/excess, million tons/year | −660 | +605 | −285 | 0 | +245 | +95 | 0 |
| Protected areas, million ha | 65 | 480 | 0 | 293 | 497 | 242 | 1577 |
| *Production scenario 2, bioenergy, 2050* | | | | | | | |
| Cultivated area for bioenergy, million ha | 25 | 220 | 0 | 120 | 150 | 70 | 585 |
| Expected yield, tons of oil equivalent (toe)/ha | 4 | 4 | 0 | 3 | 2,5 | 2 | 3,2 |
| Energy production, million toe/year | 100 | 880 | 0 | 360 | 375 | 140 | 1855 |
| Protected areas, million ha | 40 | 260 | 0 | 173 | 347 | 172 | 992 |

All these numbers are highly uncertain and sometimes based on the assumption of a linear proportion with the population. They are only orders of magnitudes, not precise estimates

in t/ha, the amount of water consumed (blue water, green water, and % of rainfall), the food deficit or excess, and finally the amount of arable land that is not cultivated and kept as "natural areas," i.e. forest or grassland. Note that these numbers come from different sources and are often not consistent (and therefore adjusted so as to be consistent in Table 5) and highly uncertain; they provide only orders of magnitude.

The water consumed by agriculture in 2000 was 8140 $km^3$/year: 1.34 billion ha of rain-fed agriculture, consuming 5500 $km^3$/year of water; 3.3 billion ha of rain-fed pasture, consuming 840 $km^3$/year; and 234 million ha of irrigated agriculture, consuming 1830 $km^3$/year of water. It represents 97 % of the total water consumption by man. Three major cereals, rice, wheat, and maize, each representing approximately one-third, constitute 60 % of the food consumption. The total food production is about 3.3 billion tons of cereal equivalents per year, for 6.2 billion people. However, about 1 billion are undernourished; the amount of the food deficit is about 40 million tons per year, mostly in Asia and Sub-Saharan Africa, as shown in Fig. 1. The current rate of food production increase does not correspond to that of the demographic growth or, at least, does not reduce the food deficit fast enough. The food yield is on average 2.11 t/ha, but varies greatly from 0.75 (Russia and the Commonwealth of Independent States, CIS), 0.92 (Sub-Saharan Africa, SS-Africa) to about 2.9 (Asia and the countries of the Organization for Economic Co-operation and Development, OECD). The water efficiency ($m^3$ of water used to produce 1 t of cereals) is on average 2460 $m^3$/t, with SS-Africa at 6150 $m^3$/t, Russia + CIS at 4600 $m^3$/t and OECD at 1040 $m^3$/t.

The first observation is that the major problems are expected to occur in Asia and in the West Asia–North Africa (WANA) countries, where the ratio of consumed water (*Blue* + *Green*) to rainfall is about 16 % (World average: 8 %) and, most importantly, the ratio of farm land to arable land is 75 and 87 %, respectively (World average: 37 %). The major issue concerning food, as we will see, is the availability of arable land, not water. The consumed water is on World average 78 % *Green water* and 22 % *Blue water*, but again Asia and WANA have quite different ratios: 70 % *Green* and 30 % *Blue*, and 53 % *Green* and 47 % *Blue*, respectively. A final observation is that "natural" (protected) land, i.e. arable land that is not cultivated and is covered by forests and grassland, is mostly found in Latin America (33 % of the total), Sub-Saharan Africa (31 %), and OECD countries (19 %).

To predict the food balance for the years 2050 or 2100, one needs to determine:

- the number of inhabitants on Earth,
- their eating habits and the amount of wasted food,
- the efficiency of food production per $m^3$ of water, i.e. the efficiency of the agricultural water use,
- the effects of climate change,
- the amount of cultivated land.

To answer the first question, recent demographic projections made by the UN (2012, see Gerland et al. 2014; Fig. 3) converge towards 9.5 billion inhabitants (from 9.1 to 9.9) in 2050 and towards 11 billion in 2100 (from 9.5 to 12.5), but the demographic growth will continue after 2100, mainly in Africa.

The second question (eating habits) is more difficult. Table 3 shows the amount of water needed to produce the different types of food consumed today, and Table 5 the water actually used per geographic zone and the yield. If a country goes from a mostly vegetarian diet to a meat-rich one, the amount of water required for food production will greatly increase, as, for example, one kg of beef requires 13 times more water than one kg of

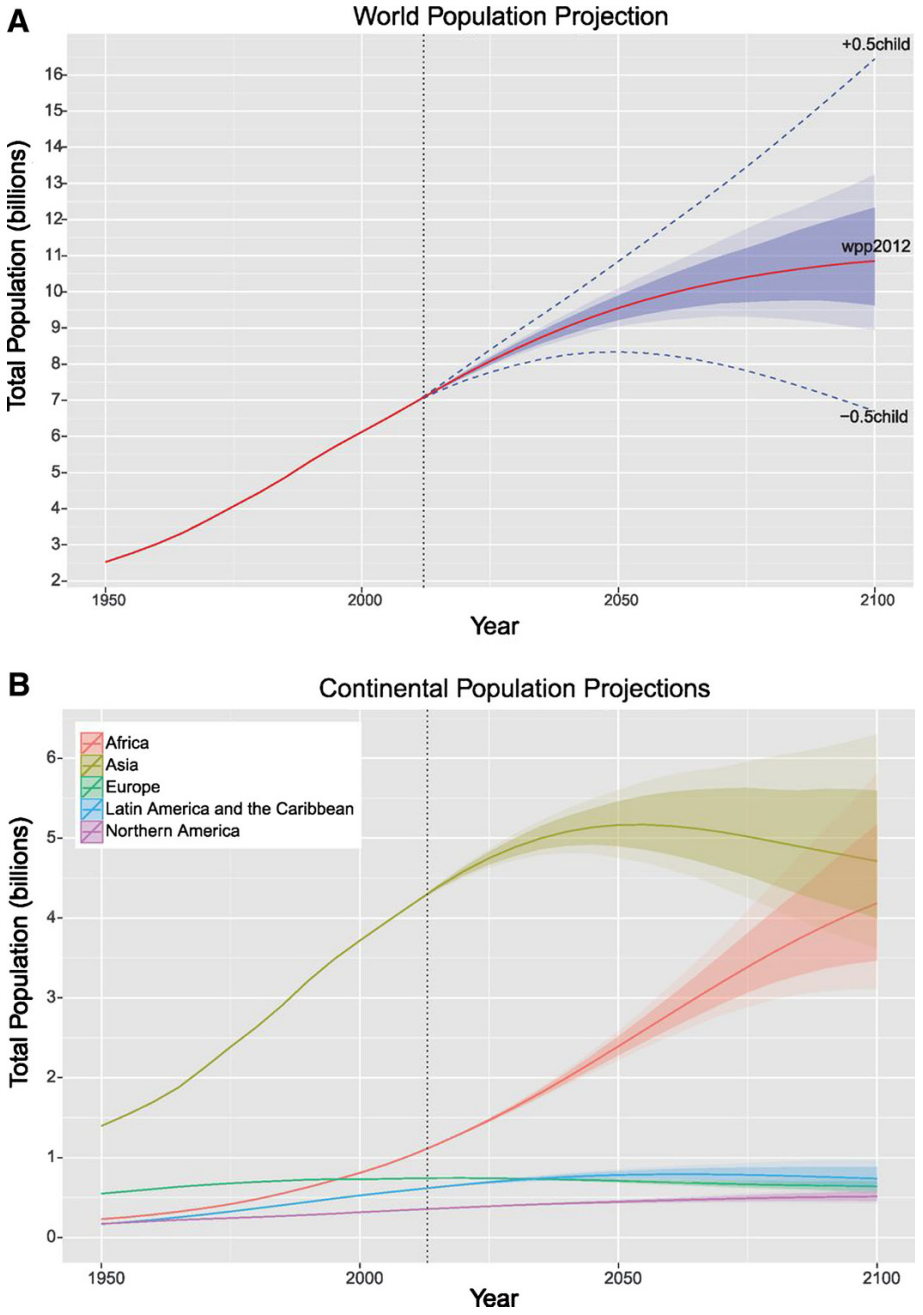


**Fig. 3** Demographic growth as projected by the UN in 2012, from Gerland et al. (2014). World and continental population projections. **A** UN 2012 World population projection (*solid red line*), with 80 % prediction interval (*dark shaded area*), 95 % prediction interval (*light shaded area*), and the traditional UN high and low variants (*dashed blue lines*). **B** UN 2012 population projections by continent. In both panels, the *vertical dashed line* denotes 2012

wheat. At this moment, Asia is more vegetarian than meat consuming, but this is changing rapidly, in particular in China and India. Assumptions have thus to be made on the evolution of food habits.

The third question concerning agricultural efficiency (see Table 5) is also difficult to answer, particularly for such a long forecasting period, i.e. 35–85 years. But it is generally assumed that water use efficiency could be increased by 20 % by 2050, i.e. that the same amount of food could be produced with 20 % less water. In short, "more crop per drop" is feasible. When the yield is good (e.g. above to 2–3 t/ha), the water consumption per ton is about that of Table 3, but when the yield is low (e.g. about 1 t/ha), the water consumption per ton becomes much higher (up to eight times more), because the plants are less developed, they do not cover the soil, and much water is evaporated, not transpired (Zimmer 2013; Rockström 2004). Increasing the yield (e.g., by better plant selection, use of fertilizers, protection against pests.) will also increase water efficiency.

The effects of climate change are discussed in Sect. 3.

Griffon (2006), Agrimonde (2010) and FAO (2015a), among many others, have built scenarios of food needs and food production increase for 2050. One of these scenarios is presented in Table 5, part 2, the situation for 2050. Compared to 2000, the increase in food production achieved by 2050 should be from 3300 to 6180 million t/year. This number takes into account population growth, the age of the population, the eradication of hunger, and diet changes as a linear continuation of what has been observed in the past 10 years. This food production increase can be obtained by:

- increasing yields and crop efficiency,
- increasing the amount of irrigated land,
- increasing the amount of cultivated rain-fed land,
- reducing food losses, which are currently estimated at 30 % of food production (SIWI 2008).

At present, the rate of areal increase in irrigated land is low, $< 2$ million ha/year. In the first few years of the new millennium, the World Bank and other funding agencies stopped financing large irrigation projects, as their technical and financial success was considered poor, but they are now revising their opinions. Unless its rate of increase is raised very rapidly, by at least a factor of ten, irrigation is not going to be the main factor of production growth. Scenario 1 in Table 5 is based on small technology changes, nominal investment in irrigation, and major increase in rain-fed agriculture in Africa, to satisfy the demand on this continent, in South America, Russia-CIS, and OECD countries, to compensate for the deficits, and in Asia and WANA, unable to be self-sufficient. Many tests have been performed, but the major conclusion is indeed that Asia and WANA countries cannot be self-sufficient food producers in 2050, as is already the case of WANA today. The limiting factor is soils for Asia and water for WANA. SS-Africa is currently in food deficit and must import food, but there is plenty of arable land and water in SS-Africa, and it could be self-sufficient, as is assumed in Table 5, but this is a very strong assumption and requires rapid development of the agricultural production in SS-Africa, which may or may not occur. The deficits from Asia and WANA are assumed to be met by extra production by Latin America, OECD countries, and Russia-CIS. But other scenarios could equally well have been built, with SS-Africa becoming an exporter, or with different ratios between the three exporting zones.

The net result of this scenario is that an increase of about 1 billion ha of rain-fed cultivated land would be required, thus reducing the "protected area" (non-cultivated arable land) by the same amount. This number is probably too large; other scenarios

produce half or even a third of that number, with different assumptions on yield and food habits. If this scenario is linearly extrapolated to 2100, with 11 billion inhabitants, a total production of 7200 million tons/year of cereal equivalents would be required, i.e. an additional increase in rain-fed cultivated land of about 0.4 billion ha and a residual "protected area" of 1.2 billion ha, instead of 2.6 today.

Scenario 2 in Table 5 is again taken from Griffon (2006). It assumes that in 2050, in addition to food production, land is also used to produce second-generation biofuels. In this scenario, 585 million ha are taken out of the pool of arable land to produce energy, at an average yield of 3.3 tons of oil equivalent (toe) per ha, producing 1.9 billion toe/year. According to Müller in FAO (2006), up to 25 % or the World energy needs could come from biofuels within 25 years. But these 1855 million toe would only represent 8 % of the energy needs of the planet in 2050, not 25 %, and would reduce the "protected area" to 1 billion ha in 2050.

Water desalination, often mentioned as the solution, is not a realistic option for food production, given its cost and energy requirements (from 2.5 to 6 kWh/$m^3$ for seawater with reverse osmosis). Just to provide an order of magnitude, if 4000 $km^3$/year of water (to produce, by irrigation, the additional food needed from 2000 to 2050) were to be produced from seawater desalination by reverse osmosis, it would require an amount of energy equal to half of that produced today per year from the current exploitation of hydrocarbons. Artificially growing food plants without soil can be efficient, but is also extremely costly and will most likely not be the solution. Increasing the food productivity by genetically selected or modified plants is certainly a fascinating research area but, according to Tardieu (2005), it is today very difficult to expect significant reduction in plant water consumption, as there is a trade-off between the evapotranspiration of water through the stomata of the leaves, and the capture of $CO_2$ for photosynthesis: reducing one also reduces the second. But plants more tolerant to droughts can probably be developed.

Raising insects to provide animal proteins as feed for farm animals, fishes, or as human food is quite often mentioned (see Rumpold and Schlueter 2013; Makkar et al. 2014; FAO 2015b). Today, about two billion inhabitants of the planet eat insects, but they are mostly gathered, not farmed. The significance of this protein input in the food balance is unknown, but assumed to be currently very small. Encouraged by FAO, insect farming is developing rapidly; the bugs can be cooked and eaten or lyophilized and used as a protein extract which is then incorporated in food or feed. The energy content of insects varies greatly (FAO 2012), in general from 90 to 200 kcal per 100 g of raw food, with extreme values for Australian ants (1272 kcal/100 g), Ivory Coast termites (535 kcal/100 g), or Mexican ants (404 kcal/100 g); for comparison, raw meat is on the order of 113–208 kcal/100 g. Is this the solution to the food problem? It may help, but it cannot be considered as a real breakthrough. Indeed, when insects are farmed, they must be fed with vegetal products or with animal or vegetal waste. But then they become competitors to other "transformers" of vegetal or waste into animal products: with 10 kg of vegetal matter, one can make 1 kg of beef, 3 kg of pork, 5 kg of chicken, and 7 kg of insects. By using insects, one only increases productivity by a factor of 1.4, at least with the current species. Many studies are furthermore required to evaluate the long-term health effects of such food.

Thus, the major conclusion of this survey is that additional food will most likely be produced by an increase in rain-fed agriculture, in those areas where land is still available: mostly South America and Africa and, to a lesser extent, Russia + CIS and OECD countries, while other regions such as Asia and WANA will not be able to be self-sufficient in food production. In conclusion, water is not likely to be the limiting factor in controlling

the current demographic growth of the planet; there will be enough land and water to produce the required food in normal years, but with:

- Enormous "*Virtual Water*" trade between continents, as Asia and North Africa will not be self-sufficient and must import food, essentially from South America; see for instance Dalin et al. (2012) who have estimated the current virtual water trade at 259 $km^3$/year in 1986 and at 567 $km^3$/year in 2007.
- Dramatic reduction in the biodiversity and of natural ecosystems all over the World, by a reduction in the "protected areas" on arable land, such as forests and grassland or bush land.

## 3 Climate Change

The above picture of the World in 2050 is already grim, but let us now look briefly at the prospects for the effects of climate change. The latest IPCC report (2014) shows that the effects of climate changes are fairly well predicted as far as the temperature is concerned, for any specified emission scenario, but that their hydrologic effects are still poorly predicted. Nevertheless, the current prediction is for a global increase in the total rainfall, the hydrologic cycle being accelerated, with a displacement towards the poles of the climate zones, which have been described above. In the Northern hemisphere, it will rain more, for example, in Northern Europe, less in Southern Europe and North Africa, as the Mediterranean climate zone will move North, and more in the tropical zone and in southern Sahara. The summer season in Southern Europe will be drier and the evaporation higher, requiring greater irrigation water supplies. The mountain glaciers will melt partly or totally (e.g., in the tropical Andes). The effects of temperature and $CO_2$ concentration changes on crop yields have been summarized by, for example, Agrimonde (2010) or Académie des Sciences (2011) but are not considered here in view of an expected impact ($\pm$5 to 20 %) much weaker than the uncertainties.

The major issue in the present discussion is whether climate changes will also affect the climate variability, i.e. the frequency or intensity of extreme events, droughts, or floods. This is still a controversial issue. The model results apparently do not show significant changes in the extreme-event frequency, unless a four times higher $CO_2$ concentration in the atmosphere is reached, which hopefully will never occur. At the very minimum, climatologists agree that if the mean of the rainfall distribution is shifted, the whole distribution curve will also be shifted, in the same direction. In other words, if the mean rainfall increases in one area, then the frequency of floods will increase and that of droughts will decrease (or, at the same frequencies, the magnitude of the floods will increase and that of the droughts will decrease), and vice versa if the mean rainfall decreases.

Whether the shape of the distribution of events will also be modified and not just shifted is debatable. When observations are considered, a record of about 40 years where a change in climate can be detected on the mean is very short for detecting changes in the frequencies of extreme events, but the latest IPCC report (2014) indicates that the variability of climate seems likely to increase. This would mean higher frequencies of extreme events, floods, or droughts.

In Table 5, it is assumed that, because of climate change, 110 million ha of arable land will be lost in the zones of Mediterranean latitudes, and 160 million ha will be gained in

the Northern latitudes because of the warming; moreover, 10 million ha would be lost because of sea-level rise, according to IPCC (2014).

## 4 Risk of Droughts

Disregarding climate changes, the Earth has always experienced great climate variability, depicted, for example, as the seven years of fat cows and lean cows in the Bible. Some archaeological studies conducted simultaneously in Greece and China seem to show that a severe drought occurred in these two countries around the year 400 AD (Cook 2013; Manning 2013), while other researchers suggest that a major climate change-induced drought may have driven the collapse of the once-flourishing Eastern Mediterranean civilizations towards the end of the thirteenth century BC, i.e. the late Bronze Age crisis (Kaniewski et al. 2013). It is likely that such events will occur again; the question is: will they severely affect food production and occur simultaneously on different continents? In 1998, following a strong El Niño event, there was a large deficit in grain production in China and Indonesia at the same time (Rojas et al. 2014; Lizumi et al. 2014). These two countries were able to import and distribute from the World stocks the required amount of grain, and no major adverse consequences were felt; the global food stock of cereals, of the order of 400–600 million tons, which is about 2–3 months of the current global consumption, falls to a very low point, but was sufficient. This stock has been decreasing regularly in the last 20 years, and, as a result, the cereal prices have greatly increased since 2006 with a peak in 2010 (the FAO food price index had doubled compared to 1990–2005). But since 2008, good harvests have brought down prices (in 2015, they are only about 30 % higher than for 1990–2005), and the cereal stocks are back to 630 million tons (March 5th, 2015) representing about 3 months of the World cereal consumption (FAO 2015a).

The current theory is that drought situations will occur in the future (Sheffield and Wood 2011), as they did before, even during the last six decades (Sheffield et al. 2012); droughts are even expected to increase in frequency and severity in the future as a result of climate change, mainly as a consequence of decreasing regional precipitation in some areas but also of increasing evapotranspiration driven by global warming (Dai 2013; Trenberth et al. 2014). However, it is assumed that these droughts will not occur at the same time on all continents and that a situation of drought here will be compensated by normal or good harvest elsewhere; therefore, no major food shortage should occur (FAO 2003, 2006).

This may be true most of the time. But a brief look at history may be of interest here. It is well known, for instance, that the major volcanic eruption on Krakatoa in 1883 had a Worldwide effect on temperature and rainfall (a global 5 % reduction in rainfall is often mentioned). In 2001, Davis published a historical analysis of the nineteenth century famines and reported on two severe drought episodes that occurred in 1876–1878 and 1896–1900, simultaneously affecting at least Brazil, China, India, and Ethiopia. Contrary to the general belief, in this case very serious droughts occurred at the same time in different places, on different continents; Davis (2001) relates these droughts to very strong El Niño events affecting the monsoon zones.

The consequences of the famines in the nineteenth century were very severe; Davis (2001) mentions, for each case, around 30 million deaths in China and India only, i.e. a total of 4 % of the World population at that time (around 1.5 billion in 1875). The Nobel Prize laureate in economy Armatyra Sen (Sen and Drèze 1999) analysed the same events

and determined that in most cases of drought, which he called "Food Availability Decline," the main cause of death and famines is not the lack of food, but rather the lack of economic resources of the poor farmers whose crops (their unique source of revenue) have been lost and who therefore can no longer afford to buy food at the inflated prices. He showed, for instance, that the same happened in Ethiopia in 1975, when a drought and agricultural disaster in one part of the country created a large famine and many deaths, while in other parts of the same country, food was available, and even the means of transporting it to the famine zone, which was situated along a major highway, but nothing was done.

In this context, it is interesting to look at observed frequencies of very strong El Niño events. Ortlieb (2000) tried to reconstruct, from historical archives in South America, the years of strong and very strong El Niño events from 1525 to 1950. In his list, 1876, 1878, and 1899 were indeed very strong El Niño years, as stated by Davis (2001), but, on average, such very strong El Niño events seem to occur about twice every century: they are indeed relatively rare.

In conclusion, what this brief survey shows is that once or twice per century, or perhaps more often if climate changes affect the El Niño variability (Cai et al. 2014), a major drought period lasting several years may affect simultaneously several continents, influencing the food production on a global scale (Vicente-Serrano et al. 2011). Stocks will probably not be sufficient to satisfy the demand, as the current level of stocks, which equals about 2–3 months of global consumption, would rapidly be used up, and its transportation to remote places would still be a problem. The international market prices of food would suddenly become very high, and "Food Availability Decline" would become a reality, generating famines of unknown magnitude. The poor countries or the poor rural communities affected by the droughts would be the first to suffer, but may not be the only ones.

There is no reason to assume that this cannot occur. What is, however, unknown is when: Next year? Ten years from now? The only means of preventing such a catastrophe would be to very significantly increase the World food stocks or water stocks. But where to put the food stocks? Near harbours for easy access and transportation? Who would pay?

## 5 Conflicts

Since at least the Neolithic Revolution, people have identified water as a commodity and source of economic power and have manipulated its flow (Mithen 2012). It is also well known that throughout the World's history, political and environmental mismanagement, associated with climatic causes, has had a catalytic effect on large-scale disasters, including the decline/demise of complex societies, such as, for example, the ancient Maya civilization (Demarest 2004). This Mayan decline is related to complex and intricate political and environmental reasons (Hodell et al. 1995; Turner and Sabloff 2012; Masson 2012), where successive dry periods were indeed the culprits (Kennett et al. 2012; Denommee et al. 2014). More recently, the Sudanese 60-year long war, which started in 1955, has also been linked to two long-lasting droughts (1967–1973 and 1980–2000) that have caused widespread population displacement during which thousands died of starvation (Welzer 2012). Similarly, in the ongoing Syrian crisis, water mismanagement and climatic conditions (Gleick 2014; Kelley et al. 2015) have played a role in the deterioration of Syria's economic conditions, magnifying religious and sociopolitical, even geopolitical, factors (Azmeh 2014).

Of course water conflicts are not only related to water scarcity. They may arise due to flooding, water-quality degradation, but, according to Wolf (1995), for the most part, they are indeed related to water deficits. As shown above, demographic growth is likely to generate water stresses, or rather, food deficits. Let us cite here two dramatic examples, Easter Island and Rwanda, as described by Diamond (2005).

1. Easter Island was discovered in 1722 (at Easter) by the Dutch navigator Jakob Roggeveen. He found a civilization that was totally isolated, devastated, and whose members thought that they were alone on Earth, in the middle of a big ocean. From the fifteenth to the seventeenth century, the inhabitants had destroyed their environment by cutting down all the trees on the island, only to use them as rollers to move the huge stone statues, the Moaï, which served as emblems of power and nobility to the priests and leaders. The soil erosion and loss of fertility that resulted made it impossible to feed a population estimated to have been in the range of 3000–30,000 individuals. In 1680, approximately, an uprising against the priests and leaders occurred, with massacres and cannibalism, reducing the population to about 30 % of its initial numbers. Food deficit can indeed generate large conflicts.
2. The second example, Rwanda, is more controversial. In 1994, genocide occurred in Rwanda (see http://en.wikipedia.org/wiki/Rwandan_Genocide), where 500,000–800,000 people (about 11–20 % of the population) were killed with machetes over a period of 100 days (from 6 April 1994 to 16 July 1994). The usual explanation is that two local tribes, the Hutus and the Tutsis, went to war for political reasons, the Hutus (usually labourers), 85 % of the population, having been kept as "second-rate" citizens inferior to the Tutsis (more frequently landowners), who considered themselves the rulers, following the European colonists who selected this group to be both privileged and educated. This situation exacerbated the tendency of the few to oppress the many, creating a legacy of hatred, resentment and tension that exploded into violence many times before and after the Hutu revolution (1959) and the independence (1962), henceforth reaching its climax in 1994.

But Diamond (2005) claims that the reality is quite different. He maintains that demographic growth had been about 3 % per year since the 1960s. In 1994, all arable land was exploited, the population density was 760 inhabitants per $km^2$, as high as in England, and the food production, given the local agricultural practices, was insufficient to meet the needs. In 1985, the agricultural production per capita, after a continuous increase from 1966 to 1981, was back to the level of 1960. For Diamond, this food deficit was the cause of the genocide; as evidence, he states that in areas where there were few or no Tutsis, the Hutus killed Hutus. Of course there was an existing tribal rivalry, which was involved in the triggering of the genocide, but the real underlying cause was a food deficit. This hypothesis is confirmed by a booklet published before the genocide by Belgian agronomists (Wils et al. 1986), who said that a major food deficit crisis was bound to occur, but nothing had been done to prevent it. In Rwanda, the food deficit was not a water deficit, the country is very humid and does not lack water, and it was an arable land deficit. But the consequences are similar: food deficits can results in major conflicts.

Does climate variability (and water scarcity) play an important part in conflicts/violence, or is it expressing a modern form of environmental determinism? This is an ongoing debate (see, for example Rahaman 2012; Hsiang and Burke 2014; Cane et al. 2014; Raleigh et al. 2014; Nordas and Gleditsch 2015; Buhaug 2015). Note that Wolf et al. at Oregon State University (see Wolf 1995; Subramanian et al. 2012; Kramer et al. 2013) have studied all the past water conflicts in the World and developed a data base: the

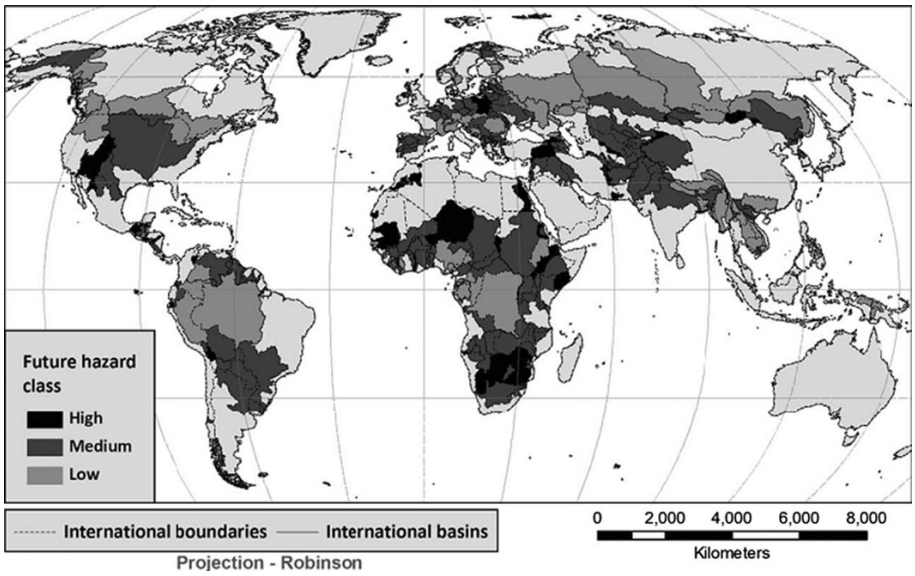


**Fig. 4** Potential water-related conflicts in 2050, with the intensity scale (high, medium, low); from De Stefano et al. (2012)

Transboundary Freshwater Dispute Database (TFDD 2015) where all the disputes, conflicts, and settlements have been documented. A map of the current 888 "hot spots" on the planet has been produced, see Wolf (2014). Based on the TFDD, De Stefano et al. (2012) have developed a map of potential future conflicts in the World in 2050 (Fig. 4). More than half of the basins at high risk are in Africa (Congo, Niger, Lake Chad), but other basins at risk exist in the Catatumbo Basin between Columbia and Venezuela, in the Middle East, and in Eastern Europe, etc.

## 6 Conclusions

As predicted by the UN in 2012, the World population growth will put the planet under intense pressure to produce what will be needed to feed this population, with little place left for producing, at the same time, second-generation biofuels, and thus to solve the energy challenge. Contrary to current beliefs, water will not be the limiting factor of food production at the global scale: there is plenty of water on Earth, mostly through the water cycle, and in some places through the groundwater stocks. The major source of water to be used for food production is *Green Water*, i.e. rainwater infiltrated into the upper soil and available to the vegetation for evapotranspiration. The real limiting factor for food production is the availability of agricultural soils that can be farmed (excluding food grown artificially without soil, due to its very high costs).

The availability of water and soil is very unequally distributed on Earth, compared to the distribution of the population. In other words, in many places on Earth, the population growth will exceed the capacity of the countries to produce the food they need, as is already the case in some countries. The forecast for 2050 is that Asia (the continent as a whole) will not be able to feed itself due to a lack of arable land, and West Asia–North

Africa even less so, due to a lack of water. Sub-Saharan Africa could have enough water and soils to feed itself, but if, and only if, intensive agricultural development takes place, mostly by increasing rain-fed agriculture and its yields and developing irrigation. The food deficit in Asia and WANA (and in SS-Africa if the required development is not sufficient) will have to come from the three remaining zones: OECD countries, which need to increase their production (through irrigation, yield increase, and new land farming), Russia and the CIS countries (mostly through yield increases), and lastly South America (through deforestation); all three zones will have to export "virtual water" to the countries with a food deficit. Sea transport of food is cheap and does not significantly harm the environment. In places where soils and water are available, but not in the same place (e.g., China and India), increasing irrigation by long-distance water transfers will be necessary to reduce the need for "virtual water" transfers.

For the countries that will need to import food, the real problem is to generate, by exports, the income required to pay for this import. It can be raw materials, e.g., minerals and oil or electric energy produced in arid zones, or industrial products, or services including tourism. It may happen that a country with water stress will be better off using the little water it has to produce goods or services rather than food, both in terms of economic and employment balance.

For countries with both arable land and water, which are obliged to increase their food production, two options are available: building dams and irrigation systems, or increasing the area of rain-fed agriculture, by deforestation. Both options have very negative consequences for the environment, the loss of natural ecosystems and biodiversity. Each situation may be different, and the two options need to be compared in each individual case, but irrigation is very efficient in reducing the surface area of land that needs to be farmed, since, on a global average, one hectare of irrigated land produces three times more food than one hectare of rain-fed land. But have we developed the tools and methodologies to compare the negative effects on the environment of each option and to develop the best mitigation strategies to minimize these effects?

However, the World can sometimes experience very severe food deficits, both spatially and temporally, when the rains fail. In such situations, we have seen that tragic conflicts or genocide can happen. The monsoon zone seems to be the most fragile in that respect, with historical famines which had extremely severe death tolls, e.g., in the nineteenth century, most likely linked to very strong El Niño events, lasting several years. Very intense volcanic eruptions can also have drastic effects on rainfall, temperature, and global food production. The World is not protected against such food deficits, even if the last large famines occurred more than 100 years ago. The only way to protect the World population against such events is to create stocks. However, economists do not favour food stocks, because of their costs, or consider them only as regulators of market prices. On 6 March 2015, China indicated, however, that it would increase by 33 % its budget for agricultural stocks, up to 24 billion dollars, or from 200 million tons to 250 (these are estimates, the exact numbers are state secrets). This seems to be a very wise decision, and other countries should follow that route. But, as hydrologists, we can offer an alternative: create water stocks. See, for instance, the immense social benefits that Egypt enjoyed with the construction of the Aswan dam: several episodes of droughts (and of floods) were prevented thanks to the dam, even if its environmental consequences were severe. No Egyptian would deny that. But how can we store water? We can build more dams, of course; the current volume of water stored in dams is about 8500 $km^3$ (Chao et al. 2008), and it could be increased, notwithstanding their environmental consequences.

But there is a better alternative: storing water underground in aquifers. The volume of water naturally stored in aquifers is huge: 15 million km$^3$. There is room for water storage in aquifers equal to 600,000 times the current amount of water stored in dams! Artificial recharge of aquifers has been tested in many places (see, for example, Dillon et al. 2009) and can be implemented relatively easily. In drought-prone areas, the aquifers should be recharged artificially in order to store water for "bad times," instead of being depleted as is currently the case. In areas where the aquifers are brackish, it is possible to inject fresh-water and create "lenses" of fresh water within the brackish aquifer, where mixing would occur only at the interfaces.

This should be the major task of the next generation of hydrologists: take good-quality surface water from rivers, when there is plenty, treat it, and store it underground (where it does not evaporate) in aquifers, to provide water and food in case of drought. Tools such as GRACE can be an efficient way to monitor the global amount of water stored on Earth.

**Acknowledgments** The authors wish to thank the two reviewers, Prof. M. Besbes and one anonymous colleague, for their help in correcting and improving this article; they also wish to express their gratitude to the Guest Editor of this issue, Dr. Anny Cazenave, for her invitation to prepare this paper together and for organizing the reviewing and final editing of this work.

## References

Académie des Sciences (2006) Les Eaux Continentales, coordinated by Marsily G de. EDP Sciences; Paris

Académie des Sciences (2011) Démographie, Climat et Alimentation Mondiale, coordinated by Leridon H and Marsily G de. EDP Sciences: Paris

Agrimonde (2010) Scénarios et défis pour nourrir le monde en 2050. Coordinated by Paillard S, Treyer S, Dorin B. Quae: Versailles

Allan JA (1998) Moving water to satisfy uneven global needs. Trading water as an alternative to engineering it. ICID J 47(2):1–8

Azmeh S (2014), The uprising of the marginalised: a socio-economic perspective of the syrian uprising. LSE Middle East Centre Paper Series 06, p 28, http://eprints.lse.ac.uk/60243/

Baraer M, Mark B, McKenzie J, Condom T, Bury J, Huh K, Portocarrero C, Gomez J, Rathay S (2012) Glacier recession and water resources in Peru's Cordillera Blanca. J Glaciol 58(207):134–150

Besbes M, Chahed J, Hamdane A, Marsily G de (2009) Water resources assessment and food production in arid zones : the example of Tunisia with a global change context. In: Courel MF, Schneider-Madanes G (eds) Water ecosystems and sustainable development in arid and semi-arid zones. Springer, Berlin

Besbes M, Chahed J, Hamdane A (2014) Sécurité Hydrique de la Tunisie, gérer l'eau en conditions de pénurie. L'Harmattan, Paris

Bradley R, Vuille M, Diaz H, Vergara W (2006) Threats to water supplies in the tropical andes. Science 312:1755–1756

Buhaug H (2015) Climate–conflict research: some reflections on the way forward. WIREs Clim Change. doi:10.1002/wcc.336

Cai W, Borlace S, Lengaigne M, Rensch PV, Collins M, Vecchi G, Timmermann A, Santoso A, McPhaden MJ, Wu L, England MH, Wang G, Guilyardi E, Jin FF (2014) Increasing frequency of extreme El Niño events due to greenhouse warming. Nat Clim Change 4(2):111–116. doi:10.1038/nclimate2100

Cane MA, Miguel E, Burke M, Hsiang SM, Lobell DB, Meng KC, Satyanath S (2014) Temperature and violence. Nat Clim Change 4:234–235. doi:10.1038/nclimate2171

Chahed J, Hamdane A, Besbes M (2008) A comprehensive water balance of Tunisia : blue water, green water and virtual water. Water Int 33:4

Chao BF, Wu YH, Li YS (2008) Impact of artificial reservoir water impoundment on global sea level. Sciencexpress 1–3www.sciencexpress.org. doi:10.1126/science.1154580

Chevallier P, Pouyaud B, Suarez W, Condom T (2011) Climate change threats to environment in the tropical Andes: glaciers and water resources. Suppl Reg Environ Change 11(1):179–187

Cook ER (2013) Megadroughts, ENSO, and the Invasion of Late-Roman Europe by the Huns and Avars, In: Harris WV (ed) The Ancient Mediterranean Environment between Sciences and History. Leiden-Boston, Brill, pp 103–170. ISBN: 978-90-04-25343-8

Dai A (2013) Increasing drought under global warming in observations and models. Nat Clim Change 3:52–58. doi:10.1038/nclimate1633
Dalin C, Konar M, Hanasaki N, Rinaldo A, Rodriguez-Iturbe I (2012) Evolution of the global virtual water trade network. Proc Nat Acad Sci PNAS 109(16). www.pnas.org/cgi/doi/10.1073/pnas.1203176109
Davies BJ, Glasser NF (2012) Accelerating recession in Patagonian glaciers from the "Little Ice Age" (c. A.D. 1870) to 2011. J Glaciol 58(212):1063–1084
Davis M (2001) Late Victorian Holocausts, El Niño Famines and the Making of the Third World, Verso, London. ISBN: 1-85984-739-0
De Stefano L, Duncan J, Dinar S, Stahl K, Strzepek K, Wolf AT (2012) Climate change and the institutional resilience of international river basins. J Peace Res 49(1):193–209
Demarest A (2004) Ancient Maya. The rise and fall of a Rainforest Civilization. Cambridge University Press. ISBN-13_: 9780521592246
Denommee KC, Bentley SJ, Droxler AW (2014) Climatic controls on hurricane patterns: a 1200-y near-annual record from Lighthouse Reef, Belize. Nat Sci Rep 4:3876. doi:10.1038/srep03876
Diamond J (2005) Collapse. How societies choose to fail or succeed. Viking Penguins, New-York. ISBN-13: 978-0670033379
Diaz HF, Bradley RS, Ning L (2014) Climatic changes in mountain regions of the American Cordillera and the Tropics: historical changes and future outlook. Arct Antarct Alp Res 46(4):1–9
Dillon P, Gale I, Contreras S, Pavelic P, Evans R, Ward (2009) Managing aquifer recharge and discharge to sustain irrigation livelihoods under water scarcity and climate change. In: Blöschl G, van de Giesen N, Muralidharan D, Ren L, Seyler F, Sharma U, Vrba J (eds) Improving integrated surface and groundwater resources management in a vulnerable and changing world. IAHS Publishers, 330, IAHS, Wallingford, pp 1–12
Döll P, Müller Schmied H, Schuh C, Portman FT, Eicker A (2014) Global-scale assessment of groundwater depletion and related groundwater abstractions: combining hydrological modeling with information from well observations and GRACE satellites. Water Resour Res. doi:10.1002/2014WR015595
Döll P, Douville H, Güntner A, Müller Schmied H, Wada Y (2015) Modelling the continental water cycle: challenges and prospects. Remote Sensing and Water Resources. In: ISSI Workshop. To appear, Survey in Geophysics, this volume
FAO Food and Agriculture Organization (2002) World agriculture: towards 2030–2050. FAO, Rome. http://www.fao.org/docrep/004/Y3557E/y3557e00.HTM
FAO Food and Agriculture Organization (2003) World agriculture : towards 2015–2030. FAO, Rome http://www.fao.org/fileadmin/user_upload/esag/docs/y4252e.pdf
FAO Food and Agriculture Organization (2006) World agriculture: towards 2030–2050 (Interim report). FAO, Rome. ftp://fao.org/docrep/fao/009/a0607e/a0607e00.pdf
FAO Food and Agricultural Organization (2012) Energy-smart food at FAO; an overview. http://www.fao.org/3/a-an913e.pdf
FAO Food and Agricultural Organization (2014) Hunger map. http://www.fao.org/fileadmin/templates/ess/foodsecurity/poster_web_001_WFS.jpg
FAO Food and Agricultural Organzation (2015a) World food situation, cereals supply and demand brief. http://www.fao.org/worldfoodsituation/csdb/en/
FAO Food and Agricultural Organization (2015b) The contribution of insects to food security, livelihood and the environment. http://www.fao.org/forestry/edibleinsects/en/
Gerland P, Raftery AE, Ševčíková H, Li N, Gu D, Spoorenberg T, Alkema L, Fosdick BK, Chunn J, Lalic N, Bay G, Buettner T, Heilig GK, Wilmoth J (2014) World population stabilization unlikely this century. Science 346:234–237. doi:10.1126/science.1257469
Gleick PH (2014) Water, drought, climate change, and conflict in Syria. Weather Clim Soc 6:331–340. doi:10.1175/WCAS-D-13-00059.1
Griffon M (2006) Nourrir la planète. Odile Jacob, Paris
Hodell DA, Curtis JH, Brenner M (1995) Possible role of climate in the collapse of Classic maya civilization. Nature 375:391–394. doi:10.1038/375391a0
Hoekstra AY, Mekonnen MM (2012) The water footprint of humanity. PNAS 109:3232–3237. doi:10.1073/pnas.1109936109
Hoekstra AY, Chapagain AK, Aldaya MM, Mekonnen MM (2011) The water footprint assessment manual: setting the global standard. Earthscan: London. ISBN: 978-1-84971-279-8
Holdridge LR (1967) Life zone ecology. Tropical Science Center, San José (Costa Rica), p 206
Hsiang SM, Burke M (2014) Climate, conflict, and social stability: What does the evidence say? Clim Change 123:39–55. doi:10.1007/s10584-013-0868-3
IPCC (2014) Fifth assessment report. Intergovernmental panel on climate change. Geneva

IWMI (2007) Water for food, water for life : the comprehensive assessment of water management in agriculture. Molden D (ed) International water management institute. Colombo; Sri Lanka. Earthscan: London

Kaniewski D, Van Campo E, Guiot J, Le Burel S, Otto T, et al (2013) Environmental roots of the late bronze age crisis. PLoS One. 8(8):e71004. doi: 10.1371/journal.pone.0071004

Kelley CP, Mohtadi S, Cane MK, Seager R, Kushnir Y (2015) Climate change in the Fertile Crescent and implications of the recent Syrian drought. PNAS. doi:10.1073/pnas.1421533112

Kennett DJ, Breitenbach SFM, Aquino VV, Asmerom Y et al (2012) Development and disintegration of maya political systems in response to climate change. Science 338(6108):788–791. doi:10.1126/science.1226299

Konikow LF (2011) Contribution of global groundwater depletion since 1900 to sea-level rise. Geophys Res Lett 38:17. doi:10.1029/2011GL048604

Kramer A, Wolf AT, Carius A, Dabeklo GD (2013) The key to managing conflict and cooperation over water. World Sci 11(1):4–12

Leemans R (1992) Global holdridge life zone classifications. In: Global Ecosystems Database Version 2.0, NOAA National Geophysical Data Center, Boulder, CO, USA

Lizumi T, Luo J, Challinor A, Sakurai G, Yokozawa M, Sakuma H, Brown M, Yamagata T (2014) Impacts of El Niño southern oscillation on the global yields of major crops. Nat Commun 5:3712. doi:10.1038/ncomms4712

Makkar HPS, Tran G, Henze V et al (2014) State-of-the-art on use of insects as animal feed. Anim Feed Sci Technol 197:1–33

Manning SW (2013) The Roman world and climate: context, relevance of climate change, and some issues. In: Harris WV (ed) The Ancient Mediterranean environment between sciences and history. pp 103–170. Leiden-Boston: Brill. ISBN: 978-90-04-25343-8

Marsily G de (2007) An overview of the world's water resources problems in 2050. Ecohydrol Hydrobiol 7(2):147–155

Marsily G de (2009) L'eau, un trésor en partage. Dunod, Paris

Masson MA (2012) Maya collapse cycles. PNAS 109(45):18237–18238. doi:10.1073/pnas.1213638109

Millennium Ecosystem Assessment (2005) Ecosystems and human well-being: synthesis. Island Press: Washington. ISBN: 1-59726-040-1

Mithen SJ (2012) Thirst: water and power in the ancient world. Weidenfeld & Nicolson: London. ISBN: 978-0-674-06693-6

Moya Quiroga V, Mano A, Asaoka Y, Udo K, Kure S, Mendoza J (2014) Estimation of glacier melt water contribution for human consumption in the royal andes considering temperature measurement errors. Open J Mod Hydrol 2014(4):27–43

Musy A, Higy C (2010) Hydrology: a science of nature. CRC Press: Boca Raton. ISBN: 9781578087099 - CAT# N10334

Nicholson L, Marin J, Lopez D, Rabatel A, Brown F, Rivera A (2009) Glacier inventory of the upper Huasco valley, Norte Chico, Chile: glacier characteristics, glacier change and comparison with central Chile. Ann Glaciol 50(53):111–118

Nordas R, Gleditsch NP (2015) Climate change and conflict. In: Hartard S, Lieber W (eds) Competition and conflicts on resource use. Natural Resources Management and Policy, 46, pp 21–38. doi:10.1007/978-3-319-10954-1_3

Ortlieb L (2000) The documented historical period of El Niño events in Peru: an update of the Quinn record (16th to 19th centuries). In: Diaz HF, Markgraf V (eds) El Niño and the southern oscillation. Multiscale variability and local and regional impacts. Cambridge University Press, Cambridge, pp 207–295

Post VEA, Groen J, Kooi H, Person M, Ge S, Edmunds WM (2013) Offshore fresh groundwater reserves as a global phenomenon. Nature 504(5):12. doi:10.1038/nature12858

Rabatel A, Francou B, Soruco A, Gomez J, Caceres B et al (2013) Current state of glaciers in the tropical Andes: a multi-century perspective on glacier evolution and climate change. The Cryosphere 7(1):81–102

Rahaman MM (2012) Water wars in 21st century: speculation or Reality? Int J Sustain Soc 4:3–10

Raleigh C, Linke A, O'Loughlin J (2014) Extreme temperatures and violence. Nat Clim Change 4:76–77

Ramirez E, Olmos C, Romàn J (2007) Deshielo de la cuenca Tuni Condoriri y su impacto sobre los recursos hídricos de las ciudades de La Paz y El Alto. Quinquenal P (ed) La Paz: GRANT—GREAT ICE, IHH-IRD

Renault D, Wallender WW (2000) Nutritional water productivity and diets: from crop per drop towards nutrition per drop. Agric Water Manag 45:275–296

Rijsberman FR (2006) Water scarcity: Fact or fiction? Agric Water Manag 80(1–3):5–22

Rockström J (2004) Magnitude of the hunger alleviation challenge—implications for consumptive use. Stockholm International Water Institute, Balancing food and environmental security. Finding opportunities for improving livelihoods, Stockholm
Rojas O, Li Y, Cumani R (2014) Understanding the drought impact of El Niño on the global agricultural areas: an assessment using FAO's Agricultural Stress Index (ASI), FAO, Climate, energy and tenure division (nRc) publications. ISBN: 978-92-5-108671-1, ISSN 2071-0992
Rumpold BA, Schlueter OK (2013) Nutritional composition and safety aspects of edible insects. Mol Nutr Food Res 57:141–160
Sen A, Drèze J (1999) Omnibus. Oxford University Press: New Delhi. ISBN: -13:978-0195648317
Sheffield J, Wood EF (2011) Drought: past problems and future scenarios. Earthscan: UK. ISBN: -13: 978-1849710824
Sheffield J, Wood EF, Roderick ML (2012) Little change in global drought over the past 60 years. Nature 491:435–438. doi:10.1038/nature11575
Shelton LM (2009) Hydroclimatology: perspectives and applications. Cambridge University Press, Cambridge, p 418
Shiklomanov IA (1999) World freshwater resources and their Use. Database on CD Rom. UNESCO, Paris
Shiklomanov IA, Rodda JC (2003) World water resources at the beginning of the twenty-first century. Cambridge University Press, Cambridge
SIWI (2008) Stockholm International Water Institute. Saving water: from field to fork. Cutting losses and wastage in the food chain. Stockholm
Soruco A (2012) Medio siglo de fluctuaciones glaciares en la Cordillera Real, y su efectos hidrológicos en la ciudad de La Paz. IRD, La Paz. ISBN: 978-99954-55-62-. pp 228
Subramanian A, Brown B, Wolf A (2012) Reaching across the waters: facing the risks of cooperation in international waters. The World Bank Press, Washington DC
Tardieu F (2005) Plant tolerance to water deficit: physical limits and possibilities for progress. Académie des Sciences, Comptes Rendus Geoscience, n 337:57–67
TFDD (2015) Transboundary freshwater dispute database, international freshwater treaty database. Oregon State University. http://www.transboundarywaters.orst.edu/database/interfreshtreatdata.html
Trenberth KE, Smith L, Qian T, Dai A, Fasulo J (2007) Estimates of the global water budget and its annual cycle using observational and model data. J Hydrometeorol Special Section 8:758–769
Trenberth KE, Dai A, van der Schrier G, Jones PD, Barichivich J, Briffa KR, Sheffield J (2014) Global warming and changes in drought. Nat Clim Change 4:17–22
Turner BL, Sabloff JA (2012), Classic period collapse of the Central Maya Lowlands: insights about human–environment relationships for sustainability. Proc Natl Acad Sci USA 109(35): 13908–13914. doi:10.1073/pnas.1210106109
Vicente-Serrano SM, López-Moreno JI, Gimeno L, Nieto R, Morán-Tejeda E, Lorenzo-Lacruz J, Beguería S, Azorin-Molina C (2011) A multiscalar global evaluation of the impact of ENSO on droughts. J Geophys Res 116:D20109. doi:10.1029/2011JD016039
Viviroli D, Dürr HH, Meybeck M, Weingartner R, Messerli B (2007) Mountains of the world—water towers for humanity: typology, mapping and global significance. Water Resour Res 43:W07447. doi:10.1029/2006WR005663
Vuille M (2013) Climate change and water resources in the tropical Andes. Interamerican Development Bank Technical Note, No. IDB-TN-515
Vuille M, Francou B, Wagnon P, Irmgard J, Kaser G, Mark B, Bradley R (2008) Climate change and tropical Andean glaciers: past, present and future. Earth-Sci Rev 89:79–96
Wada Y, Van Beek LPH, Bierkens MFP (2012) Non-sustainable groundwater sustaining irrigation : a global assessment. Water Resour Res. doi:10.1029/2011WR010562
Welzer H (2012) Climate Wars: what people will be killed for in the 21st century. Wiley. ISBN: 978-0-7456-5145-3
Willis M, Melkonian A, Pritchard M, Rivera A (2012) Ice loss from the Southern Patagonian Ice Field, South America, between 2000 and 2012. Geophys Res Lett. doi:10.1029/2012GL053136
Wils W, Carael M, Tondeur G (1986) Le Kivu Montagneux: surpopulation, sous-nutrition, érosion du sol. Mem. Acad. Royale Sc.Outremer Belgique, tome 21,fasc.no 3
Wolf A (1995) Hydropolitics along the Jordan River: the impact of scarce water resources on the Arab–Israeli conflict. United Nations University Press, New York, Paris, p 283
Wolf A (2014) Where will the world's water conflicts erupt? A heatmap of war over water. Peek K (ed). Popular Science, Posted June 13, 2014. http://www.popsci.com/article/science/where-will-worlds-water-conflicts-erupt-infographic

WWAP(2012) United Nations Educational, Scientific and Cultural Organization (UNESCO), United Nations World Water Assessment Programme (WWAP), UN-Water. March 2012; see also World Resources Institute http://www.wri.org/resource/physical-and-economic-water-scarcity

WWDR (2012) Managing Water under Uncertainty and Risk, in 4th edition of the UN World Water Development Report (WWDR4), World Water Assessment Programme (WWAP)

Zimmer D (2013) L'empreinte eau. Les faces cachées d'une ressource vitale. Charles Léopold Meyer, Paris